INSIGHTS IN PLANT PHYSIOLOGY: 2021

EDITED BY: Anna N. Stepanova

PUBLISHED IN: Frontiers in Plant Science

frontiers Research Topics

frontiers

ISSN 1664-8714
ISBN 978-2-83250-277-8
DOI 10.3389/978-2-83250-277-8

About Frontiers

Frontiers is more than just an open-access publisher of scholarly articles: it is a pioneering approach to the world of academia, radically improving the way scholarly research is managed. The grand vision of Frontiers is a world where all people have an equal opportunity to seek, share and generate knowledge. Frontiers provides immediate and permanent online open access to all its publications, but this alone is not enough to realize our grand goals.

Frontiers Journal Series

The Frontiers Journal Series is a multi-tier and interdisciplinary set of open-access, online journals, promising a paradigm shift from the current review, selection and dissemination processes in academic publishing. All Frontiers journals are driven by researchers for researchers; therefore, they constitute a service to the scholarly community. At the same time, the Frontiers Journal Series operates on a revolutionary invention, the tiered publishing system, initially addressing specific communities of scholars, and gradually climbing up to broader public understanding, thus serving the interests of the lay society, too.

Dedication to Quality

Each Frontiers article is a landmark of the highest quality, thanks to genuinely collaborative interactions between authors and review editors, who include some of the world's best academicians. Research must be certified by peers before entering a stream of knowledge that may eventually reach the public - and shape society; therefore, Frontiers only applies the most rigorous and unbiased reviews.
Frontiers revolutionizes research publishing by freely delivering the most outstanding research, evaluated with no bias from both the academic and social point of view. By applying the most advanced information technologies, Frontiers is catapulting scholarly publishing into a new generation.

What are Frontiers Research Topics?

Frontiers Research Topics are very popular trademarks of the Frontiers Journals Series: they are collections of at least ten articles, all centered on a particular subject. With their unique mix of varied contributions from Original Research to Review Articles, Frontiers Research Topics unify the most influential researchers, the latest key findings and historical advances in a hot research area! Find out more on how to host your own Frontiers Research Topic or contribute to one as an author by contacting the Frontiers Editorial Office: frontiersin.org/about/contact

INSIGHTS IN PLANT PHYSIOLOGY: 2021

Topic Editor:
Anna N. Stepanova, North Carolina State University, United States

Citation: Stepanova, A. N., ed. (2022). Insights in Plant Physiology: 2021. Lausanne: Frontiers Media SA. doi: 10.3389/978-2-83250-277-8

Table of Contents

frontiers | Frontiers in Plant Science

ORIGINAL RESEARCH
published: 19 April 2022
doi: 10.3389/fpls.2022.858519

Empirical Evaluation of Inflorescences' Morphological Attributes for Yield Optimization of Medicinal Cannabis Cultivars

Erez Naim-Feil[1,2], Edmond J. Breen[1], Luke W. Pembleton[1], Laura E. Spooner[1], German C. Spangenberg[1,2] and Noel O. I. Cogan[1,2]*

[1] Agriculture Victoria, AgriBio, Centre for AgriBioscience, Melbourne, VIC, Australia, [2] School of Applied Systems Biology, La Trobe University, Melbourne, VIC, Australia

In recent decades with the reacknowledgment of the medicinal properties of *Cannabis sativa* L. (cannabis) plants, there is an increased demand for high performing cultivars that can deliver quality products for various applications. However, scientific knowledge that can facilitate the generation of advanced cannabis cultivars is scarce. In order to improve cannabis breeding and optimize cultivation techniques, the current study aimed to examine the morphological attributes of cannabis inflorescences using novel image analysis practices. The investigated plant population comprises 478 plants ascribed to 119 genotypes of high−THC or blended THC−CBD ratio that was cultivated under a controlled environment facility. Following harvest, all plants were manually processed and an image of the trimmed and refined inflorescences extracted from each plant was captured. Image analysis was then performed using in-house custom-made software which extracted 8 morphological features (such as size, shape and perimeter) for each of the 127,000 extracted inflorescences. Our findings suggest that environmental factors play an important role in the determination of inflorescences' morphology. Therefore, further studies that focus on genotype X environment interactions are required in order to generate inflorescences with desired characteristics. An examination of the intra-plant inflorescences weight distribution revealed that processing 75% of the plant's largest inflorescences will gain 90% of its overall yield weight. Therefore, for the optimization of post-harvest tasks, it is suggested to evaluate if the benefits from extracting and processing the plant's smaller inflorescences outweigh its operational costs. To advance selection efficacy for breeding purposes, a prediction equation for forecasting the plant's production biomass through width measurements of specific inflorescences, formed under the current experimental methodology, was generated. Thus, it is anticipated that findings from the current study will contribute to the field of medicinal cannabis by improving targeted breeding programs, advancing crop productivity and enhancing the efficacy of post-harvest procedures.

Keywords: breeding, plant productivity, heritability, selection, image analysis, production

OPEN ACCESS

Edited by:
Andrea Mastinu,
University of Brescia, Italy

Reviewed by:
Nirit Bernstein,
Agricultural Research Organization (ARO), Israel
Youbin Zheng,
University of Guelph, Canada

****Correspondence:***
Erez Naim-Feil
erez.naim-feil@agriculture.vic.gov.au

Specialty section:
This article was submitted to Plant Physiology, a section of the journal Frontiers in Plant Science

Received: *20 January 2022*
Accepted: *21 March 2022*
Published: *19 April 2022*

Citation:
Naim-Feil E, Breen EJ, Pembleton LW, Spooner LE, Spangenberg GC and Cogan NOI (2022) Empirical Evaluation of Inflorescences' Morphological Attributes for Yield Optimization of Medicinal Cannabis Cultivars. Front. Plant Sci. 13:858519. doi: 10.3389/fpls.2022.858519

INTRODUCTION

For millennia, *Cannabis sativa* L. (cannabis) has been utilized by mankind as a multipurpose source for fiber and oil-seed products, as hemp, and for ritual, recreational and medicinal applications as cannabis (Abel, 1980; Small et al., 2003; Small, 2017a). The utilization of cannabis for medicinal purposes is well-documented since ancient times (Zuardi, 2006; Russo, 2014) but its breakthrough into the modern pharmacopoeia occurred only during the 19th century, when western physicians recognized its therapeutic potential (Mikuriya, 1969; Small, 2017a). However, due to advances in medicinal technology and alternative medication during the first half of the 20th century, the popularity of cannabis dwindled (Mikuriya, 1969; Hand et al., 2016; Small, 2017a) but concurrently, its recreational consumption became more prevalent (Hand et al., 2016). Over this period, international prohibition of cannabis and cannabis trafficking was initiated, labeling the cannabis plant and its products as narcotics (Erkelens and Hazekamp, 2014; Pain, 2015; Pisanti and Bifulco, 2017). As a result, scientific research on cannabis almost completely ceased (Sobo, 2017) and its medical use was diminished significantly (Mikuriya, 1969; Small, 2017a) whilst its illegal recreational use was widespread (Zuardi, 2006). In order to meet the illegal market demands, cannabis growers had to implement its cultivation under clandestine locations which necessitated plant adaptations to suboptimal growth conditions (Small, 2017a). These adaptations were successfully implemented through unofficial breeding initiatives (Clarke and Merlin, 2013; Barcaccia et al., 2020) and cannabis has become one of the most extensive and fast-growing illicit drug distributed and consumed worldwide (Hall and Degenhardt, 2007). Hence, while other commercial crops were being scientifically evaluated and improved (Godfray et al., 2010), cannabis, due to its illicit status, was not examined by advanced and contemporary scientific tools and therefore, its breeding potential is currently still in its infancy (Chouvy, 2019).

Since the turn of the century, the potential of medicinal cannabis has been scientifically reacknowledged through a large number of studies (Nahtigal et al., 2016). These have suggested that cannabis-based remedies can alleviate and treat a wide range of medical disorders (Cascio et al., 2017) such as nausea (Parker et al., 2002), psychotic symptoms of schizophrenia (Leweke et al., 2012), pediatric epilepsy (Goldstein, 2015) and pain (Baron, 2018). The pharmaceutical properties of cannabis are generally ascribed to the plant's secondary metabolites and especially to the phytocannabinoids (cannabinoids) (Jin et al., 2020). To date, 120 different cannabinoids have been scientifically identified (ElSohly et al., 2017; Radwan et al., 2017) amongst them, Δ9-tetrahydrocannabinol (THC) and cannabidiol (CBD) are the most abundant, well-known and extensively studied due to their broad medicinal attributes (Cascio et al., 2017; Chandra et al., 2020). Cannabinoids can be found across most tissues of both male and female cannabis plants (Tanaka and Shoyama, 1999; Raman et al., 2017) but the most profuse cannabinoid concentration is found over inflorescences' trichomes of pistillate plants (Potter, 2013; Thomas and ElSohly, 2015). The ovary of each floret that forms the inflorescence is surrounded by transparent perianth and green bracts which are considered to be the location of the most abundant trichome coverage within the cannabis plant (Hammond and Mahlberg, 1977). Due to the high cannabinoid concentration found over the plant's inflorescences, they are utilized as the main commercial product of the medicinal cannabis industry (Radwan et al., 2017; Hawley et al., 2018). Morphologically, cannabis florets develop close to the plant's stem in a sessile or subsessile structure and near to shoot apex, they aggregate together to form a continuous and congested inflorescence (Small, 2015; Raman et al., 2017).

Scientific research has targeted cannabis inflorescences and largely focused on microscopic aspects of the distribution, formation, structure and morphogenesis of trichomes (Hammond and Mahlberg, 1973; Dayanandan and Kaufman, 1976; Ebersbach et al., 2018; Livingston et al., 2020) as well as the biosynthesis pathways of secondary metabolites (Flores-sanchez and Verpoorte, 2008; Andre et al., 2016). However, in the last decade, the expanding market of medicinal cannabis has become a valuable industry that primarily relies on the cultivation and production of cannabis plant material (Small, 2017a; Summers, 2018; Parker et al., 2019) and therefore, there is now a strong focus on the optimization of cannabis yield in the whole-plant production level. Currently, one of the greatest challenges of this industry is to cultivate prolific and uniform plants which provide a consistent supply of homogenous plant material (Magagnini et al., 2018; Lata et al., 2019; Burgel et al., 2020). In response to this, several studies that were designed to improve plant productivity have examined the effect of key environmental factors such as exogenic growth regulators (Burgel et al., 2020), light source and light spectrum (Magagnini et al., 2018; Danziger and Bernstein, 2021a), stress (Caplan et al., 2019), plant architecture (Danziger and Bernstein, 2021b) and optimized fertilization regimes (Caplan et al., 2017; Bernstein et al., 2019a; Saloner and Bernstein, 2021) on plant yield. Although these studies have generated significant knowledge regarding the plant's secondary metabolites and yield production, studies that characterize the inflorescence as a singular entity remain scarce. Usually, cannabis yield productivity is evaluated by the total weight of milled inflorescences (per plant or unit area) and the cannabinoid content in the harvested plant material (Magagnini et al., 2018). However, for breeding initiatives that focus on the enhancement of inflorescence biomass, using the weight indication solely is incomplete as there is an abundance of information concerning attributes of the intact inflorescences such as the number per plant, the distribution of size, uniformity, length and width, shape and perimeter that remains untapped. Although this knowledge can be beneficial for crop improvement, obtaining inflorescence data is challenging and requires a rigorous preparation process of manual separation

Abbreviations: IN, Inflorescence Number; TIC, Total Inflorescence Coverage; IS, Inflorescence Size; IS-sd, Inflorescence Size standard deviation; IL, Inflorescence Length; IL-sd, Inflorescence Length standard deviation; IW, Inflorescence Width; IW-sd, Inflorescence Width standard deviation; CH, Convex Hull; CH-sd, Convex Hull standard deviation; HP, Hull perimeter; HP-sd, Hull perimeter standard deviation; ISH, Inflorescence Shape; ISH-sd, Inflorescence Shape standard deviation; IDB, Inflorescence Dry Biomass; PH, Plant Height on harvest day; DTM, Days To Maturation; CE, Controlled Environment; RH, Relative Humidity.

from the plant, trimming of vegetative parts (in order to reflect genuine sizes) and measuring a wide distribution of phenotypic traits. To overcome the challenges with many of the manual aspects of data recording and generation, the current study employed image analysis techniques that are often used to evaluate plants' characteristics (Samal et al., 2020) such as canopy growth (Kipp et al., 2014; Gage et al., 2017; Cai et al., 2018), plant architecture (Nguyen et al., 2015), seed attributes (Tanabata et al., 2012; Jahnke et al., 2016), and root characterization (Cai et al., 2015; Jeudy et al., 2016) for the assessment of inflorescence's morphological attributes. It is plausible that uncovering the inflorescences' morphological characteristics will advance breeders' capability to generate cannabis plants with a tailored and desired yield morphology. These insights can potentially advance the cannabis industry by enhancing yield productivity through inflorescence size optimization, generating specific commodities that are in line with the industry requirements and increase labor efficacy during the processing of harvested plants. To the best of our knowledge, studies applying image analysis approaches for the quantification of intact inflorescences' parameters have not been performed before.

The objective of this study is to characterize morphological inflorescence attributes that can optimize cannabis breeding and advance crop productivity. To address this goal we aim to (I) Characterize the morphological properties of cannabis inflorescences across various medicinal cannabis genotypes and estimate their variation and homogeneity within and between genotypes (II) Link the overall yield production and inflorescences' features to identify key parameters for yield enhancement (III) Examine associations between inflorescences' attributes and the plant's physiological and phenological features.

MATERIALS AND METHODS

All work in the current study was carried out under the Medicinal Cannabis Research License (RL011/18) and Permits (RL01118P6 and RLO1118P3) issued by the Department of Health (DoH), Office of Drug Control (ODC), Australia.

A detailed description of the plants' material used and the cultivation and physiological evaluation methods performed has been previously published (Naim-Feil et al., 2021). The following section will present a summarized version of the above and will expand on inflorescence evaluation techniques and image analysis methodologies.

Plant Material and Trial Design

In the current study, a heterogeneous population of 119 cannabis genotypes was assessed under controlled environment (CE) conditions. Ninety-seven genotypes of the examined plant population have been imported as genetically unique seeds of medicinal cannabis cultivars from Canadian commercial companies. The remaining twenty-two genotypes have been developed by Agriculture Victoria Research as crosses between High-THC cannabis lines and high CBD accessions which contain a genetic background of an off-type hemp plant. Major cannabinoid profiles (THC and CBD) for all of the experimented genotypes were predicted through the B1080/1192 DNA marker (Pacifico et al., 2006). The molecular data indicated that the cannabinoid profile of the plant population was segregated into 2 groups of 74 and 45 genotypes, of high-THC:low-CBD and blended THC:CBD ratio, respectively.

The trial was designed in a randomized incomplete block design manner and 4–5 plant replicates of each genotype were examined in order to refine the effect of genetic factors on the phenotypic performance (Naim-Feil et al., 2021).

Growth Conditions

Clonal replicates for each genotype were generated from a single mother plant that was maintained under long photoperiod (18 h light). Each mother plant was utilized to extract 10 cuttings, similar in size (10.5 $\pm$ 0.5 cm) and vigor. To invigorate root development, rooting hormone (Growth Technologies, Clonex, 3 g/L IBA gel, Perth, Australia) was applied at the base of each cutting before it was planted into coconut coir propagation plugs (Jiffy-7C,® 50 mm, Zwijndrecht, Netherlands). Plant establishment took place under CE conditions with a 24/18°C (day/night) temperature regime, daylight cycle of 16/8 h (day/night), light intensity (PPFD) of 360 μmol $m^{-2}s^{-1}$ (measured on cultivating shelves surface, 35 cm below the light source) and relative humidity (RH) set to 55% in an indoor room. Thirty days after propagation, 6–7 cuttings, corresponding in size and vigor were selected for each genotype and transplanted into large coconut coir plugs (Jiffypots,® ø8 cm, Zwijndrecht, Netherlands). Fourteen days later, 4–5 uniform plants of each genotype were selected and transplanted into coconut coir grow slabs (100 cm $\times$ 16 cm $\times$ 10 cm, Cazna grow slabs, Sydney, Australia) with 40 and 20 cm intervals between and within rows, respectively. The overall plant density within the CE cultivation facility was 4.3 plants $\times$ m^{-2}. Plants were cultivated over drainage trays (Danish Hydro Trays 338 cm $\times$ 148 cm, Ringe, Denmark) that were situated on a rolling bench system. The vegetative growth phase lasted 42 days (from the date of transplanting) and the transition into the reproductive growth phase was induced by shortening the daylight cycle. Light intensity (PPF, wavelength range of 400–800 nm) of 2,150 μmol s^{-1} delivered by high-pressure sodium bulbs (Philips, MASTER GreenPower Xtra 1,000 W EL/5 $\times$ 6 CT, Amsterdam, Netherland), provided photoperiodic regimes of 18 and 12 h for the vegetative and the reproductive growth phases, respectively. Total fertigation of 1.3 liters $\times$ day^{-1} $\times$ $plant^{-1}$ was delivered by a controlled drip irrigation system (Jain Octa-BubblerTM, 7.5 L/h, Fresno, California, United States), applying 1% A and B nutrient solution (THCTM, coco A + B, Melbourne, Australia) with an EC of 2.1 dS/m and pH levels of 6–6.1. Throughout the growing season, the temperature was maintained at 20°C/17°C (day/night) and the RH was set at 60%. To prevent breaking and overshading, wooden stakes were attached to tilted plants. Pest management was controlled by beneficial (arthropods) that were regularly distributed during the cultivation season.

Data Recording and Plant Processing

Physiological and phenological parameters have been recorded individually for each plant. Phenological assessment (Day to

Maturation, DTM) was performed every 3 days during the flowering phase and defined as the period that lasted between the short daylight induction and the appearance of brown-shaded stigmas on 3 independent inflorescences. Plant harvest was performed selectively when ∼70% of the overall florets' stigmas turned brown (**Supplementary Figure 1A**). The spatially adjusted genotypic mean of plant height (PH) range on harvest day spans from 95 to 157 cm with an overall mean of 122 cm (Naim-Feil et al., 2021). Harvested plants (**Figure 1**) were processed under both fresh (on harvest day) and dried (following drying) states. All plants were manually processed to separate inflorescences from vegetative substances (stems, foliage leaves) and the extracted inflorescences were further purified by removing vegetative organs (leaves and petioles) using leaves trimmers (**Supplementary Figures 1B–D**, Growlush® bowl trimmer, 19″, Melbourne, Australia) in order to capture dependable and refined parameters. The processed inflorescences were then distributed over a scaled surface (**Figure 2A**) and photographed perpendicularly above the surface center to capture 12 MP images, with square pixels, *via* a dual-pixel camera (Samsung Galaxy S8, Seoul, South Korea). Large field image optical distortion was controlled by enabling the camera's ultra-wide shape correction feature. Following this, inflorescence material was placed in a drying room (25°C, 20% humidity) for a minimum period of 14 days and the overall inflorescence dry biomass (IDB) was measured for each plant after complete dehydration was performed using a freeze dryer (VirTis, GPFD, Gardiner, NY, United States).

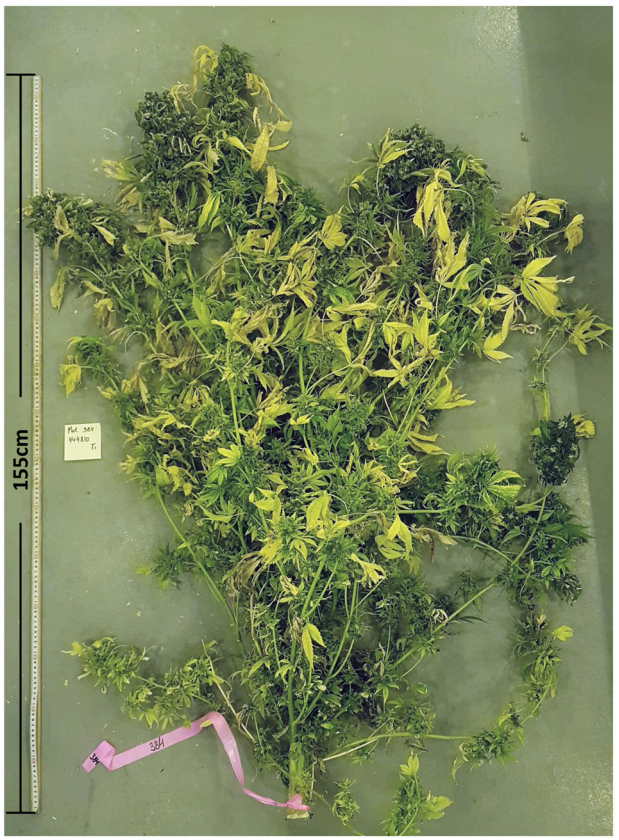

FIGURE 1 | A whole cannabis plant at the time of harvest.

Inflorescence Evaluation and Image Analysis Data Extraction

When needed, image editing was performed manually using GIMP (GIMP Development Team, 2.10.12, 2019) whereas image analysis for cannabis inflorescence shape identification and data extraction was carried out by in-house custom-made C++ (C++17 ISO standard compliant) software. A cm:pixel ratio was calculated independently for each image *via* measuring tapes that were embedded in the photo's background (**Figure 2A**) to generate metric/absolute values for recorded parameters. Raw scaled-surface images were first converted into a binary format (black and white image, **Figure 2B**). As scaled-surface images were RGB color images, it was found that a combination of the blue band, from the RGB image, and the use of minimum error thresholding (Kittler and Illingworth, 1986) was a reliable and robust approach to automate the production of inflorescence binary images (**Figure 2B**) across all captured photographs. The initial binary images were further refined manually by constructing a juxtaposed figure (**Figure 2C**) using Gimp's image layering that enabled manual elimination of undesired objects (e.g., remnant pieces of measurement scales and plant identification tags) and improvements to the segmented-image data by removing image shading or by separating any touching inflorescences that had not been correctly delimited by the software.

These manually corrected binary images were then subject to further automated image editing, using image analysis, to remove isolated inflorescences/leaf material in each image having an area of less than 1 cm^2, using area openings (Breen and Jones, 1996). All cleaned and processed binary images (**Figure 2D**) were then analyzed and inflorescence length (IL), inflorescence width (IW), convex hull (CH) area and hull perimeter (HP) of each object within each plant were recorded (**Figure 3**).

Inflorescence size (IS) was determined from the number of pixels making up the object. The length and width of each inflorescence was determined using the best-fit ellipse (**Figure 3A**) in order to account for all variances or plasticity in its shape. The best fit ellipse is a least-squares approach based on central moments derived from image pixel positions of all the boundary pixels of a given binary object, where

$$\text{object length} = 2\sqrt{\frac{2\left(u_{20}+u_{02}+\sqrt{(u_{20}-u_{02})^2+4u_{11}^2}\right)}{u_{00}}},$$

$$\text{object width} = 2\sqrt{\frac{2\left(u_{20}+u_{02}-\sqrt{(u_{20}-u_{02})^2+4u_{11}^2}\right)}{u_{00}}},$$

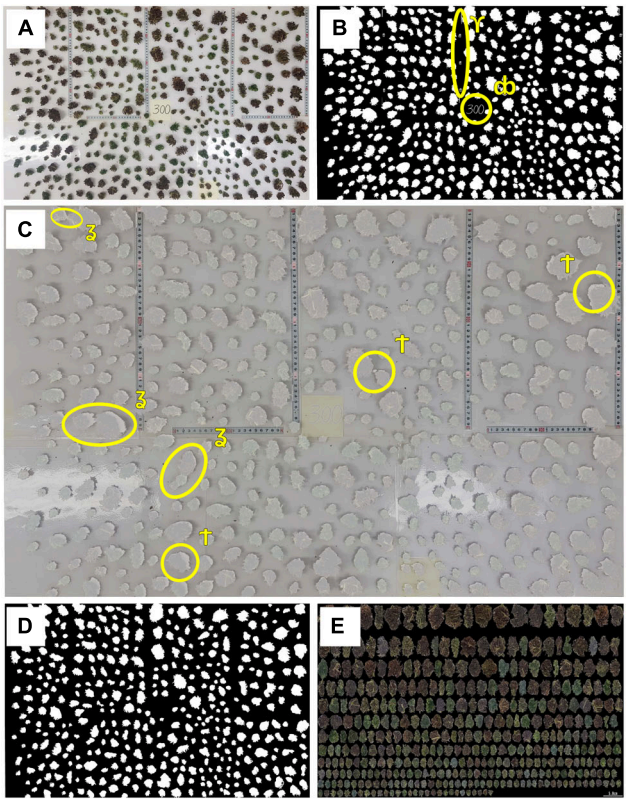

FIGURE 2 | Preparation procedure for inflorescence image analysis. **(A)** An example of the total processed inflorescences distributed over a scaled surface which formed the raw image for morphological analysis,**(B)** Binary (black and white) image of the distributed inflorescences, **(C)** Raw and binary images juxtaposed onto one figure to highlight any requirements for manual editing, **(D)** Processed (cleaned) binary image with only inflorescence material included, **(E)** Composite image containing all inflorescences within the examined plant which are ordered by size. The following symbols indicate areas of concerns in the raw data: ϒ denotes a section with non-inflorescence material which needs to be removed;db indicates the location of plant index; ʒ shows areas of inflorescences contact which need to be separated and † indicates shaded areas to be removed which could be mistaken for inflorescence.

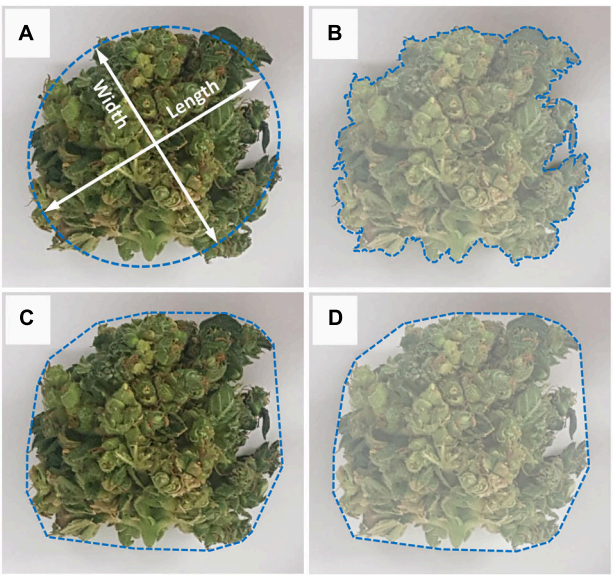

FIGURE 3 | Measurement methodology for image analysis of the inflorescence's morphological parameters. **(A)** Measurement of inflorescence length (major axis) and width (minor axis). Major axis defined as the longest line that can be drawn across the inflorescence and width defined as the longest line that can be drawn through the object while maintaining a perpendicular intersection with the major axis, **(B)** Inflorescence area is defined as the area enclosed within the object perimeter, **(C)** Convex perimeter (Hull Perimeter) measures the surrounding perimeter that contains the inflorescence object, **(D)** Convex hull is the area enclosed within the inflorescence's convex perimeter.

$u_{pq} = \sum_{i=1}^{n} (x_i - \bar{x})^p \left(y_i - \bar{y}\right)^q$ and (x_i, y_i) represent the image position of the i^{th} pixel in a boundary of n pixels.

The CH of each inflorescence was determined using Andrew's monotone chain convex hull algorithm (Andrew, 1979). A geometric approach to determine the area of a typical polygon was performed using geometrics of the locations obtained from each set of CH pixels as shown in **Supplementary Figure 2**.

The estimated length of each object in terms of pixel number was converted into an absolute value *via* $(n_l * p_l)$ where n_l is the length of an object in terms of pixel number and p_l is the length in centimeters of an image pixel. Likewise, the area of each object was converted to absolute values *via* $(n_a * p_l^2)$, where n_a represents the number of pixels making up the object and, given that the image pixels were square, then p_l^2 is the square of the length in centimeters of an image pixel. Based on these parameters, inflorescence shape (ISH) was calculated as the ratio between IW and IL and for each plant, the inflorescence number (IN) and total inflorescence coverage (TIC) were computed. Furthermore, for each plant, a composite image was constructed using its extracted inflorescence objects, sorted by surface size (**Figure 2E**).

Data Standardization and Statistical Analysis

In the current study, comprehensive morphological attributes of 127,000 inflorescences have been recorded and analyzed across 478 cannabis plants. The recorded data contains representatives of both fresh (processed and imaged on harvest day, total of 209 plants) and dried (processed and imaged after drying, total of 283 plants) inflorescence material. To allow the integration between the two data sets, images of 14 plants were captured under both fresh and dry conditions. Based on these records, regression analysis between the 2 inflorescence states was performed for each parameter and a linear trendline and R^2 values were generated to statistically evaluate the trendline prediction accuracy. Since all regressions have been characterized by R^2 values greater than 0.9, the linear trendline equation was utilized to adjust "fresh" recorded data to its "dry" equivalent values (**Supplementary Figure 3**), in order to generate a unified and intact data set. In addition, it is important to note that plant cultivation

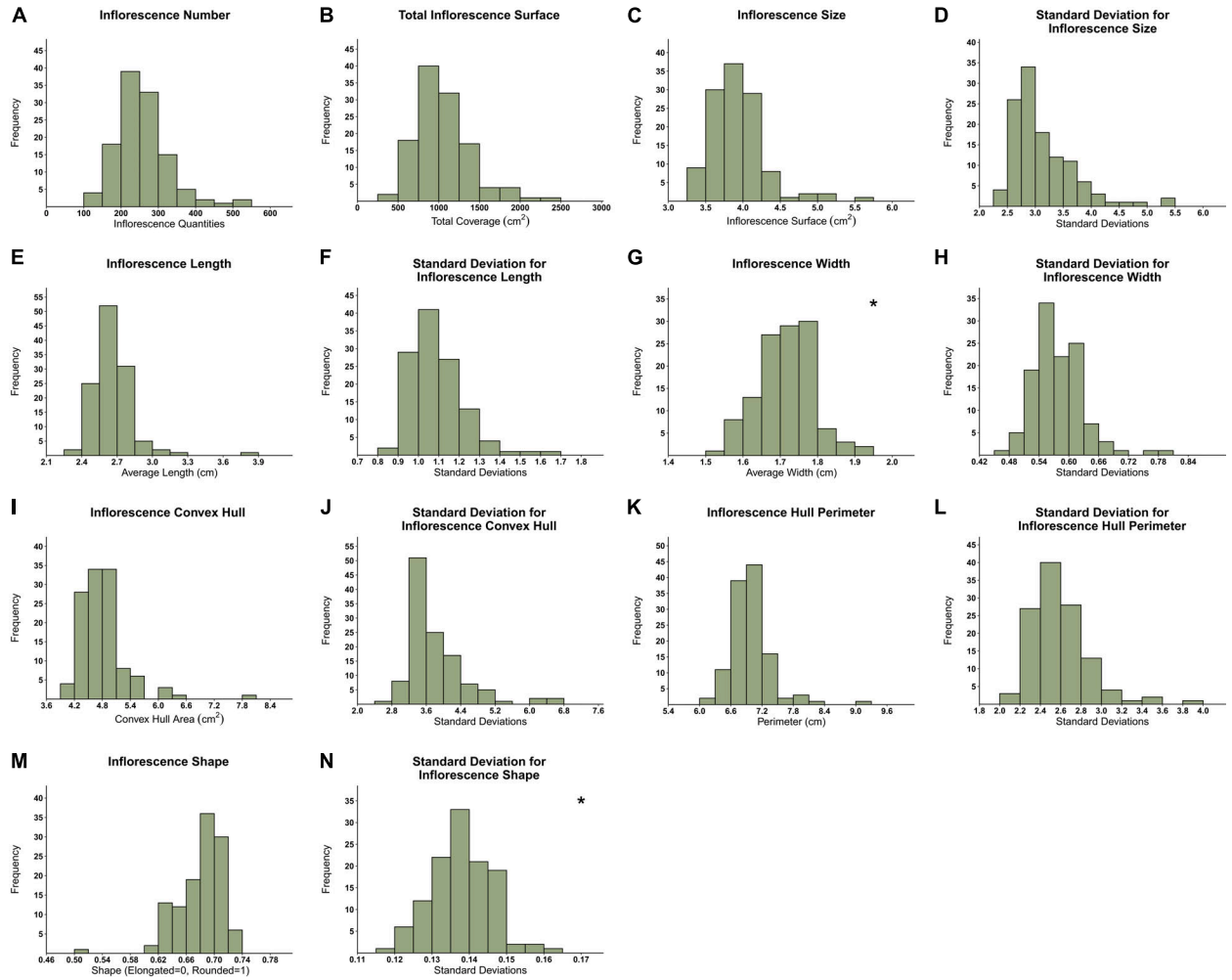

FIGURE 4 | Frequency distribution of 119 genotypes across 14 inflorescences' attributes. **(A)** Inflorescence Number (IN), **(B)** Total Inflorescence Surface Coverage (TIC), **(C)** Average Inflorescence Size (IS), **(D)** Inflorescence Size standard deviation (IS.sd), **(E)** Average Inflorescence Length (IL), **(F)** Inflorescence Length standard deviation (IL.sd), **(G)** Average Inflorescence Width (IW), **(H)** Inflorescence Width standard deviation (IW.sd), **(I)** Average Inflorescence Convex Hull (CH), **(J)** Inflorescence Convex Hull standard deviation (CH.sd), **(K)** Average Inflorescence Hull Perimeter (HP), **(L)** Inflorescence Hull Perimeter standard deviation (HP.sd), **(M)** Inflorescence Shape (ISH), **(N)** Inflorescence Shape standard deviation (ISH.sd). *Normally distributed figures marked with an asterisk on the top right corner.

methodologies which include practices such as plant pruning, vegetative growth phase duration, plant density etc., play a significant role in the determination of plant development and its inflorescence morphology. Thus, the presented absolute values reflect the growth conditions under which the current experiment took place.

Statistical analysis was performed by IBM SPSS Statistics for Windows, Version 26.0 (Armonk, NY: IBM Corp) and by R (R Core Team, 2020). For all examined inflorescences' parameters, the mean and standard deviation (σ_p) within plants were computed. Following this, phenotypic variation across clonal plant repetitions was assessed to evaluate environmental effects throughout the CE facility. Accordingly, spatial adjustments were applied to the data and an estimated value across replicates for each genotype was generated (as detailed in Naim-Feil et al., 2021). PCA (principal component analysis) and correlation matrix were generated using "corrplot" and "stats" R packages, respectively. ASReml models were used to calculate broad-sense heritability (H^2) for all recorded parameters as the proportion of phenotypic variation (V_P) that can be ascribed to genetic factors (V_G) as $H^2 = V_G/V_P$.

RESULTS

Phenotypic Diversity

The frequency distribution of the mean for all 119 examined genotypes (**Figure 4**) reflects the high variation in inflorescence morphology across all 14 recorded parameters. Although most presented histograms are not characterized by a normal distribution, in most cases, the removal of a few outlier genotypes can restore normality to the distribution. An examination of inflorescence quantity distribution (**Figure 4A**) reveals that while most genotypes are characterized by an average of 200–300

inflorescences per plant, some genotypes are typified by up to 500 per plant. Furthermore, the TIC of the examined genotypes ranges from 250 to 2,500 cm^2 (**Figure 4B**). Hence, for some genotypes, the overall coverage of inflorescence surfaces can be up to 10 times greater than others. Following this, as depicted in **Figure 4C**, the average inflorescence size ranges from 3.25 to 5.5 cm^2 across the examined plant population. Interestingly, a comparison between the distribution profile of IL (**Figure 4E**) and IW (**Figure 4G**) reveals that the latter is characterized by a narrower distribution range (0.45 cm) in comparison to the former (1.05 cm). Moreover, the standard deviation (sd) values of attributes such as IL, IW and ISH (**Figures 4F,H,N**, respectively) were found to be relatively narrow and low in comparison to the sd values of attributes such as CH and HP (**Figures 4J,L**, respectively).

Broad–Sense Heritability (H^2)

Broad-sense heritability estimations for inflorescence attributes are presented in **Table 1**. Across all indices concerning inflorescence attributes, ISH had the highest H^2 value (0.38) while all other parameters had values below 0.3 with IS and CH generating the lowest H^2 values of 0.15 and 0.16, respectively. Nevertheless, PH, DTM and IDB, physiological parameters which link to the plant performance as a whole unit, are characterized by relatively higher H^2 values in comparison to most H^2 entries recorded for inflorescences' attributes (i.e., IW, TIC, HP).

Traits Association

A principal component analysis, as well as a correlation matrix, were performed (**Figures 5**, **6**) in order to assess traits association across all recorded inflorescence parameters and key physiological traits. Although the two main components presented in **Figure 5**, jointly explain 76.7% of the variation (PC1 and PC2 accounting for 58.1 and 18.6%, respectively), a highly correlated vectors aggregate, containing parameters that are associated with the dimensions of the intact inflorescence (CH, HP, IS), was observed over the 4th quadrant of the Cartesian system. Interestingly, this group also includes the IL parameter while it does not comprise the IW vector that appears to be highly associated with the plant yield (IDB). The close association between IDB and the average IW is also corroborated through the correlation matrix (**Figure 6**) with a relatively high coefficient value ($r = 0.61$). In addition, each of the inflorescence morphological attributes that comprise this cluster was found to be highly associated with its sd parameter (**Figure 5**) that is characterized by a statistically significant ($p < 0.05$) correlation coefficient value of $r = 0.87$, $r = 0.86$, $r = 0.87$ and $r = 0.87$ for CH, HP, IS and IL, respectively (**Figure 6**).

From the correlation matrix (**Figure 6**), IDB demonstrates a stronger association with IN ($r = 0.83$) than with IS ($r = 0.48$). Yet, IS was found to be correlated with TIC ($r = 0.48$) but no correlation was demonstrated between IS and IN. Plants' precocity (low DTM) was found to be correlated with elongated (DTM to IL, $r = -0.35$), wider (DTM to IW, $r = -0.23$) and larger inflorescences (IS, $r = -0.28$) and in contrast, late maturation (high DTM) was found to be correlated with rounded inflorescences (DTM to ISH, $r = 0.29$) while no correlation was detected between a specific ISH and IDB.

TABLE 1 | Broad-sense heritability (H^2) for inflorescence morphological traits and key physiological attributes.

Trait	H^2
Inflorescence Number	0.29
Inflorescence Size	0.15
Inflorescence Size Standard Deviation	0.18
Total Inflorescence Coverage	0.28
Inflorescence Length	0.18
Inflorescence Length Standard Deviation	0.17
Inflorescence Width	0.19
Inflorescence Width Standard Deviation	0.22
Convex Hull	0.16
Convex Hull Standard Deviation	0.18
Hull Perimeter	0.17
Hull Perimeter Standard Deviation	0.19
Inflorescence Shape	0.38
Inflorescence Shape Standard Deviation	0.22
Plant Height	0.52
Days to Maturation	0.49
Inflorescence Dry Biomass	0.33

The Effect of Inflorescence Size on the Overall Yield

From the principal component analysis (**Figure 5**), despite IDB and TIC being independently recorded parameters, their vectors are completely overlapping. This association is reinforced by the high correlation coefficient value ($r = 0.96$, **Figure 6**). Accordingly, a unique ratio of gram per cm^2 was calculated for each plant by dividing the plant's IDB (gr) by its TIC (cm^2). The obtained ratio was then utilized to compute the weight of each inflorescence, in order to assess the profile of inflorescence weight distribution across the examined plants as demonstrated in **Figure 7**, from 7 selected plants, chosen to represent the IDB spectrum (range from 27.9 to 325.9 gr/plant). As depicted in **Figure 7**, the smallest inflorescences (weighing less than 200 mg) are highly prevalent but their contribution to the overall weight is limited. In addition, it was found that across most plants, the larger inflorescences, accounting for less than 50% of the overall inflorescence quantity, contributes to 75% or more of the plant's total IDB.

Furthermore, the overall percentage of inflorescences that need to be extracted and processed, in order to accumulate 50, 75, and 90% of the plant's IDB was calculated and ranged between 17–32%, 41–58% and 64–79% of the total inflorescence quantity, respectively (**Figure 8**). The trendline equations obtained by linear regressions between inflorescence quantity and the targeted yield thresholds (to accumulate 50, 75, and 90% of the overall IDB) across all genotypes are characterized by statistically significant ($P < 0.001$) coefficients values (slope) of $r = -0.025$, $r = -0.028$, $r = -0.021$, and R^2 values of 0.17, 0.16 and 0.14, respectively.

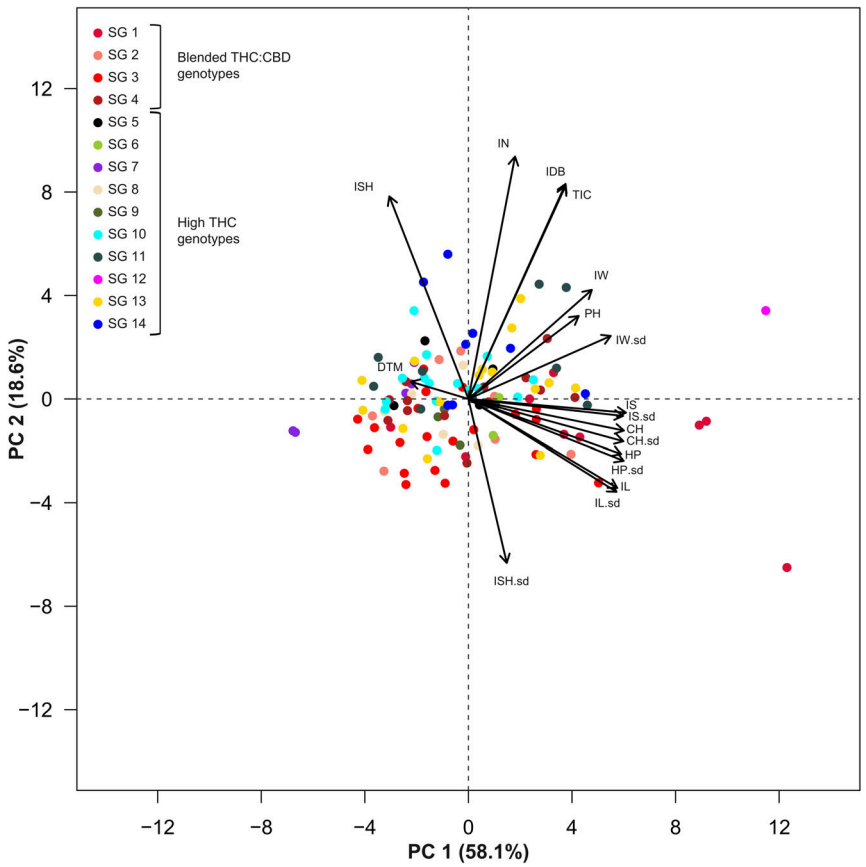

FIGURE 5 | Principal Component Analysis (PCA) for 119 genotypes across 14 Inflorescences' attributes and three physiological parameters. Colors indicate genotypic classifications into strain groups (SG) according to vernacular affiliations (for example, "Banana Kush" or "Diesel"). Genotypes marked in red (or a red shade) are characterized with a blended THC:CBD ratio while all other colors indicate high-THC genotypes (plants cannabinoid classification was assessed through DNA markers). Abbreviations: Inflorescence Size (IS), Inflorescence Size standard deviation (IS.sd), Convex Hull (CH), Convex Hull standard deviation (CH.sd), Hull Perimeter (HP), Hull Perimeter standard deviation (HP.sd), Inflorescence Length (IL), Inflorescence Length standard deviation (IL.sd), Inflorescence Width (IW), Inflorescence Width standard deviation (IW.sd), Total Inflorescence Coverage (TIC), Inflorescence Number (IN), Inflorescence Shape (ISH), Inflorescence Shape standard deviation (ISH.sd), Inflorescence Dry Biomass (IDB), Plant Height on harvest day (PH), Days To Maturation (DTM).

Yield Assessment and Prediction Equation

Due to the relatively high correlation coefficient value observed between IW and IDB (r = 0.61, **Figure 6**), a linear regression analysis was performed to predict plant productivity *via* IW measurements. To be relevant in a production environment with plants nearing harvest under cultivation conditions, the regression model was run using estimated values of fresh rather than dried IW. In addition, as cannabis plant productivity is often expressed by copious inflorescence quantities (as demonstrated through **Figures 6**, **7**), which are challenging to measure under field conditions, a limited number of inflorescences were selected and defined in order to generate a yield assessment methodology. Based on the assumption that the plant's longer inflorescences form over the branches' apex, the top 20 longer inflorescences within each plant were examined and their corresponding width data was extracted and averaged. Furthermore, to improve the prediction accuracy by focusing on a feasible IDB range desired for selection purposes (above∼ 15 gr/plant), the regression model was performed using plants with an IW average greater than 2.5 cm (n = 426). Prior to running the regression analysis, a linear relationship was observed between the examined variables for the prediction model and assumptions of homoscedasticity and normality of the residuals were met. IW predicted the plant's IDB, $F(1, 424) = 549.77$, $p < 0.001$, accounting for 56% of the variation in IDB (R^2 = 0.56). Thus, the following prediction equation for IDB was generated:

$$\mathrm{IDB}_{(gr/plant)} = 59.14 \times IW^{*}_{(cm)} - 134.97$$

*Refers to the average IW of the longest 20 inflorescences.

To simulate errors that may occur while visually evaluating the longest 20 epical inflorescences emerging on a growing plant, the mean IW of 5, 10 and 15 inflorescences that were randomly selected out of the longest 20 inflorescences was calculated. For each of the examined case groups, 10 sample rounds were applied and the dispersal of the obtained averages around the

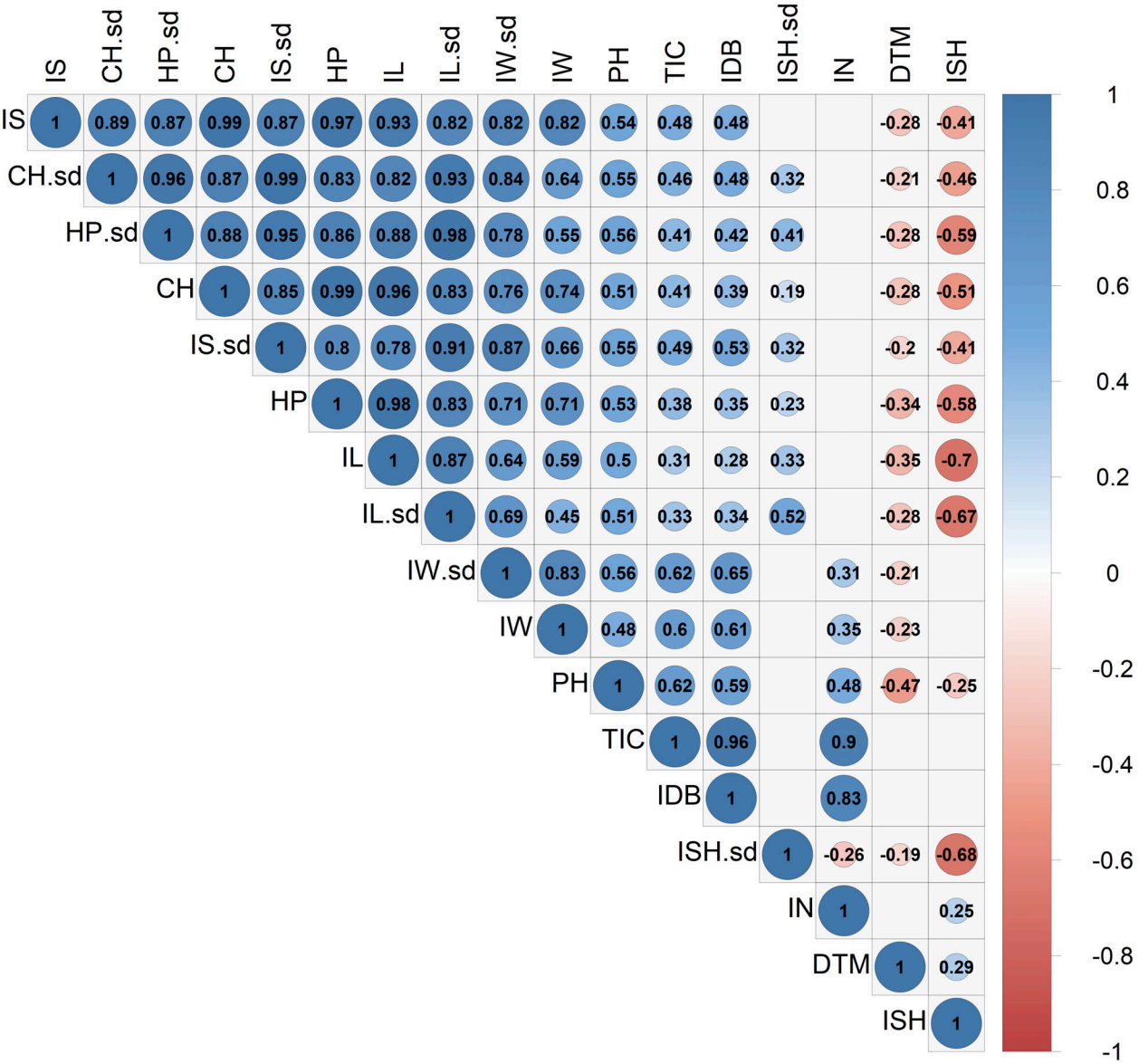

FIGURE 6 | Correlation coefficient matrix for 14 inflorescences' attributes and 3 physiological parameters. The correlation strength and direction are indicated by colors and numeric (coefficient) values. Blank cells indicate statistically insignificant correlations ($P > 0.05$). Abbreviations: Inflorescence Size (IS), Inflorescence Size standard deviation (IS.sd), Convex Hull (CH), Convex Hull standard deviation (CH.sd), Hull Perimeter (HP), Hull Perimeter standard deviation (HP.sd), Inflorescence Length (IL), Inflorescence Length standard deviation (IL.sd), Inflorescence Width (IW), Inflorescence Width standard deviation (IW.sd), Total Inflorescence Coverage (TIC), Inflorescence Number (IN), Inflorescence Shape (ISH), Inflorescence Shape standard deviation (ISH.sd), Inflorescence Dry Biomass (IDB), Plant Height on harvest day (PH), Days To Maturation (DTM).

absolute width mean of the 20 longer inflorescences was assessed (**Figure 9**). Although with more inflorescences selected, the overall variance of the predicted average IW decreases, across all examined IDB range, the presented simulation demonstrates moderate to low variation in IW for sample groups of 10 and 15 inflorescences (**Figures 9B,C**). For example, IDB prediction accuracy for the most productive plant presented in **Figure 9** (IDB = 254 gr) reveals that while the absolute IW average of the longest 20 inflorescences of this plant measured as 5.55 cm, the divergent from the actual mean is 20% in size sample of 5 (range between 4.56–6.7 cm), 15% in size sample of 10 (range between 5.05–6.4 cm) and 7% in size sample of 15 (range between 5.25–5.92 cm).

DISCUSSION

The current study focuses on the role of various cannabis inflorescence attributes in the determination of the overall plant's yield component and their association with key physiological

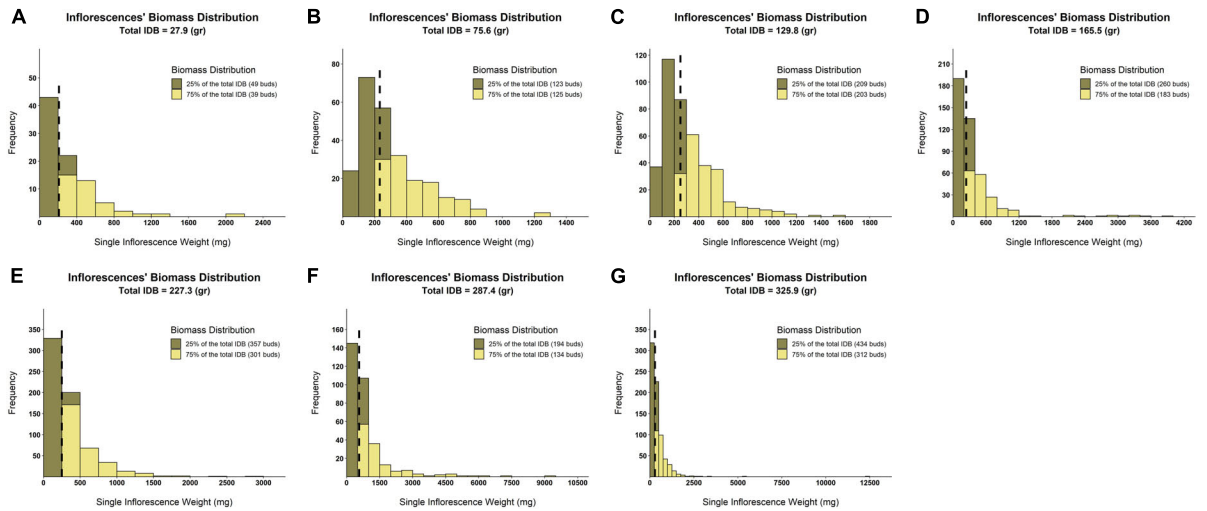

FIGURE 7 | Distribution histograms of within-plant inflorescences' weight across various levels of IDB. Surfaces colored in khaki represent the quantity of smaller inflorescences that contributes to the accumulation of 25% of plant IDB. Surfaces colored in yellow reflect the quantity of larger inflorescences that contributes to the accumulation of 75% of plant IDB. Black broken lines indicate the inflorescences' weight median for each of the examined plants. **(A)** IDB = 27.9 (gr/plant), **(B)** IDB = 75.6 (gr/plant), **(C)** IDB = 129.8 (gr/plant), **(D)** IDB = 165.5 (gr/plant), **(E)** IDB = 227.3 (gr/plant), **(F)** IDB = 287.4 (gr/plant), and **(G)** IDB = 325.9 (gr/plant).

and phenological traits. The examined germplasm includes 119 cannabis drug-type genotypes, which were obtained from legal medicinal cannabis commercial companies, and comprise 74 genotypes characterized by a high-THC:low-CBD ratio and 45 genotypes with a blended THC:CBD ratio. Although cannabis recreational breeding has reportedly impacted the cannabinoids' genetic diversity by intensifying and selecting high THC genotypes (Hazekamp, 2007; Mehmedic et al., 2010; Cascini et al., 2012; Chouvy, 2019), the current examination of inflorescence morphological attributes reveals a broad genotypic diversity across all examined parameters (**Figure 4**). These findings are aligned with the previously reported diversity that was identified across physiological and phenological attributes of the current medicinal cannabis germplasm (Naim-Feil et al., 2021). Nevertheless, to broaden this conclusion for genotypes characterized by low THC:high CBD cannabinoid profile, further studies are required.

Heritability

The broad-sense heritability (H^2) estimations presented in this study can be divided into 2 cohorts: (1) Indices associated with attributes of the intact plant (e.g., PH, TIC, IN) and (2) Indices that focus on features of processed inflorescences (e.g., IW, ISH, CH). As depicted in **Table 1**, all H^2 entries recorded for parameters within the first cohort are greater than the estimated values recorded for the second cohort (excluding ISH). These findings suggest that under the current experiment, inflorescence features are more susceptible to environmental factors as compared to physiological and phenological traits of the intact plant. Although studies examining the heritability indices of cannabis inflorescence features are scarce, a similar H^2 value to that of cannabis IS (0.15) was found among the size of safflower heads (0.21, Camas and Esendal, 2006). In addition, Gómez et al. (2009) investigated the narrow-sense heritability (h^2) of *Erysimum mediohispanicum* (Brassicaceae) flower features and reported an h^2 value of 0.24 for flower size, 0.26 for flower length (in comparison to IL H^2 of 0.18 in the current study) and 0.019 for flower width (in comparison to IW H^2 of 0.19 in the current study). Although these heritability estimations were examined across plants of different taxonomic orders, they all indicate that environmental factors play a major role in the determination of the flowers' phenotypic profile. Therefore, with the relatively low H^2 values typifying the characteristics of cannabis inflorescences, it is anticipated that these traits will have a limited response to selection. Hence, it is suggested that the production of inflorescences with desired morphology will combine breeding initiatives, studies examining the genotype X environment interactions and rigorous adjustments of environmental factors within the cultivation facility.

Traits Association

The close association between traits related to the inflorescence magnitude (e.g., IS, IL, HP) and their compatible standard deviation (sd) parameter (**Figures 5**, **6**) indicates that as the average inflorescence size increases, so does the variation across the inflorescences' size within the examined plant (increased sd). However, the significant role of environmental factors in the determination of inflorescences morphology (as depicted in **Table 1**) and the range of different microenvironmental conditions to which different areas of the plant are exposed suggest that through the implementation of adjusted cultivation methodologies such as: tailored light intensity (Rodriguez-Morrison et al., 2021) and light spectra (Reichel et al., 2021), supplemented subcanopy light (Hawley et al., 2018), pruning (Small, 2017b; Gaudreau et al., 2020) and applications of exogenous growth regulators (Burgel et al., 2020), the variability across intra-plant inflorescence characteristics might be restrained.

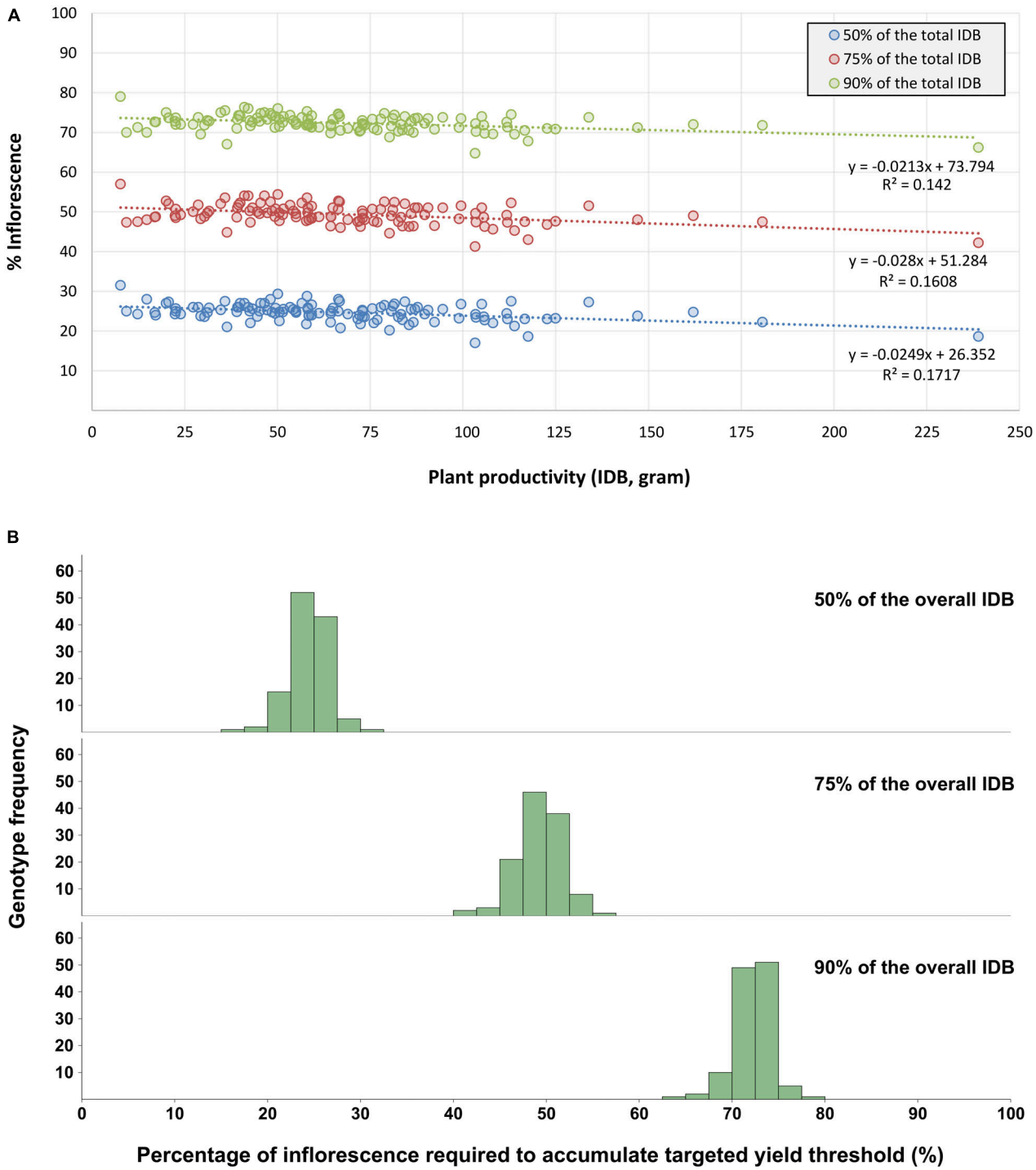

FIGURE 8 | Percentage of inflorescences required for the accumulation of 50%, 75% and 90% of the overall IDB. The presented data refers to the proportion between the larger inflorescences quantity (required to accumulate the targeted yield threshold) and the overall inflorescences quantity within each plant. **(A)** Illustrates the percentage dispersal across all genotypes for each of the targeted yield thresholds. Linear regression trendlines and their corresponding datapoints are marked with the same color, **(B)** Presents the frequency distribution of all examined genotypes across the three targeted yield thresholds.

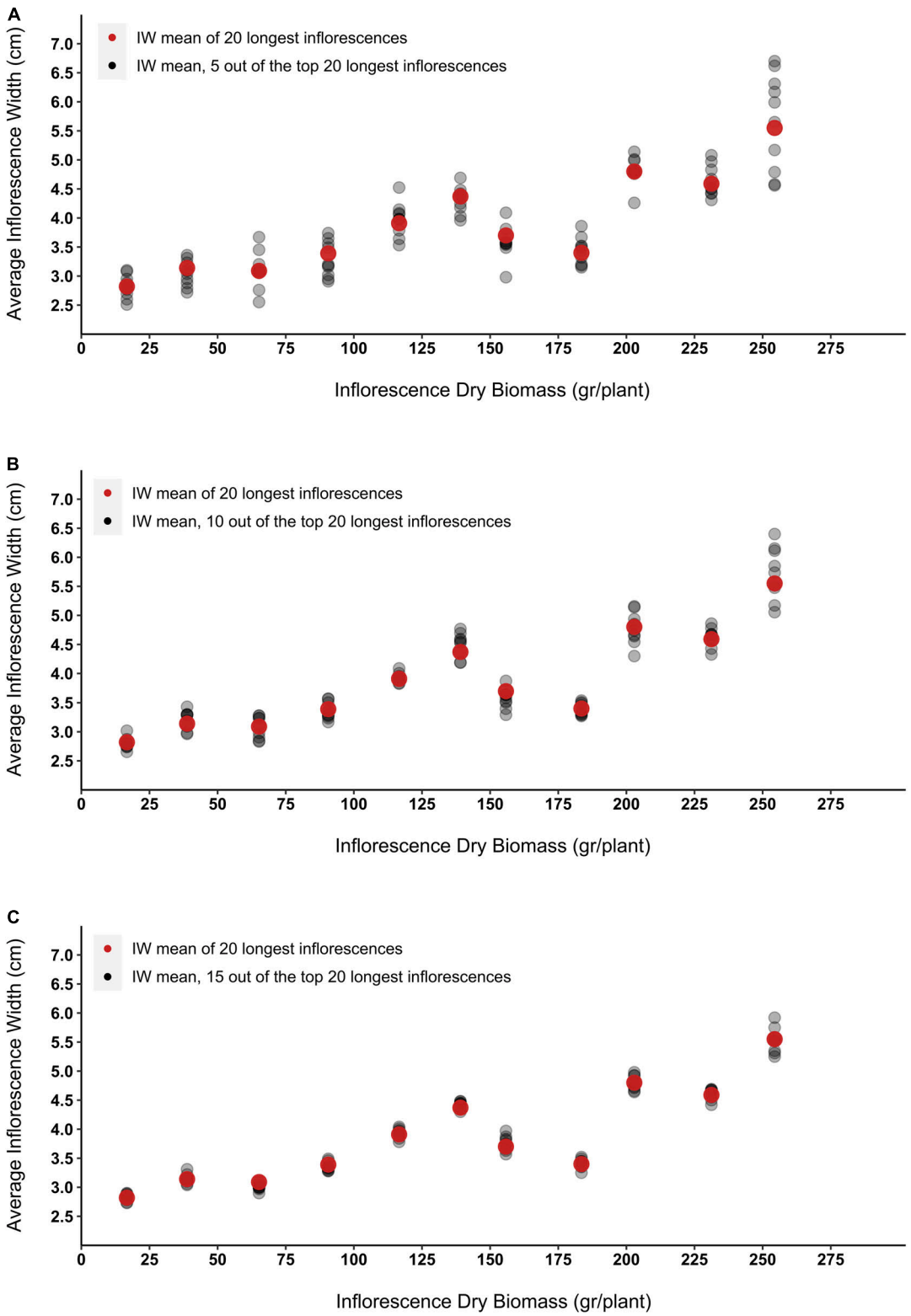

FIGURE 9 | The effect of inflorescence width (IW) measurement sample size on the accuracy of the obtained mean data. Red dots represent the mean of the entire sample group (the width of the top 20 longest inflorescences). Grey dots represent the inflorescence width average that was obtained from 10 sampling rounds of **(A)** 5 randomly selected inflorescences (out of the top 20 longest inflorescences), **(B)** 10 randomly selected inflorescences (out of the top 20 longest inflorescences), and **(C)** 15 randomly selected inflorescences (out of the top 20 longest inflorescences).

In addition, the association between ISH and ISH-sd (**Figure 6**, $r = -0.68$) indicates that rounded inflorescences (ISH closer to 1) are likely to be consistent across the plant (low ISH-sd) while a varied shape morphology (high ISH-sd) is anticipated within genotypes characterized by elongated inflorescences (ISH closer to 0). Together with the relatively high H^2 value that typifies ISH (**Table 1**, 0.38), these findings suggest that reproduction of rounded inflorescences as a commercial product can be relatively feasible to perform. Nevertheless, it should be noted that due to the correlation between ISH and DTM (**Figure 6**, $r = 0.29$), breeding for this trait might come at a cost of late-maturing phenology. In contrast to this, the association between early maturing and elongated (DTM to IL, $r = -0.35$), wider (DTM to IW, $r = -0.23$) and therefore larger inflorescences (DTM to IS, $r = -0.28$) indicate that selection for precocious genotypes is likely to be coupled with inflorescence enlargement. yet, no significant correlation was found between precocity (DTM) and productivity (IDB).

IDB displays a greater correlation coefficient value with IN than with IS (**Figure 6**, $r = 0.83$ and 0.48, respectively). Hence, for breeding initiatives striving to improve plant productivity by focusing on inflorescences' attributes, selection for high inflorescence quantity will provide greater advances on the overall yield enhancement in comparison to selection for increased individual inflorescence sizes.

In the current study, both IL and IW demonstrate significant correlations with IDB (**Figure 6**, $r = 0.28$ and $r = 0.61$, respectively). However, the correlation coefficients values generated indicate that IW can be used as a better predictor for plant productivity than IL. Interestingly, although both IW and IL determine the ISH parameter, no significant association was found between IDB and ISH (**Figure 6**), which suggests that inflorescence profiles across prolific genotypes may not be limited to specific shapes. This is not surprising as the phenomenon of weak associations between the overall plant productivity and the shape of the commercial products (rounded vs. elongated) have been previously reported for several crops such as wheat (Gegas et al., 2010; Yoshioka et al., 2019) and tomatoes (Tanksley, 2004). More specifically, these studies indicated that the independence of these parameters was due to the presence of several loci that regulate fruit shape and other loci which regulate fruit size. However, this is the first study, to the authors' knowledge to demonstrate this effect in cannabis inflorescence.

In the current study, inflorescence parameters within each plant were extracted from the analysis of a single image providing a contour-based two-dimensional (2D) assessment for each object. The high correlation found between TIC and IDB (**Figure 6**, $r = 0.96$) suggests that 2D measurements can be used for the assessment of inflorescence weight without the need for more complex volumetric (3D) measurements. This finding can be used to facilitate the characterization of cannabis plants for selection and breeding purposes as well as identifying optimal environmental conditions for enhancing crop productivity by applying a relatively simple measurement approach. This corresponds with the observations of Diago et al. (2015) in their examination of 2D vs. 3D image analysis as a tool for predicting yield weight in grapevine, where they concluded that 2D measurements can be used as a simple alternative to volumetric measurements when the examined objects are characterized by symmetrical shape.

The Association Between Intra-Plant Inflorescence Weight Distribution and the Overall Plant Productivity

Although cannabis post-harvest operations are labor intensive (Carpentier et al., 2012), formal studies that estimate the expenses of these activities are scarce as their costs appear to vary extensively (Caulkins, 2010). With regards to Inflorescence weight distribution and its association with the overall IDB (**Figure 7**), our findings suggest that a cost-benefit assessment for extracting and processing the smaller inflorescences should be performed in order to optimize labor input per processed IDB unit. Interestingly, for nearly all of the examined plants, extracting the largest 50% of inflorescences led to a gain of 75% or more of the overall IDB. Furthermore, according to **Figure 7**, processing inflorescences weighing less than 200 mg has a relatively minor contribution to the final harvested weight.

This conclusion is underpinned also by the association between yield accumulation and the percentage of processed inflorescences (**Figure 8**) when harvesting 50, 75, and 90% of the total IDB of a given plant, it is required to process (approximately) its larger 25, 50, and 75% inflorescences, respectively. Thus, these findings may indicate diminishing returns to IDB for processing the 25% smaller inflorescences as these are contributing to only 10% of the overall yield. Moreover, the association between inflorescences' proportion and gaining a comparable yield percentage was found to be consistent within each of the examined yield thresholds and across all IDB spectrum (**Figure 8**). Therefore, it is suggested that targeting desired yield threshold by processing a selected number of inflorescences can optimize cannabis production cost-benefit efficacy across a vast range of cultivated genotypes. Nevertheless, as smaller inflorescences typically form within the plant's foliage where environmental factors such as light, humidity and aerate are suboptimal, it is expected that smaller and larger inflorescences will contain different cannabinoid compositions (Bernstein et al., 2019b). Therefore, a chemotypic characterization should be performed for each of the targeted yield thresholds, in order to evaluate the precise cannabinoid content within the processed plant material.

Prediction Equation

Currently, the knowledge that can facilitate precision breeding for generating scientifically based cannabis strains is limited (Chouvy, 2019; Challa et al., 2020). Therefore, practical tools that enable accelerated plant screening and improve selection accuracy are valuable for the growing medicinal cannabis industry. However, unlike classical breeding programs aiming for the production of inbred varieties or hybrid seeds (F1) through crosses of genetically-stabilized parental lines, in cannabis, due to its typical vegetative propagation technique (Barcaccia et al., 2020), any hybrid plant in the observation facility, regardless of its parental genetic background, can result in a commercial

variety. Thus, increasing the number of screened individuals directly enhances the probability to locate desirable varieties, but at the same time requires a tedious, costly and highly time-consuming phenotypic evaluation (e.g., cannabinoids and terpenoids content, phenology and physiological traits) that first and foremost includes yield assessments. The prediction equation presented in this study will enable estimates of plant productivity (IDB) by measuring the average width of the plant's largest inflorescences which typically evolve on the branches apex (Dach et al., 2015; Reichel et al., 2021). Previously, a minimum number of 20 second-order branches per plant in the current plant population was identified (Naim-Feil et al., 2021). Thus, the proposed prediction equation was generated accordingly and requires the average width of 10 out of the top 20 randomly selected apical inflorescences of a given plant. Per the prediction equation, an increase of 1 cm in the calculated IW, will enhance the overall IDB by 59.14 gr. By using an on-site simple caliper measurement, this method allows for rapid yield forecasting estimation of diverse drug-type cannabis plant populations. However, as observed by Dach et al. (2015) and confirmed by the current study findings, environmental factors can have an extensive effect on cannabis inflorescence morphology which includes IW. Thus, the accuracy of the proposed prediction equation is expected to vary under different environmental conditions. To address this issue, one possibility is to forecast the IDB ratio between plants of a given population according to their compatible IW ratios. The linear association and the relatively high correlation coefficient between IDB and IW provide support for this method. Although this alternative approach does not provide an absolute prediction value for the plant's IDB, it can be used as a practical tool for yield estimation under diverse environmental conditions and for heterogeneous plant populations. However, as this methodology has not yet been rigorously explored, its accuracy should be evaluated and validated by future studies.

CONCLUSION

The findings presented in the current study indicate that environmental factors play a major role in the determination of inflorescences morphology. Therefore, it is suggested that the production of inflorescences with desired features will combine breeding activities, research examining the genotype X environment interactions and rigorous adjustments of environmental factors within the cultivation facility. With regards to inflorescence weight distribution, our findings suggest that processing 75% of the plant's largest inflorescence will gain 90% of the plant's yield potential. Therefore, it is worthwhile to evaluate if the benefits from extracting and processing the plant's 25% smaller inflorescences outweigh its operational costs. Based on the relatively high correlation between plant productivity (IDB) and inflorescence width (IW), a prediction equation for forecasting the plant's IDB through width measurements of specific inflorescences was generated. However, since this equation was generated based on inflorescences' width that formed under specific cultivation settings, to expand this selection methodology for diverse environmental conditions it is proposed to rate the predicted IDB values according to the IW ratios within populations cultivated under the same growth conditions.

The knowledge obtained in the current study can facilitate the generation of desired inflorescences, improve yield productivity and increase labor efficacy in commercial production pipelines. To build on this work, future studies could investigate inflorescences' features on a microscopic level to further explore trichomes morphology and density. Moreover, further research is needed to investigate the genetic factors that regulate inflorescence morphology, plant physiology and cannabinoids biosynthesis. These, together with the insights of this research, will improve our capability to generate and cultivate scientifically based cannabis cultivars for medicinal application.

DATA AVAILABILITY STATEMENT

The original contributions presented in the study are included in the article/**Supplementary Material**, further inquiries can be directed to the corresponding author/s.

AUTHOR CONTRIBUTIONS

EN-F designed the study, performed the statistical analysis, and prepared the manuscript. EN-F and LS cultivated and processed the plant material, captured, scaled, and manually refined all images. EB designed and programmed the image analysis software and extracted inflorescence evaluation data. LP performed the trial's design and implemented the spatial adjustments. NC and GS co-supervised all aspects of the project and assisted with the manuscript preparation and secured funding. All authors have approved the manuscript.

FUNDING

This work was funded by Agriculture Victoria Research and Agriculture Victoria Services.

ACKNOWLEDGMENTS

We acknowledge Alix Malthouse, Melinda Quinn, Amy Miner, Darren, Callaway, Lennon Matchett–Oates, Rebecca Baillie, Shivi Braich and Doris Ram for providing excellent technical assistance and to Jodie Naim–Feil for her insight and advice.

SUPPLEMENTARY MATERIAL

The Supplementary Material for this article can be found online at: https://www.frontiersin.org/articles/10.3389/fpls.2022.858519/full#supplementary-material

REFERENCES

Abel, E. L. (1980). *Marihuana the First Twelve Thousand Years*. Berlin: Springer Science+Business Media.

Andre, C. M., Hausman, J. F., and Guerriero, G. (2016). Cannabis sativa: the plant of the thousand and one molecules. *Front. Plant Sci.* 7:19. doi: 10.3389/fpls.2016.00019

Andrew, A. M. (1979). Another efficient algorithm for convex hulls in two dimensions. *Inf. Process. Lett.* 9, 216–219. doi: 10.1016/0020-0190(79)90072-90073

Barcaccia, G., Palumbo, F., Scariolo, F., Vannozzi, A., Borin, M., and Bona, S. (2020). Potentials and challenges of genomics for breeding cannabis cultivars. *Front. Plant Sci.* 11:573299. doi: 10.3389/fpls.2020.573299

Baron, E. P. (2018). Medicinal properties of cannabinoids, terpenes, and flavonoids in cannabis, and benefits in migraine, headache, and pain: an update on current evidence and cannabis science. *Curr. Pain Headache Rep.* 58, 1139–1186. doi: 10.1111/head.13345

Bernstein, N., Gorelick, J., and Koch, S. (2019a). Interplay between chemistry and morphology in medical cannabis (*Cannabis sativa* L.). *Ind. Crops Prod.* 129, 185–194. doi: 10.1016/j.indcrop.2018.11.039

Bernstein, N., Gorelick, J., Zerahia, R., and Koch, S. (2019b). Impact of N, P, K, and humic acid supplementation on the chemical profile of medical cannabis (*Cannabis sativa* L). *Front. Plant Sci.* 10:736. doi: 10.3389/fpls.2019.00736

Breen, E. J., and Jones, R. (1996). Attribute openings, thinnings, and granulometries. *Comput. Vis. Image Underst.* 64, 377–389. doi: 10.1006/cviu.1996.0066

Burgel, L., Hartung, J., and Schibano, D. (2020). Impact of different phytohormones on morphology, yield and cannabinoid content of *Cannabis sativa* L. *Plants* 9:725. doi: 10.3390/plants9060725

Cai, J., Kumar, P., Chopin, J., and Miklavcic, S. J. (2018). Land-based crop phenotyping by image analysis: accurate estimation of canopy height distributions using stereo images. *PLoS One* 13:e0196671. doi: 10.1371/journal.pone.0196671

Cai, J., Zeng, Z., Connor, J. N., Huang, C. Y., Melino, V., Kumar, P., et al. (2015). RootGraph: a graphic optimization tool for automated image analysis of plant roots. *J. Exp. Bot.* 66, 6551–6562. doi: 10.1093/jxb/erv359

Camas, N., and Esendal, E. (2006). Estimates of broad-sense heritability for seed yield and yield components of grass pea (*Lathyrus sativus* L.). *Hereditas* 143, 55–57. doi: 10.3906/tar-0611-622

Caplan, D., Dixon, M., and Zheng, Y. (2017). Optimal rate of organic fertilizer during the flowering stage for cannabis grown in two coir-based substrates. *HortScience* 52, 1796–1803. doi: 10.21273/HORTSCI12401-17

Caplan, D., Dixon, M., and Zheng, Y. (2019). Increasing inflorescence dry weight and cannabinoid content in medical cannabis using controlled drought stress. *HortScience* 54, 964–969. doi: 10.21273/HORTSCI13510-18

Carpentier, C., Mulligan, K., Laniel, L., Potter, D., Hughes, B., Vandam, L., et al. (2012). *Cannabis Production and Markets in Europe*. Lisbon: EMCDDA.

Cascini, F., Aiello, C., and Di Tanna, G. (2012). Increasing Delta-9-Tetrahydrocannabinol (Delta -9-THC) content in herbal cannabis over time: systematic review and meta-analysis. *Curr. Drug Abuse Rev.* 5, 32–40.

Cascio, M. G., Pertwee, R. G., and Marini, P. (2017). "The pharmacology and therapeutic potential of plant cannabinoids," in *Cannabis sativa L. - Botany and Biotechnology*, eds S. Chandra, H. Lata, and M. A. ElSohly (Berlin: Springer International Publishing), 207–225. doi: 10.1007/978-3-319-54564-6_9

Caulkins, J. P. (2010). *Estimated Cost of Production for Legalized Cannabis*. Santa Monica, CA: Rand.

Challa, S. K. R., Misra, N. N., and Martynenko, A. (2020). Drying of cannabis—state of the practices and future needs. *Dry. Technol.* 39, 2055–2064. doi: 10.1080/07373937.2020.1752230

Chandra, S., Lata, H., and ElSohly, M. A. (2020). Propagation of cannabis for clinical research: an approach towards a modern herbal medicinal products development. *Front. Plant Sci.* 11:58. doi: 10.3389/fpls.2020.00958

Chouvy, P.-A. (2019). Cannabis cultivation in the world: heritages, trends and challenges. *EchoGéo* 48, 1–20. doi: 10.4000/echogeo.17591

Clarke, R., and Merlin, M. (2013). *Cannabis- Evolution and Ethanobotany*. Los Angeles, CA: University of California Press, 771–810.

Dach, J., Moore, E. A., and Kander, J. (2015). "Cannabisbotany, taxonomy and growth," in *Cannabis Extracts in Medicine The Promise of Benefits in Seizure Disorders, Cancer and Other Conditions*, (Jefferson NC: McFarland & Company, Inc., Publishers), 21–36.

Danziger, N., and Bernstein, N. (2021a). Light matters: effect of light spectra on cannabinoid profile and plant development of medical cannabis (*Cannabis sativa* L.). *Ind. Crops Prod.* 164:113351. doi: 10.1016/j.indcrop.2021.113351

Danziger, N., and Bernstein, N. (2021b). Plant architecture manipulation increases cannabinoid standardization in 'drug-type' medical cannabis. *Ind. Crops Prod.* 167:113528. doi: 10.1016/j.indcrop.2021.113528

Dayanandan, P., and Kaufman, P. B. (1976). Trichomes of *Cannabis sativa* L. (Cannabaceae). *Am. J. Bot.* 63, 578–591. doi: 10.1002/j.1537-2197.1976.tb11846.x

Diago, M. P., Tardaguila, J., Aleixos, N., Millan, B., Prats-Montalban, J. M., Cubero, S., et al. (2015). Assessment of cluster yield components by image analysis. *J. Sci. Food Agric.* 95, 1274–1282. doi: 10.1002/jsfa.6819

Ebersbach, P., Stehle, F., Kayser, O., and Freier, E. (2018). Chemical fingerprinting of single glandular trichomes of Cannabis sativa by Coherent anti-Stokes Raman scattering (CARS) microscopy. *BMC Plant Biol.* 18:275. doi: 10.1186/s12870-018-1481-1484

ElSohly, M. A., Radwan, M. M., Gul, W., Chandra, S., and Galal, A. (2017). "Phytochemistry of *Cannabis sativa* L," in *Phytocannabinoids. Progress in the Chemistry of Organic Natural Products*, eds A. D. Kinghorn, H. Falk, S. Gibbons, and J. Kobayashi (Cham: Springer International Publishing), 1–36. doi: 10.1007/978-3-319-45541-9_1

Erkelens, J. L., and Hazekamp, A. (2014). An essay on the history of the term Indica and the taxonomical conflict between the monotypic and polytypic views of Cannabis. *Cannabinoids* 9, 9–15.

Flores-sanchez, I. J., and Verpoorte, R. (2008). Secondary metabolism in cannabis. *Phytochem. Rev.* 7, 615–639. doi: 10.1007/s11101-008-9094-9094

Gage, J. L., Miller, N. D., Spalding, E. P., Kaeppler, S. M., and de Leon, N. (2017). TIPS: a system for automated image-based phenotyping of maize tassels. *Plant Methods* 13:21. doi: 10.1186/s13007-017-0172-178

Gaudreau, S., Missihoun, T., and Germain, H. (2020). Early topping: an alternative to standard topping increases yield in cannabis production. *Plant Sci. Today* 7, 627–630. doi: 10.14719/PST.2020.7.4.927

Gegas, V. C., Nazari, A., Griffiths, S., Simmonds, J., Fish, L., Orford, S., et al. (2010). A genetic framework for grain size and shape variation in wheat. *Plant Cell* 22, 1046–1056. doi: 10.1105/tpc.110.074153

Godfray, H. C. J., Beddington, J. R., Crute, I. R., Haddad, L., Lawrence, D., Muir, J. F., et al. (2010). Food security: the challenge of Feeding 9 Billion People. *Science* 327, 812–818. doi: 10.1016/j.geoforum.2018.02.030

Goldstein, B. B. (2015). *Cannabis in the Treatment of Pediatric Epilepsy*. Chicago, IL: O'Shaughnessy's.

Gómez, J. M., Abdelaziz, M., Muñoz-Pajares, J., and Perfectti, F. (2009). Heritability and genetic correlation of corolla shape and size in erysimum mediohispanicum. *Evolution* 63, 1820–1831. doi: 10.1111/j.1558-5646.2009.00667.x

Hall, W., and Degenhardt, L. (2007). Prevalence and correlates of cannabis use in developed and developing countries. *Curr. Opin. Psychiatry* 20, 393–397. doi: 10.1097/YCO.0b013e32812144cc

Hammond, C. T., and Mahlberg, P. G. (1973). Morphology of glandular hairs of cannabis sativa from scanning electron microscopy. *Am. J. Bot.* 60, 524–528. doi: 10.1002/j.1537-2197.1973.tb05953.x

Hammond, C. T., and Mahlberg, P. G. (1977). Morphogenesis of capitate glandular hairs of *Cannabis sativa* (Cannabaceae). *Am. J. Bot.* 64, 1023–1031. doi: 10.1002/j.1537-2197.1977.tb11948.x

Hand, A., Blake, A., Kerrigan, P., Samuel, P., and Friedberg, J. (2016). History of medical cannabis. *J. Pain Manag.* 9, 387–394.

Hawley, D., Graham, T., Stasiak, M., and Dixon, M. (2018). Improving Cannabis bud quality and yield with subcanopy lighting. *HortScience* 53, 1593–1599. doi: 10.21273/HORTSCI13173-18

Hazekamp, A. (2007). "An evaluation of the quality of medicinal grade cannabis in the Netherlands," in *Cannabis; Extracting the Medicine*, ed. B. V. Ipskamp (Amsterdam: PrintPartners), 25–38.

Jahnke, S., Roussel, J., Hombach, T., Kochs, J., Fischbach, A., Huber, G., et al. (2016). phenoSeeder - a robot system for automated handling and phenotyping of individual seeds. *Plant Physiol.* 172, 1358–1370. doi: 10.1104/pp.16.01122

Jeudy, C., Adrian, M., Baussard, C., Bernard, C., Bernaud, E., Bourion, V., et al. (2016). RhizoTubes as a new tool for high throughput imaging of plant root

development and architecture: test, comparison with pot grown plants and validation. *Plant Methods* 12:31. doi: 10.1186/s13007-016-0131-139

Jin, D., Dai, K., Xie, Z., and Chen, J. (2020). Secondary metabolites profiled in cannabis inflorescences, leaves, stem barks, and roots for medicinal purposes. *Sci. Rep.* 10:3309. doi: 10.1038/s41598-020-60172-60176

Kipp, S., Mistele, B., Baresel, P., and Schmidhalter, U. (2014). High-throughput phenotyping early plant vigour of winter wheat. *Eur. J. Agron.* 52, 271–278. doi: 10.1016/j.eja.2013.08.009

Kittler, J., and Illingworth, J. (1986). Minimum error thresholding. *Pattern Recognit.* 19, 41–47. doi: 10.1016/0031-3203(86)90030-90030

Lata, H., Chandra, S., Uchendu, E. E., Khan, A. I., and ElSohly, M. A. (2019). "Cultivating research grade cannabis for the development of phytopharmaceuticals," in *Medicinal Plants From Farm to Pharmacy*, eds Joshee, Dhekney, and Parajuli (Cham: Springer Nature) 169–186.

Leweke, F. M., Piomelli, D., Pahlisch, F., Muhl, D., Gerth, C. W., Hoyer, C., et al. (2012). Cannabidiol enhances anandamide signaling and alleviates psychotic symptoms of schizophrenia. *Transl. Psychiatry* 2:e94. doi: 10.1038/tp.2012.15

Livingston, S. J., Quilichini, T. D., Booth, J. K., Wong, D. C. J., Rensing, K. H., Laflamme-Yonkman, J., et al. (2020). Cannabis glandular trichomes alter morphology and metabolite content during flower maturation. *Plant J.* 101, 37–56. doi: 10.1111/tpj.14516

Magagnini, G., Grassi, G., and Kotiranta, S. (2018). The effect of light spectrum on the morphology and cannabinoid content of *Cannabis sativa* L. *Med. Cannabis Cannabinoids* 1, 19–27. doi: 10.1159/000489030

Mehmedic, Z., Chandra, S., Slade, D., Denham, H., Foster, S., Patel, A. S., et al. (2010). Potency trends of Δ9-THC and other cannabinoids in confiscated cannabis preparations from 1993 to 2008. *J. Forensic Sci.* 55, 1209–1217. doi: 10.1111/j.1556-4029.2010.01441.x

Mikuriya, T. H. (1969). Marijuana in medicine: past, present and future. *Calif. Med.* 110, 34–40.

Nahtigal, I., Blake, A., Hand, A., Florentinus-Mefailoski, A., Haleh, H., and Friedberg, J. (2016). The pharmacological properties of cannabis. *J. Pain Manag.* 9, 481–491.

Naim-Feil, E., Pembleton, L. W., Spooner, L. E., Malthouse, A. L., Miner, A., Quinn, M., et al. (2021). The characterization of key physiological traits of medicinal cannabis (*Cannabis sativa* L.) as a tool for precision breeding. *BMC Plant Biol.* 21:294. doi: 10.1186/s12870-021-03079-3072

Nguyen, T. T., Slaughter, D. C., Max, N., Maloof, J. N., and Sinha, N. (2015). Structured light-based 3D reconstruction system for plants. *Sensors* 15, 18587–18612. doi: 10.3390/s150818587

Pacifico, D., Miselli, F., Micheler, M., Carboni, A., Ranalli, P., and Mandolino, G. (2006). Genetics and marker-assisted selection of the chemotype in *Cannabis sativa* L. *Mol. Breed.* 17, 257–268. doi: 10.1007/s11032-005-5681-x

Pain, S. (2015). A potted history. *Nature* 525, S10–S11.

Parker, K. A., Di Mattia, A., Shaik, F., Cerón Ortega, J. C., and Whittle, R. (2019). Risk management within the cannabis industry: building a framework for the cannabis industry. *Financ. Mark. Institutions Instruments* 28, 3–55. doi: 10.1111/fmii.12104

Parker, L. A., Mechoulam, R., and Schlievert, C. (2002). Cannabidiol, a non-psychoactive component of cannabis and its synthetic dimethylheptyl homolog suppress nausea in an experimental model with rats. *Neuroreport* 13, 567–570. doi: 10.1097/00001756-200204160-200204166

Pisanti, S., and Bifulco, M. (2017). Modern history of medical cannabis: from widespread use to prohibitionism and back. *Trends Pharmacol. Sci.* 38, 195–198. doi: 10.1016/j.tips.2016.12.002

Potter, D. J. (2013). A review of the cultivation and processing of cannabis (*Cannabis sativa* L.) for production of prescription medicines in the UK. *Drug Test. Anal.* 6, 31–38. doi: 10.1002/dta.1531

R Core Team (2020). *R: A Language and Environment for Statistical Computing*. Vienna: R Core Team.

Radwan, M. M., Wanas, A. S., Chandra, S., and ElSohly, M. A. (2017). "Natural cannabinoids of cannabis and methods of analysis," in *Cannabis sativa L. - Botany and Biotechnology*, eds S. Chandra, H. Lata, and M. A. ElSohly (Berlin: Springer International Publishing), 161–182. doi: 10.1007/978-3-319-54564-6_7

Raman, V., Lata, H., Chandra, S., Khan, I. A., and ElSohly, M. A. (2017). "Morpho-anatomy of marijuana (*Cannabis sativa* L.)," in *Cannabis sativa L. - Botany and Biotechnology*, eds S. Chandra, H. Lata, and M. A. ElSohly (Berlin: Springer International Publishing), 123–136. doi: 10.1007/978-3-319-54564-6_5

Reichel, P., Munz, S., Hartung, J., Präger, A., Kotiranta, S., Burgel, L., et al. (2021). Impact of three different light spectra on the yield, morphology and growth trajectory of three different *Cannabis sativa* L. strains. *Plants* 10:1866. doi: 10.3390/plants10091866

Rodriguez-Morrison, V., Llewellyn, D., and Zheng, Y. (2021). Cannabis yield, potency, and leaf photosynthesis respond differently to increasing light levels in an indoor environment. *Front. Plant Sci.* 12:646020. doi: 10.3389/fpls.2021.646020

Russo, E. B. (2014). "The pharmacological history of cannabis," in *Handbook of Cannabis*, ed. R. Pertwee (Oxford: Oxford University Press), 12–43. doi: 10.1093/acprof

Saloner, A., and Bernstein, N. (2021). Nitrogen supply affects cannabinoid and terpenoid profile in medical cannabis (*Cannabis sativa* L.). *Ind. Crops Prod.* 167:113516. doi: 10.1016/j.indcrop.2021.113516

Samal, A., Choudhury, S., Das, and Awada, T. (2020). "Part 1: basics," in *Intelligent Image Analysis for Plant Phenotyping*, eds A. Samal and S. Das Choudhury (Boca Raton, FL: CRC Press), 4–66.

Small, E. (2015). Evolution and classification of *Cannabis sativa* (Marijuana, Hemp) in relation to human utilization. *Bot. Rev.* 81, 189–294. doi: 10.1007/s12229-015-9157-9153

Small, E. (2017a). "Classification of *Cannabis sativa* L.: in relation to agricultural, biotechnological, medical and recreational utilization," in *Cannabis sativa L. - Botany and Biotechnology*, eds S. Chandra, H. Lata, and M. A. ElSohly (Berlin: Springer International Publishing), 1–62. doi: 10.1007/978-3-319-54564-6_1

Small, E. (2017b). "Medical marijuana: production," in *Cannabis: a Complete Guide*, (Boca Raton, FL: CRC Press), 351–370.

Small, E., Pocock, T., and Cavers, P. B. (2003). The biology of Canadian weeds .119. *Cannabis sativa* L. *Can. J. Plant Sci.* 83, 217–237. doi: 10.4141/P02-021

Sobo, E. J. (2017). Parent use of cannabis for intractable pediatric epilepsy: everyday empiricism and the boundaries of scientific medicine. *Soc. Sci. Med.* 190, 190–198. doi: 10.1016/j.socscimed.2017.08.003

Summers, D. J. (2018). "Supply and demand," in *The Business of Cannabis: New Policies for the New Marijuana Industry*, (California: Praeger), 1–16.

Tanabata, T., Shibaya, T., Hori, K., Ebana, K., and Yano, M. (2012). SmartGrain: high-throughput phenotyping software for measuring seed shape through image analysis. *Plant Physiol.* 160, 1871–1880. doi: 10.1104/pp.112.205120

Tanaka, H., and Shoyama, Y. (1999). Monoclonal antibody against tetrahydrocannabinolic acid distinguishes *Cannabis sativa* samples from different plant species. *Forensic Sci. Int.* 106, 135–146. doi: 10.1016/S0379-0738(99)00193-190

Tanksley, S. D. (2004). The genetic, developmental, and molecular bases of fruit size and shape variation in tomato. *Plant Cell* 16, 181–189. doi: 10.1105/tpc.018119

Thomas, B. F., and ElSohly, M. A. (2015). "The botany of *Cannabis sativa* L," in *The Analytical Chemistry of Cannabis: Quality Assessment, Assurance, and Regulation of Medicinal Marijuana and Cannabinoid Preparations*, eds B. F. Thomas and M. A. ElSohly (Amsterdam: Elsevier).

Yoshioka, M., Takenaka, S., Nitta, M., Li, J., Mizuno, N., and Nasuda, S. (2019). Genetic dissection of grain morphology in hexaploid wheat by analysis of the NBRP-Wheat core collection. *Genes Genet. Syst.* 94, 35–49. doi: 10.1266/ggs.18-00045

Zuardi, A. W. (2006). History of cannabis as a medicine: a review. *Rev. Bras. Psiquiatr.* 28, 153–157. doi: 10.1590/S1516-44462006000200015

Conflict of Interest: The authors declare that the research was conducted in the absence of any commercial or financial relationships that could be construed as a potential conflict of interest.

Publisher's Note: All claims expressed in this article are solely those of the authors and do not necessarily represent those of their affiliated organizations, or those of the publisher, the editors and the reviewers. Any product that may be evaluated in this article, or claim that may be made by its manufacturer, is not guaranteed or endorsed by the publisher.

frontiers | Frontiers in Plant Science

REVIEW
published: 21 April 2022
doi: 10.3389/fpls.2022.880423

WHIRLIES Are Multifunctional DNA-Binding Proteins With Impact on Plant Development and Stress Resistance

Karin Krupinska[1], Christine Desel[1], Susann Frank[1] and Götz Hensel[2,3]*

[1]Institute of Botany, Christian-Albrechts-University of Kiel, Kiel, Germany, [2]Centre for Plant Genome Engineering, Institute of Plant Biochemistry, Heinrich-Heine-University Düsseldorf, Düsseldorf, Germany, [3]Centre of Region Haná for Biotechnological and Agricultural Research, Czech Advanced Technology and Research Institute, Palacký University Olomouc, Olomouc, Czechia

WHIRLIES are plant-specific proteins binding to DNA in plastids, mitochondria, and nucleus. They have been identified as significant components of nucleoids in the organelles where they regulate the structure of the nucleoids and diverse DNA-associated processes. WHIRLIES also fulfil roles in the nucleus by interacting with telomers and various transcription factors, among them members of the WRKY family. While most plants have two WHIRLY proteins, additional WHIRLY proteins evolved by gene duplication in some dicot families. All WHIRLY proteins share a conserved WHIRLY domain responsible for ssDNA binding. Structural analyses revealed that WHIRLY proteins form tetramers and higher-order complexes upon binding to DNA. An outstanding feature is the parallel localization of WHIRLY proteins in two or three cell compartments. Because they translocate from organelles to the nucleus, WHIRLY proteins are excellent candidates for transducing signals between organelles and nucleus to allow for coordinated activities of the different genomes. Developmental cues and environmental factors control the expression of WHIRLY genes. Mutants and plants with a reduced abundance of WHIRLY proteins gave insight into their multiple functionalities. In chloroplasts, a reduction of the WHIRLY level leads to changes in replication, transcription, RNA processing, and DNA repair. Furthermore, chloroplast development, ribosome formation, and photosynthesis are impaired in monocots. In mitochondria, a low level of WHIRLIES coincides with a reduced number of cristae and a low rate of respiration. The WHIRLY proteins are involved in the plants' resistance toward abiotic and biotic stress. Plants with low levels of WHIRLIES show reduced responsiveness toward diverse environmental factors, such as light and drought. Consequently, because such plants are impaired in acclimation, they accumulate reactive oxygen species under stress conditions. In contrast, several plant species overexpressing WHIRLIES were shown to have a higher resistance toward stress and pathogen attacks. By their multiple interactions with organelle proteins and nuclear transcription factors maybe a comma can be inserted here? and their participation in organelle–nucleus communication, WHIRLY proteins are proposed to serve plant development and stress resistance by coordinating processes at different levels. It is proposed that the

OPEN ACCESS

Edited by:
Anna N. Stepanova, North Carolina State University, United States

Reviewed by:
Ertugrul Filiz, Duzce University, Turkey
Sujit Roy, University of Burdwan, India

****Correspondence:***
Karin Krupinska
krupinska@bot.uni-kiel.de

Specialty section:
This article was submitted to Plant Physiology, a section of the journal Frontiers in Plant Science

Received: *21 February 2022*
Accepted: *24 March 2022*
Published: *21 April 2022*

Citation:
Krupinska K, Desel C, Frank S and Hensel G (2022) WHIRLIES Are Multifunctional DNA-Binding Proteins With Impact on Plant Development and Stress Resistance. Front. Plant Sci. 13:880423. doi: 10.3389/fpls.2022.880423

multifunctionality of WHIRLY proteins is linked to the plasticity of land plants that develop and function in a continuously changing environment.

Keywords: DNA-binding, nucleoid, stress, development, WHIRLY

INTRODUCTION

Plant-specific WHIRLY proteins received increasing attention in recent years regarding their participation in development and stress resistance. WHIRLY proteins are DNA/RNA-binding proteins sharing a highly conserved WHIRLY DNA-binding domain and are present in all DNA containing compartments of the plant cell. Higher plants share a KGKAAL motif in the WHIRLY domain that mediates the binding to single-stranded DNA (ssDNA). WHIRLY-like proteins with a high structural similarity but lacking the KGKAAL motif are also found in green algae, such as *Ostreococcus taurii* (Krause et al., 2009), *Klebsormidium flaccidum*, a member of the Charophyceae that are the closest relatives of land plants, and in the liverwort *Marchantia polymorpha*, a representative of the most basal plant lineage (Kobayashi et al., 2016). While the algae and Marchantia have only one WHIRLY-like protein, higher plant species have at least two WHIRLY proteins. Both have an organelle targeting peptide at the N-terminus, directing them either to mitochondria, plastids, or both organelles (Krause et al., 2005; Golin et al., 2020).

WHIRLY1 was initially identified as the 24 kDa protein (p24) subunit of a factor binding to the promoter of the *PR-10a* gene of potato and hence named *PR-10a* binding factor 2 (PBF-2; Desveaux et al., 2000). By crystallographic analyses, PBF-2 was shown to be a p24 tetramer having a structure compared with whirligigs (Desveaux et al., 2002). A structural comparison of WHIRLY proteins from potato and Arabidopsis revealed that they share a conserved orientation of different residues providing a platform for binding ssDNA in a non-sequence-specific manner (Cappadocia et al., 2013).

The literature on WHIRLY proteins is relatively diverse, reporting on seemingly unrelated features of the members of the WHIRLY family. To gain a comprehensive understanding of the biological significance of WHIRLIES, this review aims at integrating the different findings on these multifunctional proteins.

CONSERVATION AND VARIATION OF WHIRLY SEQUENCES

Whereas most higher plants have two WHIRLY proteins, *Arabidopsis thaliana* and other members of the Brassicaceae family have three WHIRLIES, of which WHIRLY1 is targeted to chloroplasts, WHIRLY2 to mitochondria, and WHIRLY3 is dually targeted to both organelles (Krause et al., 2005; Golin et al., 2020). In different strawberry genomes, gene duplication has resulted in the presence of up to five *WHIRLY* genes (Hu and Shu, 2021).

The KGKAAL motif shared by all WHIRLY proteins in higher plants was shown to be required for binding to ssDNA and for the hexamerization of the tetramers resulting in hollow sphere structures of 12 nm in diameter (Cappadocia et al., 2012). These sphere-like structures were shown to further assemble into large protein DNA complexes by DNA-dependent joining of adjacent spheres (Cappadocia et al., 2012). Besides the DNA-binding motif (DBM), that is, KGKAAL (or KGKAAM in the case of the rice WHIRLY1), many WHIRLY proteins share a conserved cysteine whose function may be essential for redox regulation (Foyer et al., 2014). Additionally, a putative nuclear localization sequence can be found in the WHIRLY domain of plastid-targeted WHIRLY proteins (**Figure 1**). However, the functionality of this motif is questionable considering that AtWHIRLY:GFP fusion proteins are not imported into the nucleus (Krause et al., 2005).

Sequence comparisons of WHIRLY proteins from different species revealed that WHIRLY proteins possess additional motifs in the variable sequences preceding the WHIRLY domain (Desveaux et al., 2005). This result suggests that the proteins might have different functions in different species. N-terminal polyglutamine stretches shared by several dicot WHIRLY1 proteins (*St*, *Le*, *Vv*), the alternative proline-rich sequences of monocot WHIRLY1 proteins, and the serine-rich sequences of members of the Brassicaceae family were predicted to serve as transactivation motifs (Desveaux et al., 2005). The mutation of different WHIRLY sequences revealed, however, that the proline-rich PRAPP motif of monocot WHIRLY1 proteins rather contributes to the compaction of organellar nucleoids (Oetke et al., 2022).

In the C-terminal variable parts of the WHIRLY sequences, putative autoregulatory domains (pAD) have been identified (Desveaux et al., 2005). In the crystal structure of StWHIRLY1, it is evident that Glu271 and Trp272 in the C-terminal part interact with Lys188 of the WHIRLY domain. Desveaux and Brisson observed that a mutation of Trp272 resulted in a higher ssDNA-binding activity *in vitro*, suggesting that the C-terminal region might interfere with the binding to ssDNA (Desveaux et al., 2005). Sequence alignments show that Lys188 and the C-terminal Glu271 and Trp272 of StWHIRLY1 are highly conserved in all WHIRLY proteins (**Supplementary Figure 1**). Furthermore, many WHIRLY proteins possess a putative copper-binding motif (pCBM) preceding a putative transactivation domain (pAD; **Figure 1**), which has also been found in the prion protein, where it is crucial for the protection of neurons (Prince and Gunson, 1998; Nguyen et al., 2019). The pCBM is a motif shared by all monocot WHIRLIES while it is lacking in the dicot WHIRLY1 sequences. In Arabidopsis, WHIRLY2 and WHIRLY3 share this motif.

The WHIRLY sequences contain several putative sites for posttranslational modifications, including phosphorylation and sumoylation (Grabowski et al., 2008). Matching these predictions,

		OTP	PRAPP	DBM	WHIRLY	Cysteine	pNLS	pCBM	pAD
dicots	AtWHIRLY1	1-53	-	89-94	87-222	159	167-180	-	241-263
	AtWHIRLY3	1-58	-	93-98	91-227	163	171-185	233-240	246-268
	MeWHIRLY1	1-63	-	112-117	110-245	182	190-203	-	264-286
	NtWHIRLY1	1-61	-	95-100	93-228	165	173-186	-	247-269
	SlWHIRLY1	1-63	-	94-99	92-227	164	172-185	-	246-268
	StWHIRLY1	1-54	-	100-105	98-233	170	178-191	-	252-274
monocots	HvWHIRLY1	1-47	56-60	95-100	93-228	165	173-186	234-241	247-267
	OsWHIRLY1	1-51	61-65	100-105	98-233	170	178-191	239-246	252-272
	ZmWHIRLY1	1-44	62-66	94-99	92-227	164	172-185	233-240	246-266
dicots	AtWHIRLY2	1-29	-	62-67	60-195	-	-	201-208	214-238
	MeWHIRLY2	1-36	-	56-61	54-189	-	-	195-202	207-229
	MeWHIRLY3	1-40	-	56-61	54-189	-	-	195-202	207-229
	NtWHIRLY2	1-47	-	68-73	66-201	138	-	207-214	220-241
	SlWHIRLY2	1-47	-	68-73	66-201	-	-	207-214	220-241
	StWHIRLY2	1-44	-	65-70	63-198	-	-	204-211	217-238
monocots	HvWHIRLY2	1-35	-	58-63	56-191	128	-	197-204	210-233
	OsWHIRLY2	1-36	-	54-59	52-187	124	-	193-200	206-228
	ZmWHIRLY2	1-32	-	56-61	54-189	126	-	195-202	208-232

FIGURE 1 | Schematic comparison of motifs in selected WHIRLY proteins. AtWHIRLY1 (*Arabidopsis thaliana*, NP_172893), AtWHIRLY2 (*A. thaliana*, NP_177282.2), AtWHIRLY3 (*A. thaliana*, NP_178377), HvWHIRLY1 (*Hordeum vulgare*, BAJ96655), HvWHIRLY2 (*H. vulgare*, BF627441.2), SlWHIRLY1 (*Solanum lycopersicum*, AFY24240.1), SlWHIRLY2 (*S. lycopersicum*, XP_010313085.1), StWHIRLY1 (*Solanum tuberosum*, NP_001275155.1), StWHIRLY2 (*S. tuberosum*, NP_001275393.1), NtWHIRLY1 (*Nicotiana tabacum*, XP_016453689.1), NtWHIRLY2 (*N. tabacum*, XP_016511175.1), ZmWHIRLY1 (*Zea mays*, NP_001123589.1), ZmWHY2 (*Z. mays*, NP_001152589.2), OsWHIRLY1 (*Oryza sativa*, BAD68418.1), OsWHIRLY2 (*O. sativa*, NP_001045956.1). The WHIRLY domain is colored in light blue. The N-terminal organelle targeting peptides (OTP) are illustrated in grey. Below the scheme, the positions of selected amino acid residues and motifs in different WHIRLIES are listed: the PRAPP motif in yellow, the DNA-binding motif (DBM) and a putative nuclear localization motif (pNLS) in blue, a putative copper-binding motif in purple and a putative transactivation domain (pAD) in green. The organelle targeting peptides (OTP) were predicted with TargetP-2.0 (https://services.healthtech.dtu.dk/service.php?TargetP-2.0) or UniProt, (https://www.uniprot.org/), the putative nuclear localization signal (pNLS) with NLStradamus (http://www.moseslab.csb.utoronto.ca/NLStradamus/) and the putative copper-binding motif (CBM) with Motif Scan (https://myhits.sib.swiss/cgi-bin/motif_scan). The putative autoregulatory domain (pAD) was defined by Desveaux et al. (2005).

several studies report on different molecular weights of WHIRLY proteins. For example, WHIRLY1 has been detected in nuclei prepared from Arabidopsis leaves with a higher molecular weight of 29 kDa instead of 24 kDa (Lin et al., 2020). In tomato nuclei, a WHIRLY1 with the predicted size of the plastid form coexists with an additional form of higher molecular weight (Zhuang et al., 2019). The conditions leading to these putative modifications of WHIRLY1 remain to be determined. In potato, the p24 subunit of PBF, that is, WHIRLY1, was reported to be phosphorylated when binding to the *PR-10a* promoter in the nucleus (Després et al., 1995). Phosphorylation by a homolog of mammalian protein kinase C was essential for transcriptional activation of the *PR-10a* gene by PBF-2 (Subramaniam et al., 1997; Desveaux et al., 2000). Recombinant Arabidopsis WHIRLY2 was shown to be phosphorylated by a mitochondrial kinase (Tarasenko et al., 2012).

SUBCELLULAR TARGETING AND LOCALIZATION OF WHIRLY PROTEINS

For Arabidopsis, it has been shown that WHIRLY1 in fusion with the green fluorescence protein (GFP) is targeted to chloroplasts while WHIRLY2:GFP is targeted to mitochondria (Krause et al., 2005). *In organello*, import assays showed that AtWHIRLY2 is also imported into chloroplasts (Krause et al., 2005). The third WHIRLY protein of *A. thaliana* is imported into both chloroplasts and mitochondria (Golin et al., 2020). When the WHIRLY genes in fusion with fluorescent proteins

were stably overexpressed in Arabidopsis, both WHIRLY1 and WHIRLY3 were exclusively detected in chloroplasts and WHIRLY2 in mitochondria, respectively (Isemer, 2013). The discrepancies observed between the localization of the fusion proteins and the *in organello* import assays might be due to changes in size and conformation resulting from the fusion with the fluorescent protein (Sharma et al., 2018). Neither protoplasts nor transgenic plants were able to show the nuclear localization of any Arabidopsis WHIRLY protein in fusion with a fluorescent protein.

Although WHIRLY1:GFP and WHIRLY3:RFP fusion proteins were both detected in chloroplasts, they showed differences concerning their distribution in the plastids of different tissues (**Figure 2**). While in mesophyll cells, WHIRLY1 and 3 showed both the typical nucleoid association, in epidermal cells, WHIRLY3:RFP fluorescence was also seen in the frequently formed stromules (**Figure 2**). This finding indicates that the gene duplication in Arabidopsis gave rise to a specialization of the different plastid-targeted WHIRLY proteins.

The nuclear localization of WHIRLY1 has so far only been deduced from immunological analysis and Edman degradation protein sequencing of the purified PBF-2 fraction from potato tubers (Desveaux et al., 2000), and from mass spectrometry of proteins binding to single-stranded telomere sequences (Yoo et al., 2007) and of the components of the KPRE binding factor 1 binding to the kinesin gene of Arabidopsis (Xiong et al., 2009). Immunogold analysis with a specific antibody directed toward WHIRLY1 in barley showed that the WHIRLY1 protein is dually located in the same cell's chloroplasts and nucleus (Grabowski et al., 2008). Intriguingly, both isoforms have the same molecular weight as shown by immunoblot analysis of fractions from barley and maize leaves (Grabowski et al., 2008; Zhang et al., 2013), indicating that nuclear WHIRLY1 must first be processed inside chloroplasts. Indeed, in transplastomic tobacco plants synthesizing an HA-tagged form of the Arabidopsis WHIRLY1 protein in chloroplasts, WHIRLY1 was shown to translocate to the nucleus (Isemer et al., 2012b), where it acts as an activator of pathogen response genes as shown before for the potato WHIRLY1, that is, p24 (Desveaux et al., 2000). WHIRLY1 thereby is one of the few plant echoproteins described so far. These are proteins that have the same molecular weight in different compartments (Yogev and Pines, 2011; Krupinska et al., 2020). In Arabidopsis, WHIRLY2 was reported to have a triple localization in chloroplasts, mitochondria, and nucleus, with the nuclear form having a higher molecular weight (Huang et al., 2020). Putative posttranslational modifications associated with multiple compartmentation of the WHIRLY proteins remain to be identified.

SPECIFICITY OF THE BINDING OF WHIRLIES TO DNA

In the nucleus, WHIRLY1 has been found to bind to promoters of genes associated with stress responses and senescence (**Table 1**). In the first report on WHIRLY1, the 24 kDa protein had been identified as a subunit of the transcriptional activator complex PBF-2 binding to the potato *PR-10a* gene promoter (Desveaux et al., 2000). A 30-bp sequence in the promoter containing an inverted repeat sequence required for binding WHIRLY1 to the *PR10-a* promoter, that is, TGACANNNNTGTCA, has been named elicitor response element (ERE). Later on, mutational analyses have shown that the GTCAAAAA/T sequence is sufficient for ERE activity (Desveaux et al., 2004). This so-called PB (PBF-2 binding) element has been detected in the promoters of several defense genes and can overlap with the W-box (T/G)TGAC(C/T) and the TGACG element that are targets of WRKY and TGA family transcription factors, respectively (Desveaux et al., 2005). Furthermore, WHIRLY1 was identified as a repressor of senescence-associated genes, that is, *S40* of barley and *WRKY53* of *A. thaliana* (Miao et al., 2013; Krupinska et al., 2014a). The promoter of *HvS40* contains two ERE-like elements, one of them overlapping with two W-boxes (Krupinska et al., 2014a). In the promoter of *AtWRKY53*, WHIRLY1 was shown to bind to GNNNAAATT plus an AT-rich telomeric repeat-like sequence (Miao et al., 2013). Recent research with tomato plants revealed that WHIRLY1 binds to ERE-like sequences in promoters of genes involved in starch metabolism (Zhuang et al., 2019). By opposite effects on the expression of genes encoding starch degrading and starch synthesizing enzymes, WHIRLY1 contributes to an increase in soluble sugar content coinciding with enhanced chilling resistance (Zhuang et al., 2019). In Arabidopsis, WHIRLY1 was found to attach to telomers consisting of repeated TTTAGGG sequences (Yoo et al., 2007). Together with WHIRLY3, it was detected in a nuclear fraction binding to the promoter of the *KINESIN* gene, thereby repressing transcription (Xiong et al., 2009). The TGAGG(G/A) element in the *KINESIN* promoter (**Table 1**) overlaps with the W-box (T/G)TGAC(C/T) and the TGACG element recognized by the TGA family of transcription factors (Xiong et al., 2009). Overlapping of binding motifs used by WHIRLY1 and other transcription factors is in accordance with the identification of TGA1 and WRKY factors as interacting proteins of WHIRLIES (**Supplementary Table 1**).

Beyond this, the DNA sequences WHIRLIES bind to, share only little similarity (**Table 1**). Several binding motifs overlap with sequences used by other defense-related transcription factors. This might indicate an interplay between the ssDNA-binding WHIRLY and the transcription factors binding to double-stranded DNA (Desveaux et al., 2005; Krupinska et al., 2014a). It is known that several ssDNA-binding proteins regulate gene expression both positively and negatively (Rothman-Denes et al., 1998). Desveaux et al. (2005) proposed that ssDNA-binding proteins might sense twisted DNA produced during transcription and amplify gene transcription by their transactivation domains. Electrophoretic mobility shift assays (EMSA) with the ERE of *StPR-10a* and the ERE-like elements of the *HvS40* promoter revealed that the binding of WHIRLY1 is most robust to ssDNA and that the binding strength differed between coding and non-coding strands (Desveaux et al., 2000; Krupinska et al., 2014a). The *S40* promoter of barley contains two ERE-like elements in the promotor, which were shown

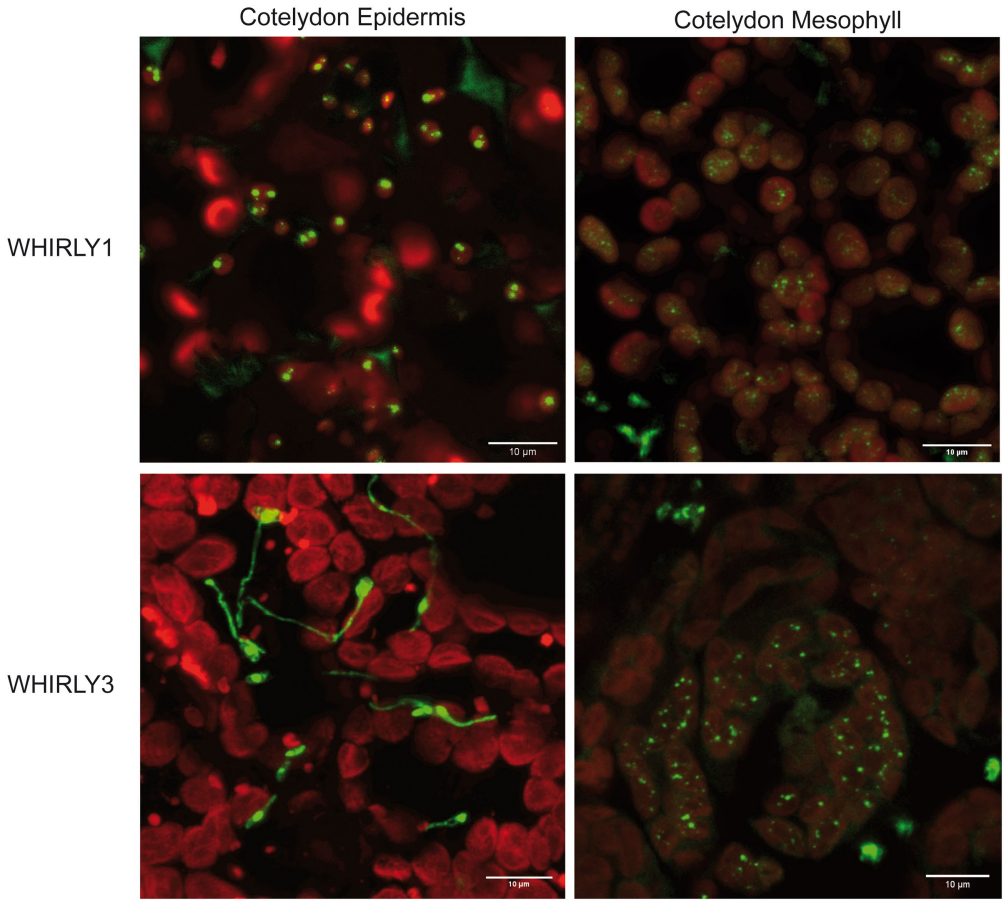

FIGURE 2 | Detection of WHIRLY1:GFP and WHIRLY3:RFP fusion proteins in epidermal cells of the cotyledons of stably transformed Arabidopsis plants. The constructs were overexpressed under the control of the CaMV *35S* promoter. The constructs were overexpressed under the control of the CaMV *35S* promoter. Leaves were imbedded in PBS:glycerol (1:1) without fixation and analyzed by a LEICA SP5 laser scanning microscope and a HCX PL Apo 63x/1.2 W objective. Sequential scans per frame for GFP [Ex 488 nm (6%), Em 510–550 nm], mRFP [Ex 543nm (14%), Em 580–610nm] and chlorophyll [Ex 633 (5%), Em 690–750 nm] were carried out. Chlorophyll fluorescence is shown in red while signals of WHIRLY1:GFP and WHIRLY3:RFP displayed both in green. A projection out of five optical layers representing 3 µm in z-direction are created by the LAS X software. The bars represent 10 µm each.

TABLE 1 | Target sequences of WHIRLY proteins in different plant species.

WHIRLY	Species	Target gene	Sequence	Method	References
WHIRLY1	*Solanum tuberosum*	*PR10-a*	ERE: TGACANNNNTGTCA	EMSA	Desveaux et al., 2000
WHIRLY1	*Solanum tuberosum*	*PR10-a*	PB element GTCAAAAA/T	ChIP	Desveaux et al., 2004
WHIRLY1	*Arabidopsis thaliana*	*Telomer*	TTTAGGG	EMSA	Yoo et al., 2007
WHIRLY1 WHIRLY3	*Arabidopsis thaliana*	*KINESIN KP1*	Promoter element KPRE including TGAGG(G/A)	ChIP	Xiong et al., 2009
WHIRLY1	*Arabidopsis thaliana*	*WRKY53*	GNNNAAATT plus an AT-rich telomeric repeat-like sequence	ChIP	Huang et al., 2018a
WHIRLY1	*Hordeum vulgare*	*HvS40*	ERE-like sequences and **W-boxes:** **TGTCA**GAAAT**GGTCAA** **GTCAA**ATAAT**GGTCAA**	EMSA	Krupinska et al., 2014a
WHIRLY1	*Lycopersicum esculentum*	*SlSA2*, starch synthesis-related gene	ERE	ChIP	Zhuang et al., 2019
WHIRLY1	*Lycopersicum esculentum*	*SlAMY3*, α-amylase	ERE-like	ChIP	Zhuang et al., 2019
WHIRLY1	*Lycopersicum esculentum*	*HSP21.5A*	ERE-like	ChIP	Zhuang et al., 2020a
WHIRLY1	*Lycopersicum esculentum*	*psbA*	TGACACGTGGCAAT GTTACCCT	Yeast 1HLUC expression Yeast 1H	Zhuang et al., 2019

to bind WHIRLY1 by electrophoretic mobility shift assays. While in senescent leaves a complex was formed only with the first motif, in non-senescent leaves a complex was formed with the second motif (Krupinska et al., 2014a). The results indicate that at least WHIRLY1 can function as repressor as well as activator of nuclear genes. Its activity might depend on interactions with other transcription factors, such as the WRKY factors binding to W-boxes included in the EREs (Ciolkowski et al., 2008).

In the organelles, the binding of WHIRLIES to DNA is somewhat independent of the DNA sequence as shown by immunoprecipitation with plastid DNA (Prikryl et al., 2008) and mitochondrial DNA (Maréchal et al., 2008; Tarasenko et al., 2012). An exception reported for tomato is its binding to the GTTACCCT sequence in the *psbA* promoter, which is proposed to ensure high expression of the *psbA* gene during chilling (Zhuang et al., 2019).

WHIRLIES CONTROL CHLOROPLAST DEVELOPMENT, SENESCENCE, EMBRYO DEVELOPMENT, AND GERMINATION

Arabidopsis T-DNA insertion mutants *why1* and *why2* as well as the tilling mutant of *WHIRLY3 (tilwhy3)*, do not show apparent changes in development (Yoo et al., 2007; Maréchal et al., 2008, 2009). Only a few plants of the progeny of the *why1tilwhy3* double mutant show variegated leaves indicating a disturbance of chloroplast development (Maréchal et al., 2009). Although several dicot species have been employed for silencing or overexpression of *WHIRLY* genes (**Table 2**), none of these studies reported a disturbance of chloroplast development.

In contrast, *ZmWHIRLY1* transposon mutants of *Zea mays* have ivory or albino leaves and die after developing three or four leaves (Prikryl et al., 2008). Biochemical analyses revealed that impaired ribosome formation and disturbed splicing might cause impaired chloroplast development (Prikryl et al., 2008). Following the positive impact of WHIRLY1 on chloroplast development in maize, a barley line with a low abundance of WHIRLY1 was shown to be delayed in the formation of ribosomes and in chloroplast development (Krupinska et al., 2019).

In many plants, including Arabidopsis, mutations with such a profound impact on plastid ribosome formation preventing chloroplast development would cause embryo lethality (Belcher et al., 2015). However, in cereals with large grain reserves supporting heterotrophic growth, the molecular defects of such mutations can be studied. Intriguingly, *ZmWHIRLY1* was shown to be identical with the gene *EMBRYO DEFECTIVE 16*, whose mutation caused embryo lethality (Zhang et al., 2013). The authors showed that the consequences of the *ZmWHIRLY1* mutation depend on the genetic background of the different maize varieties. A cross between *Zmwhy1* and *Zmemb16* resulted in defective embryos and albino seedlings in the F1 progeny (Zhang et al., 2013). The authors hypothesized that the negative impact of WHIRLY1 deficiency on embryogenesis is related to impaired plastid translation. In some genetic backgrounds of maize, embryo lethality usually resulting from impaired plastid translation might be suppressed.

It is possible that Arabidopsis mutants neither show a chloroplast development phenotype nor an embryo development phenotype because another WHIRLY protein might replace the mutated one. Indeed, due to the dual targeting of AtWHIRLY3 to chloroplasts and mitochondria (Golin et al., 2020), it is likely that WHIRLY3 can replace both WHIRLY1 and WHIRLY2. The *AtWHIRLY3* gene is apparently indispensable because there is no report on a knockout mutant of *AtWHIRLY3*. The truncated WHIRLY3 in the TILLING *why3* mutant is terminated after amino acid 98 and therefore still contains the DNA-binding motif KGKAAL (**Supplementary Figure 2**). The "*why1why3*" double mutant for *AtWHIRLY1* and *AtWHIRLY3*, which has been frequently used in studies on the WHIRLY proteins, was prepared by crossing the T-DNA insertion mutant *why1-1* and the tilling mutant *why3* from the Arabidopsis TILLING project (ATP; Till et al., 2003; Maréchal et al., 2009) and should be precisely termed *why1tilwhy3*.

So far, there is no evidence for a mutant in which all WHIRLY genes are knocked out in any plant species. Targeted mutation by CRISPR/Cas9 technology did not succeed in the mutation of the *AtWHIRLY3* gene while mutation of *AtWHIRLY1* and *AtWHIRLY2* was possible (Hensel, unpublished). These mutants show no obvious chloroplast development defects (Krupinska et al., unpublished). Considering that single mutants and even Arabidopsis double mutants can still perform essential functions shared by all WHIRLY proteins, it is reasonable to expect that all WHIRLY proteins can locate to all three DNA containing compartments of the cell.

Chloroplasts, besides mitochondria, are the powerhouses of plant cells whose operation needs to be tightly controlled. It is well-known that disturbances in chloroplast development have consequences for retrograde signaling altering nuclear gene expression during all phases of plant development (Pfannschmidt and Munné-Bosch, 2013; Chan et al., 2016). Due to the high susceptibility of the photosynthetic apparatus to environmental cues, coordination of plastidic and nuclear activities is of pivotal importance. During leaf senescence, chloroplasts are dismantled, and nutrients must be efficiently remobilized (Pfannschmidt and Munné-Bosch, 2013; Krieger-Liszkay et al., 2019). Senescence processes may be prematurely induced and accelerated by environmental factors including light, reduced water supply, and hormones known to accumulate during stress and senescence, that is, abscisic acid, jasmonic acid, and salicylic acid. While light accelerates senescence in barley wild-type plants, the RNAi-mediated *WHIRLY1* knockdown plants are compromised in response to light, albeit the senescence-associated hormones have high levels in the leaves of these plants (Kucharewicz et al., 2017). This result is in accordance with the observation that the *why1* mutant of Arabidopsis is insensitive to abscisic acid (Isemer et al., 2012a). Taken together, both studies showed that WHIRLY1 enhances the responsiveness to ABA in both dicot and monocot plants. With regard to this feature shared by WHIRLY1 of monocots and dicots, it is surprising that senescence is promoted in the *why1* mutant of *A. thaliana* (Miao et al., 2013). The

TABLE 2 | Phenotypes of plants with altered expression of WHIRLY genes, oe, overexpression, RNAi, RNA inference.

Species	Genetic modification	Development	Stress resistance	References
Arabidopsis thaliana	*why1* T-DNA mutant	Accelerated senescence		Miao et al., 2013
Arabidopsis thaliana	*why1 tilwhy3*	Leaf variegation		Maréchal et al., 2009
Arabidopsis thaliana	*tilwhy1* mutants		Reduced resistance to *Peronospora parasitica*	Desveaux et al., 2004
Arabidopsis thaliana	oe*WHIRLY1*	No phenotype	Hypersensitive to ABA	Isemer et al., 2012a
Arabidopsis thaliana	oe*WHIRLY2*	Accelerated senescence, reduced pollen growth		Maréchal et al., 2008; Cai et al., 2015
Arabidopsis thaliana	*why2 T-DNA mutant*	Reduced germination		Golin et al., 2020
Hordeum vulgare	RNAi *WHIRLY1* knockdown	Delay of chloroplast development and senescence	Reduced resistance to high light, enhanced drought resistance, reduced resistance toward powdery mildew (Hensel et al., unpublished)	Janack et al., 2016; Kucharewicz et al., 2017; Swida-Barteczka et al., 2018; Krupinska et al., 2019
Hordeum vulgare	oe*WHIRLY1*	Delay of senescence	Enhanced resistance toward powdery mildew	Krupinska, unpublished
Manihot esculenta	oe*WHIRLY1-3*		Enhanced resistance toward cassava bacterial blight	Liu et al., 2018
Manihot esculenta	Virus-induced silencing of *WHIRLY1-3*		Higher sensitivity toward cassava bacterial blight	Liu et al., 2018
Manihot esculenta	Silencing of *WHIRLY1* expression		Reduced drought resistance	Yan et al., 2020
Nicotiana tabacum	oe*SlWHIRLY2*		Enhanced resistance toward drought and *Pseudomonas solanacearum*	Zhao et al., 2018
Solanum lycopersicum	oe*SlWHIRLY1*		Enhanced chilling tolerance by upregulated expression of *RBCS1*	Zhuang et al., 2019, 2020b
Solanum lycopersicum	oe*SlWHIRLY1*		Enhanced thermotolerance by regulation of HSP21.5A expression	Zhuang et al., 2020a
Solanum lycopersicum	RNAi *SlWHIRLY1*		Reduced thermotolerance	Zhuang et al., 2020a
Solanum lycopersicum	RNAi *SlWHIRLY1*		Enhanced chilling sensitivity	Zhuang et al., 2019
Solanum lycopersicum	RNAi *SlWHIRLY2*		Reduced drought resistance	Meng et al., 2020
Zea mays	*why1* Transposon mutant	Inhibition of chloroplast development		Prikryl et al., 2008

rapid senescence in the latter has been assigned to the repressing effect of AtWHIRLY1 on the expression of *WRKY33* and *WRKY53* encoding senescence promoting transcription factors (Miao et al., 2013).

While WHIRLY1 is involved in chloroplast biogenesis and senescence, WHIRLY2 has been reported to control germination. Although the development of vegetative parts is not affected in the mature *Atwhy2* T-DNA insertion mutant, seed germination is compromised in the mutant (Golin et al., 2020). In line with this observation, the expression level of *AtWHIRLY2* in seeds is higher than that of *AtWHIRLY3*, whereas the expression of the two genes does not show differences in the vegetative parts of mature wild-type plants. The differential expression of *AtWHIRLY2* and *AtWHIRLY3* predetermines the possibility of a functional replacement of AtWHIRLY2 by AtWHIRLY3 (Golin et al., 2020).

WHIRLY PROTEINS ARE ARCHITECTURAL ORGANELLE NUCLEOID-ASSOCIATED PROTEINS

After HvWHIRLY1 was shown to be located in chloroplasts and the nucleus of the same cell (Grabowski et al., 2008), it had been suggested that transcription factors, such as WHIRLIES, might be stored in chloroplasts or mitochondria. They were proposed to rapidly translocate to the nucleus upon certain stimuli (Krause and Krupinska, 2009). However, analyses of organelle structure and nucleoid morphology in plants with reduced abundance of WHIRLY proteins clearly showed that the proteins also have essential organellar functions related to their binding to ssDNA and RNA (Prikryl et al., 2008; Melonek et al., 2010).

WHIRLY2 promotes DNA compaction in Arabidopsis mitochondria, as evident in transmission electron microscopic images of the *why2* mutant mitochondria containing largely unpacked DNA (Golin et al., 2020). Furthermore, WHIRLY2 was found together with another abundant ssDNA-binding protein (ODB1 = RAD52) in large DNA- and RNA-containing complexes likely deriving from nucleoids (**Table 3**). Both proteins were shown to interact *via* mitochondrial DNA (Janicka et al., 2012). The study's authors discussed that WHIRLY2, together with ODB1, cover the mitochondrial DNA (mtDNA) at sites where ssDNA is formed during the division of the organelles. It remained unknown whether ODB1 and WHIRLY2 compete or cooperate in recruiting different factors to ssDNA regions (Janicka et al., 2012).

In chloroplasts, WHIRLIES have been identified as significant components of the transcriptionally active chromosome (TAC;

Pfalz et al., 2006; Melonek et al., 2010; Majeran et al., 2012). Therefore, WHIRLY1 and WHIRLY3 are also called pTAC1 and pTAC11, respectively. TAC is used as a term used for nucleoids when biochemical properties rather than structural aspects are in the focus of the investigations (Krause and Krupinska, 2017). Nucleoids were proposed to be multifunctional platforms serving various DNA-associated processes, that is, replication, repair/recombination, and transcription (Sakai et al., 2004; Kobayashi et al., 2016). Moreover, their complex proteomes suggest that they serve as a docking station for proteins with key functions in metabolic processes and signaling (Melonek et al., 2016).

While WHIRLY1 and WHIRLY3 in Arabidopsis plastids have no noticeable impact on nucleoid morphology, chloroplasts of transgenic barley plants with an RNAi-mediated knockdown of *HvWHIRLY1* contain unpacked plastid DNA (ptDNA) besides a few regularly packed nucleoids (Krupinska et al., 2014b). The staining of DNA in the ivory leaves of the transposon insertion mutant *Zmwhy1-1* revealed that the ptDNA is detectable in patches without a prominent characteristic nucleoid structure (Prikryl et al., 2008; **Figure 3**). For comparison, DNA was stained in ivory leaves of other non-photosynthetic maize mutants with transposons inserted in genes encoding other TAC proteins, that is, pTAC2 (PAP2), pTAC10 (PAP3), and pTAC12 (PAP5; Williams-Carrier et al., 2014). In contrast to the morphologically of unorganized nucleoids of the *Zmwhy1-1* mutant, nucleoids of the *pap* mutants are discernible as distinct punctate speckles that form structures resembling a necklace of pearls or rings associated with the inner envelope of plastids. Similar structures have also been observed in undifferentiated plastids of wild-type meristematic cells and albino leaf sections of the barley mutant *albostrians* (Powikrowska et al., 2014).

WHIRLY1 proteins of dicot species and WHIRLY2 proteins of monocot and dicot species did not affect nucleoid compaction in *Escherichia coli* (Oetke et al., 2022). In accordance with this finding, a mutation of the conserved second lysine of the KGKAAL motif did not affect the compactness of nucleoids in *E. coli*. Surprisingly, the PRAPP motif that has been identified in monocot WHIRLY1 proteins promoted compaction in *E. coli* but not in the chloroplasts of transgenic Arabidopsis plants with PRAPP inserted into *AtWHIRLY1* (Oetke et al., 2022).

TABLE 3 | Proteins co-immunoprecipitated, pulled-down, or co-purified with WHIRLIES in protein complexes of plastids or mitochondria.

	Full name and synonymous names	WHIRLIES	Organelle protein complex	Function	References
BCCP1	Biotin carboxyl carrier protein 1 of acetyl-CoA carboxylase	WHIRLY3	Nucleoid	Fatty acid biosynthesis	Phinney and Thelen, 2005
CLPC1	CLP protease chaperon 1	WHIRLY3	Nucleoid	Proteolysis stress	Zheng et al., 2002; Olinares et al., 2011
CRS1	Chloroplast RNA Splicing 1	WHIRLY1	Ribonucleoprotein complex	Group IIA intron splicing factor	Till et al., 2001; Prikryl et al., 2008
2CPA	2-Cys-Peroxiredoxin A	WHIRLY1 WHIRLY3		Redox sensing and redox regulation	Liebthal et al., 2020; Telman et al., 2020
FIB1a	Fibrillin 1a	WHIRLY3	Network around plastoglobuli, interaction with fibrillin 1b indicative of oligomerization	Involved in partitioning of proteins in plastids protection against photodamage, stress resistance	Singh and McNellis, 2011; Gamez-Arjona et al., 2014
FIB4	Fibrillin 4	WHIRLY3	Interaction with plastoglobules, LHC, photosystem II, thylakoids	Development of plastoglobules, resistance to multiple stresses	Singh et al., 2010
pTAC4	Plastid transcriptionally active chromosome 4	WHIRLY3	Nucleoid/TAC	Chloroplast development	Kroll et al., 2001
PPR4	VIPP, vesicle inducing plastid protein Plastid pentatricopeptide repeat 4	WHIRLY3	Ribonucleoprotein complex	*rps12* trans-splicing	Xu et al., 2019
LHCA1	Light-Harvesting complex of photosystem I, subunit 1	WHIRLY1	Photosystem I	Photosynthesis, light adaptation	Huang et al., 2017
LHCB5	Light-Harvesting complex of photosystem II, subunit 5 CP26	WHIRLY3	Photosystem II	Photosynthesis, tolerance to drought, oxidative stress protection	Xu et al., 2012; Chen et al., 2018
ODB1	Organelle DNA-binding protein 1, RAD52-1	WHIRLY2	Large nucleoprotein complexes, likely nucleoids	Recombination and repair of mitochondrial DNA	Janicka et al., 2012
PetA	Cytochrome f	WHIRLY3	Cytochrome b6f complex	Photosynthesis, electron transport	
PRPS5	Plastid ribosomal protein S5, EMB3113	WHIRLY3	Essential component of plastid ribosome	16S rRNA processing, translation cold stress tolerance embryo development	Bryant et al., 2011; Zhang et al., 2016
PRPS3	Plastid ribosomal protein S3	WHIRLY3	Essential component of plastid ribosome	Translation affects leaf shape	Fleischmann et al., 2011
RECA	Recombinase A	WHIRLY2		Mitochondrial DNA recombination	Meng et al., 2020
RNaseH	Ribonuclease H	WHIRLY1 WHIRLY3	DNA gyrase complex	Maintenance of ptDNA, removal of R-loops	Yang et al., 2017

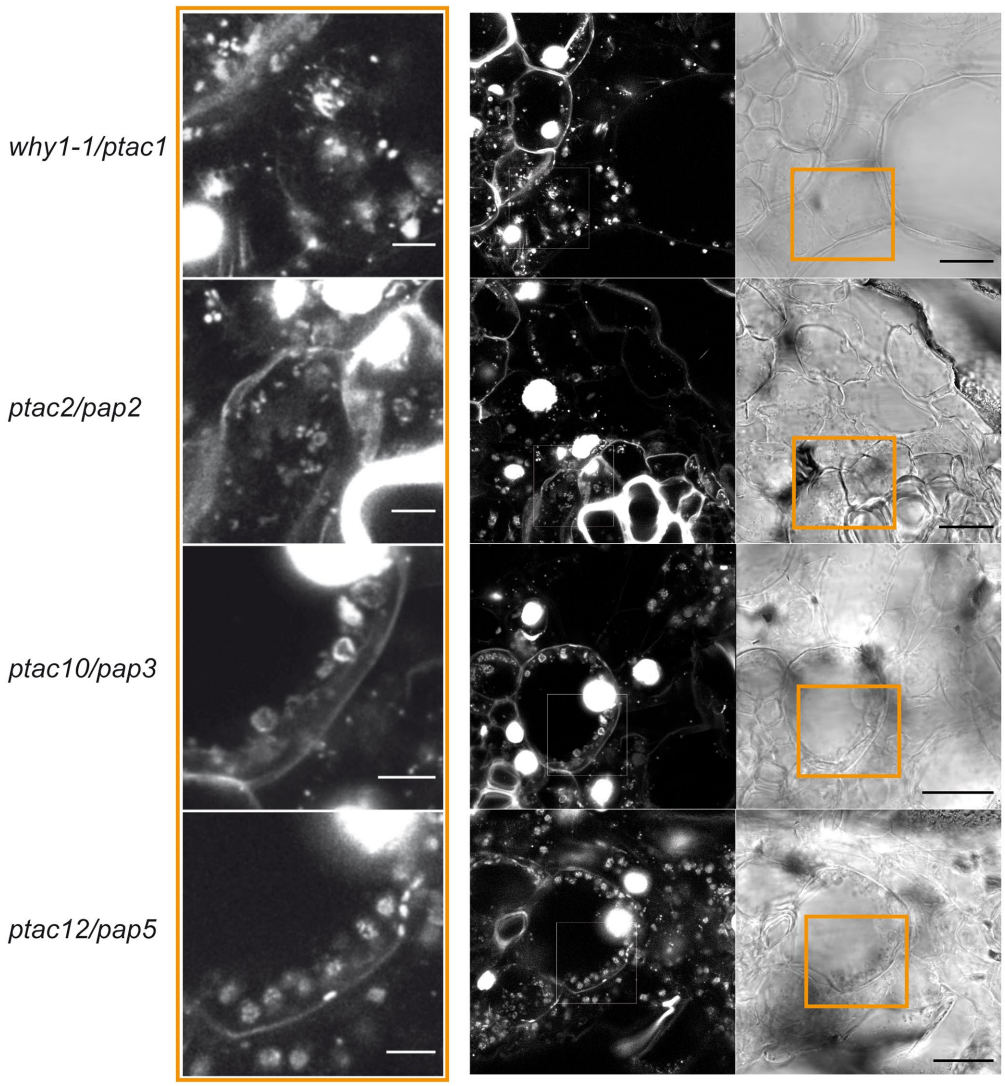

FIGURE 3 | Morphology of nucleoids in sections from albino leaves of maize transposon mutants. The *Zmwhy1*-1 mutant (Prikryl et al., 2008) is compared with selected mutants lacking PEP-associated proteins (PAP; Williams-Carrier et al., 2014). All proteins are transcriptionally active chromosomes (TAC) components and hence have pTAC names. DNA was stained by SYBR GREEN as described (Krupinska et al., 2014b). Bars in low magnification images represent 20 μm, in the higher magnifications on the left, bars represent 5 μm. Frames in the transmission images on the right indicate the sections shown in the high magnification images on the left.

Taken together, there is no evidence for compaction of plastid nucleoids by WHIRLY proteins in Arabidopsis. Alternatively, plastid nucleoid compaction might be mediated by SWIB proteins in Arabidopsis (Melonek et al., 2012) and by sulfite reductase containing a DNA compacting motif in tobacco (Cannon et al., 1999).

It is possible that the reduced compactness of nucleoids as observed in barley *WHIRLY1* knockdown plants (Krupinska et al., 2014b) and the maize *why1* mutants (**Figure 3**), but not in the *why* mutants of Arabidopsis (Oetke et al., 2022), has negative consequences for chloroplast development by impairing ribosome formation. Following the idea that nucleoids serve as platforms for the formation of ribosomes (Bohne, 2014), several components of ribosomes have been detected in the nucleoid proteomes (Melonek et al., 2016). Hence, it is conceivable that the deficiency in ribosome formation as observed in maize plastids is a consequence of uncompacted nucleoid DNA (**Figure 3**). A coincidence of unorganized nucleoids and reduced levels of plastid ribosomal RNAs indicating a reduced ribosome content was also observed in the barley *WHIRLY1*-RNAi plants with a low abundance of WHIRLY1 (Krupinska et al., 2014b, 2019).

Concerning its nucleoid compacting activity in monocot chloroplasts, WHIRLY1 belongs to the group of abundant architectural nucleoid-associated proteins (NAPs) that in bacteria have also been termed histone-like proteins (HPL; Luijsterburg et al., 2006, 2008; Dillon and Dorman, 2010). Bacterial NAPs with high abundance bind to DNA with low specificity and

protect DNA by coating/compacting in response to environmental stress (Holowka and Zakrzewska-Czerwinska, 2020). A prominent example is the HU protein which binds sequence independently to DNA and regulates global gene expression by nucleoid remodeling (Remesh et al., 2020). Indeed, several parallels between the properties of WHIRLY proteins and the bacterial HU proteins are apparent and have been discussed by Prikryl et al. (2008): both proteins bind preferentially to ssDNA in addition to RNA and are involved in recombination and repair of DNA.

The structure of the WHIRLY 24-mer shares similarity with that of the oligomeric bacterial protein Dps (DNA-binding protein of starved cells), whose gene is highly expressed during stress and which is responsible for the compaction of nucleoids in the stationary phase and during stress (Dame et al., 2020; Holowka and Zakrzewska-Czerwinska, 2020). Both, Dps and WHIRLY proteins bind non-specifically to DNA *via* lysine residues through a cooperative mechanism in which supramolecular nucleoprotein complexes are formed (Wolf et al., 1999; Cappadocia et al., 2012). Protection of DNA during stress is achieved by NAP-mediated coating and condensing of the nucleoid, thereby creating a selective physical barrier separating the DNA from the surrounding matrix (Holowka and Zakrzewska-Czerwinska, 2020). Experimentally, it has been demonstrated that the condensation of nucleoids by Dps does not affect the access of RNA polymerase (RNAP) to DNA while other proteins are prevented from interacting with DNA (Janissen et al., 2018; Abbondanzieri and Meyer, 2019). Already as early as 1984, it had been suggested that nucleoids are a membrane-less microcompartment formed by phase separation (Valkenburg and Woldringh, 1984; Odijk, 1998). It is self-evident that abundant NAPs, such as HU, Dps, and likely WHIRLIES, are the building blocks of nucleoids. A putative cage-forming activity of WHIRLY1 in plastid nucleoids is in accordance with peripheral localization of WHIRLY1 in the nucleoids (Melonek et al., 2010; Krupinska et al., 2013).

WHIRLIES IMPACT PHOTOSYNTHESIS AND RESPIRATION

Photosynthesis in chloroplasts and respiration in mitochondria provide the energy for plant development and growth. It has been reported that the expression levels of *AtWHIRLY1* and *AtWHIRLY3* increased after the application of inhibitors affecting these processes (Karpinska et al., 2017), indicating that WHIRLY proteins are required for efficient photosynthesis and respiration and that a reduction of WHIRLIES could reduce energy production. Furthermore, *WHIRLY2* expression was also shown to significantly increase after treating Arabidopsis seedlings with the translation inhibitor spectinomycin, preventing chloroplast development (Börner and Krupinska, unpublished results).

The characterization of the WHIRLY1 deficient barley plants revealed that the delay in chloroplast development coincides with disturbances in the structure of prolamellar bodies and thylakoids (**Figure 4A**). Prolamellar bodies are clearly discernible in etioplasts of WHIRLY1 deficient plants grown in darkness. However, the organization of the tubular structures is less regular than in wild-type etioplasts. In chloroplasts of the WHIRLY1 deficient plants, the organization of thylakoid membranes appears to be less regular, with grana stacks having more various heights than in wild-type chloroplasts (Saeid-Nia et al., 2022). While during growth in a daily light–dark cycle, the major part of the thylakoids stays stacked even at high irradiance (Saeid-Nia and Krupinska, unpublished), during continuous illumination at high irradiance, thylakoids of WHIRLY deficient chloroplasts get swollen (**Figure 4B**). This swelling indicates that the light stress effects accumulating during continuous illumination can be minimized by WHIRLY1.

The structural abnormalities of the thylakoid membranes observed in WHIRLY1 deficient barley plants indicate that WHIRLY1 is required for an accurate assembly of the photosynthetic apparatus. During the development of primary foliage leaves of barley with reduced abundance of WHIRLY1, chlorophyll content and the efficiency of photosystem II measured by chlorophyll fluorescence increased much slower than in wild-type leaves (Krupinska et al., 2019). When the plants were grown in continuous light of different irradiances, chlorophyll levels were severely reduced in the WHIRLY1 deficient plants grown at high irradiance. The irradiance

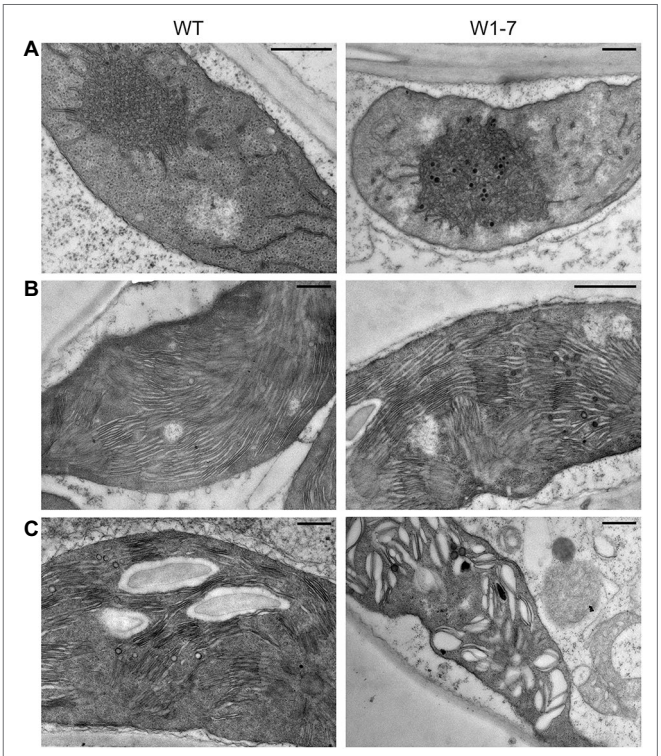

FIGURE 4 | Impact of WHIRLY1 on the structure of prolamellar bodies and prothylakoids of etioplasts **(A)** and thylakoids of barley chloroplasts **(B,C)**. Ultrathin sections were prepared from primary foliage leaves of RNAi-W1-7 and wild-type plants. For analysis of etioplast structure, plants were grown in darkness for 8 days. For studies of chloroplasts, plants were grown in continuous light of either 120 **(B)** or 320 $\mu mol\, m^{-2} s^{-1}$ **(C)**. Ultrastructural analyses were performed as described (Golin et al., 2020). Bars represent 500 nm.

dependent decline in the chlorophyll content coincided with the production of reactive oxygen species (ROS) indicating that the photosynthetic apparatus cannot be adjusted to the prevailing light conditions when the abundance of WHIRLY1 is low (Swida-Barteczka et al., 2018). Additional investigations on light acclimation revealed that the WHIRLY1 deficient barley plants show neither the typical high light-induced increase in photosynthesis nor leaf thickness as observed in wild-type plants (Saeid Nia et al., 2022). Basically, the results of these studies indicate that the WHIRLY1 deficient plants are either compromised in sensing light quantity or in reacting to a change in light intensity. Considering that the WHIRLY1 deficient plants have a lower chlorophyll a/b ratio, they are rather compromised in the measurement of light intensity, than in responding to light intensity by changes in the composition of the photosynthetic apparatus (Krupinska et al., 2019).

Curiously, WHIRLY1 deficient barley plants were reported to maintain higher assimilation rates under limiting nitrogen than wild-type plants (Comadira et al., 2015). However, they are compromised in photosynthetic performance when grown in soil (Krupinska et al., 2019; Saeid Nia et al., 2022). This finding suggests that WHIRLY1 is not only important for acclimation to light, but also to nutrient deficiency. Accordingly, the expression of *HvWHIRLY1* is upregulated in response to nitrogen deficiency (Comadira et al., 2015).

So far, the impact of WHIRLY2 on the structure and function of mitochondria could be analyzed in the *why2* T-DNA insertion mutant of *A. thaliana* (Golin et al., 2020) and tomato plants (Meng et al., 2020). Mitochondria of the Arabidopsis mutant have a lower number of cristae and a low electron density as analyzed by transmission electron microscopy. The structural changes correlate with reduced respiration activity (Golin et al., 2020). Intriguingly, the overexpression of *AtWHIRLY2* negatively affected the morphology and functionality of mitochondria (Maréchal et al., 2008). Overexpression of *AtWHIRLY2* under control of a pollen-specific promoter led to slower pollen tube growth due to an increase in ROS and a decrease in ATP production (Cai et al., 2015). Tomato plants with a reduced accumulation of WHIRLY2 were reported to have lower expression levels of mitochondrial genes encoding components of respiratory complexes, lower alternative oxidase activity, and enhanced ROS levels (Meng et al., 2020). It seems that either a reduced or an increased abundance of WHIRLY2 has detrimental effects on mitochondrial structure and function. An optimal abundance of WHIRLY2 in mitochondria seems to be critical for both structure and function, that is, respiration and ATP production.

ORGANELLE PROTEINS INTERACTING WITH WHIRLIES

To learn about the multiple functions of WHIRLIES, it is helpful to know more about their interactions with other proteins. About half of the proteins experimentally shown to interact with one or more WHIRLIES (**Supplementary Table 1**) are organellar proteins, with the majority of these being active in the plastids (**Table 3**). Concerning the localization of WHIRLIES in organelle nucleoids, the identification of further nucleoid-associated proteins (NAPs) as interacting proteins is foreseeable. Surprisingly, however, only one of the 12 proteins found to co-immunoprecipitate with an AtWHIRLY3-specific antibody (Isemer, 2013) is a NAP, that is, pTAC4. The protein that has also been named vesicle inducing plastid protein (VIPP1), is essential for the formation of thylakoids during chloroplast development (Kroll et al., 2001).

Furthermore, WHIRLIES were found to interact with the two ribosomal proteins, PRPS5 and PRPS3, also located in nucleoids (Melonek et al., 2016). Besides, WHIRLY3 interacts with BCCP1, a subunit of acetyl CoA carboxylase (ACCase) that also belong to the subgroup of "unexpected" nucleoid-associated proteins that do not have a known function associated with DNA (Melonek et al., 2016). However, in the protein repertoire of a fraction enriched in ACCase from chloroplasts, among 179 proteins, 35 proteins were predicted to be nucleoid-associated proteins (Phinney and Thelen, 2005), indicating a close link between nucleoids and biosynthetic activities in chloroplasts (Melonek et al., 2016). Another "unexpected" nucleoid protein that interacts with WHIRLY3 is the chaperone of the CLP protease, that is, CLPC1. Furthermore, WHIRLIES in chloroplasts were also found to interact with RNA-binding proteins, that is, CRS1, PPR4. WHIRLY1/3 proteins were identified by mass spectrometry in complexes that co-immunoprecipitated with Arabidopsis chloroplast RNase H1 (Yang et al., 2017). The interaction with RNase H1 was mediated by DNA and was proposed to be essential for protecting DNA by WHIRLIES (Wang et al., 2021).

With regard to the impact of WHIRLIES on chloroplast structure (see above), it is not surprising that two fibrillins, FIB1a and FIB4, are among the interacting proteins found by co-immunoprecipitation with a WHIRLY3 specific antibody. Fibrillins form a network around plastoglobules and partition plastid proteins (Singh and McNellis, 2011; Gamez-Arjona et al., 2014; Torres-Romero et al., 2022).

Furthermore, WHIRLIES in chloroplasts were found to interact with several proteins of the photosynthetic apparatus, that is, LHCA1 that has been co-immunoprecipitated with AtWHIRLY1 (Huang et al., 2017) and LHCB5 as well as cytochrome f (PetA) that have been co-immunoprecipitated with AtWHIRLY3 (Isemer, 2013). These interactions are in accordance with the impact of HvWHIRLY1 on thylakoid membrane structure (**Figures 4B,C**) and photosynthetic function (Krupinska et al., 2019). The photosynthetic apparatus undergoes redox changes in response to the environment that are signaled to the nucleus (Fey et al., 2005). The interaction of WHIRLY1 with 2-cysteine peroxiredoxin (2CPA) might be linked to redox sensing and signaling (Liebthal et al., 2020).

In mitochondria of tomato, WHIRLY2 was found to interact with RECA2, a subunit of a mitochondrial recombinase (Meng et al., 2020). Arabidopsis WHIRLY2 has been purified with the ssDNA-binding DNA-binding protein ODB1 (RAD52-1), which has a dual localization in the nucleus (Janicka et al.,

2012). Both interactions might be necessary for maintaining and repairing mitochondrial DNA.

Two proteins that were shown to interact with WHIRLY3 in yeast two-hybrid assays are enzymes: one is an isomer of mitochondrial cysteine synthase, and the second is aconitase 1 (Isemer, 2013), which belongs to the 4Fe-4S cluster enzymes and catalyzes the isomerization of citrate to isocitrate in mitochondria (Przybyla-Toscano et al., 2021). For rice aconitase, a role in iron sensing and regulation of Fe deficiency-inducible genes has been reported (Senoura et al., 2020).

IMPACT OF WHIRLIES ON ORGANELLE DNA-ASSOCIATED ACTIVITIES

Concerning their abundance in nucleoids and their binding affinities to DNA and RNA as well as the reported interactions with nucleoid-associated proteins (**Table 3**), WHIRLIES have an impact on the multiple processes associated with organelle DNA, that is, replication, recombination, and maintenance of genome stability, transcription and associated posttranscriptional processes. The effects of WHIRLIES on these processes were mainly investigated with the Arabidopsis *why1tilwhy3* mutant, maize *why1* mutants, and barley plants with a knockdown of *WHIRLY*.

Replication

Barley plants with an RNAi-mediated knockdown of *WHIRLY1* contained higher levels of ptDNA in their leaves (Krupinska et al., 2014b). This result coincided with a higher expression of plastid–mitochondria targeted plant organelle DNA polymerase (POP; Krupinska et al., 2014b), suggesting that WHIRLY1 might have a repressing effect on the expression of the POP encoding gene. In contrast, ptDNA levels are not altered in *why1* mutants of maize (Prikryl et al., 2008) and Arabidopsis (Maréchal et al., 2009).

Curiously, in pollen of Arabidopsis, the level of mtDNA was found to correlate with the abundance of AtWHIRLY2. Overexpression of *AtWHIRLY2* under control of the vegetative cell-specific promoter *Lat52* increased the mtDNA level by 10 times. In these plants, pollen were shown to have enhanced ROS levels and less ATP, coinciding with slower growth of pollen tubes (Cai et al., 2015).

Transcription

Transcription in chloroplasts is mediated by two RNA polymerases, the bacterial type plastid-encoded RNA polymerase PEP (plastid-encoded polymerase) and a nucleus-encoded polymerase resembling those of T-phages (RPOT) that is also termed NEP (nucleus-encoded polymerase; Hess and Börner, 1999b; Börner et al., 2015). Principally, both enzymes transcribe all genes, but from different promoters and with different efficiencies. While NEP provides the basic level of transcription in all types of plastids (Hess and Börner, 1999a) or chloroplasts at night (Ono et al., 2020), PEP is required for the dramatic increase in transcriptional activity required for chloroplast development (Baumgartner et al., 1989; Börner et al., 2015). In a very recent study, it has been shown that binding of PEP to DNA is reduced in chloroplasts of a triple mutant obtained from *why1tilwhy3* and a mutant lacking its interacting protein RNase H1C (**Table 3**; Wang et al., 2021). In a preceding paper, the interaction of WHIRLY proteins with RNase H1 had been suggested to promote transcription (Yang et al., 2017).

During chilling, tomato WHIRLY1 was found to bind to a specific motif (GTTACCCT) in the promoter of the *psbA* gene, which is mainly transcribed by PEP. This motif has also been detected in pepper, another chilling sensitive plant, but not in Arabidopsis, maize, and rice (Zhuang et al., 2019). Because WHIRLY1 was found neither to interact with PEP nor NEP, the significance of the sequence-specific binding remained unknown.

Barley plants with an RNAi-mediated knockdown of *WHIRLY1* showed reduced levels of PEP-dependent transcripts but high levels of NEP-dependent transcripts, such as *rpoB/C* and *clpP* encoding the subunits of PEP and the catalytic subunit of the CLP protease (Krupinska et al., 2019). This decrease in the ratio of PEP- and NEP-derived transcripts indicates an impaired function of PEP coinciding with retardation of chloroplast development. The reduced activity of PEP which requires supercoiled rather than relaxed templates (Zaitlin et al., 1989) in the WHIRLY1 deficient barley chloroplasts may be a consequence of the reduced compaction of plastid nucleoids (Krupinska et al., 2014b).

Underrepresented PEP-derived transcripts include ribosomal RNAs (Börner et al., 2015). A reduction in ribosomal RNA is shared by the barley RNAi-WHIRLY1 plants, the *Zmwhy1* mutants, and the Arabidopsis double mutant *why1tilwhy3*, as reported recently (Wang et al., 2021). Maréchal et al. (2009) did, however, not observe a reduced level of plastid ribosomal RNA in the same *why1tilwhy3* mutant and concluded that the variegation observed in a part of the mutant progeny might have another reason. Intriguingly, in all cases, the level of 23S rRNA is more affected than the level of 16S rRNA. This altered expression might be explained by replication–transcription conflicts occurring at a putative replication origin located near the 23S rDNA in the region of the inverted repeat (IR; Takeda et al., 1992).

RNA Splicing

In barley (Melonek et al., 2010) as well as in algae and liverwort (Kobayashi et al., 2016), WHIRLIES were shown to have an additional extra-nucleoid localization that might be related to their association with RNA derived from intron-containing genes, their interaction with the splicing factors PPR4 and CRS1 (**Table 3**) and their positive impact on splicing of primary transcripts (Prikryl et al., 2008; Melonek et al., 2010). It remains an open question whether the inefficient splicing of plastid transcripts in WHIRLY1 deficient plants is a direct consequence of WHIRLY1 deficiency or is caused by a disturbed formation of plastid-encoded RNA polymerase (PEP). Indeed, in transplastomic tobacco plants lacking a functional PEP, RNA processing is altered (Legen et al., 2002), indicating that the origin of transcripts determines their processing. Intriguingly,

accumulation and processing of mitochondrial transcript is also altered in Arabidopsis plants overexpressing the *AtWHIRLY2* gene (Maréchal et al., 2008).

Maintenance of Organelle Genome Stability

Organelle genomes have to be faithfully repaired to ensure the efficient functioning of organelles and overall plant performance (Maréchal and Brisson, 2010). To maintain the integrity of the genome, chloroplasts and mitochondria have efficient DNA recombination surveillance machineries (Maréchal and Brisson, 2010; Kühn and Gualberto, 2012). The involvement of plastid WHIRLIES in the repair of DNA by homologous recombination has been first reported for the double mutant *why1tilwhy3* showing a variegation phenotype in a portion of the mutant progeny (about 5%; Maréchal et al., 2009). Variegated leaf parts of the double mutant accumulated aberrant ptDNA resulting from microhomology-mediated illegitimate recombination (MMIR; Maréchal et al., 2009). Maréchal et al. (2009) reported that the frequency of illegitimate recombination is also increased in the albino *why1-1* mutant of maize (Prikryl et al., 2008), albeit in this mutant, no large rearranged ptDNA molecules were detectable.

The variegated leaf phenotype of the *why1tilwhy3* was detectable with much higher abundance when the double mutant was combined with a mutant lacking the gene encoding organelle targeted DNA polymerase Ib (*polIb*; Zampini et al., 2015). A quadruple mutant lacking in addition RecA was unable to survive (Zampini et al., 2015). These investigations showed that WHIRLY proteins, DNA polymerase Ib and the RecA protein have synergistic effects on DNA stability.

In a recent study of the group of Normand Brisson, the double mutant *why1tilwhy3* was combined with the *sig6* mutant deficient in SIGMA 6 (SIG6), that is, a significant nucleus-encoded transcription factor for PEP (Di Giorgio et al., 2019). By characterization of the triple mutant and pharmacological treatments with the transcription inhibitor rifampicin, the authors identified transcription as a major source of ptDNA instability. Recently, it has been proposed that WHIRLY proteins promote the formation of RNA/DNA hybrids (R-loops) by recruiting RNAPs to DNA and that these R-loops serve in DNA repair by homologous recombination (Wang et al., 2021).

To fulfil their function in maintaining organelle genome stability, WHIRLIES require the DNA-binding motif KGKAAL. When the AtWHIRLY1 sequence mutated for the second lysine of the KGKAAL motif (K91A) was expressed under the control of the CaMV *35S* promoter in the *why1tilwhy3* mutant of Arabidopsis, the resulting plants were more sensitive toward the gyrase inhibitor ciprofloxacin (CIF) than control plants overexpressing the non-mutated WHIRLY1 (Cappadocia et al., 2012).

PROTEINS INTERACTING WITH WHIRLIES IN THE NUCLEUS

Most interactions with nuclear proteins reported for all three Arabidopsis WHIRLIES have been shown by yeast two-hybrid assays, bimolecular fluorescence complementation, or by Cre reporter-mediated yeast two-hybrid coupled with next-generation sequencing (CrY2H) assays (Trigg et al., 2017; **Supplementary Table 1**). By the latter method, WHIRLIES were identified as components of the Arabidopsis transcription factor interactome (Trigg et al., 2017). Earlier, interactions of WHIRLIES with transcription factors were proposed to occur *via* the putative transactivation domains preceding the WHIRLY domain (Desveaux et al., 2005).

Several transcription factors interacting with WHIRLIES are involved in senescence and immune responses. One of the Arabidopsis transcription factors that interact with WHIRLY1 is WRKY53 (Trigg et al., 2017) whose gene expression during senescence is regulated by WHIRLY1 (Miao et al., 2013). Another member of the plant-specific family of WRKY transcription factors, that is, WRKY75, has been identified as WHIRLY interacting protein in cassava by yeast-2-hydrid assays and bimolecular fluorescence complementation (Liu et al., 2018). WHIRLY2 was found to interact with TGA1 (Trigg et al., 2017), belonging to the TGA motif transcription factors that have also been implicated in senescence and pathogen defense (Gatz, 2013). Both WRKY and TGA transcription factors might interact with WHIRLIES by binding to cis-elements that overlap with WHIRLY binding sequences (**Table 1**; Desveaux et al., 2005).

WHIRLY3 was found to interact with a member of the GATA transcription factor family member, that is, GATA14 belonging to the B-class of this large family (Behringer and Schwechheimer, 2015). GATA motifs are found in promoters of light-responsive genes. The B-GATA factors encoding genes are controlled by nitrogen availability, phytohormones, and light (Behringer and Schwechheimer, 2015).

Further plant-specific transcription factors interacting with WHIRLY2 or 3 are involved in growth and development, that is, the auxin response factor ARF19 involved in lateral root formation and response to phosphate starvation (Huang et al., 2018b; Lee et al., 2019), the two MADS-box class C transcription factors AGAMOUS-like 74 and 84 (AGL74 and AGL84; Castelan-Munoz et al., 2019) and WOX13 (He et al., 2019; Tvorogova et al., 2021). ARFs and WOXs are plant-specific families of transcription factors involved in regulation of developmental plasticity and responses to abiotic stress. WHIRLY2 was found to interact with the transcription factors AGL74 and AGL84 of the group of MADS-box factors (**Table 4**) involved in spatial and temporal plant developmental processes, such as flowering (Castelan-Munoz et al., 2019).

Besides transcription factor interactions, other nucleus located proteins were found to interact with WHIRLIES. As early as in 2007, WHIRLY1 had been identified as a telomer binding protein. Later on, WHIRLY1 was demonstrated to physically interact with the catalytic subunit of telomerase (Majerska et al., 2017).

Furthermore, WHIRLIES were found to interact with components of signal transduction (**Supplementary Table 1**). WHIRLY1 interacts with CIPK14, that is, a CBL-interacting serine/threonine kinase 14 (Ren et al., 2017), likely involved in calcium signaling (Qin et al., 2008). WHIRLY2 was found to interact with ATARCA, a receptor of activated kinase C1A

TABLE 4 | Transcription factors interacting with WHIRLIES.

Transcription factor	Full names, synonymous names	Family, binding motif	WHIRLIES	Functional context	References
ARF19/IAA22	Auxin response factor 19	Auxin response element	AtWHIRLY2	Ethylene responses, for example, root formation and response to phosphate starvation	Huang et al., 2018b
ARF11	Indole acetic acid inducible 22		AtWHIRLY3		
AGL74	AGAMOUS-LIKE 74	MADS-box class C $CC(A/T)_6GG$	AtWHIRLY2	Spatial and temporal development/Flowering responses to stress	Castelan-Munoz et al., 2019
AGL84	AGAMOUS-LIKE 84	MADS-box class C $CC(A/T)_6GG$	AtWHIRLY2	Plastid development and growth responses to stress	Castelan-Munoz et al., 2019
GATA14	Factor 14 binding to the cis-element GATA	Zn ion binding	AtWHIRLY3	Regulation of light-responsive genes	Reyes et al., 2004
TGA1	TGACG sequence-specific binding protein 1	bZIP basic leucine zipper	AtWHIRLY2	Redox-controlled regulation of systemic acquired resistance and different stress pathways	Gatz, 2013
WOX13	WUSCHEL-related homeobox 13, HB-4	Homeobox factor	AtWHIRLY3	Development, determination of cell fate, abiotic stress response	He et al., 2019
WRKY53	W-box binding factor 53 with WRKY motif	Group III of the WRKY transcription factors W-box	AtWHIRLY1	Leaf senescence and pathogen resistance	Miao et al., 2013, Huang et al., 2018a, Zentgraf and Doll, 2019
WRKY75	W-box binding factor 75 with WRKY motif	W-box	MeWHIRLY1, 2, 3	Disease resistance	Liu et al., 2018

(RACK1) playing a role in numerous developmental processes and hormone responses (Guo et al., 2019).

FUNCTIONS OF NUCLEUS LOCATED WHIRLIES

By their affinity to ssDNA, nucleus located WHIRLIES are likely involved in all processes associated with the formation of ssDNA, such as transcription.

Brisson and co-workers proposed that WHIRLIES bind as tetramers to melted promoter regions to modulate the expression of target genes (Desveaux et al., 2002). By stabilizing melted promoter regions, WHIRLIES were proposed to enhance the activities of transcription factors interacting with them. More detailed information on the impact of WHIRLY binding to promoters on transcription has been reported for two senescence-associated genes regulated by WHIRLY1, that is, *AtWRKY53* and *HvS40*. WHIRLY1 binding to the promoter of Arabidopsis *WRKY53* has been shown by chromatin immunoprecipitation (Huang et al., 2018a). WHIRLY1 binding inhibits methylation and promotes acetylation of histone 3 (H3K9ac), coinciding with the recruitment of RNAPII and transcriptional activation of *WRKY53* during senescence (Huang et al., 2018a). In barley, WHIRLY1 was shown to bind to the promoter of the senescence-associated gene *S40* (Krupinska et al., 2014a). Furthermore, during drought-induced senescence WHIRLY1 affects histone modifications in the promoter and the coding sequence of *HvS40*. While euchromatic H3K9ac accumulated during drought stress in the wild type, no changes were observed in the *WHIRLY1* knockdown plants produced by RNA interference (Janack et al., 2016). The impaired change in chromatin structure coincided with a lack of stress-induced changes in the expression of multiple senescence and drought stress-related genes (Janack et al., 2016).

Taken together, the findings on transcription of the two senescence-associated genes in Arabidopsis and barley indicate that WHIRLY1 is involved in chromatin remodeling and might regulate the accessibility of DNA for transcription factors. Chromatin remodeling is also crucial for the maintenance of telomers (Lee and Cho, 2019). Interestingly, the AtWHIRLY1 deficient mutant plants show a steady increase in the length of telomers over generations (Yoo et al., 2007), being in accordance with the interaction of WHIRLY1 with telomerase (**Supplementary Table 1**).

It is known that chromatin remodeling also controls microRNA biogenesis at the transcriptional level (Choi et al., 2016). Promotion of microRNA biogenesis by WHIRLY1 (Swida-Barteczka et al., 2018) could be a further link between WHIRLIES and chromatin remodeling. The microRNAs play an essential role in the interactions of plants with the environment (Song et al., 2019) and serve in the attenuation of plant growth and development by targeting the mRNAs encoding transcription factors for degradation (Sunkar et al., 2012). Recently, microRNA biogenesis has been reported to be under the control of a retrograde signaling pathway from chloroplasts that involves tocopherols and 3′-phosphoadenosin 5′-phosphate, an inhibitor of exoribonucleases (Fang et al., 2019). So far, an interaction of WHIRLIES with proteins involved in microRNA biogenesis remains to be investigated. It will be interesting to elucidate whether WHRILIES affect microRNA biogenesis directly or *via* an impact on chromatin remodeling.

WHIRLIES ARE INVOLVED IN TRANSCRIPTIONAL NETWORKS CONTROLLING DEVELOPMENT AND STRESS RESPONSES

Developmental and environmental cues control WHIRLY gene expression. Expression patterns might give information on the situations in which WHIRLIES might be necessary. In the

promoters of the tomato WHIRLY genes, 13 types of putative transcription factor binding motifs have been identified, and the most dominant bind GATA and MYB transcription factors (Akbudak and Filiz, 2019). GATA factors play roles in light- and nitrate-dependent control of transcription (Reyes et al., 2004). Among them, GATA14 has been found to interact with WHIRLY3 (**Table 4**). MYB factors are implicated in abscisic acid (ABA) responses and play roles in development and in responses to abiotic and biotic stresses (Ambawat et al., 2013).

Expression of *HvWHIRLY1* does transiently increase during chloroplast development (Krupinska et al., 2014b) and declines during leaf senescence (Kucharewicz et al., 2017). In comparison, the expression level of *HvWHIRLY2* is high in meristematic tissue where WHIRLY2 it has been proposed to function as an epigenetic regulator (McCoy et al., 2021), declines during leaf development and increases during leaf senescence (Grabowski et al., 2008; Kucharewicz et al., 2017). Treatment of barley leaf segments with different hormones showed that ABA suppressed the expression of *WHIRLY1*, whereas expression of *WHIRLY2* increased by treatment with ABA (Grabowski et al., 2008). Treatment with methyl jasmonate had inverse effects on the expression of the two genes (Grabowski et al., 2008).

While the two WHIRLY genes in barley responded differently during development and toward treatment with stress-associated hormones, both WHIRLY genes of tomato are likewise upregulated during drought and salt stress (Akbudak and Filiz, 2019). Furthermore, *WHIRLY1* of tomato was observed to have higher expression during chilling (Zhuang et al., 2019). The three *WHIRLY* genes of cassava (*Manihot esculentum*, *Me*) are upregulated by the bacterial *flg22* elicitor and treatment with Xanthomonas (Liu et al., 2018). Expression of all five *WHIRLIES* genes in strawberry was shown to be downregulated by crown rot infection (Hu and Shu, 2021). By analyses of the cis-elements in the promoters of all the five genes, several "defense and stress responsive" and "salicylic acid responsive" elements were identified. The parallel expression patterns in response to diverse stress factors observed for all WHIRLY genes in these three dicot plants suggest that all WHIRLY genes have similar functions during stress in these plants (Hu and Shu, 2021).

For Arabidopsis, it has been postulated that WHIRLIES control genes activated by salicylic acid and containing PB elements in their promoters (Desveaux et al., 2004, 2005). However, these were predictions, and although responses to high light involve salicylic acid signaling (Karpinski et al., 2013), an analysis of global gene expression performed with the *why1tilwhy3* mutant under high light conditions did not show the expected changes in gene expression (Lepage et al., 2013). Moreover, Lepage et al. (2013) reported that plastid genome instability increased when the *why1tilwhy3* mutant was combined with the *polIb-1* mutant, leading to ROS production and retrograde signaling and finally to genetic reprogramming and adaptation to oxidative stress (Lepage et al., 2013). The authors concluded that the genetic reprogramming occurring in the triple mutant is not due to the individual genetic backgrounds of *polIb-1* and *why1tilwhy3*, but instead is induced by the production of ROS resulting from enhanced genome instability in the triple mutant (Supplemental Information S9 in Lepage et al., 2013).

The most striking changes in abundances of transcripts in the barley WHIRLY1 deficient plants (Comadira et al., 2015) have been re-evaluated based on recent barley gene annotations (**Supplementary Table 2**). In accordance with the delayed chloroplast development of the WHIRLY1 deficient barley plants (Krupinska et al., 2019), the former and the new annotations revealed that the expression of genes encoding the S18 and L23 subunits of the 70S ribosomes is enhanced (**Supplementary Table 2**). Both subunits are essential for ribosome formation in green plants (Rogalski et al., 2006; Tiller and Bock, 2014). With regard to the dramatic decrease in the level of mRNA encoding the eukaryotic translation factor 4A (Comadira et al., 2015), WHIRLY1 might also promote translation at 80S ribosomes. Increased expression levels of genes encoding components of the chloroplast NADH complex (**Supplementary Table 2**) might indicate oxidative stress.

Among the genes newly identified to have an enhanced expression level in the barley WHIRLY1 deficient plants by re-evaluation of the barley gene annotations, is the gene encoding RNase J (RNJ) which belongs to the metallo-ß-lactamase family (**Supplementary Table 2**). RNJ is an abundant protein of nucleoids isolated from maize proplastids (Majeran et al., 2012). This RNase displays endo- and exonuclease activities and is conserved among bacteria, archaea, and chloroplasts. In plants, it has a GT-1 domain that was also found in transcription factors that function in light and stress responses (Halpert et al., 2019). In Arabidopsis, RNJ is required for embryogenesis and chloroplast development (Chen et al., 2015). Disturbance of chloroplast development was proposed to be the reason for the observed abortion of embryos. RNJ promotes chloroplast development by degrading aberrant RNA, such as antisense RNA produced by relaxed transcription in plastids (Sharwood et al., 2011; Hotto et al., 2020).

WHIRLY proteins might control the expression of target genes in cooperation with interacting transcription factors that have partly overlapping binding sequences with WHIRLIES. For some of the WHIRLY target genes, that is, *WRKY53* (Miao et al., 2013), it has been shown that they encode the transcription factors that were shown to interact with a WHIRLY protein, suggesting that WHIRLIES might aid in autoregulation of such genes. Vice versa, concerning the cis-elements identified in promoters of WHIRLY genes, such as W-boxes and GATA elements, it also seems that WHIRLY interacting transcription factors might also control the expression of WHIRLY genes, for example, transcriptional activation of *MeWHIRLY3* by MeWRKY75 (Liu et al., 2018). A complex consisting of MeWHIRLY3 and MeWRKY75 was found to activate genes with PB elements (Liu et al., 2018).

STRESS RESISTANCE OF PLANTS WITH ALTERED ABUNDANCES OF WHIRLIES

In all species studied so far, high levels of one or the other WHIRLY protein were observed to promote resistance toward

various pathogens. To increase stress resistance, different *WHIRLY* genes have been overexpressed in agronomically important plants (**Table 2**). Tobacco and tomato plants overexpressing *WHIRLY* genes, for example, have a higher resistance toward bacterial and fungal pathogens (**Table 2**), and overexpression of all three cassava *WHIRLY* genes enhanced resistance against cassava bacterial blight. In contrast, virus-induced gene silencing decreased resistance (Liu et al., 2018). Accordingly, Arabidopsis *TILLING why1* mutants with reduced binding of WHIRLY1 to the PB element (**Table 1**) showed reduced resistance toward *Peronospora parasitica* (Desveaux et al., 2004), and barley RNAi-WHIRLY1 plants with reduced expression *HvWHIRLY1* have reduced resistance toward powdery mildew (Hensel et al., unpublished). These results are in accordance with the characterization of WHIRLY1 as a transcriptional activator of pathogen response genes as a consequence of salicylic acid signaling (Desveaux et al., 2000, 2004). It has been suggested that WHIRLY1 moves to the nucleus upon oxidative stress-induced production of salicylic acid inside chloroplasts. This pathway would parallel SA-signaling by NPR1, which moves from the cytoplasm to the nucleus in response to salicylic acid and binds to pathogen response gene promoters in the nucleus (Foyer et al., 2014). Among the genes activated in Arabidopsis during pathogen defense is the gene encoding isochorismate synthase 1 (Lin et al., 2020), the key enzyme of the plastid located part of the salicylic acid biosynthesis pathway (Rekhter et al., 2019). Likely, WHIRLY1 and NPR1 have an additive effect on the expression of PR genes as proposed already by Desveaux et al. (2004, 2005), and WHIRLY1 is likely responsible for defense reactions independent of NPR1 (Vlot et al., 2009; An and Mou, 2011; Janda and Ruelland, 2015).

The consistent results on WHIRLY-dependent biotic stress resistance in different species contrasts with the diverse effects of WHIRLY proteins on abiotic stress resistance. While barley RNAi *WHIRLY1* knockdown plants have been reported to have an enhanced resistance toward drought (Janack et al., 2016), cassava plants with silenced *WHIRLY1* (Yan et al., 2020) and tomato lines with silenced *WHIRLY2* showed a reduced drought tolerance (Meng et al., 2020; Yan et al., 2020). The latter findings are in accordance with the enhanced drought resistance of tobacco *WHIRLY2* overexpressing tobacco plants (Zhao et al., 2018). Drought tolerance is primarily mediated by abscisic acid (ABA), which is also involved in responses to different abiotic stresses and biotic stresses (Kumar et al., 2019). Arabidopsis plants overexpressing *AtWHIRLY1* were shown to be hypersensitive to ABA, while a *why1* mutant showed insensitivity toward ABA (Isemer et al., 2012a). When overexpression was performed with a construct lacking the sequence encoding the plastid targeting sequence of AtWHIRLY1, the plants were as insensitive to ABA as the mutant plants (Isemer et al., 2012a), clearly indicating that the location of WHIRLY1 inside chloroplasts is mandatory for the perception of ABA.

In tomato, overexpression of *WHIRLY1* leads to higher chilling tolerance, coinciding with a higher level of soluble sugars and higher photosynthesis likely due to enhanced expression of *RBCS1* (Zhuang et al., 2020b) as well as to enhanced thermotolerance (Zhuang et al., 2020a). Taken together, these results indicate that the WHIRLY proteins have a positive impact on abiotic stress resistance in dicot plants. In contrast, the situation might be more complex in monocot plants, because it is impossible to distinguish direct effects of monocot WHIRLY1 proteins from indirect effects *via* their impacts on organelle DNA compaction (Oetke et al., 2022).

PUTATIVE MECHANISMS UNDERLYING ROS MANAGEMENT AND REGULATION OF STRESS RESISTANCE BY WHIRLIES

Several studies showed that the changes in abiotic stress resistance of plants with an altered abundance of WHIRLIES are accompanied by changes in organellar ROS levels. Enhanced chloroplast ROS levels were measured by EPR spectroscopy in barley plants with an RNAi-mediated knockdown of *WHIRLY1* grown at high light intensity (Swida-Barteczka et al., 2018). Higher ROS levels were also reported for old leaves of the Arabidopsis *why1* mutant (Lin et al., 2019) and the *why1tilwhy3polIb-1* triple mutant (Lepage et al., 2013). Tomato RNAi-*WHIRLY2* lines were shown to accumulate more ROS during drought and have a lower alternative oxidase activity (Meng et al., 2020). In contrast, transgenic tobacco plants overexpressing *SlWHIRLY2* have reduced ROS levels and enhanced the activities of enzymes of the antioxidative system (SOD, APX; Zhao et al., 2018).

Albeit there is consensus about the suppression of ROS production by WHIRLIES in dicot and monocot species, the suggested sources of ROS and their effectiveness in stress responses in WHIRLY deficient plants were reported to differ. While in barley WHIRLY1 deficient plants, enhanced ROS production is obviously due to an inefficient photosynthetic apparatus (Swida-Barteczka et al., 2018), the enhanced level of ROS in the Arabidopsis *why1til3polIb-1* mutant (Parent et al., 2011; Lepage et al., 2013) was suggested to be a consequence of plastid genome instability coinciding with the appearance of variegated leaves in a portion of the *why1tilwhy3* mutant (Maréchal et al., 2009). Variegation in the mutant was reported to occur more frequently when plants were grown in high light (Guan et al., 2018) and might be caused by inequal resistance of individual plastids to photooxidative stress reported for the *immutans* mutant of Arabidopsis (Yu et al., 2007). It seems that plastids can tolerate a certain level of rearranged DNA molecules as these are also detectable in green sectors of the leaves (Maréchal et al., 2009) while their accumulation gives rise to non-functional plastids. Moreover, ROS production can be promoted by treating the Arabidopsis *why1tilwhy3polIb* mutant plants with ciprofloxacin that induces double-strand break production by inhibition of gyrases during replication (Lepage et al., 2013). The findings suggest that plastid genome instability leads to an increase in the production of ROS. The redox imbalance correlates with altered nuclear gene

expression, as various abiotic stress-related genes required for acclimation, that is, *ELIP2*, NUDt4, *ACS6*, *UPOX*, *Armadillo repeat* AT3G06530, were shown to be upregulated. Lepage et al. (2013) postulated that plastid genome instability induces an oxidative burst that favors adaptation to subsequent oxidative stress. This idea got recent support by studies with the triple mutant *recA1why1tilwhy3* and ciprofloxacin. In this mutant, ROS production is promoted by DNA damage in an otherwise non-stress situation. ROS was shown to induce retrograde signaling affecting endoreplication and cell cycle *via* regulation of the nuclear SOG1 transcription factor required for plant growth and development (Duan et al., 2020).

In the *why1tilwhy3* double mutant and the triple mutants prepared by crosses of the double mutant with *polIb* and *recA*, respectively, ROS production obviously induced changes in nuclear gene expression, enabling a light acclimation response. In contrast, in WHIRLY1 deficient plants of barley, ROS production is not able to induce acclimation. Instead, these plants suffer oxidative stress when grown at high irradiance (Swida-Barteczka et al., 2018) and cannot accelerate senescence in response to light (Kucharewicz et al., 2017). Leaves of the plants indeed lack typical reactions associated with acclimation to high light (Saeid Nia et al., 2022). The plants are not only insensitive to light, but also to the supply of water (Janack et al., 2016) and nitrogen (Comadira et al., 2015). In WHIRLY1 deficient barley plants grown under nitrogen-deficient conditions, leaf chlorophyll content and photosynthesis were higher than in the wild type (Comadira et al., 2015). The results suggest that the barley plants are compromised in the measurement of light intensity and cannot activate the required stress defense programs. The function of WHIRLY1 in sensing environment is in accordance with the reduced stress resistance reported for WHIRLY1 deficient dicot plants (**Table 2**).

The capability of the Arabidopsis *why1tilwhy3* mutant to activate stress responses (Lepage et al., 2013) might be due to the presence of the truncated AtWHIRLY3 including the KGKAAL motif (see above and **Supplementary Figure 2**). In comparison, the reduced resistance to DNA damage as reported for the *why1tilwhy3* mutant might be at least partly caused by the lack of motifs downstream of the DNA-binding motif (**Figure 1**).

Considering that WHIRLY proteins are also present in the nucleus where they might aid in the regulation of the expression stress-related genes, it is difficult to distinguish the impact of organellar ROS production and subsequent retrograde signaling on nuclear gene regulation from the direct effect of chloroplast-to-nucleus translocation of WHIRLY proteins on stress resistance.

CONCLUDING REMARKS AND OUTLOOK

WHIRLIES apparently have a high impact on plant development and stress resistance. By binding to ssDNA and RNA, WHIRLY proteins influence diverse DNA and RNA associated processes in the organelles and connect them with the responsiveness to environment being important for both development and stress resistance. During stress, WHIRLIES participate in retrograde signaling in two ways: (1) retrograde signaling initiated by perturbation of electron transport leading to ROS production and hormone signaling and (2) directly as a chloroplast-to-nucleus translocating protein (Bobik and Burch-Smith, 2015). This latter pathway is likely activated by salicylic acid or other stress-related signal compounds, such as ROS and methylerythritol cyclopyrophosphate (MEcPP; Xiao et al., 2012, 2013). In bacteria, MEcPP produced during oxidative stress was reported to release histone-like proteins from DNA (Artsatbanov et al., 2012). In plants, MEcPP could be the link between the generation of chloroplast stress signals and the translocation of WHIRLY1 from chloroplasts to the nucleus (Foyer et al., 2014).

Putative and confirmed WHIRLY interacting proteins involve on one hand organellar proteins serving as components of the photosynthetic machinery, nucleoids, ribosomes, and enzymes of the primary metabolism, and on the other hand transcription factors in the nucleus. These numerous interactions might accommodate the coordination of plant functions at different levels during the plants' response to environment.

WHIRLY proteins of different species possess different motifs besides the highly conserved WHIRLY domain responsible for binding ssDNA and oligomerization. The sequence diversity outside of the WHIRLY domain indicates that WHIRLIES can serve various purposes in different species. Likely, decisions among the multiple functions of WHIRLIES and their subcellular distribution involves various posttranslational modifications which remain to be determined in the different species.

The growing knowledge on the impact of WHIRLY proteins on numerous processes affecting development and resistance to diverse abiotic and biotic stresses indicate that *WHIRLIES* belong to the group of "multi-role pleiotropic genes" which are expected to be valuable targets for developing crop plants with an inbuilt tolerance to multiple stresses (Husaini, 2022). It stands to reason that WHIRLIES' impact on resistance to multiple stresses depends on their dynamic localization in organelle nucleoids and the nucleus.

As major nucleoid-associated proteins, WHIRLIES might operate in "epigenetic reprogramming" of organelle genomes. In humans/mammals, reversible NAP-mediated changes in the structure and function of mitochondrial nucleoids were observed to affect the mitochondria–nucleus cross-talk, being of pivotal importance for an efficient operation of mitochondria in energy-demanding tissues (Arunachalam et al., 2021). Mitochondrial epigenomics and its impact on mitochondria–nucleus cross-talk offered novel perspectives for studying diseases, such as cancer (Sharma et al., 2021). A deep understanding of the mechanisms underlying the impact of WHIRLIES on nucleoid structure and the consequences for photosynthesis and respiration will increase the chances to develop plants with higher productivity and stress resistance.

AUTHOR CONTRIBUTIONS

KK has outlined and mainly written the manuscript. CD performed microscopy research and prepared the figures. SF performed sequence analyses and evaluated published data sets. GH re-evaluated published data on gene expression. All authors contributed to the article and approved the submitted version.

FUNDING

The joint research of GH and KK on WHIRLY proteins is funded by the German Research Foundation (HE6432/4-1, KR1350/25-1). GH is supported by funding of the Deutsche Forschungsgemeinschaft (DFG, German Research Foundation) under Germany's Excellence Strategy—EXC-2048/1—project ID 390686111.

ACKNOWLEDGMENTS

We thank Alice Barkan, Eugene, University of Oregon, United States, for providing *ptac* mutants of maize and Henrik Aronsson, University of Gothenburg, Sweden, to instruct Rena Isemer in co-immunoprecipitation with the AtWHIRLY3 specific antibody. We acknowledge Maria Mulisch and Marita Beese for electron microscopy in the central facility of the Biology Center of CAU. We also thank Kirsten Krause, The Arctic University of Norway, and Giannina Kunz, University of Kiel, for critical reading of the manuscript.

SUPPLEMENTARY MATERIAL

The Supplementary Material for this article can be found online at: https://www.frontiersin.org/articles/10.3389/fpls.2022.880423/full#supplementary-material

REFERENCES

Abbondanzieri, E. A., and Meyer, A. S. (2019). More than just a phase: the search for membraneless organelles in the bacterial cytoplasm. *Curr. Genet.* 65, 691–694. doi: 10.1007/s00294-018-00927-x

Akbudak, M. A., and Filiz, E. (2019). Whirly (why) transcription factors in tomato (*Solanum lycopersicum* L.): genome-wide identification and transcriptional profiling under drought and salt stresses. *Mol. Biol. Rep.* 46, 4139–4150. doi: 10.1007/s11033-019-04863-y

Ambawat, S., Sharma, P., Yadav, N. R., and Yadav, R. C. (2013). MYB transcription factor genes as regulators for plant responses: an overview. *Physiol. Mol. Biol. Plants* 19, 307–321. doi: 10.1007/s12298-013-0179-1

An, C. F., and Mou, Z. L. (2011). Salicylic acid and its function in plant immunity. *J. Integr. Plant Biol.* 53, 412–428. doi: 10.1111/j.1744-7909.2011.01043.x

Artsatbanov, V. Y., Vostroknutova, G. N., Shleeva, M. O., Goncharenko, A. V., Zinin, A. I., Ostrovsky, D. N., et al. (2012). Influence of oxidative and nitrosative stress on accumulation of diphosphate intermediates of the non-mevalonate pathway of isoprenoid biosynthesis in Corynebacteria and mycobacteria. *Biochemistry* 77, 362–371. doi: 10.1134/S0006297912040074

Arunachalam, M., Ramesh, M., Thiagarajan, V., Singla, S. K., Mudhol, S., and Muthukumar, S. P. (2021). Current perspectives of healthy mitochondrial function for healthy neurons. *Curr. Drug Targets* 22, 1688–1703. doi: 10.2174/1389450122666210222163528

Baumgartner, B. J., Rapp, J. C., and Mullet, J. E. (1989). Plastid transcription activity and DNA copy number increase early in barley chloroplast development. *Plant Physiol.* 89, 1011–1018. doi: 10.1104/pp.89.3.1011

Behringer, C., and Schwechheimer, C. (2015). B-GATA transcription factors: insights into their structure, regulation, and role in plant development. *Front. Plant Sci.* 6:90. doi: 10.3389/fpls.2015.00090

Belcher, S., Williams-Carrier, R., Stiffler, N., and Barkan, A. (2015). Large-scale genetic analysis of chloroplast biogenesis in maize. *Biochim. Biophys. Acta Bioenerg.* 1847, 1004–1016. doi: 10.1016/j.bbabio.2015.02.014

Bobik, K., and Burch-Smith, T. M. (2015). Chloroplast signaling within, between and beyond cells. *Front. Plant Sci.* 6:781. doi: 10.3389/fpls.2015.00781

Bohne, A. V. (2014). The nucleoid as a site of rRNA processing and ribosome assembly. *Front. Plant Sci.* 5:257. doi: 10.3389/fpls.2014.00257

Börner, T., Aleynikova, A. Y., Zubo, Y. O., and Kusnetsov, V. V. (2015). Chloroplast RNA polymerases: role in chloroplast biogenesis. *Biochim. Biophys. Acta Bioenerg.* 1847, 761–769. doi: 10.1016/j.bbabio.2015.02.004

Bryant, N., Lloyd, J., Sweeney, C., Myouga, F., and Meinke, D. (2011). Identification of nuclear genes encoding chloroplast-localized proteins required for embryo development in *Arabidopsis*. *Plant Physiol.* 155, 1678–1689. doi: 10.1104/pp.110.168120

Cai, Q., Guo, L., Shen, Z. R., Wang, D. Y., Zhang, Q., and Sodmergen, (2015). Elevation of pollen mitochondrial DNA copy number by WHIRLY2: altered respiration and pollen tube growth in *Arabidopsis*. *Plant Physiol.* 169, 660–673. doi: 10.1104/pp.15.00437

Cannon, G. C., Ward, L. N., Case, C. I., and Heinhorst, S. (1999). The 68 kDa DNA compacting nucleoid protein from soybean chloroplasts inhibits DNA synthesis in vitro. *Plant Mol. Biol.* 39, 835–845. doi: 10.1023/A:1006135615924

Cappadocia, L., Parent, J. S., Sygusch, J., and Brisson, N. (2013). A family portrait: structural comparison of the Whirly proteins from *Arabidopsis thaliana* and *Solanum tuberosum*. *Acta Crystallogr. F:Struct. Biol. Commun.* 69, 1207–1211. doi: 10.1107/S1744309113028698

Cappadocia, L., Parent, J. S., Zampini, E., Lepage, E., Sygusch, J., and Brisson, N. (2012). A conserved lysine residue of plant Whirly proteins is necessary for higher order protein assembly and protection against DNA damage. *Nucleic Acids Res.* 40, 258–269. doi: 10.1093/nar/gkr740

Castelan-Munoz, N., Herrera, J., Cajero-Sanchez, W., Arrizubieta, M., Trejo, C., Garcia-Ponce, B., et al. (2019). MADS-box genes are key components of genetic regulatory networks involved in abiotic stress and plastic developmental responses in plants. *Front. Plant Sci.* 10:853. doi: 10.3389/fpls.2019.00853

Chan, K. X., Phua, S. Y., Crisp, P., Mcquinn, R., and Pogson, B. J. (2016). "Learning the languages of the chloroplast: retrograde signaling and beyond" in *Annual Review of Plant Biology*. 67, 25–53.

Chen, Y. E., Ma, J., Wu, N., Su, Y. Q., Zhang, Z. W., Yuan, M., et al. (2018). The roles of *Arabidopsis* proteins of Lhcb4, Lhcb5 and Lhcb6 in oxidative stress under natural light conditions. *Plant Physiol. Biochem.* 130, 267–276. doi: 10.1016/j.plaphy.2018.07.014

Chen, H. Y., Zou, W. X., and Zhao, J. (2015). Ribonuclease J is required for chloroplast and embryo development in *Arabidopsis*. *J. Exp. Bot.* 66, 2079–2091. doi: 10.1093/jxb/erv010

Choi, K., Kim, J., Muller, S. Y., Oh, M., Underwood, C., Henderson, I., et al. (2016). Regulation of microRNA-mediated developmental changes by the SWR1 chromatin remodeling complex. *Plant Physiol.* 171, 1128–1143. doi: 10.1104/pp.16.00332

Ciolkowski, I., Wanke, D., Birkenbihl, R. P., and Somssich, I. E. (2008). Studies on DNA-binding selectivity of WRKY transcription factors lend structural clues into WRKY-domain function. *Plant Mol. Biol.* 68, 81–92. doi: 10.1007/s11103-008-9353-1

Comadira, G., Rasool, B., Karpinska, B., Garcia, B. M., Morris, J., Verrall, S. R., et al. (2015). WHIRLY1 functions in the control of responses to nitrogen deficiency but not aphid infestation in barley. *Plant Physiol.* 168, 1140–1151. doi: 10.1104/pp.15.00580

Dame, R. T., Rashid, F. Z. M., and Grainger, D. C. (2020). Chromosome organization in bacteria: mechanistic insights into genome structure and function. *Nat. Rev. Genet.* 21, 227–242. doi: 10.1038/s41576-019-0185-4

Després, C., Subramaniam, R., Matton, D., and Brisson, N. (1995). The activation of the potatoe PR-10a gene requires phosphorylation of the nuclear factor PBF-1. *Plant Cell* 7, 589–598.

Desveaux, D., Allard, J., Brisson, N., and Sygusch, J. (2002). A new family of plant transcription factors displays a novel ssDNA-binding surface. *Nat. Struct. Biol.* 9, 512–517. doi: 10.1038/nsb814

Desveaux, D., Despres, C., Joyeux, A., Subramaniam, R., and Brisson, N. (2000). PBF-2 is a novel single-stranded DNA binding factor implicated in PR-10a gene activation in potato. *Plant Cell* 12, 1477–1489. doi: 10.1105/tpc.12.8.1477

Desveaux, D., Maréchal, A., and Brisson, N. (2005). Whirly transcription factors: defense gene regulation and beyond. *Trends Plant Sci.* 10, 95–102. doi: 10.1016/j.tplants.2004.12.008

Desveaux, D., Subramanian, R., Després, C., Mess, J.-N., Lévesque, C., Fobert, P., et al. (2004). A "Whirly" transcription factor is required for salicylic acid-dependent disease resistance in *Arabidopsis*. *Dev. Cell* 6, 229–240. doi: 10.1016/S1534-5807(04)00028-0

Di Giorgio, J. A. P., Lepage, E., Tremblay-Belzile, S., Truche, S., Loubert-Hudon, A., and Brisson, N. (2019). Transcription is a major driving force for plastid genome instability in *Arabidopsis*. *PLoS One* 14. doi: 10.1371/journal.pone.0214552

Dillon, S. C., and Dorman, C. J. (2010). Bacterial nucleoid-associated proteins, nucleoid structure and gene expression. *Nat. Rev. Microbiol.* 8, 185–195. doi: 10.1038/nrmicro2261

Duan, S. J., Hu, L. L., Dong, B. B., Jin, H. L., and Wang, H. B. (2020). Signaling from plastid genome stability modulates endoreplication and cell cycle during plant development. *Cell Rep.* 32, 1–13. doi: 10.1016/j.celrep.2020.108019

Fang, X. F., Zhao, G. Z., Zhang, S., Li, Y. X., Gu, H. Q., Li, Y., et al. (2019). Chloroplast-to-nucleus signaling regulates microRNA biogenesis in *Arabidopsis*. *Dev. Cell* 48, 371.e4–382.e4. doi: 10.1016/j.devcel.2018.11.046

Fey, V., Wagner, R., Bräutigam, K., Wirtz, M., Hell, R., Dietzmann, A., et al. (2005). Retrograde plastid redox signals in the expression of nuclear genes for chloroplast proteins of *Arabidopsis thaliana*. *J. Biol. Chem.* 280, 5318–5328. doi: 10.1074/jbc.M406358200

Fleischmann, T. T., Scharff, L. B., Alkatib, S., Hasdorf, S., Schottler, M. A., and Bock, R. (2011). Nonessential plastid-encoded ribosomal proteins in tobacco: a developmental role for plastid translation and implications for reductive genome evolution. *Plant Cell* 23, 3137–3155. doi: 10.1105/tpc.111.088906

Foyer, C. H., Karpinska, B., and Krupinska, K. (2014). The functions of WHIRLY1 and REDOX-RESPONSIVE TRANSCRIPTION FACTOR 1 in cross tolerance responses in plants: a hypothesis. *Philos. Trans. R. Soc. Lond. B, Biol. Sci.* 369:20130226. doi: 10.1098/rstb.2013.0226

Gamez-Arjona, F. M., De La Concepcion, J. C., Raynaud, S., and Merida, A. (2014). *Arabidopsis thaliana* plastoglobule-associated fibrillin 1a interacts with fibrillin 1b in vivo. *FEBS Lett.* 588, 2800–2804. doi: 10.1016/j.febslet.2014.06.024

Gatz, C. (2013). From pioneers to team players: TGA transcription factors provide a molecular link between different stress pathways. *Mol. Plant-Microbe Interact.* 26, 151–159. doi: 10.1094/MPMI-04-12-0078-IA

Golin, S., Negroni, Y. L., Bennewitz, B., Klösgen, R. B., Mulisch, M., La Rocca, N., et al. (2020). WHIRLY2 plays a key role in mitochondria morphology, dynamics, and functionality in *Arabidopsis thaliana*. *Plant Direct* 4:e00229. doi: 10.1002/pld3.229

Grabowski, E., Miao, Y., Mulisch, M., and Krupinska, K. (2008). Single-stranded DNA binding protein Whirly1 in barley leaves is located in plastids and the nucleus of the same cell. *Plant Physiol.* 147, 1800–1804. doi: 10.1104/pp.108.122796

Guan, Z., Wang, W. Z., Yu, X. L., Lin, W. F., and Miao, Y. (2018). Comparative proteomic analysis of coregulation of CIPK14 and WHIRLY1/3 mediated pale yellowing of leaves in *Arabidopsis*. *Int. J. Mol. Sci.* 19:2231. doi: 10.3390/ijms19082231

Guo, J. G., Hu, Y. H., Zhou, Y. P., Zhu, Z. N., Sun, Y. J., Li, J. A., et al. (2019). Profiling of the receptor for activated C kinase 1a (RACK1a) interaction network in *Arabidopsis thaliana*. *Biochem. Biophys. Res. Commun.* 520, 366–372. doi: 10.1016/j.bbrc.2019.09.142

Halpert, M., Liveanu, V., Glaser, F., and Schuster, G. (2019). The *Arabidopsis* chloroplast RNase J displays both exo- and robust endonucleolytic activities. *Plant Mol. Biol.* 99, 17–29. doi: 10.1007/s11103-018-0799-5

He, P., Zhang, Y. Z., Liu, H., Yuan, Y., Wang, C., Yu, J. N., et al. (2019). Comprehensive analysis of WOX genes uncovers that WOX13 is involved in phytohormone-mediated fiber development in cotton. *BMC Plant Biol.* 19:12. doi: 10.1186/s12870-019-1892-x

Hess, W., and Börner, T. (1999a). Organellar RNA polymerases of higher plants. *Int. Rev. Cytol.* 190, 1–59. doi: 10.1016/S0074-7696(08)62145-2

Hess, W. R., and Börner, T. (1999b). "Organellar RNA polymerases of higher plants," in *International Review of Cytology: A Survey of Cell Biology*. ed. K. W. Jeon, *vol. 190* (San Diego: Elsevier Academic Press Inc.), 1–59.

Holowka, J., and Zakrzewska-Czerwinska, J. (2020). Nucleoid associated proteins: the small organizers that help to cope with stress. *Front. Microbiol.* 11:590. doi: 10.3389/fmicb.2020.00590

Hotto, A. M., Stern, D. B., and Schuster, G. (2020). Plant ribonuclease J: an essential player in maintaining chloroplast RNA quality control for gene expression. *Plants* 9:11. doi: 10.3390/plants9030334

Hu, Y. Y., and Shu, B. (2021). Identifying strawberry Whirly family transcription factors and their expressions in response to crown rot. *Not. Bot. Horti Agrobot. Cluj Napoca* 49:12323. doi: 10.15835/nbha49212323

Huang, D. M., Lan, W., Li, D. J., Deng, B., Lin, W. F., Ren, Y. J., et al. (2018a). WHIRLY1 occupancy affects histone lysine modification and WRKY53 transcription in *Arabidopsis* developmental manner. *Front. Plant Sci.* 9:1503. doi: 10.3389/fpls.2018.01503

Huang, D. M., Lin, W. F., Deng, B., Ren, Y. J., and Miao, Y. (2017). Dual-located WHIRLY1 interacting with LHCA1 alters photochemical activities of photosystem I and is involved in light adaptation in *Arabidopsis*. *Int. J. Mol. Sci.* 18:2352. doi: 10.3390/ijms18112352

Huang, K. L., Ma, G. J., Zhang, M. L., Xiong, H., Wu, H., Zhao, C. Z., et al. (2018b). The ARF7 and ARF19 transcription factors positively regulate PHOSPHATE STARVATION RESPONSE1 in *Arabidopsis* roots. *Plant Physiol.* 178, 413–427. doi: 10.1104/pp.17.01713

Huang, C. X., Yu, J. F., Cai, Q., Chen, Y. X., Li, Y. Y., Ren, Y. J., et al. (2020). Triple-localized WHIRLY2 influences leaf senescence and silique development via carbon allocation. *Plant Physiol.* 184, 1348–1362. doi: 10.1104/pp.20.00832

Husaini, A. M. (2022). High-value pleiotropic genes for developing multiple stress-tolerant biofortified crops for 21st-century challenges. *Heredity*. doi: 10.1038/s41437-022-00500-w [Epub ahead of print

Isemer, R. (2013). Die WHIRLY-proteine von *Arabidopsis thaliana*. dissertation/master's thesis. Kiel.

Isemer, R., Krause, K., Grabe, N., Kitahata, N., Asami, T., and Krupinska, K. (2012a). Plastid located WHIRLY1 enhances the responsiveness of *Arabidopsis* seedlings toward abscisic acid. *Front. Plant Sci.* 3:283. doi: 10.3389/fpls.2012.00283

Isemer, R., Mulisch, M., Schäfer, A., Kirchner, S., Koop, H. U., and Krupinska, K. (2012b). Recombinant Whirly1 translocates from transplastomic chloroplasts to the nucleus. *FEBS Lett.* 586, 85–88. doi: 10.1016/j.febslet.2011.11.029

Janack, B., Sosoi, P., Krupinska, K., and Humbeck, K. (2016). Knockdown of WHIRLY1 affects drought stress-induced leaf senescence and histone modifications of the senescence-associated gene *HvS40*. *Plan. Theory* 5:37. doi: 10.3390/plants5030037

Janda, M., and Ruelland, E. (2015). Magical mystery tour: salicylic acid signalling. *Environ. Exp. Bot.* 114, 117–128. doi: 10.1016/j.envexpbot.2014.07.003

Janicka, S., Kuhn, K., Le Ret, M., Bonnard, G., Imbault, P., Augustyniak, H., et al. (2012). A RAD52-like single-stranded DNA binding protein affects mitochondrial DNA repair by recombination. *Plant J.* 72, 423–435. doi: 10.1111/j.1365-313X.2012.05097.x

Janissen, R., Arens, M. M. A., Vtyurina, N. N., Rivai, Z., Sunday, N. D., Eslami-Mossallam, B., et al. (2018). Global DNA compaction in stationary-phase bacteria does not affect transcription. *Cell* 174, 1188.e14–1199.e14. doi: 10.1016/j.cell.2018.06.049

Karpinska, B., Alomrani, S. O., and Foyer, C. H. (2017). Inhibitor-induced oxidation of the nucleus and cytosol in *Arabidopsis thaliana*: implications for organelle to nucleus retrograde signalling. *Philos. Trans. R. Soc. Lond., B, Biol. Sci.* 372. doi: 10.1098/rstb.2016.0392

Karpinski, S., Szechynska-Hebda, M., Wituszynska, W., and Burdiak, P. (2013). Light acclimation, retrograde signalling, cell death and immune defences in plants. *Plant Cell Environ.* 36, 736–744. doi: 10.1111/pce.12018

Kobayashi, Y., Takusagawa, M., Harada, N., Fukao, Y., Yamaoka, S., Kohchi, T., et al. (2016). Eukaryotic components remodeled chloroplast nucleoid organization during the green plant evolution. *Genome Biol. Evol.* 8, 1–16. doi: 10.1093/gbe/evv233

Krause, K., Herrmann, U., Fuß, J., Miao, Y., and Krupinska, K. (2009). Whirly proteins as communicators between plant organelles and the nucleus? *Endocytosis Cell Res.* 19, 51–62.

Krause, K., Kilbienski, I., Mulisch, M., Rödiger, A., Schäfer, A., and Krupinska, K. (2005). DNA-binding proteins of the Whirly family in *Arabidopsis thaliana* are targeted to the organelles. *FEBS Lett.* 579, 3707–3712. doi: 10.1016/j.febslet.2005.05.059

Krause, K., and Krupinska, K. (2009). Nuclear regulators with a second home in organelles. *Trends Plant Sci.* 14, 194–199. doi: 10.1016/j.tplants.2009.01.005

Krause, K., and Krupinska, K. (2017). TAC-the transcriptionally acives chromosomes of plastids. *Endocytobiosis Cell Res.* 28, 54–61.

Krieger-Liszkay, A., Krupinska, K., and Shimakawa, G. (2019). The impact of photosynthesis on initiation of leaf senescence. *Physiol. Plant.* 166, 148–164. doi: 10.1111/ppl.12921

Kroll, D., Meierhoff, K., Bechtold, N., Kinoshita, M., Westphal, S., Vothknecht, U. C., et al. (2001). VIPP1, a nuclear gene of *Arabidopsis thaliana* essential for thylakoid membrane formation. *Proc. Natl. Acad. Sci. U. S. A.* 98, 4238–4242. doi: 10.1073/pnas.061500998

Krupinska, K., Blanco, N. E., Oetke, S., and Zottini, M. (2020). Genome communication in plants mediated by organelle-nucleus-located proteins. *Philos. Trans. R. Soc. Lond., B, Biol. Sci.* 375:20190397. doi: 10.1098/rstb.2019.0397

Krupinska, K., Braun, S., Saeid Nia, M., Schäfer, A., Hensel, G., and Bilger, W. (2019). The nucleoid-associated protein WHIRLY1 is required for the coordinate assembly of plastid and nucleus-encoded proteins during chloroplast development. *Planta* 249, 1337–1347. doi: 10.1007/s00425-018-03085-z

Krupinska, K., Dähnhardt, D., Fischer-Kilbienski, I., Kucharewicz, W., Scharrenberg, C., Trosch, M., et al. (2014a). Identification of WHIRLY1 as a factor binding to the promoter of the stress- and senescence-associated gene *HvS40*. *J. Plant Growth Regul.* 33, 91–105. doi: 10.1007/s00344-013-9378-9

Krupinska, K., Melonek, J., and Krause, K. (2013). New insights into plastid nucleoid structure and functionality. *Planta* 237, 653–664. doi: 10.1007/s00425-012-1817-5

Krupinska, K., Oetke, S., Desel, C., Mulisch, M., Schäfer, A., Hollmann, J., et al. (2014b). WHIRLY1 is a major organizer of chloroplast nucleoids. *Front. Plant Sci.* 5:432. doi: 10.3389/fpls.2014.00432

Kucharewicz, W., Distelfeld, A., Bilger, W., Muller, M., Munne-Bosch, S., Hensel, G., et al. (2017). Acceleration of leaf senescence is slowed down in transgenic barley plants deficient in the DNA/RNA-binding protein WHIRLY1. *J. Exp. Bot.* 68, 983–996. doi: 10.1093/jxb/erw501

Kühn, K., and Gualberto, J. M. (2012). "Recombination in the stability, repair and evolution of the mitochondrial genome," in *Mitochondrial Genome Evolution*. ed. L. Marechaldrouard (London: Academic Press Ltd-Elsevier Science Ltd.), 215–252.

Kumar, M., Kesawat, M. S., Ali, A., Lee, S. C., Gill, S. S., and Kim, H. U. (2019). Integration of abscisic acid signaling with other signaling pathways in plant stress responses and development. *Plan. Theory* 8:20. doi: 10.3390/plants8120592

Lee, W. K., and Cho, M. H. (2019). Epigenetic aspects of telomeric chromatin in *Arabidopsis thaliana*. *BMB Rep.* 52, 175–180. doi: 10.5483/BMBRep.2019.52.3.047

Lee, H. W., Cho, C., Pandey, S. K., Park, Y., Kim, M. J., and Kim, J. (2019). LBD16 and LBD18 acting downstream of ARF7 and ARF19 are involved in adventitious root formation in *Arabidopsis*. *BMC Plant Biol.* 19:46. doi: 10.1186/s12870-019-1659-4

Legen, J., Kemp, S., Krause, K., Profanter, B., Herrmann, R., and Maier, R. (2002). Comparative analysis of plastid transcription profiles of entire plastid chromosomes from tobacco attributed to wild-type and PEP-deficient transcription machineries. *Plant J.* 31, 171–188. doi: 10.1046/j.1365-313X.2002.01349.x

Lepage, E., Zampini, E., and Brisson, N. (2013). Plastid genome instability leads to reactive oxygen species production and plastid-to-nucleus retrograde signaling in *Arabidopsis*. *Plant Physiol.* 163, 867–881. doi: 10.1104/pp.113.223560

Liebthal, M., Schuetze, J., Dreyer, A., Mock, H. P., and Dietz, K. J. (2020). Redox conformation-specific protein–protein interactions of the 2-cysteine peroxiredoxin in *Arabidopsis*. *Antioxidants* 9:515. doi: 10.3390/antiox9060515

Lin, W. F., Huang, D. M., Shi, X. M., Deng, B., Ren, Y. J., Lin, W. X., et al. (2019). H_2O_2 as a feedback signal on dual-located WHIRLY1 associates with leaf senescence in *Arabidopsis*. *Cell* 8:1585. doi: 10.3390/cells8121585

Lin, W. F., Zhang, H., Huang, D. M., Schenke, D., Cai, D. G., Wu, B. H., et al. (2020). Dual-localized WHIRLY1 affects salicylic acid biosynthesis via coordination of ISOCHORISMATE SYNTHASE1, PHENYLALANINE AMMONIA LYASE1, and S-ADENOSYL-L-METHIONINE-DEPENDENT METHYLTRANSFERASE1. *Plant Physiol.* 184, 1884–1899. doi: 10.1104/pp.20.009964

Liu, W., Yan, Y., Zeng, H. Q., Li, X. L., Wei, Y. X., Liu, G. Y., et al. (2018). Functional characterization of WHY-WRKY75 transcriptional module in plant response to cassava bacterial blight. *Tree Physiol.* 38, 1502–1512. doi: 10.1093/treephys/tpy053

Luijsterburg, M. S., Noom, M. C., Wuite, G. J. L., and Dame, R. T. (2006). The architectural role of nucleoid-associated proteins in the organization of bacterial chromatin: a molecular perspective. *J. Struct. Biol.* 156, 262–272. doi: 10.1016/j.jsb.2006.05.006

Luijsterburg, M. S., White, M. F., Van Driel, R., and Dame, R. T. (2008). The major architects of chromatin: architectural proteins in bacteria, archaea and eukaryotes. *Crit. Rev. Biochem. Mol. Biol.* 43, 393–418. doi: 10.1016/j.jsb.2006.05.006

Majeran, W., Friso, G., Asakura, Y., Qu, X., Huang, M., Ponnala, L., et al. (2012). Nucleoid-enriched proteomes in developing plastids and chloroplasts from maize leaves; a new conceptual framework for nucleoid function. *Plant Physiol.* 158, 156–189. doi: 10.1104/pp.111.188474

Majerska, J., Schrumpfova, P. P., Dokladal, L., Schorova, S., Stejskal, K., Oboril, M., et al. (2017). Tandem affinity purification of AtTERT reveals putative interaction partners of plant telomerase in vivo. *Protoplasma* 254, 1547–1562. doi: 10.1007/s00709-016-1042-3

Maréchal, A., and Brisson, N. (2010). Recombination and the maintenance of plant organelle genome stability. *New Phytol.* 186, 299–317. doi: 10.1111/j.1469-8137.2010.03195.x

Maréchal, A., Parent, J.-B., Sabar, M., Veronneau-Laforturne, F., Abou-Rached, C., and Brisson, N. (2008). Overexpression of mtDNA-associated AtWhy2 compromises mitochondrial function. *BMC Plant Biol.* 8:42. doi: 10.1186/1471-2229-8-42

Maréchal, A., Parent, J. S., Veronneau-Lafortune, F., Joyeux, A., Lang, B. F., and Brisson, N. (2009). Whirly proteins maintain plastid genome stability in *Arabidopsis*. *Proc. Natl. Acad. Sci. U. S. A.* 106, 14693–14698. doi: 10.1073/pnas.0901710106

McCoy, R. M., Julian, R., Kumar, S. R. V., Ranjan, R., Varala, K., and Li, Y. (2021). A systems biology approach to identify essential epigenetic regulators for specific biological processes in plants. *Plan. Theory* 10:364. doi: 10.3390/plants10020364

Melonek, J., Matros, A., Trösch, C. M., Mock, H. P., and Krupinska, K. (2012). The core of chloroplast nucleoids contains architectural SWIB-domain proteins. *Plant Cell* 24, 3060–3073. doi: 10.1105/tpc.112.099721

Melonek, J., Mulisch, M., Schmitz-Linneweber, C., Grabowski, E., Hensel, G., and Krupinska, K. (2010). Whirly1 in chloroplasts associates with intron containing RNAs and rarely co-localizes with nucleoids. *Planta* 232, 471–481. doi: 10.1007/s00425-010-1183-0

Melonek, J., Oetke, S., and Krupinska, K. (2016). Multifunctionality of plastid nucleoids as revealed by proteome analyses. *Biochim. Biophys. Acta Proteins Proteom.* 1864, 1016–1038. doi: 10.1016/j.bbapap.2016.03.009

Meng, C., Yang, M. M., Wang, Y. X., Chen, C., Sui, N., Meng, Q. W., et al. (2020). SlWHY2 interacts with SlRECA2 to maintain mitochondrial function under drought stress in tomato. *Plant Sci.* 301:110674. doi: 10.1016/j.plantsci.2020.110674

Miao, Y., Jiang, J. J., Ren, Y. J., and Zhao, Z. W. (2013). The single-stranded DNA-binding protein WHIRLY1 represses WRKY53 expression and delays leaf senescence in a developmental stage-dependent manner in *Arabidopsis*. *Plant Physiol.* 163, 746–756. doi: 10.1104/pp.113.223412

Nguyen, X. T. A., Tran, T. H., Cojoc, D., and Legname, G. (2019). Copper binding regulates cellular prion protein function. *Mol. Neurobiol.* 56, 6121–6133. doi: 10.1007/s12035-019-1510-9

Odijk, T. (1998). Osmotic compaction of supercoiled DNA into a bacterial nucleoid. *Biophys. Chem.* 73, 23–29. doi: 10.1016/S0301-4622(98)00115-X

Oetke, S., Scheidig, A., and Krupinska, K. (2022). WHIRLY1 of barley and maize share a PRAPP motif conferring nucleoid compaction. *Plant Cell Physiol.* 63, 234–247. doi: 10.1093/pcp/pcab164

Olinares, P. D. B., Kim, J., and Van Wijk, K. J. (2011). The Clp protease system; a central component of the chloroplast protease network. *Biochim. Biophys. Acta Bioenerg.* 1807, 999–1011. doi: 10.1016/j.bbabio.2010.12.003

Ono, S., Suzuki, S., Ito, D., Tagawa, S., Shiina, T., and Masuda, S. (2020). Plastidial (p)ppGpp synthesis by the Ca^{2+}-dependent RelA-SpoT homolog regulates the adaptation of chloroplast gene expression to darkness in *Arabidopsis*. *Plant Cell Physiol.* 61, 2077–2086. doi: 10.1093/pcp/pcaa124

Parent, J. S., Lepage, E., and Brisson, N. (2011). Divergent roles for the two PolI-like organelle DNA polymerases of *Arabidopsis*. *Plant Physiol.* 156, 254–262. doi: 10.1104/pp.111.173849

Pfalz, J., Liere, K., Kandlbinder, A., Dietz, K.-J., and Oelmüller, R. (2006). pTAC2, −6, and −12 are components of the transcriptionally active plastid chromosome that are required for plastid gene expression. *Plant Cell* 18, 176–197. doi: 10.1105/rpc.105.036392

Pfannschmidt, T., and Munné-Bosch, S. (2013). "Plastid signaling during the plant life cycle," in *Plastid Development in Leaves during Growth and Senescence*. eds. B. Biswal, K. Krupinska and U. C. Biswal (Dordrecht, Heidelberg, New York, London: Springer), 503–528.

Phinney, B. S., and Thelen, J. J. (2005). Proteomic characterization of a triton-insoluble fraction from chloroplasts defines a novel group of proteins associated with macromolecular structures. *J. Proteome Res.* 4, 497–506. doi: 10.1021/pr049791k

Powikrowska, M., Oetke, S., Jensen, P. E., and Krupinska, K. (2014). Dynamic composition, shaping and organization of plastid nucleoids. *Front. Plant Sci.* 5:424. doi: 10.3389/fpls.2014.00424

Prikryl, J., Watkins, K. P., Friso, G., Van Wijk, K. J., and Barkan, A. (2008). A member of the Whirly family is a multifunctional RNA- and DNA-binding protein that is essential for chloroplast biogenesis. *Nucleic Acids Res.* 36, 5152–5165. doi: 10.1093/nar/gkn492

Prince, R. C., and Gunson, D. E. (1998). Prions are copper-binding proteins. *Trends Biochem. Sci.* 23, 197–198. doi: 10.1016/S0968-0004(98)01209-2

Przybyla-Toscano, J., Christ, L., Keech, O., and Rouhier, N. (2021). Iron sulfur proteins in plant mitochondria: roles and maturation. *J. Exp. Bot.* 72, 2014–2044. doi: 10.1093/jxb/eraa578

Qin, Y. Z., Li, X., Guo, M., Deng, K. Q., Lin, J. Z., Tang, D. Y., et al. (2008). Regulation of salt and ABDA responses by CIPK14, a calcium sensor interacting protein kinase in *Arabidopsis*. *Sci. China Life Sci.* 51, 391–401. doi: 10.1007/s11427-008-0059-z

Rekhter, D., Ludke, D., Ding, Y. L., Feussner, K., Zienkiewicz, K., Lipka, V., et al. (2019). Isochorismate-derived biosynthesis of the plant stress hormone salicylic acid. *Science* 365, 498–502. doi: 10.1126/science.aaw1720

Remesh, S. G., Verma, S. C., Chen, J. H., Ekman, A. A., Larabell, C. A., Adhya, S., et al. (2020). Nucleoid remodeling during environmental adaptation is regulated by HU-dependent DNA bundling. *Nat. Commun.* 11:2905. doi: 10.1038/s41467-020-16724-5

Ren, Y. J., Li, Y. Y., Jiang, Y. Q., Wu, B. H., and Miao, Y. (2017). Phosphorylation of WHIRLY1 by CIPK14 shifts its localization and dual functions in *Arabidopsis*. *Mol. Plant* 10, 749–763. doi: 10.1016/j.molp.2017.03.011

Reyes, J. C., Muro-Pastor, M. I., and Florencio, F. J. (2004). The GATA family of transcription factors in *Arabidopsis* and rice. *Plant Physiol.* 134, 1718–1732. doi: 10.1104/pp.103.037788

Rogalski, M., Ruf, S., and Bock, R. (2006). Tobacco plastid ribosomal protein S18 is essential for cell survival. *Nucleic Acids Res.* 34, 4537–4545. doi: 10.1093/nar/gkl634

Rothman-Denes, L. B., Dai, X., Davydova, E., Carter, R., and Kazmierczak, K. (1998). Transcriptional regulation by DNA structural transitions and single-stranded DNA-binding proteins. *Cold Spring Harb. Symp. Quant. Biol.* 63, 63–74. doi: 10.1101/sqb.1998.63.63

Saeid-Nia, M., Repnik, U., Krupinska, K., and Bilger, W. (2022). The plastid-nucleus localized DNA-binding protein WHIRLY1 is required for acclimation of barley leaves to high light. *Planta* 255:84. doi: 10.1007/s00425-022-03854-x

Sakai, A., Takano, H., and Kuroiwa, T. (2004). Organelle nuclei in higher plants: structure, composition, function and evolution. *Int. Rev. Cytol.* 238, 59–118. doi: 10.1016/S0074-7696(04)38002-2

Senoura, T., Kobayashi, T., An, G., Nakanishi, H., and Nishizawa, N. K. (2020). Defects in the rice aconitase-encodingOsACO1gene alter iron homeostasis. *Plant Mol. Biol.* 104, 629–645. doi: 10.1007/s11103-020-01065-0

Sharma, M., Bennewitz, B., and Klösgen, R. B. (2018). Dual or not dual? Comparative analysis of fluorescence microscopy-based approaches to study organelle targeting specificity of nuclear-encoded plant proteins. *Front. Plant Sci.* 9:1350. doi: 10.3389/fpls.2018.01350

Sharma, J., Kumari, R., Bhargava, A., Tiwari, R., and Mishra, P. K. (2021). Mitochondrial-induced epigenetic modifications: from biology to clinical translation. *Curr. Pharm. Des.* 27, 159–176. doi: 10.2174/1381612826666200826165735

Sharwood, R. E., Halpert, M., Luro, S., Schuster, G., and Stern, D. B. (2011). Chloroplast RNase J compensates for inefficient transcription termination by removal of antisense RNA. *RNA* 17, 2165–2176. doi: 10.1261/rna.028043.111

Singh, D. K., Maximova, S. N., Jensen, P. J., Lehman, B. L., Ngugi, H. K., and Mcnellis, T. W. (2010). FIBRILLIN4 is required for plastoglobule development and stress resistance in apple and *Arabidopsis*. *Plant Physiol.* 154, 1281–1293. doi: 10.1104/pp.110.164095

Singh, D. K., and Mcnellis, T. W. (2011). Fibrillin protein function: the tip of the iceberg? *Trends Plant Sci.* 16, 432–441. doi: 10.1016/j.tplants.2011.03.014

Song, X. W., Li, Y., Cao, X. F., and Qi, Y. J. (2019). MicroRNAs and their regulatory roles in plant-environment interactions. *Annu. Rev. Plant Biol.* 70, 489–525. doi: 10.1146/annurev-arplant-050718-100334

Subramaniam, R., Despres, C., and Brisson, N. (1997). A functional homolog of mammalian protein kinase C participates in the elicitor-induced defense response in potato. *Plant Cell* 9, 653–664.

Sunkar, R., Li, Y. F., and Jagadeeswaran, G. (2012). Functions of microRNAs in plant stress responses. *Trends Plant Sci.* 17, 196–203. doi: 10.1016/j.tplants.2012.01.010

Swida-Barteczka, A., Krieger-Liszkay, A., Bilger, W., Voigt, U., Hensel, G., Szweykowska-Kulinska, Z., et al. (2018). The plastid-nucleus located DNA/RNA binding protein WHIRLY1 regulates microRNA-levels during stress in barley (*Hordeum vulgare* L.). *RNA Biol.* 15, 886–891. doi: 10.1080/15476286.2018.1481695

Takeda, Y., Hirokawa, H., and Nagata, T. (1992). The replication of origin of proplastid DNA in cultured cells of tobacco. *Mol. Gen. Genet.* 232, 191–198. doi: 10.1007/BF00279996

Tarasenko, V. I., Katyshev, A. I., Subota, I. Y., and Konstantinov, Y. M. (2012). Recombinant *Arabidopsis* WHY2 protein binds unspecifically to single-stranded DNA and is phosphorylated by mitochondrial protein kinases. *Plant Omics* 5, 372–375.

Telman, W., Liebthal, M., and Dietz, K. J. (2020). Redox regulation by peroxiredoxins is linked to their thioredoxin-dependent oxidase function. *Photosynth. Res.* 145, 31–41. doi: 10.1007/s11120-019-00691-0

Till, B. J., Reynolds, S. H., Greene, E. A., Codomo, C. A., Enns, L. C., Johnson, J. E., et al. (2003). Large-scale discovery of induced point mutations with high-throughput TILLING. *Genome Res.* 13, 524–530. doi: 10.1101/gr.977903

Till, B., Schmitz-Linneweber, C., Williams-Carrier, R., and Barkan, A. (2001). CRS1 is a novel group II intron splicing factor that was derived from a domain of ancient origin. *RNA* 7, 1227–1238. doi: 10.1017/S1355838201010445

Tiller, N., and Bock, R. (2014). The translational apparatus of plastids and its role in plant development. *Mol. Plant* 7, 1105–1120. doi: 10.1093/mp/ssu022

Trigg, S. A., Garza, R. M., Macwilliams, A., Nery, J. R., Bartlett, A., Castanon, R., et al. (2017). CrY2H-seq: a massively multiplexed assay for deep-coverage interactome mapping. *Nat. Methods* 14, 819–825. doi: 10.1038/nmeth.4343

Torres-Romero, D., Gómez-Zambrano, Á., Serrato, A. J., Sahrawy, M., and Mérida, À. (2022). Arabidopsis fibrillin 1-2 subfamily members exert their functions via specific protein-protein interactions. *J. Exp. Bot.* 73, 903–914. doi: 10.1093/jxb/erab452

Tvorogova, V. E., Krasnoperova, E. Y., Potsenkovskaia, E. A., Kudriashov, A. A., Dodueva, I. E., and Lutova, L. A. (2021). What does the WOX say? Review of regulators, targets, partners. *Mol. Biol.* 55, 311–337. doi: 10.1134/S002689332102031X

Valkenburg, J. A. C., and Woldringh, C. L. (1984). Phase-separation between nucleoid and cytoplasm in *Escherichia coli* as defined by immersive

refractometry. *J. Bacteriol.* 160, 1151–1157. doi: 10.1128/jb.160.3.1151-1157.1984

Vlot, A. C., Dempsey, D. A., and Klessig, D. F. (2009). Salicylic acid, a multifaceted hormone to combat disease. *Annu. Rev. Phytopathol.* 47, 177–206. doi: 10.1146/annurev.phyto.050908.135202

Wang, W. J., Li, K., Yang, Z., Hou, Q. C., Zhao, W. W., and Sun, Q. W. (2021). RNase H1C collaborates with ssDNA binding proteins WHY1/3 and recombinase RecA1 to fulfill the DNA damage repair in *Arabidopsis* chloroplasts. *Nucleic Acids Res.* 49, 6771–6787. doi: 10.1093/nar/gkab479

Williams-Carrier, R., Zoschke, R., Belcher, S., Pfalz, J., and Barkan, A. (2014). A major role for the plastid-encoded RNA polymerase complex in the expression of plastid transfer RNAs. *Plant Physiol.* 164, 239–248. doi: 10.1104/pp.113.228726

Wolf, S. G., Frenkiel, D., Arad, T., Finkel, S. E., Kolter, R., and Minsky, A. (1999). DNA protection by stress-induced biocrystallization. *Nature* 400, 83–85.

Xiao, Y. M., Savchenko, T., Baidoo, E. E. K., Chehab, W. E., Hayden, D. M., Tolstikov, V., et al. (2012). Retrograde signaling by the plastidial metabolite MEcPP regulates expression of nuclear stress-response genes. *Cell* 149, 1525–1535. doi: 10.1016/j.cell.2012.04.038

Xiao, Y. M., Wang, J. Z., and Dehesh, K. (2013). Review of stress specific organelles-to-nucleus metabolic signal molecules in plants. *Plant Sci.* 212, 102–107. doi: 10.1016/j.plantsci.2013.08.003

Xiong, J. Y., Lai, C. X., Qu, Z., Yang, X. Y., Qin, X. H., and Liu, G. Q. (2009). Recruitment of AtWHY1 and AtWHY3 by a distal element upstream of the kinesin gene AtKP1 to mediate transcriptional repression. *Plant Mol. Biol.* 71, 437–449. doi: 10.1007/s11103-009-9533-7

Xu, Y. H., Liu, R., Yan, L., Liu, Z. Q., Jiang, S. C., Shen, Y. Y., et al. (2012). Light-harvesting chlorophyll a/b-binding proteins are required for stomatal response to abscisic acid in Arabidopsis. *J. Exp. Bot.* 63, 1095–1106. doi: 10.1093/jxb/err315

Xu, F., Tang, J. Y., Gao, S. P., Chang, X., Du, L., and Chu, C. C. (2019). The coordinated action of PPR4 and EMB2654 on each intron half mediates trans-splicing of *rps12* transcripts in plant chloroplasts. *Plant J.* 100, 1193–1207. doi: 10.1111/tpj.14509

Yan, Y., Liu, W., Wei, Y. X., and Shi, H. T. (2020). MeCIPK23 interacts with Whirly transcription factors to activate abscisic acid biosynthesis and regulate drought resistance in cassava. *Plant Biotechnol. J.* 18, 1504–1506. doi: 10.1111/pbi.13321

Yang, Z., Hou, Q. C., Cheng, L. L., Xu, W., Hong, Y. T., Li, S., et al. (2017). RNase H1 cooperates with DNA gyrases to restrict R-loops and maintain genome integrity in *Arabidopsis* chloroplasts. *Plant Cell* 29, 2478–2497. doi: 10.1105/tpc.17.00305

Yogev, O., and Pines, O. (2011). Dual targeting of mitochondrial proteins: mechanism, regulation and function. *Biochim. Biophys. Acta* 1808, 1012–1020. doi: 10.1016/j.bbamem.2010.07.004

Yoo, H. H., Kwon, C., Lee, M. M., and Chung, I. K. (2007). Single-stranded DNA binding factor AtWHY1 modulates telomere length homeostasis in *Arabidopsis*. *Plant J.* 49, 442–451. doi: 10.1111/j.1365-313X.2006.02974.x

Yu, F., Fu, A. G., Aluru, M., Park, S., Xu, Y., Liu, H. Y., et al. (2007). Variegation mutants and mechanisms of chloroplast biogenesis. *Plant Cell Environ.* 30, 350–365. doi: 10.1111/j.1365-3040.2006.01630.x

Zampini, E., Lepage, E., Tremblay-Belzile, S., Truche, S., and Brisson, N. (2015). Organelle DNA rearrangement mapping reveals U-turn-like inversions as a major source of genomic instability in *Arabidopsis* and humans. *Genome Res.* 25, 645–654. doi: 10.1101/gr.188573.114

Zaitlin, D., Hu, J., and Bogorad, L. (1989). Binding and transcription of relaxed DNA templates by fractions of maize chloroplast extracts. *Proc. Natl. Acad. Sci. U.S.A.* 86, 876–880.

Zentgraf, U., and Doll, J. (2019). Arabidopsis WRKY53, a node of multi-layer regulation in the network of senescence. *Plants* 8:578. doi: 10.3390/plants8120578

Zhang, Y. F., Hou, M. M., and Tan, B. C. (2013). The requirement of WHIRLY1 for embryogenesis is dependent on genetic background in maize. *PLoS One* 8:12. doi: 10.1371/journal.pone.0067369

Zhang, J. X., Yuan, H., Yang, Y., Fish, T., Lyi, S. M., Thannhauser, T. W., et al. (2016). Plastid ribosomal protein S5 is involved in photosynthesis, plant development, and cold stress tolerance in *Arabidopsis*. *J. Exp. Bot.* 67, 2731–2744. doi: 10.1093/jxb/erw106

Zhao, S. Y., Wang, G. D., Zhao, W. Y., Zhang, S., Kong, F. Y., Dong, X. C., et al. (2018). Overexpression of tomato WHIRLY protein enhances tolerance to drought stress and resistance to *pseudomonas solanacearum* in transgenic tobacco. *Biol. Plant.* 62, 55–68. doi: 10.1007/s10535-017-0714-y

Zheng, B., Halperin, T., Hruskova-Heidingsfeldova, O., Adam, Z., and Clarke, A. K. (2002). Characterization of chloroplast Clp proteins in *Arabidopsis*: localization, tissue specificity and stress responses. *Physiol. Plant.* 114, 92–101. doi: 10.1034/j.1399-3054.2002.1140113.x

Zhuang, K. Y., Gao, Y. Y., Liu, Z. B., Diao, P. F., Sui, N., Meng, Q. W., et al. (2020a). WHIRLY1 regulates HSP21.5A expression to promote thermotolerance in tomato. *Plant Cell Physiol.* 61, 169–177. doi: 10.1093/pcp/pcz189

Zhuang, K. Y., Kong, F. Y., Zhang, S., Meng, C., Yang, M. M., Liu, Z. B., et al. (2019). Whirly1 enhances tolerance to chilling stress in tomato via protection of photosystem II and regulation of starch degradation. *New Phytol.* 221, 1998–2012. doi: 10.1111/nph.15532

Zhuang, K. Y., Wang, J. Y., Jiao, B. Z., Chen, C., Zhang, J. J., Ma, N. N., et al. (2020b). WHIRLY1 maintains leaf photosynthetic capacity in tomato by regulating the expression of RbcS1 under chilling stress. *J. Exp. Bot.* 71, 3653–3663. doi: 10.1093/jxb/eraa145

Conflict of Interest: The authors declare that the research was conducted in the absence of any commercial or financial relationships that could be construed as a potential conflict of interest.

Publisher's Note: All claims expressed in this article are solely those of the authors and do not necessarily represent those of their affiliated organizations, or those of the publisher, the editors and the reviewers. Any product that may be evaluated in this article, or claim that may be made by its manufacturer, is not guaranteed or endorsed by the publisher.

frontiers | Frontiers in Plant Science

MINI REVIEW
published: 25 April 2022
doi: 10.3389/fpls.2022.897549

Recent Developments in Deciphering the Biological Role of Plant Complex *N*-Glycans

*Richard Strasser**

Department of Applied Genetics and Cell Biology, Institute of Plant Biotechnology and Cell Biology, University of Natural Resources and Life Sciences, Vienna, Austria

Asparagine (*N*)-linked protein glycosylation is a ubiquitous co- and posttranslational modification which has a huge impact on the biogenesis and function of proteins and consequently on the development, growth, and physiology of organisms. In mammals, *N*-glycan processing carried out by Golgi-resident glycosidases and glycosyltransferases creates a number of structurally diverse *N*-glycans with specific roles in many different biological processes. In plants, complex *N*-glycan modifications like the attachment of β1,2-xylose, core α1,3-fucose, or the Lewis A-type structures are evolutionary highly conserved, but their biological function is poorly known. Here, I highlight recent developments that contribute to a better understanding of these conserved glycoprotein modifications and discuss future directions to move the field forward.

Keywords: glycan, glycoprotein, glycosylation, posttranslational modification, secretory pathway

OPEN ACCESS

Edited by:
Anna N. Stepanova,
North Carolina State University,
United States

Reviewed by:
Takeshi Ishimizu,
Ritsumeikan University, Japan
Jianming Li,
University of Michigan, United States
Kazuhito Fujiyama,
Osaka University, Japan
Naoki Hirotsu,
Toyo University, Japan

***Correspondence:**
Richard Strasser
richard.strasser@boku.ac.at

Specialty section:
This article was submitted to Plant Physiology, a section of the journal Frontiers in Plant Science

Received: *16 March 2022*
Accepted: *06 April 2022*
Published: *25 April 2022*

Citation:
Strasser R (2022) Recent Developments in Deciphering the Biological Role of Plant Complex N-Glycans. Front. Plant Sci. 13:897549. doi: 10.3389/fpls.2022.897549

INTRODUCTION

N-glycosylation of proteins is initiated in the lumen of the endoplasmic reticulum (ER) by the oligosaccharyltransferase (OST) complex which transfers a preassembled oligosaccharide to an asparagine residue within the Asn-X-Ser/Thr consensus sequence of a nascent polypeptide. While the total number of proteins in the plant *N*-linked glycoproteome is unknown, every protein that has the consensus *N*-glycosylation site in its sequence and is targeted to the secretory pathway is a potential substrate for *N*-glycosylation and *N*-glycan dependent folding. The transferred oligosaccharide can directly influence polypeptide folding by stabilizing protein conformations. In addition to the direct effect of the attached oligosaccharide, specific *N*-glycans are recognized as signals by lectins which assist in protein folding, retain folding intermediates in the ER, or trigger ER-associated degradation (ERAD) if proper folding cannot be achieved (Strasser, 2018; Zhang et al., 2021).

Initial trimming by ER-resident α-glucosidases (GCSI and GCSII, **Figure 1A**) generates a monoglucosylated *N*-glycan that allows the transient interaction with the lectins calnexin or calreticulin and entry into an ER-quality control cycle. Further trimming of mannose residues is carried out by ER- (MNS3) and Golgi-α-mannosidases (GMI; Liebminger et al., 2009; Kajiura et al., 2010). The resulting $Man_5GlcNAc_2$ *N*-glycan is used as acceptor substrate by the *cis*/*medial*-Golgi-resident *N*-acetylglucosaminyltransferase I (GNTI). GNTI transfers a single *N*-acetylglucosamine (GlcNAc) residue and initiates the formation of characteristic complex *N*-glycans carrying β1,2-linked xylose and an α1,3-fucose attached to the innermost GlcNAc, respectively (GnGnXF structures, **Figure 1B**). While the core complex *N*-glycan is identical in mammals and plants,

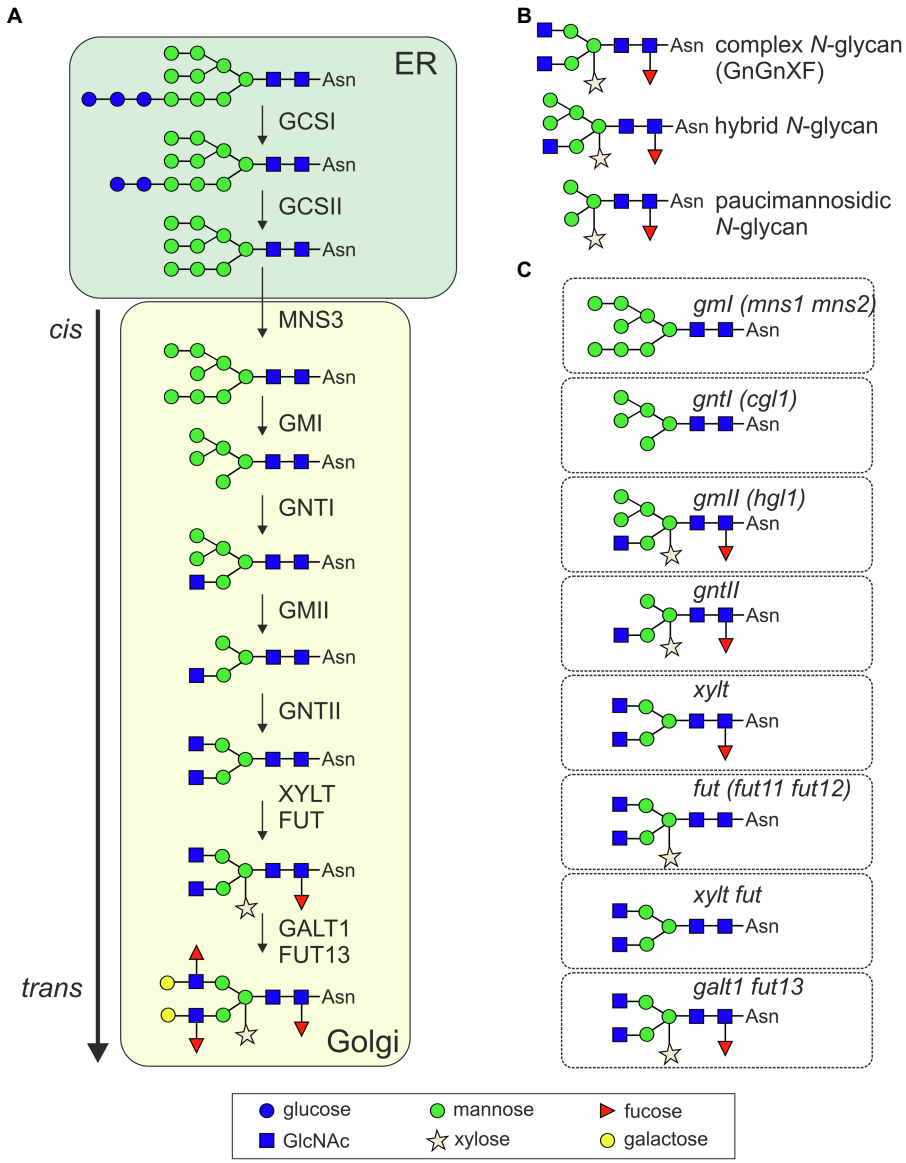

FIGURE 1 | (A) Illustration of the processing pathway for the formation of complex *N*-glycans in plants. GCSI, α-glucosidases I (GCSI); GCSII, α-glucosidases II; MNS3, ER α-mannosidase; GMI, Golgi α-mannosidase I (two forms termed MNS1 and MNS2 with redundant function are present in *Arabidopsis thaliana*); GNTI, β1,2-*N*-acetylglucosaminyltransferase I; GMII, Golgi α-mannosidase II; GNTII, β1,2-*N*-acetylglucosaminyltransferase II; XYLT, β1,2-xylosyltransferase; FUT, core α1,3-fucosyltransferases (two forms termed FUT11 and FUT12 with redundant function are present in *A. thaliana*); GALT1, Lewis type β1,3-galactosyltransferase; and FUT13, α1,4-fucosyltransferase. Not shown: the removal of terminal GlcNAc residues by β-hexosaminidases, which generates paucimannosidic *N*-glycans in post-Golgi compartments, at the plasma membrane or in the extracellular space. **(B)** Illustration of typical complex, hybrid, and paucimannosidic *N*-glycans. **(C)** Illustration of the predominate *N*-glycan structure of the indicated knockout mutants. Alternative names of the mutants are given in brackets. Symbols are used according to the suggestions from the Consortium for Functional Glycomics (http://www.functionalglycomics.org/).

β1,2-xylose and core α1,3-fucose modifications are not found on mammalian glycoproteins (Strasser, 2016). Their biosynthesis is carried out by β1,2-xylosyltransferase (XYLT) and core α1,3-fucosyltransferase (FUT; Strasser et al., 2004). While GnGnXF is the dominant structure on many glycoproteins (Zeng et al., 2018), on a rather small number of glycoproteins, the GnGnXF *N*-glycan is further modified by β1,3-galactosyltransferase (GALT1) and α1,4-fucosyltransferase (FUT13) to generate Lewis A-type structures (Strasser et al., 2007a; Beihammer et al., 2021). In the vacuole, at the plasma membrane or in the apoplast, different β-hexosaminidases can cleave off terminal GlcNAc residues from exposed complex *N*-glycans resulting in the formation of truncated or paucimannosidic *N*-glycans (Strasser et al., 2007b; Alvisi et al., 2021). The biosynthetic pathway and involved enzymes are well characterized and have been reviewed in detail recently (Strasser et al., 2021). Notably, the whole machinery for complex

N-glycan formation appears conserved in vascular plants and in mosses like *Physcomitrella patens* (Koprivova et al., 2003; Viëtor et al., 2003; Strasser, 2016; Stenitzer et al., 2022). Complex GnGnXF and Lewis A-type structures are ubiquitously found in plants (Fitchette-Lainé et al., 1997; Wilson et al., 2001; Beihammer et al., 2021) which point to a selective pressure and a functional advantage to maintain these *N*-glycans. Despite this conservation, the knowledge about the physiological role of complex *N*-glycan modifications is still limited. However, in the last decade, considerable progress has been made and different processes have been revealed where complex *N*-glycans play an important role in plant physiology, development, and under various stress conditions. This has been spurred by in-depth analysis of Arabidopsis mutants and gene knockouts generated by CRISPR/Cas9 genome editing or other technologies in different plant species.

THE ACHIEVEMENTS IN THE PAST DECADE: DECIPHERING THE BIOLOGICAL ROLE OF COMPLEX *N*-GLYCANS BY PHENOTYPIC CHARACTERIZATION OF GENE KNOCKOUTS

Our knowledge about the role of complex *N*-glycans stems mainly from the analysis of mutants deficient in *N*-glycan processing steps. The Arabidopsis *complex glycan1* (*cgl1* or *gntI*) mutant that lacks GNTI activity and thus displays $Man_5GlcNAc_2$ instead of complex *N*-glycans was first described almost three decades ago (von Schaewen et al., 1993; **Figure 1C**). In this pioneering study on the role of complex *N*-glycans in plants, no obvious growth or developmental phenotype was reported for *cgl1* plants grown under controlled growth conditions. This lack of a severe phenotype in Arabidopsis *cgl1* was a surprise because the consequence of GNTI-deficiency in mammals was embryonic lethality (Ioffe and Stanley, 1994; Metzler et al., 1994). Later it was, however, shown that Arabidopsis *cgl1* displayed reduced root growth when subjected to osmotic stress or high salt concentrations (Kang et al., 2008) and a recent study observed that *cgl1* has reduced photosynthetic efficiency (Jiao et al., 2020). This link to photosynthesis suggests that glycoproteins carrying complex *N*-glycans are transported from the Golgi apparatus or a post-Golgi compartment to chloroplasts where they fulfill important functions. Of note, a detailed analysis of the root system in Arabidopsis seedlings showed that root hairs are significantly longer in *cgl1* plants which for the first time revealed a developmental phenotype in Arabidopsis plants with abrogated complex *N*-glycan formation (Frank et al., 2021). The *cgl1* roots appeared generally more responsive to synthetic phytohormones suggesting that complex *N*-glycans on one or several glycoproteins are critical for phytohormone homeostasis.

A knockdown of *GnTI* expression in *Nicotiana benthamiana* resulted in a decrease in the amounts of complex type *N*-glycans from 90% to less than 10% without any growth or reproduction defects (Limkul et al., 2016). This is consistent with previous data showing that *N. benthamiana*, which is frequently used as a production platform for protein-based biopharmaceuticals, tolerates the virtual absence of GnGnXF *N*-glycans very well (Strasser et al., 2008). While a *GnTI* knockdown in tomato resulted in abnormal fruit ripening (Kaulfürst-Soboll et al., 2021), an *Oryza sativa* GNTI-deficient line that displayed a similar *N*-glycan profile as Arabidopsis *cgl1* showed a severe growth phenotype with arrested seedling development and lethality before reaching the reproductive stage (Fanata et al., 2013). In line with this finding, *GnTI* gene disruption in the legume *Lotus japonicus* caused a severe growth defect with lethality before reaching the flowering stage (Pedersen et al., 2017). Taken together, our knowledge on the role of GNTI in Arabidopsis and other plants has enormously increased in the last decade.

Upon transfer of the single GlcNAc by GNTI, two mannose residues are removed by Golgi-α-mannosidase II (GMII). In contrast to GNTI, GMII deficiency does not block further processing completely and results in hybrid *N*-glycans that are still modified with β1,2-xylose and core α1,3-fucose (Strasser et al., 2006; Kaulfürst-Soboll et al., 2011). Tomatoes with reduced *GMII* expression produced fewer and enlarged seeds (Kaulfürst-Soboll et al., 2021) and Arabidopsis *gmII* plants displayed similar differences in root hair density and length as Arabidopsis *cgl1*/*gntI* (Frank et al., 2021). The finding in Arabidopsis suggests that terminal modifications (presence of mannose residues or absence of GlcNAc residues on both antennae or blocked terminal elongations) rather than core glycan modifications (attachment of xylose or fucose) are important for the function in root hair elongation (**Figure 1C**). Consistent with this, *galt1 fut13* double mutants lacking *N*-glycan modifications that form the Lewis A structure are partially impaired in root hair elongation (Frank et al., 2021) indicating a specific role for these terminal complex *N*-glycan modifications.

After the removal of the two terminal mannose residues by GMII, the free α1,6-mannose of the core glycan is used by *N*-acetylglucosaminyltransferase II (GNTII) for the attachment of a single GlcNAc residue (Strasser et al., 1999). Consequently, *GnTII* loss-of-function in Arabidopsis prevents the formation of GnGnXF glycans and *gntII* mutants displayed numerous phenotypes including slightly early flowering, accelerated dark-induced leaf senescence and altered responses to NaCl, the *N*-glycosylation inhibitor tunicamycin, a synthetic cytokinin, and a polar auxin transport inhibitor (Yoo et al., 2021). These pleiotropic effects suggest that several glycoproteins involved in different processes are affected in the *gntII* mutant. Consistent with the impaired auxin transport, the abundance of the auxin transporter PIN2 fused to GFP and its subcellular localization were altered in *gntII*. However, PIN2 is likely not *N*-glycosylated because all potential *N*-glycosylation sites are in the hydrophilic loop that faces the cytosol. Therefore, it is more likely that other glycoproteins involved in auxin signaling or transport are directly affected by incomplete processing of the α1,6-mannose on the complex *N*-glycan.

No phenotype has so far been described for the Arabidopsis FUT loss-of-function mutant lacking core α1,3-fucose residues

(Strasser et al., 2004). In line with the crucial role of complex *N*-glycans in other plant species, growth defects, reduced seed number, impaired pollen viability, and morphology were observed in rice and *L. japonicus fut* lines (Harmoko et al., 2016; Pedersen et al., 2017; Sim et al., 2018). By contrast, genome-edited *Nicotiana benthamiana* completely lacking β1,2-xylose and core α1,3-fucose did not display any growth abnormalities or reproduction defects (Jansing et al., 2019). Overall, the function of the β1,2-xylose residue is poorly understood, and phenotypes have only been described for a rice XYLT-deficient mutant. Rice *xylt* plants are impaired in their growth under adverse environmental conditions including extreme temperatures, drought, or salt stress (Takano et al., 2015). Rice callus lacking XYLT and FUT activities grew normal, but plants could not be regenerated from *xylt fut* rice callus which is likely caused by the altered phytohormone responsiveness (Jung et al., 2021). Taken together, these findings indicate that complex *N*-glycans are essential in many plant species for growth, reproduction, phytohormone homeostasis, and for the response to different stresses (**Table 1**). In Arabidopsis, complex *N*-glycans play an important role for root hair elongation in addition to the role in abiotic stress tolerance. Like pollen, root hairs are formed through tip growths and secrete numerous cell wall components which could be impaired in the *N*-glycan processing mutants. In line with described phenotypes for pollen, FUT13 which catalyzes the final *N*-glycan processing step in the Golgi (**Figure 1**) appears highly regulated during pollen development (Joly et al., 2002). Transcription of glycosidases or glycosyltransferases involved in *N*-glycan processing provides another level for regulating the abundance of certain *N*-glycan structures. While glycoenzyme-specific transcription factors have not been identified in plants yet, the transcriptional regulation of *GALT1* and *FUT13* likely contributes to the abundance of Lewis A structures in different Arabidopsis organs (Strasser et al., 2007a; Stefanowicz et al., 2016). Furthermore, β-hexosaminidases or other degrading glycosidases that act on complex *N*-glycans may have a physiological role that is largely unknown (Strasser et al., 2007b; Kato et al., 2018).

THE CHALLENGE FOR THE NEXT 10 YEARS: UNDERSTANDING THE ROLE OF DISTINCT *N*-GLYCAN MODIFICATIONS ON INDIVIDUAL GLYCOPROTEINS TO OBTAIN MECHANISTIC INSIGHTS

For almost all the identified biological processes where complex *N*-glycans are involved, an insight into the underlying mechanisms and molecular function of a distinct complex *N*-glycan linked to an individual protein is missing. The disadvantage of characterization of *N*-glycan processing mutants is their pleiotropic effect on numerous glycoproteins and an inherent difficulty to identify individual *N*-glycans on a distinct glycoprotein that are involved in a specific process. In a recent glycoproteome study (Liu et al., 2021), differentially abundant proteins were identified in Arabidopsis wild type, *cgl1* and the *gmI* mutant when grown under elevated salt conditions. Among the proteins increased under salt stress were proteins involved in glycoprotein biosynthesis, stress response, signal transduction, and oxidation–reduction processes. Two peroxidases (PRX32 and PRX34) were, for example, differentially abundant in the mutants under salt stress. The two peroxidases have several potential *N*-glycosylation sites in their amino acid sequence, were *N*-glycosylated, and seedlings of the peroxidase double knockout mutant were salt-sensitive (Liu et al., 2021). While such studies provide a starting point for the characterization of *N*-glycan modifications on individual proteins, there is no direct evidence that the *N*-glycosylation and distinct *N*-glycan modifications are indeed relevant for the function of the two peroxidases. Because of impaired complex *N*-glycan processing, many different processes are affected leading to massive changes in the transcriptome and proteome that are indirect due to alterations of key signaling pathways (Sim et al., 2018). In mammalian cells, there is evidence that Golgi-mediated complex *N*-glycan modifications like core α1,6-fucosylation regulate the *N*-glycosylation efficiency on different glycoproteins (Huang et al., 2021). The regulation of the upstream *N*-glycosylation process catalyzed by the ER-resident OST complex by downstream *N*-glycan modifications could be mediated by Golgi feedback events as part of poorly understood Golgi-quality control mechanisms (Sun and Brodsky, 2019). This further complicates the interpretation of quantitative glycoproteomics data obtained from *N*-glycan processing mutants. Moreover, underglycosylated proteins are more instable, prone to aggregation and therefore less efficiently enriched by commonly used lectin-based affinity purification approaches. Lectins typically show a preference for a certain type of *N*-glycan causing a bias when samples with different *N*-glycan compositions are analyzed. Collectively, this makes the comparison of the *N*-glycoproteome abundance from different mutants impossible. Even when all these difficulties can be overcome, a confirmed differentially abundant glycoprotein with altered *N*-glycans in a mutant background might not be involved in the process and a comprehensive characterization of the glycoprotein and its fate in the mutant background are required to unravel the underlying mechanisms. Approaches to understand the role of complex *N*-glycans on individual proteins include the analysis of the molecular function (e.g., enzymatic activity), protein stability, cellular interaction partners, and the subcellular localization when the *N*-glycan composition is altered on the protein. As mentioned before, the difficulty is to distinguish between specific and pleiotropic effects in the mutant background. Despite some tremendous progress in glycoengineering in plants (Schoberer and Strasser, 2018), controlled site-specific modification of *N*-glycans (e.g., to furnish one *N*-glycan with Lewis A-type structures while another *N*-glycan attached to a different position on the same protein stays GnGnXF) is currently not possible *in vivo*. Therefore, multiple tedious approaches are required with the generation of mutant variants that lack individual *N*-glycosylation sites and careful examination of the protein fate and function.

TABLE 1 | Overview of phenotypes in vascular plants with aberrant *N*-glycans.

Species	Gene[1]	Technology[2]	Phenotype[3]	Reference
Arabidopsis thaliana	*GMI*	T-DNA	Altered root morphology	Liebminger et al., 2009
			No obvious phenotype	Kajiura et al., 2010
			Increased salt sensitivity	Liu et al., 2018
			Increased sensitivity to *Pseudomonas syringae*	Jia et al., 2020
	GnTI	EMS/T-DNA	No obvious phenotype	von Schaewen et al., 1993
			Increased salt sensitivity	Kang et al., 2008
			Decreased photosynthetic efficiency	Jiao et al., 2020
			Altered auxin responsiveness Altered root hair development	Frank et al., 2021
	GMII	T-DNA	No obvious phenotype	Strasser et al., 2006
			Increased salt sensitivity	Kang et al., 2008 Kaulfürst-Soboll et al., 2011
			Altered auxin responsiveness Altered root hair development	Frank et al., 2021
	GnTII	T-DNA	Altered growth under stress Altered phytohormone response	Yoo et al., 2021
	Xylt	T-DNA	No obvious phenotype	Strasser et al., 2004 Kang et al., 2008
	Fut	T-DNA	No obvious phenotype	Strasser et al., 2004 Kang et al., 2008
	Xylt + Fut	T-DNA	No obvious phenotype	Strasser et al., 2004
	Galt1 + Fut13	T-DNA	Increased salt sensitivity	Kang et al., 2008
			No obvious phenotype	Strasser et al., 2007a
			Altered root hair development	Frank et al., 2021
Oryza sativa	*GnTI*	T-DNA	Reduced growth, altered seed set	Fanata et al., 2013
	Xylt	Gamma-ray	Plant growth affected under various stresses, affected seed germination	Takano et al., 2015
	Fut	T-DNA	Pollen viability affected	Sim et al., 2018
	Fut	T-DNA	Developmental abnormalities Increased sensitivity to *Magnaporthe oryzae*	Harmoko et al., 2016
	Xylt + Fut	CRISPR/Cas9	No phenotype in callus	Jung et al., 2021
Lotus japonicus	*GMI*	LORE1 retrotransposon	Reduced growth Reduced seed number	Pedersen et al., 2017
	GnTI	LORE1 retrotransposon	Severe growth defect, lethality	Pedersen et al., 2017
	Fut	LORE1 retrotransposon	Reduced growth Reduced seed number	Pedersen et al., 2017
Nicotiana benthamiana	*GnTI*	RNAi	No obvious phenotype	Limkul et al., 2016
	Xylt	CRISPR/Cas9	No obvious phenotype	Jansing et al., 2019
	Fut	CRISPR/Cas9	No obvious phenotype	Jansing et al., 2019
	Xylt + Fut	CRISPR/Cas9	No obvious phenotype	Jansing et al., 2019
	Xylt + Fut	RNAi	No obvious phenotype	Strasser et al., 2008
Nicotiana tabacum	*GnTI*	antisense	No obvious phenotype	Wenderoth and von Schaewen, 2000
tobacco BY-2 cells	*GnTI*	CRISPR/Cas9	No obvious phenotype	Herman et al., 2021
	Xylt + Fut	CRISPR/Cas9	No obvious phenotype	Hanania et al., 2017
	Xylt + Fut	CRISPR/Cas9	No obvious phenotype	Mercx et al., 2017
Solanum lycopersicum	*GnTI*	RNAi	Abnormal fruit ripening	Kaulfürst-Soboll et al., 2021
	GMII	RNAi	Fewer, enlarged seeds	Kaulfürst-Soboll et al., 2021
Solanum tuberosum	*GnTI*	antisense	No obvious phenotype	Wenderoth and von Schaewen, 2000

[1]*N-glycan processing defects of Golgi located enzymes are listed.*
[2]*This indicates the technology used to generate the mutants.*
[3]*For mutants with various phenotypes, only some characteristic phenotypes are shown.*

An in-depth analysis of *N*-glycan function has been done for KORRIGAN 1 (KOR1), a β1,4-endoglucanase involved in cellulose biosynthesis (Lane et al., 2001; Liebminger et al., 2013; Rips et al., 2014; Nagashima et al., 2020). KOR1 is a membrane-anchored glycoprotein with eight *N*-glycosylation sites in its extracellular domain. *N*-glycan analysis of a recombinant variant as well as the analysis of *N*-glycosylation site mutants expressed in plants confirmed that all sites are *N*-glycosylated (Liebminger et al., 2013; Rips et al., 2014). KOR1 is glycosylated with oligomannosidic *N*-glycans as well as with Golgi-processed complex ones. While *N*-glycosylation is essential for the enzymatic function, analysis of purified recombinant KOR1 carrying different *N*-glycan compositions showed that *N*-glycan processing in the Golgi is not important for KOR1 enzymatic activity (Mølhøj et al., 2001; Liebminger et al., 2013). Of note, genetic interaction analysis between a KOR1 partial loss-of-function allele (*rsw2-1*) and *N*-glycan processing mutants like *cgl1* revealed strong synergistic effects on the plant growth (Kang et al., 2008). Moreover, a non-glycosylated KOR1 variant could partially complement the root growth phenotype of a KOR1-deficient mutant (Rips et al., 2014). The data from the enzymatic activity assays and complementation of the *rsw2-1* mutant strongly suggest that other glycoproteins are affected which require complex *N*-glycans for their function and thus contribute to the phenotype when KOR1 is compromised (Liebminger et al., 2013; Rips et al., 2014; Nagashima et al., 2020). Biochemical analysis indicated that KOR1 protein abundance is affected under salt stress when mannose-trimming is blocked in the Arabidopsis *gmI* mutant suggesting the involvement of a yet to be discovered mechanism that regulates glycoprotein stability or trafficking under different environmental conditions (Liu et al., 2018). Taken together, these findings highlight the complexity in the analysis of *N*-glycan function on individual proteins and the difficulty to separate effects from oligomannosidic *N*-glycans in the ER (e.g., protein folding, quality control, and degradation) and processed *N*-glycans in the Golgi (e.g., conformational changes and protein–protein interactions).

To overcome current hurdles and move the field forward, more efforts should be made to purify individual glycoproteins from different plant organs, cell-types, or different growth conditions and perform a comprehensive analysis of their *N*-glycosylation status including the number of *N*-glycans, the degree of site occupancy, and the *N*-glycan composition. Using such approaches, it may be possible to reveal potential changes in *N*-glycan structures on an individual glycoprotein that point toward a specific function during development or under stress conditions. While there are indications that *N*-glycans vary under different growth conditions or developmental stages (Elbers et al., 2001; Horiuchi et al., 2016; Kaulfürst-Soboll et al., 2021), the underlying cause of the differences is less clear. Changes may be attributed to variations in protein abundance, expression of glycoproteins, *N*-glycosylation efficiency, or altered *N*-glycan structures. In addition to ER-quality control, there are data suggesting a role of lectin-glycoprotein interactions in the Golgi, *trans*-Golgi network (TGN) or another post-Golgi compartment that may provide another layer of quality control or regulation of transport to specific organelles (Rips et al., 2014; Liu et al., 2018; Veit et al., 2018; Nagashima et al., 2020). In the future, we will gain more insights into these processes involving complex *N*-glycans.

The conserved nature of many complex *N*-glycan modifications could be the result of a selection pressure mediated by pathogens (Gagneux and Varki, 1999). While the impact of *N*-glycosylation and glycan-mediated folding on pattern recognition receptors is well known (Nekrasov et al., 2009; Saijo et al., 2009; Häweker et al., 2010), the role of complex *N*-glycans under biotic stress conditions is still poorly understood. The Arabidopsis *gmI* mutant is more susceptible to *Pseudomonas syringae* (Jia et al., 2020) and rice *fut* plants are more susceptible to *Magnaporthe oryzae* (Harmoko et al., 2016) providing hints that complex *N*-glycans have crucial roles in plant immunity during pathogen infection. In the next decade, we will likely uncover many more examples of interactions of plants with symbiotic or pathogenic organisms that depend on specific *N*-glycan modifications and interacting lectins. In conclusion, numerous biological processes with functional roles of complex *N*-glycans are known now. These discoveries lay the foundation to examine the role of complex *N*-glycans on individual proteins and decipher the underlying mechanisms in the fascinating world of plant protein glycosylation.

AUTHOR CONTRIBUTIONS

RS wrote and edited the manuscript. The author confirms being the sole contributor of this work and has approved it for publication.

FUNDING

This work was supported by the Austrian Science Fund (FWF) Project P31920-B32.

ACKNOWLEDGMENTS

I would like to thank all members from my group for their support and inspiring discussions during the last years.

REFERENCES

Alvisi, N., Van Noort, K., Dwiani, S., Geschiere, N., Sukarta, O., Varossieau, K., et al. (2021). β-Hexosaminidases along the secretory pathway of *Nicotiana benthamiana* have distinct specificities toward engineered helminth N-glycans on recombinant glycoproteins. *Front. Plant Sci.* 12:638454. doi: 10.3389/fpls.2021.638454

Beihammer, G., Maresch, D., Altmann, F., Van Damme, E. J. M., and Strasser, R. (2021). Lewis A glycans are present on proteins involved in cell wall biosynthesis and appear evolutionarily conserved among natural. *Front. Plant Sci.* 12:630891. doi: 10.3389/fpls.2021.630891

Elbers, I. J., Stoopen, G. M., Bakker, H., Stevens, L. H., Bardor, M., Molthoff, J. W., et al. (2001). Influence of growth conditions and developmental stage on N-glycan heterogeneity of transgenic immunoglobulin G and endogenous

proteins in tobacco leaves. *Plant Physiol.* 126, 1314–1322. doi: 10.1104/pp.126.3.1314

Fanata, W. I., Lee, K. H., Son, B. H., Yoo, J. Y., Harmoko, R., Ko, K. S., et al. (2013). N-glycan maturation is crucial for cytokinin-mediated development and cellulose synthesis in *Oryza sativa*. *Plant J.* 73, 966–979. doi: 10.1111/tpj.12087

Fitchette-Lainé, A., Gomord, V., Cabanes, M., Michalski, J., Saint Macary, M., Foucher, B., et al. (1997). N-glycans harboring the Lewis a epitope are expressed at the surface of plant cells. *Plant J.* 12, 1411–1417. doi: 10.1046/j.1365-313x.1997.12061411.x

Frank, M., Kaulfürst-Soboll, H., Fischer, K., and Von Schaewen, A. (2021). Complex-type N-glycans influence the root hair landscape of Arabidopsis seedlings by altering the auxin output. *Front. Plant Sci.* 12:635714. doi: 10.3389/fpls.2021.635714

Gagneux, P., and Varki, A. (1999). Evolutionary considerations in relating oligosaccharide diversity to biological function. *Glycobiology* 9, 747–755. doi: 10.1093/glycob/9.8.747

Hanania, U., Ariel, T., Tekoah, Y., Fux, L., Sheva, M., Gubbay, Y., et al. (2017). Establishment of a tobacco BY2 cell line devoid of plant-specific xylose and fucose as a platform for the production of biotherapeutic proteins. *Plant Biotechnol. J.* 15, 1120–1129. doi: 10.1111/pbi.12702

Harmoko, R., Yoo, J. Y., Ko, K. S., Ramasamy, N. K., Hwang, B. Y., Lee, E. J., et al. (2016). N-glycan containing a core α1,3-fucose residue is required for basipetal auxin transport and gravitropic response in rice (*Oryza sativa*). *New Phytol.* 212, 108–122. doi: 10.1111/nph.14031

Häweker, H., Rips, S., Koiwa, H., Salomon, S., Saijo, Y., Chinchilla, D., et al. (2010). Pattern recognition receptors require N-glycosylation to mediate plant immunity. *J. Biol. Chem.* 285, 4629–4636. doi: 10.1074/jbc.M109.063073

Herman, X., Far, J., Courtoy, A., Bouhon, L., Quinton, L., De Pauw, E., et al. (2021). Inactivation of N-acetylglucosaminyltransferase I and α1,3-fucosyltransferase genes in *Nicotiana tabacum* BY-2 cells results in glycoproteins with highly homogeneous *high-mannose N-glycans*. *Front. Plant Sci.* 12:634023. doi: 10.3389/fpls.2021.634023

Horiuchi, R., Hirotsu, N., and Miyanishi, N. (2016). N-glycan transition of the early developmental stage in *Oryza sativa*. *Biochem. Biophys. Res. Commun.* 477, 426–432. doi: 10.1016/j.bbrc.2016.06.082

Huang, Y., Zhang, H. L., Li, Z. L., Du, T., Chen, Y. H., Wang, Y., et al. (2021). FUT8-mediated aberrant N-glycosylation of B7H3 suppresses the immune response in triple-negative breast cancer. *Nat. Commun.* 12:2672. doi: 10.1038/s41467-021-22618-x

Ioffe, E., and Stanley, P. (1994). Mice lacking N-acetylglucosaminyltransferase I activity die at mid-gestation, revealing an essential role for complex or hybrid N-linked carbohydrates. *Proc. Natl. Acad. Sci. U. S. A.* 91, 728–732. doi: 10.1073/pnas.91.2.728

Jansing, J., Sack, M., Augustine, S. M., Fischer, R., and Bortesi, L. (2019). CRISPR/Cas9-mediated knockout of six glycosyltransferase genes in *Nicotiana benthamiana* for the production of recombinant proteins lacking β-1,2-xylose and core α-1,3-fucose. *Plant Biotechnol. J.* 17, 350–361. doi: 10.1111/pbi.12981

Jia, X., Zeng, H., Bose, S. K., Wang, W., and Yin, H. (2020). Chitosan oligosaccharide induces resistance to Pst DC3000 in Arabidopsis via a non-canonical N-glycosylation regulation pattern. *Carbohydr. Polym.* 250:116939. doi: 10.1016/j.carbpol.2020.116939

Jiao, Q. S., Niu, G. T., Wang, F. F., Dong, J. Y., Chen, T. S., Zhou, C. F., et al. (2020). N-glycosylation regulates photosynthetic efficiency of *Arabidopsis thaliana*. *Photosynthetica* 58, 72–79. doi: 10.32615/ps.2019.153

Joly, C., Léonard, R., Maftah, A., and Riou-Khamlichi, C. (2002). alpha4-fucosyltransferase is regulated during flower development: increases in activity are targeted to pollen maturation and pollen tube elongation. *J. Exp. Bot.* 53, 1429–1436. doi: 10.1093/jexbot/53.373.1429

Jung, J. W., Shin, J. H., Lee, W. K., Begum, H., Min, C. H., Jang, M. H., et al. (2021). Inactivation of the β (1,2)-xylosyltransferase and the α (1,3)-fucosyltransferase gene in rice (*Oryza sativa*) by multiplex CRISPR/Cas9 strategy. *Plant Cell Rep.* 40, 1025–1035. doi: 10.1007/s00299-021-02667-8

Kajiura, H., Koiwa, H., Nakazawa, Y., Okazawa, A., Kobayashi, A., Seki, T., et al. (2010). Two *Arabidopsis thaliana* Golgi alpha-mannosidase I enzymes are responsible for plant N-glycan maturation. *Glycobiology* 20, 235–247. doi: 10.1093/glycob/cwp170

Kang, J., Frank, J., Kang, C., Kajiura, H., Vikram, M., Ueda, A., et al. (2008). Salt tolerance of *Arabidopsis thaliana* requires maturation of N-glycosylated proteins in the Golgi apparatus. *Proc. Natl. Acad. Sci. U. S. A.* 105, 5933–5938. doi: 10.1073/pnas.0800237105

Kato, S., Hayashi, M., Kitagawa, M., Kajiura, H., Maeda, M., Kimura, Y., et al. (2018). Degradation pathway of plant complex-type N-glycans: identification and characterization of a key α1,3-fucosidase from glycoside hydrolase family 29. *Biochem. J.* 475, 305–317. doi: 10.1042/BCJ20170106

Kaulfürst-Soboll, H., Mertens-Beer, M., Brehler, R., Albert, M., and von Schaewen, A. (2021). Complex N-glycans are important for normal fruit ripening and seed development in tomato. *Front. Plant Sci.* 12:635962. doi: 10.3389/fpls.2021.635962

Kaulfürst-Soboll, H., Rips, S., Koiwa, H., Kajiura, H., Fujiyama, K., and von Schaewen, A. (2011). Reduced immunogenicity of Arabidopsis *hgl1* mutant N-glycans caused by altered accessibility of xylose and core fucose epitopes. *J. Biol. Chem.* 286, 22955–22964. doi: 10.1074/jbc.M110.196097

Koprivova, A., Altmann, F., Gorr, G., Kopriva, S., Reski, R., and Decker, E. (2003). N-glycosylation in the moss *Physcomitrella patens* is organized similarly to that in higher plants. *Plant Biol.* 5, 582–591. doi: 10.1055/s-2003-44721

Lane, D., Wiedemeier, A., Peng, L., Höfte, H., Vernhettes, S., Desprez, T., et al. (2001). Temperature-sensitive alleles of RSW2 link the KORRIGAN endo-1,4-beta-glucanase to cellulose synthesis and cytokinesis in Arabidopsis. *Plant Physiol.* 126, 278–288. doi: 10.1104/pp.126.1.278

Liebminger, E., Grass, J., Altmann, F., Mach, L., and Strasser, R. (2013). Characterizing the link between glycosylation state and enzymatic activity of the endo-β1,4-glucanase KORRIGAN1 from *Arabidopsis thaliana*. *J. Biol. Chem.* 288, 22270–22280. doi: 10.1074/jbc.M113.475558

Liebminger, E., Hüttner, S., Vavra, U., Fischl, R., Schoberer, J., Grass, J., et al. (2009). Class I alpha-mannosidases are required for N-glycan processing and root development in *Arabidopsis thaliana*. *Plant Cell* 21, 3850–3867. doi: 10.1105/tpc.109.072363

Limkul, J., Iizuka, S., Sato, Y., Misaki, R., Ohashi, T., and Fujiyama, K. (2016). The production of human glucocerebrosidase in glyco-engineered *Nicotiana benthamiana* plants. *Plant Biotechnol. J.* 14, 1682–1694. doi: 10.1111/pbi.12529

Liu, C., Niu, G., Li, X., Zhang, H., Chen, H., Hou, D., et al. (2021). Comparative label-free quantitative proteomics analysis reveals the essential roles of N-glycans in salt tolerance by modulating protein abundance in Arabidopsis. *Front. Plant Sci.* 12:646425. doi: 10.3389/fpls.2021.646425

Liu, C., Niu, G., Zhang, H., Sun, Y., Sun, S., Yu, F., et al. (2018). Trimming of N-glycans by the Golgi-localized α-1,2-Mannosidases, MNS1 and MNS2, is crucial for maintaining RSW2 protein abundance during salt stress in Arabidopsis. *Mol. Plant* 11, 678–690. doi: 10.1016/j.molp.2018.01.006

Mercx, S., Smargiasso, N., Chaumont, F., De Pauw, E., Boutry, M., and Navarre, C. (2017). Inactivation of the β(1,2)-xylosyltransferase and the α(1,3)-fucosyltransferase genes in *Nicotiana tabacum* BY-2 cells by a multiplex CRISPR/Cas9 strategy results in glycoproteins without plant-specific Glycans. *Front. Plant Sci.* 8:403. doi: 10.3389/fpls.2017.00403

Metzler, M., Gertz, A., Sarkar, M., Schachter, H., Schrader, J. W., and Marth, J. D. (1994). Complex asparagine-linked oligosaccharides are required for morphogenic events during post-implantation development. *EMBO J.* 13, 2056–2065. doi: 10.1002/j.1460-2075.1994.tb06480.x

Mølhøj, M., Ulvskov, P., and Dal Degan, F. (2001). Characterization of a functional soluble form of a Brassica napus membrane-anchored endo-1,4-beta-glucanase heterologously expressed in *Pichia pastoris*. *Plant Physiol.* 127, 674–684. doi: 10.1104/pp.010269

Nagashima, Y., Ma, Z., Liu, X., Qian, X., Zhang, X., von Schaewen, A., et al. (2020). Multiple quality control mechanisms in the ER and TGN determine subcellular dynamics and salt-stress tolerance function of KORRIGAN1. *Plant Cell* 32, 470–485. doi: 10.1105/tpc.19.00714

Nekrasov, V., Li, J., Batoux, M., Roux, M., Chu, Z. H., Lacombe, S., et al. (2009). Control of the pattern-recognition receptor EFR by an ER protein complex in plant immunity. *EMBO J.* 28, 3428–3438. doi: 10.1038/emboj.2009.262

Pedersen, C. T., Loke, I., Lorentzen, A., Wolf, S., Kamble, M., Kristensen, S. K., et al. (2017). N-glycan maturation mutants in *Lotus japonicus* for basic and applied glycoprotein research. *Plant J.* 91, 394–407. doi: 10.1111/tpj.13570

Rips, S., Bentley, N., Jeong, I. S., Welch, J. L., Von Schaewen, A., and Koiwa, H. (2014). Multiple N-glycans cooperate in the subcellular targeting and functioning of Arabidopsis KORRIGAN1. *Plant Cell* 26, 3792–3808. doi: 10.1105/tpc.114.129718

Saijo, Y., Tintor, N., Lu, X., Rauf, P., Pajerowska-Mukhtar, K., Häweker, H., et al. (2009). Receptor quality control in the endoplasmic reticulum for plant innate immunity. *EMBO J.* 28, 3439–3449. doi: 10.1038/emboj.2009.263

Schoberer, J., and Strasser, R. (2018). Plant glyco-biotechnology. *Semin. Cell Dev. Biol.* 80, 133–141. doi: 10.1016/j.semcdb.2017.07.005

Sim, J. S., Kesawat, M. S., Kumar, M., Kim, S. Y., Mani, V., Subramanian, P., et al. (2018). Lack of the α1,3-Fucosyltransferase gene (*Osfuct*) affects anther development and pollen viability in Rice. *Int. J. Mol. Sci.* 19:1225. doi: 10.3390/ijms19041225

Stefanowicz, K., Lannoo, N., Zhao, Y., Eggermont, L., Van Hove, J., Al Atalah, B., et al. (2016). Glycan-binding F-box protein from *Arabidopsis thaliana* protects plants from *Pseudomonas syringae* infection. *BMC Plant Biol.* 16:213. doi: 10.1186/s12870-016-0905-2

Stenitzer, D., Mócsai, R., Zechmeister, H., Reski, R., Decker, E. L., and Altmann, F. (2022). O-methylated N-glycans distinguish mosses from vascular plants. *Biomolecules* 12:136. doi: 10.3390/biom12010136

Strasser, R. (2016). Plant protein glycosylation. *Glycobiology* 26, 926–939. doi: 10.1093/glycob/cww023

Strasser, R. (2018). Protein quality control in the endoplasmic reticulum of plants. *Annu. Rev. Plant Biol.* 69, 147–172. doi: 10.1146/annurev-arplant-042817-040331

Strasser, R., Altmann, F., Mach, L., Glössl, J., and Steinkellner, H. (2004). Generation of *Arabidopsis thaliana* plants with complex N-glycans lacking beta1,2-linked xylose and core alpha1,3-linked fucose. *FEBS Lett.* 561, 132–136. doi: 10.1016/S0014-5793(04)00150-4

Strasser, R., Bondili, J., Schoberer, J., Svoboda, B., Liebminger, E., Glössl, J., et al. (2007b). Enzymatic properties and subcellular localization of Arabidopsis beta-N-acetylhexosaminidases. *Plant Physiol.* 145, 5–16. doi: 10.1104/pp.107.101162

Strasser, R., Bondili, J. S., Vavra, U., Schoberer, J., Svoboda, B., Glössl, J., et al. (2007a). A unique beta1,3-galactosyltransferase is indispensable for the biosynthesis of N-glycans containing Lewis a structures in *Arabidopsis thaliana*. *Plant Cell* 19, 2278–2292. doi: 10.1105/tpc.107.052985

Strasser, R., Schoberer, J., Jin, C., Glössl, J., Mach, L., and Steinkellner, H. (2006). Molecular cloning and characterization of *Arabidopsis thaliana* Golgi alpha-mannosidase II, a key enzyme in the formation of complex N-glycans in plants. *Plant J.* 45, 789–803. doi: 10.1111/j.1365-313X.2005.02648.x

Strasser, R., Seifert, G., Doblin, M. S., Johnson, K. L., Ruprecht, C., Pfrengle, F., et al. (2021). Cracking the "sugar code": A snapshot of N- and O-glycosylation pathways and functions in plants cells. *Front. Plant Sci.* 12:640919. doi: 10.3389/fpls.2021.640919

Strasser, R., Stadlmann, J., Schähs, M., Stiegler, G., Quendler, H., Mach, L., et al. (2008). Generation of glyco-engineered *Nicotiana benthamiana* for the production of monoclonal antibodies with a homogeneous human-like N-glycan structure. *Plant Biotechnol. J.* 6, 392–402. doi: 10.1111/j.1467-7652.2008.00330.x

Strasser, R., Steinkellner, H., Borén, M., Altmann, F., Mach, L., Glössl, J., et al. (1999). Molecular cloning of cDNA encoding N-acetylglucosaminyltransferase II from *Arabidopsis thaliana*. *Glycoconj J* 16, 787–791. doi: 10.1023/a:1007127815012

Sun, Z., and Brodsky, J. L. (2019). Protein quality control in the secretory pathway. *J. Cell Biol.* 218, 3171–3187. doi: 10.1083/jcb.201906047

Takano, S., Matsuda, S., Funabiki, A., Furukawa, J., Yamauchi, T., Tokuji, Y., et al. (2015). The rice RCN11 gene encodes β1,2-xylosyltransferase and is required for plant responses to abiotic stresses and phytohormones. *Plant Sci.* 236, 75–88. doi: 10.1016/j.plantsci.2015.03.022

Veit, C., König, J., Altmann, F., and Strasser, R. (2018). Processing of the terminal alpha-1,2-linked mannose residues from oligomannosidic. *Front. Plant Sci.* 9:1807. doi: 10.3389/fpls.2018.01807

Viëtor, R., Loutelier-Bourhis, C., Fitchette, A., Margerie, P., Gonneau, M., Faye, L., et al. (2003). Protein N-glycosylation is similar in the moss *Physcomitrella patens* and in higher plants. *Planta* 218, 269–275. doi: 10.1007/s00425-003-1099-z

von Schaewen, A., Sturm, A., O'neill, J., and Chrispeels, M. (1993). Isolation of a mutant Arabidopsis plant that lacks N-acetyl glucosaminyl transferase I and is unable to synthesize Golgi-modified complex N-linked glycans. *Plant Physiol.* 102, 1109–1118. doi: 10.1104/pp.102.4.1109

Wenderoth, I., and von Schaewen, A. (2000). Isolation and characterization of plant N-acetyl glucosaminyltransferase I (GntI) cDNA sequences. Functional analyses in the Arabidopsis *cgl* mutant and in antisense plants. *Plant Physiol.* 123, 1097–1108. doi: 10.1104/pp.123.3.1097

Wilson, I., Zeleny, R., Kolarich, D., Staudacher, E., Stroop, C., Kamerling, J., et al. (2001). Analysis of Asn-linked glycans from vegetable foodstuffs: widespread occurrence of Lewis a, core alpha1,3-linked fucose and xylose substitutions. *Glycobiology* 11, 261–274. doi: 10.1093/glycob/11.4.261

Yoo, J. Y., Ko, K. S., Vu, B. N., Lee, Y. E., Yoon, S. H., Pham, T. T., et al. (2021). N-acetylglucosaminyltransferase II is involved in plant growth and development under stress conditions. *Front. Plant Sci.* 12:761064. doi: 10.3389/fpls.2021.761064

Zeng, W., Ford, K. L., Bacic, A., and Heazlewood, J. L. (2018). N-linked glycan micro-heterogeneity in glycoproteins of Arabidopsis. *Mol. Cell. Proteomics* 17, 413–421. doi: 10.1074/mcp.RA117.000165

Zhang, J., Wu, J., Liu, L., and Li, J. (2021). The crucial role of demannosylating asparagine-linked glycans in ERADicating misfolded glycoproteins in the endoplasmic reticulum. *Front. Plant Sci.* 11:625033. doi: 10.3389/fpls.2020.625033

Conflict of Interest: The author declares that the research was conducted in the absence of any commercial or financial relationships that could be construed as a potential conflict of interest.

Publisher's Note: All claims expressed in this article are solely those of the authors and do not necessarily represent those of their affiliated organizations, or those of the publisher, the editors and the reviewers. Any product that may be evaluated in this article, or claim that may be made by its manufacturer, is not guaranteed or endorsed by the publisher.

frontiers | Frontiers in Plant Science

ORIGINAL RESEARCH
published: 13 May 2022
doi: 10.3389/fpls.2022.858652

Grain-Filling Rate Improves Physical Grain Quality in Barley Under Heat Stress Conditions During the Grain-Filling Period

Hamid Shirdelmoghanloo[1], Kefei Chen[2], Blakely H. Paynter[1], Tefera Tolera Angessa[3,4], Sharon Westcott[3,4], Hammad Aziz Khan[1,4], Camilla Beate Hill[4] and Chengdao Li[3,4]**

[1] Department of Primary Industries and Regional Development, Northam, WA, Australia, [2] School of Molecular and Life Sciences, Curtin University, Perth, WA, Australia, [3] Department of Primary Industries and Regional Development, Perth, WA, Australia, [4] Western Crop Genetics Alliance, College of Science, Health, Engineering and Education, Murdoch University, Perth, WA, Australia

OPEN ACCESS

Edited by:
Nigel G. Halford,
Rothamsted Research,
United Kingdom

Reviewed by:
Cara Griffiths,
Rothamsted Research,
United Kingdom
Dirk Boudreaux Hays,
Texas A&M University, United States

***Correspondence:**
Hamid Shirdelmoghanloo
hamid.shirdelmoghanloo@dpird.wa.gov.au
Chengdao Li
c.li@murdoch.edu.au

Specialty section:
This article was submitted to Plant Physiology, a section of the journal Frontiers in Plant Science

Received: 20 January 2022
Accepted: 28 March 2022
Published: 13 May 2022

Citation:
Shirdelmoghanloo H, Chen K, Paynter BH, Angessa TT, Westcott S, Khan HA, Hill CB and Li C (2022) Grain-Filling Rate Improves Physical Grain Quality in Barley Under Heat Stress Conditions During the Grain-Filling Period. Front. Plant Sci. 13:858652. doi: 10.3389/fpls.2022.858652

Heat stress is a primary constraint to Australia's barley production. In addition to impacting grain yield, it adversely affects physical grain quality (weight and plumpness) and market value. The incidence of heat stress during grain filling is rising with global warming. However, breeding for new superior heat-tolerant genotypes has been challenging due to the narrow window of sensitivity, the unpredictable nature of heat stress, and its frequent co-occurrence with drought stress. Greater scientific knowledge regarding traits and mechanisms associated with heat tolerance would help develop more efficient selection methods. Our objective was to assess 157 barley varieties of contrasting genetic backgrounds for various developmental, agro-morphological, and physiological traits to examine the effects of heat stress on physical grain quality. Delayed sowing (i.e., July and August) increased the likelihood of daytime temperatures above 30°C during grain-filling. Supplementary irrigation of field trials ensured a reduced impact of drought stress. Heat tolerance appeared to be the primary factor determining grain plumpness. A wide variation was observed for heat tolerance, particularly among the Australian varieties. Genotypic variation was also observed for grain weight, plumpness, grain growth components, stay-green and stem water-soluble carbohydrates (WSC) content, and mobilisation under normal and delayed sown conditions. Compared to normal sowing, delayed sowing reduced duration of developmental phases, plant height, leaf size, head length, head weight, grain number, plumpness, grain width and thickness, stem WSC content, green leaf area retention, and harvest index (HI), and increased screenings, grain length, grain-filling rate (GFR), WSC mobilisation efficiency (WSCME), and grain protein content. Overall, genotypes with heavier and plumper grains under high temperatures had higher GFR, longer grain-filling duration, longer green leaf area retention, higher WSCME, taller stature, smaller leaf size, greater HI, higher grain weight/plumpness potentials, and earlier flowering. GFR played a significant role in determining barley grain weight and plumpness under heat-stress conditions. Enhancing GFR may provide a new avenue for improving heat tolerance in barley.

Keywords: grain weight, plumpness, heat stress, grain-filling, stay-green, water-soluble carbohydrates, barley

INTRODUCTION

Barley (*Hordeum vulgare* L.) is an important temperate cereal crop best adapted to environments with an optimum temperature of 15°C during grain-filling to achieve maximum grain mass (Chowdhury and Wardlaw, 1978). However, in many growing regions, including the Australian grain belt, the barley crop is frequently exposed to high-temperature damage (days above 30°C) during flowering and grain development (Wardlaw and Wrigley, 1994; Asseng et al., 2011). During flowering and grain development, high-temperature damage can be classified as acute or chronic. Acute damage results from short exposure to high temperatures (heat shock and typically temperatures above 35°C), while chronic damage results from exposure to elevated temperature for a long duration during flowering and grain development (heat stress and typically temperatures above 30°C). The increasing frequency and severity of heat extremes predicted due to climate change are likely to challenge global food security in the future (Asseng et al., 2011; Xie et al., 2018).

Heat stress causes an average of 15% yield loss p.a. in temperate cereals in Australia (Wardlaw and Wrigley, 1994; Telfer et al., 2013). Using a panel of 138 barley genotypes, a study in Denmark reported a 56% grain yield reduction caused by heat stress (Ingvordsen et al., 2015). While most studies report reductions in grain yield, heat stress dramatically reduces barley grain weight and plumpness and increase grain size inconsistency (Macnicol et al., 1993; Savin and Nicolas, 1996). The resultant downgrading of malt barley to feed can cause a significant loss of market value for barley growers. Heat stress, therefore, has severe implications for the future of the Australian grain crop industry and highlights an urgent need to develop heat-tolerant barley varieties.

Heat stress during meiosis leads to floret sterility and, consequently, failed seed set (Saini and Aspinall, 1982; Sakata et al., 2000). At the early grain-filling stage, heat reduces final grain weight and size (Macnicol et al., 1993; Savin and Nicolas, 1996). Direct selection for heat tolerance is difficult due to the apparent narrow window of sensitivity, the unpredictable nature of heat stress (i.e., timing, magnitude, and duration), and its frequent co-occurrence with drought stress. Therefore, a greater scientific knowledge regarding traits and mechanisms associated with heat tolerance (and its genetic variability) would help develop more efficient selection methods.

A range of physiological and biochemical processes are adversely affected by high temperatures, resulting in reduced grain yields and quality (Cossani and Reynolds, 2012). These processes, exclusively and in combination, could potentially represent the basis for genotypic variation in heat tolerance. Approximately 70% of the barley grain mass consists of starch, which is the grain component most diminished under high-temperature conditions, and its synthesis depends on both the supply of assimilates to the developing grain and their conversion into starch within the grain (Wallwork et al., 1998; Shirdelmoghanloo et al., 2016b). Heat stress accelerates the rate of senescence and leaf chlorophyll loss, leading to reduced photosynthetic capacity and assimilate supply to the developing grains. The ability to retain green leaf area during grain-filling (stay-green) under stress conditions would help assimilate supply and lead to a higher rate and a longer duration of grain-filling under such conditions. Maintenance of grain weight under field and controlled conditions for heat and drought are often associated with the stay-green trait in wheat (Kumari et al., 2007; Lopes and Reynolds, 2012; Shirdelmoghanloo et al., 2016b,c) and sorghum (Borrell et al., 2014a,b). Water-soluble carbohydrate (WSC) reserves in the stems and leaf sheaths serve as an alternative source of assimilates, significantly buffering against the loss of green area and photosynthetic capacity during reproductive stages under heat and drought stress (Blum, 1998). Stem WSC content is dynamic and is the net outcome of deposition, remobilisation, and losses caused by other processes (e.g., respiration). Talukder et al. (2013) reported a positive association between stem WSC mobilisation and the heat stability of grain-filling in wheat. Evidence on the contribution of WSCs to variability in the ability of barley genotypes to maintain grain weight and size under heat stress is scarce.

Nevertheless, mobilised WSCs can be estimated from the difference between peak and minimum WSCs content during grain-filling. Sensitivity of processes within or close to the developing grain may also be crucial factors. These processes include heat sensitivity and recovery of lost activity following heat relief of several enzymes in the starch biosynthesis pathway of the developing grain (Wallwork et al., 1998) and accelerated maturation of the grain by heat stress, provoked by stress signals such as ethylene (Hays et al., 2007). Studying these traits in a diverse range of barley genotypes exposed to natural heat stress could explain the underlying tolerance mechanisms and drivers of better physical grain quality under heat stress and genetic variability. Shirdelmoghanloo et al. (2016a) suggested that this would allow complementary selection criteria when breeding for heat tolerance.

For experimental purposes, heat stress can be mimicked in the field by late sowing, covering plots with tunnels, or using in-field

Abbreviations: DT49, Days to awn emergence (Z49); DTM, Days to physiological maturity; GDD, Growing degree days (thermal time, GDD); GFD, Grain-filling duration (GDD); GFR, Average grain-filling rate (mg GDD^{-1}, dry basis); GFRmax, Maximum grain-filling rate (mg GDD^{-1}, dry basis); GLe, Grain length (mm); GNS, Grain number $spike^{-1}$ (number); GP, Grain plumpness (% grain above 2.8 mm); GP.HTI, Grain plumpness heat tolerance index; GPr, Grain protein content (%, dry basis); GTh, Grain thickness (mm); GWi, Grain width (mm); GWS, Grain weight $spike^{-1}$ (g); HI, Harvest index (%); HL, Head length (cm); HTI, Heat tolerance index; LL, Penultimate leaf length (cm); LS, Late sown; LW, Penultimate leaf width (cm); MK, Muresk; MWSC, Absolute mobilised stem water-soluble carbohydrates during grain-filling (mg); NAUSC, Normalised area under the penultimate leaf SPAD decline curve; NS, Normal sown; PCA, Principal component analysis; PC, Principal component; Ret, Retention (% grain above 2.5 mm); Ret.HTI, Retention heat tolerance index; Scr, Screenings (% grain below 2.2 mm); SFNS, Sterile floret number $spike^{-1}$ (number); SGW, Single grain weight (mg, dry basis); SL, Stem length (cm); SSS, Soluble starch synthase; TGW, Thousand-grain weight (g, dry basis); TGW.HTI, Thousand-grain weight heat tolerance index; TIP, Thermal time from awn emergence to grain growth inflection point (GDD); TW, Test weight (kg/hL); VLS, Very late sown; WH, Wongan Hills; WSC, Water-soluble carbohydrates; WSCmax, Maximum stem water-soluble carbohydrates content (mg); WSCME, Stem water-soluble carbohydrates mobilisation efficiency (%); WSCmin, Minimum stem water-soluble carbohydrates content (mg).

heat chambers. Under more controlled conditions, temperature-controlled growth rooms or glasshouse compartments can be used to grow plants and transfer them at specific developmental stages to defined heat stress treatments (Borghi et al., 1995; Savin and Nicolas, 1996; Passarella et al., 2008; Talukder et al., 2013; Thistlethwaite et al., 2020). However, a greater emphasis should be placed on field responses when breeding for heat tolerance to relate the relevance of the results to the barley industry (Passioura, 2006).

The present study measured physiological processes, phenology, and plant architecture in a diverse set of 157 barley genotypes. The aim was to gain insights into their relative contributions to physical grain quality stability, genetic variability, and their interactions under heat stress conditions during the grain-filling period. Barley plants were sown later than standard farming practise to ensure heat stress coincided with grain-filling. Such an approach allows the evaluation of large numbers of lines for heat tolerance under field conditions (Abou-Elwafa and Amein, 2016; Sissons et al., 2018; Thistlethwaite et al., 2020).

MATERIALS AND METHODS

Germplasm

In 2016 and 2017, a collection of flowering date and grain plumpness characteristics of 300 barley (*Hordeum vulgare* L.) genotypes occurred across various environments (unpublished data). A subset of 157 two-row barley genotypes was selected for this study's detailed phenotyping (**Supplementary Table S1**). The genotypes selected comprised released varieties, advanced breeding lines, and landraces, with 106 originating from Australia, 18 from North America, 11 from Europe, nine from South Africa, eight from South America, three from the International Center for Agricultural Research in the Dry Areas (ICARDA), and two from Asia. Seven lines were only screened in one location (**Supplementary Table S1**).

Field Experiments

Wongan Hills (WH) and Muresk (MK) in Western Australia were the locations of the field trials in 2018 and 2019 (**Table 1**). At WH, three planting dates represented normal (NS), late (LS), and very late sowing (VLS) conditions, while there was only LS at MK. The LS and VLS increased the probability of heat stress occurring during barley's reproductive development. Except for the first sowing date at WH in 2018 (WH18NS), the trials were supplementarily irrigated during grain filling to reduce the confounding effect of drought.

The randomised complete block designs (RCBD) were applied for all field experiments and were generated using the experimental design tool DiGGer in R (Coombes, 2018). Each plot was 10 m long, with seed sown over seven rows (22 cm row spacing). Trimming before harvest reduced the plot length to ∼8 m. At MK in 2018 (MK18LS), each plot was 5 m long, trimmed to 3.5 m before harvest, with the seed sown over four rows (20 cm row spacing). The seeder was a breeding seeder with discs. MK18LS was planted as paired plots due to the shorter plot length. The left plot was used for destructive measurements and the right for grain yield and quality. The seed was sown at 2 to 4 cm depth, targeting a plant density of 150 plants m^{-2} by adjusting for kernel weight. Plots were fertilised by drilling a compound fertiliser below the seed and topdressing another compound fertiliser in front of the seeder to supply 30 kg N/ha, 28 kg P/ha, and 40.5 kg K/ha. Eight weeks after sowing, a further 40 kg N/ha was applied as a foliar fertiliser. Treating the seed and fertiliser with fungicide suppressed early disease infection, with no in-crop fungicide required. Glyphosate controlled early emerging weeds before crop establishment. In-crop weeds and diseases were controlled as needed using products registered for barley in Western Australia.

Weather Data

Temperature data loggers (Tinytag, Hastings, UK) installed at 90 cm above the ground recorded air temperature in a bare area near each trial. Daily minimum and maximum temperatures were used to calculate the thermal time (GDD; at a base temperature of 0°C). Rainfall data (mm) was obtained from the nearest Department of Primary Industries and Regional Development (DPIRD) weather station (https://weather.agric.wa.gov.au/).

Trait Evaluation

A total of 29 traits were measured (**Supplementary Table S2**) as described below.

Flowering time (DT49) was defined for each plot as the days from sowing to when 50% of plants exhibited 1 cm of awn emergence above the flag leaf (Z49) (Zadoks et al., 1974; Alqudah and Schnurbusch, 2017). Z49 is an equivalent for flowering time in barley (Alqudah and Schnurbusch, 2017). At Z49, at least 65 tillers with 1 cm of awn protruding from the boot were tagged per plot, except WH18NS, where 55 primary tillers were tagged on average. Five tagged spikes from each plot were collected at 2–3-day intervals from 7 to 14 days after flowering. and then every week to shortly after physiological maturity, except in WH18NS, where four spikes were sampled on average. The collected spikes were oven-dried for 5 days at 65°C, and the four middle grains of each spike were removed and weighed. Single grain weight (SGW, mg) was calculated by dividing the total weight of the removed grains by their number.

Grain growth characteristics were estimated by fitting a logistic function to the SGW data collected over time (Equation 1) (Zahedi and Jenner, 2003), where SGW(t) is SGW at thermal time t (GDD) after flowering, the Theoretical Final SGW at maturity (mg), s is the slope parameter that controls the steepness of the curve, TIP (GDD) is the thermal time from flowering to the inflection point (TIP), the inflection point is the point of maximum grain growth, and e is Napier's number (a mathematical constant of ∼2.71828).

$$SGW(t) = \frac{Theoretical\ Final\ SGW}{1 + e^{(-s(t-TIP))}} \quad (1)$$

The GFR reaches maximum at the inflection point when $SGW(t) = 0.5 \times (Theoretical\ Final\ SGW)$, so the maximum GRF (GFRmax, mg GDD^{-1}) can be calculated using the first derivative of the logistic curve (Equation 2):

TABLE 1 | Summary of sowing dates, awn emergence times, and weather experienced in trials at Wongan Hills (WH) and Muresk (MK) in 2018 and 2019 crop growing seasons.

Location	Wongan hills						Muresk	
GPS location	30° 50' S, 116° 45' E						31° 45' S, 116° 40' E	
Soil description	Grey sandy duplex						Brown loamy earth	
Year	2018			2019			2018	2019
Annual precipitation (mm)	414			246			383	270
Environment	WH18NS	WH18LS	WH18VLS	WH19NS[b]	WH19LS	WH19VLS	MK18LS	MK19LS
Sowing date description	Normal	Late	Very late	Normal	Late	Very late	Late	Late
Sowing date	15-May	5-Jul	31-Jul	16-May	8-Jul	5-Aug	28-Jun	11-Jul
GDD from sowing to Z49 (awn emergence)	1,325	1,013	894	1,214	962	894	1,018	947
Days from sowing to Z49	105	84	69	95	72	61	89	77
Ave. daily max. temp., sowing to Z49 (°C)	18.6	18.8	20.2	19.0	20.3	22.5	18.0	20.2
Ave. daily max. temp., Z49 to physiological maturity (°C)	22.7	26.4	28.0	24.0	27.3	29.2	26.5	27.1
Days ≥30°C, sowing to Z49	0.0	1.8	2.7	0.0	3.9	7.0	0.0	2.4
Days ≥30°C, Z49 to physiological maturity	4.1	9.0	12.9	8.1	11.2	18.2	9.7	10.5
Days ≥30°C, booting/flowering[a]	0.0	1.8	2.3	0.0	3.5	3.5	0.0	1.1
Days ≥30°C, early grain filling[a]	1.1	4.6	6.9	2.6	4.6	7.5	4.2	5.1
Irrigation during grain filling (mm)	0	40	40	60	75	75	30	75

[a]*Based on averages for all genotypes evaluated, with "booting/flowering" defined as the period 10 days before- to 4 days after-awn emergence and "early grain-filling" from 5 to 25 days after awn emergence, respectively.*
[b]*Irrigated with 40 mm at sowing due to the dry season start.*

$$GFR_{\max} = \left.\frac{d\left(SGW(t)\right)}{d\left(t\right)}\right|_{SGW(t)=0.5\cdot(\text{Theoretical Final } SGW)}$$
$$= \left.\frac{s \cdot SGW(t) \cdot \left((\text{Theoretical Final } SGW) - SGW(t)\right)}{(\text{Theoretical Final } SGW)}\right|_{SGW(t)=0.5\cdot(\text{Theoretical Final } SGW)}$$
$$= \frac{s \cdot (\text{Theoretical Final } SGW)}{4} \quad (2)$$

The grain-filling duration (GFD, in GDD) was considered to be the period until $SGW\ (t) = 0.95 \times Theoretical\ Final\ SGW$. Thus, GFD can be calculated by using (Equation 3):

$$GFD = \frac{s.TIP + 2.944}{s} \quad (3)$$

The average grain-filling rate (GFR; mg GDD^{-1}) was calculated using Equation 4 (Wang et al., 2009).

$$GFR = \frac{Theoretical\ Final\ SGW}{GFD} \quad (4)$$

Tagged tillers were collected at 7, 14, and 49 days after Z49, except in WH19NS, in which stem samples were also collected at 21 days after Z49 in addition to 7 and 14 days after Z49, with the spikes used in the grain growth study. At each sampling time, the tillers were cut at the soil surface, and the leaf blades, at the auricle, and the spike, at the junction of the peduncle and head, were removed. The stem samples (whole stem and peduncle) were then oven-dried for 5 days at 65°C. Each dried sample was weighed, chopped into 5 mm segments, placed in a cyclone twister mill (ZM200, Retsch Co., Germany), and reduced to a fine powder. The ground samples (200 mg) were transferred into 125 ml Erlenmeyer flasks, to which 30 ml of deionized water were added. For 1 h, the flasks were sealed and placed in a shaking hot water bath (90°C; 100 RPM). After cooling, the samples were filtered into tubes, diluted to 50 ml, and refrigerated at −20°C until analysis. The WSC of each sample was quantified using the anthrone method (Yemm and Willis, 1954), using absorbance at 620 nm on a UV-visible light spectrophotometer (Model UV-120, MIOSTECH, USA) and fructose as the standard.

Water-soluble carbohydrate content (mg) was calculated by multiplying WSC concentration (mg g^{-1}) by stem dry weight (g). Maximum WSC (WSCmax, mg) was defined as the highest WSC content from the samples collected at either 7, 14, or 21 days after Z49, and the minimum WSC (WSCmin, mg) was defined as the WSC content at 49 days after Z49. The amount of mobilised WSC (MWSC, mg) was calculated as the difference between the WSCmax and WSCmin. WSC mobilisation efficiency (WSCME, %) was calculated as the fraction of the maximum WSC content mobilised (Equation 5).

$$WSCME = \frac{MWSC}{WSCmax} \times 100 \quad (5)$$

Mean relative chlorophyll content of the penultimate leaves of three to five tagged primary tillers per plot was measured using a portable SPAD chlorophyll metre (SPAD-502, Minolta Co. Ltd.,

Japan) weekly starting at 14 days after Z49 and concluding at 42 days after Z49. Measurements were taken from the same tagged plants in each plot over time. The SPAD values were normalised to the SPAD value at 14 days after Z49 and the area under the curve of the normalised SPAD values (NAUSC) during grain-filling (Equation 6).

$$NAUSC = \sum_{i=1}^{n-1}\left[\left(\frac{x_i + x_{i+1}}{2}\right) \times (t_{i+1} - t_i)\right] \quad (6)$$

x_i is the relative chlorophyll content (normalised SPAD units) on the i^{th} date, t_i is the corresponding thermal time after flowering of the date on which the chlorophyll content was measured, and n is the number of dates on which chlorophyll content was recorded.

The penultimate leaf length and width were measured as the length of the blade, and width was recorded at the widest point using a ruler at ∼20 days after Z49 on five randomly selected tagged tillers per plot.

Each plot's duration to physiological maturity was the period from sowing to when 75% of the plants exhibited 95% spike and peduncle senescence (DTM). At physiological maturity, before harvest, five tagged tillers were randomly selected to estimate the following traits after being oven-dried for 5 days at 65°C. Head length was measured from the peduncle collar to the tip of the spike, excluding awns (HL, cm) using a ruler. Grain number spike^{-1} (GNS) counts fertile grains per spike, while sterile kernels are reflected in the sterile floret number per spike (SFNS). After removing all the grains, grain weight per spike (GWS, g) was calculated. The harvest index (HI, %) was calculated as (GWS/the primary tiller above ground biomass) × 100. Stem length (SL, cm) was measured from five randomly selected tagged tillers per plot from the soil surface to below the collar using a metre ruler.

Plots were harvested at maturity with an experimental harvester when the grain moisture was at ∼11% moisture, with a subsample collected (∼1 kg). Grain yield data was collected for each genotype in all environments (except WH18NS). The influence of heat stress on grain yield will be presented in a separate paper. This paper focuses on the implication of heat stress on physical grain quality traits like grain plumpness, which are vital in managing future climate change risk for malting and brewing end-use. The grain subsample was de-awned, cleaned over a 1.5 mm slotted screen (Pfeuffer Sample Cleaner Model SLN3, Pfeuffer GmbH, Germany), and used for the physical grain quality measurements. Test weight (TW, kg/hl) was determined by a chondrometer equipped with a 500 ml cylinder (or 210 ml cylinder if there was not enough sample to fill the 500 ml cylinder). Kernel weight (TGW, g) from a thousand-grain sample (Pfeuffer Contador V1 seed counter, Pfeuffer GmbH, Germany) was calculated after oven drying for 5 days at 65°C. Grain length (GLe, mm), width (GWi, mm), and thickness (GTh, mm) were measured on a 300- to 400-grain sample using a digital image analyser (SeedCount SC6000R, Next Instruments, NSW). A 100 g sample from each plot was graded on a screening machine (Pfeuffer 4K Sortimat, Pfeuffer GmbH, Germany) with a 2.2, 2.5, 2.8, and 3.1 mm screen stack for 2 min. Screening's (Scr, %) data are presented as percent of grain passing through the 2.2 mm screen, while retention (Ret, %) is the percent retained on a 2.5 mm screen (Ret), and grain plumpness (GP, %) is the percent retained on a 2.8 mm screen. Grain protein percent (GPr, %) was predicted by near-infrared (NIR) analysis (FOSS XDS, FOSS NIR Systems Inc., USA) using calibrations developed by DPIRD in partnership with the Australian Export Grains Innovation Centre (AEGIC).

Estimation of Heat Tolerance Index (HTI)

To mitigate differences in crop phenology (heat escape) and trait potential (i.e., the trait value under normal growing conditions), and to calculate the heat tolerance indices for TGW, GP, and Ret, the multiple regression approach by Bidinger et al. (1987) was employed. This approach has shown that the residual trait value after removing the effects of heat escape and the trait potential of a genotype gives a good indication of the heat response of that genotype. The approach considers the trait value under stress conditions ($\hat{Y}_s$) as a function of the trait potential (i.e., the trait value under NS condition, Y_p), time to flowering under stress condition (i.e., delayed sown condition, F_s), and a stress tolerance index (Equation 7).

$$\hat{Y}_s = a + b.Y_p + c.F_s + HTI + E \quad (7)$$

E is the random error with zero mean and the variances σ, b, and c are regression coefficients, while a is the intercept.

The heat tolerance index (HTI) is then calculated (Equation 8). Y_s is the actual trait value under heat stress conditions, $\hat{Y}_s$ is the estimated trait value under heat stress by the multiple regression model, and *S.E.* indicates the standard error of the estimated trait value.

$$HTI = \frac{Y_s - \hat{Y}_s}{S.E\left(\hat{Y}_s\right)} \quad (8)$$

WH18NS and WH19NS were chosen as the baseline for calculating HTI for each WH and MK late or very late sown environment. In each growing season, they were exposed to the lowest average temperature and least number of days above 30°C. An assumption made in calculating the HTI at MK was that the main difference between the WH and MK environments was air temperature. Both sites were irrigated fortnightly during grain filling with an overhead boom irrigator (**Supplementary Figure S1**) supplying 15–20 mm unless there was precipitation at or around that target rate. The purpose of the irrigation was to reduce the confounding effect of drought, but there may have been further factors that influenced the HTI.

Statistical Analysis

Each year-by-location-by-sowing date combination was considered as a separate environment, giving a total of eight environments. Linear mixed models were fitted with ASReml-R (version 4.1.0) (Butler et al., 2018) in the analyses of the evaluated traits in each environment, where the variance parameters in the mixed models were estimated using the residual maximum likelihood (REML) procedure of Patterson and Thompson (1971). For each trait in each environment, spatial variations were examined, including local autocorrelations, global trends,

and extraneous variations. The blocking structures of the experiments were fitted as random effects. Spatial trends and residual variances with auto-regressive correlation at first-order for rows and columns were examined and fitted when the global trends and autocorrelations were significant. Likelihood ratio tests were used for random effects, and conditional Wald tests (Kenward and Roger, 1997) were used for fixed effects. Residual diagnostics were performed to examine the validity of the model assumption of normality and homogeneity of variance. For each fitted model, the empirical best unbiased linear estimates (eBLUEs) were produced. Broad sense heritability (H^2) was estimated for each trait across all environments (Equation 9), where r is the number of replicates, e is the number of environments, σ^2 is error variance, σ_g^2 is genotypic variance, and σ_{ge}^2 is genotype by environment interaction variance.

$$H^2 = \sigma_g^2 / [\sigma_g^2 + (\sigma_{ge}^2/e) + (\sigma^2/r.e)] \quad (9)$$

The static stability index was calculated according to environmental variance (S^2) (Roemer, 1917) (Equation 10).

$$S^2{}_{xi} = \frac{\sum (X_{ij} - \overline{X}_{i.})^2}{(E-1)} \quad (10)$$

In the static stability index, X_{ij} is the observed trait value of the genotype i in the environment j, $\overline{X}_{i.}$ is the average trait value of the genotype i across environments, and E is the number of environments. The dynamic stability index was calculated according to Wricke's ecovalence (W^2) (Wricke, 1962) (Equation 11).

$$W^2{}_i = \sum (X_{ij} - \overline{X}_{i.} - \overline{X}_{.j} + \overline{X}_{..})^2 \quad (11)$$

In the dynamic stability index, X_{ij} is the observed trait value of the genotype i in the environment j; $\overline{X}_{i.}$ is the average trait value of the genotype i across treatments; $\overline{X}_{.j}$ is the average trait value across environment j of all genotypes; and $\overline{X}_{..}$ is the grand mean and average of all $\overline{X}_{.j}$. Hence, W^2 states the stability dependent on the pool of genotypes evaluated by taking averages of all genotypes ($\overline{X}_{i.}$ and $\overline{X}_{..}$) into account. At the same time, S^2 is a function of only the specific genotype in question.

Pearson correlation coefficients and stepwise multiple regression analyses studied the relationship between the primary traits of interest and the traits measured under normal or delayed conditions, and between HTIs and traits measured under delayed sown conditions. Principal component analyses (PCA) were also conducted and provided as **Supplementary Materials**.

RESULTS

Exposure of Genotypes to Heat Stress

Across both growing seasons, air temperatures were milder during the vegetative stage (before Z49) than during flowering and grain filling (after Z49) (**Table 1** and **Figure 1**). The 2019 growing season was hotter with more heat events (days $> 30^\circ$C) at early to mid-grain-filling, lower total precipitation, and a generally shorter growing season than 2018. Z49 occurred in mid- to late-August in NS trials and mid-September to early-October in delayed sown trials, depending on the growing season, location, and sowing time (**Figure 1**). Exposure to higher daily maximum temperatures and a higher number of heat events, especially during the booting and grain-filling stages of development, was seen in delayed sown plots. At WH on average, VLS barley was exposed to 15 days above 30°C after Z49, compared to 10 days for LS and 6 days for NS barley. There were, on average, 7 days above 30°C for VLS barley during early grain filling compared to 5 for LS and 2 for NS barley. In some of the trials, a few frost events (−1.3 to 2.0°C) occurred during the booting and early grain-filling development stages (**Figure 1**). However, it is unlikely that those frost events significantly impacted plant performance, as crop canopy air temperatures of −3.5 to −4.5°C and below are required to damage barley when it is at its sensitive reproductive stage (Frederiks et al., 2015).

Variance Components, Broad-Sense Heritability, and the Association of Each Trait Across Environments

The analysis of variance for genotype (G), environment (E), and G × E effects were highly significant (**Table 2**). Variation (%) attributed to G was more significant in 50% of the traits than that attributed to E or the interaction between G × E. The E effects were, however, more prominent than G or G × E effects for 7 of the 29 traits (DT49, GNS, SFNS, GFD, MWSC, LL, and LW), while the impact of G × E was greater than those of G or E effects for four traits (GFRmax, WSCmin, WSCME, and NAUSC). There was also a similar variation for three traits (GWS, TIP, and WSCmax).

Broad-sense heritability estimates were high (range, 0.70 to 0.99), except for WSCM which had a moderate heritability (0.45) (**Table 2**). Heritability was very strong (above 0.90) for DT49, DTM, grain weight, and size parameters (TW, TGW, GP, Scr, GLe, GWi, GTh, and SGW), HL, SL and GPr. GFR had the highest heritability (0.89), followed by WSCmax and TIP (0.84 and 0.83, respectively) among the physiological traits.

The correlations of trait values across environments were computed using Pearson's correlation coefficients (**Supplementary Figure S2**). The traits values were significantly positively correlated across environments for all traits in most cases, reflecting the strong genetic effect and high heritability observed for the traits. The exceptions being WSCmin, WSCME, and NAUSC, which were less correlated across environments, reflecting a lower heritability and/or a strong G × E effect for these traits.

Overall Environmental Effects

The expression of each trait varied with growing environment and genotype (**Figure 2** and **Supplementary Figure S3**), with environmental conditions during 2018 generally more favourable than those in 2019. The delayed sown effects were smaller in 2018 than in 2019, while VLS had a larger response than LS at WH in

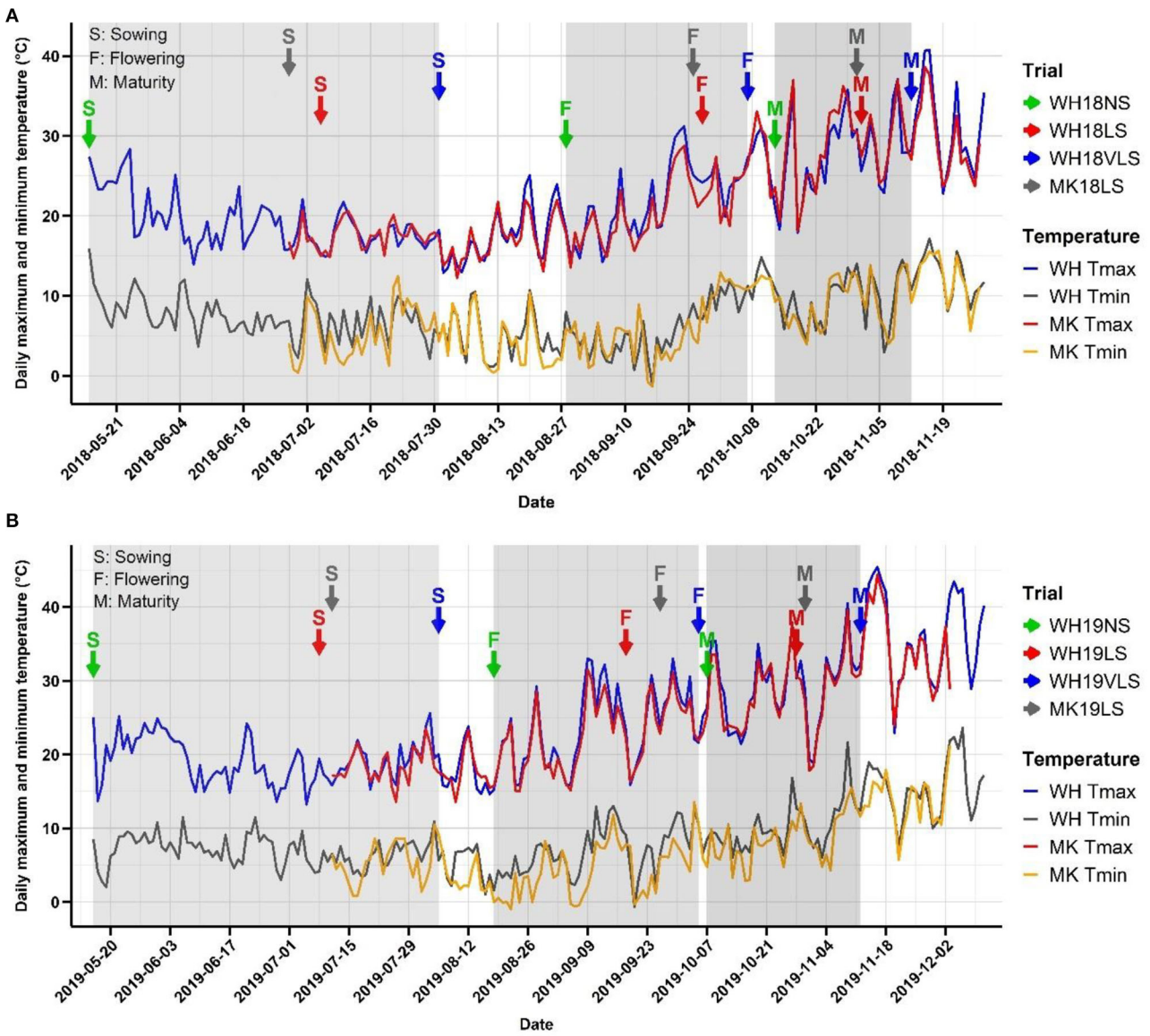

FIGURE 1 | Minimum and maximum temperatures experienced in each trial at Wongan Hills (WH) and Muresk (MK) in **(A)** 2018 and **(B)** 2019 crop growing seasons. The time series line plots in blue and grey, and red and orange indicate the daily maximum and minimum temperature at WH and MK, respectively. The arrows in green, red, and blue colours indicate normal (NS), late (LS), and very late sown (VLS) trials at WH, respectively, and the grey arrows indicate LS trials at MK. S, F, and M indicate sowing, average flowering, and physiological maturity dates in each trial, respectively.

both seasons. The larger responses observed with VLS at WH in 2019 are consistent with higher levels of heat stress.

Delayed sowing plants generally had the following characteristics: shorter durations of their developmental phases (DT49, DTM, GFD, and TIP), reduced primary tiller fertility, shorter plants with smaller leaves (width and length), smaller and lighter heads with fewer grains per head of smaller grain size, lower maximum and minimum WSC, lower MWSC during grain-filling, shorter green leaf area duration, lower HI; higher WSCME, and faster GFR (**Figure 2**). Overall, delayed sowing increased the risk of delivering feed grade barley due to lower grain plumpness, higher screenings, and higher grain protein. The effect on test weight was generally small (and often insignificant).

On average, delayed sowing reduced DT49 and DTM in 16–36 days and 26–46 days, respectively. The reduction in DT49 and DTM relative to NS were similar across the two seasons and were largest for VLS, with higher average temperatures and longer days during the entire growing period.

Spike sterility behaved differently in the two seasons due to delayed sowing. Particularly, lower in 2018 and higher in 2019. Delayed sowing considerably affected the grain growth

TABLE 2 | Percent of variance attributable to genetic (G), environment (E), G × E, and other effects, and broad-sense heritability estimates (H^2).

Trait	Variance component¥				
	G	E	G × E	Residual	H^2
DT49 (days)	33.11***	55.66***	9.70***	1.53	0.96
DTM (days)	43.51***	30.75***	20.12***	5.62	0.93
TW (kg/hL)	62.10***	2.54***	25.01***	10.35	0.94
TGW (g)	74.71***	1.69***	18.45***	5.15	0.96
GP (%)	68.66***	8.99***	19.05***	3.30	0.96
Ret (%)	45.67***	12.78***	35.70***	5.85	0.88
Scr (%)	41.50***	23.96***	24.56***	9.98	0.91
GLe (mm)	88.74***	0.67***	6.54***	4.05	0.99
GWi (mm)	57.46***	11.93***	22.51***	8.10	0.94
GTh (mm)	61.18***	4.16***	24.89***	9.77	0.94
GWS (g)	26.00***	26.78***	30.34***	16.88	0.83
GNS	28.05***	50.38***	13.56***	8.01	0.93
SFNS	13.03***	39.76***	25.96***	21.25	0.70
SGW (mg)†	57.07***	8.65***	24.26***	10.02	0.93
GFR (mg GDD^{-1})†	43.82***	11.51***	28.08***	16.59	0.89
GFRmax (mg GDD^{-1})†	29.12***	8.41***	36.40***	26.07	0.78
GFD (GDD)†	16.85***	39.23***	24.76***	19.16	0.75
TIP (GDD)†	28.01***	27.86***	26.94***	17.19	0.83
WSCmax (mg)†	28.85***	29.52***	26.77***	14.86	0.84
WSCmin (mg)†	23.32***	9.00***	40.01***	27.67	0.70
MWSC (mg)†	22.81***	32.46***	27.33***	17.40	0.79
WSCME (%)†	16.04***	3.60***	51.25***	29.11	0.45
NAUSC†	22.95***	18.65***	35.08***	23.32	0.73
HL (cm)	65.89***	2.21***	20.33***	11.57	0.95
SL (cm)	48.68***	10.04***	30.66***	10.62	0.91
LL (cm)†	16.88***	59.79***	15.04***	8.29	0.85
LW (cm)†	19.32***	57.88***	12.84***	9.96	0.88
HI (%)	36.25***	10.14***	35.10***	18.51	0.86
GPr (%)	38.49***	25.18***	23.75***	12.58	0.91

DT49, days from sowing to awn emergence; DTM, days from sowing to physiological maturity; TW, test weight; TGW, thousand-grain weight; GP, grain plumpness (% grains >2.8 mm); Ret, retention (% grains >2.5 mm); Scr, screenings (% grains <2.2 mm), GLe, grain length; GWi, grain width; GTh, grain thickness; GWS, grain weight $spike^{-1}$; GNS, grain number $spike^{-1}$; SFNS, sterile floret number $spike^{-1}$; SGW, single grain weight; GFR, grain-filling rate; GFRmax, maximum grain-filling rate; GFD, grain-filling duration; TIP, thermal time from awn emergence to grain growth inflection point; WSCmax, maximum stem water-soluble carbohydrate (WSC) content; WSCmin, minimum stem WSC content; MWSC, mobilised WSC during grain-filling; WSCME, WSC mobilisation efficiency; NAUSC, normalised area under SPAD curve; HL, head length; SL, stem length; LL, penultimate leaf length; LW, penultimate leaf width; HI, harvest index; GPr, grain protein percentage.

¥ Variance component of each effect divided by the total of all variance components, genotype (G), environment (E), G × E and residual.

† Measured in seven environments except WH18VLS.

H^2 is broad-sense heritability.

**** Showing significance level at $p < 0.001$.*

components. On average, relative to NS, delayed sowing significantly increased GFR and GFRmax (3.1–21.4%, except GFRmax in WH19LS and WH19VLS), whereas significantly reduced GFD and the related trait TIP (5.1–19.0%).

Single grain weight behaved differently in the two seasons. Generally, the GFR was increased larger than the concomitant decrease in grain-filling duration at delayed sown environments relative to NS in 2018, while the reverse happened in 2019. In line with this, relative to NS, delayed sowing slightly increased SGW in 2018, whereas it tended to reduce SGW in 2019 (by 1.3–6.2%; the effect was insignificant in WH19LS).

Stem WSC content was generally much higher at early grain-filling (∼375.0–431.0 mg under NS and ∼153.0–336.0 mg under delayed sown) than maturity (∼26.0–72.0 mg under NS and ∼5.0–19.0 mg under delayed sowing). Reduced stem volume and less WSC deposition (probably due to reduced photosynthesis; data not shown) were associated with the decline in WSCmax by 22.2–59.3%. In line with this, MWSC was lower by 31.3–59.1% in delayed sown environments relative to NS (excluding WH18LS which had only slightly lower MWSC relative to NS). Stem WSCmin at maturity were also lower by 28.3–92.9%, with delayed sowing indicating higher exhaustion of WSC. Nevertheless, WSCME was only significantly increased in response to delayed sowing in 2018 (29.2–33.5) and only showed an insignificant increase in 2019 (except in MK19LS, which had slightly lower WSCME relative to NS).

Generally, delayed sowing accelerated senescence and reduced normalised area under the penultimate leaf's SPAD decline curve (NAUSC). NAUSC was significantly decreased in WH18LS, MK18LS, and MK19LS relative to the respective NS (16.0–40.1%), while it showed an insignificant decline in WH19VLS and a negligible increase in WH19LS relative to the respective NS.

The general reduction in HI with delayed sowing was only significant in MK18LS, WH19VLS, and MK19LS (11.8, 8.8, and 11.7%, respectively), except for WH18VLS which showed 19.7% higher HI relative to respective NS.

Physical Grain Quality Heat Tolerance Index (HTI)

Thousand grain weight (TGW), GP, and Ret values in delayed sown conditions were significantly correlated with their potentials (i.e., the trait *per se* value under NS conditions) and DT49 (**Supplementary Table S3**). Therefore, a considerable variation in physical grain quality among the genotypes due to delayed sowing could be attributed to variation in their trait potential (genetic weight and size) and DT49 (heat escape). Due to these confounding factors, HTIs were calculated for TGW, GP, and Ret using linear terms for both the trait potentials and time to flowering as described by Bidinger et al. (1987). In calculating HTIs, its distribution is symmetric with a mean of 0.

Genotypes varied substantially for the physical grain quality heat responses and their heat response stability (**Supplementary Table S4**). TGW, GP, and Ret HTIs (TGW.HTI, GP.HTI, and Ret.HTI, respectively) ranged from 1.99 to −2.30, 1.72 to −2.33, and 1.86 to −2.35, respectively (**Supplementary Table S4**). TGW.HTI, GP.HTI, and Ret.HTI was moderate to strongly correlated across environments (**Supplementary Table S5**), suggesting that HTI is a universal response index to heat stress.

There was good correspondence between genotypes that responded the least or the most to delayed sowing for TGW.HTI,

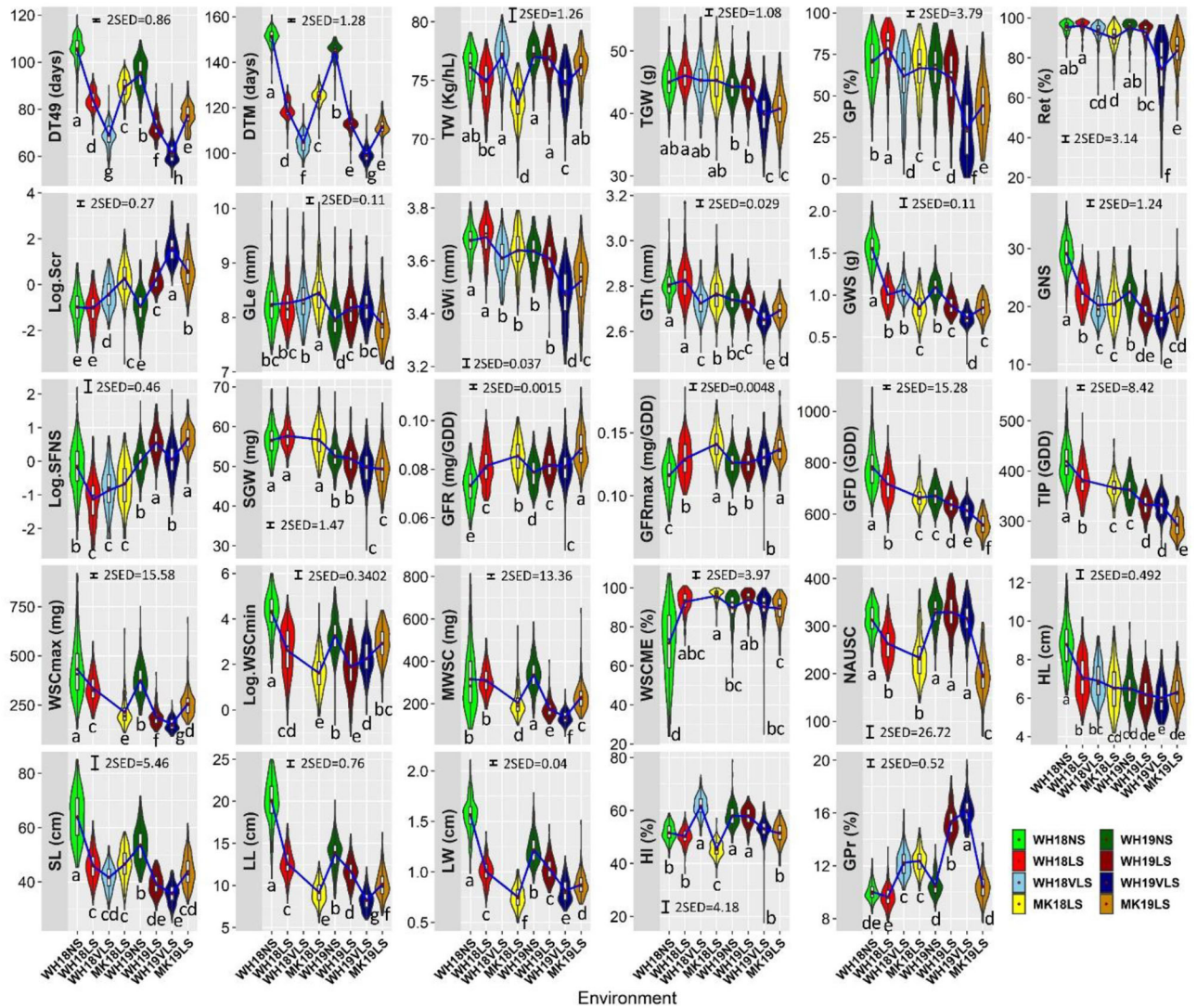

FIGURE 2 | Trait distributions in WH18NS (light green), WH18LS (light red), WH18VLS (sky blue), MK18LS (yellow), WH19NS (dark green), WH19LS (dark red), WH19VLS (navy blue), and MK19LS (orange) environments. The length of the boxes show the interquartile range, the horizontal line within the box indicating the median, red diamonds within the box representing the mean, the whiskers the variability within 1.5 interquartile range of the upper and lower quartiles, and the widths of the violin plots indicate the probability density of the data at different values. The blue lines connect the means of each environment for each trait. Environment and trait definitions are as defined for **Tables 1**, **2**, respectively. Bars represent 2 × standard error of differences (SED) with $\alpha = 0.05$. Different letters below the violin plots represent significant differences between environments for each trait at significance level of 0.05.

GP.HTI, and Ret.HTI. For TGW.HTI, Capstan, Fathom, Lockyer, Sloop VIC, and VB0916 were the best, while Baudin-Hs 2, Dampier, Tallon, and Yan 95168 were the worst-performing. For GP, Lockyer, Cowabbie, and 08S917N-226 were the best, while Fitzgerald, Tallon and Yan 95168 were the worst-performing. For Ret, Capstan, Lockyer, and VB0916 were the best, while Tallon, WA8964, and Yan 95168 were the worst-performing. The heat-tolerant genotypes tended to have more stability. In contrast, the susceptible genotypes appeared to be more responsive to the environmental changes and consequently had less stability in their response (**Supplementary Table S4**).

The Relative Contribution of Physical Grain Quality Potentials, Time to Flowering, and Heat Tolerance to Physical Grain Quality Performance Under Delayed Sowing

The HTI explained 37.2, 44.1, and 53.4% of the variation in TGW, GP, and Ret, respectively (**Figure 3** and **Supplementary Table S6**). On average, TGW, GP, and Ret potentials explained ∼48.6, 42.7, and 28.7% of the variations in TGW, GP, and Ret, while DT49 made a lower contribution to physical grain quality. DT49 accounted for 14.2, 13.2, and 17.5%

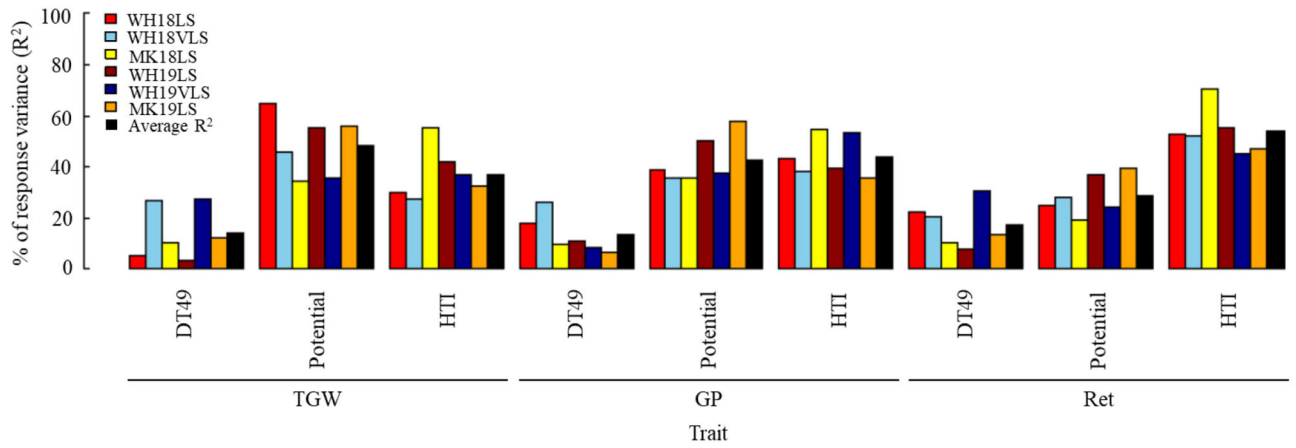

FIGURE 3 | Estimated contribution (% of the variance, R^2) of the trait potential, time to flowering, and heat tolerance index to thousand-grain weight (TGW), grain plumpness (GP), and retention (Ret) under delayed sown/heat-stress conditions. Environment definitions are as defined in **Table 1**.

of the observed variation in TGW, GP, and Ret under delayed sown, respectively.

Heat tolerance index appeared to be the primary factor determining Ret, while TGW potential was the main determinant of TGW, and GP potential and HTI were equally crucial in determining GP. The combined factors accounted for 100% of the observed variability for the physical grain quality parameters. This suggests that this analysis method effectively estimates major determinants of physical grain quality under delayed sown/heat-stressed growing conditions.

Association of Selected Physical Grain Quality Parameters With the Traits Evaluated Within Environments

Thousand grain weight (TGW), GP, and Ret were negatively correlated with DT49 and DTM in pairwise correlations across delayed sown environments in both seasons (**Table 3** and **Supplementary Table S7**). The negative correlations between phenology (DT49 and DTM) and the physical grain quality parameters were either missing or weaker in NS environments than delayed sown environments. Genotypes with heavier and plumper grains tended to have earlier flowering and maturity under delayed sowing. Unsurprisingly, TGW, GP, and Ret were significantly correlated with one another and with other grain weight and size parameters (i.e., TW, Scr, GLe, GWi, GTh, SGW and GWS) across environments (**Table 3**). TGW, GP, and Ret showed stronger correlations with GWi and GTh than GLe in delayed sown environments, suggesting that the alteration in lateral dimension was probably more important in determining grain weight and size under heat-stress conditions. TGW, GP, and Ret were negatively correlated (moderate to relatively strong) with GNS and HL across all environments (except in WH18NS). Therefore, genotypes with heavier and plumper grains tended to have shorter heads with lower grain numbers (i.e., smaller sink size), which probably led to less competition between grains for photosynthates.

While most physiological attributes influenced physical grain quality *per se*, grain quality was best correlated with GFR. GFR was strongly and positively correlated with SGW and TGW, with the correlation stronger with delayed sowing (**Supplementary Table S7**). GFR was also positively correlated (moderate to relatively strong) with GP and Ret across all delayed sown environments (except WH18LS). It only showed a weak positive correlation with GP in one NS environment (WH18NS). GFD and the related trait TIP showed weak to moderate positive correlations with TGW, GP, and Ret under normal and delayed sown conditions, mainly in the 2019 growing season. These correlations indicate that genotypes with heavier and plumper grains had higher GFRs and longer grain-filling durations. However, the GFR rate may play a relatively more important role in determining TGW, GP, and Ret (and other grain weight and size parameters) (**Table 3** and **Supplementary Table S7**).

Normalised area under the penultimate leaf's SPAD decline curve (NAUSC) was positively correlated (moderate) with GP and Ret across all environments (except in MK18LS) and with TGW only in late sown trials at MK (i.e., MK18LS and MK19LS). Therefore, the penultimate leaf chlorophyll retention during grain-filling (stay-green) contributed to better physical grain quality under normal and delayed sown conditions. NAUSC was positively correlated with GFD and TIP across environments (**Supplementary Table S7**), indicating that the stay-green contributed to better physical grain quality performance via stabilisation of GFD.

The stem WSC parameters behaved differently to TGW, GP, and Ret. WSCmin and WSCME showed weak to moderate positive and negative correlations, respectively, with TGW, GP, and Ret under NS conditions, while the reverse held under delayed sown conditions. These correlations indicate that genotypes with better physical grain quality tended to have higher WSC mobilisation efficiency and lower stem WSC residuals at physiological maturity under delayed sown/heat-stress conditions. The reverse was true under NS conditions. MWSC and WSCME were positively correlated with GFR and GFRmax across environments (**Supplementary Table S7**), indicating a link between WSC mobilisation with better physical grain quality performance via stabilisation of GFR. WSCmax

TABLE 3 | Correlations between thousand-grain weight (TGW), grain plumpness (GP), and retention (Ret), and traits measured in each environment.

	Environment																							
	WH18NS			WH18LS			WH18VLS			MK18LS			WH19NS			WH19LS			WH19VLS			MK19LS		
Trait	**TGW**	**GP**	**Ret**	**TGW**	**GP**	**Ret**	**TGW**	**GP**	**Ret**	**TGW**	**GP**	**Ret**	**TGW**	**GP**	**Ret**	**TGW**	**GP**	**Ret**	**TGW**	**GP**	**Ret**	**TGW**	**GP**	**Ret**
DT49	−0.03	−0.09	−0.04	−0.25**	−0.46***	−0.48***	−0.53***	−0.54***	−0.46***	−0.34***	−0.31***	−0.31***	−0.20*	−0.28***	−0.29***	−0.24**	−0.43***	−0.38***	−0.60***	−0.38***	−0.64***	−0.42***	−0.34***	−0.46***
DTM	0.00	−0.07	−0.05	−0.28***	−0.42***	−0.47***	−0.55***	−0.50***	−0.43***	−0.14	−0.21**	−0.19*	−0.18*	−0.30***	−0.23**	−0.14	−0.32***	−0.25**	−0.49***	−0.28***	−0.52***	−0.33***	−0.34***	−0.46***
TW	−0.04	0.22**	0.23**	−0.24**	0.06	0.05	−0.01	0.43***	0.48***	0.24**	0.42***	0.47***	−0.12	0.33***	0.36***	−0.19*	0.19*	0.35***	0.40***	0.59***	0.70***	0.15	0.40***	0.47***
TGW		0.53***	0.48***		0.56***	0.55***		0.58***	0.46***		0.58***	0.66***		0.48***	0.47***		0.43***	0.38***		0.58***	0.75***		0.58***	0.71***
GP	0.53***		0.89***	0.56***		0.94***	0.58***		0.84***	0.58***		0.90***	0.48***		0.88***	0.43***		0.87***	0.58***		0.81***	0.58***		0.86***
Ret	0.48***	0.89***		0.55***	0.94***		0.46***	0.84***		0.66***	0.90***		0.47***	0.88***		0.38***	0.87***		0.75***	0.81***		0.71***	0.86***	
Scr	−0.41***	−0.74***	−0.91***	−0.58***	−0.83***	−0.91***	−0.46***	−0.78***	−0.88***	−0.64***	−0.79***	−0.88***	−0.48***	−0.74***	−0.90***	−0.28***	−0.50***	−0.76***	−0.73***	−0.63***	−0.90***	−0.70***	−0.70***	−0.91***
GLe	0.63***	−0.08	−0.08	0.61***	−0.11	−0.07	0.65***	−0.06	−0.15	0.46***	−0.16*	−0.04	0.60***	−0.26**	−0.22**	0.60***	−0.19*	−0.26**	0.38***	−0.30***	−0.17*	0.61***	−0.07	0.07
GWi	0.55***	0.68***	0.62***	0.69***	0.77***	0.76***	0.75***	0.70***	0.61***	0.72***	0.73***	0.77***	0.63***	0.78***	0.69***	0.65***	0.65***	0.59***	0.86***	0.71***	0.80***	0.85***	0.72***	0.80***
GTh	0.31***	0.64***	0.47***	0.52***	0.75***	0.68***	0.46***	0.76***	0.65***	0.51***	0.75***	0.66***	0.35***	0.82***	0.68***	0.33***	0.74***	0.62***	0.25**	0.58***	0.49***	0.28***	0.69***	0.53***
GWS	0.33***	0.17*	0.13	−0.16*	−0.25**	−0.21*	0.03	−0.07	0.00	−0.12	−0.12	−0.18*	0.13	−0.09	−0.12	0.02	−0.22**	−0.16	0.14	−0.08	0.04	0.16	0.03	0.07
GNS	−0.13	−0.01	−0.02	−0.53***	−0.40***	−0.35***	−0.51***	−0.41***	−0.29***	−0.47***	−0.37***	−0.47***	−0.44***	−0.32***	−0.33***	−0.45***	−0.40***	−0.31***	−0.49***	−0.41***	−0.41***	−0.38***	−0.30***	−0.33***
SFNS	−0.19*	−0.26**	−0.21**	−0.22**	−0.33***	−0.33***	−0.19*	−0.26**	−0.23**	−0.24**	−0.17*	−0.16*	−0.15	−0.21*	−0.23**	−0.13	−0.26**	−0.28***	−0.23**	−0.15	−0.28***	−0.09	−0.17*	−0.20*
SGW	0.76***	0.32***	0.27***	0.80***	0.33***	0.32***	–	–	–	0.82***	0.49***	0.58***	0.81***	0.34***	0.31***	0.82***	0.27***	0.19*	0.87***	0.48***	0.64***	0.89***	0.44***	0.58***
GFR	0.55***	0.17*	0.10	0.47***	0.06	0.05	–	–	–	0.63***	0.34***	0.41***	0.58***	0.05	0.03	0.62***	0.19*	0.07	0.70***	0.32***	0.43***	0.68***	0.29***	0.41***
GFRmax	0.46***	0.18*	0.11	0.37***	0.02	0.00	–	–	–	0.49***	0.29***	0.33***	0.51***	0.05	0.01	0.48***	0.06	−0.03	0.56***	0.28***	0.39***	0.56***	0.22**	0.32***
GFD	−0.01	0.06	0.11	0.04	0.13	0.15	–	–	–	0.21**	0.15	0.15	0.17*	0.33***	0.32***	0.21**	0.09	0.15	0.20*	0.22**	0.29***	0.37***	0.24**	0.29***
TIP	−0.01	0.13	0.17*	0.03	0.13	0.13	–	–	–	0.19*	0.18*	0.17*	0.10	0.30***	0.27***	0.12	−0.03	0.05	0.10	0.20*	0.29***	0.26**	0.19*	0.22**
WSCmax	0.10	−0.04	0.02	0.04	−0.16	−0.12	–	–	–	0.08	0.05	0.13	0.05	−0.03	−0.04	−0.03	−0.19*	−0.18*	−0.03	−0.17*	−0.08	−0.04	−0.13	−0.09
WSCmin	0.17*	0.17*	0.17*	−0.11	−0.19*	−0.13	–	–	–	−0.04	0.06	0.05	0.22**	0.23**	0.22**	−0.36***	−0.34***	−0.39***	−0.17*	−0.17*	−0.27***	−0.16*	0.01	−0.10
MWSC	0.02	−0.16	−0.12	0.06	−0.12	−0.11	–	–	–	0.11	0.05	0.15	−0.06	−0.15	−0.15	0.06	−0.11	−0.09	0.05	−0.09	0.06	0.01	−0.12	−0.05
WSCME	−0.11	−0.16*	−0.15	0.09	0.17*	0.09	–	–	–	0.20*	0.10	0.13	−0.23**	−0.30***	−0.29***	0.34***	0.31***	0.36***	0.16*	0.19*	0.31***	0.14	−0.04	0.09
NAUSC	0.11	0.31***	0.26**	−0.04	0.26**	0.19*	–	–	–	0.32***	0.12	0.15	0.14	0.30***	0.29***	0.10	0.31***	0.29***	0.16	0.31***	0.31***	0.29***	0.27***	0.30***
HL	−0.04	−0.06	0.00	−0.43***	−0.42***	−0.37***	−0.48***	−0.47***	−0.32***	−0.40***	−0.38***	−0.44***	−0.30***	−0.33***	−0.30***	−0.33***	−0.44***	−0.32***	−0.54***	−0.50***	−0.56***	−0.39***	−0.42***	−0.44***
SL	0.26**	0.32***	0.33***	0.13	0.11	0.16**	0.09	0.06	0.13	−0.05	0.14	0.06	0.25**	0.35***	0.30***	0.24**	0.25**	0.16*	−0.07	0.03	−0.03	0.31***	0.35***	0.39***
LL	0.38***	0.10	0.21**	0.12	0.13	0.16	–	–	–	−0.03	−0.17*	−0.21**	0.23**	0.04	0.10	0.18*	−0.04	−0.10	−0.09	−0.28***	−0.25**	0.19*	−0.03	0.10
LW	0.14	0.13	0.18*	0.01	0.01	0.01	–	–	–	0.01	−0.16*	−0.15	0.17*	−0.09	−0.02	0.02	−0.18*	−0.26**	−0.19*	−0.34***	−0.34***	0.13	−0.08	0.02
HI	−0.13	−0.25**	−0.31***	−0.27***	−0.13	−0.18*	0.10	0.21**	0.11	−0.19*	−0.19*	−0.19*	0.11	−0.08	−0.07	0.14	0.09	0.20*	0.24**	0.11	0.30***	0.13	0.01	0.09
GPr	0.26**	0.27***	0.34***	0.31***	0.34***	0.39***	0.25**	0.20*	0.08	0.20*	0.13	0.18*	0.15	0.12	0.18*	−0.18*	−0.26**	−0.33***	0.15	0.11	0.24**	0.01	0.00	−0.02

*Environment and trait definitions are as defined for **Tables 1**, **2**, respectively.*

Values are Pearson correlation coefficients and significance level indicated by $^{*}p < 0.05$, $^{**}p < 0.01$, and $^{***}p < 0.001$.

–Indicates that the trait was not evaluated in the respective environment.

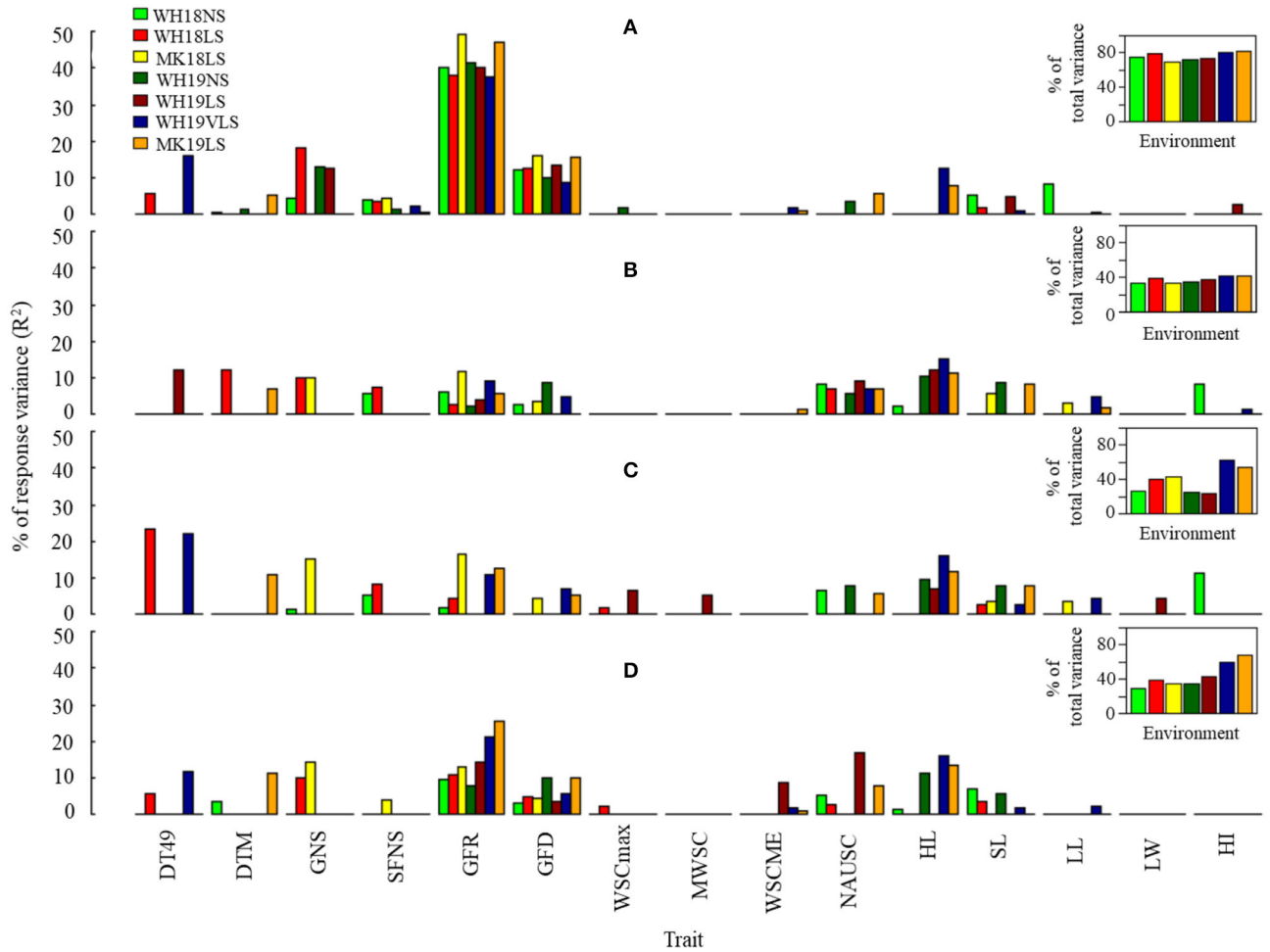

FIGURE 4 | Estimated contribution (% of variance, R^2) of selected phenological, agro-morphological and physiological traits to **(A)** TGW, **(B)** GP, **(C)** Ret, and **(D)** grain width (GWi) in WH18NS (light-green), WH18LS (light-red), MK18LS (yellow), WH19NS (dark-green), WH19LS (dark-red), WH19VLS (navy-blue), and MK19LS (orange) environments. Insets show the total variability explained by the best significant model in each environment ($p < 0.0001$). Environment and trait definitions are as defined for **Tables 1**, **2**, respectively.

showed weak negative correlations with GP and Ret only in WH19LS and WH19VLS. This was in contrast to what was expected if higher WSC content *per se* at early grain-filling contributed to better physical grain quality under heat.

Thousand grain weight (TGW), GP, and Ret showed moderate positive correlations with SL under NS, WH19LS and MK19LS. LL was positively correlated (weak to moderate) with TGW in NS, WH19LS and MK19LS environments. It was positively correlated with Ret in WH18NS and negatively correlated with GP and Ret in MK18LS and WH19VLS. LW was positively correlated (weak) with TGW and Ret in NS and negatively correlated with TGW and grain size in some delayed sown environments, mainly WH in 2019.

Grain protein percent was generally positively correlated with the physical grain quality parameters across environments except for WH19LS, which was negatively correlated.

The relationship between the physical grain quality parameters and other traits in PCA analyses was similar to the correlation tests. The PCA indicate that most of the variation among the genotypes could be accounted for by the physical grain quality parameters and GFR under delayed sown/heat stress conditions and that they (i.e., TGW, GP, Ret, and GFR) were positively correlated to one another under such conditions (**Supplementary Figure S4**).

The associations between TGW, GP, Ret, and GWi (as dependent variables) and selected phenological, agro-morphological, and physiological parameters (as independent variables) were tested in a stepwise multiple linear regression analysis (except for WH19VLS) (**Figure 4** and **Supplementary Table S8**). The best model accounted for 69.7–81.8%, 32.7–41.9%, 23.1–62.8%, and 29.3–68.4% of the variation for TGW, GP, Ret, and GWi, respectively, depending on the environment (**Figure 4**). Grain growth components (GFR and GFD), sink size (HL and GNS), and plant stature (SL) were significant when added to the model. GP and GWi models included stay-green (NAUSC) in most environments.

Grain-filling rate was the most potent predictor for TGW and GWi across the environments. In contrast, the best predictor

for GP and Ret varied across environments (generally HL and GFR in most cases). Interestingly, GFR's contribution to explaining grain size variation (GP, Ret, and GWi) was considerably stronger under delayed sown conditions in comparison with NS.

Associations of HTIs and the Traits Evaluated Within Delayed Sown Environments

The considerable variation in agro-morphological and physiological traits' expression across delayed sown/heat-stressed environments, together with considerable variation for heat tolerance among the genotypes, provided an opportunity to test the associations of heat tolerance with other traits. This was explored to see whether the expression of specific traits was more advantageous under heat stress than others. If this were the case, selection for genotypes adapted to heat stress would be considerably simplified (**Table 4**).

The HTIs for TGW, GP, and Ret were strongly and positively correlated with TGW, GP, and Ret, respectively, across all delayed sown environments, indicating the strong reflection of genotypic differences for the traits into the HTIs. The HTIs were not related to the trait potentials ($r = 0$ in all cases, data not shown) or flowering time ($r = 0$; **Table 4**). Therefore, their relationship to the physical grain quality parameters under delayed sown conditions was independent of the effects of these confounding factors.

The HTIs showed moderate to strong correlations with the grain weight and size parameters. The HTIs were positively correlated with TW, TGW, GP, Ret, GWi, GTh, and SGW, and were negatively associated with Scr across delayed sown environments in both seasons (**Table 4**). TGW.HTI was correlated positively with GLe, whereas GP.HTI and Ret.HTI were correlated negatively with GLe (except Ret.HTI in MK19LS). Grain weight and size HTIs were generally better correlated with GWi and GTh than GLe, indicating that physical grain quality heat tolerance was more related to alteration of the grain's lateral dimensions.

Grain weight per spike showed only a few weak correlations with HTIs (**Table 4**), reflecting how it was better correlated with GNS than grain weight or size (**Supplementary Table S7**). Grain weight and size HTIs were consistently negatively correlated (weak to moderate) with GNS and HL across delayed sown environments. Therefore, genotypes with shorter heads and lower grain numbers (i.e., smaller sink size) maintained better grain weight and size under heat. Grain weight and size HTIs showed weak to moderate negative correlations with SFNS in 2018, reflecting the association of both traits with sink size.

Physiological traits generally had weak to moderate correlations with grain weight and size HTIs. Among the physiological characteristics, GFR and GFRmax showed relatively stronger and more consistent correlations with grain weight and size HTIs across delayed sown environments. The positive correlations of GFR and GFRmax with TGW.HTI, GP.HTI, and Ret.HTI across delayed sown environments indicate genotypes with better grain weight and size maintenance under heat had faster GFR. GFD and the related trait TIP showed weak and inconsistent correlations with TGW.HTI.

Relationships between WSC measures and grain weight and size maintenance appeared complex. WSCmax and MWSC had few weak to moderate negative correlations with grain weight and size HTIs. These correlations were opposite to expected if stem WSCs and absolute WSCs mobilisation contribute to maintaining grain weight and size under heat stress. HTI showed few negative correlations with WSCmin and a positive correlation with WSCME, demonstrating that genotypes with higher grain weight heat tolerance had a more efficient WSC mobilisation. WSCmin and WSCME also showed few weak to moderate correlations with grain size HTIs that were variable in direction. WSCmin was negatively correlated with GP.HTI and Ret.HTI in WH19LS and was positively correlated with Ret.HTI in WH19VLS. WSCME was positively correlated with grain size HTIs in WH19LS, while the reverse held in MK19LS. TGW.HTI and GP.HTI were positively correlated (weak to moderate) with NAUSC during grain-filling in WH19LS and MK19LS, indicating that stay-green contributed to better grain weight and size maintenance.

The penultimate leaf dimensions were negatively (weak to moderate) correlated with grain weight and grain size HTIs in WH19LS and WH19VLS. Therefore, smaller leaf sizes may have adaptive value in hot environments, probably through the heat avoidance mechanism. HI showed positive correlations with grain weight and size HTIs in WH18VLS and WH19LS, indicating that HI was favoured and may contribute to grain weight and size maintenance under heat conditions. GPr showed a weak positive correlation with TGW.HTI in WH18LS and moderate negative correlations with grain weight and size HTIs in WH19LS.

The relationship between the physical grain quality HTIs and other traits in PCA analyses were similar to those of the correlation tests. The PCA results indicate a substantial contribution of the GFR to the explained variation by the first two PCs and the consistent positive correlation between the physical grain quality HTIs and GFR across delayed sown/heat-stressed environments (**Supplementary Figure S5**).

The associations between TGW.HTI, GP.HTI, and Ret.HTI (as dependent variables) and selected phenological, agro-morphological, and physiological parameters (as independent variables) were tested in a stepwise multiple linear regression analysis for each delayed sown environment separately (except for WH19VLS) (**Figure 5** and **Supplementary Table S9**). The included independent variables in the model accounted for 20.5–40.9%, 13.4–24.1%, and 12.4–29.1% of the variation for TGW.HTI, GP.HTI, and Ret.HTI, respectively, depending on the environment. GFR accounted for the most significant proportion of the contribution to HTIs (explained 10–22%, 6–13%, and 7–18% of variability for TGW.HTI, GP.HTI, and Ret.HTI, respectively). GFR is likely the most crucial trait in determining physical grain quality under heat stress. The exception was WH19VLS, in which GFR was not added to the model for grain size HTI (GP.HTI and Ret.HTI). HL and LL explained much of the variation in that environment. No HTI model included NAUSC or LW.

TABLE 4 | Correlations between thousand-grain weight, grain plumpness, and retention heat tolerance indices (TGW.HTI, GP.HTI, and Ret. HTI, respectively), and traits measured within each delayed sown environment.

	Environment																	
	WH18LS			WH18VLS			MK18LS			WH19LS			WH19VLS			MK19LS		
Trait	**TGW.HTI**	**GP.HTI**	**Ret.HTI**	**TGW.HTI**	**GP.HTI**	**Ret.HTI**	**TGW.HTI**	**GP.HTI**	**Ret.HTI**	**TGW.HTI**	**GP.HTI**	**Ret.HTI**	**TGW.HTI**	**GP.HTI**	**Ret.HTI**	**TGW.HTI**	**GP.HTI**	**Ret.HTI**
DT49	0.00	0.00	0.00	0.00	0.00	0.00	0.00	0.00	0.00	0.00	0.00	0.00	0.00	0.00	0.00	0.00	0.00	0.00
DTM	−0.13	−0.13	−0.12	−0.24**	−0.18*	−0.11	0.02	−0.08	−0.05	0.14	0.03	0.09	−0.06	0.04	0.00	0.01	−0.02	−0.05
TW	−0.04	0.19*	0.21**	0.08	0.36***	0.42***	0.20*	0.34***	0.41***	0.07	0.28***	0.46***	0.33***	0.32***	0.43***	0.22**	0.19*	0.32***
TGW	0.55***	0.38***	0.40***	0.52***	0.30***	0.18*	0.74***	0.50***	0.57***	0.65***	0.38***	0.30***	0.61***	0.33***	0.43***	0.57***	0.48***	0.62***
GP	0.34***	0.66***	0.62***	0.22**	0.62***	0.48***	0.38***	0.74***	0.68***	0.15	0.63***	0.52***	0.41***	0.73***	0.63***	0.26**	0.60***	0.56***
Ret	0.34***	0.63***	0.73***	0.11	0.43***	0.72***	0.48***	0.71***	0.84***	0.21*	0.59***	0.74***	0.46***	0.45***	0.67***	0.37***	0.48***	0.69***
Scr	−0.32***	−0.55***	−0.65***	−0.14	−0.42***	−0.58***	−0.48***	−0.62***	−0.73***	−0.37***	−0.47***	−0.77***	−0.44***	−0.26**	−0.53***	−0.38***	−0.38***	−0.61***
GLe	0.20*	−0.14	−0.12	0.28***	−0.15	−0.26**	0.22**	−0.11	−0.01	0.24**	−0.13	−0.25**	0.08	−0.22**	−0.21*	0.28***	0.15	0.21*
GWi	0.47***	0.56***	0.59***	0.40***	0.41***	0.34***	0.58***	0.61***	0.65***	0.48***	0.43***	0.42***	0.63***	0.45***	0.55***	0.49***	0.45***	0.58***
GTh	0.32***	0.38***	0.41***	0.16*	0.36***	0.33***	0.37***	0.55***	0.51***	0.18*	0.38***	0.38***	0.26**	0.37***	0.32***	0.13	0.34***	0.30***
GWS	−0.14	−0.07	0.05	−0.07	−0.10	0.05	−0.05	−0.03	−0.07	0.02	−0.16	−0.08	−0.03	−0.22**	−0.17*	0.16*	0.01	0.06
GNS	−0.31***	−0.18*	−0.08	−0.30***	−0.23**	−0.06	−0.24**	−0.20*	−0.30***	−0.23**	−0.29***	−0.16*	−0.30***	−0.35***	−0.34***	−0.11	−0.22**	−0.27**
SFNS	−0.12	−0.18*	−0.22**	−0.14	−0.20*	−0.15	−0.24**	−0.12	−0.09	0.06	−0.03	−0.12	0.01	0.08	0.08	0.01	0.06	0.04
SGW	0.34***	0.22**	0.27**	–	–	–	0.48***	0.38***	0.46***	0.43***	0.23**	0.12	0.32***	0.16	0.22**	0.44***	0.30***	0.44***
GFR	0.37***	0.27**	0.24**	–	–	–	0.45***	0.37***	0.43***	0.28***	0.26**	0.06	0.30***	0.12	0.15	0.36***	0.26**	0.42***
GFRmax	0.29***	0.22**	0.20*	–	–	–	0.35***	0.31***	0.35***	0.18*	0.12	−0.03	0.25**	0.11	0.14	0.28***	0.16	0.32***
GFD	−0.17*	−0.14	−0.08	–	–	–	0.01	−0.02	0.00	0.16*	−0.03	0.07	0.00	0.06	0.10	0.16	0.10	0.08
TIP	−0.20*	−0.14	−0.09	–	–	–	−0.01	0.01	0.04	0.06	−0.13	−0.01	−0.05	0.01	0.05	0.08	0.00	0.00
WSCmax	−0.16	−0.18*	−0.13	–	–	–	−0.02	0.05	0.11	−0.19*	−0.21**	−0.26**	−0.08	−0.19*	−0.03	−0.08	−0.11	−0.08
WSCmin	−0.16*	−0.12	−0.08	–	–	–	−0.06	0.00	0.00	−0.32***	−0.26**	−0.30***	0.11	0.13	0.17*	0.08	0.16	0.12
MWSC	−0.13	−0.16*	−0.13	–	–	–	0.00	0.07	0.12	−0.12	−0.16	−0.19*	−0.11	−0.23**	−0.07	−0.11	−0.14	−0.11
WSCME	0.12	0.08	0.01	–	–	–	0.07	0.06	0.08	0.23**	0.18*	0.21**	−0.09	−0.10	−0.07	−0.13	−0.20*	−0.17*
NAUSC	−0.14	0.00	−0.06	–	–	–	0.09	0.01	0.04	0.11	0.10	0.16*	−0.03	0.12	0.07	0.24**	0.16	0.16*
HL	−0.29***	−0.15	−0.09	−0.32***	−0.28***	−0.09	−0.22**	−0.20*	−0.29***	−0.12	−0.26**	−0.14	−0.29***	−0.35***	−0.38***	−0.22**	−0.32***	−0.33***
SL	−0.10	−0.11	−0.03	−0.16*	−0.07	0.01	−0.13	−0.01	−0.06	−0.01	−0.01	−0.10	−0.08	−0.13	−0.07	0.09	0.11	0.15
LL	−0.05	0.02	0.07	–	–	–	0.06	−0.05	−0.11	−0.05	−0.22**	−0.28***	−0.26**	−0.36***	−0.34***	−0.02	−0.10	−0.04
LW	−0.01	0.00	−0.02	–	–	–	0.14	−0.02	−0.06	−0.13	−0.24**	−0.32***	−0.11	−0.25**	−0.17*	0.02	−0.05	0.01
HI	0.04	0.14	0.08	0.23**	0.27**	0.15	0.03	0.04	−0.02	0.27***	0.18*	0.28***	0.06	0.00	−0.01	0.16	0.04	0.04
GPr	0.18*	0.07	0.10	0.10	0.08	−0.16	0.07	−0.01	0.03	−0.23***	−0.24**	−0.38***	−0.04	0.00	0.05	0.08	0.15	0.10

*Environment and trait definitions are as defined for **Tables 1**, **2**, respectively.*

Values are Pearson correlation coefficients and significance level indicated by $^{*}p < 0.05$, $^{**}p < 0.01$, and $^{***}p < 0.001$.

–Indicates that the trait was not evaluated in the respective environment.

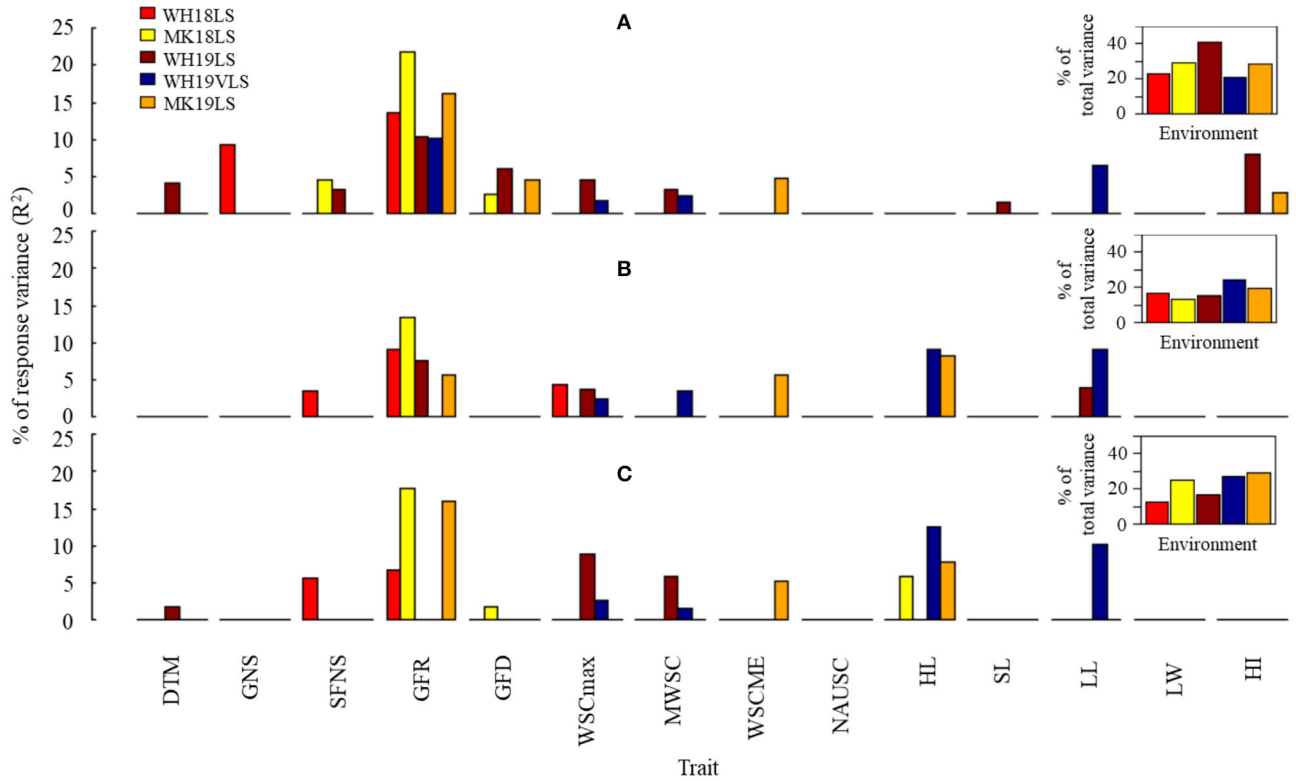

FIGURE 5 | Estimated contribution (% of the variance, R^2) of selected phenological, agro-morphological, and physiological traits to **(A)** thousand-grain weight heat tolerance (TGW.HTI), **(B)** grain plumpness heat tolerance (GP.HTI), and **(C)** retention heat tolerance (Ret.HTI) in WH18LS (light-red), MK18LS (yellow), WH19LS (dark-red), WH19VLS (navy-blue), and MK19LS (orange) environments. Insets show the total variability explained by the best significant model in each environment ($p < 0.001$). Environment and trait definitions are as defined for **Tables 1**, **2**, respectively.

DISCUSSION

Late sowing with supplementary irrigation increased the probability of days with temperatures of above 30°C during grain filling in assessing a diverse set of barley genotypes for heat tolerance. GFR was the trait most highly and consistently associated with physical grain quality stability, indicating this trait as potentially linked to barley heat tolerance.

Grain Weight, Plumpness, and Dimensions

The change in grain weight (TGW and SGW), plumpness (GP and Ret), and dimensions (GLe, GWi, and GTh) was not consistent with increasing average temperature and frequency and intensity of hot days (≥30°C) with later sowing (**Table 1** and **Figures 1**, **2**).

The lack of general grain weight response with delayed sowing may be explained to some degree by the compensatory relationship between GLe and GWi or GTh, even though the sites were irrigated to minimise the effects of drought stress during grain filling. Although not always significant, delayed sowing generally increased GLe (except in MK19LS, which was slightly lower) and reduced average GWi and GTh (except in WH18LS, which was slightly higher) (**Figure 2**). GWi and GTh tended to show lower reductions (or even an increase in the case of WH18LS) in delayed sown environments in which grain weight did not significantly differ from the respective NS. It appears that the GLe increased large enough (although not always significant; **Figure 2**) to compensate for the concomitant decrease in GWi and GTh, leading to an insignificant grain weight difference in those delayed sown environments with a respective NS. By contrast, in WH19VLS, the significant increase in GLe could not compensate for a large concomitant decrease in GWi and GTh. In MK19LS, the significant reduction in GLe and grain lateral dimensions (GWi and GTh) led to a significantly lower grain weight relative to the respective NS.

The contrasting response of grain length to grain width and thickness under high temperatures is also reported elsewhere. Watt (2020) observed an increase in grain length and a reduction in grain width and thickness in response to high field temperatures during grain-filling in barley. Li et al. (2018) observed a grain length increase, while the width was reduced in response to high temperature during grain-filling in wheat under late sown field heat-stressed conditions. Shi et al. (2016) reported the grain length and width effect of high night-time temperature under controlled conditions in rice. They concluded that grain length was not significantly changed in response to the heat treatment, whereas grain width was reduced considerably. By contrast, Aiqing et al. (2018) reported a more significant effect of heat stress on grain length than the width in wheat. Grain length growth occurs early in grain development in response

to cell division and elongation in the caryopsis, whereas filling out (width/thickness) occurs later in grain development due to starch deposition in the developing endosperm. Tashiro and Wardlaw (1990) found that grain length was most sensitive to high temperature 7 days after flowering and was unaffected by the heat treatment, which commenced 8 days later. Grain width was highly responsive to high temperature at 12–20 days after anthesis. Therefore, the high-temperature effects on GLe and the grain lateral dimensions may have partly depended on the exact timing of heat stress in this study and the studies, as mentioned earlier.

The average grain plumpness (GP and Ret) trend across environments closely followed the trend in grain lateral dimensions (in particular GWi), reflecting that the width of the grain defines plumpness. Grain plumpness and lateral dimensions showed a more transparent relationship with hot days, heat intensity, and frequency during grain-filling (**Table 1**; **Figures 1**, **2**).

Grain weight (TGW and SGW) and plumpness (GP, Ret; and Scr) were better correlated with GWi in environments with a higher degree of heat stress during grain-filling (**Table 3** and **Supplementary Table S7**). Additionally, the HTI for TGW, GP, and Ret were more correlated with GWi and GTh than GLe (**Table 4**). These observations suggest that the observed genotypic variation for grain weight, plumpness, and size under delayed sown conditions (higher heat stress) was mainly related to the grain width response. The observed stronger environmental and genetic-by-environment effects for GWi than GLe reinforce this idea (**Table 2**). These results are similar to those of Li et al. (2018) who reported a stronger heat stress effect on GWi than GLe and a stronger correlation of grain weight response with grain width, but not grain length in wheat under field grain-filling heat stress conditions. In contrast, Aiqing et al. (2018) observed a larger effect of heat stress on grain length than grain width in response to 10 days heat stress commenced at anthesis under controlled environment conditions in wheat. They also found a positive correlation between grain weight and length, but not between grain weight and width.

Heat stress affects starch accumulation in grains by affecting enzyme activity in the starch synthesis pathway (Hawker and Jenner, 1993; Jenner, 1994; Keeling et al., 1994; Wallwork et al., 1998). It can also alter amylose and amylopectin deposition and the number and size of different types of starch granules (Bhullar and Jenner, 1985; Hurkman et al., 2003; Li et al., 2018). These factors could have contributed to the observed variation in grain weight and width among the genotypes in response to high temperatures in this study. For further discussion, see Section Grain Growth and Development.

Grain Growth and Development

The final grain weight and grain size of barley is a function of the rate and the duration of grain-filling. This study's genotypic variation was larger for rate than duration (**Table 2**), with delayed sowing truncating the GFD and TIP, but enhancing GFR and GFRmax (**Figure 2**). These findings agree with several studies which demonstrated that genotype determines the GFR, while environmental factors (e.g., temperature) mainly affect the duration of the grain-filling period (Bruckner and Frohberg, 1987; Wardlaw and Moncur, 1995; Zahedi and Jenner, 2003; Dias and Lidon, 2009).

Grain weight (TGW and SGW) and plumpness (GP and Ret) were more highly correlated with GFR (and GFRmax) than GFD (and TIP) under heat stress conditions (**Table 3** and **Supplementary Table S7**). Interestingly, GWi, which was the grain dimension best correlated with TGW, plumpness (GP and Ret), and HTIs (**Tables 3**, **4**), showed a more consistent and much stronger correlation with GFR (and GFRmax) than GFD or TIP under delayed sown conditions (**Figure 4** and **Supplementary Table S7**). Furthermore, TGW.HTIs, GP.HTIs, and Ret.HTIs were positively correlated with GFR (and GFRmax), but did not show a clear relationship with GFD and TIP (**Table 4**). Overall, these findings suggest that GFR and GFRmax plays an essential role in determining physical grain quality performance/maintenance under heat-stress conditions.

Research with wheat has similarly observed greater genotypic variation in GFR than GFD. In those studies, genotypes with higher grain weight (the most heat-tolerant) were those with higher GFR under high-temperature conditions in the field (Bruckner and Frohberg, 1987; Motzo et al., 1996) and in the controlled environmental conditions (Wardlaw and Moncur, 1995; Zahedi and Jenner, 2003; Dias and Lidon, 2009). Savin and Nicolas (1996) and Santiveri et al. (2002) reported similar relations between grain growth components and grain weight in barley and triticale. Additionally, Tashiro and Wardlaw (1989) observed that the greater tolerance of the rice (a subtropical cereal) grain to high temperature in comparison with wheat (a temperate cereal) was associated with an ability to increase the rate of grain-filling with increasing temperature. These studies reinforce GFR as a critical trait determining grain weight and size under high-temperature conditions. By contrast, a few studies found that grain weight was more closely associated with GFD than GFR under heat stress conditions (Stone and Nicolas, 1995; Shirdelmoghanloo et al., 2016a).

The finding provides an opportunity for breeding programs to enhance heat tolerance by selecting for higher GFRs. It also gives greater validity to studies on isolating biochemical and physiological characteristics within the grain that are sensitive to heat stress, especially as starch accounts for most of the grain's dry matter (∼70%). The time-course of the grain growth is dominated by the kinetics of starch accumulation, with starch reduced proportionately more than protein by heat stress (Bhullar and Jenner, 1985). Many studies suggest that the supply of assimilates to the developing grains is not limiting the production of starch under high temperature in barley (MacLeod and Duffus, 1988; Wallwork et al., 1998) and wheat (Wardlaw et al., 1980; Jenner, 1994; Wardlaw and Wrigley, 1994). Stronger correlations between GFR and grain weight (TGW and SGW) and plumpness (GP and Ret, and also GWi and GLe) than between GFR and mobilised stem WSCs (MWSC and WSCME), and also lack of or even negative correlation between GFR and NAUSC under delayed sown conditions observed in this study may support that notion (**Supplementary Table S7**).

Under heat stress, starch synthesis may be the limiting factor. Wallwork et al. (1998) in barley and Jenner (1994) in

wheat have shown reduced conversion of sucrose to starch in the endosperm under high temperatures. They related the reduction to the heat sensitivity of several enzymes in the starch synthesis pathway, particularly soluble starch synthase (SSS). While there was a general trend for high temperature to increase the average GFR across genotypes (**Figure 2**), some genotypes, however, appeared to show a reduction in GFR in this study (**Supplementary Figure S3**). With several isoforms of SSS identified in wheat endosperm (Denyer et al., 1995), isoforms of SSS may exist in barley, accounting for the observed genotypic variation response to heat stress for GFR. Another heat-tolerance mechanism reported is the recovery of lost enzyme activity following heat relief (Hawker and Jenner, 1993; Wallwork et al., 1998). The transfer of photosynthate from the crease vascular system of the grain into the endosperm could also possibly explain part of the temperature response among wheat genotypes (Wardlaw et al., 1995). A combination of the factors mentioned above may have contributed to the variation in grain growth rate under delayed sowing in this study.

Keeling et al. (1994) and Wallwork et al. (1998) suggest that increased GFR under high temperatures may be associated with increased rates of chemical reactions due to greater kinetic energy of molecules (e.g., enzymes and substrates) and more frequent collisions between them. High temperatures also increase the rate of import of photosynthate into the grain (Wardlaw et al., 1980), which may, at least in part, relate to the enhanced rate of grain-filling under high-temperature conditions.

The most noticeable effect of delayed sowing on grain growth was a premature truncation in grain-filling and is possibly due to the decline in activity of the starch biosynthetic system in barley (Wallwork et al., 1998) and wheat (Jenner, 1986). Alternatively, truncation in the GFD may be partly due to the grain's heat-induced accelerated senescence, limiting its development and ability to convert the delivered sugars into starch (Shirdelmoghanloo et al., 2016a). Furthermore, the earlier TIP and shorter GFD under high temperature may relate to temperature impacts on the expression of genes encoding starch synthesis enzymes and shortening the time to reach the maximum expression levels of the transcripts of the starch biosynthetic enzymes (Hurkman et al., 2003).

Rate and duration of grain-filling were negatively correlated across all environments in this study, with similar observations by Al-Karaki (2012), Bruckner and Frohberg (1987), and Wardlaw and Moncur (1995). The correlation was generally more robust in low-stressed environments compared with environments with a greater degree of heat stress (**Supplementary Table S7**). Environmental and genetic factors resulting in rapid GFR were associated with short GFD and compensation between both variables. Because the correlation between GFR and grain weight/plumpness was much greater than between GFD and grain weight/plumpness, particularly under heat conditions, selection for higher GFR and grain weight/plumpness without lengthening GFD may be plausible. Indeed, a high rate of grain growth over a shorter period of grain-filling (and an earlier inflection point) would be a desirable, risk-reducing pattern of grain-filling in barley in rain-fed environments. Such a breeding strategy has been suggested for other crops, such as wheat (Bruckner and Frohberg, 1987) and maize (Daynard and Kannenberg, 1976), in environments where temperature extremes can shorten the growing season.

Green Leaf Area Duration

Scientific consensus suggests that grain-filling in wheat and barley is not source-limited under favourable growing conditions. Flag and penultimate leaf photosynthesis provide a significant proportion of assimilates to fill the developing grains in barley (Jebbouj and El Yousfi, 2009), but assimilate supply can become a limiting factor under stress (e.g., drought and heat) due to the loss of chlorophyll and, thus, reduced photosynthetic activity (Serrago et al., 2013).

This study used the penultimate leaf NAUSC during grain-filling to measure green leaf area retention (stay-green). Delayed sowing was associated with accelerated chlorophyll loss and reduced NAUSC (**Figure 2**). While the mechanisms of heat-induced chlorophyll loss resulting in a reduction in green leaf area and photosynthetic capacity are unknown, it could be associated with injury to thylakoid membranes that harbour chlorophyll. Harding et al. (1990) concluded that heat stress accelerates thylakoid component breakdown and induces a destabilising imbalance between component reaction rates. Ristic et al. (2007) found strong correlations between heat-induced injuries to thylakoids (and losses of PSII functionality) and chlorophyll loss.

Normalised area under the SPAD decline curve (NAUSC) was positively correlated with grain weight (TGW and SGW) and plumpness (GP and Ret, and also the grain lateral dimensions GWi and GTh) and duration (GFD and TIP) across environments (**Table 3** and **Supplementary Table S7**). NAUSC was also correlated (albeit weakly) HTIs of the physical grain quality parameters in a few environments (**Table 4**). These results suggest that maintaining green leaf area for a more extended period during grain-filling (stay-green) may have contributed to some of the observed genotypic variations for grain weight and plumpness/size, particularly under delayed sown conditions. There are many reports of an association between stay-green, grain weight/size, and yield performance under drought or heat conditions in barley (Emebiri, 2013; Gous et al., 2016), wheat (Reynolds et al., 1994; Kumari et al., 2007; Lopes and Reynolds, 2012; Shirdelmoghanloo et al., 2016a) and sorghum (Borrell et al., 2014a,b). Furthermore, the higher grain weight of durum wheat stay-green mutants was related to the delayed loss of chlorophyll content, more extended photosynthetic competence (Spano et al., 2003), and longer expression of Rubisco activase, SSS, and glycine decarboxylase (Rampino et al., 2006). Further support for the idea that stay-green prolongs photosynthesis and GFD.

It is worth noting that NAUSC was negatively associated with SFNS across environments, indicating that stay-green has a role in higher spike fertility rate, particularly in environments exposed to a greater degree of heat stress (**Supplementary Table S7**).

Stem Water-Soluble Carbohydrate

Water-soluble carbohydrates stored in stems also contribute to grain-filling in barley. Their contribution to final grain dry matter can increase under any stress which inhibits current assimilation,

such as heat and drought (Austin et al., 1980; Blum et al., 1994; Blum, 1998; Ehdaie et al., 2006; Talukder et al., 2013). In this study, delayed sowing reduced stem WSC, which was associated with reduced stem volume (**Figure 2**) and WSCs accumulation (probably due to reduced photosynthesis; data not shown). Delayed sowing also reduced the absolute mobilised stem WSCs, but improved WSC mobilisation efficiency, particularly in 2018. Similar effects under heat or drought stress conditions have been reported in barley (Austin et al., 1980; Méndez et al., 2011) and wheat (Ehdaie et al., 2006; Talukder et al., 2013).

Maximum WSC and MWSC showed few negative correlations with plumpness (GP and Ret) and HTIs (**Tables 3**, **4**). These correlations, however, were in the opposite directions to those expected if those parameters contribute to better physical grain quality performance under heat conditions. There were also few correlations between WSCME and the HTIs (**Table 4**). There was no clear relationship between stem WSCs content or the absolute stem WSCs remobilisation and the physical grain quality performance. However, grain weight (TGW and SGW) and plumpness (GP, Ret, and grain lateral dimensions) showed some positive correlations (weak to moderate) with WSCME (and in line with this negatively correlated with WSCmin) under delayed sown conditions, particularly in 2019. Genotypes with heavier and plumper grain potentials tended to have higher WSCME under heat-stress conditions. Furthermore, MWSC and WSCME showed positive correlations (albeit weak) with grain growth rate (GFR and GFRmax), particularly in delayed sown environments (**Supplementary Table S7**).

The results presented here suggest that stem reserves may not be an advantage unless plants can efficiently mobilise the reserves to the developing grains or convert delivered carbohydrates to starch in the grain (e.g., as a result of heat-stable SSS activity). It also suggests that the mobilised stem reserves may contribute to better physical grain quality performance *per se* through stabilising GFR, particularly under high-temperature conditions.

The Trade-Off Between Grain Weight and Grain Plumpness With Grain Number

Grain number spike^{-1} (GNS) and HL showed a relatively consistent negative correlation with grain weight (TGW and SGW), grain plumpness (GP and Ret; and also grain dimensions) (**Table 3** and **Supplementary Table S7**), and HTIs (**Table 4**). Sadras (2007) reported a similar trade-off between grain number and grain weight as observed in higher temperature conditions in this study. However, neither the physiological and genetic basis underlying this trade-off (Quintero et al., 2018) nor the environmental effect is well-understood.

Removal of florets before grain filling can increase the weight of the remaining grains (Fischer and HellieRisLambers, 1978; Calderini and Reynolds, 2000; Golan et al., 2019). A single amino acid substitution at a putative phosphorylation site in the *VRS1* gene in two-rowed barley *deficiens* mutants severely suppressed lateral florets and promoted grain weight (Sakuma et al., 2017). A recent study demonstrated a 12% improvement in grain weight without a negative effect on grain number due to increased levels of α-expansin in developing wheat grains by the ectopic expression of *TaExpA6* under control of a grain-specific gene promoter (Calderini et al., 2021). Therefore, the trade-off could stem from a growth limitation imposed by competition for an inadequate assimilate source (sink competition) or intrinsic limitations in grain weight potential.

The positive correlations between GNS with WSC content and mobilisation *per se* and for grain weight and plumpness with WSC mobilisation efficiency and stay-green (**Table 3** and **Supplementary Table S7**) support the notion that assimilate supply probably had a role in determining grain weight, plumpness, and number. However, as those correlations were generally weak to moderate, other factors may have been in play, influencing the trade-off.

Quintero et al. (2018) found the trade-off to be very strong in environments with high temperatures and very low in cool favourable growing environments. In this study, the trade-off between GNS and HL with grain weight and plumpness was missing in the coolest growing environment (WH18NS). It was generally stronger in heat-stressed environments, suggesting a similar observation to Quintero et al. (2018). Interestingly, GFR was also negatively correlated with GNS, particularly in 2019 (**Supplementary Table S7**), indicating some compensating variability among the genotypes in both the GNS and GFR. A similar relationship was noted by Egli (2006) and Wu et al. (2018).

Implications for Breeding

The present study identified heat-tolerant genotypes useful for barley breeding programs and identified traits for complementary selection criteria for heat tolerance. Heat tolerance, the physical grain quality potential, and heat escape (early flowering) all appeared to play a role in determining the barley genotypes' physical grain quality (TGW, GP, and Ret) assessed under the delayed sown conditions. However, they differed in their relative contribution, with heat tolerance and physical grain quality potential more important than heat escape. The accelerated development with later sowing may have reduced the contribution of heat escape as a mechanism.

Selection for high grain plumpness under low-stress conditions could enhance the breeding for heat stress tolerance, as genotypes with plump grain were less prone to small grain when exposed to higher temperatures under later sowing. However, the most efficient approach would be concurrent selection for factors affecting physical grain quality under heat stress. Selecting for high GFR, in particular, is likely to improve the future heat tolerance of barley as there was a highly significant positive correlation with physical grain quality parameters under heat stress conditions and with heat tolerance (**Tables 3**, **4**, and **Figures 4**, **5**). There was also strong genetic variation and very high heritability for GFR (**Table 2**).

CONCLUSIONS

Responses to high temperature at the reproductive stage in barley have received less attention than other cereal

crops such as wheat and rice. In this study, physical grain quality and a range of physiological, developmental, and agro-morphological traits were concurrently tested for their responses to natural heat events during reproductive stages of development in a diverse set of barley genotypes. Results presented here demonstrate a considerable heat impact on barley physical grain quality, but with a genetic variation.

Maximum progress in improving the physical quality of barley grain (weight and plumpness/size) in a future warmer climate could be achieved through combining physical grain quality potential, an appropriate developmental cycle (heat scape), and attributes associated with a high positive HTI (heat-tolerance) and physical grain quality *per se* under heat conditions. Generally, genotypes with better grain weight and plumpness performance *per se* and heat-tolerance under high temperatures tended to have high GFR, long grain-filling duration, long green leaf area retention, high WSC mobilisation efficiency, shorter heads with lower grain number, taller stature, smaller leaf size, and greater harvest index. GFR, however, had a significant role in determining barley grain weight and plumpness/size under grain-filling heat-stress conditions.

Additionally, results presented here suggest that stem WSC mobilisation and stay-green may contribute to better physical grain quality performance through their effect in stabilising GFR and duration, respectively. However, the stable GFR correlated with WSC mobilisation might be more influential in determining physical grain quality performance under heat stress conditions than grain-filling duration (and TIP) correlated with stay-green. The assimilates generated through ongoing photosynthesis and carbon losses due to other processes, such as respiration, were not estimated in this study. Further research considering these factors is required to get a better insight into contribution of the stem WSCs to physical grain quality performance/maintenance under heat conditions. The negative relationship between grain number and grain weight/plumpness performance and heat tolerance (and also GFR) suggest some level of compensating variability among the genotypes for these traits, particularly under heat-stress conditions. As heat tolerance and the associated traits presented here are challenging to measure in a breeding program, further work is required to detect genomic regions/genes controlling heat-tolerance traits, particularly GFR, and their use in heat-tolerance breeding through the delivery of validated DNA markers.

The irrigated conditions used in the current study may have favoured the expression of heat-tolerance mechanisms related to transpirational cooling. Furthermore, reductions in grain weight and plumpness/size in response to delayed sowing may stem from the accelerated development caused by exposing the crop to higher average temperature (in the non-stressful range) throughout the growing cycle, and also from an increased incidence of heat events at grain-filling. Transpirational cooling and accelerated development could have influenced the performance of the genotypes under delayed sowing. Therefore, it is essential to test heat-tolerant genotypes using in-field heat chambers when sown under normal rain-fed, not delayed sowing conditions.

DATA AVAILABILITY STATEMENT

The original contributions presented in the study are included in the article and **Supplementary Materials**. Further inquiries can be directed to the corresponding authors.

AUTHOR CONTRIBUTIONS

HS contributed to the project development and study design, conducted the experiments, contributed to the data collection and analysis, interpreted the data, and drafted the manuscript. KC made the experimental designs and undertook the data analysis, wrote the statistical methods section, and contributed to the data interpretation and preparation of the manuscript. BP contributed to the project development, study design, phenotyping, data interpretation, and manuscript preparation. TA conducted preliminary screening work, identified and provided germplasm, and contributed to the project development, study design, and manuscript preparation. SW contributed to the coordination, phenotyping, and preparation of the manuscript. HK and CH contributed to data interpretation and preparation of the manuscript. CL conceived of the study, contributed to its design and coordination, and contributed to data interpretation and preparation of the manuscript. All authors have read and approved the final version of the manuscript.

FUNDING

This project was funded by the Grains Research and Development Corporation (GRDC; project UMU00049), with support from the Western Australian Department of Primary Industries and Regional Development (DPIRD) and Murdoch University.

ACKNOWLEDGMENTS

We thank Shari Dougall, Bruce Thorpe, Tracey Mouritzen, Robert De Gruchy, Julie Roche, David Farleigh, and the staff of DPIRD's Wongan Hills and Northam research facilities for plant care and growth facilities. We are also grateful to Monica Elliott, Amanuel Bekuma, Deborah Barker, Lee-Anne McFawn, Jenifer Bussanich, and Amber Balfour-Cunningham for their contribution to phenotyping. We thank the Western Crop Genetics Alliance (WCGA) for providing barley germplasm used in this study.

SUPPLEMENTARY MATERIAL

The Supplementary Material for this article can be found online at: https://www.frontiersin.org/articles/10.3389/fpls.2022.858652/full#supplementary-material

REFERENCES

Abou-Elwafa, S. F., and Amein, K. A. (2016). Genetic diversity and potential high temperature tolerance in barley (*Hordeum vulgare*). *World J. Agric. Res.* 4, 1–8. doi: 10.12691/wjar-4-1-1

Aiqing, S., Somayanda, I., Sebastian, S. V., Singh, K., Gill, K., Prasad, P. V. V., et al. (2018). Heat stress during flowering affects time of day of flowering, seed set, and grain quality in spring wheat. *Crop Sci.* 58, 380–392. doi: 10.2135/cropsci2017.04.0221

Al-Karaki, G. N. (2012). Phenological development-yield relationships in durum wheat cultivars under late-season high-temperature stress in a semiarid environment. *ISRN Agron.* 2012, 1–7. doi: 10.5402/2012/456856

Alqudah, A. M., and Schnurbusch, T. (2017). Heading date is not flowering time in spring barley. *Front. Plant Sci.* 8, 896. doi: 10.3389/fpls.2017.00896

Asseng, S., Foster, I., and Turner, N. C. (2011). The impact of temperature variability on wheat yields. *Glob. Change Biol.* 17, 997–1012. doi: 10.1111/j.1365-2486.2010.02262.x

Austin, R. B., Morgan, C. L., Ford, M. A., and Blackwell, R. D. (1980). Contributions to grain yield from pre-anthesis assimilation in tall and dwarf barley phenotypes in two contrasting seasons. *Ann. Bot.* 45, 309–319. doi: 10.1093/oxfordjournals.aob.a085826

Bhullar, S. S., and Jenner, C. F. (1985). Differential responses to high temperatures of starch and nitrogen accumulation in the grain of four cultivars of wheat. *Aust. J. Plant Physiol.* 12, 363–375. doi: 10.1071/PP9850363

Bidinger, F. R., Mahalakshmi, V., and Rao, G. D. P. (1987). Assessment of drought resistance in pearl millet [*Pennisetum americanum* (L.) leeke]. II* estimation of genotype response to stress. *Aust. J. Agric. Res.* 38, 49–59. doi: 10.1071/AR9870049

Blum, A. (1998). Improving wheat grain filling under stress by stem reserve mobilisation. *Euphytica* 100, 77–83. doi: 10.1023/A:1018303922482

Blum, A., Sinmena, B., Mayer, J., Golan, G., and Shpiler, L. (1994). Stem reserve mobilisation supports wheat-grain filling under heat stress. *Aust. J. Plant Physiol.* 21, 771–781. doi: 10.1071/PP9940771

Borghi, B., Corbellini, M., Ciaffi, M., Lafiandra, D., De Stefanis, E., Sgrulletta, D., et al. (1995). Effect of heat shock during grain filling on grain quality of bread and durum wheats. *Aust. J. Agric. Res.* 46, 1365–1380. doi: 10.1071/AR9951365

Borrell, A. K., Mullet, J. E., George-Jaeggli, B., Van Oosterom, E. J., Hammer, G. L., Klein, P. E., et al. (2014a). Drought adaptation of stay-green sorghum is associated with canopy development, leaf anatomy, root growth, and water uptake. *J. Exp. Bot.* 65, 6251–6263. doi: 10.1093/jxb/eru232

Borrell, A. K., van Oosterom, E. J., Mullet, J. E., George-Jaeggli, B., Jordan, D. R., Klein, P. E., et al. (2014b). Stay-green alleles individually enhance grain yield in sorghum under drought by modifying canopy development and water uptake patterns. *New Phytol.* 203, 817–830. doi: 10.1111/nph.12869

Bruckner, P. L., and Frohberg, R. C. (1987). Stress tolerance and adaptation in spring wheat1. *Crop Sci.* 27, 31–36. doi: 10.2135/cropsci1987.0011183X002700010008x

Butler, D. G., Cullis, B. R., Gilmour, A. R., Gogel, B. J., and Thompson, R. (2018). *ASReml-R reference manual version 4*. VSN International Ltd, Hemel Hempstead, HPI 1ES, UK. Available online at:http://www.vsni.co.uk/ (accessed December 20, 2021).

Calderini, D. F., Castillo, F. M., Arenas-M, A., Molero, G., Reynolds, M. P., et al. (2021). Overcoming the trade-off between grain weight and number in wheat by the ectopic expression of expansin in developing seeds leads to increased yield potential. *New Phytol.* 230, 629–640. doi: 10.1111/nph.17048

Calderini, D. F., and Reynolds, M. P. (2000). Changes in grain weight as a consequence of de-graining treatments at pre- and post-anthesis in synthetic hexaploid lines of wheat (*Triticum durum* × *T. tauschii). Aust. J. Plant Physiol.* 27, 183–191. doi: 10.1071/PP99066

Chowdhury, S. I., and Wardlaw, I. F. (1978). The effect of temperature on kernel development in cereals. *Aust. J. Agvic. Res.* 29, 205–223. doi: 10.1071/AR9780205

Coombes, N. (2018). *DiGGer: DiGGer design generator under correlation and blocking*. R Package Version 1.0.3. Available online at: http://nswdpibiom.org/austatgen/software (accessed December 20, 2021).

Cossani, C. M., and Reynolds, M. P. (2012). Physiological traits for improving heat tolerance in wheat. *Plant Physiol.* 160, 1710–1718. doi: 10.1104/pp.112.207753

Daynard, T. B., and Kannenberg, L. W. (1976). Relationship between length of actual and effective grain filling periods and the grain yield of corn. *Can. J. Plant Sci.* 56, 237–242. doi: 10.4141/cjps76-038

Denyer, K., Hyiton, C. M., Jenner, C. F., and Smith, A. M. (1995). Identification of multiple isoforms of soluble and granule-bound starch synthase in developing wheat endosperm. *Planta* 196, 256–265. doi: 10.1007/BF00201382

Dias, A. S., and Lidon, F. C. (2009). Evaluation of grain filling rate and duration in bread and durum wheat, under heat stress after anthesis. *J. Agron. Crop Sci.* 195, 137–147. doi: 10.1111/j.1439-037X.2008.00347.x

Egli, D. B. (2006). The role of seed in the determination of yield of grain crops. In *Aust. J. Agric. Res.* 57, 1237–1247. doi: 10.1071/AR06133

Ehdaie, B., Alloush, G. A., Madore, M. A., and Waines, J. G. (2006). Genotypic variation for stem reserves and mobilization in wheat: II. Postanthesis changes in internode water-soluble carbohydrates. *Crop Sci.* 46, 2093–2103. doi: 10.2135/cropsci2006.01.0013

Emebiri, L. C. (2013). QTL dissection of the loss of green colour during post-anthesis grain maturation in two-rowed barley. *Theor. Appl. Genet.* 126, 1873–1884. doi: 10.1007/s00122-013-2102-0

Fischer, R. A., and HellieRisLambers, D. (1978). Effect of environment and cultivar on source limitation to grain weight in wheat. *Aust. J. Agric. Res.* 29, 443–458. doi: 10.1071/AR9780443

Frederiks, T. M., Christopher, J. T., Sutherland, M. W., and Borrell, A. K. (2015). Post-head-emergence frost in wheat and barley: defining the problem, assessing the damage, and identifying resistance. *J. Exp. Bot.* 66, 3487–3498. doi: 10.1093/jxb/erv088

Golan, G., Ayalon, I., Perry, A., Zimran, G., Ade-Ajayi, T., Mosquna, A., et al. (2019). GNI-A1 mediates trade-off between grain number and grain weight in tetraploid wheat. *Theor. Appl. Genet.* 132, 2353–2365. doi: 10.1007/s00122-019-03358-5

Gous, P. W., Hickey, L., Christopher, J. T., Franckowiak, J., and Fox, G. P. (2016). Discovery of QTL for stay-green and heat-stress in barley (*Hordeum vulgare*) grown under simulated abiotic stress conditions. *Euphytica* 207, 305–317. doi: 10.1007/s10681-015-1542-9

Harding, S. A., Guikema, J. A., and Paulsen, G. M. (1990). Photosynthetic decline from high temperature stress during maturation of wheat: I. Interaction with source and sink processes. *Plant Physiol.* 92, 648–653. doi: 10.1104/pp.92.3.648

Hawker, J. S., and Jenner, C. F. (1993). High temperature affects the activity of enzymes in the committed pathway of starch synthesis in developing wheat endosperm. *Aust. J. Plant Physiol.* 20, 197–209. doi: 10.1071/PP9930197

Hays, D. B., Do, J. H., Mason, R. E., Morgan, G., and Finlayson, S. A. (2007). Heat stress induced ethylene production in developing wheat grains induces kernel abortion and increased maturation in a susceptible cultivar. *Plant Sci.* 172, 1113–1123. doi: 10.1016/j.plantsci.2007.03.004

Hurkman, W. J., McCue, K. F., Altenbach, S. B., Korn, A., Tanaka, C. K., Kothari, K. M., et al. (2003). Effect of temperature on expression of genes encoding enzymes for starch biosynthesis in developing wheat endosperm. *Plant Sci.* 164, 873–881. doi: 10.1016/S0168-9452(03)00076-1

Ingvordsen, C. H., Backes, G., Lyngkjær, M. F., Peltonen-Sainio, P., Jensen, J. D., Jalli, M., et al. (2015). Significant decrease in yield under future climate conditions: stability and production of 138 spring barley accessions. *Eur. J. Agron.* 63, 105–113. doi: 10.1016/j.eja.2014.12.003

Jebbouj, R., and El Yousfi, B. (2009). Barley yield losses due to defoliation of upper three leaves either healthy or infected at boot stage by *Pyrenophora teres* f. teres. *Eur. J. Plant Pathol.* 125, 303–315. doi: 10.1007/s10658-009-9483-6

Jenner, C. (1986). "End product storage in cereals," in *Phloem Transport*, eds J. Cronshaw, W. J. Lucas, and R. T. Giaquinta (New York, NY: Alan R. Liss), 561–572.

Jenner, C. F. (1994). Starch synthesis in the kernel of wheat under high temperature conditions. *Aust. J. Plant Physiol.* 21, 791–806. doi: 10.1071/PP9940791

Keeling, P. L., Banisadr, R., Barone, L., Wasserman, B. P., and Singletary, G. W. (1994). Effect of temperature on enzymes in the pathway of starch biosynthesis in developing wheat and maize grain. *Aust. J. Plant Physiol.* 21, 807–827. doi: 10.1071/PP9940807

Kenward, M. G., and Roger, J. H. (1997). Small sample inference for fixed effects from restricted maximum likelihood. *Biometrics* 53, 983–997. doi: 10.2307/2533558

Kumari, M., Singh, V. P., Tripathi, R., and Joshi, A. K. (2007). "Variation for staygreen trait and its association with canopy temperature depression and yield traits under terminal heat stress in wheat," in *Wheat Production in Stressed Environments. Developments in Plant Breeding, Vol 12*, eds H. T. Buck, J. E. Nisi, and N. Salomón (Springer, Dordrecht), 357–363. doi: 10.1007/1-4020-5497-1_44

Li, R., Hou, L., Zhang, A., Lu, Y., Song, W., Tadesse, W., et al. (2018). Heat stress in filling stage confers distinct effect on starch granules formation in different thermotolerant wheat accessions. *Pak. J. Bot.* 50, 913–920. Available online at: http://www.pakbs.org/pjbot/

Lopes, M. S., and Reynolds, M. P. (2012). Stay-green in spring wheat can be determined by spectral reflectance measurements (normalized difference vegetation index) independently from phenology. *J. Exp. Bot.* 63, 3789–3798. doi: 10.1093/jxb/ers071

MacLeod, L. C., and Duffus, C. M. (1988). Reduced starch content and sucrose synthase activity in developing endosperm of barley plants grown at elevated temperatures. *Aust. J. Plant Physiol.* 15, 367–375. doi: 10.1071/PP9880367

Macnicol, P. K., Jacobsen, J. V., Keys, M. M., and Stuart, I. M. (1993). Effects of heat and water stress on malt quality and grain parameters of schooner barley grown in cabinets. *J. Cereal Sci.* 18, 61–68. doi: 10.1006/jcrs.1993.1034

Méndez, A. M., Castillo, D., Del Pozo, A., Matus, I., and Morcuende, R. (2011). Differences in stem soluble carbohydrate contents among recombinant chromosome substitution lines (RCSLs) of barley under drought in a mediterranean-type environment. *Agron. Res.* 9, 433–438. Available online at: https://agronomy.emu.ee/category/volume-09-2011/special-issue-ii-volume-9-2011/ (accessed November 30, 2021).

Motzo, R., Giunta, F., and Deidda, M. (1996). Relationships between grain-filling parameters, fertility, earliness and grain protein of durum wheat in a Mediterranean environment. *Field Crops Res.* 47, 129–142. doi: 10.1016/0378-4290(96)00021-4

Passarella, V. S., Savin, R., and Slafer, G. A. (2008). Are temperature effects on weight and quality of barley grains modified by resource availability? *Aust. J. Agric. Res.*, 59, 510–516. doi: 10.1071/AR06325

Passioura, J. B. (2006). The perils of pot experiments. *Funct. Plant Biol.* 33, 1075–1079. doi: 10.1071/FP06223

Patterson, H., and Thompson, R. (1971). Recovery of inter-block information when block size are unequal. *Biometrika* 58, 545–554. doi: 10.1093/biomet/58.3.545

Quintero, A., Molero, G., Reynolds, M. P., and Calderini, D. F. (2018). Trade-off between grain weight and grain number in wheat depends on GxE interaction: a case study of an elite CIMMYT panel (CIMCOG). *Eur. J. Agron.* 92, 17–29. doi: 10.1016/j.eja.2017.09.007

Rampino, P., Spano, G., Pataleo, S., Mita, G., Napier, J. A., Di Fonzo, N., et al. (2006). Molecular analysis of a durum wheat "stay green" mutant: expression pattern of photosynthesis-related genes. *J. Cereal Sci.* 43, 160–168. doi: 10.1016/j.jcs.2005.07.004

Reynolds, M. P., Balota, M., Delgado, M. I. B., Amani, I., and Fischer, R. A. (1994). Physiological and morphological traits associated with spring wheat yield under hot, irrigated conditions. *Aust. J. Plant Physiol.* 21, 717–730. doi: 10.1071/PP9940717

Ristic, Z., Bukovnik, U., and Prasad, P. V. V. (2007). Correlation between heat stability of thylakoid membranes and loss of chlorophyll in winter wheat under heat stress. *Crop Sci.* 47, 2067–2073. doi: 10.2135/cropsci2006.10.0674

Roemer, T. (1917). Sind die ertragsreichen Sorten ertragssicherer? *Mitteilung Deutsche Landwirtschafts-Gesellschaft* 32, 87–89.

Sadras, V. O. (2007). Evolutionary aspects of the trade-off between seed size and number in crops. *Field Crops Res.* 100, 125–138. doi: 10.1016/j.fcr.2006.07.004

Saini, H. S., and Aspinall, D. (1982). Abnormal sporogenesis in wheat (*Triticum aestivum* L.) induced by short periods of high temperature. *Ann. Bot.* 49, 835–846. doi: 10.1093/oxfordjournals.aob.a086310

Sakata, T., Takahashi, H., Nishiyama, I., and Higashitani, A. (2000). Effects of high temperature on the development of pollen mother cells and microspores in Barley *Hordeum vulgare* L. *J. Plant Res.* 113, 395–402. doi: 10.1007/PL00013947

Sakuma, S., Lundqvist, U., Kakei, Y., Thirulogachandar, V., Suzuki, T., Hori, K., et al. (2017). Extreme suppression of lateral floret development by a single amino acid change in the VRS1 transcription factor. *Plant Physiol.* 175, 1720–1731. doi: 10.1104/pp.17.01149

Santiveri, F., Royo, C., and Romagosa, I. (2002). Patterns of grain filling of spring and winter hexaploid triticales. *Eur. J. Agron.* 16, 219–230. doi: 10.1016/S1161-0301(01)00127-7

Savin, R., and Nicolas, M. E. (1996). Effects of short periods of drought and high temperature on grain growth and starch accumulation of two malting barley cultivars. *Aust. J. Plant Physiol.* 23, 201–210. doi: 10.1071/PP9960201

Serrago, R. A., Alzueta, I., Savin, R., and Slafer, G. A. (2013). Understanding grain yield responses to source-sink ratios during grain filling in wheat and barley under contrasting environments. *Field Crops Res.* 150, 42–51. doi: 10.1016/j.fcr.2013.05.016

Shi, W., Yin, X., Struik, P. C., Xie, F., Schmidt, R. C., and Jagadish, K. S. V. (2016). Grain yield and quality responses of tropical hybrid rice to high night-time temperature. *Field Crops Res.* 190, 18–25. doi: 10.1016/j.fcr.2015.10.006

Shirdelmoghanloo, H., Cozzolino, D., Lohraseb, I., and Collins, N. C. (2016a). Truncation of grain filling in wheat (Triticum aestivum) triggered by brief heat stress during early grain filling: association with senescence responses and reductions in stem reserves. *Funct. Plant Biol.* 43, 919–930. doi: 10.1071/FP15384

Shirdelmoghanloo, H., Lohraseb, I., Rabie, H. S., Brien, C., Parent, B., and Collins, N. C. (2016b). Heat susceptibility of grain filling in wheat (*Triticum aestivum* L.) linked with rapid chlorophyll loss during a 3-day heat treatment. *Acta Physiol. Plant* 38, 208. doi: 10.1007/s11738-016-2208-5

Shirdelmoghanloo, H., Taylor, J. D., Lohraseb, I., Rabie, H., Brien, C., Timmins, A., et al. (2016c). A QTL on the short arm of wheat (*Triticum aestivum* L.) chromosome 3B affects the stability of grain weight in plants exposed to a brief heat shock early in grain filling. *BMC Plant Biol.* 16, 100. doi: 10.1186/s12870-016-0784-6

Sissons, M., Pleming, D., Taylor, J. D., Emebiri, L., and Collins, N. C. (2018). Effects of heat exposure from late sowing on the agronomic and technological quality of tetraploid wheat. *Cereal Chem.* 95, 274–287. doi: 10.1002/cche.10027

Spano, G., Di Fonzo, N., Perrotta, C., Platani, C., Ronga, G., Lawlor, D. W., et al. (2003). Physiological characterization of "stay green" mutants in durum wheat. *J. Exp. Bot.* 54, 1415–1420. doi: 10.1093/jxb/erg150

Stone, P. J., and Nicolas, M. E. (1995). Effect of timing of heat stress during grain filling on two wheat varieties differing in heat tolerance. I. Grain Growth. *Aust. J. Plant Physiol.* 22, 927–934. doi: 10.1071/PP9950927

Talukder, A. S. M. H. M., McDonald, G. K., and Gill, G. S. (2013). Effect of short-term heat stress prior to flowering and at early grain set on the utilization of water-soluble carbohydrate by wheat genotypes. *Field Crops Res.* 147, 1–11. doi: 10.1016/j.fcr.2013.03.013

Tashiro, T., and Wardlaw, I. F. (1989). A comparison of the effect of high temperature on grain development in wheat and rice. *Ann. Bot.* 64, 59–65. doi: 10.1093/oxfordjournals.aob.a087808

Tashiro, T., and Wardlaw, I. F. (1990). The effect of high temperature at different stages of ripening on grain set, grain weight and grain dimensions in the semi-dwarf wheat "Banks." *Ann. Bot.* 65, 51–61. doi: 10.1093/oxfordjournals.aob.a087908

Telfer, P., Edwards, J., Kuchel, H., Reinheimer, J., and Bennett, D. (2013). *Heat Stress Tolerance of Wheat*. 2013 GRDC Research Updates, Adelaide, SA. Available online at: https://grdc.com.au/resources-and-publications/grdc-update-papers/tab-content/grdc-update-papers/2013/02/heat-stress-tolerance-of-wheat (accessed November 30, 2021).

Thistlethwaite, R. J., Tan, D. K. Y., Bokshi, A. I., Ullah, S., and Trethowan, R. M. (2020). A phenotyping strategy for evaluating the high-temperature tolerance of wheat. *Field Crops Res.* 255, 107905. doi: 10.1016/j.fcr.2020.107905

Wallwork, M. A. B., Jenner, C. F., Logue, S. J., and Sedgley, M. (1998). Effect of high temperature during grain-filling on the structure of developing and malted barley grains. *Ann. Bot.* 82, 587–599. doi: 10.1006/anbo.1998.0721

Wang, R. X., Hai, L., Zhang, X. Y., You, G. X., Yan, C. S., and Xiao, S. H. (2009). QTL mapping for grain filling rate and yield-related traits in RILs of the Chinese winter wheat population Heshangmai x Yu8679. *Theor. Appl. Genet.* 118, 313–325. doi: 10.1007/s00122-008-0901-5

Wardlaw, F., Sofield, I., and Cartwright, P. M. (1980). Factors Limiting the rate of dry matter accumulation in the grain of wheat grown at high temperature. *Austral. J. Plant Physiol.* 7, 387–400. doi: 10.1071/PP9800387

Wardlaw, I. F., and Moncur, L. (1995). The responsse of wheat to high temperature following anthesis. I. The rate and duration of kernel filling. *Austral. J. Plant Physiol.* 22, 391–397. doi: 10.1071/PP9950391

Wardlaw, I. F., Moncur, L., and Patrick, J. W. (1995). The response of wheat to high temperature following anthesis. II.* Sucrose accumulation and metabolism by isolated kernels. *Aust. J. Plant Physiol.* 22, 399–407. doi: 10.1071/PP9950399

Wardlaw, I. F., and Wrigley, C. W. (1994). Heat tolerance in temperate cereals: an overview. *Aust. J. Plant Physiol.* 21, 695–703. doi: 10.1071/PP9940695

Watt, C. (2020). *An in-depth interrogation of the genetic control of grain size and response to heat stress in barley (Hordeum vulgare L.)* (PhD Thesis). Murdoch University. Available online at: https://researchrepository.murdoch.edu.au/id/eprint/59276/1/Watt2020.pdf (accessed November 30, 2021).

Wricke, G. (1962). Über eine Methode zur Erfassung der okologischen Streubreite in Feldversuchen. *Z. Pflanzenzuchtg* 47, 92–96.

Wu, X., Tang, Y., Li, C., and Wu, C. (2018). Characterization of the rate and duration of grain filling in wheat in southwestern China. *Plant Prod. Sci.* 21, 358–369. doi: 10.1080/1343943X.2018.1518722

Xie, W., Xiong, W., Pan, J., Ali, T., Cui, Q., Guan, D., et al. (2018). Decreases in global beer supply due to extreme drought and heat. *Nat. Plants* 4, 964–973. doi: 10.1038/s41477-018-0263-1

Yemm, E. W., and Willis, A. J. (1954). The estimation of carbohydrates in plant extracts by anthrone. *Biochem. J.* 57, 508–514. doi: 10.1042/bj0570508

Zadoks, J. C., CHANGt, T. T., Konzak, C. F., and Fryer, J. D. (1974). A decimal code for the growth stages of cereals. *Weed Res.* 14, 415–421. doi: 10.1111/j.1365-3180.1974.tb01084.x

Zahedi, M., and Jenner, C. F. (2003). Analysis of effects in wheat of high temperature on grain filling attributes estimated from mathematical models of grain filling. *J. Agric. Sci.* 141, 203–212. doi: 10.1017/S0021859603003411

Conflict of Interest: The authors declare that the research was conducted in the absence of any commercial or financial relationships that could be construed as a potential conflict of interest.

Publisher's Note: All claims expressed in this article are solely those of the authors and do not necessarily represent those of their affiliated organizations, or those of the publisher, the editors and the reviewers. Any product that may be evaluated in this article, or claim that may be made by its manufacturer, is not guaranteed or endorsed by the publisher.

frontiers | Frontiers in Plant Science

MINI REVIEW
published: 23 May 2022
doi: 10.3389/fpls.2022.916948

Maturation and Assembly of Iron-Sulfur Cluster-Containing Subunits in the Mitochondrial Complex I From Plants

*Alicia López-López[1,2], Olivier Keech[2] and Nicolas Rouhier[1]**

[1] INRAE, IAM, Université de Lorraine, Nancy, France, [2] Department of Plant Physiology, Umeå Plant Science Centre, Umeå University, Umeå, Sweden

In plants, the mitochondrial complex I is the protein complex encompassing the largest number of iron-sulfur (Fe-S) clusters. The whole, membrane-embedded, holo-complex is assembled stepwise from assembly intermediates. The Q and N modules are combined to form a peripheral arm in the matrix, whereas the so-called membrane arm is formed after merging a carbonic anhydrase (CA) module with so-called Pp (proximal) and the Pd (distal) domains. A ferredoxin bridge connects both arms. The eight Fe-S clusters present in the peripheral arm for electron transfer reactions are synthesized *via* a dedicated protein machinery referred to as the iron-sulfur cluster (ISC) machinery. The *de novo* assembly occurs on ISCU scaffold proteins from iron, sulfur and electron delivery proteins. In a second step, the preformed Fe-S clusters are transferred, eventually converted and inserted in recipient apo-proteins. Diverse molecular actors, including a chaperone-cochaperone system, assembly factors among which proteins with LYR motifs, and Fe-S cluster carrier/transfer proteins, have been identified as contributors to the second step. This mini-review highlights the recent progresses in our understanding of how specificity is achieved during the delivery of preformed Fe-S clusters to complex I subunits.

Keywords: complex I, mitochondria, iron-sulfur cluster, maturation factors, assembly factors, plants

OPEN ACCESS

Edited by:
Anna N. Stepanova, North Carolina State University, United States

Reviewed by:
Simone Ciofi Baffoni, University of Florence, Italy
Yan Lu, Western Michigan University, United States

***Correspondence:**
Nicolas Rouhier
Nicolas.Rouhier@univ-lorraine.fr

Specialty section:
This article was submitted to Plant Physiology, a section of the journal Frontiers in Plant Science

Received: *10 April 2022*
Accepted: *04 May 2022*
Published: *23 May 2022*

Citation:
López-López A, Keech O and Rouhier N (2022) Maturation and Assembly of Iron-Sulfur Cluster-Containing Subunits in the Mitochondrial Complex I From Plants. Front. Plant Sci. 13:916948. doi: 10.3389/fpls.2022.916948

INTRODUCTION

Complex I, also defined as NADH-ubiquinone oxidoreductase, is one of the four complexes constituting the mitochondrial electron transport chain. In plants, this enzymatic complex, which catalyzes the NADH-dependent coenzyme Q reduction, is composed of at least 45 subunits including 14 conserved core subunits and additional accessory subunits (Subrahmanian et al., 2016; Meyer et al., 2019; Soufari et al., 2020). As in other organisms, this protein complex adopts a L-shape formed by two main arms (Maldonado et al., 2020). The hydrophobic "membrane arm," which participates in proton pumping, is embedded in the inner membrane, and is composed of so-called Pp (proximal) and the Pd (distal) domains (**Figure 1A**). The hydrophilic "peripheral arm" resides in the mitochondrial matrix but is attached to the membrane arm. It is composed of a N module where NADH oxidation takes place, and a Q module where coenzyme Q reduction occurs. Plants, but not yeast or human, have another spherical matrix-exposed domain attached to the membrane arm, known as the carbonic anhydrase (CA) domain (Fromm et al., 2016; Soufari et al., 2020).

In addition, a protein bridge connects the Q domain of the peripheral arm (B14 subunit) to the membrane arm (ND2 subunit) and CA domain (γCAL2 subunit) (Klusch et al., 2021). This protein bridge is formed by the acyl-carrier protein 2 (mtACP2/SDAP2) and a ferredoxin-like subunit or complex 1 ferredoxin (C1-FDX). Klusch et al. (2021) proposed that this bridge would regulate complex I activity by setting the angle between its two arms, which would be essential to control the different conformational states of complex I (close and open conformations).

MODULAR ASSEMBLY OF COMPLEX I

The assembly of complex I is a stepwise, precisely orchestrated process. Assembly intermediates (CA, Pd, Pp, Q, and N modules) are initially formed, and then assembled to form the whole holocomplex (Ligas et al., 2019). While the principle of stepwise assembly process is conserved among species, the intermediates are not assembled in the same order in plants as in mammals (Meyer et al., 2019). This process requires several assembly factors, i.e., proteins that contribute to the assembly of the different subunits and domains, but are not part of the final active complex. Although a dozen proteins were identified in mammals, only seven of these exist in plants, namely NDUFAF1 to NDUFAF7 (Meyer et al., 2019). Furthermore, whether they have a similar role remains unclear, notably because they were not found associated with complex I subassemblies so far. Noteworthy, while maturation factors, which are required for the assembly and insertion of iron-sulfur (Fe-S) clusters into functional respiratory subunits, are not part of the final complex I, they are usually not included among assembly factors. Hence, to date, there are only two assembly factors characterized in plants, and in *Arabidopsis thaliana* (Arabidopsis) in particular L-galactonolactone dehydrogenase (GLDH) (Schertl et al., 2012; Ligas et al., 2019) and complex I assembly factor 1 (CIAF1) (Wang et al., 2012; Ivanova et al., 2019).

The peripheral arm is assembled from N and Q modules formed independently (**Figure 1B**). The N module is formed at least by four subunits. The 51-kDa and 24-kDa subunits in combination with an unknown assembly factor form an assembly intermediate of 120 kDa, to which B8 and 75-kDa subunits associate. It releases the assembly factor to form an assembly intermediate of 170 kDa. The Q module is formed at least by five different subunits: Nad7, Nad9, and B13 that form an assembly intermediate of 80 kDa to which PSST and TYKY subunits are subsequently incorporated thus forming a 120 kDa intermediate (Zhu et al., 2016). Finally, the N and Q modules merge in a 350 kDa assembly intermediate that corresponds to the peripheral arm (Ligas et al., 2019). Some additional subunits (13-kDa, B14, B14.5a, B17.2) are likely added at one of these steps based on the recent *Brassica oleracea* complex I structure (Soufari et al., 2020). All cofactors ensuring electron transfer reactions, i.e., FMN and eight Fe-S clusters, are bound by five subunits of the peripheral arm.

The assembly of the membrane arm also proceeds stepwise. The CA domain (85 kDa intermediate), containing three of the five CAs present in Arabidopsis, i.e., two CAs and one CA-like (CAL) (Fromm et al., 2016), associates with B14.5b, P2, Nad2, and 20.9-kDa subunits leading to the formation of a 200 kDa intermediate. The following assembly of Nad4L, Nad3, Nad6 subunits and of the GLDH assembly factor results in the formation of a 400 kDa intermediate that forms the Pp module of 450 kDa after addition of B9, B16.6, and Nad1 subunits. Association of the Pp module with the peripheral arm results in the formation of an assembly intermediate of 800 kDa (C1*) (Ligas et al., 2019). Finally, the Pd module, which contains among other P1, AGGG, ESSS, B12, B18, Nad4, and Nad5 subunits, is the last functional submodule assembled with the intermediate of 800 kDa to form the whole complex I of 1,000 kDa. GLDH has been identified within the 400, 450, and 850 kDa subcomplexes, but never in the final complex. In its absence, the whole mature complex I is not detectable, whereas the 200 kDa intermediate accumulates (Schertl et al., 2012; Schimmeyer et al., 2016). It was proposed that the final linkage between the Pp and Pd modules is regulated/prevented by GLDH (Soufari et al., 2020). The function of GLDH as an assembly factor of the membrane arm seems independent of its catalytic role in ascorbate synthesis (Schimmeyer et al., 2016). The following sections detail the current state of knowledge about Fe-S cluster synthesis in mitochondria and their insertion into complex I subunits.

IRON-SULFUR CLUSTER ASSEMBLY AND TRANSFER IN PLANT MITOCHONDRIA

The maturation of mitochondrial Fe-S proteins relies on the iron-sulfur cluster (ISC) machinery and is divided in two basic steps, i.e., Fe-S cluster assembly and transfer (Przybyla-Toscano et al., 2021b).

De novo Assembly of Iron-Sulfur Clusters

The NFS1 cysteine desulfurase is the sulfur donor protein catalyzing cysteine desulfurization. It forms a core complex with ISD11 and acyl-carrier protein (ACP) with the following stoichiometry $[NFS1]_2$:$[ISD11]_2$:$[ACP]_2$ (Boniecki et al., 2017). ISD11 stabilizes NFS1 and contains a conserved Leu-Tyr-Arg motif, which is present in members of the small, eukaryote-specific LYRM protein family (Adam et al., 2006; Wiedemann et al., 2006). ACP interacts with ISD11 through a covalently bound 4′-phosphopantetheine-conjugated acyl chain, further stabilizing the assembly complex. In addition to being essential for Fe-S cluster assembly, ACP provides fatty acid precursors necessary for lipoic acid biosynthesis. In Arabidopsis, there are three mitochondrial ACPs known as mACP1, mACP2, and mACP3 but their respective contribution and interchangeable nature remain unclear (Meyer et al., 2007; Fu et al., 2020).

In the NFS1 reaction mechanism, a conserved Cys becomes persulfidated, and the sulfur atoms are transferred to the ISU/ISCU scaffold protein to be combined with iron atoms to form the Fe-S clusters. Three ISU proteins are present in Arabidopsis and possess the three conserved cysteinyl residues

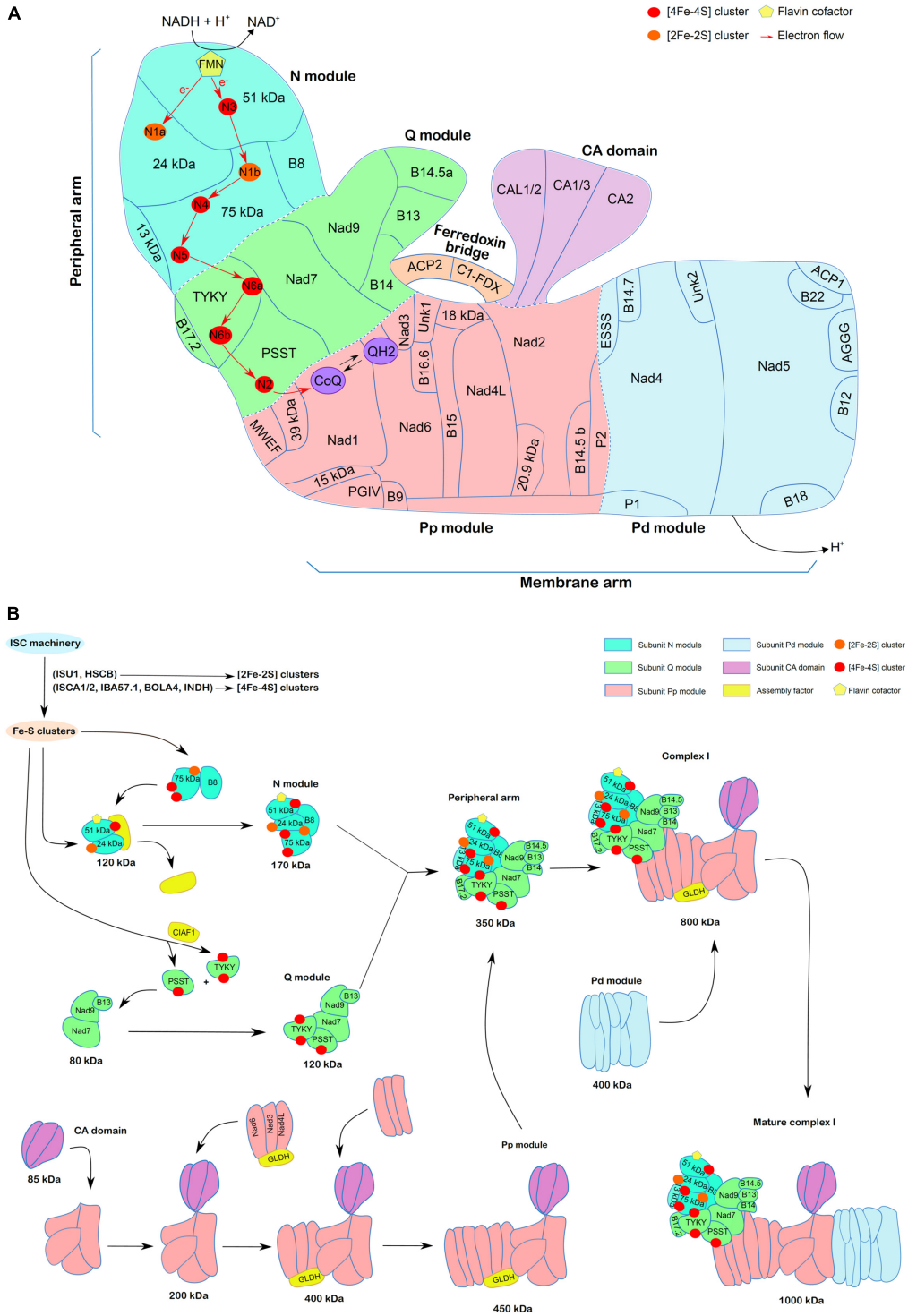

FIGURE 1 | Complex I structure and assembly in plants. **(A)** Schematic representation of complex I structure based on the 3D structure of *Brassica oleracea* complex I (Soufari et al., 2020), including the ferredoxin bridge described in Klusch et al. (2021). Arabidopsis nomenclature is used for the 46 subunits shown here. The CA domain, ferredoxin bridge, modules of the peripheral arm (N and Q modules) and of the membrane arm (Pp and Pd modules) have been represented in different colors. The electron flow from FMN to coenzyme Q *via* the 7 Fe-S clusters present in the different subunits of the peripheral arm is shown. **(B)** Model of the assembly steps of complex I. The figure is adapted from Ligas et al. (2019). Emphasis is made on Fe-S cluster-containing subunits present in the N and Q modules of the peripheral arm. It is thought that they are assembled prior to their insertion in larger subassemblies. Both [2Fe-2S] clusters (orange) and [4Fe-4S] clusters (red) are synthesized *via* the mitochondrial ISC machinery but HSCB and ISCU1/3 scaffold proteins may be sufficient for [2Fe-2S] clusters whereas additional maturation

(Continued)

FIGURE 1 | factors such as ISCA1/2, IBA57.1, BOLA4, or INDH and assembly factor (CIAF1) are required at least for some [4Fe-4S] clusters. The N and Q modules, including the Fe-S containing subunits, assemble in parallel following a two-step process forming complexes of 170 and 120 kDa, respectively, and which associate with a few additional subunits in a larger complex of 350 kDa, forming the peripheral arm. In an independent manner, the CA domain (85 kDa) is integrated in a 200 kDa intermediate containing early inserted subunits of the membrane arm. Two further steps are needed to obtain the Pp module of 450 kDa. The L-galactonolactone dehydrogenase (GLDH) assembly factor is present at these steps. The Pp module is then assembled with the 350 kDa to form a 800 kDa complex to which the Pd module is associated to form the mature complex I of 1 MDa. The recently identified ferredoxin bridge is not represented here, but it is likely assembled lately.

required for Fe-S cluster binding (Léon et al., 2005). While their respective biochemical and structural properties have not yet been compared, expression data indicate that ISU1 is predominant, being constitutively expressed unlike AtISU2 and AtISU3, whose expression seems restricted to pollen (Przybyla-Toscano et al., 2021b). Using mammalian proteins, it was shown that iron binding to ISCU2 drives persulfide uptake from NFS1 before persulfide reduction by FDX2 occurs (Webert et al., 2014; Gervason et al., 2019). Two mitochondrial ferredoxins (MFDX1/2) exist in Arabidopsis, and their redox-active [2Fe-2S] cluster is reduced by a NADPH-dependent mitochondrial ferredoxin reductase (mFDR). Frataxin (FH) is the final key player in this assembly process. It stabilizes NFS1 loops present at the NFS1-ISCU2 interface (Fox et al., 2019), thus accelerating persulfide transfer from NFS1 to ISCU2 (Gervason et al., 2019).

Transfer of Preformed Iron-Sulfur Clusters to Acceptor Proteins

A chaperone-cochaperone system is required to transfer the preformed [2Fe-2S] cluster bound to ISCU/ISU scaffold proteins either directly to apoproteins (notably respiratory complex subunits) or to other maturation factors. ISCU interacts both with the heat shock protein 70 (HSP70)-type chaperones known as HSCA1/2 in plants (HSPA9 in human) and with the HSP40-type cochaperone HSCB in plants (HSC20 in human) that stimulates the ATPase activity of HSCAs. ATP reloading is performed by MGE1a/b nucleotide exchange factors. HSCB is a key factor recruiting either acceptor proteins or adaptor proteins with a LYR motif (see below) (Maio et al., 2014, 2017).

Based on the yeast model for the ISC machinery, the first receiving maturation factor is glutaredoxinS15 (GRXS15) (Przybyla-Toscano et al., 2021b). Recruitment of GRXS15 by HSCB may rely on a positively charged motif present at the C-terminus of mitochondrial GRXs, but the identified $KKX_{10}KK$ in human GRX5 is not conserved as such in plant isoforms, which have more dispersed K residues (Maio et al., 2014). GRXS15 binds a [2Fe-2S] cluster into a homodimer, and transfers it to acceptor proteins such as mFDX1 (Moseler et al., 2015; Azam et al., 2020b). As shown for non-plant proteins (Uzarska et al., 2016), GRXS15 should also bind a [2Fe-2S] cluster in heterodimer with BOLA proteins. A GRXS15-BOLA4 interaction was reported both by yeast-two-hybrid experiments and *in planta* by bimolecular fluorescence complementation assays (Couturier et al., 2014).

Finally, GRXS15 also promotes the formation of [4Fe-4S] clusters onto A-type carrier (ATC) maturation factors referred to as ISCA1a/b and ISCA2 in plants (Azam et al., 2020b). This step consists in the reductive coupling of two [2Fe-2S] clusters into one [4Fe-4S] cluster (Brancaccio et al., 2014; Azam et al., 2020b). In human, the electrons needed for this reaction are brought by FDX2 while another protein named IBA57 assists electron entry into the system (Weiler et al., 2020). IBA57 may also have a role in the Fe-S cluster transfer reaction since a heterodimeric complex formed by human IBA57 and ISCA2 bridges a [2Fe-2S] cluster (Gourdoupis et al., 2018). Further exchange of the [4Fe-4S] cluster bound by ISCA1a/2 heterodimer with other maturation factors named NFU4/5 likely provides specificity toward the numerous recipient mitochondrial Fe-S proteins (Azam et al., 2020a). The observed lethality of *grxs15*, *iba57.1*, and *nfu4 nfu5* Arabidopsis mutant lines demonstrates the critical nature of this pathway for mitochondrial metabolism (Waller et al., 2012; Moseler et al., 2015; Przybyla-Toscano et al., 2022). A complex I-specific maturation factor, INDH, comes into play (discussed below) but its relationship with other ISC maturation factors is unknown.

MATURATION OF IRON-SULFUR CLUSTER-CONTAINING SUBUNITS PRESENT IN THE N AND Q MODULES

In complex I, eight Fe-S clusters are bound by five subunits localized in the peripheral arm (**Figure 1**). In the N module, the 24-kDa subunit binds one [2Fe-2S] cluster, the 51-kDa subunit one [4Fe-4S] cluster and the 75-kDa subunit one [2Fe-2S] cluster and two [4Fe-4S] clusters. In the Q module, PSST binds one [4Fe-4S] cluster and TYKY two [4Fe-4S] clusters (Maldonado et al., 2020). The exact players, mechanisms and specificities by which the different Fe-S clusters are inserted into apoproteins by the ISC machinery only emerged recently.

The Presence of LYR Motifs in Assembly Factors or Acceptor Proteins Seems to Guide the Insertion of Iron-Sulfur Clusters in Complex I Subunits

In a study performed in human, it was demonstrated that the HSCB cochaperone co-immunoprecipitates all complex I subunits (Maio et al., 2017). Moreover, it was shown that HSCB makes interactions with proteins containing a LYR motif, either present in Fe-S cluster-containing subunits themselves such as SDHB from complex II or in LYRM proteins (Maio et al., 2014, 2017). By recruiting these proteins, HSCB allows substrate discrimination by assisting the guide delivery of nascent [2Fe-2S] clusters bound to the ISCU scaffold to specific subsets of Fe-S recipients. Accordingly, the activity of complex I, and of complexes II and III, is systematically affected in human patients with mutations in the ISCU2, frataxin, ISD11/LYRM4,

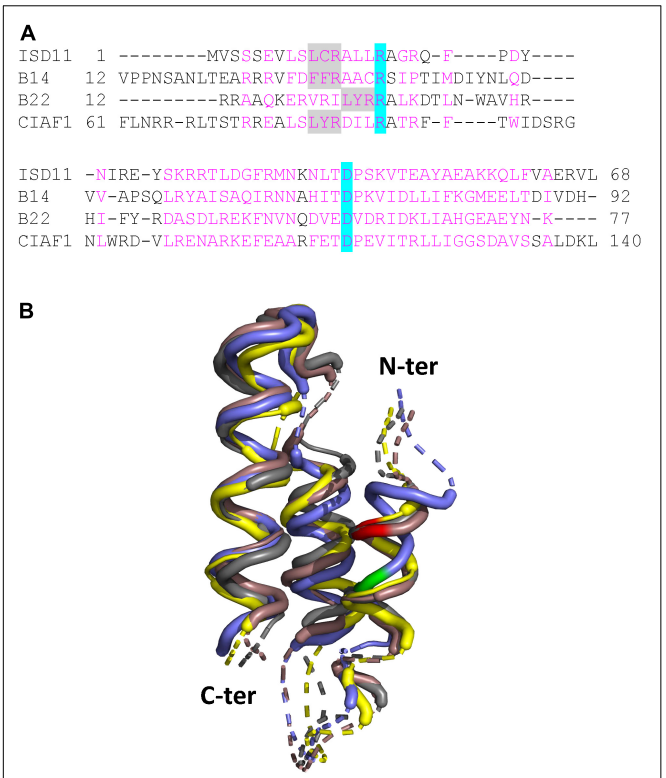

FIGURE 2 | LYRM proteins associated with complex I in plants.
(A) Structure-based sequence alignment. The alignment was generated with mTM-align (Dong et al., 2018) and manually adjusted to focus on the LYRM common core regions (amino acids are numbered on both sides). We used the structures of the B14 and B22 subunits present in the *Brassica oleracea* complex I cryo-EM structure (Soufari et al., 2020) and structural models of Arabidopsis ISD11 and CIAF1 generated by alphafold (Jumper et al., 2021). Amino acids in magenta correspond to common core regions. The only two conserved residues are highlighted in blue; the LYR motif in gray. Noteworthy, in the B14 protein the FFR motif is degenerated, and the conserved Arginine (R) is not even present in some algal sequences. **(B)** 3D structure superimposition of the core helices. The superimposed structure file in common core regions generated by mTM-align was visualized with Pymol. The ISD11, B14, CIAF1, and B22 proteins are represented in brown, yellow, gray and violet, respectively. Dashed lines represent variable spacing regions. The LYR motif in ISD11, B14, CIAF1 is colored in red, whereas for the B22 protein it is in green and shifted by one helix turn.

and FDX2 genes (Selvanathan and Parayil Sankaran, 2022). In studies focusing on complexes II and III, it was shown that Fe-S cluster insertion into target proteins (SDHB or Rieske protein of complex III) is mandatory for the formation of larger complexes (Maio et al., 2014, 2017). This suggests that cluster-free subunits should not assemble into the subcomplexes, and that Fe-S cluster insertion into apo-subunits should not occur in proteins engaged in multipartite protein complex.

In Arabidopsis, the LYRM protein family consists of 10 members (Ivanova et al., 2019). This includes ISD11 and two complex I subunits (B14 and B22). Although their primary sequences are very divergent, they adopt a similar core 3D structure formed by three α-helices (**Figure 2**) and all interact with ACPs (Angerer, 2013). The rest supposedly represents assembly factors for mitochondrial complexes (Maio et al., 2014, 2017; Ivanova et al., 2019). A recent study highlighted a possible role of the LYRM, plant-specific CIAF1 assembly factor for Fe-S cluster maturation of TYKY. A specific interaction of CIAF1 with TYKY was observed using yeast-two-hybrid assays (Ivanova et al., 2019). Moreover, a 650 kDa intermediate representing the fully assembled membrane arm accumulates in Arabidopsis *ciaf1* knock-down mutants as in mutants for the 24-kDa, 51-kDa, 75-kDa, and PSST subunits (Ivanova et al., 2019; Ligas et al., 2019). All these mutants do not assemble the whole complex I or the supercomplex I + III (Ivanova et al., 2019; Ligas et al., 2019). Arabidopsis *ciaf1* mutants accumulate also 800 kDa intermediates. Therefore, it is possible that, in this case, cluster-free subunits assemble into larger subcomplexes. Alternatively, the remaining CIAF1 protein allows to some extent Fe-S cluster insertion in TYKY, or TYKY maturation also occurs without CIAF1. Interestingly, plant TYKYs possess a strictly conserved LYR motif at the C-terminus that might be sufficient for Fe-S cluster insertion. The 75-kDa subunits from plants also contain a conserved, internal VYR motif unlike the three remaining Fe-S cluster binding subunits.

Additional Candidate Maturation Factors for the Formation and Insertion of [4Fe-4S] Clusters

Since most Fe-S clusters in complex I are of the [4Fe-4S]-type, the question arises whether the reductive coupling of two [2Fe-2S] clusters donated by ISCU operates despite the existence of several specific maturation factors (ISCA, IBA57, BOLA, NFU4/5, and INDH protein families), which are relevant for direct [4Fe-4S] cluster insertion. This possibility is reinforced by the observation that ISCA1, IBA57, and NFU1 co-immunoprecipitates with HSCB in human (Maio et al., 2017). Moreover, while the [2Fe-2S] containing NDUFV2 (24-kDa ortholog) interacted with HSC20/HSCB, HSPA9/HSCA, and ISCU in a single complex, NDUFS8 (TYKY ortholog) and NDUFS1 were found in higher molecular weight complexes (Maio et al., 2017), possibly including some [4Fe-4S] transfer proteins.

Additional evidence for the contribution of these late-acting maturation factors come from the biochemical phenotypes of human patients or Arabidopsis mutated lines. In human, mutations in *NFU1*, *BOLA3*, *IBA57*, *ISCA2*, and *ISCA1* genes lead to Multiple Mitochondrial Dysfunctions Syndromes 1 to 5 (MMDS1 to MMDS5) respectively (Selvanathan and Parayil Sankaran, 2022). For *BOLA*3, *IBA*57, and *ISCA*1, gene depletion in human cell lines or mutations in human patients consistently lead to defects in complex I assembly/activity, in complex II activity and in enzymes that depend on lipoic acid, the synthesis of which requires the [4Fe-4S]-containing lipoate synthase (Sheftel et al., 2012; Haack et al., 2013; Debray et al., 2015; Torraco et al., 2018). Although the corresponding Arabidopsis mutants have not been investigated, defects associated with defaults in Fe-S cluster assembly and trafficking in Δ*bol1-3*, Δ*iba57*, and Δ*isca1/2* yeast mutants were functionally complemented with Arabidopsis BOLA, IBA57, and ISCA proteins (Uzarska et al., 2018), suggesting that the corresponding plant proteins

contribute to the assembly of an holo-complex I (absent in *Saccharomyces cerevisiae*). Concerning NFU1, contrasting results have been obtained since a complex I activity decrease to ∼30% was noticed in some patients (Cameron et al., 2011), but not reported in another study (Navarro-Sastre et al., 2011). In both cases, lipoic acid-dependent enzymes were affected. Accordingly, protein lipoylation was defective in Arabidopsis *nfu4 nfu5* lines unlike complex I activity (Przybyla-Toscano et al., 2022), likely excluding a role of NFUs for complex I assembly.

So far, INDH protein, also referred to as Ind1 or NUBPL in human, is the sole Fe-S cluster maturation factor specifically associated with complex I assembly. The IND1/INDH/NUBPL proteins belong to a subfamily of P-loop NTPases. *In vitro* reconstitution assays using *Yarrowia lipolytica* Ind1 and human IND1/NUBPL showed that they bind a [4Fe-4S] cluster using a conserved CxxC motif at the C-terminus (Bych et al., 2008; Sheftel et al., 2009). Genetic studies, either performed in HeLa cells by RNAi, with a *Y. lipolytica* deletion mutant or with Arabidopsis T-DNA insertion lines, evidenced a strong decrease in complex I protein and activity levels, and an accumulation of subcomplexes representing part or the totality of the membrane arm (Bych et al., 2008; Sheftel et al., 2009; Wydro et al., 2013), corroborating results in human patients presenting *IND1* mutations (Friederich et al., 2020). Importantly, the functional complementation of the *Y. lipolytica* deletion mutant by *Y. lipolytica* Ind1 variants recapitulating mutations found in human patients pointed to the accumulation of the Q module intermediate (Maclean et al., 2018). Overall, this indicates that INDH may be responsible for the delivery of [4Fe-4S] clusters to at least one subunit of the matrix arm. Analysis of the Arabidopsis *indh* mutant phenotypes also showed a translational defect affecting the matrix arm subunit Nad9, which suggests a role for INDH in mitochondrial translation as well (Wydro et al., 2013). Therefore, additional work is needed to clarify the exact role of INDH during complex I assembly.

CONCLUSION

There are about 40 Fe-S proteins in Arabidopsis mitochondria present either in respiratory complexes or in the matrix (Przybyla-Toscano et al., 2021a). Only two types of proteins (ISU and GRXS15) should be involved in the maturation of [2Fe-2S] clusters and four types of proteins or protein couples (NFU, GRXS15/BOLA, ISCA/IBA57, INDH) in the maturation of [4Fe-4S] clusters. This indicates that these proteins likely contribute to the maturation of multiple acceptor proteins, but how specificity is achieved remains largely uncharacterized. For proteins integrated into larger complexes, it seems that Fe-S cluster insertion occurs in apo-proteins prior to their incorporation in complexes. Recent studies highlighted that complexes I–III share a common molecular mechanism at least for [2Fe-2S] cluster insertion. The current view is that the HSCB cochaperone recruits LYRM-bound target proteins for [2Fe-2S] cluster insertion by ISU proteins as exemplified by the requirement of LYRM7 for the Rieske subunit of complex III or of SDHAF1/SDHAF3 for complex II (Maio et al., 2017). The presence of additional LYR motif(s) in target proteins themselves likely participate in protein recognition as shown for complex II SDHB subunit (Maio et al., 2014). The maturation of [4Fe-4S] containing proteins is less clear but it should also require LYRM proteins and additional factors such as the complex I specific IND1/INDH maturation factors. The first example in plants is CIAF1 that may recruit TYKY for [4Fe-4S] cluster insertion by a yet unknown ISC maturation factor (Ivanova et al., 2019). In conclusion, the complete set of assembly and maturation factors required as well as the molecular mechanisms supporting the insertion of the different types of Fe-S clusters present in the peripheral arm remain largely elusive. In particular, biochemical and structural data are urgently needed to obtain direct evidence of (i) whether additional LYR-M proteins, either uncharacterized or yet unidentified, are necessary, (ii) which maturation factors are required for the insertion of the [4Fe-4S] clusters, and more generally (ii) how interactions between LYRM, maturation factors and acceptor proteins occur.

AUTHOR CONTRIBUTIONS

All authors have read and approved the manuscript.

FUNDING

The UMR 1136 was supported by the Agence Nationale de la Recherche as part of the "Investissements d'Avenir" program (ANR-11-LABX-0002-01, Lab of Excellence ARBRE). The Ph.D. salary of AL-L was provided by a funding from the Lorraine University of Excellence (LUE). OK was supported by an SSF grant (FFF20-008). UPSC was supported by grants from the Knut and Alice Wallenberg Foundation (KAW 2016.0341 and 2016.0352) and the Swedish Governmental Agency for Innovation Systems (VINNOVA; 2016-00504).

ACKNOWLEDGMENTS

We are grateful to Claude Didierjean for his help with 3D structure modeling.

REFERENCES

Adam, A. C., Bornhövd, C., Prokisch, H., Neupert, W., and Hell, K. (2006). The Nfs1 interacting protein Isd11 has an essential role in Fe/S cluster biogenesis in mitochondria. *EMBO J.* 25, 174–183. doi: 10.1038/sj.emboj.7600905

Angerer, H. (2013). The superfamily of mitochondrial Complex1_LYR motif-containing (LYRM) proteins. *Biochem. Soc. Trans.* 41, 1335–1341. doi: 10.1042/BST20130116

Azam, T., Przybyla-Toscano, J., Vignols, F., Couturier, J., Rouhier, N., and Johnson, M. K. (2020b). The *Arabidopsis* mitochondrial glutaredoxin GRXS15 Provides

[2Fe-2S] clusters for ISCA-Mediated [4Fe-4S] cluster maturation. *Int. J. Mol. Sci.* 21:E9237. doi: 10.3390/ijms21239237

Azam, T., Przybyla-Toscano, J., Vignols, F., Couturier, J., Rouhier, N., and Johnson, M. K. (2020a). [4Fe-4S] cluster trafficking mediated by *Arabidopsis* mitochondrial ISCA and NFU proteins. *J. Biol. Chem.* 295, 18367–18378. doi: 10.1074/jbc.RA120.015726

Boniecki, M. T., Freibert, S. A., Mühlenhoff, U., Lill, R., and Cygler, M. (2017). Structure and functional dynamics of the mitochondrial Fe/S cluster synthesis complex. *Nat. Commun.* 8:1287. doi: 10.1038/s41467-017-01497-1

Brancaccio, D., Gallo, A., Mikolajczyk, M., Zovo, K., Palumaa, P., Novellino, E., et al. (2014). Formation of [4Fe-4S] clusters in the mitochondrial iron-sulfur cluster assembly machinery. *J. Am. Chem. Soc.* 136, 16240–16250. doi: 10.1021/ja507822j

Bych, K., Kerscher, S., Netz, D. J. A., Pierik, A. J., Zwicker, K., Huynen, M. A., et al. (2008). The iron-sulphur protein Ind1 is required for effective complex I assembly. *EMBO J.* 27, 1736–1746. doi: 10.1038/emboj.2008.98

Cameron, J. M., Janer, A., Levandovskiy, V., Mackay, N., Rouault, T. A., Tong, W.-H., et al. (2011). Mutations in iron-sulfur cluster scaffold genes NFU1 and BOLA3 cause a fatal deficiency of multiple respiratory chain and 2-oxoacid dehydrogenase enzymes. *Am. J. Hum. Genet.* 89, 486–495. doi: 10.1016/j.ajhg.2011.08.011

Couturier, J., Wu, H.-C., Dhalleine, T., Pégeot, H., Sudre, D., Gualberto, J. M., et al. (2014). Monothiol glutaredoxin-BolA interactions: redox control of *Arabidopsis thaliana* BolA2 and SufE1. *Mol. Plant* 7, 187–205. doi: 10.1093/mp/sst156

Debray, F.-G., Stümpfig, C., Vanlander, A. V., Dideberg, V., Josse, C., Caberg, J.-H., et al. (2015). Mutation of the iron-sulfur cluster assembly gene IBA57 causes fatal infantile leukodystrophy. *J. Inherit. Metab. Dis.* 38, 1147–1153. doi: 10.1007/s10545-015-9857-1

Dong, R., Pan, S., Peng, Z., Zhang, Y., and Yang, J. (2018). mTM-align: a server for fast protein structure database search and multiple protein structure alignment. *Nucleic Acids Res.* 46, W380-W386. doi: 10.1093/nar/gky430

Fox, N. G., Yu, X., Feng, X., Bailey, H. J., Martelli, A., Nabhan, J. F., et al. (2019). Structure of the human frataxin-bound iron-sulfur cluster assembly complex provides insight into its activation mechanism. *Nat. Commun.* 10:2210. doi: 10.1038/s41467-019-09989-y

Friederich, M. W., Perez, F. A., Knight, K. M., Van Hove, R. A., Yang, S. P., Saneto, R. P., et al. (2020). Pathogenic variants in NUBPL result in failure to assemble the matrix arm of complex I and cause a complex leukoencephalopathy with thalamic involvement. *Mol. Genet Metab.* 129, 236–242. doi: 10.1016/j.ymgme.2019.12.013

Fromm, S., Braun, H.-P., and Peterhansel, C. (2016). Mitochondrial gamma carbonic anhydrases are required for complex I assembly and plant reproductive development. *New Phytol.* 211, 194–207. doi: 10.1111/nph.13886

Fu, X., Guan, X., Garlock, R., and Nikolau, B. J. (2020). Mitochondrial fatty acid synthase utilizes multiple acyl carrier protein isoforms. *Plant Physiol.* 183, 547–557. doi: 10.1104/pp.19.01468

Gervason, S., Larkem, D., Mansour, A. B., Botzanowski, T., Müller, C. S., Pecqueur, L., et al. (2019). Physiologically relevant reconstitution of iron-sulfur cluster biosynthesis uncovers persulfide-processing functions of ferredoxin-2 and frataxin. *Nat. Commun.* 10:3566. doi: 10.1038/s41467-019-11470-9

Gourdoupis, S., Nasta, V., Calderone, V., Ciofi-Baffoni, S., and Banci, L. (2018). IBA57 Recruits ISCA2 to Form a [2Fe-2S] cluster-mediated complex. *J. Am. Chem. Soc.* 140, 14401–14412. doi: 10.1021/jacs.8b09061

Haack, T. B., Rolinski, B., Haberberger, B., Zimmermann, F., Schum, J., Strecker, V., et al. (2013). Homozygous missense mutation in BOLA3 causes multiple mitochondrial dysfunctions syndrome in two siblings. *J. Inherit. Metab. Dis.* 36, 55–62. doi: 10.1007/s10545-012-9489-7

Ivanova, A., Gill-Hille, M., Huang, S., Branca, R. M., Kmiec, B., Teixeira, P. F., et al. (2019). A mitochondrial LYR protein is required for complex I assembly. *Plant Physiol.* 181, 1632–1650. doi: 10.1104/pp.19.00822

Jumper, J., Evans, R., Pritzel, A., Green, T., Figurnov, M., Ronneberger, O., et al. (2021). Highly accurate protein structure prediction with AlphaFold. Nature 596, 583–589. doi: 10.1038/s41586-021-03819-2

Klusch, N., Senkler, J., Yildiz, Ö, Kühlbrandt, W., and Braun, H.-P. (2021). A ferredoxin bridge connects the two arms of plant mitochondrial complex I. *Plant Cell* 33, 2072–2091. doi: 10.1093/plcell/koab092

Léon, S., Touraine, B., Briat, J.-F., and Lobréaux, S. (2005). Mitochondrial localization of *Arabidopsis thaliana* Isu Fe-S scaffold proteins. *FEBS Lett.* 579, 1930–1934. doi: 10.1016/j.febslet.2005.02.038

Ligas, J., Pineau, E., Bock, R., Huynen, M. A., and Meyer, E. H. (2019). The assembly pathway of complex I in *Arabidopsis thaliana*. *Plant J.* 97, 447–459. doi: 10.1111/tpj.14133

Maclean, A. E., Hertle, A. P., Ligas, J., Bock, R., Balk, J., and Meyer, E. H. (2018). Absence of complex i is associated with diminished respiratory chain function in european mistletoe. *Curr. Biol.* 28, 1614.e–1619.e. doi: 10.1016/j.cub.2018.03.036

Maio, N., Kim, K. S., Singh, A., and Rouault, T. A. (2017). A single adaptable cochaperone-scaffold complex delivers nascent iron-sulfur clusters to mammalian respiratory chain complexes I-III. *Cell Metab.* 25, 945.e–953.e. doi: 10.1016/j.cmet.2017.03.010

Maio, N., Singh, A., Uhrigshardt, H., Saxena, N., Tong, W.-H., and Rouault, T. A. (2014). Cochaperone binding to LYR motifs confers specificity of iron sulfur cluster delivery. *Cell Metab.* 19, 445–457. doi: 10.1016/j.cmet.2014.01.015

Maldonado, M., Padavannil, A., Zhou, L., Guo, F., and Letts, J. A. (2020). Atomic structure of a mitochondrial complex I intermediate from vascular plants. *Elife* 9:e56664. doi: 10.7554/eLife.56664

Meyer, E. H., Heazlewood, J. L., and Millar, A. H. (2007). Mitochondrial acyl carrier proteins in *Arabidopsis thaliana* are predominantly soluble matrix proteins and none can be confirmed as subunits of respiratory Complex I. *Plant Mol. Biol.* 64, 319–327. doi: 10.1007/s11103-007-9156-9

Meyer, E. H., Welchen, E., and Carrie, C. (2019). Assembly of the complexes of the oxidative phosphorylation system in land plant mitochondria. *Annu. Rev. Plant Biol.* 70, 23–50. doi: 10.1146/annurev-arplant-050718-100412

Moseler, A., Aller, I., Wagner, S., Nietzel, T., Przybyla-Toscano, J., Mühlenhoff, U., et al. (2015). The mitochondrial monothiol glutaredoxin S15 is essential for iron-sulfur protein maturation in *Arabidopsis thaliana*. *Proc. Natl. Acad. Sci. U.S.A.* 112, 13735–13740. doi: 10.1073/pnas.1510835112

Navarro-Sastre, A., Tort, F., Stehling, O., Uzarska, M. A., Arranz, J. A., Del Toro, M., et al. (2011). A fatal mitochondrial disease is associated with defective NFU1 function in the maturation of a subset of mitochondrial Fe-S proteins. *Am. J. Hum. Genet.* 89, 656–667. doi: 10.1016/j.ajhg.2011.10.005

Przybyla-Toscano, J., Boussardon, C., Law, S. R., Rouhier, N., and Keech, O. (2021a). Gene atlas of iron-containing proteins in *Arabidopsis thaliana*. *Plant J.* 106, 258–274. doi: 10.1111/tpj.15154

Przybyla-Toscano, J., Christ, L., Keech, O., and Rouhier, N. (2021b). Iron-sulfur proteins in plant mitochondria: roles and maturation. *J. Exp. Bot.* 72, 2014–2044. doi: 10.1093/jxb/eraa578

Przybyla-Toscano, J., Maclean, A. E., Franceschetti, M., Liebsch, D., Vignols, F., Keech, O., et al. (2022). Protein lipoylation in mitochondria requires Fe-S cluster assembly factors NFU4 and NFU5. *Plant Physiol.* 188, 997–1013. doi: 10.1093/plphys/kiab501

Schertl, P., Sunderhaus, S., Klodmann, J., Grozeff, G. E. G., Bartoli, C. G., and Braun, H.-P. (2012). L-galactono-1,4-lactone dehydrogenase (GLDH) forms part of three subcomplexes of mitochondrial complex I in *Arabidopsis thaliana*. *J. Biol. Chem.* 287, 14412–14419. doi: 10.1074/jbc.M111.305144

Schimmeyer, J., Bock, R., and Meyer, E. H. (2016). L-Galactono-1,4-lactone dehydrogenase is an assembly factor of the membrane arm of mitochondrial complex I in Arabidopsis. *Plant Mol. Biol.* 90, 117–126. doi: 10.1007/s11103-015-0400-4

Selvanathan, A., and Parayil Sankaran, B. (2022). Mitochondrial iron-sulfur cluster biogenesis and neurological disorders. *Mitochondrion* 62, 41–49. doi: 10.1016/j.mito.2021.10.004

Sheftel, A. D., Stehling, O., Pierik, A. J., Netz, D. J. A., Kerscher, S., Elsässer, H.-P., et al. (2009). Human ind1, an iron-sulfur cluster assembly factor for respiratory complex I. *Mol. Cell Biol.* 29, 6059–6073. doi: 10.1128/MCB.00817-09

Sheftel, A. D., Wilbrecht, C., Stehling, O., Niggemeyer, B., Elsässer, H.-P., Mühlenhoff, U., et al. (2012). The human mitochondrial ISCA1. ISCA2, and IBA57 proteins are required for [4Fe-4S] protein maturation. *Mol. Biol Cell* 23, 1157–1166. doi: 10.1091/mbc.E11-09-0772

Soufari, H., Parrot, C., Kuhn, L., Waltz, F., and Hashem, Y. (2020). Specific features and assembly of the plant mitochondrial complex I revealed by cryo-EM. *Nat. Commun.* 11:5195. doi: 10.1038/s41467-020-18814-w

Subrahmanian, N., Remacle, C., and Hamel, P. P. (2016). Plant mitochondrial Complex I composition and assembly: a review. *Biochim. Biophys. Acta* 1857, 1001–1014. doi: 10.1016/j.bbabio.2016.01.009

Torraco, A., Stehling, O., Stümpfig, C., Rösser, R., De Rasmo, D., Fiermonte, G., et al. (2018). ISCA1 mutation in a patient with infantile-onset leukodystrophy causes defects in mitochondrial [4Fe-4S] proteins. *Hum. Mol. Genet* 27, 2739–2754. doi: 10.1093/hmg/ddy183

Uzarska, M. A., Nasta, V., Weiler, B. D., Spantgar, F., Ciofi-Baffoni, S., Saviello, M. R., et al. (2016). Mitochondrial Bol1 and Bol3 function as assembly factors for specific iron-sulfur proteins. *Elife* 5:e16673. doi: 10.7554/eLife.16673

Uzarska, M. A., Przybyla-Toscano, J., Spantgar, F., Zannini, F., Lill, R., Mühlenhoff, U., et al. (2018). Conserved functions of Arabidopsis mitochondrial late-acting maturation factors in the trafficking of iron-sulfur clusters. *Biochim. Biophys. Acta Mol. Cell Res.* 1865, 1250–1259. doi: 10.1016/j.bbamcr.2018.06.003

Waller, J. C., Ellens, K. W., Alvarez, S., Loizeau, K., Ravanel, S., and Hanson, A. D. (2012). Mitochondrial and plastidial COG0354 proteins have folate-dependent functions in iron-sulphur cluster metabolism. *J. Exp. Bot.* 63, 403–411. doi: 10.1093/jxb/err286

Wang, Y., Carrie, C., Giraud, E., Elhafez, D., Narsai, R., Duncan, O., et al. (2012). Dual location of the mitochondrial preprotein transporters B14.7 and Tim23-2 in complex I and the TIM17:23 complex in Arabidopsis links mitochondrial activity and biogenesis. *Plant Cell* 24, 2675–2695. doi: 10.1105/tpc.112.098731

Webert, H., Freibert, S.-A., Gallo, A., Heidenreich, T., Linne, U., Amlacher, S., et al. (2014). Functional reconstitution of mitochondrial Fe/S cluster synthesis on Isu1 reveals the involvement of ferredoxin. *Nat. Commun.* 5:5013. doi: 10.1038/ncomms6013

Weiler, B. D., Brück, M.-C., Kothe, I., Bill, E., Lill, R., and Mühlenhoff, U. (2020). Mitochondrial [4Fe-4S] protein assembly involves reductive [2Fe-2S] cluster fusion on ISCA1-ISCA2 by electron flow from ferredoxin FDX2. *Proc. Natl. Acad. Sci. U.S.A.* 117, 20555–20565. doi: 10.1073/pnas.2003982117

Wiedemann, N., Urzica, E., Guiard, B., Müller, H., Lohaus, C., Meyer, H. E., et al. (2006). Essential role of Isd11 in mitochondrial iron-sulfur cluster synthesis on Isu scaffold proteins. *EMBO J.* 25, 184–195. doi: 10.1038/sj.emboj.7600906

Wydro, M. M., Sharma, P., Foster, J. M., Bych, K., Meyer, E. H., and Balk, J. (2013). The evolutionarily conserved iron-sulfur protein INDH is required for complex I assembly and mitochondrial translation in *Arabidopsis* [corrected]. *Plant Cell* 25, 4014–4027. doi: 10.1105/tpc.113.117283

Zhu, J., Vinothkumar, K. R., and Hirst, J. (2016). Structure of mammalian respiratory complex I. *Nature* 536, 354–358. doi: 10.1038/nature19095

Conflict of Interest: The authors declare that the research was conducted in the absence of any commercial or financial relationships that could be construed as a potential conflict of interest.

Publisher's Note: All claims expressed in this article are solely those of the authors and do not necessarily represent those of their affiliated organizations, or those of the publisher, the editors and the reviewers. Any product that may be evaluated in this article, or claim that may be made by its manufacturer, is not guaranteed or endorsed by the publisher.

frontiers | Frontiers in Plant Science

ORIGINAL RESEARCH
published: 26 May 2022
doi: 10.3389/fpls.2022.902705

There Is No Carbon Transfer Between Scots Pine and Pine Mistletoe but the Assimilation Capacity of the Hemiparasite Is Constrained by Host Water Use Under Dry Conditions

*Ao Wang[1,2], Marco M. Lehmann[1], Andreas Rigling[1,2], Arthur Gessler[1,2], Matthias Saurer[1], Zhong Du[1,3] and Mai-He Li[1]**

[1] Forest Dynamics, Swiss Federal Institute for Forest, Snow and Landscape Research WSL, Birmensdorf, Switzerland, [2] Institute of Terrestrial Ecosystems, ETH Zürich, Zurich, Switzerland, [3] School of Geographical Sciences, China West Normal University, Nanchong, China

OPEN ACCESS

Edited by:
Sebastian Leuzinger,
Auckland University of Technology,
New Zealand

Reviewed by:
Juan Pedro Ferrio,
Fundacion Agencia Aragonesa Para la Investigacion y el Desarrollo, Spain
Néstor Fernández Del-Saz,
University of Concepcion, Chile

***Correspondence:**
Mai-He Li
maihe.li@wsl.ch

Specialty section:
This article was submitted to Plant Physiology, a section of the journal Frontiers in Plant Science

Received: 23 March 2022
Accepted: 09 May 2022
Published: 26 May 2022

Citation:
Wang A, Lehmann MM, Rigling A, Gessler A, Saurer M, Du Z and Li M-H (2022) There Is No Carbon Transfer Between Scots Pine and Pine Mistletoe but the Assimilation Capacity of the Hemiparasite Is Constrained by Host Water Use Under Dry Conditions. Front. Plant Sci. 13:902705. doi: 10.3389/fpls.2022.902705

Pine mistletoe is a hemiparasitic shrub that can produce its own photosynthates. There is a lack of knowledge about the interaction of mistletoe and host under varying environmental condition that might influence carbon gain and allocation. In a ^{13}C-pulse labeling experiment with mature *Pinus sylvestris* (pine) infected by mistletoes grown in naturally dry or irrigated conditions, (1) mistletoe clusters were shielded from $^{13}CO_2$ added, and (2) mistletoes or host needles were removed to manipulate the local assimilate and water availability. No ^{13}C signal was found in shielded mistletoes, indicating no carbon transfer from the host to the mistletoe. When the pine needles were removed from girdled branches, no ^{13}C signal was found in the host tissues, implying no carbon transfer from mistletoe to the host. However, mistletoes on needle-removed pine trees accumulated more labeled assimilates and had higher non-structural carbohydrate (NSC) concentrations only under naturally dry conditions but not in irrigated plots. Our results suggest that mistletoes show full carbon autonomy, as they neither receive carbon from nor provide carbon resource to the host trees. Moreover, the high assimilation capacity of mistletoes seems to be constrained by the host water use under dry conditions, suggesting that drought stress is not only negatively impacting trees but also mistletoes. Therefore, we conclude that the hemiparasites live on their own in terms of carbon gain which, however, depends on the water provided by the host tree.

Keywords: ***Viscum album* ssp. *austriacum*, *Pinus sylvestris*, ^{13}C assimilates, non-structural carbohydrate (NSC), host water, carbon relationship**

INTRODUCTION

The relationship between a parasite and its host is important ecologically and widely discussed in animal and plant pathology and physiology. Most research on parasite–host relationships in plants has concentrated on host responses to infections by parasites (Streicker et al., 2013; Solomon et al., 2015). In contrast, the interactions between plant hosts and plant parasites, especially the effects

of hosts on parasites in different habitats and varying site conditions, have rarely been studied. However, such parasite–host relationships, including a possible feedback system between the host and parasite, are of central interest because they can strongly affect the growth and survival of the higher plants serve as hosts.

Mistletoes are well-known hemiparasitic plants that maintain their own carbon assimilation by photosynthesis and can infect many tree species in various ecosystem types worldwide, making them an important and relevant species in parasitism research (Zuber, 2004; Glatzel and Geils, 2009). *Viscum album* ssp. *austriacum* (Santalaceae), pine mistletoe, is the most widely distributed species across the European continent (Zuber, 2004; Dobbertin and Rigling, 2006). Pine mistletoe survival and development in forest ecosystems mainly rely on water and mineral resources obtained from the xylem sap of the host tree (Dobbertin and Rigling, 2006; Rigling et al., 2010). If water availability is high and nutrients are not limited, pine mistletoes and their hosts co-exist for years without major restrictions for the host tree (Zuber, 2004; Solomon et al., 2015). However, if water is limited during dry periods, the high-water consumption and low water-use efficiency of pine mistletoes may exacerbate drought stress in the host tree, with negative consequences on the host's physiology and growth performance (Dobbertin and Rigling, 2006; Rigling et al., 2010; Zweifel et al., 2012). As a consequence, pine mistletoe infection leads to a reduction of branching and of branch and needle growth (Rigling et al., 2010), resulting in an increased risk of mortality for the host tree (Dobbertin and Rigling, 2006). This contribution of pine mistletoe to drought-induced forest decline processes has been demonstrated in several xeric forest ecosystems in Spain (Galiano et al., 2011; Sangüesa-Barreda et al., 2012, 2013; Scalon et al., 2013) and inner-Alpine regions in Switzerland and Italy (Dobbertin and Rigling, 2006; Rigling et al., 2010; Vacchiano et al., 2012).

Along with the negative effects of mistletoes on the host water balance, pine mistletoes have also been found to affect the carbon balance of the host in a variety of ways (Glatzel and Geils, 2009; Scalon and Wright, 2015; Le et al., 2016b). High water use of mistletoes and thus considerable water loss from the whole host–parasite system may induce closure of the stomata in host trees to save water (Rigling et al., 2010; Zweifel et al., 2012), resulting in lower photosynthesis rates of the trees (Dobbertin and Rigling, 2006; Yan et al., 2016). Therefore, pine mistletoe can indirectly reduce the host's ability to acquire carbon resources, especially under drought-stress conditions (Sangüesa-Barreda et al., 2013; Yan et al., 2016).

Mistletoes perform photosynthesis at a rate similar to that of the host (Lüttge et al., 1998; Scalon and Wright, 2017). In some studies, however, it has been reported that mistletoes are able to additionally acquire organic carbon from the host in the form of xylem-mobile organic acids and amino acids (Escher et al., 2004b; Těšitel et al., 2010). Richter et al. (1995) estimated that mistletoe leaves take up over 50% of its required heterotrophic carbon from its host. Nevertheless, according to Smith and Gledhill (1983), the haustorium of *V. album* grows only within the host's xylem and does not connect to the host's phloem. This means that there should be only acropetal carbon transport from the host xylem to the mistletoe via the transpiration stream, with no basipetal carbon flow from the mistletoe to the host, even under strong carbon limitation of the host (Glatzel and Geils, 2009; Scalon and Wright, 2015). Hence, it remains unclear whether mistletoes can directly absorb carbon resources from host tissues in considerable amounts, in addition to their own photosynthetic activities. By utilizing the stable ^{13}C isotope tracer technique, it is possible to determine the direction and quantity of carbon assimilate flow between mistletoe and host, and also to assess how this process depends on carbon and water availability.

Most studies on mistletoe–host relationships have been conducted by comparing trees infected by mistletoes with non-infected trees growing under the same conditions (Dobbertin and Rigling, 2006; Dobbertin et al., 2010; Rigling et al., 2010; Yan et al., 2016). Whether the host's carbon resource availability, which is strongly associated with its growth conditions (e.g., soil water moisture), affects the mistletoe–host relationship has only been investigated in a few studies, and these studies were only focused on the response of hosts to mistletoe infection (Zweifel et al., 2012; Sangüesa-Barreda et al., 2013; Le et al., 2016a). It is still unclear if the carbon dynamics in the mistletoe and in its host, as well as the potential exchange of assimilates between the two, changes in response to the local water availability of both the host tree and the mistletoe.

To address these unresolved questions, we conducted two separate experiments under the umbrella of a whole-tree ^{13}C-pulse labeling experiment with mature Scots pine (*Pinus sylvestris*) trees infected by pine mistletoe (*V. album*). Host trees whose crowns were exposed to $^{13}CO_2$ were growing either in naturally dry conditions (∼600 mm precipitation per year) or in irrigated areas (+ 700 mm per year, applied during the growing season) for 15 years in the Swiss Pfynwald forest ecosystem experimental platform (Schaub et al., 2016; Joseph et al., 2020).

In a wrapping experiment (Exp. 1), we shielded mistletoe clusters with gas-tight plastic foil and darkened them with aluminum foil before the whole-tree labeling to prevent ^{13}C assimilation by these clusters. We investigated the ^{13}C values in both wrapped and non-wrapped mistletoes, as well as in their host twigs, to test the hypothesis (**H1**) that *V. album* takes up carbon resources from its host via the haustorium. Any signal in the wrapped mistletoes (shielding from $^{13}CO_2$ and light exclusion) would originate from the host and we assumed the contribution of the host (if any) to be higher in irrigated vs. drought-stressed trees due to increased assimilation rates in irrigated trees (Schonbeck et al., 2021).

To change source–sink carbon and water relationships, we performed a tissue removal experiment (Exp. 2). We girdled pine branches infected with mistletoes of drought-stressed and irrigated host trees to restrict the phloem carbon translocation between the remaining tree and the girdled branch (Andersen et al., 2005; De Schepper and Steppe, 2013), while keeping a constant water and nutrient flow. Beyond the girdling point, we then removed all pine needles or all mistletoe tissues (including stem and leaves) from the girdled pine branches to manipulate source-sink relationships and water relations locally on the branch level. Through Exp. 2, we aimed to test the hypothesis

(**H2a**) that local changes in source–sink relationships by reducing assimilate ability (i.e., host needle removal), would decrease the mistletoes' carbon level due to lower amounts of carbon obtained from the host (conditional H1 is supported). An alternative hypothesis (**H2b**) is that needle removal increases the mistletoes' carbon level due to increased carbon assimilation by the hemiparasite itself as a result of decreased competition for water with the host. This effect would be more pronounced under the dry control conditions. Finally, we hypothesize (**H3**) that mistletoes do not provide any carbon to the host, even when the host is carbon limited due to needle removal.

MATERIALS AND METHODS

Study Site

Our experiment was conducted in a naturally regenerated, mature Scots pine (*Pinus sylvestris*) forest in Pfynwald, Valais, Switzerland (46°19′27″N, 7°34′40″E, 610 m a.s.l.). The forest site is located in a dry, inner-Alpine region of Switzerland with repeated occurrence of Scots pine mortality events within the last decades (Dobbertin et al., 2005; Rigling et al., 2013). The mean annual precipitation is around 657 mm and the mean annual temperature is 9.7°C (Dobbertin et al., 2010). A long-term irrigation experiment was started in 2003, where four plots of 1,000 m^2 are irrigated with water from a nearby channel during the growing season (+ 700 mm $year^{-1}$, resulting in 1,300–1,400 mm total precipitation per year = irrigated). Four additional plots of the same size are used as a naturally dry control (= non-irrigated). The dominant species in this forest (> 10 km^2) is *P. sylvestris*, with *Quercus pubescens* occurring occasionally. The pine trees are over 100 years old, with a mean height of ∼11 m and a diameter at breast height (DBH) of ∼12 cm (Schaub et al., 2016). The soil type is a Rendzic Leptosol derived from limestone (Brunner et al., 2009). Many of the Scots pine trees are severely infected by pine mistletoe (*V. album*), with variations in the density and age of the mistletoes (mostly more than 10 years old) (Dobbertin et al., 2010). Since the irrigation experiment started, the environmental conditions (i.e., air temperature, air humidity, precipitation, soil temperature, and soil water potential) have been continuously monitored.

^{13}C Labeling at the Whole-Tree Level

We conducted whole-tree-crown ^{13}C labeling experiments in summer 2017, i.e., in the 15th year of irrigation treatment (Joseph et al., 2020). Six mature pine trees that were severely infected (over) by mistletoes (three control and three irrigated) were selected from the labeling experiment for the present study. For each selected tree, the whole tree crown was enclosed within a large temperature controlled transparent chamber, and approx. 10 g of CO_2 with > 99 atom% ^{13}C (Cambridge Isotopes, Tewksbury, MA, United States) was released into the chamber over a period of 3.5 h. Pulse labeling of the six trees was applied from 29 to 31 August 2017 (one pair of trees (control/irrigated) per day) (**Supplementary Figure 1**). Within this whole-tree labeling experiment, we conducted the following two experiments for the present study (**Figure 1**).

Wrapping Experiment (Exp. 1)

We selected six to eight mistletoe clusters from each of the six ^{13}C-labeled trees. Half of them (three to four) were randomly selected and wrapped with gas-tight plastic sheets to avoid direct

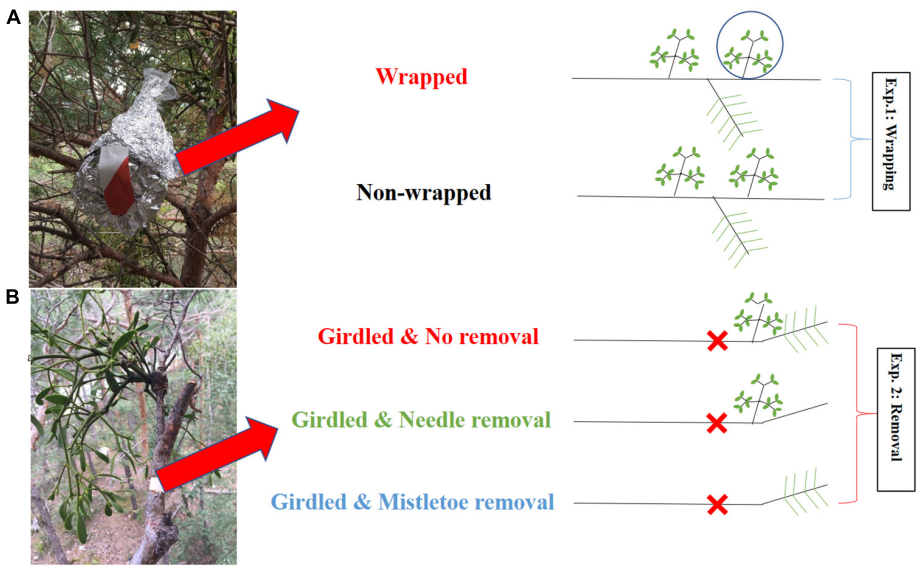

FIGURE 1 | Scheme of the wrapping experiment [**(A)**: Exp. 1] and the girdling and removal experiment [**(B)**: Exp. 2], with drawings showing the treatments applied to mistletoes and pine twigs on the right-hand site. In Exp. 1, mistletoe clusters were covered with gas-tight plastic sheets and aluminum foil to prevent direct ^{13}C label uptake during the whole-tree $^{13}CO_2$ labeling experiment; non-wrapped controls were allowed to take up $^{13}CO_2$. In Exp. 2, the bark including phloem was girdled for three branches per tree before the whole-tree labeling to create an isolated environment without top-down carbon transportation via the host's phloem, and each of these three branches was randomly assigned to mistletoe removal, pine needle removal, or intact control.

uptake and assimilation of $^{13}CO_2$, and additionally darkened with aluminum foil to avoid exposure to sunlight before the chamber was closed (**Figure 1**). The other three to four clusters selected per tree remained unwrapped and were allowed to take up $^{13}CO_2$ during the 3.5 h of labeling. We did not cover pine needles with gas-tight plastic sheets and aluminum foil because we expected that *V. album* takes up carbon resources with increased ^{13}C signal labeled from its host via the haustorium, but not vice versa (see our hypothesis H1). Tissues from the host (needle, twig xylem and phloem) and mistletoe clusters (leaf and shoot) were sampled at –1 day (the day before labeling) and at 4, 8, 24 h, 3, 7, 14, 30, 60, and 180 days after the start of labeling for analysis of the ^{13}C abundance.

Removal Experiment (Exp. 2)

In each of the six ^{13}C labeled trees considered in this study, three well-foliaged branches (around 1 m in length) that were infected by mistletoes were selected for a girdling treatment (**Figure 1**). A bark strip (including the phloem) of 2 cm width was removed over the entire circumference of the branch, basipetal to the mistletoe, to stop the basipetal transport of photo assimilates but to keep the xylem intact for the upward water and nutrient transport (**Figure 1**), 1 day before the whole-tree labeling started. In one of the three girdled branches per tree, all mistletoe tissues (leaf and shoot) were completely removed from the host branch at the point of injection with scissors before the $^{13}CO_2$-labeling (mistletoe removal), while in a second girdled branch, all host needles were easily removed from the host branch by bare hand (needle removal). The third one was kept intact and was used as a control (no removal). Plant material from the host (needle, twig xylem and phloem) and mistletoe (leaf and shoot) were sampled at –1 day (the day before labeling) and at 4, 8, 24 h, 3, 8, and 15 days after the start of labeling for ^{13}C abundance measurements. Measurement of non-structural carbohydrate (NSC) concentrations was conducted for the sampling at –1 day, label 1, 3, 8, and 15 days.

Analysis of Morphological Traits in Pine Needles and Mistletoe Leaves

One day before the labeling, 10 mistletoe leaves and 20 pine needles of each selected tree were harvested separately for leaf morphological measurements. Leaf area was measured using a scanner and image analysis software (PIXSTAT v1.3, WSL, Birmensdorf, Switzerland). Fresh weight of all leaves was firstly measured, and dry weight was measured after oven-drying the samples at 65°C for 5 days, and leaf water content on a fresh weight basis and leaf dry mass per unit leaf area (LMA) were then calculated.

Analysis of Non-structural Carbohydrate Concentrations

All tissues harvested for NSC and isotope analyses were dried in an oven at 65°C for 5 days. After drying, each sample was ground with a Retsch MM 300 ball mill (Retsch, Germany) until finely and homogeneously ground. NSCs are defined here as low-molecular-weight sugars and starch, and analysis followed the protocol by Schönbeck et al. (2018). About 10 mg of the sample powder was first vortexed with 2 ml of deionized water and then boiled in the steam for 30 min. For free-sugar analysis, a 200 μl aliquot of the extract was treated with invertase and isomerase (in 0.4 M Na-acetate buffer; Sigma-Aldrich, St. Louis, MO, United States) to break down sucrose to fructose and glucose. For the total NSC_T (NSC_T = soluble sugars + starch) analysis, a 500 μl aliquot of the extract (sugars and starch) was incubated with a fungal amyloglucosidase from *Aspergillus niger* (Sigma-Aldrich, St Louis, MO, United States) for 15 h at 49°C to digest starch into glucose. Both soluble sugars and NSC_T concentrations were determined at 340 nm in a 96-well microplate photometer (Multiskan GO, Thermo Fisher Scientific, Waltham, MA, United States) after enzymatic conversion of glucose molecules derived from sugars and starch to gluconate-6-phosphate (via isomerase, hexokinase, and glucose-6-P dehydrogenase; all supplied by Sigma-Aldrich). NSC concentrations are expressed as a percentage of dry matter, and the concentration of starch was calculated as NSC_T minus free sugars.

Analysis of ^{13}C Abundance

Around 1 mg of ground tissue material (same as used for the NSC analysis) was weighed into tin capsules. Organic carbon was converted to CO_2 in an elemental analyzer Euro EA3000 (Hekatech GmbH, Wegberg, Germany) connected to an isotope ratio mass spectrometer (IRMS; Delta V Advantage, Thermo Fisher Scientific, Bremen, Germany) to determine the total carbon and carbon isotopic composition. Laboratory standards with known $\eth^{13}C$ values were measured with a precision of 0.1‰. The isotopic ratios in all samples were expressed in δ notation (‰) relative to the international standard Vienna Pee Dee Belemnite (VPDB). The carbon isotope ratio was corrected to account for pre-labeling isotope ratios of bulk material to indicate the extent of ^{13}C-label incorporation in different tissues.

$$\Delta\delta^{13}C = \delta^{13}C_L - \delta^{13}C_{NA} \quad (1)$$

where $\delta^{13}C_L$ is the isotope ratio after the start of the labeling and $\delta^{13}C_{NA}$ is the natural (pre-labeling) isotope abundance.

Data Analysis

All data (i.e., $\delta^{13}C$, NSC_T and its components) were first tested for normality with Kolmogorov–Smirnov tests to assess the within- and between-subject effects in different tissues of pine (i.e., needle, xylem, phloem) and mistletoe (i.e., leaf, shoot).

For the wrapping experiment (Exp. 1), a linear mixed model (tree replicates as random effect) was used for testing the effects of time (sampling time), irrigation treatment (i.e., non-irrigated vs. irrigated), wrapping treatment (i.e., wrapping vs. non-wrapped), and their interactions on the carbon isotopic composition in different mistletoe tissues (i.e., leaf, shoot). The assessment of residuals normality and homoscedasticity were tested before analysis.

For the removal experiment (Exp. 2) (above the girdled branches), the assessment of residuals normality and homoscedasticity were tested before analysis. A linear mixed

model (tree replicates as random effect) was used for testing the effects of time (sampling time), irrigation treatment (i.e., non-irrigated vs. irrigated), removal treatments (i.e., needle removal for phloem, xylem and mistletoe tissues; mistletoe removal for pine tissues; and no removal for both pine and mistletoe tissues), and their interactions on $\delta^{13}C$ and NSC_T concentrations. For each sampling time point, one-way ANOVA and a Tukey-HSD *post hoc* test were used to investigate the difference in $\delta^{13}C$ and NSC_T concentrations in different pine and mistletoe tissues under different irrigation and removal treatments. R version 4.1.0 was used for all statistical analyses (R Core Team, 2021).

RESULTS

Irrigation Effects on the Morphology of Pine Needles and Mistletoe Leaves

Long-term irrigation significantly influenced the morphological traits of both pine needles and mistletoe leaves. Host leaf mass per unit leaf area (LMA) was significantly higher in control trees than in irrigated ones, but mistletoe leaves showed the opposite pattern (**Figure 2A**). There was no detectable difference in leaf water content between irrigated and control pine needles (**Figure 2B**). In contrast, leaf water content was significantly higher in control compared with irrigated mistletoe leaves (**Figure 2B**). The area of single pine needles was not affected by the irrigation treatment, but mistletoe had significantly larger leaves under control dry conditions than when irrigated (**Figure 2C**).

Wrapping Effects on ^{13}C Assimilates in Mistletoe Tissues (Exp. 1: Wrapping)

Irrigation had no significant effects on the ^{13}C assimilates of mistletoe tissues in the wrapping experiment, whereas the wrapping treatment had a strong effect on the ^{13}C accumulation in mistletoe tissues (**Table 1**). Strong labeling signals were found in the non-wrapped mistletoe leaves and shoots, while in the wrapped mistletoe clusters no ^{13}C signal was found in leaves or shoots (**Figure 3**). The peak value of $\Delta\delta^{13}C$ in non-wrapped leaves occurred approximately 8 h after the labeling started, after which point $\Delta\delta^{13}C$ values decreased gradually (**Figure 3A**). $\Delta\delta^{13}C$ values reached a peak in wrapped mistletoe shoots at the first sampling time after labeling, remained at a relatively stable high level until 15 days after labeling, and decreased slowly thereafter (**Figure 3B**).

Removal Effects on Carbon Assimilates in Pine and Mistletoe Tissues (Exp. 2: Girdling and Removal)

The irrigation treatment and its interaction with other factors (time or removal treatment) did not affect $\Delta\delta^{13}C$ or NSC concentration (NSC_T, sugars, starch) in the pine tissues (**Table 2**). However, there was a direct effect of the removal treatments on the carbon assimilates in host tissues (**Table 2**). Mistletoe removal resulted in significantly lower needle $\Delta\delta^{13}C$ at 24 h after labeling (**Figure 4A**), but did not affect needle NSC concentrations (**Table 2** and **Figure 5A**). Mistletoe removal did not affect new carbon assimilates in the host phloem (**Figures 4B**, **5B**) but led to significantly lower $\Delta\delta^{13}C$ in the pine xylem tissue at 3 and 15 days after labeling (**Figures 4C**, **5C**). When the needles were removed, no significant ^{13}C signals were found anymore in host phloem or xylem (**Figures 4B,C**). Needle and mistletoe removal did not affect the NSC concentrations in pine phloem (**Figure 5B**). Needle removal decreased the host xylem NSC concentrations, while such effects were not observed in the mistletoe removal treatment (**Figure 5C**).

Irrigation significantly ($P < 0.05$) or marginally significantly ($P < 0.10$) influenced the $\Delta\delta^{13}C$ and NSC concentrations (except sugars) in both mistletoe leaves and shoots (**Table 2**), and host needle removal also significantly affected the carbon assimilates and NSC concentrations in both mistletoe leaves and shoots (**Table 2**). In addition, host needle removal interacted with irrigation to significantly affect both $\Delta\delta^{13}C$ and NSC concentrations in mistletoe leaves and only $\Delta\delta^{13}C$ in mistletoe shoots (**Table 2**). Mistletoe leaves and shoots on trees grown under dry control conditions tended to have higher $\Delta\delta^{13}C$ levels than those on irrigated trees, especially when the host needles were removed (**Figures 4D,E**). Similarly, NSC concentrations in

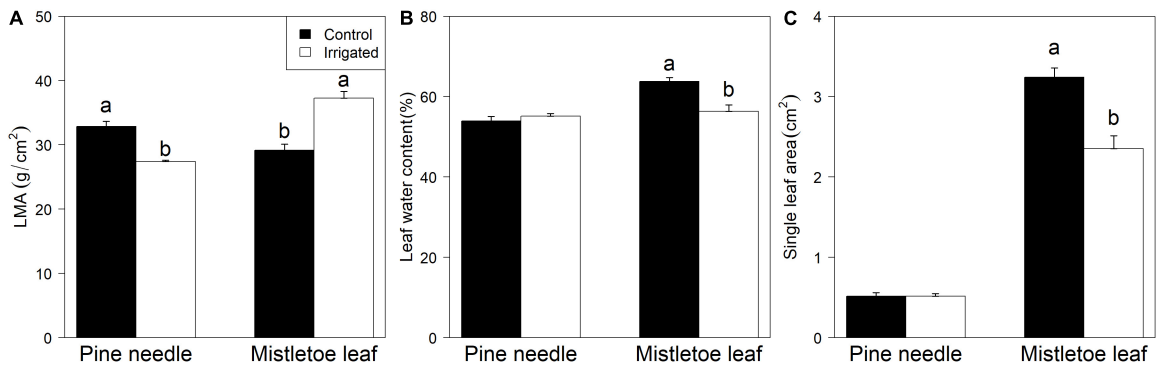

FIGURE 2 | Comparison of the leaf traits between *Pinus sylvestris* and *Viscum album* ssp. *austriacum* in the control and irrigation treatments ($n = 3$ trees per treatment). **(A)** Leaf mass per unit leaf area (LMA) of mistletoe leaves and pine needles, **(B)** leaf water content of mistletoe leaves and pine needles, **(C)** single leaf area of mistletoe leaves and pine needles. Different letters indicate significant differences ($P < 0.05$) for each tissue between dry controls and irrigated trees.

TABLE 1 | Results of linear mixed models for $\Delta\delta^{13}C$ values (uptake and incorporation of ^{13}C) of bulk material in different tissues of *Viscum album* ssp. *austriacum* in the wrapping experiment (Exp. 1).

Factors	df	Mistletoe leaf $\Delta\delta^{13}C$	Mistletoe shoot $\Delta\delta^{13}C$
Time (T)	9	9.08***	3.43**
Irrigation (I)	1	1.11	0.47
Wrapping (W)	1	185.99***	137.74***
T × I	9	1.99	1.03
T × W	9	8.70***	3.49**
I × W	1	2.72	3.41
T × I × W	9	1.80	0.47

$^{**}P < 0.01$, $^{***}P < 0.001$.
Degrees of freedom (df) and F-values are given for time, irrigation treatment and wrapping treatment (i.e., wrapped vs. non-wrapped; n = 3).

mistletoe leaves were higher in the control compared with the irrigated trees, but mainly when the pine needles were removed (**Figures 5D,E**).

DISCUSSION

No Transport of Newly Assimilated Carbon From Host to Mistletoes

The wrapping experiment showed that non-wrapped mistletoes efficiently assimilate carbon (**Figure 3**), although the incorporation of ^{13}C originating from the labeled CO_2 in mistletoe leaves was only half of that in pine needles (**Figures 3**, **4**). We did not find a strong effect of irrigation on the ^{13}C incorporation in mistletoe leaves or shoots (**Table 1**), indicating that the carbon assimilation capacity of mistletoes was not affected by restricted soil water availability, although mistletoes are known to rely on acquiring water resources via the xylem of the host tree (Glatzel and Geils, 2009; Zweifel et al., 2012). Scalon and Wright (2017) investigated 42 mistletoe–host species pairs sampled from 5 sites in Australia and Brazil under different soil water availability and found that the photosynthetic capacity of mistletoes and their hosts were on a similar level, but that mistletoes had leaf dark respiration rates that were twice that of the hosts at a given photosynthetic capacity, resulting in higher leaf maintenance costs for these hemiparasitic plants. In our study, it is possible that higher respiration rates, and thus loss of previously fixed ^{13}C, contributed to the lower overall incorporation of ^{13}C in bulk organic matter of mistletoe leaves compared with pine needles.

In contrast, wrapped mistletoes were not able to assimilate new carbon assimilates after the labeling event (**Figure 3**). This clearly shows that new carbon assimilates are not transported from the host to any mistletoe tissue in significant amounts, which is consistent with the concept suggested in previous studies assuming that no phloem connection is established between hemiparasite and host (Glatzel and Geils, 2009; Těšitel et al., 2010; Scalon and Wright, 2015). In contrast, Marshall and Ehleringer (1990) compared the nature abundance of ^{13}C values measured with gas exchange measurement-based theoretical ^{13}C values in mistletoe leaves, and found that only part of the carbon in the biomass of *V. album* originated from its own photosynthesis activities. Escher et al. (2004a) speculated that pine mistletoes gained heterotrophic carbon from the host via the xylem sap, based on significantly positive correlations of soluble carbohydrate between mistletoe and host. However, such "extra" carbon gain of mistletoe derived from xylem (i.e., from needles, downwards to roots, and then upwards to xylem) was not evidenced by our labeling experiment. Even after 180 days, we did not find any ^{13}C signal in the wrapped mistletoe clusters, indicating that, in

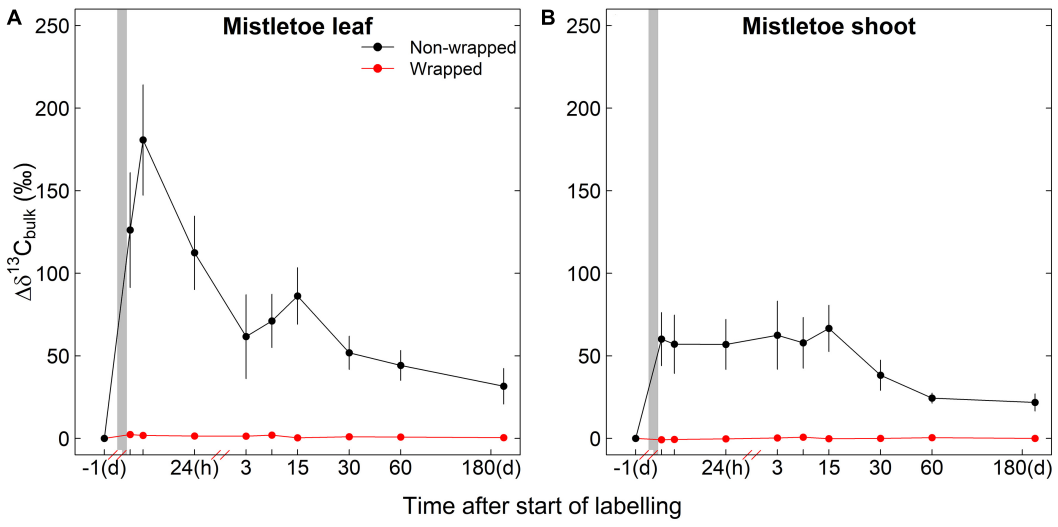

FIGURE 3 | Incorporation of the ^{13}C label into the bulk organic matter ($\Delta\delta^{13}C_{bulk}$) of mistletoe leaves **(A)** and shoots **(B)** in the wrapping experiment (i.e., wrapped vs. non-wrapped; *n* = 3) after a 3.5 h of exposure to ^{13}C-enriched CO_2 (gray shaded area). Please note that the initial point is from 1 day before the labeling and that the scaling of the *x*-axis changes after each break.

TABLE 2 | Results of linear mixed models for $\Delta\delta^{13}C$ values (uptake and incorporation of ^{13}C) of bulk material, as well as the concentration of NSC_T and its compounds (i.e., soluble sugars and starch) in different tissues of *Pinus sylvestris* and *Viscum album* ssp. *austriacum* in the removal experiment (Exp. 2).

	df	$\Delta\delta^{13}C$	df	NSC_T	Sugar	Starch
Pine needle						
Time (T)	6	18.25***	4	0.89	0.14	0.87
Irrigation (I)	1	0.11	1	0.06	1.01	0.01
Mistletoe removal (MR)	1	9.94***m	1	2.11	2.64	0.38
T × I	6	0.58	4	0.54	0.72	0.89
T × R	6	1.13	4	1.31	1.54	0.96
I × MR	1	0.43	1	0.11	0.36	1.02
Pine phloem						
Time (T)	6	3.26*	4	0.33	1.99	1.93
Irrigation (I)	1	0.17	1	1.40	0.01	2.61
Removal (R)	2	10.23***	2	11.35***	6.49*	5.39*
T × I	6	0.14	4	1.59	1.22	1.08
T × R	12	1.15	8	1.23	1.66	1.74
I × R	2	0.48	2	0.31	1.73	1.38
Pine xylem						
Time (T)	6	2.29*	4	2.36	2.06	1.71
Irrigation (I)	1	0.08	1	0.63	1.21	2.21
Removal (R)	2	11.89***	2	23.58***	21.93***	9.87**
T × I	6	0.14	4	1.20	1.51	0.89
T × R	12	1.13	8	3.25**	2.63*	2.95*
I × R	2	0.06	2	2.04	1.11	0.84
Mistletoe leaf						
Time (T)	6	9.24***	4	2.71	0.44	2.28
Irrigation (I)	1	11.89***	1	5.14†	0.59	3.04†
Needle removal (NR)	1	25.93***	1	7.69*	5.23*	6.01*
T × I	6	10.35***	4	1.22	1.02	0.87
T × NR	6	8.21***	4	2.83†	2.54†	2.77†
I * NR	1	15.47***	1	17.62***	14.54***	11.25***
Mistletoe shoot						
Time (T)	6	16.03***	4	2.41	0.44	1.88
Irrigation (I)	1	4.45†	1	3.74†	2.05	3.03†
Needle removal (NR)	1	25.11***	1	9.08*	4.72*	4.09*
T × I	6	4.11**	4	1.13	1.17	1.24
T × NR	6	2.62*	4	0.93	0.87	0.74
I * NR	1	35.15***	1	0.12	0.05	2.64

*$P < 0.05$, **$P < 0.01$, ***$P < 0.001$, †$P < 0.1$.

The degrees of freedom (df) and F-values are given (P-values are given with the significance level indicated, with values corresponding to $P < 0.05$ given in red) for time, irrigation treatment and different removal treatments (i.e., mistletoe removal for pine needle, needle removal and mistletoe removal for pine phloem, and xylem, needle removal for mistletoe leaf and shoot; n = 3).

the longer term, no labeled carbon was obtained from the host. Within the same whole-tree labeling experiment, Gao et al. (2021) showed that even 10 months after labeling, tree's respired CO_2 still had $\delta^{13}C$ values of up to 25‰. This indicates that significant amounts of label were still present in the host's tissues and transport systems on our final sampling date, yet not transferred to the mistletoes. We conclude that mistletoes are complete carbon autotrophs and do not receive significant amounts of carbon directly from the host; thus, we can reject **H1**.

The Photosynthetic Capacity of Pine Mistletoes Is Suppressed by the Host Trees Under Drier Conditions

Although we did not find a significant effect of the irrigation treatment on mistletoe ^{13}C uptake and incorporation in the wrapping experiment (**Figure 3**), mistletoe leaves and shoots accumulated more ^{13}C-labeled assimilates in trees grown in the dry control conditions than in the irrigated conditions, when the needles of trees in both conditions were removed from the girdled branches (**Table 2** and **Figure 4**). As photosynthetic carbon acquisition is normally greater in an environment with higher soil moisture (Wang et al., 1998; Reich et al., 2018; Joseph et al., 2020), our results may be attributed to an increased water supply to mistletoes due to reduced water use by needle removal in the dry conditions which had significantly lower soil moisture than the irrigated plots (**Supplementary Figure 2**). Such an abrupt water release may result in a short-term pulse effect (<3 days; **Figure 4D**) of water on the photosynthetic capacity and thus ^{13}C levels in mistletoe leaves (**Figure 4D**). This may imply that mistletoes compete for water with the host in dry but not in wetter conditions, as the former had significantly lower soil water moisture showing possible water limitation while the latter had higher soil moisture remaining near optimal water conditions (**Supplementary Figure 2**). Similarly, Zweifel et al. (2012) found that the stomatal conductance of pine needles was significantly negatively correlated with the levels of mistletoe infection in *P. sylvestris* trees grown in conditions with ∼600 mm precipitation, suggesting water competition between mistletoe and its host in dry environment. Moreover, mistletoe leaves were larger and had a higher water content under the dry control conditions (**Figure 2**), and thus may have a higher photosynthetic potential, leading to increased ^{13}C signal (**Figures 4D,E**). Similarly, previous studies suggested that changes in host water and nutrient condition can regulate the water and carbon uptake efficiency of a hemiparasitic mistletoe (*Phoradendron juniperinum*) (Marshall et al., 1994), and a holoparasitic mistletoe (*Arceuthobium vaginatum* subsp. *Cryptopodum*) (Bickford et al., 2005). These results further signify that host needle removal not only affected source–sink carbon relationships in the girdled branch but might also result in more available water for the mistletoe due to discontinued host transpiration. The reduced competition for water may allow the mistletoes to keep stomates more open, thus allowing for higher photosynthesis rates.

We also found that mistletoe leaf NSC_T concentrations were significantly higher in the control trees compared with the irrigated trees when pine needles were not present anymore (**Table 2** and **Figure 5**), which corroborates our assumption of higher assimilation by mistletoes when there were no needles to demand water under dry conditions. The high carbon accumulation capacity of mistletoes in a stressful environment also demonstrates the competitive ability of the hemiparasite. However, it seemed that mistletoes with bigger leaf size and higher assimilation potential benefit more from pine needle removal than the pine needles benefit from mistletoe removal (see discussion below). Still, mistletoes are known to exacerbate

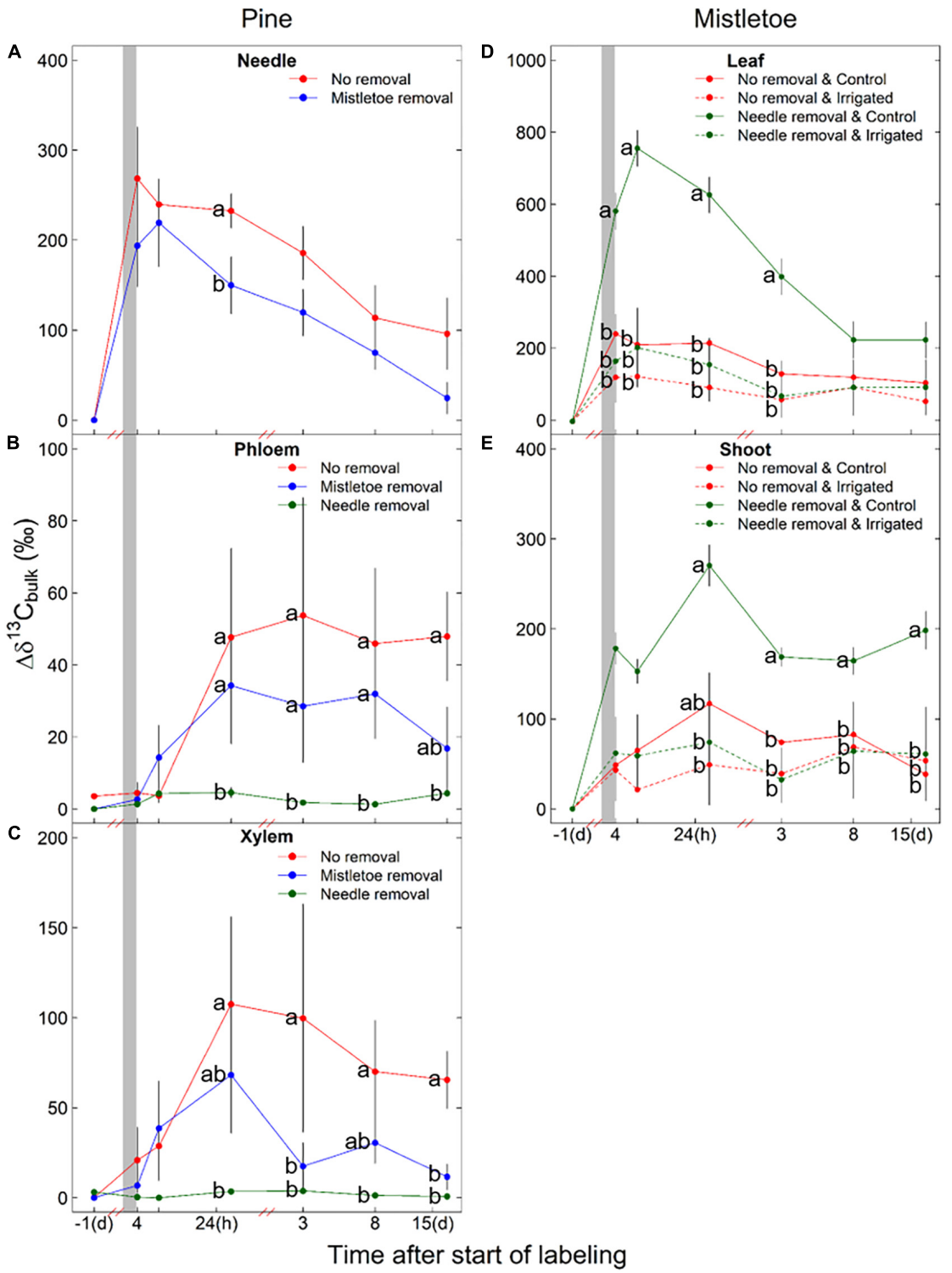

FIGURE 4 | Initial (1 day before the labeling) and incorporation of the ^{13}C label into the bulk organic matter ($\Delta\delta^{13}C_{bulk}$) of different pine (*Pinus sylvestris*) **(A–C)** and mistletoe (*Viscum album* ssp. *austriacum*) **(D,E)** tissues under different removal treatments (i.e., pine needle removal for pine phloem and xylem, mistletoe leaf and shoot; mistletoe removal for pine needle, phloem and xylem). Girdled branches were exposed to ^{13}C-enriched CO_2 (shaded area) for 3.5 h. Dashed lines **(D,E)** are used to indicate where the $\Delta\delta^{13}C$ values of mistletoe leaves and shoots showed a significant difference ($P < 0.05$) between irrigated and non-irrigated trees (see **Table 2**). Different letters indicate significant differences among treatments at the same sampling time ($n = 3$). Please note the difference in scale of the *x*-axis before and after the red break points and the difference in *y*-axis scale among panels.

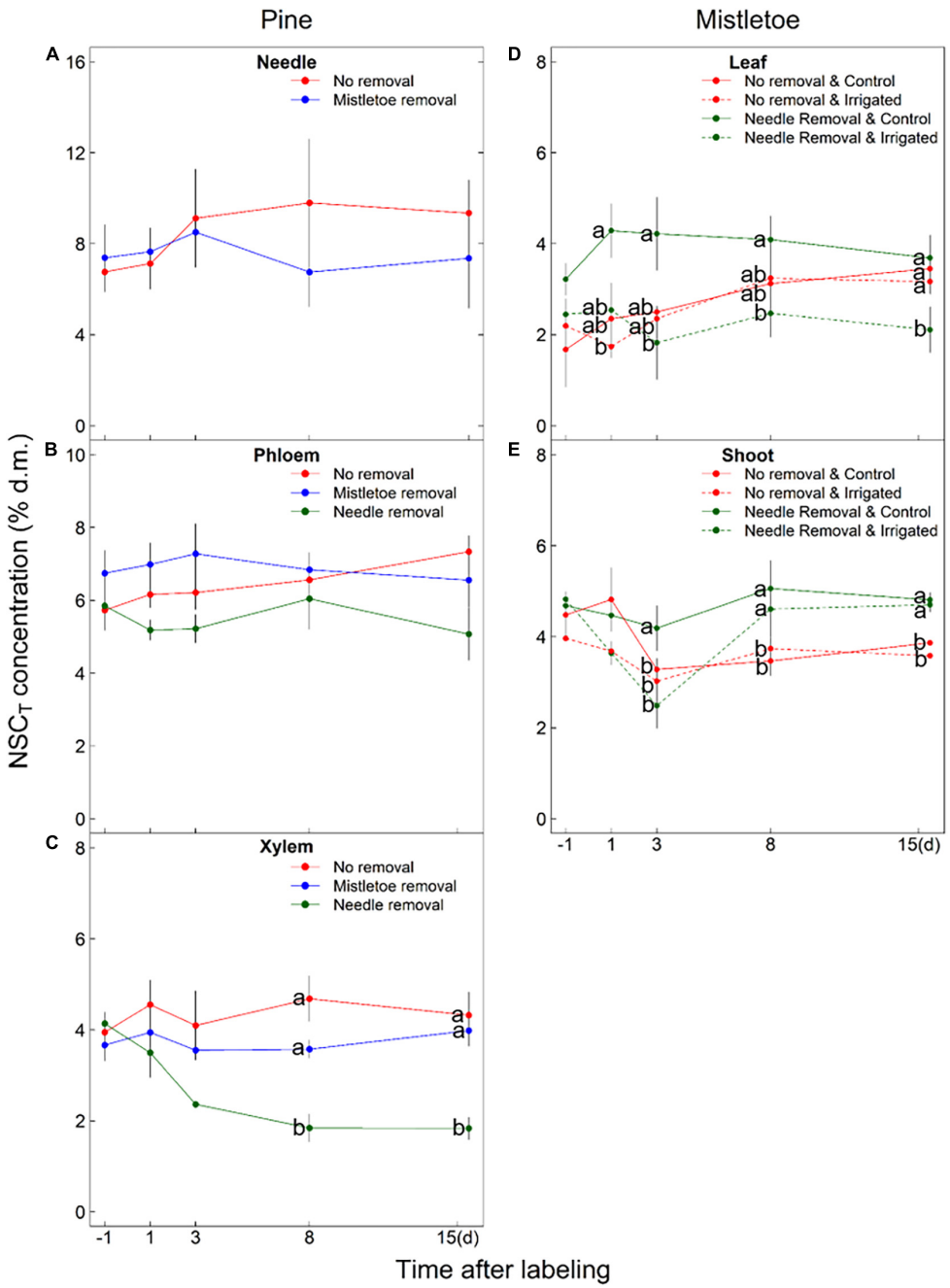

FIGURE 5 | NSC_T concentration [% of dry matter (d.m.)] in different pine (*Pinus sylvestris*) **(A–C)** and mistletoe (*Viscum album* ssp. *austriacum*) **(D,E)** tissues under different removal treatments (i.e., pine needle removal for pine phloem and xylem, mistletoe leaf and shoot; mistletoe removal for pine needle, phloem and xylem) applied to the girdled branches. The initial samples were collected 1 day before the labeling. Dashed lines **(D,E)** are used to indicate where the irrigation treatment had significant effect ($P < 0.05$) on NSC_T concentration (see **Table 2**). Different letters indicate significant differences among treatments at the same sampling time ($n = 3$). Please note the difference in *y*-axis scale among panels.

tree mortality in drought-exposed regions (Dobbertin and Rigling, 2006; Rigling et al., 2010; Zweifel et al., 2012; Sangüesa-Barreda et al., 2013; Durand-Gillmann et al., 2014). Our findings support our hypothesis **H2b** that expected an increased carbon level in mistletoes due to increased carbon assimilation by the hemiparasite itself as a result of decreased competition for water with the host after host needle removal. In contrast to our hypothesis **H2a**, an increase in carbon level and carbon assimilation of mistletoes after host needle removal was found, which is not related to a change in source activity of the host but is rather due to the released water restrictions of the mistletoe by removing the transpiring host needles under dry conditions.

Mistletoes Cannot Act as a Carbon Provider, Even When the Host Is Carbon Limited

In the needle removal treatment, no strong ^{13}C signal was found upon ^{13}C labeling in the pine sink tissues (i.e., phloem and xylem). The minimal ^{13}C traces detected (**Figures 4B,C**) might be due to bark photosynthesis (Aschan and Pfanz, 2003; Simkin et al., 2020). This finding suggests that mistletoe assimilates do not act as a significant carbon source for the host sink tissues. We thus conclude that there is no exchange of carbon assimilates between mistletoe and host. Neither do mistletoes use host carbon resources nor do they provide any carbon to the host, even when the host is carbon limited in special situations (needle removal treatment, drought). These results support **H3** and prove that mistletoes and hosts are carbon-independent and that only water and nutrients are transported from the host to the mistletoes.

Meanwhile, needle removal also resulted in a decrease in NSC_T concentrations in pine xylem tissue after 1 week, which can be explained by the lack of delivery of new assimilates to the sink tissues. Pine xylem, as well as needles and phloem, however, also tended to accumulate less ^{13}C-labeled carbon assimilates when mistletoes were removed from the branches (**Figures 4A–C**). Since there is no transport of assimilates from the mistletoe to the host tissues, we propose the following explanation: mistletoe tissues have lower water potentials compared with host tissues, which ensures continuous water uptake from the host xylem (Schulze et al., 1984; Zweifel et al., 2012; Scalon and Wright, 2015), and continuously compete for water with pine tissues. Removing the mistletoe might reduce the need to incorporate large amounts of osmotically active compounds, and thus decrease the transport of new ^{13}C-labeled soluble carbon compounds to pine tissues. Moreover, mistletoe removal could also lower the sap flow rate of the whole branch (Zweifel et al., 2012), leading to a reduction of carbon assimilates refixation in xylem tissues and further in needles and phloem (**Figures 4A–C**).

CONCLUSION

Our results demonstrate that pine mistletoes are fully carbon-autonomous: they do not provide carbon to the host and are also not supplied with carbon compounds by the host. We also observed that mistletoes are constrained in their photosynthesis by the host when soil water availability is low, most likely due to competition for xylem water—when the competition is released by removing the host needles, the ^{13}C assimilation of the mistletoe increases. This result provides physiological evidences that mistletoes do increase the drought stress of their hosts, resulting in an increased mortality risk during severely dry periods previously proposed. We, therefore, conclude that the hemiparasites live on their own in terms of carbon gain which, however, depends on the water provided by the host tree.

DATA AVAILABILITY STATEMENT

The raw data supporting the conclusions of this article will be made available by the authors, without undue reservation.

AUTHOR CONTRIBUTIONS

M-HL, AG, and AR planned the labeling experiment. M-HL and AW designed the treatment and sampling experiment. AW and ML conducted the field work. AW and ZD conducted the experiment work and analyzed the data. AW wrote the manuscript. M-HL, AG, AR, ML, and MS revised the manuscript. All authors contributed to the article and approved the submitted version.

FUNDING

This study was supported by the Chinese Scholarship Council (Grant No. 201706510023). The labeling event was based on a long-term irrigation experiment in Pfynwald, Switzerland, which was part of the Swiss Long-term Forest Ecosystem Research Programme LWF (www.lwf.ch). Open access funding provided by the Swiss Federal Institute For Forest, Snow And Landscape Research.

SUPPLEMENTARY MATERIAL

The Supplementary Material for this article can be found online at: https://www.frontiersin.org/articles/10.3389/fpls.2022.902705/full#supplementary-material

REFERENCES

Andersen, C. P., Nikolov, I., Nikolova, P., Matyssek, R., and Haberle, K. H. (2005). Estimating "autotrophic" belowground respiration in spruce and beech forests: decreases following girdling. *Eur. J. For. Res.* 124, 155–163. doi: 10.1007/s10342-005-0072-8

Aschan, G., and Pfanz, H. (2003). Non-foliar photosynthesis–a strategy of additional carbon acquisition. *Flora Morphol. Distrib. Funct. Ecol. Plants* 198, 81–97.

Bickford, C. P., Kolb, T. E., and Geils, B. W. (2005). Host physiological condition regulates parasitic plant performance: *Arceuthobium vaginatum* subsp. cryptopodum on *Pinus ponderosa*. *Oecologia* 146, 179–189. doi: 10.1007/s00442-005-0215-0

Brunner, I., Pannatier, E. G., Frey, B., Rigling, A., Landolt, W., Zimmermann, S., et al. (2009). Morphological and physiological responses of Scots pine fine roots to water supply in a dry climatic region in Switzerland. *Tree Physiol.* 29, 541–550. doi: 10.1093/treephys/tpn046

De Schepper, V., and Steppe, K. (2013). "Tree girdling: a tool to improve our understanding of coupled sugar and water transport," in *Proceedings of the II International Symposium on Woody Ornamentals of the Temperate Zone*, Gent, 313–320.

Dobbertin, M., Eilmann, B., Bleuler, P., Giuggiola, A., Pannatier, E. G., Landolt, W., et al. (2010). Effect of irrigation on needle morphology, shoot and stem growth in a drought-exposed *Pinus sylvestris* forest. *Tree Physiol.* 30, 346–360. doi: 10.1093/treephys/tpp123

Dobbertin, M., Mayer, P., Wohlgemuth, T., Feldmeyer-Christe, E., Graf, U., Zimmermann, N., et al. (2005). The decline of *Pinus sylvestris* L. forests in the Swiss Rhone valley-a result of drought stress? *Phyton* 45:153.

Dobbertin, M., and Rigling, A. (2006). Pine mistletoe (*Viscum album* ssp. austriacum) contributes to Scots pine (*Pinus sylvestris*) mortality in the Rhone valley of Switzerland. *For. Pathol.* 36, 309–322.

Durand-Gillmann, M., Cailleret, M., Boivin, T., Nageleisen, L.-M., and Davi, H. (2014). Individual vulnerability factors of Silver fir (*Abies alba* Mill.) to parasitism by two contrasting biotic agents: mistletoe (*Viscum album* ssp. abietis) and bark beetles (Coleoptera: Curculionidae: Scolytinae) during a decline process. *Ann. For. Sci.* 71, 659–673.

Escher, P., Eiblmeier, M., Hetzger, I., and Rennenberg, H. (2004b). Spatial and seasonal variation in amino compounds in the xylem sap of a mistletoe (*Viscum album*) and its hosts (*Populus* spp. and *Abies alba*). *Tree Physiol.* 24, 639–650. doi: 10.1093/treephys/24.6.639

Escher, P., Eiblmeier, M., Hetzger, I., and Rennenberg, H. (2004a). Seasonal and spatial variation of carbohydrates in mistletoes (*Viscum album*) and the xylem sap of its hosts (*Populus euamericana* and *Abies alba*). *Physiol. Plant.* 120, 212–219. doi: 10.1111/j.0031-9317.2004.0230.x

Galiano, L., Martínez-Vilalta, J., and Lloret, F. (2011). Carbon reserves and canopy defoliation determine the recovery of Scots pine 4 yr after a drought episode. *New Phytol.* 190, 750–759. doi: 10.1111/j.1469-8137.2010.03628.x

Gao, D., Joseph, J., Werner, R. A., Brunner, I., Zürcher, A., Hug, C., et al. (2021). Drought alters the carbon footprint of trees in soils—tracking the spatio-temporal fate of 13C-labelled assimilates in the soil of an old-growth pine forest. *Glob. Change Biol.* 27, 2491–2506. doi: 10.1111/gcb.15557

Glatzel, G., and Geils, B. (2009). Mistletoe ecophysiology: host–parasite interactions. *Botany* 87, 10–15. doi: 10.1111/plb.12638

Joseph, J., Gao, D., Backes, B., Bloch, C., Brunner, I., Gleixner, G., et al. (2020). Rhizosphere activity in an old-growth forest reacts rapidly to changes in soil moisture and shapes whole-tree carbon allocation. *Proc. Natl. Acad. Sci. U.S.A.* 117, 24885–24892. doi: 10.1073/pnas.2014084117

Le, Q., Tennakoon, K. U., Metali, F., Lim, L. B., and Bolin, J. F. (2016b). Host specific variation in photosynthesis of an obligate xylem-tapping mistletoe *Dendrophthoe curvata* in a Bornean heath forest. *Nordic J. Bot.* 34, 235–243.

Le, Q., Tennakoon, K., Metali, F., Lim, L., and Bolin, J. (2016a). Ecophysiological responses of mistletoe Dendrophthoe curvata (Loranthaceae) to varying environmental parameters. *J. Trop. For. Sci.* 28, 59–67.

Lüttge, U., Haridasan, M., Fernandes, G. W., de Mattos, E. A., Trimborn, P., Franco, A. C., et al. (1998). Photosynthesis of mistletoes in relation to their hosts at various sites in tropical Brazil. *Trees* 12, 167–174.

Marshall, J. D., Dawson, T. E., and Ehleringer, J. R. (1994). Integrated nitrogen, carbon, and water relations of a xylem-tapping mistletoe following nitrogen fertilization of the host. *Oecologia* 100, 430–438. doi: 10.1007/BF00317865

Marshall, J. D., and Ehleringer, J. R. (1990). Are xylem-tapping mistletoes partially heterotrophic? *Oecologia* 84, 244–248. doi: 10.1007/BF00318279

R Core Team (2021). *R: A Language and Environment for Statistical Computing. Version 3.5.1*. Vienna: R foundation for statistical computing.

Reich, P. B., Sendall, K. M., Stefanski, A., Rich, R. L., Hobbie, S. E., and Montgomery, R. A. (2018). Effects of climate warming on photosynthesis in boreal tree species depend on soil moisture. *Nature* 562, 263–267. doi: 10.1038/s41586-018-0582-4

Richter, A., Popp, M., Mensen, R., Stewart, G., and Willert, D. (1995). Heterotrophic carbon gain of the parasitic angiosperm *Tapinanthus oleifolius*. *Funct. Plant Biol.* 22, 537–544.

Rigling, A., Bigler, C., Eilmann, B., Feldmeyer-Christe, E., Gimmi, U., Ginzler, C., et al. (2013). Driving factors of a vegetation shift from scots pine to pubescent oak in dry alpine forests. *Glob. Change Biol.* 19, 229–240. doi: 10.1111/gcb.12038

Rigling, A., Eilmann, B., Koechli, R., and Dobbertin, M. (2010). Mistletoe-induced crown degradation in scots pine in a xeric environment. *Tree Physiol.* 30, 845–852. doi: 10.1093/treephys/tpq038

Sangüesa-Barreda, G., Linares, J. C., and Camarero, J. J. (2012). Mistletoe effects on scots pine decline following drought events: insights from within-tree spatial patterns, growth and carbohydrates. *Tree Physiol.* 32, 585–598. doi: 10.1093/treephys/tps031

Sangüesa-Barreda, G., Linares, J. C., and Camarero, J. J. (2013). Drought and mistletoe reduce growth and water-use efficiency of Scots pine. *For. Ecol. Manag.* 296, 64–73.

Scalon, M., Haridasan, M., and Franco, A. (2013). A comparative study of aluminium and nutrient concentrations in mistletoes on aluminium-accumulating and non-accumulating hosts. *Plant Biol.* 15, 851–857. doi: 10.1111/j.1438-8677.2012.00713.x

Scalon, M. C., and Wright, I. J. (2015). A global analysis of water and nitrogen relationships between mistletoes and their hosts: broad-scale tests of old and enduring hypotheses. *Funct. Ecol.* 29, 1114–1124.

Scalon, M. C., and Wright, I. J. (2017). Leaf trait adaptations of xylem-tapping mistletoes and their hosts in sites of contrasting aridity. *Plant Soil* 415, 117–130.

Schaub, M., Haeni, M., Hug, C., Gessler, A., and Rigling, A. (2016). *Tree Measurements 2002-2016 From the Long-Term Irrigation Experiment Pfynwald*. Valais. Swiss Federal Research Institute WSL SwissForestLab.

Schönbeck, L., Gessler, A., Hoch, G., McDowell, N. G., Rigling, A., Schaub, M., et al. (2018). Homeostatic levels of nonstructural carbohydrates after 13 yr of drought and irrigation in *Pinus sylvestris*. *New Phytol.* 219, 1314–1324. doi: 10.1111/nph.15224

Schonbeck, L., Grossiord, C., Gessler, A., Gisler, J., Meusburger, K., D'Odorico, P., et al. (2021). Photosynthetic acclimation and sensitivity to short-and long-term environmental changes. *bioRxiv*[Preprint] doi: 10.1101/2021.01.04.425174

Schulze, E. D., Turner, N., and Glatzel, G. (1984). Carbon, water and nutrient relations of two mistletoes and their hosts: a hypothesis. *Plant Cell Environ.* 7, 293–299.

Simkin, A. J., Faralli, M., Ramamoorthy, S., and Lawson, T. (2020). Photosynthesis in non-foliar tissues: implications for yield. *Plant J.* 101, 1001–1015. doi: 10.1111/tpj.14633

Smith, P. L., and Gledhill, D. (1983). Anatomy of the endophyte of *Viscum album* L.(Loranthaceae). *Bot. J. Linn. Soc.* 87, 29–53.

Solomon, N. U., James, I. M., Alphonsus, N. O.-O., and Nkiruka, R. U. (2015). A review of host-parasite relationships. *Annu. Res. Rev. Biol.* 5, 372–384.

Streicker, D. G., Fenton, A., and Pedersen, A. B. (2013). Differential sources of host species heterogeneity influence the transmission and control of multihost parasites. *Ecol. Lett.* 16, 975–984.

Těšitel, J., Plavcová, L., and Cameron, D. D. (2010). Interactions between hemiparasitic plants and their hosts: the importance of organic carbon transfer. *Plant Signal. Behav.* 5, 1072–1076. doi: 10.4161/psb.5.9.12563

Vacchiano, G., Garbarino, M., Mondino, E. B., and Motta, R. (2012). Evidences of drought stress as a predisposing factor to scots pine decline in Valle d'Aosta (Italy). *Eur. J. For. Res.* 131, 989–1000.

Wang, J. R., Hawkins, C., and Letchford, T. (1998). Photosynthesis, water and nitrogen use efficiencies of four paper birch (*Betula papyrifera*) populations grown under different soil moisture and nutrient regimes. *For. Ecol. Manag.* 112, 233–244.

Yan, C. F., Gessler, A., Rigling, A., Dobbertin, M., Han, X. G., and Li, M. H. (2016). Effects of mistletoe removal on growth, N and C reserves, and carbon and oxygen isotope composition in scots pine hosts. *Tree Physiol.* 36, 562–575. doi: 10.1093/treephys/tpw024

Zuber, D. (2004). Biological flora of central Europe: *Viscum album* L. *Flora Morphol. Distrib. Funct. Ecol. Plants* 199, 181–203.

Zweifel, R., Bangerter, S., Rigling, A., and Sterck, F. J. (2012). Pine and mistletoes: how to live with a leak in the water flow and storage system? *J. Exp. Bot.* 63, 2565–2578. doi: 10.1093/jxb/err432

Conflict of Interest: The authors declare that the research was conducted in the absence of any commercial or financial relationships that could be construed as a potential conflict of interest.

Publisher's Note: All claims expressed in this article are solely those of the authors and do not necessarily represent those of their affiliated organizations, or those of the publisher, the editors and the reviewers. Any product that may be evaluated in this article, or claim that may be made by its manufacturer, is not guaranteed or endorsed by the publisher.

frontiers | Frontiers in Plant Science

ORIGINAL RESEARCH
published: 26 May 2022
doi: 10.3389/fpls.2022.918673

WATER-SOAKED SPOT1 Controls Chloroplast Development and Leaf Senescence *via* Regulating Reactive Oxygen Species Homeostasis in Rice

Jiangmin Xu[1,2†], Zhiyuan Ji[1†], Chunlian Wang[1†], Feifei Xu[1], Fujun Wang[1,3], Yuhan Zheng[1], Yongchao Tang[1], Zheng Wei[1], Tianyong Zhao[2] and Kaijun Zhao[1]**

[1] National Key Facility for Crop Gene Resources and Genetic Improvement, Institute of Crop Sciences, Chinese Academy of Agricultural Sciences, Beijing, China, [2] State Key Laboratory of Crop Stress Biology for Arid Areas, College of Life Sciences, Northwest A&F University, Xianyang, China, [3] Rice Research Institute, Guangdong Academy of Agricultural Sciences, Guangzhou, China

OPEN ACCESS

Edited by:
Lei Wang,
Institute of Botany (CAS), China

Reviewed by:
Yasuhito Sakuraba,
The University of Tokyo, Japan
Zhonghai Li,
Beijing Forestry University, China

***Correspondence:**
Kaijun Zhao
zhaokaijun@caas.cn
Tianyong Zhao
tzhao2@nwafu.edu.cn

† These authors have contributed equally to this work

Specialty section:
This article was submitted to Plant Physiology, a section of the journal Frontiers in Plant Science

Received: 12 April 2022
Accepted: 26 April 2022
Published: 26 May 2022

Citation:
Xu J, Ji Z, Wang C, Xu F, Wang F, Zheng Y, Tang Y, Wei Z, Zhao T and Zhao K (2022) WATER-SOAKED SPOT1 Controls Chloroplast Development and Leaf Senescence via Regulating Reactive Oxygen Species Homeostasis in Rice. Front. Plant Sci. 13:918673. doi: 10.3389/fpls.2022.918673

Transmembrane kinases (TMKs) play important roles in plant growth and signaling cascades of phytohormones. However, its function in the regulation of early leaf senescence (ELS) of plants remains unknown. Here, we report the molecular cloning and functional characterization of the *WATER-SOAKED SPOT1* gene which encodes a protein belongs to the TMK family and controls chloroplast development and leaf senescence in rice (*Oryza sativa* L.). The *water-soaked spot1* (*oswss1*) mutant displays water-soaked spots which subsequently developed into necrotic symptoms at the tillering stage. Moreover, *oswss1* exhibits slightly rolled leaves with irregular epidermal cells, decreased chlorophyll contents, and defective stomata and chloroplasts as compared with the wild type. Map-based cloning revealed that *OsWSS1* encodes transmembrane kinase TMK1. Genetic complementary experiments verified that a Leu396Pro amino acid substitution, residing in the highly conserved region of leucine-rich repeat (LRR) domain, was responsible for the phenotypes of *oswss1*. *OsWSS1* was constitutively expressed in all tissues and its encoded protein is localized to the plasma membrane. Mutation of *OsWSS1* led to hyper-accumulation of reactive oxygen species (ROS), more severe DNA fragmentation, and cell death than that of the wild-type control. In addition, we found that the expression of senescence-associated genes (SAGs) was significantly higher, while the expression of genes associated with chloroplast development and photosynthesis was significantly downregulated in *oswss1* as compared with the wild type. Taken together, our results demonstrated that OsWSS1, a member of TMKs, plays a vital role in the regulation of ROS homeostasis, chloroplast development, and leaf senescence in rice.

Keywords: transmembrane kinases, water-soaked spot, leaf senescence, chloroplast development, reactive oxygen species, rice

INTRODUCTION

Plant leaf is photosynthetic organ for energy production and nutrient assimilation during plant growth. Plant leaf senescence is the final stage of leaf development and controlled by programmed cell death (PCD) (Lim et al., 2007). During leaf senescence, reactive oxygen species (ROS) accumulate, malondialdehyde (MDA) content increases, the antioxidant enzyme activity decreases, chlorophyll degrades, photosynthesis efficiency reduces, and cell membrane gets damaged (Lim et al., 2007; Woo et al., 2019; Domínguez and Cejudo, 2021). ROS, including singlet oxygen ($^1O_2$), superoxide anions (O_2^-), hydroxyl radicals (OH), and hydrogen peroxide (H_2O_2), are important signaling molecules that trigger PCD and leaf senescence in plants (Wang et al., 2013; Mittler, 2017). Hyper-accumulation of ROS can disrupt the redox balance in cells and cause severe damage to lipids, proteins, and DNA. In addition, ROS affect the fluidity of biofilm, resulting in enzyme inactivation (Foyer and Noctor, 2005; Saed-Moucheshi et al., 2014). Therefore, production and scavenging of ROS must be tightly controlled by the antioxidant defense system to maintain a dynamic balance of the ROS level in plants (Lee S. et al., 2012; Mittler, 2017). The major antioxidant enzymes are catalase (CAT), superoxide dismutase (SOD), peroxidase (POD), and ascorbate peroxidase (APX) (Saed-Moucheshi et al., 2014).

In agriculture, plant leaves undergo normal leaf senescence positively contributes to crop yield by transferring its photosynthetic products into grains or other crop harvest organs (Wu et al., 2012). Early leaf senescence (ELS) means premature leaf yellowing and/or withering compared to wild type during reproductive growth, which decreases the functional period of leaves, thus affecting crop yield and quality (Lim et al., 2007). Leaf senescence is associated with the expression of specific genes (Woo et al., 2019). More than 185 senescence-associated genes (SAGs) have been identified in rice (Li et al., 2020). These genes are mainly associated with chloroplast development (Yang Y. et al., 2016; Chen et al., 2021), chlorophyll degradation (Kusaba et al., 2007; Morita et al., 2009; Jiang et al., 2011; Yamatani et al., 2013; Cui et al., 2021), hormone signal transduction (Kong et al., 2006; Chen et al., 2013; Liang et al., 2014), protease transport metabolism (Wu et al., 2016; Hong et al., 2018), and energy transport metabolism (Huang et al., 2007; Qiao et al., 2010).

Receptor-like kinases (*RLKs*) consist in one of the ubiquitous and most abundant gene families in plants. There are more than 1130 *RLK* genes in rice, twice as many as in *Arabidopsis* due to gene duplication (Shiu et al., 2004). A typical RLK is composed of a variable extracellular domain to perceive specific ligands, a transmembrane domain to connect the extracellular and intracellular parts for signal transmission, and an intracellular domain to transduce external signals into the cell to activate or inactivate the downstream regulatory components *via* phosphorylation (Morillo and Tax, 2006; Gish and Clark, 2011). The common structural element of many plant RLKs is an extracellular leucine-rich repeats (LRRs) domain, often referred to as LRR-RLK (Kinoshita et al., 2005). Each LRR is typically 20–30 residues long that has a high portion of leucine and other hydrophobic residues. The number of LRR motifs ranges between 3 and 27, and the distribution interval of LRR varies in different LRR-RLKs (Bella et al., 2008).

The transmembrane kinases (TMKs) of LRR-RLKs family play an important role in regulating plant growth and development (Xu et al., 2014). In *Arabidopsis*, unique double and triple TMK mutant combinations lead to serious growth defects, such as late flowering and seed sterility (Dai et al., 2013). The *Arabidopsis* TMK4 acts as a node in auxin and ABA signaling pathways (Wang et al., 2020; Li et al., 2021). In addition, TMKs have vital roles in non-canonical auxin signaling in regulating pavement cell morphogenesis, differential growth of the apical hook, lateral root formation, root gravitropic response, and thermomorphogenesis in *Arabidopsis* (Lin et al., 2021). Up to the present, only one rice TMK-encoding gene (*OsTMK*) has been characterized, and it is involved in gibberellin signal transduction (van der Knaap et al., 1999). Whether rice TMKs play a role in regulation of leaf senescence remains unknown.

In this study, we isolated and characterized the rice mutant *water-soaked spot1* (*oswss1*), which exhibits water-soaked spots and necrotic symptoms on leaves. *OsWSS1* encodes a member of the TMK subfamily of RLKs. The single amino acid substitution (Leu396Pro) in OsWSS1 results in the water-soaked spots and early leaf senescence phenotypes of the mutant *oswss1*. These results demonstrated that *OsWSS1* encodes a TMK that plays an important role in regulation of rice leaf senescence.

MATERIALS AND METHODS

Plant Materials and Growth Conditions

The rice early leaf senescence mutant *oswss1* was identified from the ethyl methane sulphonate (EMS) mutagenesis library of the *indica* rice cultivar JG30. The mutant *oswss1* was crossed with two *japonica* cultivars (02428 and Nipponbare) and the *indica* line JG30 for genetic analysis and gene mapping. The F_1 plants were self-pollinated to produce F_2 seeds. Unless specified otherwise, all parents, F_1 hybrids, F_2 populations, and transgenic plants were grown under natural conditions in paddy fields in Beijing and Hainan province, China.

Measurement of Chlorophyll Concentrations and Relative Water Content

For determination of the content of chlorophyll *a* (Chl *a*), chlorophyll *b* (Chl *b*), and carotenoid (Car), 10–30 mg wild-type leaves and *oswss1* green leaves and water-soaked spot leaves were cut into small pieces and chlorophylls were extracted in 95% ethanol solution for 48 h at 4°C in the dark. The absorbance values at wavelengths of 665, 649, and 470 nm were measured using a BioPhotometer plus (Eppendorf, Germany). The 95% ethanol was used as a blank control. The concentrations of Chl *a*, Chl *b*, and Car were calculated following

a published method (Lichtenthaler, 1987). There are six biological replicates for each group.

For measurement of RWC, the fully expanded leaves of wild type and *oswss1* were excised from plants in the field, and the fresh weight was measured and recorded as m1. The leaves were soaked in distilled water in a 50 mL centrifuge tube for 2 h, weighed, and recorded as m2. The leaves were then dried in a 60°C drying oven for 48 h, weighed, and recorded as m3. The percentage of RWC was calculated as $(m1 - m3)/(m2 - m3) \times 100$.

Transmission Electron Microscopy and Scanning Electron Microscopy

Wild-type leaves, *oswss1* green leaves, and water-soaked spot leaves were cut into pieces and were immersed in 2.5% pre-cooled glutaraldehyde solution, vacuumed for 60 min, and then kept at 4°C overnight. Subsequent procedures were performed following a published protocol (Zheng et al., 2021). Briefly, the samples were washed with phosphate buffer (0.1 M, pH 7.0) and fixed with 1% osmic acid stationary solution (pH 7.3), then dehydrated using a graded ethanol series. After dehydration, samples were embedded in epoxy resin. Afterward, sections were stained with uranyl acetate and examined with a Hitachi HT7700 transmission electron microscope.

For scanning electron microscopy analysis of the leaf epidermis, the samples were fixed in 2.5% glutaraldehyde solution and washed using phosphate buffer, and then dehydrated through a graded ethanol series. The samples were dried by the critical-point drying method and coated with gold, and then observed using a Hitachi TM-1000 scanning electron microscope (Rao et al., 2015).

Observation of Leaf Cell Morphology

At the tillering stage (87 days after sowing, DAS), leaves of wild type and *oswss1* mutant were fixed with formalin/acetic acid/alcohol fixative (FAA, 3.7% formaldehyde, 5% glacial acetic acid, and 50% ethanol) for 24 h, then dehydrated with 40, 60, 80, and 100% alcohol for 50 min, respectively. After that, the leaves were placed in 1.25 g/mL chloral hydrate solution for 60 min at 96°C. The upper epidermal tissues of leaves were scraped, and the lower epidermal cells were examined and photographed using BX43 light microscope (Tokyo, Japan).

For paraffin sectioning, leaves of wild type and *oswss1* mutant were fixed in FAA fixative overnight at 4°C. The paraffin sectioning procedures were performed following a published protocol (Ren et al., 2016). In brief, the samples were dehydrated with graded ethanol series, infiltrated with graded xylene series, and embedded in paraffin. The embedded samples were sliced into 10 μm thickness pieces and stained with a solution containing 1% safranine and 1% Fast Green. The sections were observed and photographed using BX43 light microscope (Tokyo, Japan).

Map-Based Cloning of *OsWSS1*

The phenotypes of F_1 plants and the segregation ratio of F_2 population were identified for genetic analysis. F_2 individuals with mutant phenotype were selected for DNA extraction and gene mapping. The parents and 21 F_2 individuals with mutant phenotype from the 02428/*oswss1* cross were subjected to initial linkage analysis by genotyping using 189 polymorphic insertion/deletion (InDel) markers covering 12 rice chromosomes. Subsequently, a large F_2 population with 1184 mutant individuals were used for fine mapping. New polymorphic primers were developed based on DNA sequence differences between the *japonica* cultivar Nipponbare (NIP) and *indica* cultivar JG30 to further narrow down the *OsWSS1* locus. The wild type and *oswss1* mutants were amplified by PCR using the marker primers (**Supplementary Table 2**). The results were analyzed using DNAMAN software.

For complementary experiment of *oswss1*, a 10 kb genomic DNA fragment containing the 6.6 kb wild type *OsWSS1* coding sequence (CDS), 2.3 kb upstream and 1.1 kb downstream, was amplified by PCR using primers pWSS1-CF and pWSS1-CR (**Supplementary Table 3**). The amplified fragment was cloned into the binary vector pCAMBIA1300 using the ClonExpress® II One Step Cloning Kit (Vazyme, China). The constructed vector was transformed into callus cells of *oswss1* by *Agrobacterium tumefaciens*-mediated transformation and the transgenic plants were regenerated.

Subcellular Localization

To detect the subcellular localization of OsWSS1, the full-length CDS of *OsWSS1* without the termination codon was amplified by PCR using primers WSS1-GFP-F and WSS1-GFP-R (**Supplementary Table 3**) and fused into the N-terminal of enhanced green fluorescent protein (eGFP) in the pCAMBIA1300 vector under the control of the CaMV 35S promoter to generate a *p35S:OsWSS1:eGFP* vector. The constructs were then transiently expressed or co-expressed with PIP2-mCherry, a plasma membrane marker, in rice protoplasts derived from the wild-type rice seedlings following a published protocol (Rao et al., 2015). In addition, the constructs were transiently expressed or co-expressed in *Nicotiana benthamiana* leaves by *Agrobacterium tumefaciens*-mediated infiltration following the methods described previously (Gao et al., 2016). GFP fluorescence signals in rice protoplasts and epidermal cell of *N. benthamiana* leaves were observed using a Zeiss LSM700 laser scanning confocal microscope.

RNA Extraction and Quantitative Real-Time PCR

Total RNA was extracted using the RNAiso Plus reagent (Takara, Japan) according to the manufacturer's manual. Total of 1 μg RNA was reversely transcribed into complementary DNA (cDNA) using a FastQuant RT Kit with gDNA remover (Tiangen, China). Quantitative reverse transcription PCR (qRT-PCR) was performed on an ABI 7500 Real-Time PCR system (Life Technologies, Carlsbad, CA, United States) with an SYBR® Premix ExTaq™ II (Takara). Rice *OsActin* (*LOC_Os03g50885*) was used as an internal reference gene. The relative quantitative analysis was performed by $2^{-\Delta\ \Delta CT}$ method (Livak and Schmittgen, 2001). Primers used for qRT-PCR are listed in **Supplementary Table 4**.

Measurement of Hydrogen Peroxide (H_2O_2) and Malondialdehyde Contents, and Antioxidants Activities

At the tillering stage, fresh leaves (0.3 g) of wild type and *oswss1* were collected and ground into homogenate in a precooled mortar with 2 mL 50 mmol L^{-1} precooled sodium phosphate buffer (pH 7.8). The homogenate was centrifuged at 12, 000 × *g* at 4°C for 10 min. The supernatant was collected for determination of the content of H_2O_2 and MDA, the activities of SOD and CAT, using the kits (A064-1-1, A003-1-2, A001-1-2, and A007-1-1) following the manufacturer's manuals (Nanjing Jiancheng Bioengineering Institute, China).

Histochemical Analysis and TUNEL Assay

The 3,3′-diaminobenzidine (DAB) and nitroblue tetrazolium (NBT) staining assays were performed as described previously (Thordal-Christensen et al., 1997). Briefly, leaves of wild type and *oswss1* were collected at the tillering stage, then soaked in 0.1% (w/v) DAB (Sigma) or 0.05% (w/v) NBT (Duchefa) solution and dyed for more than 8 h under dark conditions. The staining leaves were transferred into 95% ethanol for decolorization. Trypan blue staining was used to detect dead cells according to the method of a published protocol (Zheng et al., 2021). In brief, leaves at the same part were cut off and immersed in trypan blue solution and boiled for 10 min. After being kept in dark overnight, the leaves were transferred to 25 mg/mL chloral hydrate to decolorize for 3 days.

Terminal deoxynucleotidyl transferase dUTP nick-end labeling (TUNEL) assay was performed following a published protocol (Huang et al., 2007). Briefly, leaves of wild type and *oswss1* were collected and fixed in FAA solution for 24 h, then embedded in paraffin and cut into thin slices. Slides were hydrated with ethanol series and treated with proteinase K in phosphate buffer (pH 7.4). The TUNEL assay was performed using a Fluorescein *In Situ* Cell Death Detection Kit (Roche) according to the manufacturer's instructions.

Bioinformatics Analyses

OsWSS1 protein transmembrane domain prediction was performed using TMHMM server v. 2.0[1]. Conserved domains of the OsWSS1-encoded proteins were analyzed using SMART[2]. The sequences used for phylogenetic analysis were obtained from the NCBI Blast website[3] using OsWSS1 protein sequence (BAF28192) as the query. Alignment of the full-length amino acid sequences was performed using the DNAMAN software, and sequence logos of each protein were generated online with WebLogo3 (Crooks et al., 2004). The phylogenetic trees were constructed using MAGE 7.0 version software using the bootstrap method with 1000 bootstrap replicates. Protein sequence alignment was performed among OsWSS1 and its homologs from *Oryza brachyantha* (XP_006663422.1), *Sorghum bicolor* (XP_002450707.1), *Setaria italic* (XP_004979222.1), *Zea mays* (XP_008670729.1, PWZ25297.1), *Panicum hallii* (XP_025827113.1), *Triticum dicoccoides* (XP_037421068.1), *Triticum aestivum* (KAF7042763.1), *Aegilops tauschii* subsp. *tauschii* (XP_020188972.1), *Brachypodium distachyon* (XP_003576062.1), *Panicum miliaceum* (RLM70345.1), *Ananas comosus* (OAY69618.1), *Triticum urartu* (EMS63078.1), *Triticum turgidum* subsp. *durum* (VAH91395.1), *Hordeum vulgare* (KAE8766681.1), *Musa balbisiana* (THU51216.1), *Carex littledalei* (KAF3334352.1), *Phoenix dactylifera* (XP_008812470.1), *Capsicum annuum* (XP_016551399.1), *Cocos nucifera* (AID55112.1), *Cannabis sativa* (XP_030507417.1), *Vitis vinifera* (RVW82026.1), *Camellia sinensis* (XP_028113257.1), *Helianthus annuus* (XP_021981103.1), *Medicago truncatula* (XP_003601704.1), *Nelumbo nucifera* (XP_010246532.1), and *Arabidopsis thaliana* (AAP04161.1).

[1]http://www.cbs.dtu.dk/services/TMHMM

[2]http://smart.embl-heidelberg.de/

[3]http://www.ebi.ac.uk/Tools/sss/ncbiblast/

RESULTS

The *Oswss1* Mutant Exhibits Water-Soaked Spots and Withered Leaves

The rice *oswss1* mutant was isolated from the *indica* rice cultivar JG30 that was treated with EMS mutagenesis. Under natural conditions of the paddy field, light green water-soaked spots gradually appeared on *oswss1* leaves at the initial tillering stage (60 days after sowing, DAS), the water-soaked spot leaves gradually withered, while the wild-type (WT) leaves remain green (**Figure 1A** and **Supplementary Figures 1A–C**). An abundance of light green spots appeared on the *oswss1* leaves at the booting stage (105 DAS, **Supplementary Figure 1D**). We measured the chlorophyll (Chl) content of the water-soaked spots and green parts of *oswss1* leaves at the initial tillering stage. The results showed no significant difference between the green part of *oswss1* and WT leaves, while the contents of Chl *a*, Chl *b,* and Car in the water-soaked zone of *oswss1* leaves were significantly lower than those in the WT leaves (**Figure 1B**). At the heading stage (118 DAS), the panicle length of *oswss1* was shorter than that of the WT (**Figures 1C,D**). The lengths of the internodes I, II, III, IV, and V of *oswss1* were shortened by 22.6, 30.2, 33.8, 22.5, and 32.8%, respectively, in comparison with WT (**Supplementary Figure 2**). In addition, the plant height, seed-setting rate, and 1000-grain weight were lower in *oswss1* than that of the WT (**Figures 1E–G**). In short, the water-soaked spots of *oswss1* have an obvious negative effect on the agronomic traits.

Irregular Cell Structure and Abnormal Chloroplast Development in the *Oswss1* Leaves

At the maximum tillering stage (87 DAS), the water-soaked zone of *oswss1* leaves were slightly curled (**Figure 2A**). Paraffin sectioning assay showed that the mesophyll cells were arranged normally and regularly in the WT leaves (**Figure 2B**). In contrast, the volume of bulliform cells (BCs) in the water-soaked zone of *oswss1* leaves was significantly reduced; the mesophyll cells (MCs) were abnormal, and the cell arrangement was irregular

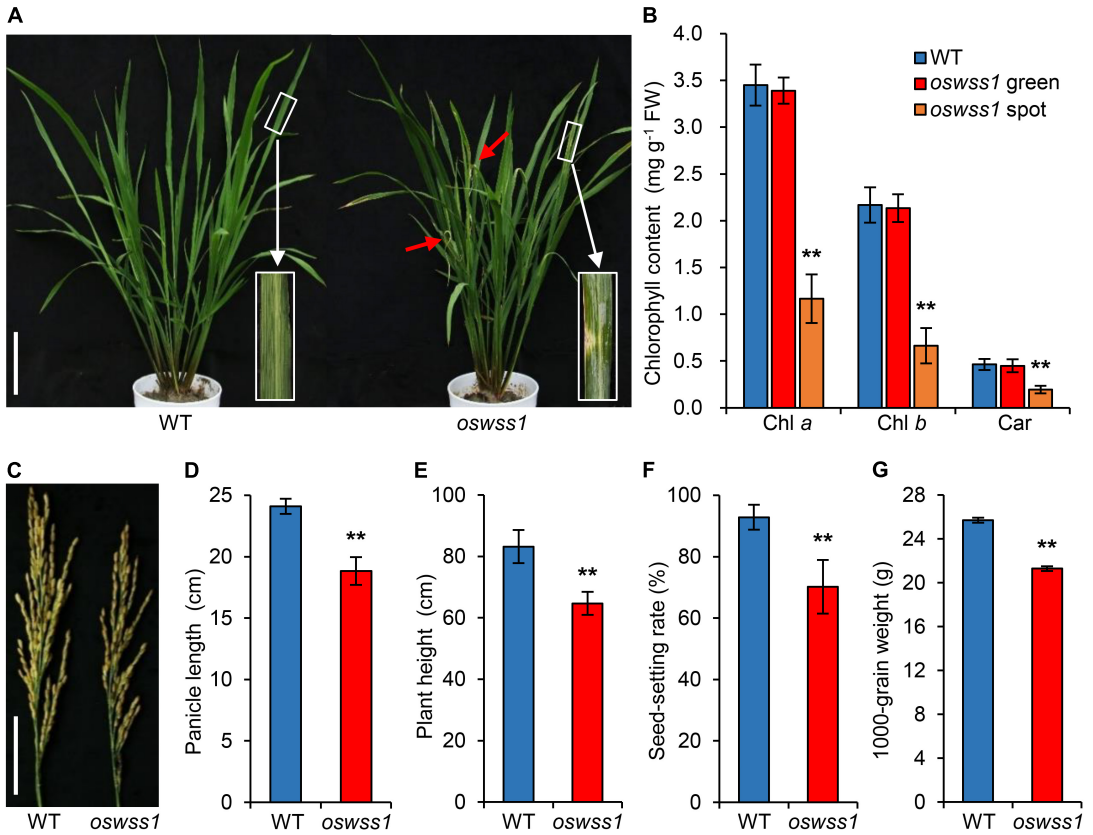

FIGURE 1 | Phenotype characterization and major agronomical traits of the rice *oswss1* mutant. **(A)** Phenotype of wild type (WT) and *oswss1* at the initial tillering stage (60 days after sowing, DAS). Inset shows a magnified view of a water-soaked spot of *oswss1* leaves. Scale bar = 14 cm. **(B)** Comparison of chlorophyll content between WT and *oswss1* at the initial tillering stage (60 DAS). Values are mean ± SD (n = 6). **(C)** Panicle morphology comparison between WT and *oswss1* at the heading stage (118 DAS). Scale bar = 6 cm. **(D–G)** Agronomic traits of WT and *oswss1* plants. **(D)** Panicle length; **(E)** plant height; **(F)** seed-setting rate; **(G)** 1,000-grain weight. Values are mean ± SD (n = 10). $^{**}P < 0.01$ (Student's t-test).

(**Figure 2B**). The leaf width of the water-soaked zone of *oswss1* mutant was narrower than that of WT (**Figure 2C**). In addition, the relative water content (RWC) of the water-soaked zone of *oswss1* leaves was lower, compared with that of WT leaves (**Figure 2D**). These results implied that the slightly rolled *oswss1* leaves may be caused by the atrophied BCs and MCs.

Scanning electron microscopy (SEM) assays showed the leaf surface in the water-soaked zone of *oswss1* leaves was seriously shrunk, the cuticular papillae were reduced, the stomatal morphology was deformed, and the stomatal density was also significantly reduced compared with that of WT (**Figures 2E–H**). Furthermore, the lower epidermal cells of the leaves were observed under light microscope. The leaf epidermal cells of WT showed regular rectangular shape, tightly arranged and had a complete cell structure (**Supplementary Figure 3A**). However, the leaf epidermal cell shape in the water-soaked zone of *oswss1* leaves was irregular, the cell arrangement was loose, and the cell structure changed significantly (**Supplementary Figure 3B**). Overall, these results suggested that *OsWSS1* play a role in regulation of leaf development.

The chloroplast ultrastructure of the WT leaves, the green parts and water-soaked zone of *oswss1* leaves were compared by transmission electron microscopy (TEM) at the tillering stage (87 DAS). TEM observation revealed that the chloroplasts were normal and structural integrity in the WT and the green part of *oswss1*, including intact membrane and dense grana lamella (**Figures 3A–D**). In contrast, in the water-soaked zone of *oswss1* leaves, the chloroplast development was impaired, the thylakoid lamellar structure was abnormal, and the grana lamellar was severely reduced, the number of chloroplasts was decreased (**Figures 3E,F**). The results suggested that *OsWSS1* plays an important role in chloroplast development.

Map-Based Cloning of *OsWSS1*

The *oswss1* was crossed with two *japonica* rice cultivars (NIP and 02428) and the *indica* line JG30, respectively. The leaves of F_1 plants were the same as the WT. The phenotype of leaf morphology showed 3:1 (WT: mutant) segregation ratio in the F_2 populations (**Supplementary Table 1**). These results indicated that the water-soaked spot phenotype of *oswss1* was controlled by a single recessive gene.

For molecular cloning of *OsWSS1* locus, the polymorphism between the parents of *oswss1* and 02428 was analyzed, a

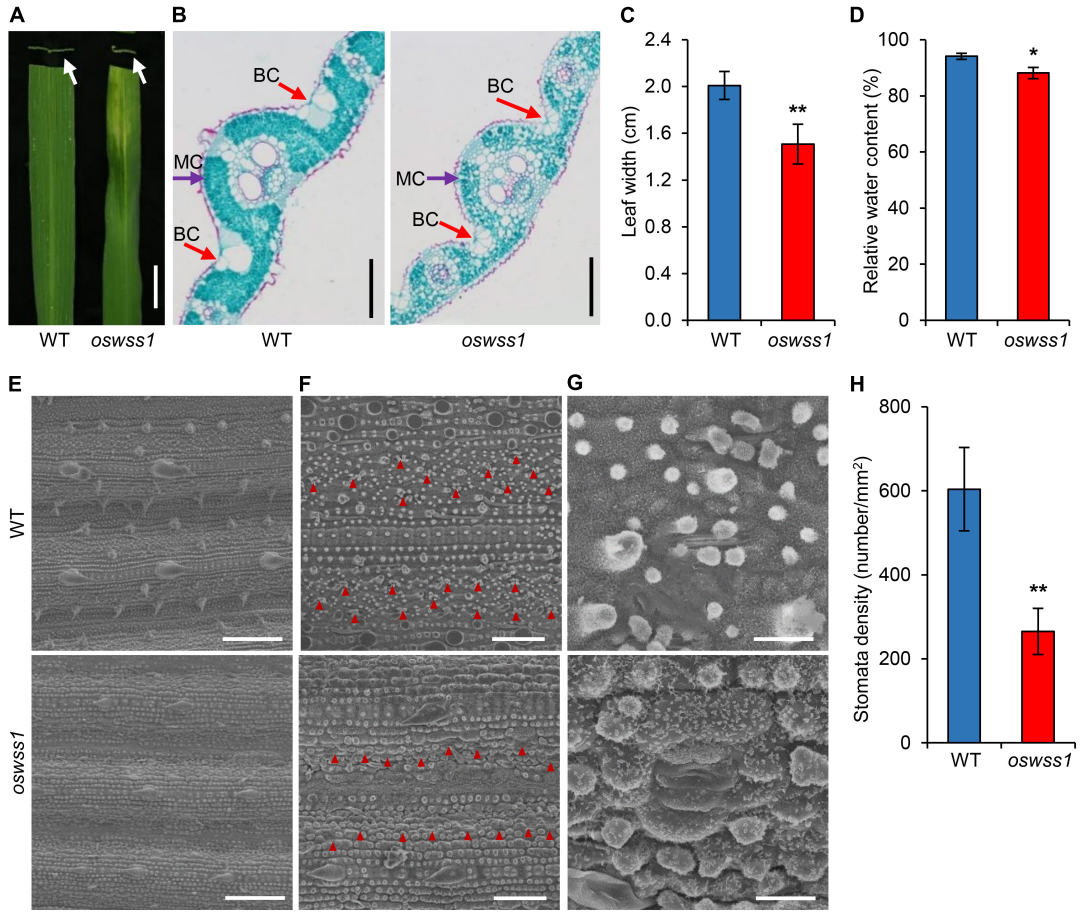

FIGURE 2 | Morphology comparison between wild type (WT) and *oswss1* leaves at the tillering stage (87 DAS). **(A)** Close-up image and cross section of WT and *oswss1* mutant leaves. Arrows indicate the cross section of water-soaked spot leaf. Scale bar = 2 cm. **(B)** Comparison of cell structure between WT and *oswss1* leaves. BC, bulliform cell; MC, mesophyll cell. Scale bars = 200 μm. **(C)** Comparison of leaf width between WT and *oswss1* leaves. **(D)** Comparison of relative water content between WT and *oswss1* leaves. **(E)** Scanning electron microscopy analysis of leaf morphological characteristics between WT and *oswss1* leaves. Scale bars = 100 μm. **(F)** Comparison of stomata density between WT and *oswss1* leaves. The red triangles indicate the positions of stomata. Scale bars = 50 μm. **(G)** Morphological characteristics of stomata between WT and *oswss1* leaves. Scale bars = 10 μm. **(H)** Statistical analysis of stomata density between WT and *oswss1*. Values are mean ± SD (n = 6). $^{*}P < 0.05$; $^{**}P < 0.01$ (Student's t-test).

total of 189 pairs of polymorphic insertion/deletion (InDel) markers were screened. Subsequently, 21 mutant individuals from the 02428/*oswss1* F_2 populations were used for linkage analysis. The *OsWSS1* locus was preliminarily mapped on chromosome 11 between the markers ID11-131 and ID11-12 (**Figure 4A**). For fine mapping of *OsWSS1*, nine new InDel markers were developed (**Supplementary Table 2**). Through genotyping of 1184 mutant individuals from the F_2 populations, *OsWSS1* was narrowed down to an 89.53 kb region between the markers Ch11-38 and Ch11-42 (**Figure 4A**). This region contains 13 annotated open reading frames (ORFs). Sequencing of these 13 ORFs revealed a T-to-C single-base substitution in the first exon of *LOC_Os11g26130*. This T to C change results in an amino acid substitution from leucine (Leu) to proline (Pro) in the 396th residue (**Figures 4B,C**). Additionally, the mutation of the *OsWSS1* gene was verified by a cleaved amplified polymorphic sequence (CAPS) marker which was developed based on this point mutation (**Figure 4D**).

The genetic complementation was performed to confirm that the mutation in *LOC_Os11g26130* is responsible for the *oswss1* mutant phenotype. The complementation vector pCAMBIA1300:*OsWSS1* with a WT genomic fragment containing the entire coding region of *OsWSS1* along with 2.3 kb upstream sequence and 1.1 kb downstream sequence was constructed and transformed into the *oswss1*-derived callus through *Agrobacterium tumefaciens*-mediated transformation. A total of 25 transgenic lines were generated, among them, 19 independent and positive complementary lines (including *pWSS1-C1*) exhibited the WT normal leaf phenotype (**Figures 4E,F** and **Supplementary Figure 4A**). Sequencing revealed that the *pWSS1-C1* transgenic line was heterozygous for the *oswss1* mutation in the T0 transgenic plant (**Supplementary Figure 4B**). There was no significant difference

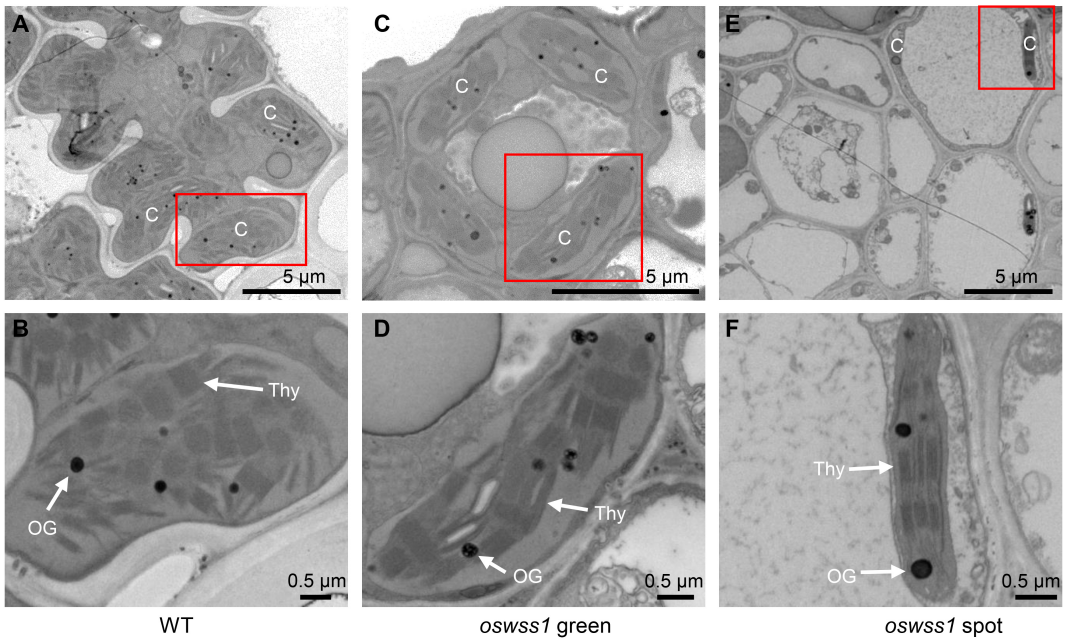

FIGURE 3 | Comparison of chloroplast ultrastructural between wild type (WT) and *oswss1* leaves at the tillering stage (87 DAS). Transmission electron microscopy (TEM) was used to detect the chloroplasts ultrastructural in WT leaves **(A,B)**, *oswss1* green sectors **(C,D)** and *oswss1* spot sectors **(E,F)**. C, chloroplast; OG, osmiophilic plastoglobuli; Thy, thylakoid. The red box indicates the area magnified.

in the leaf width, chlorophyll content, and RWC between the WT and *pWSS1-C1* complementary lines (**Figures 4G–I**). Furthermore, the plant height, panicle length, 1,000-grain weight, and seed-setting rate of 10 *pWSS1-C* complementary lines tested were recovered to the WT level (**Supplementary Figures 5A–E** and **Supplementary Table 5**). Quantitative real-time PCR (qRT-PCR) analysis revealed that expression of *OsWSS1* in *oswss1* was similar to that of the WT plants, whereas the relative transcript level of *OsWSS1* was markedly increased in the *pWSS1-C1* compared with that in the WT and *oswss1* plants (**Supplementary Figure 5F**), indicating that the phenotype of *oswss1* is not caused by the difference in *OsWSS1* expression. Taken together, these data confirmed that the mutation of *LOC_Os11g26130* was responsible for the early leaf senescence phenotype of *oswss1*.

OsWSS1 Encodes a TMK1 Type LRR-RLK

According to the RAP-DB database[4], the coding sequence of *OsWSS1* is composed of 2 exons with 2739 bp of cDNA sequence. Using the deduced OsWSS1 protein sequence as a query to search on the NCBI database[5], an identical protein which annotated as receptor protein kinase TMK1 was found. TMK1 belongs the LRR-RLK subfamily of the RLK family. SMART (see Text Footnote 2) analysis showed that OsWSS1 contains an N-terminal signal peptide domain (SP), seven LRR domains, a transmembrane domain (TM), and a serine/threonine kinase domain (**Figure 5A** and **Supplementary Figure 6**).

A total of 27 OsWSS1 homologous proteins (more than 60% identity with OsWSS1) were identified from different plant species to determine their evolutionary relationship. Phylogenetic analysis showed that OsWSS1 homologs were conserved in both monocots and dicots, and *OsWSS1* was closely related to the homologous genes in *S. bicolor*, *Z. mays*, and *T. aestivum* (**Figure 5C**). In addition, multiple alignment analysis of protein sequences revealed that most OsWSS1-like proteins have a highly conserved serine/threonine kinase domain (**Supplementary Figure 7**). Multiple sequence alignment and motif analysis revealed that the Leu396Pro amino acid substitution site in the *oswss1* mutant was located in a highly conserved LRR region (**Figure 5B**), suggesting that this site is critical for the function of OsWSS1.

OsWSS1 Is Constitutively Expressed and the Encoded Protein Localizes to the Plasma Membrane

The qRT-PCR was performed to detect the relative expression level of *OsWSS1* in different organs of the WT plants. *OsWSS1* was constitutively expressed in all tissues at young seedlings stage and heading stage, its expression level was relatively lower in roots, stems, and panicles, and relatively higher in leaves (**Figure 6A**). To further assess the transcript level of *OsWSS1* during leaf senescence, we tested *OsWSS1* expression in WT leaves at different developmental stages by qRT-PCR.

[4]https://rapdb.dna.affrc.go.jp/#

[5]https://www.ncbi.nlm.nih.gov/

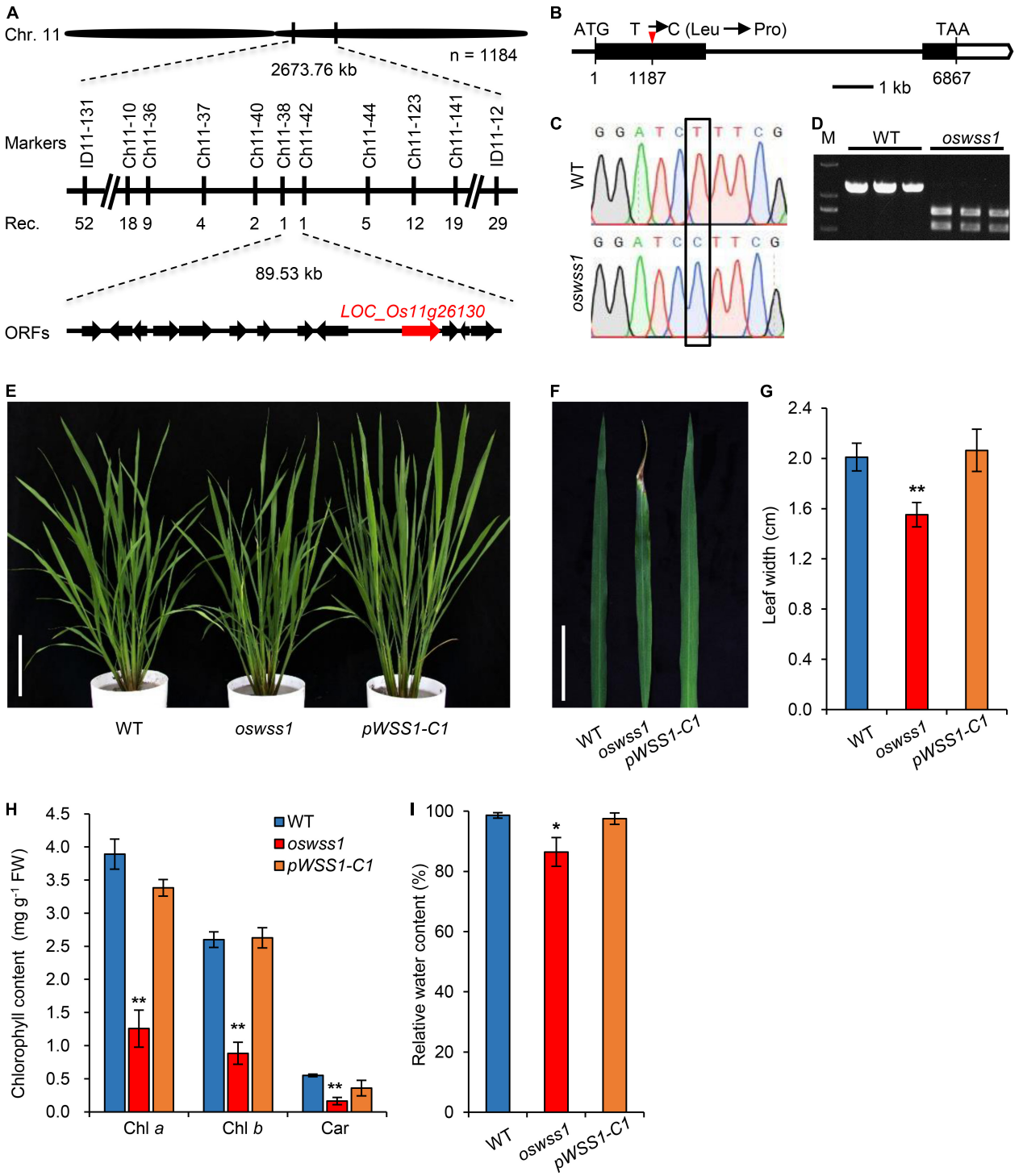

FIGURE 4 | Map-based cloning of *OsWSS1* and complementation test. **(A)** Fine mapping of *OsWSS1*. The *OsWSS1* locus was mapped to an 89.53 kb genomic region on chromosome 11 between markers Ch11-38 and Ch11-42. The molecular markers and recombinant numbers are displayed. **(B)** The structure and mutation site in *OsWSS1*. The white boxes, black boxes, and black lines represent untranslated regions, exons, and introns, respectively. **(C)** DNA sequencing to confirm the point mutation of the *OsWSS1* in the *oswss1* mutant. The black box indicates the mutation position. **(D)** Confirmation of the mutation by cleaved amplified polymorphic sequence. PCR products from *oswss1* were digested by *Bam*HI while PCR products from wild type (WT) were not digested by *BamH*1. **(E)** The plant morphology among WT, *oswss1,* and complementation transgenic line at the initial tillering stage (60 DAS). Scale bar = 15 cm. **(F)** Leaf morphology among WT, *oswss1* and complementation transgenic line at the tillering stage. Scale bar = 5 cm. **(G)** Comparison of leaf width of WT, *oswss1,* and complementation plants. **(H)** Comparison of chlorophyll content of WT, *oswss1,* and complementation plants. **(I)** Relative water content among WT, *oswss1,* and complementation leaves. Values are mean ± SD (n = 6). *P < 0.05, **P < 0.01 (Student's t-test).

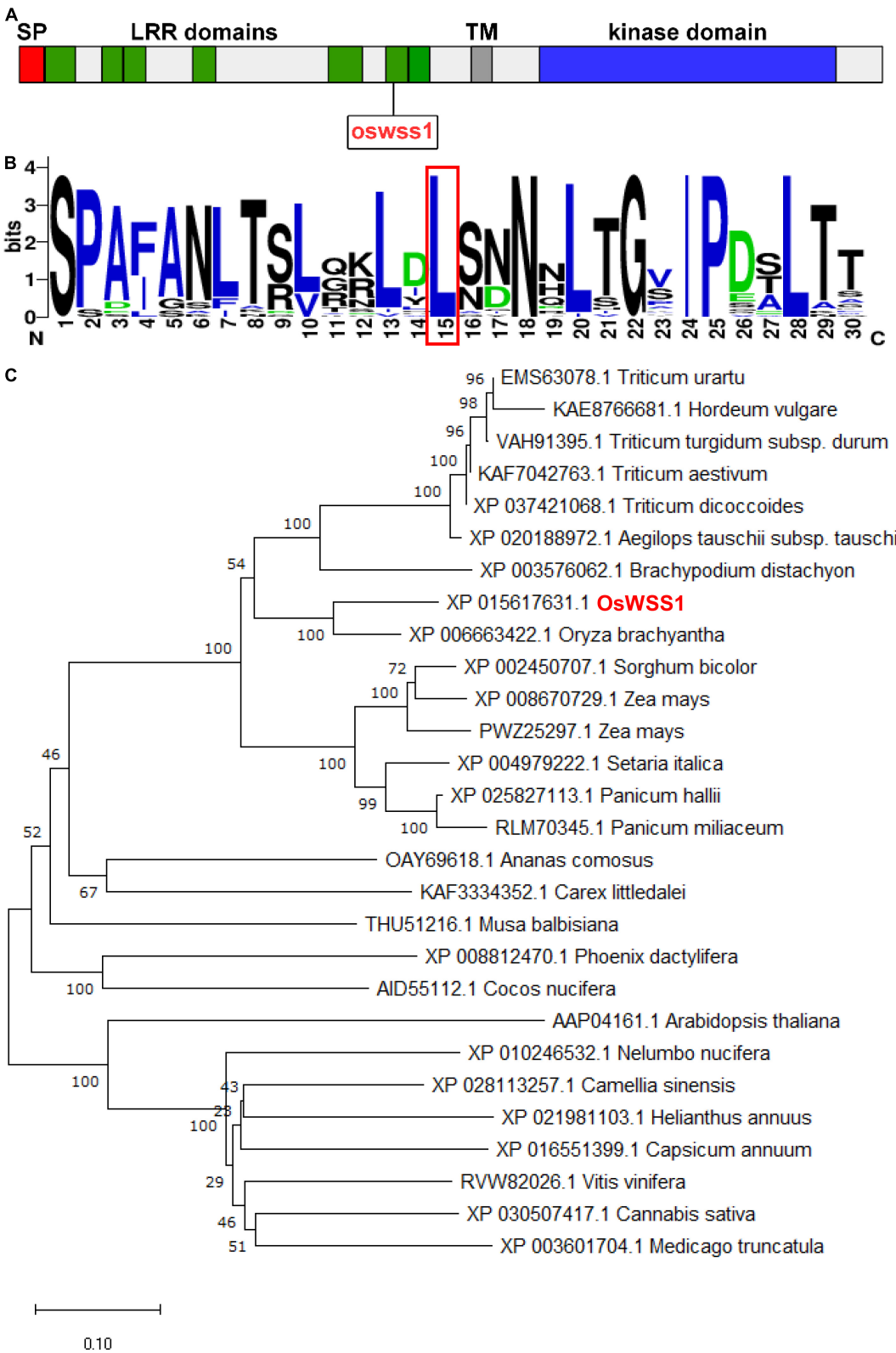

FIGURE 5 | Phylogenic analysis of OsWSS1. **(A)** Schematic diagram of the OsWSS1 protein. SP, signal peptide; LRR domain, leucine-rich repeat region; TM, transmembrane domain. The rectangle indicates the position of the point mutation of the *OsWSS1* in the *oswss1* mutant. **(B)** Conservation analysis of the amino acid substitution region and the frequency of the 50 homologous genes. The red-boxed region indicates the position of the amino acid transition. **(C)** Phylogenetic tree of the OsWSS1 protein. OsWSS1 is highlighted in red. The phylogenetic tree was constructed using MEGA 7.0 with the neighbor-joining method and 1,000 bootstrap replicates.

The *OsWSS1* transcript levels were not significantly different in various ages and regions of WT leaves (**Supplementary Figure 8**), indicating that *OsWSS1* is not induced by senescence.

Using the Cell-PLoc 2.0 program[6], OsWSS1 was predicted to be localized in plasma membrane. To confirm OsWSS1 localization, the expression vector of the *OsWSS1* and *eGFP* fusion was constructed and co-expressed with the plasma membrane marker PIP2-mCherry (Heng et al., 2018) in rice leaf sheath protoplasts (**Figure 6B**). Confocal laser-scanning microscopy revealed that the green fluorescent signal of OsWSS1-eGFP was indeed colocalized with PIP2 on the plasma membrane, while the negative control, 35S-eGFP, was localized at both the cytoplasm and nucleus (**Figures 6C–G**). Similar results were obtained in *Nicotiana benthamiana* leaf epidermal cells (**Figures 6H–L**). These results demonstrated that OsWSS1 is a plasma membrane protein.

Mutation of *OsWSS1* Causes Early Leaf Senescence and Premature Cell Death

Besides the water-soaked spots on leaves, *oswss1* mutant displays early leaf senescence (**Figure 7A**). The *oswss1* leaves exhibit water-soaked spots which subsequently developed into necrotic symptoms. Since the expression levels of many *SAGs* will change during leaf senescence, we determined the expression levels of *SAGs* in *oswss1* and WT plants by qRT-PCR. Results showed that the expression levels of all tested *SAGs* were significantly upregulated in *oswss1* (**Figure 7B**). In addition, the content of the lipid peroxidation product MDA was increased in *oswss1* by 1.4 times as compared with the WT (**Figure 7C**).

Trypan blue is an indicator of leaf cell death. After trypan blue staining, large area of the *oswss1* leaves was stained blue while only small area of the WT leaves was stained blue (**Figure 7D**). The TUNEL assay can detect DNA fragmentation that results from apoptotic signaling cascades by labeling the terminal end of nucleic acids. We accordingly used TUNEL assays to determine cell death in the *oswss1* mutant. As expected, there were few TUNEL positive signal spots in the WT leaves, whereas there were many strong and high TUNEL positive signals in *oswss1* leaves (**Figure 7E** and **Supplementary Figure 9**). These data indicated that DNA damage was more serious in *oswss1* leaves compared with that of WT leaves. Overall, these results suggested that the *oswss1* mutant stimulated premature cell death (PCD) and accelerated the leaf senescence.

Reactive Oxygen Species Is Highly Accumulated in the *Oswss1* Leaves

The ROS accumulation usually causes severe damage to most tissues and cells in plant leaves, leading to leaf senescence (Khanna-Chopra, 2012; Xu et al., 2022). To detect the ROS level in the water-soaked spots of the *oswss1* mutant, we used DAB and NBT staining to detect H_2O_2 and O_2^- accumulation, respectively. The *oswss1* leaves showed dark brownish red color while the WT leaves exhibited white color after DAB staining (**Figure 8A**). NBT stained blue spots were densely distributed in the *oswss1* leaves and sparsely distributed in WT leaves (**Figure 8B**). We also measured the H_2O_2 concentration in the leaves and results showed the H_2O_2 content in *oswss1* leaves was increased by 40.4% compared with that of WT leaves at the tillering stage (**Figure 8C**). These data showed that ROS accumulated at a higher level in *oswss1* leaves compared with that of WT. To determine whether hyper-accumulation of ROS would activate the antioxidant enzymes, the activities of SOD and CAT were detected. The activities of SOD and CAT of *oswss1* leaves were significantly lower compared with that of the WT control (**Figures 8D,E**). Our findings suggested that mutation of *OsWSS1* results in ROS accumulation in rice leaves.

The Expression of Genes Related to Chloroplast Development, Chlorophyll Synthesis and Photosynthesis Altered in *Oswss1* Mutant

To investigate the role of OsWSS1 in chloroplast development, the expression of genes related to chloroplast development and photosynthesis (*psaA*, *psbA*, *rbcL*, *rbcS*, *Cab1R*, *Cab2R*, *RpoA*, and *RpoB*) (Huang et al., 2020) was compared between WT and *oswss1* leaves. The expression of all the tested genes except *RpoA* was significantly lower in *oswss1* as compared with that of the WT (**Figure 9A**). Since the chlorophyll content of *oswss1* decreased (**Figure 1B**), the expression of 12 chlorophyll biosynthesis-related genes (*HEMA*, *HEMC*, *HEMD*, *HEME*, *OsPORA*, *OsPORB*, *OsCAO1*, *OsCAO2*, *V1*, *V2*, *OsDVR*, and *OschlH*) were compared between WT and *oswss1* leaves. The expression of chloroplast biosynthesis-related genes, such as *OsPORB* (Sakuraba et al., 2013), *OsCAO1* (Lee S. et al., 2005), *OsCAO2* (Lee S. et al., 2005), and *V2* (Sugimoto et al., 2007), were significantly less in *oswss1* leaves than that of the WT (**Figure 9B**). These data suggest the *OsWSS1* mutation (Leu396Pro amino acid substitution) affects the expression of genes related to chloroplast development, photosynthesis, and chloroplast biosynthesis. These results also imply that OsWSS1 is involved in chloroplast development in rice.

DISCUSSION

OsWSS1 Encodes a Transmembrane Kinases Which Is Essential for Normal Growth and Development of Rice

Despite the extensive studies of some RLKs (including TMK) on regulation of plant growth and development (Clark et al., 1997; Diévart and Clark, 2004; Lee L. Y. et al., 2012; He et al., 2021), up to the present, the function of TMK controlling plant leaf senescence and cell death remains unknown. In this study, we have revealed that rice OsWSS1, a TMK protein, affects plant leaf senescence and cell death. The mutant *oswss1* showed reduced chlorophyll content, abnormal chloroplast development, reduced plant height, reduced seed-setting rate, and decreased 1,000-grain weight (**Figures 1–3** and **Supplementary Figure 1**). Unlike rice, there is no significant difference of plant growth and development between *Arabidopsis TMK* T-DNA insertion

[6]http://www.csbio.sjtu.edu.cn/bioinf/Cell-PLoc-2/

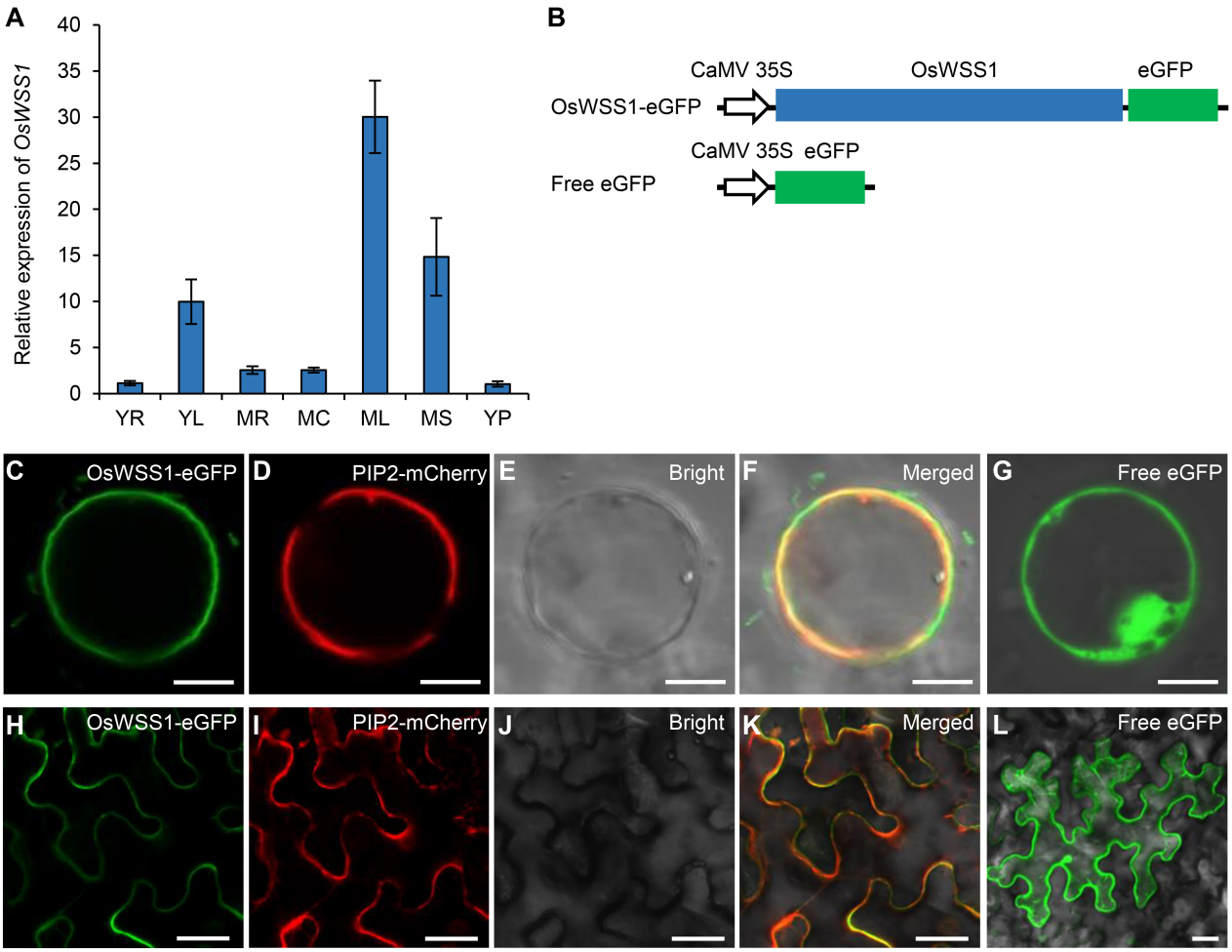

FIGURE 6 | Expression pattern of *OsWSS1* and subcellular localization of the OsWSS1-eGFP protein. **(A)** Expression pattern of *OsWSS1* in different tissues of the wild type plants. YR, Young root; YL, young leaf; MR, mature root; MC, mature culm; ML, mature leaf; MS, mature sheath; YP, young panicle. *OsWSS1* expression was normalized using the *OsActin* gene as an internal control. *OsWSS1* expression of YR was normalized to 1 after the normalization with the value of *OsActin*. Values are mean ± SD (n = 3). **(B)** A schematic diagram of the constructs used for subcellular localization. **(C–F)** Subcellular localization of OsWSS1 in rice protoplast. The fusion protein (OsWSS1-eGFP) **(C)** was co-expressed with the plasma membrane marker (PIP2-mCherry) **(D)**. **(G)** Subcellular localization of the control (Free-eGFP) in rice protoplast. **(H–K)** Subcellular localization of OsWSS1 in epidermal cell of *Nicotiana benthamiana* leaves. The fusion protein (OsWSS1-eGFP) **(H)** was co-expressed with the plasma membrane marker (PIP2.1-mCherry) **(I)**. **(L)** Subcellular localization of the control (Free-eGFP) epidermal cell of *N. benthamiana* leaves. Scale bars: 5 μm **(C–G)**; 15 μm **(H–L)**.

single mutant and the wild type (Dai et al., 2013). This is possibly due to the difference of redundancy of TMK genes between *Arabidopsis* and rice. There are four *TMK* genes in *Arabidopsis* (Dai et al., 2013) but only one *TMK* gene in rice genome. The mutant phenotype of *oswss1* was complemented by expressing the wild type *OsWSS1* gene (**Figure 4** and **Supplementary Figure 4**), demonstrating that OsWSS1 plays an important role in the growth and development of rice plants.

OsWSS1 Is Involved in the Leaf Epidermal Development and Chloroplast Development in Rice Leaves

The lesion-mimic and necrotic lesion in the leaf suggested that major changes in cell structure have occurred (Qiu et al., 2019; Cui et al., 2021). In this study, we observed changes in leaf cell structure between *oswss1* and WT plants. Paraffin section showed atrophy in the BCs and MCs in the water-soaked zone of *oswss1* leaves compared to the WT leaves (**Figure 2B**). Light microscope revealed the abnormal leaf epidermal cell shape in *oswss1* and the significantly changed cell structure (**Supplementary Figure 3**). It has been reported that the defective leaf epidermis is the main contributors to leaf rolling (Li et al., 2017). Thus, the rolled *oswss1* leaves may be caused by the defective leaf cell development in the epidermis. Moreover, the surface of water-soaked spots was severely shrunk in *oswss1* leaves (**Figures 2E–G**). The shrunken BCs (**Figure 2B**) explained the wrinkled leaf epidermal cell shape (**Figure 2G** and **Supplementary Figure 3**) observed on the *oswss1* mutant. Stomata is a key channel for water and

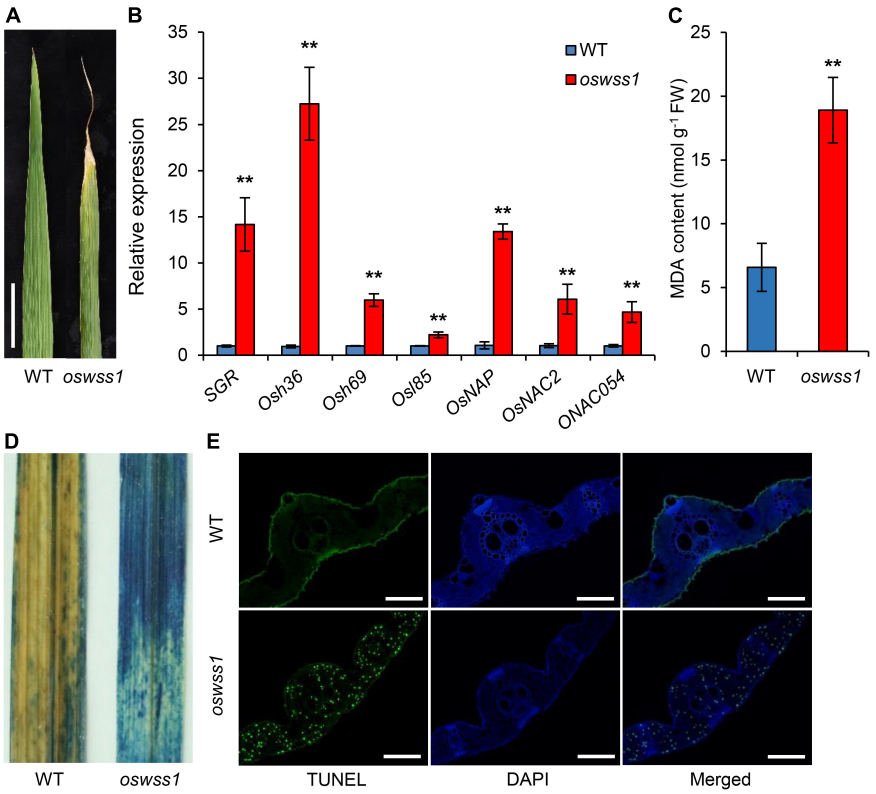

FIGURE 7 | Mutation of *OsWSS1* causes early leaf senescence and premature cell death. **(A)** Leaf morphology between wild type (WT) and *oswss1* plants at the heading stage (118 DAS). Scale bar = 4 cm. **(B)** Transcriptional level analysis of senescence-related genes between WT and *oswss1* plants at the tillering stage (87 DAS) by qRT-PCR. *OsActin* was used as an internal control. The gene expression of WT was normalized to 1 after the normalization with the value of *OsActin*. Values are mean ± SD (n = 3). $^{**}P < 0.01$ (Student's t-test). **(C)** Comparison of the malondialdehyde (MDA) contents between WT and *oswss1* leaves at the tillering stage. Values are mean ± SD (n = 6). $^{**}P < 0.01$ (Student's t-test). **(D)** The trypan blue staining of leaves between WT and *oswss1* plants at the tillering stage. **(E)** TUNEL assay of WT and *oswss1* leaves at the tillering stage. Blue signal is 4′,6-diamino-phenylindole (DAPI) staining, green fluorescence represents TUNEL-positive signals. Scale bars = 50 μm.

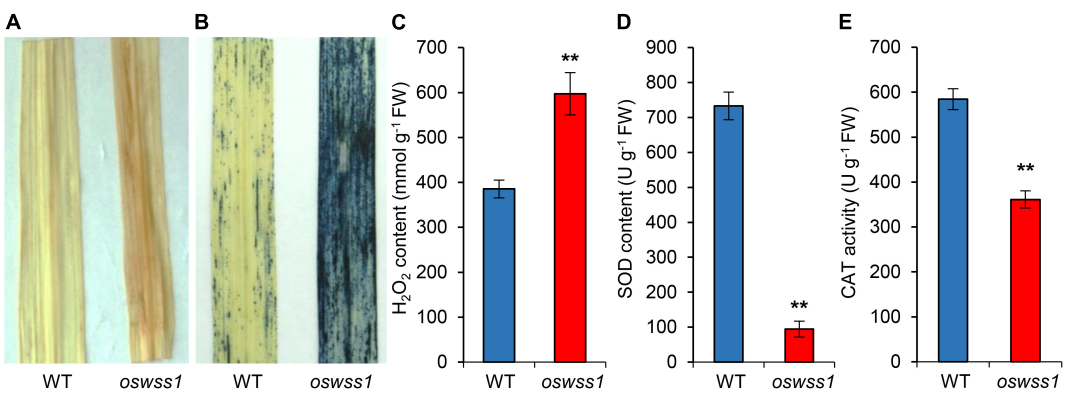

FIGURE 8 | Reactive oxygen species is highly accumulated in the *oswss1* leaves at the tillering stage (87 DAS). **(A)** 3,3′-diaminobenzidine (DAB) staining of leaves between wild type (WT) and *oswss1* plants. **(B)** The nitroblue tetrazolium (NBT) staining of leaves between WT and *oswss1* plants. **(C–E)** Quantification of H_2O_2 contents **(C)**, SOD activity **(D)**, and CAT activity **(E)** in leaves between the WT and *oswss1* plants. Values are mean ± SD (n = 6). $^{**}P < 0.01$ (Student's t-test).

gas exchange, which acts an important role to regulate water evapotranspiration and water utilization (Buckley, 2005). The *es1* (*early senescence1*) (Rao et al., 2015) and *ospls1* (*Oryza sativa premature leaf senescence 1*) (Yang X. et al., 2016) mutants exhibited excessive water loss due to increased stomatal density. However, the *oswss1* mutant exhibited lower stomatal density,

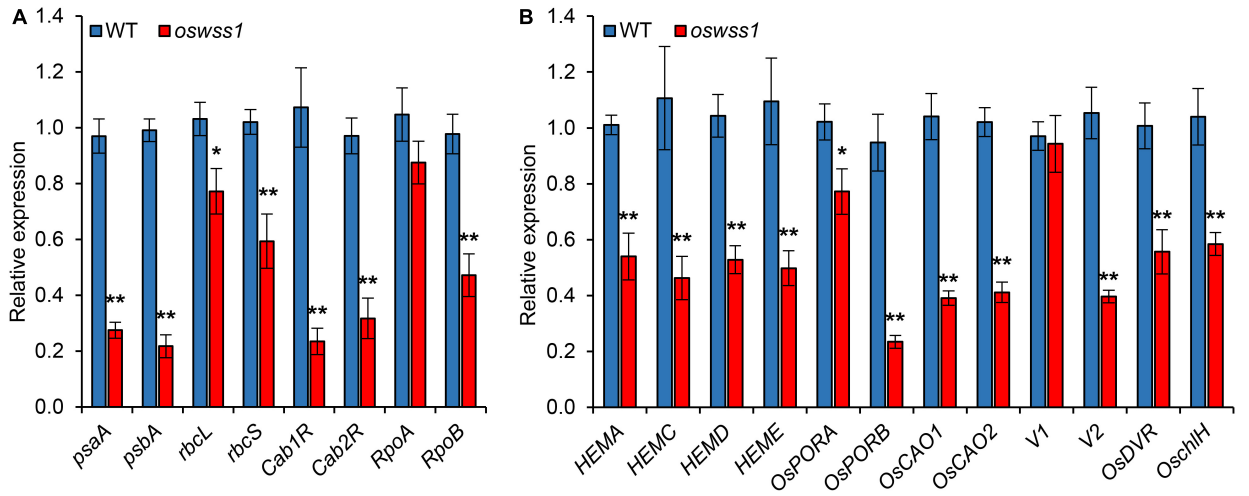

FIGURE 9 | The expression of genes related to chloroplast development, chlorophyll synthesis and photosynthesis altered in *oswss1* mutant at the tillering stage (87 DAS) by qRT-PCR. **(A)** The expression of genes involved in photosynthesis between wild type (WT) and *oswss1* mutant. **(B)** Transcriptional level analysis of expression of genes involved in chlorophyll synthesis and chloroplast development between WT and *oswss1* mutant. *OsActin* was used as an internal control. The gene expression of WT was normalized to 1 after the normalization with the value of *OsActin*. Values are mean ± SD ($n = 3$). $^*P < 0.05$, $^{**}P < 0.01$ (Student's *t*-test).

altered stomatal morphology, and decreased cuticular papillae (**Figures 2E–H**), indicating that the water evapotranspiration capacity was reduced in *oswss1*. We speculate that the weakening of water transpiration leads to transpiration force reduction and organic transport obstruction, then would obstruct the leaf normal physiological activities, resulting in water-soaked spots of leaves.

Another typical feature of lesion formation is the change of chloroplast development and the chloroplast degradation (Cui et al., 2021). The chlorophyll content in the water-soaked spots of *oswss1* decreased by 30% compared to the WT (**Figure 1B**). In general, changes in chlorophyll content are associated with chloroplast development in rice (Zhang et al., 2017; Cui et al., 2019; Sun et al., 2019; He et al., 2020). As expected, TEM observation showed that chloroplast development was impaired, chloroplast number was reduced, and there were more degraded chloroplasts in the water-soaked zone of *oswss1* compared with that of the WT and the green part of *oswss1* plants (**Figure 3**). The formation of a functional chloroplast requires the coordinated expression of nuclear and chloroplastic genes (He et al., 2018; Chen et al., 2019). This process involves two types of RNA polymerases, nucleus-encoded polymerase (NEP) and plastid-encoded polymerase (PEP) (Jarvis and López-Juez, 2013). PEP transcribes chloroplast genes involved in photosynthesis, such as *psaA*, *psbA*, and *rbcL*; NEP largely transcribes housekeeping genes, such as *rpoA* and *rpoB*, which regulate plastid development at the early stages of plant growth (Shiina et al., 2005). In this study, we found the transcripts of PEP-dependent genes were significantly decreased, and the expression of chlorophyll synthesis-associated genes, including *HEMA*, *HEMC*, *HEMD*, *HEME*, *OsPORA*, *OsPORB*, *OsCAO1*, *OsCAO2*, *V2*, *OsDVR*, and *OschlH*, were also downregulated in the *oswss1* mutant (**Figure 9**). Overall, these results indicate that OsWSS1 may play a vital role in regulating leaf epidermal development and chloroplast development.

Mutation of *OsWSS1* Promotes Reactive Oxygen Species Hyper-Accumulation and Cell Death

Reactive oxygen species are important signaling molecules and able to interact with many kinds of target molecules and metabolites, like DNA, proteins, lipids, and other cellular molecules, ROS accumulation can highly oxidative damage in cell structure and cellular components (Triantaphylidès et al., 2008; Ge et al., 2015). The *oswss1* exhibited hyper-accumulation of ROS in the water-soaked spots manifested by NBT and DAB staining, and measurement of H_2O_2 concentration (**Figures 8A–C**). ROS is generally in a dynamic balance in plant cells, and its content is determined by the delicate balance between ROS scavenging and ROS generation (Hu et al., 2011). SOD is the first defense line of plant ROS scavenging system to remove O_2^- in the cell. CAT is another main ROS scavenging enzyme which catalyzes H_2O_2 to form H_2O and O_2 (Scandalios, 2002; Mittler et al., 2004). The activities of SOD and CAT were decreased in *oswss1* leaves (**Figures 8D,E**), suggesting that the hyper-accumulation of ROS may be caused by the reduction in the activity of these two key enzymes, thereby resulting in the water-soaked spots phenotype of *oswss1*. Taken together, these findings suggest that OsWSS1 plays a key role in maintaining ROS homeostasis during rice leaf development and chloroplast development. In addition, ROS can act as a signal to activate defense and offer wide possibilities for broad-spectrum disease resistance (Qi et al., 2017), future studies can examine whether OsWSS1 is involved in the disease resistance in rice.

Reactive oxygen species are also important factors in triggering early leaf senescence and PCD in plants (Loor et al., 2010; Wang et al., 2013; Mittler, 2017; Chen et al., 2021). The *oswss1* mutant exhibited remarkable increased amounts of oxidative-stress-induced toxic compound MDA, enhanced PCD (**Figures 7C–E** and **Supplementary Figure 9**). During leaf senescence, the expression of some *SAGs* is promoted (Lim et al., 2007; Yang et al., 2020). The results also showed that the expression levels of *SAGs*, *SGR* (Jiang et al., 2011), *Osh36*, *Osh69*, *Osl85* (Lee et al., 2001), *OsNAP* (Liang et al., 2014), *OsNAC2* (Mao et al., 2017), and *ONAC054* (Sakuraba et al., 2020) were significantly upregulated in the *oswss1* mutant (**Figure 7B**). Collectively, we predicted that the early leaf senescence of *oswss1* was caused by ROS-mediated PCD. In addition, leaf senescence is also influenced by various phytohormones, including abscisic acid (ABA) and jasmonic acid (JA) (Lim et al., 2007; Liang et al., 2014). The *Arabidopsis* TMK1 and TMK4 act as key regulators in the signaling cascades of ABA (Li et al., 2021; Yang et al., 2021); the *Nicotiana tabacum NtTMK1* was strongly induced by the treatment with JA (Cho and Pai, 2000), thus it is possible that *OsWSS1* is involved in the regulation of leaf senescence partially by modulating the signaling responses of phytohormones.

The Putative Molecular Mechanism of OsWSS1 in Regulation of Reactive Oxygen Species Homeostasis

Plant LRR-RLKs are important membrane receptors that regulate plant development by sensing various ligands (Man et al., 2020). The LRR domain binds to ligands and transmits extracellular signals to the downstream (Chen, 2021). There was a point mutation in the 7th LRR domain of OsWSS1, in which the hydrophobic residue Leu396 was replaced by Pro amino acid in *oswss1* mutant (**Figure 5B** and **Supplementary Figure 7**). The hydrophobic residues play key roles in protein folding, ligand-protein and protein–protein binding, protein-nucleic acid interactions (Southall et al., 2002; Matsushima et al., 2005). Several pieces of evidence suggest that LRR-RLKs play a role in ROS homeostasis (Ouyang et al., 2010; Lin et al., 2020). Overexpression of *OsSIK2* in rice reduced ROS accumulation by enhancing the activities of POD, SOD, and CAT (Ouyang et al., 2010). *OsSTLK*-overexpressing rice plants remarkably reduced ROS concentration by upregulating ROS-scavenging activities (Lin et al., 2020). In this study, the *oswss1* mutant exhibits hyper-accumulation of ROS and lower SOD and CAT activities (**Figures 8C–E**). The expression levels of *OsWSS1* were not significantly different between WT and *oswss1* mutant (**Supplementary Figure 5F**), and there was no distinct difference in *OsWSS1* expression during leaf senescence (**Supplementary Figure 8**), suggesting that the expression level of *OsWSS1* may not affect the aging process. Based on these results, we speculate that OsWSS1 probably stimulates the activities of the SOD or CAT and regulates ROS homeostasis through phosphorylation and activation of unknown proteins.

DATA AVAILABILITY STATEMENT

The original contributions presented in the study are included in the article/**Supplementary Material**, further inquiries can be directed to the corresponding authors.

AUTHOR CONTRIBUTIONS

KZ, JX, CW, and ZJ conceived and designed the research. JX, FX, FW, and YZ performed the experiments. TZ, ZJ, YT, and ZW participated in data analysis. JX, KZ, and TZ wrote the manuscript. All authors contributed to the article and approved the submitted version.

FUNDING

This work was supported by grants from the National Science Foundation of China (U20A2035 to KZ), National Natural Science Foundation of China (31801729 to ZJ), and the Innovation Program of Chinese Academy of Agricultural Sciences to KZ and CW.

SUPPLEMENTARY MATERIAL

The Supplementary Material for this article can be found online at: https://www.frontiersin.org/articles/10.3389/fpls.2022.918673/full#supplementary-material

REFERENCES

Bella, J., Hindle, K. L., Mcewan, P. A., and Lovell, S. C. (2008). The leucine-rich repeat structure. *Cell. Mol. Life Sci.* 65, 2307–2333. doi: 10.1007/s00018-008-8019-0

Buckley, T. N. (2005). The control of stomata by water balance. *New Phytol.* 168, 275–292. doi: 10.1111/j.1469-8137.2005.01543.x

Chen, D., Qiu, Z., He, L., Hou, L., Li, M., Zhang, G., et al. (2021). The rice LRR-like1 protein YELLOW AND PREMATURE DWARF 1 is involved in leaf senescence induced by high light. *J. Exp. Bot.* 72, 1589–1605. doi: 10.1093/jxb/eraa532

Chen, L., Huang, L., Dai, L., Gao, Y., Zou, W., Lu, X., et al. (2019). *PALE-GREEN LEAF12* encodes a novel pentatricopeptide repeat protein required for chloroplast development and 16S rRNA processing in rice. *Plant Cell Physiol.* 60, 587–598. doi: 10.1093/pcp/pcy229

Chen, T. (2021). Identification and characterization of the LRR repeats in plant LRR-RLKs. *BMC Mol. Cell Biol.* 22:9. doi: 10.1186/s12860-021-00344-y

Chen, Y., Xu, Y., Luo, W., Li, W., Na, C., and Chong, Z. K. (2013). The F-box protein OsFBK12 targets OsSAMS1 for degradation and affects pleiotropic phenotypes, including leaf senescence, in rice. *Plant Physiol.* 163, 1673–1685. doi: 10.1104/pp.113.224527

Cho, H. S., and Pai, H. S. (2000). Cloning and characterization of *NtTMK1* gene encoding a TMK1-homologous receptor-like kinase in tobacco. *Mol. Cells* 10, 317–324. doi: 10.1016/S0014-5793(00)01678-1

Clark, S. E., Williams, R. W., and Meyerowitz, E. M. (1997). The *CLAVATA1* gene encodes a putative receptor kinase that controls shoot and floral meristem size in Arabidopsis. *Cell* 89, 575–585. doi: 10.1016/s0092-8674(00)80239-1

Crooks, G. E., Hon, G., Chandonia, J. M., and Brenner, S. E. (2004). WebLogo: a sequence logo generator. *Genome Res.* 14, 1188–1190. doi: 10.1101/gr.849004

Cui, X., Wang, Y., Wu, J., Han, X., Gu, X., Lu, T., et al. (2019). The RNA editing factor DUA1 is crucial to chloroplast development at low temperature in rice. *New Phytol.* 221, 834–849. doi: 10.1111/nph.15448

Cui, Y., Peng, Y., Zhang, Q., Xia, S., Ruan, B., Xu, Q., et al. (2021). Disruption of *EARLY LESION LEAF 1*, encoding a cytochrome P450 monooxygenase, induces ROS accumulation and cell death in rice. *Plant J.* 105, 942–956. doi: 10.1111/tpj.15079

Dai, N., Wang, W., Patterson, S. E., and Bleecker, A. B. (2013). The TMK subfamily of receptor-like kinases in Arabidopsis display an essential role in growth and a reduced sensitivity to auxin. *PLoS One* 8:e60990. doi: 10.1371/journal.pone.0060990

Diévart, A., and Clark, S. E. (2004). LRR-containing receptors regulating plant development and defense. *Development* 131, 251–261. doi: 10.1242/dev.00998

Domínguez, F., and Cejudo, F. J. (2021). Chloroplast dismantling in leaf senescence. *J. Exp. Bot.* 72, 5905–5918. doi: 10.1093/jxb/erab200

Foyer, C. H., and Noctor, G. (2005). Redox homeostasis and antioxidant signaling: a metabolic interface between stress perception and physiological responses. *Plant Cell* 17, 1866–1875. doi: 10.1105/tpc.105.033589

Gao, Y., Jia, S., Wang, C., Wang, F., Wang, F., and Zhao, K. (2016). BjMYB1, a transcription factor implicated in plant defence through activating *BjCHI1* chitinase expression by binding to a W-box-like element. *J. Exp. Bot.* 67, 4647–4658. doi: 10.1093/jxb/erw240

Ge, C. W., Zhi-Guo, E., Pan, J. J., Jiang, H., Zhang, X. Q., Zeng, D. L., et al. (2015). Map-based cloning of a spotted-leaf mutant gene *OsSL5* in Japonica rice. *Plant Growth Regul.* 75, 595–603. doi: 10.1007/s10725-014-9962-4

Gish, L. A., and Clark, S. E. (2011). The RLK/Pelle family of kinases. *Plant J.* 66, 117–127. doi: 10.1111/j.1365-313X.2011.04518.x

He, L., Zhang, S., Qiu, Z., Zhao, J., Nie, W., Lin, H., et al. (2018). FRUCTOKINASE-LIKE PROTEIN 1 interacts with TRXz to regulate chloroplast development in rice. *J. Integr. Plant Biol.* 60, 94–111. doi: 10.1111/jipb.12631

He, Y., Shi, Y., Zhang, X., Xu, X., Wang, H., Li, L., et al. (2020). The OsABCI7 transporter interacts with OsHCF222 to stabilize the thylakoid membrane in rice. *Plant Physiol.* 184, 283–299. doi: 10.1104/pp.20.00445

He, Z., Zou, T., Xiao, Q., Yuan, G., Liu, M., Tao, Y., et al. (2021). An L-type lectin receptor-like kinase promotes starch accumulation during rice pollen maturation. *Development* 148, dev196378. doi: 10.1242/dev.196378

Heng, Y., Wu, C., Long, Y., Luo, S., Ma, J., Chen, J., et al. (2018). OsALMT7 maintains panicle size and grain yield in rice by mediating malate transport. *Plant Cell* 30, 889–906. doi: 10.1105/tpc.17.00998

Hong, Y., Zhang, Y., Sinumporn, S., Yu, N., Zhan, X., Shen, X., et al. (2018). Premature leaf senescence 3, encoding a methyltransferase, is required for melatonin biosynthesis in rice. *Plant J.* 95, 877–891. doi: 10.1111/tpj.13995

Hu, L., Liang, W., Yin, C., Cui, X., Zong, J., Wang, X., et al. (2011). Rice MADS3 regulates ROS homeostasis during late anther development. *Plant Cell* 23, 515–533. doi: 10.1105/tpc.110.074369

Huang, L., Sun, Q., Qin, F., Li, C., Zhao, Y., and Zhou, D. X. (2007). Down-regulation of a *SILENT INFORMATION REGULATOR2*-related histone deacetylase gene, OsSRT1, induces DNA fragmentation and cell death in rice. *Plant Physiol.* 144, 1508–1519. doi: 10.1104/pp.107.099473

Huang, W., Zhang, Y., Shen, L., Fang, Q., Liu, Q., Gong, C., et al. (2020). Accumulation of the RNA polymerase subunit RpoB depends on RNA editing by OsPPR16 and affects chloroplast development during early leaf development in rice. *New Phytol.* 228, 1401–1416. doi: 10.1111/nph.16769

Jarvis, P., and López-Juez, E. (2013). Biogenesis and homeostasis of chloroplasts and other plastids. *Nat. Rev. Mol. Cell Biol.* 14, 787–802. doi: 10.1038/nrm3702

Jiang, H., Chen, Y., Li, M., Xu, X., and Wu, G. (2011). Overexpression of *SGR* results in oxidative stress and lesion-mimic cell death in rice seedlings. *J. Integr. Plant Biol.* 53, 375–387. doi: 10.1111/j.1744-7909.2011.01037.x

Khanna-Chopra, R. (2012). Leaf senescence and abiotic stresses share reactive oxygen species-mediated chloroplast degradation. *Protoplasma* 249, 469–481. doi: 10.1007/s00709-011-0308-z

Kinoshita, T., Caño-Delgado, A., Seto, H., Hiranuma, S., Fujioka, S., Yoshida, S., et al. (2005). Binding of brassinosteroids to the extracellular domain of plant receptor kinase BRI1. *Nature* 433, 167–171. doi: 10.1038/nature03227

Kong, Z., Li, M., Yang, W., Xu, W., and Xue, Y. (2006). A novel nuclear-localized CCCH-type zinc finger protein, OsDOS, is involved in delaying leaf senescence in rice. *Plant Physiol.* 141, 1376–1388. doi: 10.1104/pp.106.082941

Kusaba, M., Ito, H., Morita, R., Iida, S., Sato, Y., Fujimoto, M., et al. (2007). Rice NON-YELLOW COLORING1 is involved in light-harvesting complex II and grana degradation during leaf senescence. *Plant Cell* 19, 1362–1375. doi: 10.1105/tpc.106.042911

Lee, S., Seo, P. J., Lee, H. J., and Park, C. M. (2012). A NAC transcription factor NTL4 promotes reactive oxygen species production during drought-induced leaf senescence in Arabidopsis. *Plant J.* 70, 831–844. doi: 10.1111/j.1365-313X.2012.04932.x

Lee, L. Y., Hou, X., Fang, L., Fan, S., Kumar, P. P., and Yu, H. (2012). STUNTED mediates the control of cell proliferation by GA in Arabidopsis. *Development* 139, 1568–1576. doi: 10.1242/dev.079426

Lee, R. H., Wang, C. H., Huang, L. T., and Chen, S. C. (2001). Leaf senescence in rice plants: cloning and characterization of senescence up-regulated genes. *J. Exp. Bot.* 52, 1117–1121. doi: 10.1093/jexbot/52.358.1117

Lee, S., Kim, J. H., Yoo, E. S., Lee, C. H., Hirochika, H., and An, G. (2005). Differential regulation of *chlorophyll a oxygenase* genes in rice. *Plant Mol. Biol.* 57, 805–818. doi: 10.1007/s11103-005-2066-9

Li, L., Li, B., Zhu, S., Wang, L., Song, L., Chen, J., et al. (2021). TMK4 receptor kinase negatively modulates ABA signaling by phosphorylating ABI2 and enhancing its activity. *J. Integr. Plant Biol.* 63, 1161–1178. doi: 10.1111/jipb.13096

Li, W. Q., Zhang, M. J., Gan, P. F., Qiao, L., Yang, S. Q., Miao, H., et al. (2017). *CLD1/SRL1* modulates leaf rolling by affecting cell wall formation, epidermis integrity and water homeostasis in rice. *Plant J.* 92, 904–923. doi: 10.1111/tpj.13728

Li, Z., Zhang, Y., Zou, D., Zhao, Y., Wang, H. L., Zhang, Y., et al. (2020). LSD 3.0: a comprehensive resource for the leaf senescence research community. *Nucleic Acids Res.* 48, D1069–D1075. doi: 10.1093/nar/gkz898

Liang, C., Wang, Y., Zhu, Y., Tang, J., Hu, B., and Liu, L. (2014). OsNAP connects abscisic acid and leaf senescence by fine-tuning abscisic acid biosynthesis and directly targeting senescence-associated genes in rice. *Proc. Natl. Acad. Sci. U.S.A.* 111, 10013–10018. doi: 10.1073/pnas.1321568111

Lichtenthaler, H. K. (1987). Chlorophylls and carotenoids: Pigments of photosynthetic biomembranes. *Method. Enzymol.* 148, 350–382. doi: 10.1016/0076-6879(87)48036-1

Lim, P. O., Kim, H. J., and Nam, H. G. (2007). Leaf senescence. *Annu. Rev. Plant Biol.* 58, 115–136. doi: 10.1146/annurev.arplant.57.032905.105316

Lin, F., Li, S., Wang, K., Tian, H., Gao, J., Zhao, Q., et al. (2020). A leucine-rich repeat receptor-like kinase, OsSTLK, modulates salt tolerance in rice. *Plant Sci.* 296:110465. doi: 10.1016/j.plantsci.2020.110465

Lin, W., Zhou, X., Tang, W., Takahashi, K., Pan, X., Dai, J., et al. (2021). TMK-based cell-surface auxin signalling activates cell-wall acidification. *Nature* 599, 278–282. doi: 10.1038/s41586-021-03976-4

Livak, K. J., and Schmittgen, T. D. (2001). Analysis of relative gene expression data using real-time quantitative PCR and the 2(-Delta Delta C(T)) Method. *Methods* 25, 402–408. doi: 10.1006/meth.2001.1262

Loor, G., Kondapalli, J., Schriewer, J. M., Chandel, N. S., Vanden Hoek, T. L., and Schumacker, P. T. (2010). Menadione triggers cell death through ROS-dependent mechanisms involving PARP activation without requiring apoptosis. *Free Radic. Biol. Med.* 49, 1925–1936. doi: 10.1016/j.freeradbiomed.2010.09.021

Man, J., Gallagher, J. P., and Bartlett, M. (2020). Structural evolution drives diversification of the large LRR-RLK gene family. *New Phytol.* 226, 1492–1505. doi: 10.1111/nph.16455

Mao, C., Lu, S., Lv, B., Zhang, B., Shen, J., He, J., et al. (2017). A rice NAC transcription factor promotes leaf senescence *via* ABA biosynthesis. *Plant Physiol.* 174, 1747–1763. doi: 10.1104/pp.17.00542

Matsushima, N., Tachi, N., Kuroki, Y., Enkhbayar, P., Osaki, M., Kamiya, M., et al. (2005). Structural analysis of leucine-rich-repeat variants in proteins associated with human diseases. *Cell. Mol. Life Sci.* 62, 2771–2791. doi: 10.1007/s00018-005-5187-z

Mittler, R. (2017). ROS are good. *Trends Plant Sci.* 22, 11–19. doi: 10.1016/j.tplants.2016.08.002

Mittler, R., Vanderauwera, S., Gollery, M., and Van Breusegem, F. (2004). Reactive oxygen gene network of plants. *Trends Plant Sci.* 9, 490–498. doi: 10.1016/j.tplants.2004.08.009

Morillo, S. A., and Tax, F. E. (2006). Functional analysis of receptor-like kinases in monocots and dicots. *Curr. Opin. Plant Biol.* 9, 460–469. doi: 10.1016/j.pbi.2006.07.009

Morita, R., Sato, Y., Masuda, Y., Nishimura, M., and Kusaba, M. (2009). Defect in non-yellow coloring 3, an alpha/beta hydrolase-fold family protein, causes a stay-green phenotype during leaf senescence in rice. *Plant J.* 59, 940–952. doi: 10.1111/j.1365-313X.2009.03919.x

Ouyang, S. Q., Liu, Y. F., Liu, P., Lei, G., He, S. J., Ma, B., et al. (2010). Receptor-like kinase OsSIK1 improves drought and salt stress tolerance in rice (*Oryza sativa*) plants. *Plant J.* 62, 316–329. doi: 10.1111/j.1365-313X.2010.04146.x

Qi, J., Wang, J., Gong, Z., and Zhou, J. M. (2017). Apoplastic ROS signaling in plant immunity. *Curr. Opin. Plant Biol.* 38, 92–100. doi: 10.1016/j.pbi.2017.04.022

Qiao, Y., Jiang, W., Lee, J., Park, B., Choi, M. S., Piao, R., et al. (2010). *SPL28* encodes a clathrin-associated adaptor protein complex 1, medium subunit micro 1 (AP1M1) and is responsible for spotted leaf and early senescence in rice (*Oryza sativa*). *New Phytol.* 185, 258–274. doi: 10.1111/j.1469-8137.2009.03047.x

Qiu, Z., Zhu, L., He, L., Chen, D., Zeng, D., Chen, G., et al. (2019). DNA damage and reactive oxygen species cause cell death in the rice *local lesions 1* mutant under high light and high temperature. *New Phytol.* 222, 349–365. doi: 10.1111/nph.15597

Rao, Y., Yang, Y., Xu, J., Li, X., Leng, Y., Dai, L., et al. (2015). *EARLY SENESCENCE 1* encodes a SCAR-like protein2 that affects water loss in rice. *Plant Physiol.* 169, 1225–1239. doi: 10.1104/pp.15.00991

Ren, D., Rao, Y., Wu, L., Xu, Q., Li, Z., Yu, H., et al. (2016). The pleiotropic *ABNORMAL FLOWER AND DWARF1* affects plant height, floral development and grain yield in rice. *J. Integr. Plant Biol.* 58, 529–539. doi: 10.1111/jipb.12441

Saed-Moucheshi, A., Shekoofa, A., and Pessarakli, M. (2014). Reactive oxygen species (ROS) generation and detoxifying in plants. *J. Plant Nutr.* 37, 1573–1585. doi: 10.1080/01904167.2013.868483

Sakuraba, Y., Kim, D., Han, S. H., Kim, S. H., Piao, W., Yanagisawa, S., et al. (2020). Multilayered regulation of membrane-bound ONAC054 is essential for abscisic acid-induced leaf senescence in rice. *Plant Cell* 32, 630–649. doi: 10.1105/tpc.19.00569

Sakuraba, Y., Rahman, M. L., Cho, S. H., Kim, Y. S., Koh, H. J., Yoo, S. C., et al. (2013). The rice *faded green leaf* locus encodes protochlorophyllide oxidoreductase B and is essential for chlorophyll synthesis under high light conditions. *Plant J.* 74, 122–133. doi: 10.1111/tpj.12110

Scandalios, J. G. (2002). The rise of ROS. *Trends Bioche. Sci.* 27, 483–486. doi: 10.1016/s0968-0004(02)02170-9

Shiina, T., Tsunoyama, Y., Nakahira, Y., and Khan, M. S. (2005). Plastid RNA polymerases, promoters, and transcription regulators in higher plants. *Int. Rev. Cytol.* 244, 1–68. doi: 10.1016/S0074-7696(05)44001-2

Shiu, S. H., Karlowski, W. M., Pan, R., Tzeng, Y. H., Mayer, K. F., and Li, W. H. (2004). Comparative analysis of the receptor-like kinase family in Arabidopsis and rice. *Plant Cell* 16, 1220–1234. doi: 10.1105/tpc.020834

Southall, N. T., Dill, K. A., and Haymet, A. (2002). A view of the hydrophobic effect. *J. Phy. Chem. B* 106, 521–533. doi: 10.1021/jp015514e

Sugimoto, H., Kusumi, K., Noguchi, K., Yano, M., Yoshimura, A., and Iba, K. (2007). The rice nuclear gene, *VIRESCENT 2*, is essential for chloroplast development and encodes a novel type of guanylate kinase targeted to plastids and mitochondria. *Plant J.* 52, 512–527. doi: 10.1111/j.1365-313X.2007.03251.x

Sun, Y., Tian, Y., Cheng, S., Wang, Y., Hao, Y., Zhu, J., et al. (2019). *WSL6* encoding an Era-type GTP-binding protein is essential for chloroplast development in rice. *Plant Mol. Biol.* 100, 635–645. doi: 10.1007/s11103-019-00885-z

Thordal-Christensen, H., Zhang, Z., Wei, Y., and Collinge, D. B. (1997). Subcellular localization of H_2O_2 in plants. H_2O_2 accumulation in papillae and hypersensitive response during the barley-powdery mildew interaction. *Plant J.* 11, 1187–1194. doi: 10.1046/j.1365-313X.1997.11061187.x

Triantaphylidès, C., Krischke, M., Hoeberichts, F. A., Ksas, B., Gresser, G., Havaux, M., et al. (2008). Singlet oxygen is the major reactive oxygen species involved in photooxidative damage to plants. *Plant Physiol.* 148, 960–968. doi: 10.1104/pp.108.125690

van der Knaap, E., Song, W. Y., Ruan, D. L., Sauter, M., Ronald, P. C., and Kende, H. (1999). Expression of a gibberellin-induced leucine-rich repeat receptor-like protein kinase in deepwater rice and its interaction with kinase-associated protein phosphatase. *Plant Physiol.* 120, 559–570. doi: 10.1104/pp.120.2.559

Wang, Q., Qin, G., Cao, M., Chen, R., He, Y., Yang, L., et al. (2020). A phosphorylation-based switch controls TAA1-mediated auxin biosynthesis in plants. *Nat. Commun.* 11:679. doi: 10.1038/s41467-020-14395-w

Wang, Y., Lin, A., Loake, G. J., and Chu, C. (2013). H_2O_2-induced leaf cell death and the crosstalk of reactive nitric/oxygen species. *J. Integr. Plant Biol.* 55, 202–208. doi: 10.1111/jipb.12032

Woo, H. R., Kim, H. J., Lim, P. O., and Nam, H. G. (2019). Leaf senescence: systems and dynamics aspects. *Annu. Rev. Plant biol.* 70, 347–376. doi: 10.1146/annurev-arplant-050718-095859

Wu, L., Ren, D., Hu, S., Li, G., Dong, G., Jiang, L., et al. (2016). Down-regulation of a nicotinate phosphoribosyl transferase gene, *OsNaPRT1*, leads to withered leaf tips. *Plant Physiol.* 171, 1085–1098. doi: 10.1104/pp.15.01898

Wu, X. Y., Kuai, B. K., Jia, J. Z., and Jing, H. C. (2012). Regulation of leaf senescence and crop genetic improvement. *J. Integr. Plant Biol.* 54, 936–952. doi: 10.1111/jipb.12005

Xu, J., Pan, C., Lin, H., Ye, H., Wang, S., Lu, T., et al. (2022). A rice *XANTHINE DEHYDROGENASE* gene regulates leaf senescence and response to abiotic stresses. *Crop J.* 10, 310–322. doi: 10.1016/j.cj.2021.05.011

Xu, T., Dai, N., Chen, J., Nagawa, S., Cao, M., Li, H., et al. (2014). Cell surface ABP1-TMK auxin-sensing complex activates ROP GTPase signaling. *Science* 343, 1025–1028. doi: 10.1126/science.1245125

Yamatani, H., Sato, Y., Masuda, Y., Kato, Y., Morita, R., Fukunaga, K., et al. (2013). *NYC4*, the rice ortholog of Arabidopsis THF1, is involved in the degradation of chlorophyll - protein complexes during leaf senescence. *Plant J.* 74, 652–662. doi: 10.1111/tpj.12154

Yang, J., He, H., He, Y., Zheng, Q., Li, Q., Feng, X., et al. (2021). TMK1-based auxin signaling regulates abscisic acid responses *via* phosphorylating ABI1/2 in *Arabidopsis*. *Proc. Natl. Acad. Sci. U.S.A.* 118:e2102544118. doi: 10.1073/pnas.2102544118

Yang, S., Fang, G., Zhang, A., Ruan, B., Jiang, H., Ding, S., et al. (2020). Rice *EARLY SENESCENCE 2*, encoding an inositol polyphosphate kinase, is involved in leaf senescence. *BMC Plant Biol.* 20:393. doi: 10.1186/s12870-020-02610-1

Yang, X., Gong, P., Li, K., Huang, F., Cheng, F., and Pan, G. (2016). A single cytosine deletion in the *OsPLS1* gene encoding vacuolar-type H^+-ATPase subunit A1 leads to premature leaf senescence and seed dormancy in rice. *J. Exp. Bot.* 67, 2761–2776. doi: 10.1093/jxb/erw109

Yang, Y., Xu, J., Huang, L., Leng, Y., Dai, L., Rao, Y., et al. (2016). *PGL*, encoding chlorophyllide a oxygenase 1, impacts leaf senescence and indirectly affects grain yield and quality in rice. *J. Exp. Bot.* 67, 1297–1310. doi: 10.1093/jxb/erv529

Zhang, Z., Cui, X., Wang, Y., Wu, J., Gu, X., and Lu, T. (2017). The RNA editing factor WSP1 is essential for chloroplast development in rice. *Mol. Plant* 10, 86–98. doi: 10.1016/j.molp.2016.08.009

Zheng, Y., Xu, J., Wang, F., Tang, Y., Wei, Z., Ji, Z., et al. (2021). Mutation types of CYP71P1 cause different phenotypes of mosaic spot lesion and premature leaf senescence in rice. *Front. Plant Sci.* 12:641300. doi: 10.3389/fpls.2021.641300

Conflict of Interest: The authors declare that the research was conducted in the absence of any commercial or financial relationships that could be construed as a potential conflict of interest.

frontiers | Frontiers in Plant Science

REVIEW
published: 02 June 2022
doi: 10.3389/fpls.2022.920494

Xyloglucan Biosynthesis: From Genes to Proteins and Their Functions

*Jordan D. Julian and Olga A. Zabotina**

Roy J. Carver Department of Biochemistry, Biophysics and Molecular Biology, Iowa State University, Ames, IA, United States

The plant's recalcitrant cell wall is composed of numerous polysaccharides, including cellulose, hemicellulose, and pectin. The most abundant hemicellulose in dicot cell walls is xyloglucan, which consists of a β-(1->4) glucan backbone with α-(1->6) xylosylation producing an XXGG or XXXG pattern. Xylose residues of xyloglucan are branched further with different patterns of arabinose, fucose, galactose, and acetylation that varies between species. Although xyloglucan research in other species lag behind *Arabidopsis thaliana*, significant advances have been made into the agriculturally relevant species *Oryza sativa* and *Solanum lycopersicum*, which can be considered model organisms for XXGG type xyloglucan. In this review, we will present what is currently known about xyloglucan biosynthesis in *A. thaliana*, *O. sativa*, and *S. lycopersicum* and discuss the recent advances in the characterization of the glycosyltransferases involved in this complex process and their organization in the Golgi.

Keywords: polysaccharide biosynthesis, hemicellulose, glycosyltransferase, protein structure, sub-Golgi localization, multiprotein complex

OPEN ACCESS

Edited by:
Anna N. Stepanova, North Carolina State University, United States

Reviewed by:
SangJin Kim, Michigan State University, United states
Huiling Li, South China Agricultural University, China

***Correspondence:**
Olga A. Zabotina
zabotina@iastate.edu

Specialty section:
This article was submitted to Plant Physiology, a section of the journal Frontiers in Plant Science

Received: *14 April 2022*
Accepted: *13 May 2022*
Published: *02 June 2022*

Citation:
Julian JD and Zabotina OA (2022) Xyloglucan Biosynthesis: From Genes to Proteins and Their Functions. Front. Plant Sci. 13:920494. doi: 10.3389/fpls.2022.920494

INTRODUCTION

Within the plant cell wall, numerous polysaccharides and a group of proteins are involved in one of the strongest natural barriers. These polysaccharides are categorized as either cellulose, hemicellulose, or pectin. The abundant plant hemicellulose xyloglucan (XyG) is the most common hemicellulose in dicots and has been found in numerous monocots (Pauly and Keegstra, 2016). XyG was named for its cellulose-like β-(1->4) glucan backbone that is heavily xylosylated. The patterns of XyG xylosylation are found in two forms, XXGG and XXXG, depending on the species. The complexity of XyG varies throughout plants, with various branches composed of xylose (Xyl), galactose (Gal), arabinose (Ara), and fucose (Fuc) monosaccharides, as well as the C6 acetylation of Glc or Gal residues. XyG nomenclature is denoted by single letters, which were introduced by Fry et al. (1993) and have been expanded upon. G represents β-D-Glucose (Glc) with no branching, and X represents a xylosylated Glc, α-D-Xyl-(1->6)-β-D-Glc. These Xyl residues can be further branched with Gal, Ara, or another Xyl residue denoted as L, S, and U, respectively. Modifications such as acetylation are denoted with an underlined symbol, such as XXGG, with acetylation of the Glc in the third position. Recent literature has proposed new nomenclature for acetylated XyG branches, but this nomenclature has not been commonly used so far, and as such, this review will utilize the underlined nomenclature (Fry et al., 1993; Tuomivaara et al., 2015). Many additional linkages

have been identified, of which most have been compiled by multiple reviews and research articles (Fry et al., 1993; Zabotina, 2012; Schultink et al., 2015; Tuomivaara et al., 2015; Pauly and Keegstra, 2016).

In *Arabidopsis thaliana*, the β-D-Gal-(1->2)-α-D-Xyl glycosylation only occurs in the second and third position of the tri-xylosylated pattern resulting in XLXG, XXLG, and XLLG subunits. The third side chain can be extended with an α-L-Fuc *via* an α-(1->2) glycosidic linkage [α-L-Fuc-(1->2)-β-D-Gal-(1->2)-α-D-Xyl] to form XLFG, the most complex naturally occurring XyG subunit within most *Arabidopsis* tissues (**Figure 1A**; Pauly and Keegstra, 2016). Other species, such as *Oryza sativa*, *Solanum lycopersicum* (rice and tomato), and many types of grasses contain XXGG type XyG in their cell walls. Tomato cell walls lack fucosylated XyG and instead are constituted by mono- (S) and di-arabinosylated (T) XyG side chains with *O*-6-acetylation of the glucan backbone, resulting in XSGG and XTGG (**Figures 1B,C**; Jia et al., 2005; Schultink et al., 2013; Pauly and Keegstra, 2016). Additionally, a unique subunit of XyG has been found within the roots of *Arabidopsis*, with the first and third branches modified with galacturonic acid (GalA) to form YXYG and YXZG. GalA is the only monosaccharide to be attached to the first Xyl in *Arabidopsis* XXXG type XyG (**Figure 1D**; Peña et al., 2012).

Synthesis of XyG and most polysaccharides is carried out by glycosyltransferases (GTs). GTs are enzymes that utilize nucleotide-activated sugars such as UDP-Glc, UDP-Xyl, UDP-Gal, GDP-Fuc, UDP-Ara, or UDP-GalA as substrates (donors) and catalyze the transfer of the specific monosaccharides to a specific acceptor. Acceptors have been found to include the four building blocks of life: nucleotides, proteins, lipids, and other glycans, producing glycosylated RNA, glycoproteins, glycolipids, and polysaccharides (Reichmann and Gründling, 2011; Riley et al., 2019; Flynn et al., 2021). GTs have been believed to be very specific in the binding of both donors and acceptors *in vivo*; however, more recent *in vitro* studies have demonstrated that their specificity to be more promiscuous than originally thought (Ohashi et al., 2019; Ruprecht et al., 2020; Ehrlich et al., 2021). GTs have been divided into more than 110 families within the CAZy database,[1] demonstrating a vast variety between GTs (Drula et al., 2022). Classification of GTs is based on their fold, mechanism, and biochemical pathway. GT-A and GT-B are the most common Rossman folds of GTs, while a third fold has been proposed to have a GT-C fold (Lairson et al., 2008; Chang et al., 2011). Furthermore, GTs can either retain or invert the stereochemistry of the sugar in regard to the donor substrate. For example, most donors that are commonly used exhibit an α-bond. GTs with the retaining mechanism link *via* the same α bond, whereas inverting GTs produce a β-bond attaching the sugar to the acceptor. It is accepted that inverting GTs catalyze reaction using an S_N2-like mechanism, where an amino acid of the GT acts as the general base to deprotonate the acceptor. The deprotonated acceptor then performs a nucleophilic attack on the donor carbon, displacing the nucleotide pyrophosphate molecule. For retaining GTs, the mechanism is still up for debate. The leading two proposed mechanisms include either a double displacement reaction or a front-sided SN_i like displacement mechanism (Gómez et al., 2012; Schuman et al., 2013; Albesa-Jové et al., 2015; Zabotina et al., 2021).

All GTs are membrane proteins classified as either type II membrane proteins or integral membrane proteins, localized to a lipid bilayer within the cell. Type II membrane proteins are single-pass membrane proteins localized to the endomembrane system. Type II GTs have a short N terminal region in the cytoplasm with a single transmembrane domain (TMD) that passes through the Golgi membrane. Inside the

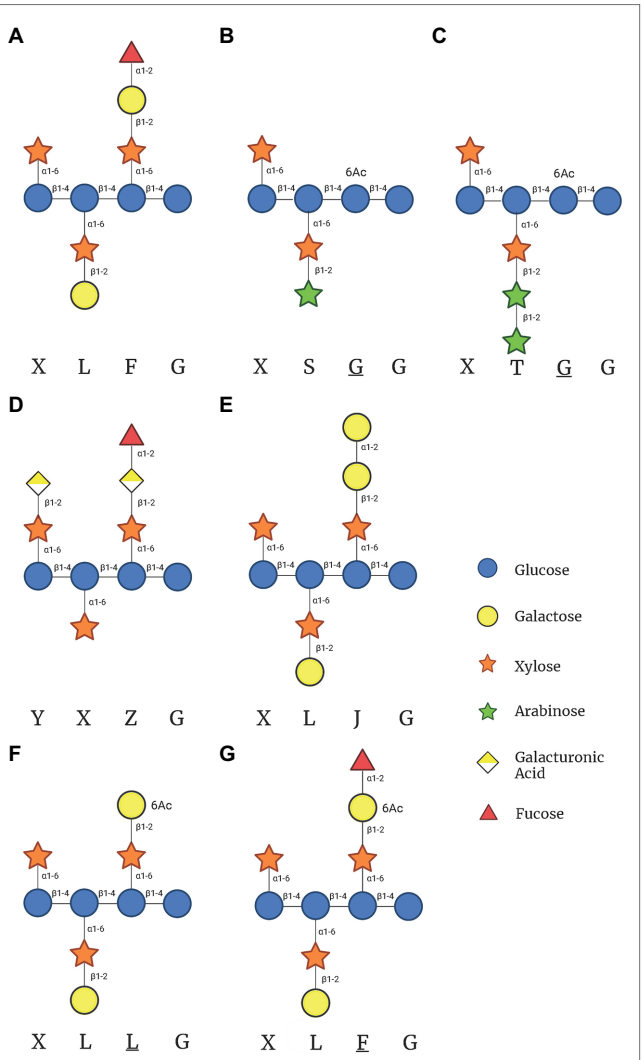

FIGURE 1 | Xyloglucan (XyG) subunits mentioned in this review found within hemicellulose extracts of plant cells walls. **(A)** The common XyG subunit XLFG found in *Arabidopsis* cell walls. **(B)** XyG subunit found in XXGG type XyG from plants such as tomato and rice. **(C)** Diarabinosylated XyG subunit in XXGG type xyloglucan of tomato. **(D)** Fully branched XyG subunit found in *Arabidopsis* root hairs. **(E)** XyG subunit synthesized in the absence of GDP-Fuc in *mur1* mutant plants. **(F)** Gal-6-*O*-acetylated XXXG type XyG after the hypothetical removal of fucose by Axy8. **(G)** Fucosylated XXXG XyG subunit with Gal-6-*O*-acetylation. This figure was created with Biorender.com.

[1]http://www.cazy.org/

Golgi lumen, the GT C-terminal catalytic domain is connected to the TMD through a stem region of variable lengths (Lairson et al., 2008). Integral membrane proteins are multi-pass membrane proteins with 6–8 TMDs embedded into the lipid bilayer. Integral membrane GTs localize to both the Golgi and the plasma membrane (Cocuron et al., 2007; Morgan et al., 2013). XyG biosynthesis is carried out entirely within the Golgi, and once XyG is fully synthesized, it is transported to the cell wall through transport vesicles (Wilkop et al., 2019).

The most recent review on XyG biosynthesis by Pauly and Keegstra (2016) goes into great depth on XyG structural diversity and the known enzymes involved in its biosynthesis. Later that year, FUT1's structure was reported, the first 3D structure for plant cell wall synthesizing enzyme. Since then, further study has elucidated another structure, XXT1, along with several insights into the other proteins involved in XyG biosynthesis. This review expands the information on XyG biosynthesis to the current standing in the field of XyG biosynthesis and presents the current views and notations about the GTs involved in the process and their mechanisms.

PROTEINS INVOLVED IN XYLOGLUCAN BIOSYNTHESIS

Biosynthesis of XyG is a complex process that involves several GTs that are presumed to be specific towards a particular acceptor structure, e.g., specificity towards the Gal in the third position vs. the second in the XLLG subunit. To date, 13 GTs have been identified which are directly involved in XyG biosynthesis in all *Arabidopsis* tissues, five cellulose synthase-like C proteins (CSLC), five xylosyltransferases (XXTs), two galactosyltransferases (GalT), and one fucosyltransferase (FUT; Faik et al., 2002; Madson et al., 2003; Perrin et al., 2003; Cavalier and Keegstra, 2006; Cocuron et al., 2007; Jensen et al., 2012; Zabotina et al., 2012; Culbertson et al., 2016). All 13 enzymes are localized to the phospholipid bilayer of the Golgi membrane *via* at least one transmembrane domain (TMD). Less studied enzymes, such as galacturonosyltransferases (GalATs), arabinosyltransferases (AraTs), and acetyltransferases (AceTs), have also been demonstrated to be involved in XyG biosynthesis.

Glucan Backbone Synthesis

CSLC enzymes are members of CAZy GT family 2, a family of inverting integral membrane GTs, and are responsible for the synthesis of the glucan backbone of XyG (Cocuron et al., 2007; Bi et al., 2015). CSLC enzymes are predicted to be integral membrane proteins composed of six TMDs (Davis et al., 2010). The expression of the five CSLC enzymes—CSLC4, 5, 6, 8, and 12—varies throughout different plant tissue (Kim et al., 2020; **Tables 1** and **2**). CSLC4 and CSLC5 have the highest levels of expression in most vegetive tissues, whereas expression of CSLC6 and CSLC12 is specific to flowers and seeds. Recombinant CSLC4 has been confirmed to synthesize β-glucan in *Pichia pastoris*, while the deletion of all five CSLC GTs in *Arabidopsis* resulted in no detectable XyG in *Arabidopsis* (Cocuron et al., 2007; Kim et al., 2020). The donor substrate for CSLC enzymes, UDP-Glc, is thought to be delivered to the cytoplasmic catalytic domain of the enzymes, which elongates the glucan backbone, moving the polysaccharide through the opening created by the transmembrane helices of the CSLC protein, translocating the glucan chain through the Golgi membrane (Bi et al., 2015). Once the chain enters the lumen of the Golgi, the glucan backbone is then further glycosylated by the other type II membrane proteins described below. It is currently

TABLE 1 | Summary of effects of XyG glycosyltransferases (GT) mutants in *Arabidopsis*.

Mutant	Type	Effects on plant	Effects on XyG structure	Citations
cslc	Knockout	Small rosettes, shorter inflorescence stems, short root hairs	No detectable XyG	Kim et al., 2020
xxt1	Knockout	None	None	Cavalier et al., 2008; Zabotina et al., 2012
xxt2	Knockout	None	None	Cavalier et al., 2008; Zabotina et al., 2012
xxt1 xxt2	Knockout	Short root hairs, shorter stems, and smaller leaves	No detectable XyG	Cavalier et al., 2008; Zabotina et al., 2012
xxt5	Knockout	Shorter root hairs, not as severe as *xxt1 xxt2* double mutant	50% Reduction in IP, higher levels of XXGG subunits	Zabotina et al., 2012
mur3	Point mutation	None	Very low levels of Gal and Fuc in third position (XLXG and XXXG only)	Madson et al., 2003; Kong et al., 2015
mur3	Knockout	Dwarfed cabage-like growth, short petioles, endomembrane aggregates	No galactosylation of third branch, lacks fucose	Tamura et al., 2005; Kong et al., 2015
xlt2	Knockout	None	No galactosylation of second branch	Jensen et al., 2012
mur3 xlt2	Knockout	Severely dwarfed plant height	No Gal or Fuc branches	Jensen et al., 2012
fut1	Point mutation	None	More than 99% reduction of fucsoylated XyG	Vanzin et al., 2002
fut1	Knockout	None	No fucosylation	Perrin et al., 2003
xut1	Knockout	Short root hairs	No branches with GalA	Peña et al., 2012
XyBat	Knockout	None	30% Reduction in XyG acetylation	Liu et al., 2016
axy4/axy4l	Knockout	None	No Gal *O*-6-acetylation	Gille et al., 2011
AraTs	N/A	Not attempted	Not attempted	

TABLE 2 | Current understanding of substrate specificity of XyG synthesizing GTs.

GT	Enzyme	Acceptor	Donor	Product	Notes	Citations
CLSC	AtCSLC4/5/6/8/12	G_n	UDP-Glc	G_{n+1}	Currently unknown if G_1 can act as an acceptor	Cocuron et al., 2007; Kim et al., 2020
XXT	AtXXT1/2	GGGGGG	UDP-Xyl	XXGGGG		Culbertson et al., 2018
	AtXXT3/4/5	XXGGGG	UDP-Xyl	XXXGGG	Requires XXT1/XXT2 to add first two Xyl	Culbertson et al., 2016
GalT	AtXLT2	XXXG	UDP-Gal	XLXG		Jensen et al., 2012
	AtMUR3	XXXG	UDP-Gal	XXLG		Madson et al., 2003
FucT	AtFUT1	XLLG	GDP-Fuc	XLFG		Rocha et al., 2016; Urbanowicz et al., 2017
		XXLG		XXFG		
GalAT	AtXUT1	XXXG	UDP-GalA	YXYG	Only found within the root hairs of *Arabidopsis*	Peña et al., 2012
AraT	SlMUR3	XXXG	UDP-Ara	XXXG	Not observed, only presumed	Schultink et al., 2013
	SlXST1/2	XXXG	UDP-Ara	XXSG	Product found only within *Arabidopsis* mutant cell walls	Schultink et al., 2013
AceT	XyBAT*	XXGG	Acetyl-CoA	XXGG		Liu et al., 2016; Zhong et al., 2020
		XSGG		XSGG		
	AXY4/AXY4L/XGOATs**	XXFG	Acetyl-CoA	XXFG		Gille et al., 2011; Zhong et al., 2018
		XLFG		XLFG		

*Includes XyBATs from both Brachypodium and Populus plants.

**AXY4, AXY4L, and XGOATs are different names proposed for the same AceT homologs. Includes homologs from Arabidopsis, rice, and tomato plants.

unclear if the CSLC enzymes require an acceptor to begin elongation or if they can synthesize the glucan chain *de novo*.

Besides CSLC proteins, the CAZy GT2 family also includes cellulose synthases (CeS) from plants (CesA) and bacteria (BcsA), the enzymes responsible for the biosynthesis of cellulose, the major polysaccharide within the plant cell wall (Morgan et al., 2013, 2016; Bi et al., 2015; McNamara et al., 2015; Purushotham et al., 2020). Both CesA and BcsA are localized to the plasma membrane and synthesize β-(1->4) glucan, a similar product as CSLC enzymes. As mentioned previously, these enzymes have two functions: synthesis of β-(1->4) glucan polymers (cellulose) and the translocation of the nascent polymers through the plasma membrane. Synthesis of the glucan polymer is carried out by the cytoplasmic catalytic domain of CeS GTs. The leading hypothesis of catalytic synthesis is that CeS's catalyze the transfer of Glc from UDP-Glc to the β-glucan polymer through an S_n2 reaction, inverting the sugar from α to β (Morgan et al., 2013). The elongated polymer is then shifted to empty the catalytic site, translocating through the plasma membrane (Bi et al., 2015; Morgan et al., 2016). Translocation of the acceptor is carried out by three conserved features: a QxxRW motif, a finger helix with a TED motif, and a gating loop. The conserved QxxRW sequence is located near the channel's entrance and is responsible for the stabilization of the acceptor through π and hydrogen bonds (Morgan et al., 2016; Zimmer, 2019). Additionally, the finger helix's TED motif interacts with the acceptor polysaccharide by forming hydrogen bonds with three hydroxyls of terminal Glc. After the transfer of Glc (N) to the acceptor, the finger motif shifts from the previous terminal Glc (N + 1) back into the catalytic domain to interact with the newly added Glc (N). An incoming UDP-Glc along with the gating loop then pushes the finger motif up into the transmembrane domain, shifting the glucan polysaccharide by one sugar residue. The rest of the Glc chain is stabilized by numerous π interactions within the channel, with only strong hydrogen bonds interacting with the terminal Glc.

This same translocation may be shared by CSLC enzymes as well, but within the Golgi membrane instead of the plasma membrane. Utilizing the new revolutionary software AlphaFold 2.0 to predict CSLCs' structure, we observed that CSLCs are highly homologous to the known BcsA structure (PDBID 4P00; Jumper et al., 2021). The predicted structures mentioned in this review (besides AraTs) are publicly available on websites such as UniProt[2] for download, and alignment can be carried out by PyMol modeling software (Schrödinger and DeLano, 2020). AlphaFold is also publicly available for free, with recent updates including a multimer prediction function, although the software can be demanding and require sophisticated hardware. In the highly homologous structures of CSLCs and CeS, CSLCs share the QxxRW motif with CeS enzymes but lack the TED motif, instead encoding a VED motif. Structural prediction of CSLCs aligns the VED motif of the CSLC GTs with the TED motif from BcsA. A T341V mutation of BcsA or CeSA has never been attempted, so it is challenging to predict how the hydrogen bonding would change the function. However, mutation of both Glu and Asp residues within the TED motif have resulted in reduced cellulose content (Kumar et al., 2018). Homology and computational modeling provide insightful hypotheses for the CSLC mechanisms and structure, while the experiments that have been carried out with CeS GTs provide an excellent model for future studies on CSLCs.

Arabidopsis lines lacking a single CSLC protein did not display any noticeable phenotypes. Combinations of *cslc* knockouts resulted in various phenotypes, including smaller rosettes, shorter inflorescence stems and short root hairs

[2]https://www.uniprot.org

(Kim et al., 2020; **Table 1**). Digestion of the mutant *cslc45812* cell wall with driselase, a cocktail of glycosyl hydrolases lacking α-(1->6) xylosidase, resulted in no detectable isoprimeverose [IP; Xyl α-(1->6) Glc], resembling that of the *xxt1 xxt2* double mutant described below.

Xylosylation of the Glucan Backbone

XXTs have been more extensively studied compared to other XyG synthesizing GTs aside from FUT1. In *Arabidopsis*, five XXTs from the retaining CAZy GT family 34 have been identified. XXTs appear to be biochemically redundant, catalyzing the xylosylation of the first three positions in the XXXG subunit. Reverse-genetic studies have demonstrated that the *Arabidopsis* double knockout mutant *xxt1 xxt2* did not produce any detectable XyG, which was confirmed by the lack of IP released by driselase (Cavalier et al., 2008; Zabotina et al., 2012). Knockout of *xxt5* alone significantly reduced levels of detectable IP by 50%, while the altered XyG patterns displayed higher levels of XXGG subunits and lower levels of the typical XXXG subunits (Zabotina et al., 2008, 2012). Similar results were observed when the *xxt5* mutation was paired with either *xxt1* or *xxt2*, suggesting that XXT5 was also required for normal XyG biosynthesis alongside XXT1 and XXT2 *in vivo* (Zabotina et al., 2012). Furthermore, the *xxt1 xxt2* double mutant plants had initial growth defects resulting in shorter stems and smaller leaves (**Table 1**), although this phenotype disappeared as the plant matured, resembling wild-type *Arabidopsis* (Cavalier et al., 2008; Zabotina et al., 2012). These double mutants also have root hairs that are much shorter, with a rounded structure, as compared to the long, thin wild-type *Arabidopsis* root hairs. The *xxt5* single mutant also had the same root hair phenotype although not as pronounced.

XXT1 is the only XXT structurally characterized to date, which was the second structure of cell wall synthesizing GTs to be described, following the characterization of FUT1. XXT1 was crystallized as a homodimer (PDBIDs: 6BSU, 6BSV 6BSW) which has a GT-A fold (Culbertson et al., 2018). For structural characterization, truncated XXT1 was expressed in HEK293F cells with amino acids 45–460, removing its TMD. Each dimer subunit was structurally oriented in opposite directions, meaning that the dimer likely acts on two separate glucan chains rather than both interacting with the same chain. Mechanistically, XXT1 binds to the donor UDP-Xyl and a β-(1–4) glucan chain acceptor molecule of at least 3 Glc in length, which is the proposed minimum required to be active (Culbertson et al., 2018; Zhong et al., 2021). Like most GT-A folded GTs, XXTs require the metal cofactor Mn^{2+} to be catalytically active, which is coordinated by the DXD motif in XXT1's binding site (Culbertson et al., 2018). Cocrystalization of UDP-Xyl with XXT1 failed to reveal any bound UDP-Xyl. Instead, UDP was bound in its place, requiring computer modeling to simulate Xyl interactions. This modeling of UDP-Xyl suggested that XXT1's dominant interactions with the donor substrate occur *via* the sugar molecule rather than the high-energy UDP. These models also suggest that Phe 203 interacts with C5 of the Xyl sugar, which would presumably impair binding to hexose sugars, increasing affinity for UDP-Xyl. The acceptor molecule, cellohexaose, is bound by XXT1 through a mix of hydrogen bonding of the inner for Glc molecules, with weaker water and hydrophobic interactions stabilizing the end Glc sugars (Glc 1 and Glc 6). These interactions orient the C6-hydroxyl of the fourth Glc into the active site of XXT1. As stated previously in this review, the mechanism for retaining GTs is still debated. Of the two prominent theories, double displacement and SN_i-like displacement, evidence suggests that XXT1 favors an SN_i-like mechanism. Likely candidate residues for double displacement included two Asp residues that were positioned a large distance (>5 Å) from the anomeric carbon of UDP-Xyl. Mutations of these two Asp to Asn impaired XXT1's activity, but did not prevent the xylosylation of cellohexaose. G319, the likely residue involved in the SN_i-like displacement mechanism, was also positioned a significant distance (4.7 Å) from the anomeric carbon. However, a G319A mutation resulted in significantly less activity, ~40% less activity than the double Asp mutant normalization to wild-type XXT1 activity (Culbertson et al., 2018).

Structural characterization of XXTs allowed Culbertson et al. (2018) to propose the N + 2 rule for glucan backbone xylosylation in *Arabidopsis*. The N + 2 rule states that XXTs that fall into this category—XXT1 and XXT2—have steric hindrance preventing the xylosylation of the N + 2 position on the glucan backbone after the N position has already been xylosylated. This steric hindrance is hypothesized to be caused by I391 in both XXT1 and XXT2. Both sequence alignment and structural prediction software such as AlphaFold predict that XXT3, XXT4, and XXT5 encode a G392 in that space instead, providing adequate capacity for the Xyl residue at the N position to fit within the binding cavity of these XXTs (Culbertson et al., 2018).

In vitro biochemical assays have confirmed the activity of XXT1, XXT2, XXT4, and XXT5, with varying rates of catalysis and different patterns of xylosylation of cellohexaose, the acceptor molecule used in most XXT *in vitro* assays (Culbertson et al., 2016, 2018; Zhong et al., 2021). XXT1 and XXT2 are kinetically similar and have been shown to synthesize XGGGGG, XXGGGG, XXXGGG, and even XXXXGG patterns in biochemical assays (Culbertson et al., 2016, 2018; Zhong et al., 2021; **Table 2**). XXT4 and XXT5 have been shown to be significantly slower, requiring a higher enzyme concentration and appear to only synthesize the XGGGGG and XXGGGG pattern in *in vitro* studies (Culbertson et al., 2016; Zhong et al., 2021). Zhong et al. (2021) showed that XXT1/XXT2 are able to add up to four Xyl residues to cellohexaose in *in vitro* assays and proposed that XXT1 and XXT2 are solely responsible for *in vivo* xylosylation of XyG.

Culbertson et al. (2018) proposed an alternative hypothesis, suggesting that the addition of three consecutive Xyl residues is likely due to the ability of truncated XXT1 and XXT2 to differently bind the glucan oligosaccharide in solution, shifting and rotating the acceptor glucan chain to prevent the previously attached Xyl from being placed in restrictive orientations (**Figure 2A**; Culbertson et al., 2018). On the contrary, full-length XXTs are attached to the plant Golgi membrane *via* their TMD and likely do not have such motional freedom as truncated XXTs in solution. Within

the Golgi, XXTs must continuously xylosylate a constantly elongating glucan chain synthesized by CSLCs. This imposes limitations on both the rotational movement and direction the glucan acceptor moves in the binding site of XXTs, limiting the XXTs' ability to bind in different positions along the glucan chain (**Figure 2B**). Such limitations in both the glucan chain interactions with XXTs and the XXTs' own restricted motions would prevent XXT1 and XXT2 from accommodating the glucan chain with XXGG pattern of substitution, as the first position (N+2) Xyl residue would be blocked by the side chain of the I391 (Culbertson et al., 2018). Thus, the results obtained from structural and reverse-genetic studies suggest a different hypothesis about the mechanism of xylosylation of the XyG backbone by XXTs within the Golgi lumen. It is likely that XXT1 and XXT2 are responsible for adding Xyl to the first two consecutive Glcs, synthesizing XXGG patterns. Whereas XXT5 and its homologs—XXT3 and XXT4—finish xylosylation by adding the third Xyl, completing the XXXG pattern in *Arabidopsis* XyG (**Table 2**; Culbertson et al., 2018; Zabotina et al., 2021).

Another study also using *in vitro* assays demonstrated that XXT1 is capable of using multiple activated sugars as donor substrates: UDP-Glc, UDP-Gal, and UDP-Ara in addition to UDP-Xyl (Ehrlich et al., 2021). It is worth to note that the rates of XXT1 catalysis using other nucleotide sugars were significantly lower in comparison to UDP-Xyl. Although *in vitro* enzymatic assays demonstrate the tetraxylosylation of sequential glucan residues and the ability to utilize different donor substrates (Zhong et al., 2021), there is no experimental evidence of this occurring *in vivo*. This suggests that there is control of XyG patterns synthesized *in vivo*, which can either be through enzyme substrate specificity or donor substrate availability in the Golgi lumen.

Galactosylation of Xylose in XyG

To date, only two galactosyltransferases (GalT) have been shown to be involved in *Arabidopsis* XyG biosynthesis, MUR3 and XLT2. XyG galactosylation occurs to the second and third positions of the XyG subunits. Both are members of the inverting CAZy GT family 47. These two GalTs have high sequence homology and have highly homologous structures predicted by AlphaFold. Both GalTs seem to be highly selective towards a specific Xyl residue in the XXXG subunit of *Arabidopsis* XyG. The mutation of *mur3* leads to a lack of both galactosylation and fucosylation of the third Xyl residue, resulting in XLXG (Madson et al., 2003). Recombinant expression in *Pichia pastoris* showed activity of MUR3 after incubation with XXXG/XLXG XyG as an acceptor and radioactive UDP-Gal as the donor (Madson et al., 2003). XLT2 is believed to galactosylate the second Xyl residue, forming XLXG. Analysis of digested XyG from *xlt2* knockout *Arabidopsis* plants displayed a lack of detectable XLXG or XLFG subunits (Jensen et al., 2012). This leads to the conclusion that galactosylation of both Xyl residues of *Arabidopsis* XyG is carried out by separate GalTs that are highly specific to the position of the Xyl residues in the acceptor molecules (**Table 2**). Both GalTs have been expressed in HEK293S cells, while MUR3 has been expressed in *Pichia*, but as of

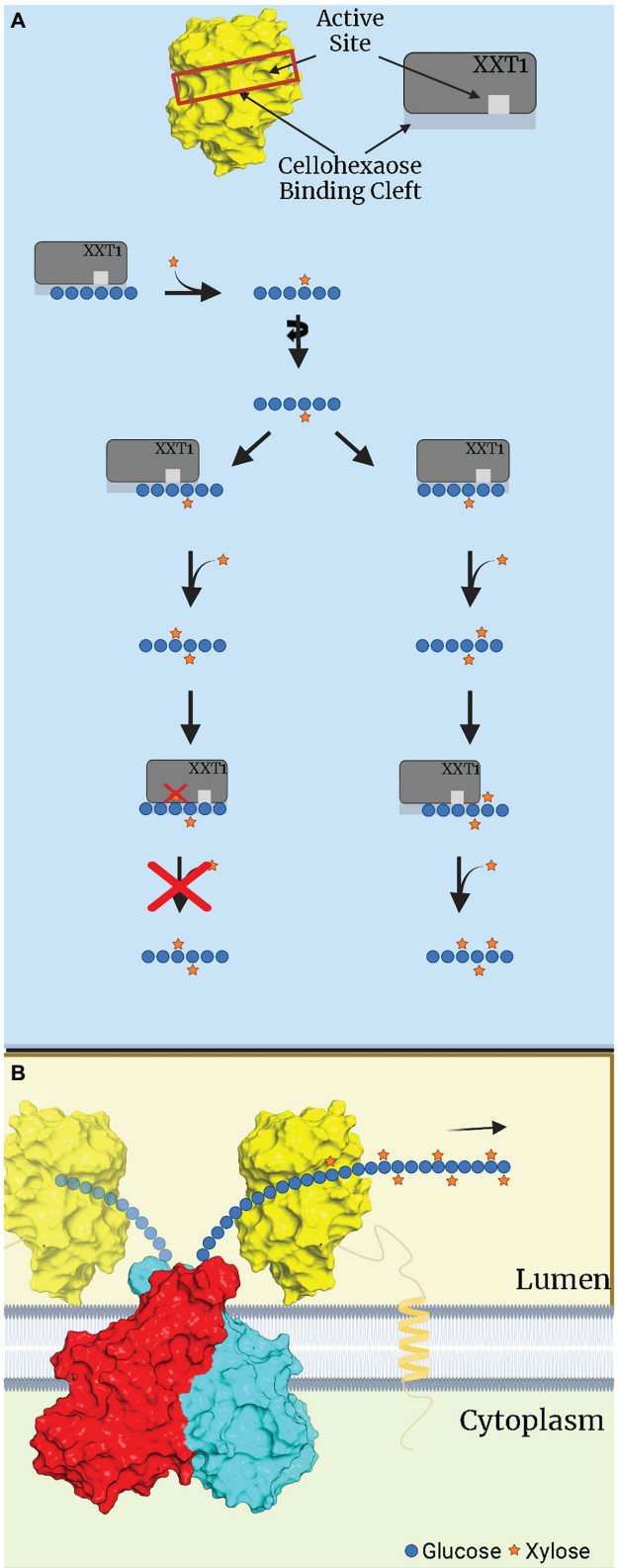

FIGURE 2 | Hypothetical depiction of xylosylation of a glucan substrate by XXT1. **(A)** *In vitro* xylosylation of cellohexaose by XXT1. XXT1 mono- and

(Continued)

FIGURE 2 | dixylosylates cellohexose without significant steric restriction, resulting in XXGGGG. Once cellohexaose is dixylosylated, XXT1 can accommodate the XXGGGG acceptor by binding it in the proper position lacking steric hinderance, e.g., all Xyl attached earlier are localized outside the binding cleft of XXT1. XXT1 can trixylosylate and tetraxylosylate the cellohexaose substrate due to motional freedom of both XXT1 and the glucan acceptor in solution. **(B)** *In vivo* xylosylation by XXT1 within the Golgi lumen. The glucan backbone is constantly elongated by a CSLC dimer (red, cyan), which is then xylosylated by XXT1 (yellow) attached to membrane *via* transmembrane domain (TMD). The TMD/stem region limits mobility of XXT1, while the glucan backbone is elongated and moves only in one direction, depicted by an arrow. The glucan backbone's rotational movement is also limited by being bound to CSLC while elongation occurs. CSLC structure was predicted by AlphaFold, while for XXT1 the crystal structure was used (PDBID:6BSW). This figure was created with Biorender.com.

this review have yet to have activity and specificity reported from *in vitro* assays (Prabhakar et al., 2020).

Aside from changes in XyG, mutant *mur3* lines with a point mutation lacked any noticeable phenotype, while still having low levels of galactosylation and fucosylation of XyG. Mutants with complete deletion of *mur3* resulted in a dwarf cabbage-like phenotype, short petioles and endomembrane aggregates, while some lines were shown to be more salt sensitive (**Table 1**; Madson et al., 2003; Tamura et al., 2005; Li et al., 2013; Kong et al., 2015). Interestingly, overexpression of *xlt2* resulting in higher levels of XLXG subunits suppressed these phenotypes (Kong et al., 2015). Additionally, double mutants *xxt2 mur3* and *xxt5 mur3* also recovered from these phenotypes, resembling wild-type plants. Cell wall analysis of these plants detected higher levels of XLXG subunits than that of the single *mur3* mutant indicating that these phenotypes are a result of shorter XyG branches.

Fucosylation of Galactose

Only one XyG synthesizing fucosyltransferase, FUT1, is encoded by *Arabidopsis* and is a member of the inverting GT37 family (Cicéron et al., 2016; Rocha et al., 2016). FUT1 catalyzes the fucosylation of Gal in the third branch of the XLLG and XXLG subunits using GDP-fucose as a donor substrate. Mutations in the FUT1 protein (*mur2*) in *Arabidopsis* led to a reduction in fucosylation of the cell wall by 50%, while only 2% of XyG was fucosylated (**Table 1**; Vanzin et al., 2002). The mutation in *mur2 Arabidopsis* plants was identified to be D550N mutation, replacing a carbocyclic group with a carboxamide that can potentially be N-glycosylated. From the crystal structure, FUT1 amino acid 550 is found located in the extra C-terminal region, which is involved in the binding of the XyG acceptor substrate (Rocha et al., 2016). FUT1 was the first plant cell wall synthesizing GT to be structurally characterized. For structural analysis, two independent groups expressed FUT1 in two different eukaryotic cells, insect and HEK293S, which were truncated at the 68th and 80th amino acids, respectively, to remove its TMD (Cicéron et al., 2016; Rocha et al., 2016; Urbanowicz et al., 2017). Each truncation of FUT1 formed a homodimer in solution and crystalized as a homotetramer (Rocha et al., 2016; Urbanowicz et al., 2017). Similarly, full-length FUT1 has been reported to also form a homodimer *in vivo* (Chou et al., 2015). Although crystal structures were unable to capture FUT1 bound to GDP-Fuc, GDP was successfully bound (Rocha et al., 2016, Urbanowicz et al., 2017). Rocha et al. (2016) proposed that D300 of FUT1 acts as a catalytic base for an S_N2 reaction, confirmed by the reported mutation of D300A, which resulted in a lack of activity. Alternatively, Urbanowicz et al. (2017) concluded that D300 is not actually a catalytic base; rather water is necessary for a two-step S_n2 reaction (Urbanowicz et al., 2017). This was concluded because 1- a lack of residue conservation by other presumed homologs; 2- a large distance of 5 Å between D300 and the XXLG's Gal-O acceptor; 3- a repetitive presence of a water molecule within the active site in all reported crystal structures, including those from Rocha et al. (2016); Urbanowicz et al. (2017). Mutation of D300A in the later study led to reduced kinetics but failed to completely inactivate FUT1 activity, contradicting the earlier results reported by Rocha et al. (2016). It should be noted that both studies differed in their activity assays, with Rocha et al. (2016) utilizing a radioactive C_{14} labeled assay and Tamarind XyG as an acceptor. Urbanowicz et al. (2017) utilized the commercially available GDP-Glo kit and used highly purified XXLG fragments as the acceptor substrate. Urbanowicz et al. (2017) also suggested that the previous study of Rocha et al. (2016) may not have used sufficient concentration of FUT1 enzyme, which resulted in a lack of activity seen in D300 and other impaired mutants. Although both studies present plausible mechanisms, it remains unclear which mechanism FUT1 follows. Further comprehensive studies with improved dynamic analysis such as Cryo-EM is likely needed to further clarify the mechanism of fucosylation catalyzed by FUT1.

Recent biochemical studies suggest that FUT1 may be less specific than initially suggested. While FUT1 has been observed to only glycosylate the third branch in the XXXG subunit, its substrate recognition has been shown to be versatile. Besides fucosylation, FUT1 also may act as a GalT in the absence of GDP-Fuc. *In vitro* assays demonstrated that FUT1 transfers Gal to an XLLG or XXLG substrate at the third position, resulting in an XLJG or XXJG product, respectively (**Figure 1E**; Ohashi et al., 2019). While capable, the activity was 1/3 that of a GDP-Fuc substrate, indicating that FUT1 has a higher affinity for GDP-Fuc rather than for GDP-Gal. The above XLJG product is observed in a mutant strain of *Arabidopsis*, *mur1*, which also produced an XLJG product (Zablackis et al., 1996). The *mur1* mutation has been linked to an epimerase (GDP-D-Mannose-4,6-Dehydratase 2) responsible for the *de novo* synthesis of GTP-Fuc, leading to defects in all cell wall polysaccharides that contain Fuc (Bonin et al., 1997). Additionally, when the *mur1* mutant was crossed with *mur2* mutant, a lack of both galactosylation and fucosylation of XyG was observed, providing further evidence that the galactosylation was carried out by FUT1 due to a lack of GDP-Fuc availability (Vanzin et al., 2002). Acceptor recognition may also be flexible as FUT1 recognizes GalA in place of Gal. XyG in root hairs with GalA residues [β-D-Gal*p*A-(1→2)-α-D-Xyl*p*-(1→6)-β-D-Glc*p*; denoted Y; XXYG] are still fucosylated, resulting in an XXZG subunit (**Figure 1C**) [α-L-Fuc*p*-(1→2)-β-D-Gal*p*A-(1→2)-α-D-Xyl*p*-(1→6)-β-D-Glc*p*; denoted J] (Peña et al., 2012).

Arabinosylation of XXGG Type Xyloglucan

XyG arabinosylation is not well characterized, as it does not naturally occur in *Arabidopsis*. XyG arabinosylation occurs in the second position in XXGG type XyG, although the third position is arabinosylated in mutant plants that have XXXG type XyG. Arabinosylated XyG is prominently found in many Solanaceous plants, such as tomatoes and potatoes, which synthesize the XXGG pattern of XyG. In these species, the dominant subunits of XyG are found as XXGG, XSGG, and LSGG with acetylation of the third Glc in the glucan chain (**Figure 1B**; Jia et al., 2003). Similar to MUR3 and XLT2, arabinosyltransferases (AraT) are members of the GT47 family and are sequentially and functionally homologous to GalTs. Predictions from AlphaFold indicate that GalTs and AraTs have high structural homology. These structures are not available on uniprot.com and have been provided in this review (**Figure 3**). Instead of the galactosylation of the second and third XyG side chains, homologs of MUR3 and XLT2 within Solanaceous plants are suspected to transfer L-arabinofuranose rather than L-galactopyranose (Madson et al., 2003). Three putative AraT homologs in tomatoes were identified and transfected into *mur3 xlt2 Arabidopsis* mutants (Schultink et al., 2013). Independent expression of SlMUR3 (homolog to MUR3), SlXST1, and SlXST2 (both homologous to XLT2) in *mur3 xlt2 Arabidopsis* mutants resulted in XyG with XXSG structure. XST1 mutants produced higher levels of XXSG XyG than other transfected AraT homologs, while the SlMUR3 expressing plants did not produce any XXSG (**Table 2**; Schultink et al., 2013).

The effect of AraTs on tomato cell walls and growth is currently unknown. It is suspected that they arabinosylate the second position in the XXGG subunit to form XSGG, but it is unknown why tomato plants encode three separate AraTs for this task. Expression of AraTs in dwarfed *mur3 xlt2* mutant *Arabidopsis* plants resulted in comparable plant height to wild-type *Arabidopsis* plants. Due to predicted high structural homology between GalTs and AraTs, most likely, the former can easily occupy the same position in the XyG synthesizing complex in *Arabidopsis* Golgi to be discussed below, as they likely share similar recognition mechanisms. This will be interesting to investigate in the future, as the activity of these AraT have yet to be demonstrated.

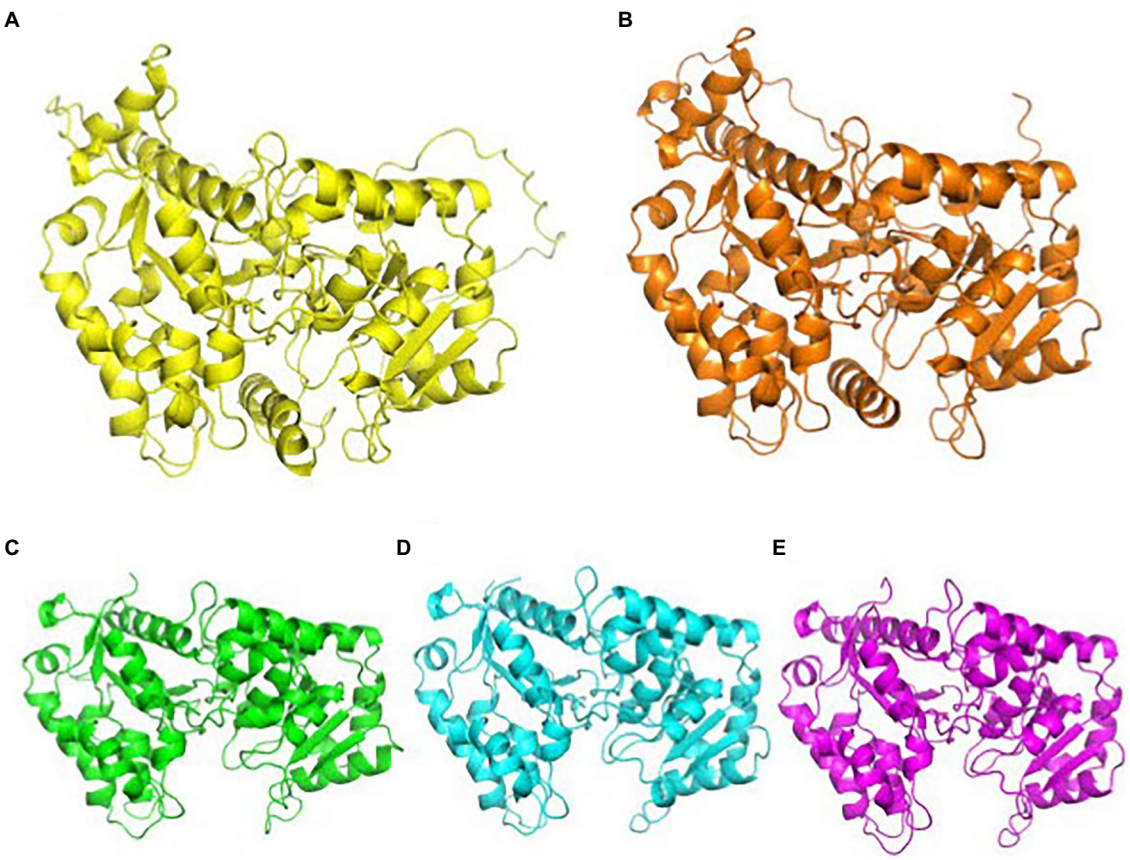

FIGURE 3 | AlphaFold predictions of CAZy family 47 GalTs and AraTs. GalTs are readily available at uniport.org, while AraTs were generated by AlphaFold for this review. **(A)** Structural prediction of AtMUR3, color: yellow. **(B)** Structural prediction of SlMUR3, color: orange. **(C)** Structural prediction of AtXLT2, color: green. **(D)** Structural prediction of SlXST1, color: cyan. **(E)** Structural prediction of SlXST2, color, magenta. The TMD and stem regions were removed for clarity. AlphaFold's prediction of the TMD and stem regions of these proteins are highly inaccurate, as computation software still struggles with transmembrane proteins. Images were aligned and generated using PyMOL.

Galacturonic Acid Substitution of Galactose

Xyloglucan-specific Galacturonosyltransferase1 (XUT1) is another predicted homolog to GalTs and is also a member of the CAZy family 47. XUT1 has only been found within the root hairs of *Arabidopsis* (Jensen et al., 2012; Peña et al., 2012). Previously reported as GT16 through transcriptome analysis, the activity of XUT1 has not been reported (Jensen et al., 2012). The current evidence suggests it transfers GalA to the first and third Xyl residues in the XyG subunit, resulting in the acidic YXXG, XXYG, and YXYG XyG subunits found only within the roots of *Arabidopsis* plants (**Figure 1D, Table 2**). Once XUT1 was deleted, XyG within the roots resembled that of XyG from vegetative tissue (XLFG), lacking acidic subunits. Plants with the *xut1* mutation also had significantly shorter root hairs than wild type *Arabidopsis* plants when grown on nutrient media (**Table 1**). *In vitro* activity of XUT1 has yet to be reported, although recombinant expression has been successful (Prabhakar et al., 2020). Interestingly, the GalA residue in the third chain can still be fucosylated in place of the typical Gal, resulting in the XXZG and YXZG XyG subunits (**Figure 1D**; Peña et al., 2012; Urbanowicz et al., 2017).

O-Acetylation of XyG

Currently, there are two distinct forms of *O*-acetylation in XyG molecules: acetylation of Gal residues and 6-*O*-acetylation of the glucan-backbone. *O*-Acetylating enzymes are classified into three families: Trichome-Birefringence-Like (TBL), Reduced-Wall-*O*-Acetylation (RWA), and a family represented by the enzyme Altered Xyloglucan 9 (AXY9; Schultink et al., 2015; Pauly and Ramírez, 2018). Members of each family are likely involved in the *O*-acetylation of several polysaccharides within the cell wall, including mannans, xylan, and XyG. Members of both TBL and AXY9 families are predicted to be type-2 membrane proteins, with their C-terminal catalytic domains within the Golgi lumen, similar to the GTs described above. Alternatively, RWA proteins are predicted to be integral membrane proteins, with up to 10 predicted transmembrane domains. These RWA proteins may act as transporters for unknown donors of acetyl groups rather than polysaccharide-specific acetyltransferases, although it is not confirmed (Pauly and Ramírez, 2018).

O-acetylation of Gal residues in the XyG side chain has been found in several organisms with XXXG type of XyG. XyG from sycamore and *Arabidopsis* cell walls were found to exhibit predominantly 6-*O*-monoacetylation of Gal residues, but 3-*O* and 4-*O*-monoacetylation and 3,4- and 4-6-di-*O*-acetylation has been observed (York et al., 1988; Zhong et al., 2018). Two proteins have been linked to the *O*-acetylation of Gal in *Arabidopsis* XyG: AXY4 and AXY4L. Single mutants lacking each gene indicated that AXY4 is responsible for *O*-acetylation in sprouting plants while AXY4L is active in seeds (**Table 2**; Gille et al., 2011). *O*-acetylation only occurs on the third Gal in the XXLG subunit, resulting in XXL̲G-like subunits (**Figure 1F**). XyG extracted from *Arabidopsis* cell walls exhibit acetylation of Gal residues in XLXG/XXLG, XLLG, XXFG and XLFG subunits. *In vitro* activity assays of AtAXY4, AtAXY4L, and homologs from *Populus trichocarpa* referred to as XGOATs, demonstrated that *O*-acetylation of Gal only occurred in subunits that had been pre-fucosylated, i.e., XXFG and XLFG. Gal residues in subunits lacking fucosylation, XLXG, XXLG, and XLLG, were not *O*-acetylated. This led Zhong et al. (2018) to propose that AXY4 and AXY4L are both specific towards Gal residues that have been fucosylated. They suggest that after the XyG is transported to the cell wall, AXY8, a fucosidase localized to the apoplast, defucosylates both acetylated and non-acetylated XyG, resulting in the reported XL̲LG and XX̲LG subunits within the cell walls (**Figures 1F,G**; **Table 2**; Zhong et al., 2018). Other putative acetyltransferases, such as AXY9, have been shown to be involved in the *O*-acetylation of multiple hemicelluloses, as knockout resulted in an overall reduction in cell wall acetylation. So AXY9 has been proposed to have an independent mode of acetylation from that of AXY4 and AXY4L and may function upstream of the two enzymes (Schultink et al., 2015). *In vitro*, AXY9 displayed minimal activity when incubated with mixed XyG acceptors, similar to the activity of AXY4 and AXY4L incubated with non-fucosylated XyG acceptors. This suggested that AXY9 is not specific for XyG acetylation, but still acts as an acetylesterase (Pauly and Ramírez, 2018; Zhong et al., 2018).

The glucan backbone is also directly *O*-acetylated at the C6 carbon of the third Glc in XXGG type XyG, resulting in XXG̲G (Jia et al., 2005). *O*-acetylation of the glucan chain has only been observed in species that produce the XXGG pattern of XyG, such as tomatoes. Glucan backbone acetylation has been linked to the protein XyBAT1, first discovered in *Brachypodium distachyon* (Liu et al., 2016). Upon the knockout of XyBAT1 in *Brachypodium*, there was a mass shift in the XyG profile, resulting in a new pattern of xylosylation resembling that of XXXG type XyG. Additionally, *xybat1* mutant plants displayed a 30% reduction in XyG acetylation (**Table 1**), while a reduction in other hemicellulose acetylation was not detected, indicating XyBat1 is specific for XyG acetylation. Using enzymatic assays, several homologs of XyBAT1 from rice and tomato have also been confirmed as acetyltransferases that are specific for the β-glucan backbone of XyG (Zhong et al., 2020). Upon expression of BdXyBAT1 in *Arabidopsis mur3 xlt2* mutant plants, the growth defect was rescued while the XyG mass-profile changed again with a low level of XyG resembling that of the *Brachyprodium* XXG̲G type (Liu et al., 2016). Furthermore, the dwarfism phenotype caused by the deletion of XLT2 and MUR3 was rescued by the expression of BdXyBAT1, resulting in the formation of acetylated XyG (Liu et al., 2016). On the other hand, rice XyBAT (OsXyBAT6) was expressed in wild-type *Arabidopsis*, which led to a severe growth defect phenotype. Cell wall analysis revealed that XyG from OsXyBAT1 transfected plants had subunits that were vastly different, with rarely detected patterns such as XG̲, FG, XFG̲, and more (Zhong et al., 2020). It appears that acetylation of the glucan backbone may compete with xylosylation and potentially be responsible for the lack of xylosylation on the third Glc in XXGG subunits in grass and tomato XyG. Further study is necessary to understand

the specificity of each acetyltransferase and the XyG biosynthesis process in regard to acetylation.

COMPLEX FORMATION AND LOCALIZATION OF XYG SYNTHESIZING ENZYMES WITHIN THE GOLGI

Like most polysaccharide synthesizing GTs, GTs involved in XyG synthesis are localized to the Golgi. The specific localization of GTs within the Golgi can promote the formation of multiprotein complexes differentially localized in the Golgi cisternae. Separation of Golgi stacks (*cis*, *medial*, and *trans*) using free-flow electrophoresis (FFE) paired with immunodetection of XyG using carbohydrate specific antibodies and immunogold labeling depicted the localization of XyG molecules throughout the Golgi stacks of *Arabidopsis* have provided insight into sub-Golgi localization (Parsons et al., 2019). High levels of only xylosylated XyG (XXXG subunit) were detected within the *cis*-cisternae with limited detection of low levels of galactosylated and fucosylated XyG. Xylosylated XyG was found to be similarly distributed throughout the *medial*-Golgi, with a moderate increase in galactosylated and fucosylated forms of XyG substitution. Finally, within the *trans*-Golgi, xylosylated XyG levels decreased slightly, while high levels of XLFG and XLLG were detected (Parsons et al., 2019). Independently, heterologous expression of GFP-tagged *Arabidopsis* GTs XXT1, MUR3, and FUT1 using tobacco BY-2 suspension-cultured cells demonstrated somewhat similar results of localization to that of the XyG polysaccharides (Chevalier et al., 2010). In the latter study, immunogold electroscopic microscopy showed XXT1 was localized to both *cis*- and *medial*-cisternae, where xylosylated XyG was most abundant. MUR3 and FUT1 localized to the *medial*- and *trans*-Golgi, where higher levels of completely branched XyG was localized. It is currently unknown what controls the localization of GTs in the Golgi, but it has been proposed that the GTs form a dynamic multicomplex in which proteins interact and separate in different cisternae (Chevalier et al., 2010; Zabotina et al., 2021). As to localization control, small peptide motifs within the N-terminals of GTs may be responsible for transportation and localization throughout the Golgi, localizing each to the correct cisternae. While a signaling peptide has yet to be confirmed for GTs and many plant localized Golgi proteins, yeast and mammalian cells have been thoroughly investigated and suggest plants may share the same machinery (Zhang and Zabotina, 2022).

Larger order complexes are quite common in many biosynthetic pathways, and some earlier evidence suggests XyG biosynthesis is not an exception. Several examples of the formation of complexes among GTs involved in the synthesis of different polysaccharides have been reported (Zabotina et al., 2021 and citations within). Some studies have given compelling evidence that some of these protein complexes may even be required for efficient biosynthesis (Atmodjo et al., 2011; Purushotham et al., 2020; Zabotina et al., 2021). The CeSA proteins, homologs to CSLCs, form large complexes known as cellulose synthesizing rosettes, synthesizing 18–24 glucan chains in close proximity to allow for twisting and assembly into large microfilaments (Purushotham et al., 2020). In the case of XyG, when CSLC4 was recombinantly expressed in *Pichia pastoris*, together with XXT1, it produced long insoluble oligomers of β-(1->4) glucan. While CSLC4 expressed alone only produced small soluble β-(1->4) glucan (Cocuron et al., 2007). These experiments confirmed that CLSC4 was responsible for XyG glucan backbone synthesis, and strongly indicated that CSLC4 requires the presence of XXTs, most likely within a multiprotein complex, to synthesize longer glucan chains of the glucan backbone. It is well known that glucan oligosaccharides are insoluble in aqueous solutions unless they are branched.

Chou et al. (2012, 2015) investigated the interactions among XyG synthesizing proteins (CSLC4, XXTs, MUR3, XLT2, and FUT1) utilizing bimolecular fluorescent complementation (BiFC) and coimmunoprecipitation (co-IP) with *Arabidopsis* protoplasts as an expression system. Additionally, *in vitro* pull-down assays of BL21 *Escherichia coli* cells expressed truncated GTs were used to further confirm the results from protoplasts, suggesting that XyG GTs indeed interact with one another (Chou et al., 2012, 2015). Only three proteins were shown to strongly interact with themselves, forming homodimers of CSLC4, XXT2, and FUT1. XXT1 has been confirmed to homodimerize at high concentrations required for crystallization, but *in vivo*, XXT1 dimers were not detected (Chou et al., 2012; Culbertson et al., 2018). Homodimers of MUR3 and XXT5 were not detected with BiFC. It was also shown that XXT2 competes with XXT5 homodimers, reducing the levels of XXT5 homooligomerization *in vivo*. However, MUR3 homooligomerization was detected in another study using a Renilla luciferase complementation assay in *N. benthamiana* (Lund et al., 2015). Interactions with the CSLC proteins are likely central to anchoring GTs together to form the complex, as BiFC experiments show heterocomplexes of CSLC4-MUR3, CSLC4-XLT2, CSLC4-FUT1 and both XXT2 and XXT5 formed (Chou et al., 2012, 2015). CSLC4s' distribution throughout all Golgi cisternae and interactions with other GTs provide a plausible indication that CSLCs recruit the other GTs to form a larger complex. Other interactions detected *via* both BiFC fluorescence and Renilla luciferase complementation included the XXT1-XXT2, XXT1-XXT5, XXT2-XLT2, and XLT2-FUT1 heterodimers (Chou et al., 2012, 2015; Lund et al., 2015). Additionally, pull-down assays confirmed the strong interactions between truncated variants of XXT2-XXT5, XXT2-FUT1, XXT5-FUT1, and MUR3-FUT1 expressed in *E. coli*, suggesting that GTs possibly interact *via* both their TMDs and catalytic domains localized to the Golgi lumen (Chou et al., 2012, 2015).

The types of interactions and how they may compete with one another among the different GTs within the multiprotein complexes have been proposed. Co-IP assays had demonstrated that homodimerization of XXT2 and FUT1 may be held together by disulfide bonds, as in reducing conditions, both proteins were exhibited in monomeric form, whereas homodimers were detected under non-reducing conditions (Chou et al., 2012, 2015). On the other hand, heterodimer XXT2-XXT5 is likely formed through non-covalent interactions, as XXT5 was only detected as a monomer (Chou et al., 2012, 2015). Alternatively,

the crystal structure of XXT1 suggests another hypothesis, as XXT1 and XXT2 share the same amino acids involved in dimer formation. XXT5 has one mutation of an amino acid involved in the XXT1 homodimer, but shares the other amino acids involved in dimerization. It is likely that the XXT2-XXT5 dimer is formed *via* non-covalent interactions involving the same residues observed in the crystal structure of the XXT1 homodimer. This notion is supported by BiFC, Co-IP assays, and results from reverse genetics, as XXT2-XXT5 was the most stable and preferred form of both XXT2 and XXT5 (Chou et al., 2012).

Although compelling evidence shows dimer formation, the larger multiprotein complexes have yet to be studied. The interactions of two proteins between multiple combinations provide reasonable evidence that they likely interact with more than one at a time. Combined with localization evidence, the GTs likely interchange throughout different cisternae. It is highly likely these multiprotein complexes are not required for GT catalytic activity, as many of them are active alone in solution in *in vitro* assays (Culbertson et al., 2016, 2018; Rocha et al., 2016; Urbanowicz et al., 2017; Zhong et al., 2018, 2020, 2021; Ehrlich et al., 2021). In context to complexes, the formation of multiprotein structures likely increases their efficiency and the overall rate of XyG synthesis. Spatial consolidation of GTs activities together, rather than the random binding of freely moving XyG molecules between individual proteins on one hand, supports fast and reproducible synthesis of completely branched XyG molecules and, on another hand, prevents termination of reaction due to low solubility of the long unsubstituted glucan chains. The current hypothesis suggests that XyG synthesizing multiprotein complex in *Arabidopsis* is composed of a CSLC homodimer, with at least three XXTs (1, 2, and 5), both GalTs, and a Fut1 dimer.

Due to high homology, GTs such as AraTs and GalATs likely interact similarly within such complexes, with recombinant AraT replacing GalT in the *Arabidopsis* protein complexes. It is currently unknown how AceTs interact with XyG, but given the current evidence, acetylation likely occurs after fucosylation (Zhong et al., 2020). Therefore, it is reasonable to suggest that AceTs may not be involved in this complex. However, the acetylation of the glucan backbone may be necessary to increase the solubility of XXGG type XyG. The potential competition for the third Glc in the XXGG repeat indicates that these AceTs likely interact closely with the other GTs, but this is still only hypothetical and requires further investigation (Liu et al., 2016; Zhong et al., 2018). There is still much to be understood in how XyG synthesizing GTs interact with one another, and current information is insufficient to completely reveal the mechanism of XyG biosynthesis.

CONCLUSION

This review presents the current state of knowledge about XyG biosynthesis. XyG synthesis is one of the most characterized polysaccharide biosynthesis processes in plants and serves as an excellent model for glycobiology by defining likely mechanisms and protein–protein interactions of the GTs involved in these processes. Most recent findings have focused on structural characterization, extending what is known about the protein structures and their homologs through numerous novel techniques that continue to evolve. Reverse genetics studies have elucidated numerous GTs and their effects on the plant's cell wall, providing evidence for recent research focusing on enzyme structure and substrate specificity (**Table 1**). While a considerable amount of work has been done in elucidating XyG biosynthesis since the last reviews (**Table 2**), many aspects of this process are still unclear.

The regulation and quality control of XyG biosynthesis is still unknown. Regulation likely occurs either within the Golgi during synthesis of XyG, or post-synthetically in the apoplast. Golgi localized regulation likely occurs through the concentration of donor substrates and activity of synthesizing GTs. Low concentrations of either molecules could explain the variety of branching of *Arabidopsis* XyG found in the cell walls, such as XXG, XLXG/XXLG, XLLG, and XLFG. Alternatively, hydrolases within the plant cell wall may cleave mature XyG branches after its incorporation into cell wall, such as the fucosidase AXY8 and other less characterized hydrolases. Another interesting question to understand is how XyG structures are synthesized with high-fidelity. Since the promiscuity of XXTs and FUT1 was observed, what prevents the promiscuous binding of "incorrect" donor substrates in the Golgi is still unknown. Wide variations in the XyG monosaccharide composition are not detected in wild-type *Arabidopsis* XyG, suggesting the promiscuity observed in *in vitro* reactions is not observed *in vivo*. Although structural constraints of GTs are likely the most effective mechanism, these constraints clearly do not completely prevent binding of different substrates when natural donor substrates are absent, as observed in the *mur2* plants. Further research is required to understand how reproduction of the same structural pattern with high-fidelity is controlled and at what stage, either during synthesis, post-synthetically or, most likely, both.

Unfortunately, only two GTs involved in XyG biosynthesis have been structurally characterized to date. Due to significant advances in bioinformatics, reasonably accurate structural predictions of any GT are available *via* advanced software such as AlphaFold. However, structural characterization using biophysical techniques, such as X-ray crystallography or cryo-EM, is still required because prediction software is far from reliably predicting protein folding, particularly when dealing with TMDs and random coiling (stem regions) of GTs. Furthermore, the understanding of details in enzyme-substrate binding to provide accurate description of the catalytic mechanisms of GTs still requires biophysical methods.

Another largely under-investigated aspect of XyG biosynthesis is the understanding of protein–protein interactions and complex formation. Structures of FUT1 and XXT1 provided new hypotheses for understanding the mechanisms of FUT1 and XXT1 catalysis using their 3D structures. Structural studies of GTs were slow before due to their low expression, potential glycosylation, and tendency to oligomerize or even aggregate. New recent developments in using HEK293 cells and advances in sensitivity

and accuracy of biophysical techniques allow for faster progress towards revealing structural organizations not only of single GTs but also their complexes. Co-expression of GTs in heterologous cells, utilization of artificial liposomes, nanodiscs, or more recently proposed amphipathic polymers together with high-resolution cryo-EM technology open new capabilities in advancing the studies of protein complex quaternary structures and the functions of GTs within such complexes.

While a considerable amount of work has been done in elucidating XyG biosynthesis in the last 5 years, there is much more to learn at the genetic, protein, and multiprotein level. To fully understand polysaccharide biosynthesis in plant Golgi, future protein work is urgently needed to elucidate GT mechanisms of enzymatic activity and substrate specificity, their localization and ER-Golgi transport, and their structural organization not only as an individual protein but, most importantly, their complexes.

AUTHOR CONTRIBUTIONS

All authors listed have made a substantial, direct, and intellectual contribution to the work and approved it for publication.

FUNDING

This research was funded by a grant from the National Science Foundation (NSF), grant number NSF-MCB #1856477.

ACKNOWLEDGMENTS

We apologize in advance to those whose work was not mentioned and cited in this review due to space limitations.

REFERENCES

Albesa-Jové, D., Mendoza, F., Rodrigo-Unzueta, A., Gomollón-Bel, F., Cifuente, J. O., Urresti, S., et al. (2015). A native ternary complex trapped in a crystal reveals the catalytic mechanism of a retaining glycosyltransferase. *Angew. Chem. Int. Ed. Eng.* 54, 9898–9902. doi: 10.1002/anie.201504617

Atmodjo, M. A., Sakuragi, Y., Zhu, X., Burrell, A. J., Mohanty, S. S., Atwood, J. A., et al. (2011). Galacturonosyltransferase (GAUT)1 and GAUT7 are the core of a plant cell wall pectin biosynthetic homogalacturonan:galacturonosyltransferase complex. *Proc. Natl. Acad. Sci. U. S. A.* 108, 20225–20230. doi: 10.1073/pnas.1112816108

Bi, Y., Hubbard, C., Purushotham, P., and Zimmer, J. (2015). Insights into the structure and function of membrane-integrated processive glycosyltransferases. *Curr. Opin. Struct. Biol.* 34, 78–86. doi: 10.1016/j.sbi.2015.07.008

Bonin, C. P., Potter, I., Vanzin, G. F., and Reiter, W. D. (1997). The MUR1 gene of *Arabidopsis thaliana* encodes an isoform of GDP-D-mannose-4,6-dehydratase, catalyzing the first step in the de novo synthesis of GDP-L-fucose. *Proc. Natl. Acad. Sci. U. S. A.* 94, 2085–2090. doi: 10.1073/pnas.94.5.2085

Cavalier, D. M., and Keegstra, K. (2006). Two xyloglucan xylosyltransferases catalyze the addition of multiple xylosyl residues to cellohexaose. *J. Biol. Chem.* 281, 34197–34207. doi: 10.1074/jbc.M606379200

Cavalier, D. M., Lerouxel, O., Neumetzler, L., Yamauchi, K., Reinecke, A., Freshour, G., et al. (2008). Disrupting two *Arabidopsis thaliana* xylosyltransferase genes results in plants deficient in xyloglucan, a major primary cell wall component. *Plant Cell* 20, 1519–1537. doi: 10.1105/tpc.108.059873

Chang, A., Singh, S., Phillips, G. N., and Thorson, J. S. (2011). Glycosyltransferase structural biology and its role in the design of catalysts for glycosylation. *Curr. Opin. Biotechnol.* 22, 800–808. doi: 10.1016/j.copbio.2011.04.013

Chevalier, L., Bernard, S., Ramdani, Y., Lamour, R., Bardor, M., Lerouge, P., et al. (2010). Subcompartment localization of the side chain xyloglucan-synthesizing enzymes within Golgi stacks of tobacco suspension-cultured cells. *Plant J.* 64, 977–989. doi: 10.1111/j.1365-313X.2010.04388.x

Chou, Y. H., Pogorelko, G., Young, Z. T., and Zabotina, O. A. (2015). Protein-protein interactions among xyloglucan-synthesizing enzymes and formation of Golgi-localized multiprotein complexes. *Plant Cell Physiol.* 56, 255–267. doi: 10.1093/pcp/pcu161

Chou, Y. H., Pogorelko, G., and Zabotina, O. A. (2012). Xyloglucan xylosyltransferases XXT1, XXT2, and XXT5 and the glucan synthase CSLC4 form Golgi-localized multiprotein complexes. *Plant Physiol.* 159, 1355–1366. doi: 10.1104/pp.112.199356

Cicéron, F., Rocha, J., Kousar, S., Hansen, S. F., Chazalet, V., Gillon, E., et al. (2016). Expression, purification and biochemical characterization of AtFUT1, a xyloglucan-specific fucosyltransferase from *Arabidopsis thaliana*. *Biochimie* 128-129, 183–192. doi: 10.1016/j.biochi.2016.08.012

Cocuron, J. C., Lerouxel, O., Drakakaki, G., Alonso, A. P., Liepman, A. H., Keegstra, K., et al. (2007). A gene from the cellulose synthase-like C family encodes a beta-1,4 glucan synthase. *Proc. Natl. Acad. Sci. U. S. A.* 104, 8550–8555. doi: 10.1073/pnas.0703133104

Culbertson, A. T., Chou, Y. H., Smith, A. L., Young, Z. T., Tietze, A. A., Cottaz, S., et al. (2016). Enzymatic activity of xyloglucan xylosyltransferase 5. *Plant Physiol.* 171, 1893–1904. doi: 10.1104/pp.16.00361

Culbertson, A. T., Ehrlich, J. J., Choe, J. Y., Honzatko, R. B., and Zabotina, O. A. (2018). Structure of xyloglucan xylosyltransferase 1 reveals simple steric rules that define biological patterns of xyloglucan polymers. *Proc. Natl. Acad. Sci. U. S. A.* 115, 6064–6069. doi: 10.1073/pnas.1801105115

Davis, J., Brandizzi, F., Liepman, A. H., and Keegstra, K. (2010). Arabidopsis mannan synthase CSLA9 and glucan synthase CSLC4 have opposite orientations in the Golgi membrane. *Plant J.* 64, 1028–1037. doi: 10.1111/j.1365-313X.2010.04392.x

Drula, E., Garron, M. L., Dogan, S., Lombard, V., Henrissat, B., and Terrapon, N. (2022). The carbohydrate-active enzyme database: functions and literature. *Nucleic Acids Res.* 50, D571–D577. doi: 10.1093/nar/gkab1045

Ehrlich, J. J., Weerts, R. M., Shome, S., Culbertson, A. T., Honzatko, R. B., Jernigan, R. L., et al. (2021). Xyloglucan xylosyltransferase 1 displays promiscuity toward donor substrates during in vitro reactions. *Plant Cell Physiol.* 62, 1890–1901. doi: 10.1093/pcp/pcab114

Faik, A., Price, N. J., Raikhel, N. V., and Keegstra, K. (2002). An Arabidopsis gene encoding an alpha-xylosyltransferase involved in xyloglucan biosynthesis. *Proc. Natl. Acad. Sci. U. S. A.* 99, 7797–7802. doi: 10.1073/pnas.102644799

Flynn, R. A., Pedram, K., Malaker, S. A., Batista, P. J., Smith, B. A. H., Johnson, A. G., et al. (2021). Small RNAs are modified with N-glycans and displayed on the surface of living cells. *Cell* 184, 3109.e22–3124.e22. doi: 10.1016/j.cell.2021.04.023

Fry, S. C., York, W. S., Albersheim, P., Darvill, A., Hayashi, T., Joseleau, J. P., et al. (1993). An unambiguous nomenclature for xyloglucan-derived oligosaccharides. *Physiol. Plant.* 89, 1–3. doi: 10.1111/j.1399-3054.1993.tb01778.x

Gille, S., de Souza, A., Xiong, G., Benz, M., Cheng, K., Schultink, A., et al. (2011). O-acetylation of *Arabidopsis* hemicellulose xyloglucan requires AXY4 or AXY4L, proteins with a TBL and DUF231 domain. *Plant Cell* 23, 4041–4053. doi: 10.1105/tpc.111.091728

Gómez, H., Polyak, I., Thiel, W., Lluch, J. M., and Masgrau, L. (2012). Retaining glycosyltransferase mechanism studied by QM/MM methods: lipopolysaccharyl-α-1,4-galactosyltransferase C transfers α-galactose via an oxocarbenium ion-like transition state. *J. Am. Chem. Soc.* 134, 4743–4752. doi: 10.1021/ja210490f

Jensen, J. K., Schultink, A., Keegstra, K., Wilkerson, C. G., and Pauly, M. (2012). RNA-Seq analysis of developing nasturtium seeds (*Tropaeolum majus*): identification and characterization of an additional galactosyltransferase involved in xyloglucan biosynthesis. *Mol. Plant* 5, 984–992. doi: 10.1093/mp/sss032

Jia, Z., Cash, M., Darvill, A. G., and York, W. S. (2005). NMR characterization of endogenously O-acetylated oligosaccharides isolated from tomato (*Lycopersicon esculentum*) xyloglucan. *Carbohydr. Res.* 340, 1818–1825. doi: 10.1016/j.carres.2005.04.015

Jia, Z., Qin, Q., Darvill, A. G., and York, W. S. (2003). Structure of the xyloglucan produced by suspension-cultured tomato cells. *Carbohydr. Res.* 338, 1197–1208. doi: 10.1016/s0008-6215(03)00079-x

Jumper, J., Evans, R., Pritzel, A., Green, T., Figurnov, M., Ronneberger, O., et al. (2021). Highly accurate protein structure prediction with AlphaFold. *Nature* 596, 583–589. doi: 10.1038/s41586-021-03819-2

Kim, S. J., Chandrasekar, B., Rea, A. C., Danhof, L., Zemelis-Durfee, S., Thrower, N., et al. (2020). The synthesis of xyloglucan, an abundant plant cell wall polysaccharide, requires CSLC function. *Proc. Natl. Acad. Sci. U. S. A.* 117, 20316–20324. doi: 10.1073/pnas.2007245117

Kong, Y., Pena, M. J., Renna, L., Avci, U., Pattathil, S., Tuomivaara, S. T., et al. (2015). Galactose-depleted xyloglucan is dysfunctional and leads to dwarfism in *Arabidopsis*. *Plant Physiol.* 167, 1296–1306. doi: 10.1104/pp.114.255943

Kumar, M., Mishra, L., Carr, P., Pilling, M., Gardner, P., Mansfield, S. D., et al. (2018). Exploiting CELLULOSE SYNTHASE (CESA) class specificity to probe cellulose microfibril biosynthesis. *Plant Physiol.* 177, 151–167. doi: 10.1104/pp.18.00263

Lairson, L. L., Henrissat, B., Davies, G. J., and Withers, S. G. (2008). Glycosyltransferases: structures, functions, and mechanisms. *Annu. Rev. Biochem.* 77, 521–555. doi: 10.1146/annurev.biochem.76.061005.092322

Li, W., Guan, Q., Wang, Z. Y., Wang, Y., and Zhu, J. (2013). A bi-functional xyloglucan galactosyltransferase is an indispensable salt stress tolerance determinant in *Arabidopsis*. *Mol. Plant* 6, 1344–1354. doi: 10.1093/mp/sst062

Liu, L., Hsia, M. M., Dama, M., Vogel, J., and Pauly, M. (2016). A Xyloglucan backbone 6-O-Acetyltransferase from *Brachypodium distachyon* modulates xyloglucan xylosylation. *Mol. Plant* 9, 615–617. doi: 10.1016/j.molp.2015.11.004

Lund, C. H., Bromley, J. R., Stenbæk, A., Rasmussen, R. E., Scheller, H. V., and Sakuragi, Y. (2015). A reversible Renilla luciferase protein complementation assay for rapid identification of protein-protein interactions reveals the existence of an interaction network involved in xyloglucan biosynthesis in the plant Golgi apparatus. *J. Exp. Bot.* 66, 85–97. doi: 10.1093/jxb/eru401

Madson, M., Dunand, C., Li, X., Verma, R., Vanzin, G. F., Caplan, J., et al. (2003). The MUR3 gene of *Arabidopsis* encodes a xyloglucan galactosyltransferase that is evolutionarily related to animal exostosins. *Plant Cell* 15, 1662–1670. doi: 10.1105/tpc.009837

McNamara, J. T., Morgan, J. L., and Zimmer, J. (2015). A molecular description of cellulose biosynthesis. *Annu. Rev. Biochem.* 84, 895–921. doi: 10.1146/annurev-biochem-060614-033930

Morgan, J. L., McNamara, J. T., Fischer, M., Rich, J., Chen, H. M., Withers, S. G., et al. (2016). Observing cellulose biosynthesis and membrane translocation in crystallo. *Nature* 531, 329–334. doi: 10.1038/nature16966

Morgan, J. L., Strumillo, J., and Zimmer, J. (2013). Crystallographic snapshot of cellulose synthesis and membrane translocation. *Nature* 493, 181–186. doi: 10.1038/nature11744

Ohashi, H., Ohashi, T., Misaki, R., and Fujiyama, K. (2019). *Arabidopsis thaliana* α1,2-l-fucosyltransferase catalyzes the transfer of l-galactose to xyloglucan oligosaccharides. *FEBS Lett.* 593, 187–194. doi: 10.1002/1873-3468.13303

Parsons, H. T., Stevens, T. J., McFarlane, H. E., Vidal-Melgosa, S., Griss, J., Lawrence, N., et al. (2019). Separating Golgi proteins from *cis* to *trans* reveals underlying properties of cisternal localization. *Plant Cell* 31, 2010–2034. doi: 10.1105/tpc.19.00081

Pauly, M., and Keegstra, K. (2016). Biosynthesis of the plant cell wall matrix polysaccharide xyloglucan. *Annu. Rev. Plant Biol.* 67, 235–259. doi: 10.1146/annurev-arplant-043015-112222

Pauly, M., and Ramírez, V. (2018). New insights into wall polysaccharide *O*-acetylation. *Front. Plant Sci.* 9:1210. doi: 10.3389/fpls.2018.01210

Peña, M. J., Kong, Y., York, W. S., and O'Neill, M. A. (2012). A galacturonic acid-containing xyloglucan is involved in *Arabidopsis* root hair tip growth. *Plant Cell* 24, 4511–4524. doi: 10.1105/tpc.112.103390

Perrin, R. M., Jia, Z., Wagner, T. A., O'Neill, M. A., Sarria, R., York, W. S., et al. (2003). Analysis of xyloglucan fucosylation in *Arabidopsis*. *Plant Physiol.* 132, 768–778. doi: 10.1104/pp.102.016642

Prabhakar, P. K., Wang, H. T., Smith, P. J., Yang, J. Y., Barnes, W. J., Peña, M. J., et al. (2020). Heterologous expression of plant glycosyltransferases for biochemistry and structural biology. *Methods Cell Biol.* 160, 145–165. doi: 10.1016/bs.mcb.2020.05.002

Purushotham, P., Ho, R., and Zimmer, J. (2020). Architecture of a catalytically active homotrimeric plant cellulose synthase complex. *Science* 369, 1089–1094. doi: 10.1126/science.abb2978

Reichmann, N. T., and Gründling, A. (2011). Location, synthesis and function of glycolipids and polyglycerolphosphate lipoteichoic acid in gram-positive bacteria of the phylum firmicutes. *FEMS Microbiol. Lett.* 319, 97–105. doi: 10.1111/j.1574-6968.2011.02260.x

Riley, N. M., Hebert, A. S., Westphall, M. S., and Coon, J. J. (2019). Capturing site-specific heterogeneity with large-scale N-glycoproteome analysis. *Nat. Commun.* 10:1311. doi: 10.1038/s41467-019-09222-w

Rocha, J., Cicéron, F., de Sanctis, D., Lelimousin, M., Chazalet, V., Lerouxel, O., et al. (2016). Structure of *Arabidopsis thaliana* FUT1 reveals a variant of the GT-B class fold and provides insight into xyloglucan fucosylation. *Plant Cell* 28, 2352–2364. doi: 10.1105/tpc.16.00519

Ruprecht, C., Bartetzko, M. P., Senf, D., Lakhina, A., Smith, P. J., Soto, M. J., et al. (2020). A glycan array-based assay for the identification and characterization of plant glycosyltransferases. *Angew. Chem. Int. Ed. Eng.* 59, 12493–12498. doi: 10.1002/anie.202003105

Schrödinger, L., and DeLano, W. (2020). PyMOL. Available at: http://www.pymol.org/pymol (Accessed April 14, 2022).

Schultink, A., Cheng, K., Park, Y. B., Cosgrove, D. J., and Pauly, M. (2013). The identification of two arabinosyltransferases from tomato reveals functional equivalency of xyloglucan side chain substituents. *Plant Physiol.* 163, 86–94. doi: 10.1104/pp.113.221788

Schultink, A., Naylor, D., Dama, M., and Pauly, M. (2015). The role of the plant-specific ALTERED XYLOGLUCAN9 protein in *Arabidopsis* cell wall polysaccharide O-acetylation. *Plant Physiol.* 167, 1271–1283. doi: 10.1104/pp.114.256479

Schuman, B., Evans, S. V., and Fyles, T. M. (2013). Geometric attributes of retaining glycosyltransferase enzymes favor an orthogonal mechanism. *PLoS One* 8:e71077. doi: 10.1371/journal.pone.0071077

Tamura, K., Shimada, T., Kondo, M., Nishimura, M., and Hara-Nishimura, I. (2005). KATAMARI1/MURUS3 is a novel Golgi membrane protein that is required for endomembrane organization in *Arabidopsis*. *Plant Cell* 17, 1764–1776. doi: 10.1105/tpc.105.031930

Tuomivaara, S. T., Yaoi, K., O'Neill, M. A., and York, W. S. (2015). Generation and structural validation of a library of diverse xyloglucan-derived oligosaccharides, including an update on xyloglucan nomenclature. *Carbohydr. Res.* 402, 56–66. doi: 10.1016/j.carres.2014.06.031

Urbanowicz, B. R., Bharadwaj, V. S., Alahuhta, M., Peña, M. J., Lunin, V. V., Bomble, Y. J., et al. (2017). Structural, mutagenic and in silico studies of xyloglucan fucosylation in *Arabidopsis thaliana* suggest a water-mediated mechanism. *Plant J.* 91, 931–949. doi: 10.1111/tpj.13628

Vanzin, G. F., Madson, M., Carpita, N. C., Raikhel, N. V., Keegstra, K., and Reiter, W. D. (2002). The mur2 mutant of *Arabidopsis thaliana* lacks fucosylated xyloglucan because of a lesion in fucosyltransferase AtFUT1. *Proc. Natl. Acad. Sci. U. S. A.* 99, 3340–3345. doi: 10.1073/pnas.052450699

Wilkop, T., Pattathil, S., Ren, G., Davis, D. J., Bao, W., Duan, D., et al. (2019). A hybrid approach enabling large-scale glycomic analysis of post-Golgi vesicles reveals a transport route for polysaccharides. *Plant Cell* 31, 627–644. doi: 10.1105/tpc.18.00854

York, W. S., Oates, J. E., van Halbeek, H., Darvill, A. G., Albersheim, P., Tiller, P. R., et al. (1988). Location of the O-acetyl substituents on a nonasaccharide repeating unit of sycamore extracellular xyloglucan. *Carbohydr. Res.* 173, 113–132. doi: 10.1016/s0008-6215(00)90807-3

Zablackis, E., York, W. S., Pauly, M., Hantus, S., Reiter, W. D., Chapple, C. C., et al. (1996). Substitution of L-fucose by L-galactose in cell walls of *Arabidopsis* mur1. *Science* 272, 1808–1810. doi: 10.1126/science.272.5269.1808

Zabotina, O. A. (2012). Xyloglucan and its biosynthesis. *Front. Plant. Sci.* 3:134. doi: 10.3389/fpls.2012.00134

Zabotina, O. A., Avci, U., Cavalier, D., Pattathil, S., Chou, Y. H., Eberhard, S., et al. (2012). Mutations in multiple XXT genes of *Arabidopsis* reveal the complexity of xyloglucan biosynthesis. *Plant Physiol.* 159, 1367–1384. doi: 10.1104/pp.112.198119

Zabotina, O. A., van de Ven, W. T., Freshour, G., Drakakaki, G., Cavalier, D., Mouille, G., et al. (2008). *Arabidopsis* XXT5 gene encodes a putative alpha-1,6-xylosyltransferase that is involved in xyloglucan biosynthesis. *Plant J.* 56, 101–115. doi: 10.1111/j.1365-313X.2008.03580

Zabotina, O. A., Zhang, N., and Weerts, R. (2021). Polysaccharide biosynthesis: glycosyltransferases and their complexes. *Front. Plant Sci.* 12:625307. doi: 10.3389/fpls.2021.625307

Zhang, N., and Zabotina, O. A. (2022). Critical determinants in ER-Golgi trafficking of enzymes involved in glycosylation. *Plants* 11:428. doi: 10.3390/plants11030428

Zhong, R., Cui, D., Phillips, D. R., Richardson, E. A., and Ye, Z. H. (2020). A group of O-acetyltransferases catalyze xyloglucan backbone acetylation and can alter xyloglucan xylosylation pattern and plant growth when expressed in *Arabidopsis*. *Plant Cell Physiol.* 61, 1064–1079. doi: 10.1093/pcp/pcaa031

Zhong, R., Cui, D., and Ye, Z. H. (2018). Xyloglucan O-acetyltransferases from *Arabidopsis thaliana* and *Populus trichocarpa* catalyze acetylation of fucosylated galactose residues on xyloglucan side chains. *Planta* 248, 1159–1171. doi: 10.1007/s00425-018-2972-0

Zhong, R., Phillips, D. R., and Ye, Z. H. (2021). A single xyloglucan xylosyltransferase is sufficient for generation of the XXXG xylosylation pattern of xyloglucan. *Plant Cell Physiol.* 62, 1589–1602. doi: 10.1093/pcp/pcab113

Zimmer, J. (2019). Structural features underlying recognition and translocation of extracellular polysaccharides. *Inter. Focus* 9:20180060. doi: 10.1098/rsfs.2018.0060

Conflict of Interest: The authors declare that the research was conducted in the absence of any commercial or financial relationships that could be construed as a potential conflict of interest.

Publisher's Note: All claims expressed in this article are solely those of the authors and do not necessarily represent those of their affiliated organizations, or those of the publisher, the editors and the reviewers. Any product that may be evaluated in this article, or claim that may be made by its manufacturer, is not guaranteed or endorsed by the publisher.

frontiers | Frontiers in Plant Science

ORIGINAL RESEARCH
published: 16 June 2022
doi: 10.3389/fpls.2022.875799

Late Embryogenesis Abundant (LEA)5 Regulates Translation in Mitochondria and Chloroplasts to Enhance Growth and Stress Tolerance

*Barbara Karpinska[1], Nurhayati Razak[1], Daniel S. Shaw[2], William Plumb[1], Eveline Van De Slijke[3,4], Jennifer Stephens[5], Geert De Jaeger[3,4], Monika W. Murcha[6] and Christine H. Foyer[1]**

[1] School of Biosciences, College of Life and Environmental Sciences, University of Birmingham, Birmingham, United Kingdom, [2] Centre for Plant Sciences, School of Biology, Faculty of Biological Sciences, University of Leeds, Leeds, United Kingdom, [3] Department of Plant Biotechnology and Bioinformatics, Ghent University, Ghent, Belgium, [4] VIB Center for Plant Systems Biology, Ghent, Belgium, [5] Cell and Molecular Sciences, The James Hutton Institute, Dundee, United Kingdom, [6] School of Molecular Sciences, Perth, WA, Australia

OPEN ACCESS

Edited by:
Vasileios Fotopoulos, Cyprus University of Technology, Cyprus

Reviewed by:
Ghazala Nawaz, Kohat University of Science and Technology, Pakistan
Elina Welchen, National University of Littoral, Argentina

***Correspondence:**
Christine H. Foyer
C.H.Foyer@bham.ac.uk

Specialty section:
This article was submitted to Plant Physiology, a section of the journal Frontiers in Plant Science

Received: *14 February 2022*
Accepted: *01 April 2022*
Published: *16 June 2022*

Citation:
Karpinska B, Razak N, Shaw DS, Plumb W, Van De Slijke E, Stephens J, De Jaeger G, Murcha MW and Foyer CH (2022) Late Embryogenesis Abundant (LEA)5 Regulates Translation in Mitochondria and Chloroplasts to Enhance Growth and Stress Tolerance. Front. Plant Sci. 13:875799. doi: 10.3389/fpls.2022.875799

The late embryogenesis abundant (LEA)5 protein is predominantly expressed in Arabidopsis leaves in the dark, the levels of *LEA5* transcripts decreasing rapidly upon illumination. LEA5 is important in plant responses to environmental stresses but the mechanisms involved have not been elucidated. We therefore explored LEA5 functions in Arabidopsis mutants (*lea5*) and transgenic Arabidopsis plants constitutively expressing LEA5 (OEX 2-5), as well as in transgenic barley lines expressing the Arabidopsis *LEA5* gene. The OEX 2-5 plants grew better than controls and *lea5* mutants in the presence of the prooxidants methyl viologen and menadione. Confocal microscopy of Arabidopsis mesophyll protoplasts expressing a LEA5-YFP fusion protein demonstrated that LEA5 could be localized to chloroplasts as well as mitochondria in Arabidopsis protoplasts. Tandem affinity purification (TAP) analysis revealed LEA5 interacts with the chloroplast DEAD-box ATP-dependent RNA helicase 22 (RH22) in Arabidopsis cells. Split YFP analysis confirmed the interaction between RH22 and LEA5 in chloroplasts. The abundance of translated protein products in chloroplasts was decreased in transgenic Arabidopsis plants and increased in *lea5* knockout mutants. Conversely, the abundance of translated mitochondrial protein products was increased in OEX 2-5 plants and decreased in *lea5* mutants. Mitochondrial electron transport rates were higher in the OEX 2-5 plants than the wild type. The transformed barley lines expressing the Arabidopsis LEA5 had increased seed yields, but they showed a greater drought-induced inhibition of photosynthesis than controls. Taken together, these data demonstrate that LEA5 regulates organellar translation, in order to enhance respiration relative to photosynthesis in response to stress.

Keywords: respiration, mitochondria, chloroplasts, translation, signaling

INTRODUCTION

Late embryogenesis abundant (LEA) proteins are a diverse family of small and hydrophilic polypeptides (10–30 kD) that protect plant tissues against a wide range of abiotic stresses by acting as molecular chaperones that bind to enzymes, membranes, DNA/RNA, and ROS (Umezawa et al., 2006; Tunnacliffe and Wise, 2007; Lan et al., 2013; Lee et al., 2013). They accumulate at the later stages of embryogenesis during seed desiccation and they are also abundant in vegetative organs (Shao et al., 2005; Lan et al., 2013; Hatanaka et al., 2015). LEA proteins, which are rich in alanine, glycine and serine, are characterized by different conserved sequence motifs composed of repeating arrangements of hydrophilic amino acids. They are intrinsically disordered in the fully hydrated state, but they form α-helical ordered structures upon exposure to stresses such as drought. For example, overexpression of a melon Y3SK2-type LEA, which belongs to the dehydrin (DHNs) group, in tobacco conferred drought and salt tolerance (Poku et al., 2020).

LEA proteins are found in many subcellular compartments, particularly mitochondria, chloroplasts, and the cytosol (Huang et al., 2016; Magwanga et al., 2018). Phytohormones such as abscisic acid (ABA) and stress-driven signals regulate LEA expression (Artur et al., 2019). For example, LEA5 (also called LEA 38, At4g02380), which belongs to an anomalous LEA protein group (type 3) in Arabidopsis (Avelange-Macherel et al., 2018), is expressed in response to ABA and oxidative stress (Mowla et al., 2006). In addition to transcriptional regulation, LEA proteins undergo translational or posttranslational modifications, reflecting the complexity of the regulation of these proteins (Sun et al., 2013; Verdier et al., 2013).

The LEA type 3 family are characterized by the presence of a tryptophan-containing W-motif (Singh and Graether, 2020). They are small (11.1 kD) in size, having an 11-amino acid sequence (TAQAAKEKAGE) repeated 13-times and they are disordered in solution (Jaspard et al., 2012). Over 450 LEA3 proteins are found in the Phytozome v13 database (Singh and Graether, 2020). LEA5 is paralogous to LEA2 (At1g02820). However, LEA5 has an additional 11 residue-long stretch of amino acids (AQGSVSSGGRS), which is required for mitochondrial targeting (Avelange-Macherel et al., 2018).

Earlier reports had shown that LEA5 fulfills functions in plant growth and abiotic stress tolerance (Mowla et al., 2006; MohdSalleh et al., 2012). Moreover, LEA5 was identified in a genome-wide association study (GWAS) seeking to identify Arabidopsis loci involved in local geographic adaptation, suggesting that LEA5 plays an important role in adaptations to environmental conditions (Fournier-Level et al., 2011). A single nucleotide polymorphism (SNP) at position 1046738 (A/T), which is in the first exon of *AtLEA5*, was associated with local adaptation to temperature stress in Finland (Fournier-Level et al., 2011). The T allele, which is the less frequent allele across Arabidopsis ecotypes, was associated with poor survival in Finland, in relation to low-temperature stress. It is likely therefore that LEA5 contributes to stress tolerance under field conditions (Fournier-Level et al., 2011).

In the absence of stress, LEA5 is expressed in leaves only in the dark and the levels of *LEA5* transcripts decline rapidly when leaves are exposed to light (Mowla et al., 2006). The dark-induced expression of LEA5 does not appear to be subject to circadian regulation. LEA5 expression is triggered in the light upon exposure to biotic or abiotic stresses or stress hormones (Mowla et al., 2006; MohdSalleh et al., 2012). Transgenic Arabidopsis lines overexpressing *AtLEA5* had similar photosynthesis rates to the wild type plants under optimal growth conditions. Interestingly, photosynthetic CO_2 assimilation rates were more severely inhibited by drought in the LEA5 overexpression lines than the wild type controls (Mowla et al., 2006). However, LEA5 overexpression had a beneficial impact on plant growth even under drought stress (Mowla et al., 2006). The following studies were performed to explore the mechanisms by which LEA5 regulates plant growth, development and stress tolerance in model, and crop plants.

MATERIALS AND METHODS

Plant Material and Growth Conditions

Seeds of wild type Arabidopsis (Col-0), a transgenic line overexpressing LEA5 (OEX2-5; Mowla et al., 2006) and T-DNA insertion mutant lines (*lea5*) were used in the following studies. The *lea5* T-DNA SALK line (SALK_099663), which has an insertion in the second exon of AT4G02380, was obtained from TAIR. A T-DNA insertion *rh22* mutant line with a T-DNA insertion in sixth intron of the At1g59990 gene, was also used in these studies. The seeds of this line were a gift from Professor Masatake Kanai (Kanai et al., 2013). Genotyping was performed as recommended by the T-DNA primer design website http://signal.salk.edu/tdnaprimers.2.html.

Arabidopsis seeds were vapor-sterilized using commercial bleach with concentrated HCL for 2 h, then sown onto Petri dishes containing 0.5x Murashige and Skoog (MS) basal salts, 1% agar, pH 5.7 and sealed with micro pore tape and later stratified for 2 days at 4°C.

The plates were then either transferred to controlled environment chambers at 20°C and grown under a long photoperiod (16 h light and 8 h dark), with a light intensity of 150 μmol m^{-2} s^{-1} and relative humidity (70%) for 14 days, or germinating seeds were transplanted to soil and grown in controlled environment chambers, under growth conditions, as described above.

Seeds of wild type barley (*Hordeum vulgare* CV Golden Promise) and transgenic barley lines expressing the Arabidopsis LEA5 sequence (9.1, 10.1, and 11.2) were sterilized using 10% ($^{v}/_{V}$) bleach for 15 min, followed by 3 washes (each 10 min) with 80% of ethanol and 5 washes with 50 ml of sterilized water in a laminar flow cabinet. Plants were grown on compost under controlled environment conditions with a 16 h light/8 h dark photoperiod regime (400 μmol m^{-2} s^{-1}).

Oxidative Stress Treatments

For these studies, seeds were sown onto Petri dishes, as described above, except that the plates contained either no added oxidants

(Control), or methyl viologen (0.1 μM), or menadione (0.1 mM). Seedlings were grown under a 16 h photoperiod (150 $\mu mol.m^{-2}.s^{-1}$ irradiance) at 22°C ± 2°C for 21 days prior to analysis.

Drought Treatments

For these studies, seedlings of wild type barley, transgenic lines expressing the Arabidopsis LEA5 sequence (9.1, 10.1, and 11.2) and empty vector and GUS controls were grown for 7 days on soil under well-watered conditions in controlled environments, as described above. Thereafter, half of the plants were maintained under well-watered conditions and half were deprived of water for 7 days. Photosynthesis measurements were then performed.

Organelle and Protoplast Isolation

Intact chloroplast and mitochondria fractions were isolated from 14-day old plate-grown seedlings according to protocols described by Aronsson and Jarvis (2011) and Murcha and Whelan (2015), respectively. Tape-Arabidopsis Sandwich protocols were used for protoplast isolation and PEG transformation (Wu et al., 2009).

Measurements of the Integrity of Mitochondrial Fractions

The percentage of intact mitochondria present in isolated fractions was measured via the latency of cytochrome C oxidase (COX) activity in the absence and presence of Triton X-100 using Clark-type oxygen electrode (Neuberger et al., 1982; Shaw et al., 2017).

Complex II Respiratory Control

Respiratory control at the level of Complex 1 was measured as described by Shaw et al. (2017). Firstly, mitochondria were added to a 1 ml liquid phase oxygen electrode chamber at final concentration 100 μg/ml. Pyruvate, thiamine pyrophosphate (TPP) and malate were added to the final concentrations of 2, 3, and 2 mM, respectively. After 2 min 20 μl of 100 mM ADP was added and after a further 2 min the reaction was stopped with the addition of 2 μg/ml oligomycin. Then 0.5 μM carbonyl cyanide p-trifluoromethoxyphenylhydrazone (FCCP) was added.

Complex II Respiratory Control

Respiratory control at the level of Complex II was measured as described by Shaw et al. (2017). Mitochondria were first added to a 1 ml liquid phase oxygen electrode chamber at final concentration 100 μg/ml. Then 10 mM succinate was added to the chamber. After 1 min, 0.5 μM rotenone was added to inhibit complex I activity. Thereafter, 20 μl of 100 mM ADP was added followed 2 μg/ml oligomycin and 0.5 μM FCCP.

Labeling of Mitochondrial and Chloroplast Translation Products With [^{35}S] Met "in Organello"

Intact organelle fractions were suspended in assay buffer, prior to analysis. Aliquots (60–100 μg protein) were added to buffer containing the mixture of 19 amino acids. Reactions were started by the addition of 225 uCi [35S] methionine (1,000 Ci/mM) and incubated at 25°C with constant rotatory shaking for 60 min. Mitochondrial fractions were incubated in the dark, while chloroplast fractions were incubated at low light conditions (100 $\mu mol\ m^{-2}\ s^{-1}$). Reactions were stopped by the addition of cold buffer containing non-labeled methionine. Proteins were separated on 14% SDS-PAGE gels. The incorporation of [35S]-Met into protein bands was determined by soaking the gels in ENLIGHTNING^{TM} Rapid Autoradiography Enhancer. After drying, the gels were analyzed using a phosphorimager (Bio Rad) at high resolution for 48 h.

PCR Reactions

Reverse transcription of 1 μg of RNA aliquots into cDNA was performed using the QuantiTect Reverse Transcription Kit (Qiagen). Thereafter, qPCR was performed using QuantiFast SYBR Green PCR kit (Qiagen) in the presence of 0.5 μM primers in a CFX96 thermocycler (Biorad, Hercules, CA, United States) following the manufacturer's instructions. The two-step cycling protocol was programmed as follows: incubation at 95°C for 5 min; 40 cycles of amplification comprised of 95°C for 10 s, 60°C for 30 s and 72°C for 30 s. The mean value of three replicates was normalized using actin 11 as internal controls. All amplifications for the cloning purposes were done with Thermo Scientific Phusion High-Fidelity DNA Polymerase according to manufacturer's instructions. All primer sequences are listed in **Supplementary Table 2**.

Confocal Microscopy

Intact leaf mesophyll protoplasts were prepared from 14-day old Arabidopsis seedlings expressing the LEA5-YFP protein. Images of these protoplasts or 5 days old plate-grown seedlings expressing the LEA5-YFP protein were prepared using a Zeiss LSM700 laser scanning confocal microscope using 20×/0.8 Plan-Apochromat, 40×/1.2 W C-Apochromat or 63 × /1.4 Oil Plan-Apochromat in multi-track channel mode. Three fluorescent proteins were excited with the following excitation wavelengths: GFP with 488 nm, YFP with 514 nm, and RFP with 651 nm. Mitochondria were labeled with red-fluorescent dye, Mitotracker Red CMXRos (Thermo Fisher Scientific) after excitation at 578 nm. Images were collected using LP emission filters 500–710 nm and processed using Zeiss ZEN 2011 (black edition).

Preparation of the Late Embryogenesis Abundant 5 and RNA Helicase 22 Constructs

Cloning Late Embryogenesis Abundant 5-YFP Fusion Protein Constructs

PCR products containing LEA5 joined in frame to YFP were cloned into pDONR207 using the Gateway BP recombination reaction (Invitrogen). After verification of the nucleotide sequence of the fragment, Gateway LR recombination reaction (Invitrogen) was used to transfer the LEA5-YFP into pBRACT214 vector containing ubiquitin promoter and hygromycin B resistance for positive selection of transformed plants.

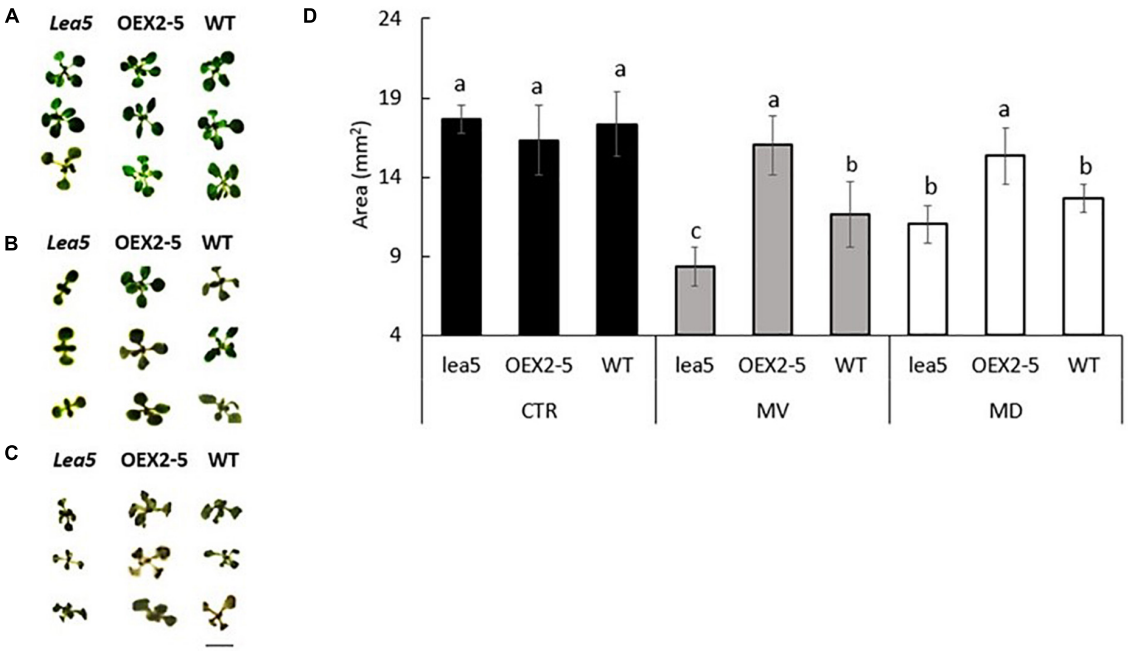

FIGURE 1 | The rosette phenotypes **(A–C)** and growth (determined as rosette area) of wild type Arabidopsis (WT), mutants defective in LEA 5 (*lea5*) and a transgenic line overexpressing the LEA5 protein (OEX2-5) in the absence or presence of the prooxidants menadione and paraquat **(D)**. **(A)** Controls, **(B)** seedlings grown in the presence of 0.1 μM paraquat or **(C)** 0.1 mM menadione. Error bars represent mean +/– standard error. Different letters indicate significance. Statistical analysis was performed using One Way ANOVA and *post hoc* Tukey test. Scale bar is 5 mm.

Cloning for Split YFP Experiments

The DEA (D/H)-box RNA helicase 22 (AT1G59990) and LEA5 sequences were cloned without a STOP codon into the pDONR201 Gateway vector and then transferred to the split YFP vectors (pDH51-GW-YFPn and pDH51-GW-YFPc).

Cloning of Constructs Containing Late Embryogenesis Abundant 5 Used for Tandem Affinity Purification Experiments

Forward primers contained the Kozak sequence, while the reverse primers were designed without a stop codon in order to perform C-terminal fusion. Fragments were then cloned in pDONR201 and used to produce constructs for TAP tagging. All cloning steps were performed using Gateway Technology.

Split YFP Experiments

A range of constructs (RH22-YFPn and LEA5-YFPc or RH22-YFPc and LEA5-YFPn) were designed to study protein-protein interactions and transiently expressed in Arabidopsis mesophyll protoplasts. Homologous co-transfections using either LEA5-YFPn and LEA5-YFPc or RH22-YFPn and RH22-YFPc were performed as controls. For these studies protoplasts were co-transfected with 10 μg of plasmid mixture the appropriate constructs, as described by Wu et al. (2009). Images of the interactions were prepared using confocal microscopy (Horstman et al., 2014).

Barley Transformation

Barley immature embryos were extracted and co-cultivated with Agrobacterium cells containing the BRACT214_SAG21-YFP for 3 days in the dark (Comadira, 2015). After callus induction and regeneration of shoots on hygromycin selection, putative transgenic plantlets were transferred to soil and grown in the glasshouse. PCR was performed using hygromycin B and Arabidopsis-YFP primers to confirm the presence of transgene. Thirty-six lines were selected as positive. Homozygous seedlings were selected from T3 generation in 0.5x MS plates supplemented with hygromycin B. Three lines with the closest 3:1 ratio (resistant: sensitive) were subsequently chosen; 9.1; 10.1 and 11.2. For controls, barley plants were transformed in parallel with pBRACT214 empty vector and pBRACT204 vector containing the GUS fragment (Comadira, 2015).

Biomass and Seed Yield Measurements

T3 generation plants, control lines and the wild type were grown to maturity in compost in glasshouses at the University of Leeds and the James Hutton Institute in Scotland under a 16 h/8 h day photoperiod regime with supplemental lighting. The number of fertile tillers were counted and the total seed yield quantified.

Tandem Affinity Purification

Arabidopsis cell suspension cultures (PSB-D) were transformed using a co-cultivation method with direct selection in liquid medium, as described previously (Van Leene et al., 2011). TAP tagging of protein complexes was performed using a GS^{rhino}

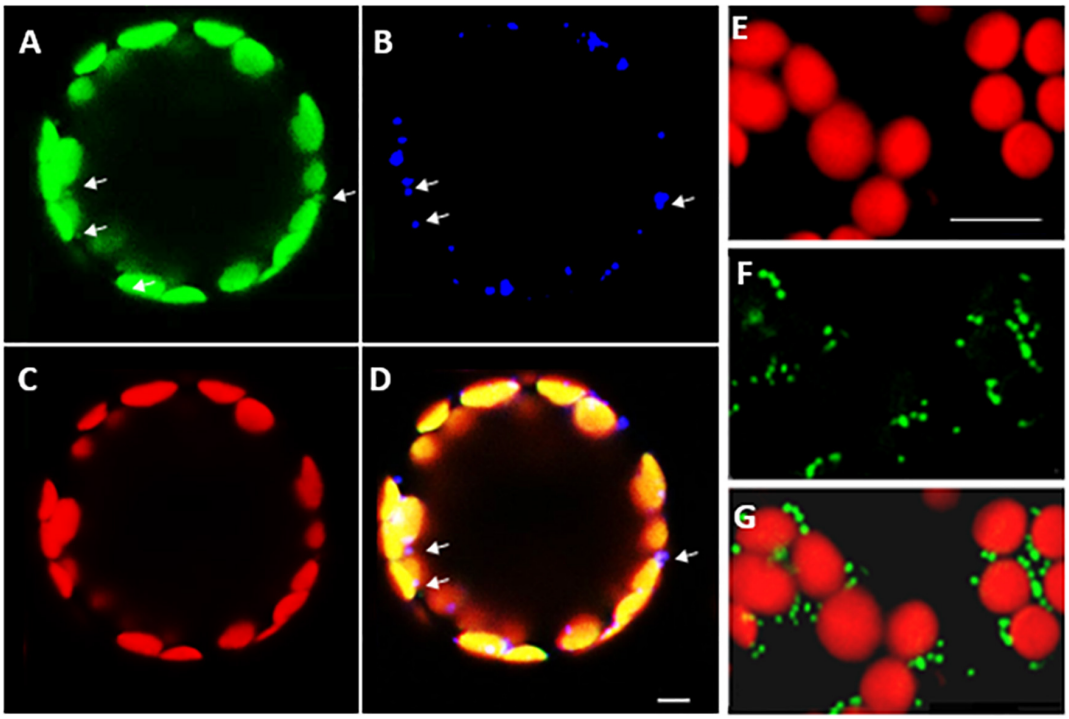

FIGURE 2 | Intracellular localization of LEA5 in mesophyll protoplasts and mesophyll tissue of Arabidopsis leaves. Mesophyll protoplasts **(A–D)** and leaf mesophyll cells **(E–G)** taken from 5 days old *Arabidopsis* seedlings (T_5 generation) expressing the LEA5-YFP protein. Green: YFP signal **(A)**, blue: MitoTracker Red CMXRos **(B)**, red: chlorophyll autofluorescence **(C)** and overlay **(D)**. The detection of the LEA5-YFP protein in the mitochondria of the mesophyll cells of 5-day old leaves of Arabidopsis seedlings **(F,G)**. Arrows indicate mitochondria. Scale bar = 10 μm.

tag (Van Leene et al., 2015). Aliquots (200 mg) of protein were precipitated. Proteins were then separated on SDS-PAGE as described by Bürckstümmer et al. (2006) and Van Leene et al. (2015). Protein interactors were identified by mass spectrometry using an LTQ Orbitrap Velos mass spectrometer. Proteins with at least two matched high confident peptides were retained for further analysis (**Supplementary Table 1**). Background proteins were filtered out based on the frequency of occurrence in the co-purified proteins in a large dataset containing 543 TAP experiments using 115 different baits (Van Leene et al., 2015).

Northern Blot Analysis

Samples (5 μg of total RNA) were denatured in 1 volume of NorthernMax^{TM}-Gly Sample Loading Dye for 30 min at 50°C. They were then separated on a 1.2% (w/v) agarose gel, blotted to positively charged nylon membrane by capillary blotting, and then fixed by cross-linking. Hybridization was performed with ^{32}P-labeled probes in 5 × SSC, 5 × Denhardt's solution, and 0.5% SDS at 65°C overnight. The membranes were washed twice in 2 × SSC, 0.1% SDS and once in 1 × SSC, 0.1% SDS at 65°C.

Hybridization probes were prepared by PCR amplification of *23S-4.5S rrn* region (primer sequences listed in **Supplementary Table 2**). The fragments were separated on 1.5% agarose gels and extracted using QIAquick Gel extraction kit (Qiagen). They were then labeled with 20 μCi [α-32P]dCTP, 3000 Ci/mmol (PerkinElmer) using a "Random primed" DNA labeling kit (Roche).

Photosynthesis Measurements

Light response curves for photosynthesis were measured using a portable Infrared Gas Analyzer (model LI-6400XT) LI-COR. Measurements were performed at 20°C and a CO2 concentration of (400 μmol mol^{-1}) in the leaf chamber. The leaves were exposed to each of the following light intensities: [(0, 50, 250, 500, 750, 1,000, 1,250, 1,500, and 1,750 μmol m^{-2} s^{-1}) photosynthetically active radiation (PAR)] allowing the leaves to acclimatize to each irradiance for at least 15 min prior to measurement to allow stabilization of parameters. Measurements were made on 3 plants per line per experiment.

RESULTS

The Late Embryogenesis Abundant 5 Protein Plays a Role in Protection Against Oxidative Stress

The *lea5* mutants and the transgenic plants overexpressing the LEA5 protein (OEX2-5) had a similar vegetative growth phenotype to the wild type (**Figures 1A,D**). The growth of the wild type seedlings was decreased in the presence of the prooxidants menadione (**Figures 1B,D**). and paraquat

TABLE 1 | Tandem affinity purification tagging identification of proteins interacting with LEA5.

Gene accession	Annotation	Dark $-H_2O_2$	Dark $+H_2O_2$	Light $-H_2O_2$	Light $+H_2O_2$
At1g59990	RH22/DEA(D/H)-box helicase family protein 22, regulates ribosome assembly and rRNA processing.	*	*	*	*
At3g16810	PUM24/pumilio 24, mRNA degradation and translation repression	*	*	*	
At1g55150	RH20/DEA(D/H)-box RNA helicase family protein.	*	*		
At2g02100	PDF2.2/low molecular weight cysteine-rich 69		*	*	
At2g36200	P-loop containing nucleoside triphosphate hydrolases superfamily protein		*	*	

The asterisks denote the presence of an interaction.

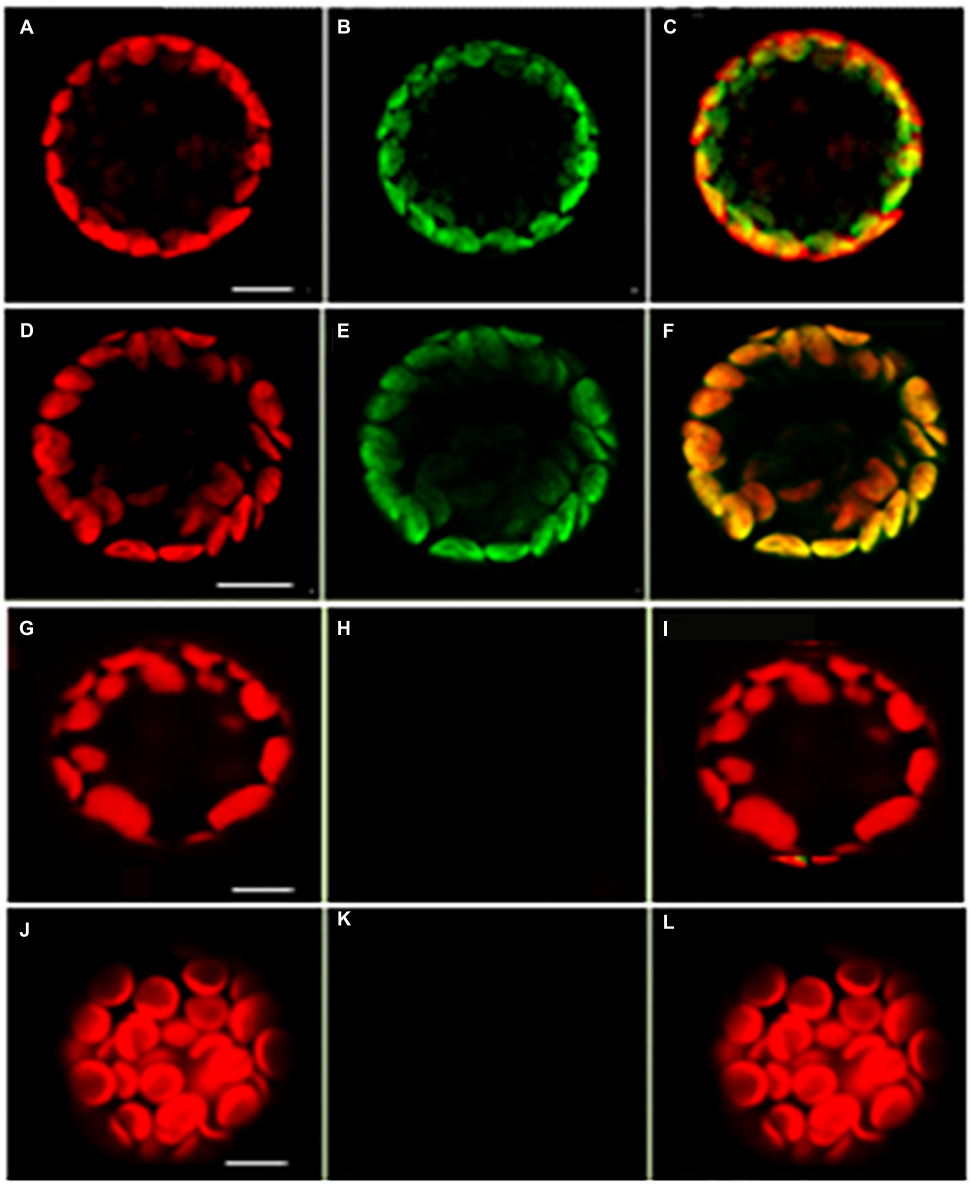

FIGURE 3 | Confocal microscopy images of Arabidopsis mesophyll protoplasts showing interactions between LEA5 and DEA (D/H)-box RNA helicase 22. Protoplasts were co-transfected with LEA5-YFPc and DEA (D/H)-box RNA helicase 22-YFPn **(A–C)** and LEA5-YFPn with DEA (D/H)-box RNA helicase 22-YFPc **(D–F)**. Co-transfection of DEA (D/H)-box RNA helicase 22-YFPn and DEA (D/H)-box RNA helicase 22-YFPc gives no positive signal of interaction **(G–I)**. Overlay of fluorescence signals **(C,F,I,L)**. The interaction between LEA5-YFPn and LEA5-YFPc in mitochondria is demonstrated by co-transfection of LEA5-YFPn and LEA-YFPc **(J–L)**. Scale bar = 10 μm.

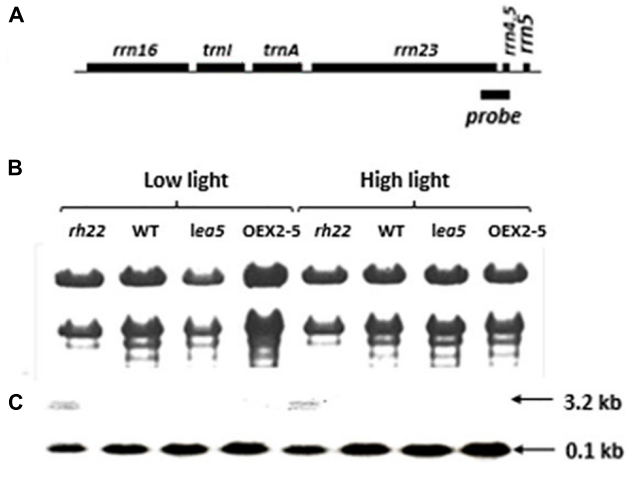

FIGURE 4 | Expression and processing of chloroplast rRNA in Wild type (WT) Arabidopsis, a knockout line defective in DEA (D/H)-box RNA helicase 22 (Δrh22), a knockout line defective in LEA5 (*lea5*) and a transformed Arabidopsis line overexpressing LEA5 (OEX2-5). **(A)** A diagram of the chloroplast rRNA operon showing the location of the probe used for the RNA gel-blot analysis. **(B)** Ethidium bromide staining of glyoxylated RNA separated on 1.2% agarose extracted from plants grown under either low or high light conditions. **(C)** Northern blot analysis.

(**Figures 1C,D**). The prooxidant-related decreases in plant growth were greater in the *lea5* mutant seedlings than the wild type (**Figures 1B–D**). However, decreases in growth caused by the prooxidants were much less pronounced in the OEX2-5 seedlings than the wild type (**Figures 1B–D**).

Intracellular Localization of the Late Embryogenesis Abundant 5 Protein

Confocal microscopy of Arabidopsis mesophyll protoplasts expressing a LEA5-YFP fusion protein, revealed that the LEA5 protein was localized to the chloroplasts as well as the mitochondria (**Figures 2A–D**). In contrast, LEA5-YFP protein was only detected in the mitochondria of the mesophyll cells of 5-day old leaves of Arabidopsis seedlings (**Figures 2F,G**).

Analysis of the Late Embryogenesis Abundant 5 Interactome

A tandem affinity purification (TAP) approach was used to identify protein interaction partners for LEA5. For these studies, a LEA5-*YFP* construct was constitutively expressed in transgenic Arabidopsis ecotype Landsberg *erecta* suspension cultures grown either in the dark (PSB-D) or the light (PSB-L). We characterized the proteins that interacted with *LEA5* in the absence or presence of hydrogen peroxide (H_2O_2) in order to determine whether oxidative stress altered the repertoire of LEA5 protein binding partners. Several proteins that interacted with the LEA5 protein in the cultures grown in the absence or presence of H_2O_2 were identified (**Table 1**). The list includes a chloroplast-localized DEA (D/H)-box RNA helicase family protein (RH22; AT1G59990), which is involved in chloroplast ribosome biogenesis and plays a key role in Arabidopsis growth and stress responses (Gu et al., 2014; Liu and Imai, 2018), as well as another DEA(D/H)-box RNA helicase family protein (RH20) and pumilio (PUM) 24, which regulates mRNA degradation and translation repression. Since LEA5 interacted with RH22 in all tagging experiments, we analyzed this interaction further using bimolecular fluorescence complementation (BIFC) assays. This method confirmed the interaction of LEA5 with RH22 specifically in the chloroplasts of Arabidopsis leaf protoplasts (**Figure 3**).

Late Embryogenesis Abundant 5 Modulates Organellar Translation and Increases Respiratory Electron Transport

To explore the functions of LEA5 in organelles, the expression and processing of chloroplast rRNA was measured in wild type Arabidopsis and in mutants lacking RH22 (*rh22*), *lea5* mutants and in plants overexpressing LEA5 (OEX2-5; **Figure 4**). In contrast to the *rh22* mutant, which showed aberrant chloroplast ribosome processing, the *lea5* mutant and OEX2-5 plants showed similar levels of chloroplast rRNAs to the wild type (**Figure 4**).

Finally, organellar translation in chloroplasts and mitochondria was analyzed in wild type, OEX 2-5 and *lea5* by *in organello* translation assays which measures the incorporation [35S] methionine to newly synthesized proteins of isolated organelles (**Figure 5**). The intensity of labeling for some mitochondrial protein products was seen to be decreased in mitochondria isolated from *lea5* and increased in mitochondria isolated from OEX 2-5 relative to the wild type (**Figure 5A**). Conversely, the intensity of labeling of some translated chloroplast protein products was observed to increase in chloroplasts isolated from *lea5* mutants and decreased in chloroplasts isolated from OEX 2-5 relative to the wild type (**Figure 5B**). Measurement of mitochondrial respiration revealed that mitochondria isolated from the OEX 2-5 exhibited significantly higher rates of respiratory electron transport to the cytochrome C oxidase than mitochondria from wild type controls (**Table 2**).

The Expression of *AtLEA5* in Barley Increases Seed Production

LEA5 overexpression has previously been reported to increase the growth and flowering of Arabidopsis plants (Mowla et al., 2006; MohdSalleh et al., 2012). We therefore set out to investigate whether LEA5 overexpression also had a positive effect on the growth and productivity of crop species. Barley was selected for these studies because an efficient transformation system is available for this important crop. The Arabidopsis LEA5 protein in barley was characterized for the growth phenotypes, yield parameters and photosynthesis in a large number of independent transgenic lines. Vegetative and reproductive phenotypes were compared in three overexpression lines (9, 10, and 11) that had high levels of *LEA5* expression compared to the wild type barley plants and empty vector and GUS control lines (**Figure 6**). Total biomass, the number of tillers, flowers, heads numbers, total seed yield per plant and seed yield per tiller were measured in

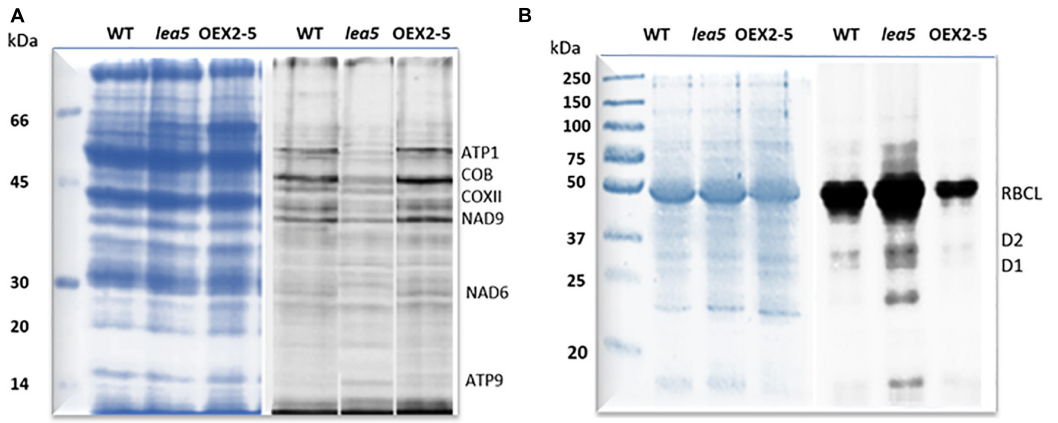

FIGURE 5 | A comparison of mitochondrial and chloroplast translation products in wild type (WT) Arabidopsis, a knockout line defective in LEA5 (*lea5*) and a transformed Arabidopsis line overexpressing LEA5 (OEX2-5). Mitochondrial **(A)** and chloroplast proteins **(B)** were labeled with ^{35}S-Met. A shows the ATP synthase subunits, ATP1 and ATP9, the NADH:ubiquinone oxidoreductase (NAD) 7 and 9 subunits, cytochrome b (cob), and cytochrome c oxidase subunit II (COXII). **(B)** Shows labeling in the photosystem II reaction center proteins D1 and D2 proteins and the large subunit of ribuoose-1, 5-bisphosphate carboxylase oxygenase (RBCL).

TABLE 2 | Respiratory electron transport rates in isolated intact mitochondria from intact wild type Arabidopsis leaves.

A					
Maximal COX activity		**Percentage of intact mitochondria**			
WT	**OEX2-5**	**WT**	**OEX2-5**		
142.9 ± 7.9	166.2 ± 9.8*	85.4 ± 3.2	89.8 ± 1.3		N=24
B					
Genotype	**CI substrates**	**ADP**	**Oligomycin**	**FCCP**	
WT	23.0 ± 2.5	18.6 ± 1.1	1.0 ± 0.5	20.4 ± 3.8	
OEX2-5	22.0 ± 2.5	22.5 ± 5.2	1.4 ± 0.3	14.0 ± 4.1	N=4
C					
	Succinate	**Rotenone**	**ADP**	**Oligomycin**	**FCCP**	
WT	23.1 ± 3.4	26.2 ± 3.0	41.0 ± 3.3	26.2 ± 4.6	32.6 ± 3.4	
OEX2-5	22.8 ± 4.2	24.2 ± 2.6	33.4 ± 3.9	27.5 ± 3.5	24.3 ± 4.6	N=15

*(A) Maximal respiration rates through complex I (CI) cytochrome C oxidase (COX). COX activity expressed as nmol O_2 * min^{-1} * mg $protein^{-1}$; (B) electron transport through respiratory complex I (CI) in the absence or presence of ADP, oligomycin or p-triflouromethoxyphenylhydrazone (FCCP); (C) electron transport through respiratory complex II.*

T3 generation plants that had been grown for 6 months under glasshouse conditions (**Figure 6** and **Table 3**). The number of fertile tillers and seeds produced in transformed barley lines (9; 10, and 11) were significantly higher than the controls (**Table 3**).

The Expression of *AtLEA5* Increases the Drought-Induced Inhibition of Photosynthesis

We have previously shown that the expression of AtLEA5 was strongly induced by drought, such that the levels of transcripts correlated with the drought-dependent inhibition of photosynthesis (Mowla et al., 2006). Moreover, Arabidopsis lines LEA5 were more susceptible to drought than the wild type, in terms of the drought-induced inhibition of photosynthesis (Mowla et al., 2006). We therefore next explored the responses of the transformed barley lines (9.1; 10.1, and 11.2) to drought by withholding water for 7 days. Photosynthetic CO2 assimilation was monitored throughout the period of drought course using infrared gas analysis. The AtLEA5-overexpressing barley lines exhibited comparable rates of photosynthesis to the wild type under water-replete conditions (**Figure 7A**), with comparable rates of stomatal conductance (**Figure 7C**). The light response curves for photosynthesis were similar in all lines grown under well-watered conditions (**Figure 7A**). Photosynthetic CO_2 assimilation rates were decreased in all lines following exposure to drought (**Figure 7B**). However, the light-saturated rates of photosynthesis were lower in the overexpression lines than controls after 7 days of water deprivation (**Figure 7B**). Stomatal conductance was decreased in all lines following exposure to drought (**Figure 7D**). All lines showed similar changes in stomatal

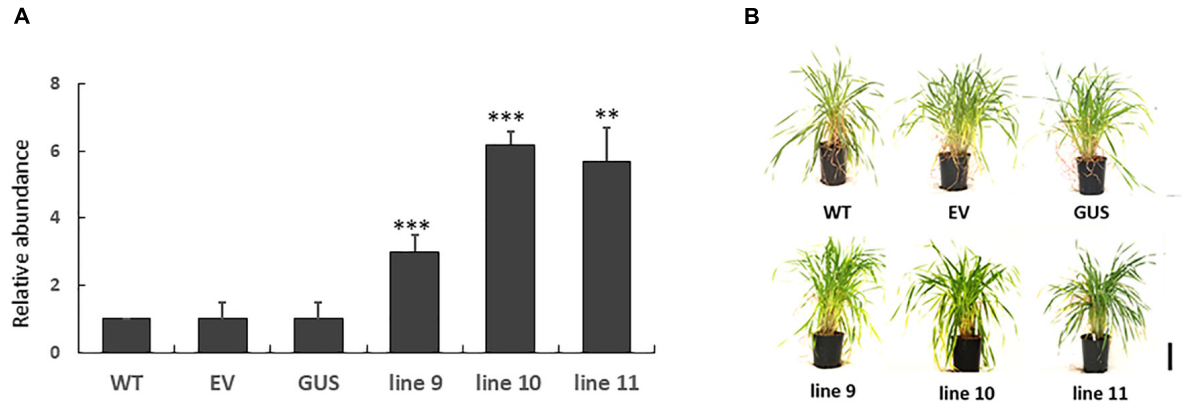

FIGURE 6 | The expression of Arabidopsis *LEA5* in transgenic barley lines (9, 10, 11) relative to controls (WT, EV, GUS) and the growth phenotypes of these lines. The relative abundance of *LEA5* in barley lines expressing the *Arabidopsis* LEA5 sequence (9, 10, 11), control lines expressing empty vector (EV) and beta-glucuronidase (GUS) and WT **(A)**. The shoot phenotypes of the lines at 4 weeks **(B)**. Two asterisks indicates significant differences at $p < 0.001$ and three asterisks indicates significance at $p < 0.0001$.

TABLE 3 | Yield parameters in transgenic barley lines expressing LEA5 in comparison to the wild type (WT) and a control barley line expressing beta-glucuronidase (GUS).

	WT	GUS	Line 9	Line 10	Line 11
Number of fertile tillers	12	13	22**	25***	19**
Total seed yield (g)	4.37	4.51	8.09**	8.16**	6.57**
Seed yield per fertile tiller (g)	0.36	0.38	0.67**	0.68**	0.55**

Data are mean values ± SE (n = 10). Significantly differences according to the Students t-test are indicated by asterisk.

conductance in response to increasing irradiance under these conditions (**Figure 7D**).

AtLEA5 Is Localized in the Mitochondria of Transgenic Barley Lines

To investigate the subcellular localization of the Arabidopsis LEA5 protein in the leaves and roots of the transgenic barley lines, lines expressing 35S-LEA5-YFP were generated and analyzed. Confocal microscopy images revealed that the LEA5-YFP protein was present exclusively in the mitochondria of the leaves and roots of the transgenic barley lines (**Figure 8**).

DISCUSSION

Chloroplasts and mitochondria are the powerhouses of plant cells that drive cell metabolism, plant growth and development. The photosynthetic and respiratory electron transport chains have the potential to produce reactive oxygen species (ROS) as signals that alter gene expression and facilitate responses to environmental stress (Foyer and Hanke, 2022). Chloroplasts act as environmental sensors, the rates of photosynthesis decreasing and respiration rates increasing in response to abiotic stresses such as drought, when leaf relative water contents decline (Chaves et al., 2002; Xu et al., 2015). Drought inhibits photosynthesis through effects on stomatal aperture, alterations in the stromal redox state, inhibition of enzyme activities and changes in gene expression.

The control of organellar translation contributes to the regulation of plastome and chondrome gene expression in response to developmental, environmental, and physiological cues (Planchard et al., 2018; Zoschke and Bock, 2018). We present evidence that altered expression of LEA5 influences the levels of mitochondrial and chloroplast translation products, as indicated by labeling with ^{35}S-Methionine. The *lea5* mutants have less mitochondrial translation products than the wild type and transformed plants overexpressing LEA5 (OEX2-5). Conversely, the transformed plants overexpressing LEA5 (OEX2-5) have less chloroplast translation products than the wild type or *lea5* mutants. The mechanisms by which the LEA5 protein is able to achieve this regulation are unknown but it must occur via interactions with other proteins involved in organellar translation in the mitochondria and chloroplasts. Our studies on the LEA5 protein interactome revealed that LEA5 interacts with the RH22/DEA(D/H)-box helicase family protein 22 (HS3) that regulates ribosome assembly and rRNA processing in the chloroplasts (Kanai et al., 2013).

Organellar protein synthesis is performed on bacteria-like 70S ribosomes, which are composed of a small 30S and a large 50S subunit. RNA processing, intron splicing, RNA editing, turnover and translational control are regulated by a variety of nucleus-encoded RNA-binding proteins (RBPs) that are targeted to chloroplasts or mitochondria, where they play essential roles in organellar RNA metabolism. The RBPs include DEAD-box RNA helicases (RHs) that regulate RNA structures and metabolism and abiotic stress responses (Nawaz and Kang, 2017). The *rh22* mutants that lack RH22 clearly

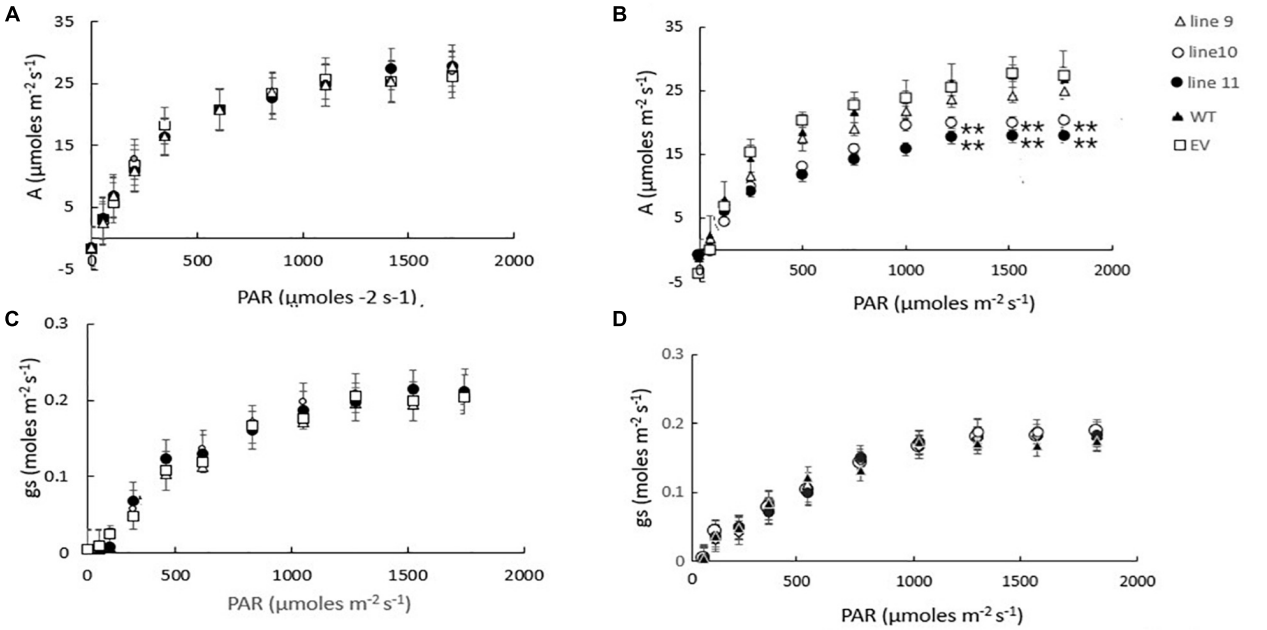

FIGURE 7 | A comparison of the light saturation curves for photosynthesis **(A,B)** and stomatal conductance **(C,D)** in wild type barley plants (WT), transgenic lines expressing the Arabidopsis LEA 5 sequence (lines 9, 10, and 11) and empty vector (EV) controls. Plants were grown for either 14 days under well-watered conditions **(A,C)** or for 7 days under well-watered conditions followed by 7 days without watering **(B,D)**. Asterisks indicate significant differences between the transgenic lines and control as estimated by the Student's *t*-test (**$p < 0.01$).

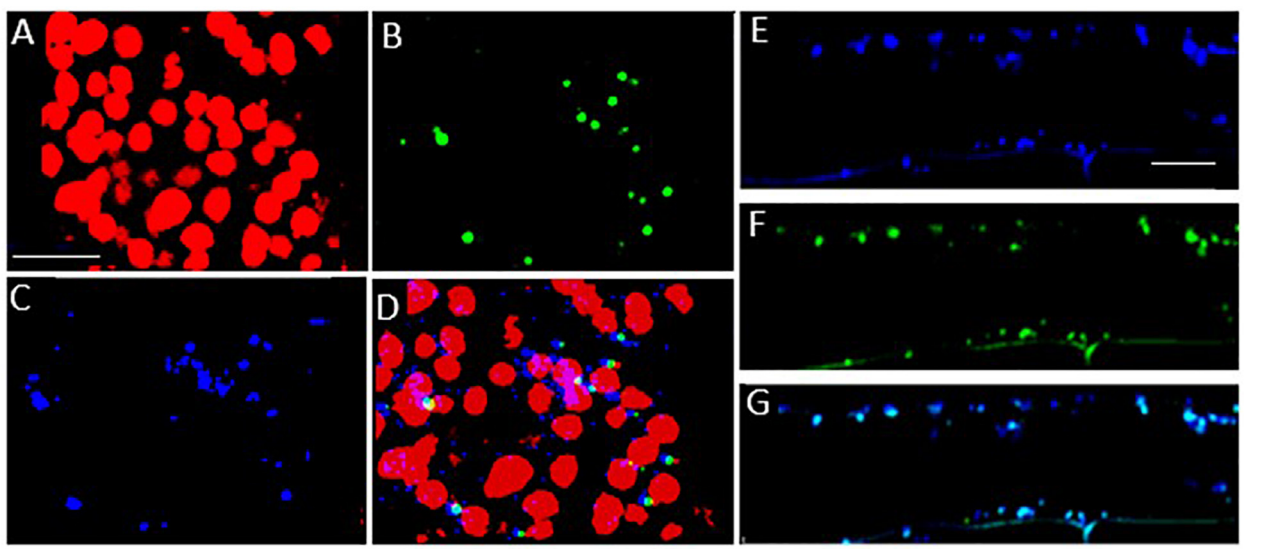

FIGURE 8 | Subcellular localization of the *Arabidopsis* LEA5 in barley leaves and roots. Confocal microscopy of 5-day old transgenic barley leaves **(A–D)** and roots **(E–G)** expressing the 35S-LEA5-YFP fusion protein. Chlorophyll autofluorescence is shown in red **(A,D)**, YFP signal is in green **(B,F)**, MitoTracker Red CMXRos is in blue **(C,E)**. **(D and G)** are merged images of **(A–C,E,F)**, respectively. All scale bars are set to 10 μm.

show aberrant chloroplast ribosome processing compared to the wild type (**Figure 4**). However, the *lea5* mutants and OEX2-5 plants showed similar levels of chloroplast rRNAs to the wild type (**Figure 4**), demonstrating that LEA5 is not involved in pre-rRNA processing in chloroplasts. We therefore explored the physiological roles of LEA5 in organellar translation via incorporation [35S] methionine into newly synthesized proteins (**Figure 4**). Data are presented showing that the presence of LEA5 increases the abundance of some translated mitochondrial protein products and decreases chloroplast protein products. Moreover, isolated intact mitochondria from the OEX 2-5 plants exhibited higher rates of cytochrome C oxidase activity than

the wild type controls (**Table 2**). Taken together, these findings show that the LEA5 protein is able to modify the abundance of specific translation products in mitochondria and chloroplasts. Specifically, the levels of the photosystem II reaction center proteins D1 and D2 proteins and the large subunit of ribulose-1, 5-bisphosphate carboxylase oxygenase (RBCL) were decreased in the chloroplasts from the OEX 2-5 plants and increased in *lea5* mutant chloroplasts relative to the wild type. These results suggest that presence of the LEA5 protein specifically decreases proteins involved in photosynthetic electron transport and carbon assimilation. This result is surprising given that the LEA5 protein is targeted to mitochondria and not to chloroplasts. We could not detect the LEA5 protein in intact 35S-LEA5-YFP expressing Arabidopsis leaves or the leaves or roots of the transformed barley lines. In all cases the LEA5 protein was detected only in mitochondria. While we were able to detect the LEA5-YFP in the chloroplasts of the mesophyll protoplasts isolated from the Arabidopsis leaves (**Figure 2**), other authors have reported that the LEA5 protein is only present in the mitochondria of isolated Arabidopsis protoplasts (Candat et al., 2014). Further studies are required to determine whether the LEA5 protein can re-distribute to the chloroplasts as well as mitochondria of certain tissues, under specific developmental or stress conditions. It may be that the LEA5 protein can localize in specialized sensory plastids that have been described in the epidermis and vascular parenchyma. These "sensory" plastids participate in environmental stress sensing and trigger tissue-specific signaling and systemic stress responses (Beltrán et al., 2018). Moreover, accumulating evidence suggests that the protein complement of any given intracellular compartment is not precisely fixed and that some proteins can move between compartments in response to metabolic or environmental triggers (Foyer et al., 2020). A recent example is the WHIRLY2 protein that is targeted in mitochondria but can also localize to chloroplasts (Huang et al., 2020). In addition, the LEA5 protein may function in the integration of chloroplast- and mitochondria-derived signals that are processed by the nuclear gene expression system. For example, the nuclear cyclin-dependent kinase E is implicated in the expression of both chloroplast and mitochondrial components in response to limitations in either the chloroplast or mitochondrial electron transport chains or H_2O_2 treatment (Blanco et al., 2014; Ng et al., 2014). Similarly, the RADICAL-INDUCED CELL DEATH1 (RCD1) protein integrates oxidative signals emitted by both mitochondria and chloroplasts to suppress ANAC013 and ANAC017 functions (Shapiguzov et al., 2019). The presence of LEA5 in the mitochondria of leaves in the light may result in signaling that modulates chloroplast translation, as well as mitochondrial translation.

Mitochondrial respiration involves five multi-subunit protein complexes, four of which (Complexes I–IV) constitute the mitochondrial respiratory chain that moves electrons from NADH and succinate to oxygen, activating the ATP synthase. The levels of the alpha subunit of the ATP synthase (ATP1) and ATP9, which encodes subunit 9, were higher in the mitochondria from the OEX 2-5 plants and lower in *lea5* mutants. Similarly the levels of the NADH:ubiquinone oxidoreductase (NAD) 7 and 9 subunits of Complex I (CI) were higher in OEX 2-5 the mitochondria from lower in *lea5* mitochondria, as were the levels of mitochondrial cytochrome b (cob), and cytochrome c oxidase subunit II (COXII). These findings suggest that mitochondrial electron transport and oxidative phosphorylation are higher when LEA5 is present in the mitochondria. The LEA5 protein therefore has a positive function in plant mitochondria, support mitochondrial respiration, and ATP synthesis.

The precise mechanisms by which LEA5 regulates chloroplast and mitochondrial ribosomal functions remains to be elucidated. However, the data presented here suggest that LEA binds to organellar proteins that regulate mRNA stability and translation in chloroplasts. In this way, LEA5 is likely to modify the responses of photosynthesis and respiration to environmental stresses such as drought. The expression patterns of LEA5 would support this notion. LEA5 is not normally expressed in leaves in the light (Mowla et al., 2006). However, the expression of LEA5 is triggered in leaves in the light by abiotic stresses such as drought and by stress hormones such as abscisic acid (ABA) and jasmonate (Mowla et al., 2006; MohdSalleh et al., 2012). Stress-induced expression of LEA5 in the light may serve to decrease oxidative pressure in chloroplasts under stress conditions by decreasing the synthesis of essential components of the photosynthetic electron transport chain, particularly D1 and D2, while stimulating respiration to maintain ATP production. Chloroplast translation is regulated in response to light through changes in the redox state of chloroplast components such as NADPH thioredoxin reductase C (NTRC; González et al., 2019). The data presented here suggests that LEA5 may be an additional major player in the regulation of chloroplast translation.

We have previously shown that photosynthesis is decreased to a greater extent in transgenic Arabidopsis lines overexpressing LEA5 than the wild type under drought stress conditions (Mowla et al., 2006). We discussed these findings in terms of the decreased stress-induced oxidative load that would occur as a consequence of an increased inhibition of photosynthesis in the transformed lines under these conditions (Mowla et al., 2006). The expression of *AtLEA5* is induced in leaves in the light by oxidants and by oxidative stress. Moreover, as shown in **Figure 1**, overexpression of *AtLEA5* enhances tolerance to oxidate stress. One might predict therefore that overexpression of *AtLEA5* would increase photosynthesis rates in plants subjected to stresses such as drought. However, the opposite effect was observed both in Arabidopsis (Mowla et al., 2006) and in barley, as shown in **Figure 7**. The data presented in **Figure 7B** clearly demonstrate that drought-induced inhibition of photosynthetic carbon assimilation is increased when the Arabidopsis LEA5 protein is constitutively expressed in barley (**Figure 7B**). While photosynthetic CO_2 assimilation rates were comparable in all lines in the absence of stress (**Figure 7A**), the light-saturated rates of photosynthesis were significantly lower in barley lines 9.1; 10.1, and 11.2 under drought stress conditions than controls (**Figure 7B**). Since stomatal conductance was decreased to a similar extent in all lines in response to drought (**Figure 7D**), we conclude that overexpression of *AtLEA5* in barley has no effect on stomatal regulation and hence it exerts effects directly in the photosynthetic mesophyll cells. Taken together, findings

suggest that the expression of the Arabidopsis LEA5 protein limits chloroplast translation when the barley plants are exposed to drought and that this in turn has a negative impact on photosynthesis rates. However, the concurrent stimulation of mitochondrial translation and respiration rates must be sufficient to offset and compensate for any restrictions on metabolism caused by impaired chloroplast translation. Moreover, the LEA5-dependent increases in mitochondrial translation and respiration are likely to underpin the greater seed yields observed in the transgenic barley lines overexpressing LEA5 compared to controls (**Figure 6**).

The Arabidopsis LEA5 protein was localized in the mitochondria of the leaves and roots of the transgenic barley lines expressing 35S-LEA5-YFP. While the protein sequence contains a putative chloroplast transit peptide (Emanuelsson et al., 2000), it is not clear whether or how AtLEA5 can localize to plastids. We conclude that the improved yields observed in the barley lines expressing the Arabidopsis LEA5 protein are related to improved regulation of organellar translation in these lines, particularly under stress conditions. These data not only provide new evidence of LEA5 functions in plants, but they also shed new light on the factors that regulate translation in order to facilitate energy and metabolite homeostasis.

DATA AVAILABILITY STATEMENT

The original contributions presented in the study are included in the article/**Supplementary Material**, further inquiries can be directed to the corresponding author/s.

AUTHOR CONTRIBUTIONS

CF, MM, and GD planned the experiments. BK, JS, NR, and DSS undertook the experimental work and data analysis. BK produced the figures. CF wrote the manuscript. All authors contributed to the article and approved the submitted version.

FUNDING

DSS thanks Bayer Crop Science and BBSRC for a CASE studentship (BB/J011363/1).

ACKNOWLEDGMENTS

We are indebted to Michael Considine for his help in the isolation of intact mitochondria, measurements of the integrity of mitochondrial fractions and respiratory electron transport. We thank Gloria Comadira for the production of the transformed barley lines used in these experiments (Comadira, 2015). DSS thanks Bayer Crop Science and BBSRC for a CASE studentship (BB/J011363/1).

SUPPLEMENTARY MATERIAL

The Supplementary Material for this article can be found online at: https://www.frontiersin.org/articles/10.3389/fpls.2022.875799/full#supplementary-material

REFERENCES

Aronsson, H., and Jarvis, P. (2011). Rapid isolation of *Arabidopsis* chloroplasts and their use for in vitro protein import assays. *Methods Mol. Biol.* 774, 281–305. doi: 10.1007/978-1-61779-234-2_17

Artur, M. A. S., Zhao, T., Ligterink, W., Schranz, E., and Hilhorst, H. W. M. (2019). Dissecting the genomic diversification of late embryo-genesis abundant (LEA) protein gene families in plants. *Genome Biol. Evol.* 11, 459–471. doi: 10.1093/gbe/evy248

Avelange-Macherel, M.-H., Candat, A., Neveu, M., and Tolleter, D. (2018). Decoding the divergent subcellular location of two highly similar paralogous LEA proteins. *Int. J. Mol. Sci.* 19:1620. doi: 10.3390/ijms19061620

Beltrán, J., Wamboldt, Y., Sanchez, R., LaBrant, E. W., Kundariya, H., Virdi, K. S., et al. (2018). Specialized plastids trigger tissue-specific signaling for systemic stress response in plants. *Plant Physiol.* 178, 672–683. doi: 10.1104/pp.18.00804

Blanco, N. E., Guinea-Diaz, M., Whelan, J., and Strand, Å (2014). Interaction between plastid and mitochondrial retrograde signalling pathways during changes to plastid redox status. *Phils. Trans. Roy. Soc. B.* 369:20130231. doi: 10.1098/rstb.2013.0231

Bürckstümmer, T., Bennett, K. L., Preradovic, A., Schutze, G., Hantschel, O., Superti-Furga, G., et al. (2006). An efficient tandem affinity purification procedure for interaction proteomics in in mammalian cells. *Nat. Methods* 3, 1013–1019. doi: 10.1038/nmeth968

Candat, A., Paszkiewicz, G., Neveu, M., Gautier, R., Logan, D. C., Avelange-Macherel, M. H., et al. (2014). The ubiquitous distribution of late embryogenesis abundant proteins across cell compartments in *Arabidopsis* offers tailored protection against abiotic stress. *Plant Cell* 26, 3148–3166. doi: 10.1105/tpc.114.127316

Chaves, M. M., Pereira, J. S., Maroco, J., Rodriques, M. L., Ricardo, C. P. P., Osório, M. L., et al. (2002). How plants cope with water stress in the field? *Photosyn. Growth Ann. Bot.* 89, 907–916. doi: 10.1093/aob/mcf105

Comadira, G. (2015). *Regulation of Senescence in Arabidopsis thaliana and Barley Ph. D, Thesis*.

Emanuelsson, O., Nielsen, H., Brunak, S., and von Heijne, G. (2000). Predicting subcellular localization of proteins based on their Nterminal amino acid sequence. *J. Mol. Biol.* 300, 1005–1016. doi: 10.1006/jmbi.2000.3903

Fournier-Level, A., Korte, A., Cooper, M. D., Nordborg, M., Schmitt, J., and Wilczek, A. M. (2011). A map of local adaptation in Arabidopsis thaliana. *Science* 334, 86–89. doi: 10.1126/science.1209271

Foyer, C. H., Baker, A., Wright, M., Sparkes, I., Mhamdi, A., Schippers, J. H. M., et al. (2020). On the move: redox –dependent protein relocation. *J. Expt. Bot.* 71, 620–631. doi: 10.1093/jxb/erz330

Foyer, C. H., and Hanke, G. (2022). "Regulation of the production and processing of ROS signals in chloroplasts," in *Photosynthesis in Action: Harvesting Light, Generating Electrons, Fixing Carbon*, eds A. Ruban, C. H. Foyer, and E. H. Murchie (Elsevier).

González, M., Delgado-Requerey, V., Ferrández, J., Serna, A., and Cejudo, F. J. (2019). Insights into the function of NADPH thioredoxin reductase C (NTRC) based on identification of NTRC-interacting proteins in vivo. *J. Expt. Bot.* 70, 5787–5798. doi: 10.1093/jxb/erz326

Gu, L., Xu, T., Lee, K., Lee, K. H., and Kang, H. (2014). A chloroplast-localized DEAD-box RNA helicase AtRH3 is essential for intron splicing and plays an important role in the growth and stress response in *Arabidopsis thaliana*. *Plant Physiol. Biochem.* 82, 309–318. doi: 10.1016/j.plaphy.2014.07.006

Horstman, A., Nougalli Tonaco, I. A., Boutilier, K., and Immink, R. G. H. (2014). A cautionary note on the use of split-YFP/BiFC in plant protein-protein interaction studies. *Int. J. Mol. Sci.* 15, 9628–9643. doi: 10.3390/ijms15069628

Hatanaka, R., Gusev, O., Cornette, R., Shimura, S., Kikuta, S., Okada, J., et al. (2015). Diversity of the expression profiles of late embryogenesis abundant (LEA) protein encoding genes in the anhydrobiotic midge *Polypedilum vanderplanki*. *Planta* 242, 451–459. doi: 10.1007/s00425-015-2284-6

Huang, A., Zhong, X. J., He, J., Jin, S. H., Guo, H. D., Yu, X. F., et al. (2016). Genome-wide identification, characterization, and stress-responsive expression profiling of genes encoding LEA (late embryogenesis abundant) proteins in Moso bamboo (*Phyllostachys edulis*). *PLoS One* 1:e0165953. doi: 10.1371/journal.pone.0165953

Huang, C., Yu, J., Cai, Q., Chen, Y., Li, Y., Ren, Y., et al. (2020). Triple-localized WHIRLY2 influences leaf senescence and silique development via carbon allocation. *Plant Physiol.* 184, 1348–1362. doi: 10.1104/pp.20.00832

Jaspard, E., Macherel, D., and Hunault, G. (2012). Computational and statistical analyses of amino acid usage and physico-chemical properties of the twelve late embryogenesis abundant protein classes. *PLos One* 7:1–20. doi: 10.1371/journal.pone.0036968

Kanai, M., Hayashi, M., Kondo, M., and Nishimura, M. (2013). The plastidic DEAD-box RNA helicase 22, HS3, is essential for plastid functions both in seed development and in seedling growth. *Plant Cell Physiol.* 9, 1431–1440. doi: 10.1093/pcp/pct091

Lan, T., Gao, J., and Zeng, Q. Y. (2013). Genome-wide analysis of the LEA (late embryogenesis abundant) protein gene family in *Populus trichocarpa*. *Tree Genet. Genom.* 9, 253–264. doi: 10.1007/s11295-012-0551-2

Lee, Y. P., Giorgi, F. M., Lohse, M., Kvederaviciute, K., Klages, S., Usadel, B., et al. (2013). Transcriptome sequencing and microarray design for functional genomics in the extremophile *Arabidopsis* relative *Thellungiella salsuginea* (*Eutrema salsugineum*). *BMC Genom.* 14:793. doi: 10.1186/1471-2164-14-793

Liu, Y., and Imai, R. (2018). Function of plant DExD/H-Box RNA helicases associated with ribosomal RNA biogenesis. *Front. Plant Sci.* 9:125. doi: 10.3389/fpls.2018.00125

Magwanga, R. O., Lu, P., Kirungu, J. N., Lu, H., Wang, X., Cai, X., et al. (2018). Characterization of the late embryogenesis abundant (LEA) proteins family and their role in drought stress tolerance in upland cotton. *BMC Genet.* 19:6. doi: 10.1186/s12863-017-0596-1

Mowla, S. B., Cuypers, A., Driscoll, S. P., Thompson, J., Foyer, C. H., and Theodoulou, F. L. (2006). Yeast complementation reveals a role for an Arabidopsis thaliana late embryogenesis abundant (LEA)-like protein in oxidative stress tolerance. *Plant J.* 48, 743–756. doi: 10.1111/j.1365-313X.2006.02911.x

MohdSalleh, F., Evans, K., Goodall, B., Machin, H., Mowla, S. B., Mur, L. A. J., et al. (2012). A novel function for a redox-related LEA protein (SAG21/AtLEA5) in root development and biotic stress responses. *Plant Cell Environ.* 35, 418–429. doi: 10.1111/j.1365-3040.2011.02394.x

Murcha, M. W., and Whelan, J. (2015). Isolation of intact mitochondria from the model plant species *Arabidopsis thaliana* and *Oryza sativa*. *Methods Mol. Biol.* 1305, 1–12. doi: 10.1007/978-1-4939-2639-8_1

Nawaz, G., and Kang, H. (2017). Chloroplast- or mitochondria-targeted DEAD-Box RNA helicases play essential roles in organellar RNA metabolism and abiotic stress responses. *Front. Plant Sci.* 8:871. doi: 10.3389/fpls.2017.00871

Neuberger, M., Journet, E. P., Bligny, R., Carde, J. P., and Douce, R. (1982). Purification of plant mitochondria by isopycnic centrifugation in destiny gradients of Percoll. *Arch. Biochem. Biophys.* 217, 312–323. doi: 10.1016/0003-9861(82)90507-0

Ng, S., De Clercq, I., Van Aken, O., Law, S. R., Ivanova, A., Willems, P., et al. (2014). Anterograde and retrograde regulation of nuclear genes encoding mitochondrial proteins during growth, development, and stress. *Mol. Plant.* 7, 1075–1093. doi: 10.1093/mp/ssu037

Planchard, N., Bertin, P., Quadrado, M., Dargel-Graffin, C., Hatin, I., Namy, O., et al. (2018). The translational landscape of *Arabidopsis mitochondria*. *Nucleic Acids Res.* 46, 6218–6228. doi: 10.1093/nar/gky489

Poku, S. A., Chukwurah, P. N., Aung, H. H., and Nakamura, I. (2020). Over-expression of a melon Y3SK2-type LEA gene confers drought and salt tolerance in transgenic tobacco plants. *Plants* 9:1749. doi: 10.3390/plants9121749

Shao, H. B., Liang, Z. S., and Shao, M. A. (2005). LEA proteins in higher plants: structure, function, gene expression and regulation. *Colloids Surfaces B Bio.* 45, 131–135. doi: 10.1016/j.colsurfb.2005.07.017

Shaw, D. S., Meitha, K., Considine, M. J., and Foyer, C. H. (2017). Mitochondrial respiration and oxygen tension. in: plant respiration and internal oxygen. *Methods Mol. Biol.* 1670, 97–113. doi: 10.1111/j.1399-3054.2009.01253.x

Singh, K. K., and Graether, S. P. (2020). Conserved sequence motifs in the abiotic stress response protein late embryogenesis abundant 3. *PLoS One* 15:e0237177. doi: 10.1371/journal.pone.0237177

Sun, X., Rikkerink, E. H., Jones, W. T., and Uversky, V. N. (2013). Multifarious roles of intrinsic disorder in proteins illustrate its broad impact on plant biology. *Plant Cell* 25, 38–55. doi: 10.1105/tpc.112.106062

Shapiguzov, A., Vainonen, J. P., Hunter, K., Tossavainen, H., Tiwari, A., Järvi, S., et al. (2019). Arabidopsis RCD1 coordinates chloroplast and mitochondrial functions through interaction with ANAC transcription factors. *eLife* 8:e43284. doi: 10.7554/eLife.43284

Tunnacliffe, A., and Wise, M. J. (2007). The continuing conundrum of the LEA proteins. *Naturwissenschaften* 94, 791–812. doi: 10.1007/s00114-007-0254-y

Umezawa, T., Fujita, M., Fujita, Y., Yamaguchi-Shinozaki, K., and Shinozaki, K. (2006). Engineering drought tolerance in plants: discovering and tailoring genes unlock the future. *Curr. Opin. Biotechnol.* 17, 113–122. doi: 10.1016/j.copbio.2006.02.002

Verdier, J., Lalanne, D., Pelletier, S., Torres-Jerez, I., Righetti, K., Bandyopadhyay, K., et al. (2013). A regulatory network-based approach dissects late maturation processes related to the acquisition of desiccation tolerance and longevity of *Medicago truncatula* seeds. *Plant Physiol.* 163, 757–774. doi: 10.1104/pp.113.222380

Van Leene, J., Eeckhout, D., Persiau, G., Van De Slijke, E., Geerinck, J., Van Isterdael, G., et al. (2011). Isolation of transcription factor complexes from Arabidopsis cell suspension cultures by tandem affinity purification. *Methods Mol. Biol.* 754, 195–218. doi: 10.1007/978-1-61779-154-3_11

Van Leene, J., Eeckhout, D., Cannoot, B., De Winne, N., Persiau, G., Van De Slijke, E., et al. (2015). An improved toolbox to unravel the plant cellular machinery by tandem affinity purification of *Arabidopsis* protein complexes. *Nat. Prot.* 10, 169–187. doi: 10.1038/nprot.2014.199

Wu, F. H., Shen, S. C., Lee, L. Y., Lee, S. H., Chan, M. T., and Lin, C. S. (2009). Tape-*Arabidopsis sandwich*—a simpler *Arabidopsis protoplast* isolation method. *Plant Methods* 5, 16–18. doi: 10.1186/1746-4811-5-16

Xu, Z., Jiang, Y., and Zhou, G. (2015). Response and adaptation of photosynthesis, respiration, and antioxidant systems to elevated CO2 with environmental stress in plants. *Front. Plant Sci.* 6:701. doi: 10.3389/fpls.2015.00701

Zoschke, R., and Bock, R. (2018). Chloroplast translation: structural and functional organization, operational control, and regulation. *Plant Cell* 30, 745–770. doi: 10.1105/tpc.18.00016

Conflict of Interest: The authors declare that the research was conducted in the absence of any commercial or financial relationships that could be construed as a potential conflict of interest.

Publisher's Note: All claims expressed in this article are solely those of the authors and do not necessarily represent those of their affiliated organizations, or those of the publisher, the editors and the reviewers. Any product that may be evaluated in this article, or claim that may be made by its manufacturer, is not guaranteed or endorsed by the publisher.

frontiers | Frontiers in Plant Science

ORIGINAL RESEARCH
published: 22 June 2022
doi: 10.3389/fpls.2022.928386

The Indole-3-Acetamide-Induced *Arabidopsis* Transcription Factor MYB74 Decreases Plant Growth and Contributes to the Control of Osmotic Stress Responses

*Paloma Ortiz-García[1†], Marta-Marina Pérez-Alonso[1,2†], Adrián González Ortega-Villaizán[1], Beatriz Sánchez-Parra[1,3], Jutta Ludwig-Müller[4], Mark D. Wilkinson[1] and Stephan Pollmann[1,5]**

[1]Centro de Biotecnología y Genómica de Plantas,Universidad Politécnica de Madrid (UPM)–Instituto Nacional de Investigación y Tecnología Agraria y Alimentación (INIA/CSIC), Madrid, Spain, [2]Umeå Plant Science Center, Umeå University, Umeå, Sweden, [3]Institute of Biology, University of Graz, Graz, Austria, [4]Institute of Botany, Technische Universität Dresden, Dresden, Germany, [5]Departamento de Biotecnología-Biología Vegetal, Escuela Técnica Superior de Ingeniería Agronómica, Alimentaria y de Biosistemas, Universidad Politécnica de Madrid (UPM), Madrid, Spain

OPEN ACCESS

Edited by:
Anna N. Stepanova, North Carolina State University, United States

Reviewed by:
Dior Rose Kelley, Iowa State University, United States
Javier Brumos, Polytechnic University of Valencia, Spain

***Correspondence:**
Stephan Pollmann
stephan.pollmann@upm.es

[†]These authors have contributed equally to this work

Specialty section:
This article was submitted to Plant Physiology, a section of the journal Frontiers in Plant Science

Received: *25 April 2022*
Accepted: *10 June 2022*
Published: *22 June 2022*

Citation:
Ortiz-García P, Pérez-Alonso M-M, González Ortega-Villaizán A, Sánchez-Parra B, Ludwig-Müller J, Wilkinson MD and Pollmann S (2022) The Indole-3-Acetamide-Induced Arabidopsis Transcription Factor MYB74 Decreases Plant Growth and Contributes to the Control of Osmotic Stress Responses. Front. Plant Sci. 13:928386. doi: 10.3389/fpls.2022.928386

The accumulation of the auxin precursor indole-3-acetamide (IAM) in the *ami1* mutant has recently been reported to reduce plant growth and to trigger abiotic stress responses in *Arabidopsis thaliana*. The observed response includes the induction of abscisic acid (ABA) biosynthesis through the promotion of *NCED3* expression. The mechanism by which plant growth is limited, however, remained largely unclear. Here, we investigated the transcriptional responses evoked by the exogenous application of IAM using comprehensive RNA-sequencing (RNA-seq) and reverse genetics approaches. The RNA-seq results highlighted the induction of a small number of genes, including the R2R3 MYB transcription factor genes *MYB74* and *MYB102*. The two MYB factors are known to respond to various stress cues and to ABA. Consistent with a role as negative plant growth regulator, conditional *MYB74* overexpressor lines showed a considerable growth reduction. RNA-seq analysis of *MYB74* mutants indicated an association of MYB74 with responses to osmotic stress, water deprivation, and seed development, which further linked MYB74 with the observed *ami1* osmotic stress and seed phenotype. Collectively, our findings point toward a role for MYB74 in plant growth control and in responses to abiotic stress stimuli.

Keywords: auxin, plant hormone crosstalk, growth repression, plant stress response, *Arabidopsis thaliana*

INTRODUCTION

Plants are continually challenged by an ever-changing environment. Many environmental alterations are unfavorable and affect the development of plants negatively. In fact, plants must endure a wide variety of abiotic stress conditions, including drought, salinity, and adverse temperatures. These stressors greatly limit plant growth and productivity, forcing plants to

adjust their developmental programs accordingly to cope with environmental variations and ensure the survival of their progeny. Over recent years, our understanding of the multifaceted and comprehensive molecular processes that contribute to orchestrating adequate abiotic stress responses in plants, including stress perception, signal transduction, and transcriptional reprogramming, has made substantial progress but is still far from being complete (Zhang et al., 2022).

Phytohormones are key drivers of plant stress responses. They are well-known small signaling molecules that show quick responses to environmental changes and act at submicromolar concentrations (Davies, 2010). The plant hormones abscisic acid (ABA), salicylic acid (SA), and jasmonic acid (JA) have been recognized as classical stress hormones, as a wealth of studies reported their key roles in plant stress responses. However, there is also mounting evidence that the crosstalk of these stress hormones with the remaining plant hormones, including brassinosteroids, ethylene, and auxin, is an important factor that is reported to determine the adequate level of response (Verma et al., 2016).

Currently, not much is known about the molecular basis of ABA–auxin crosstalk, although several studies point to the cooperation of these two plant hormones in a number of physiological processes (Emenecker and Strader, 2020). For example, both plant hormones inhibit primary root growth in light-grown Arabidopsis seedlings (Thole et al., 2014). Furthermore, a recent study reported that both the endogenous accumulation of the auxin precursor indole-3-acetamide (IAM) and the exogenous application of IAM can trigger ABA biosynthesis through the transcriptional activation of *NCED3* (Pérez-Alonso et al., 2021a). 9-*cis*-Epoxycarotenoid dioxygenases (NCEDs) are key rate-limiting enzymes in the ABA biosynthesis pathway (Huang et al., 2018b). Pérez-Alonso and colleagues (2021) reported that the abiotic stress-mediated repression of *AMIDASE 1* (*AMI1*) and the therewith coupled accumulation of IAM provide a molecular link that connects auxin and ABA biosynthesis pathways. In this way, plants are assumed to be able to marshal their energy resources and to fine-tune their growth with adequate responses to abiotic stress conditions. Moreover, another study has shown that ABA has a repressive effect on lateral root formation through the crosstalk with auxin in maize (Lu et al., 2019). It is assumed that the ABA receptor PYL9 enhances the transcription of *MYB77* (Xing et al., 2016), which is an interactor of ARF7 (Shkolnik-Inbar and Bar-Zvi, 2010). The latter is a key determinant of lateral root formation. In this manner, PYL9 can exert a direct impact on lateral root formation through transcriptional control of *MYB77*.

The myeloblastosis (MYB) transcription factor (TF) superfamily is large and functionally extremely diverse. Members of the MYB TF family share the conserved MYB DNA-binding domain, which generally consists of up to four imperfect amino acid sequence repeats (R) that span approx. 52 amino acids and form three α-helices. The second and third helix of each repeat fold into a helix-turn-helix (HTH) motif (Ogata et al., 1996). Regarding the number of MYB domains in the conserved N-terminal DNA binding domain, MYB factors can be divided into four classes: 1R, R2R3, 3R, and 4R-MYB proteins (Stracke et al., 2001; Dubos et al., 2010). Notably, the R2R3-MYB TF class is specific to the plant kingdom and the most abundant class of MYB factors in plants. As an example, the MYB superfamily in *Arabidopsis thaliana* is composed of only five 3R-MYB proteins and about 190 R2R3-MYB factors. The C-terminal regions of MYB family proteins are less conserved and contain a highly diverse modulator region that is responsible for the regulatory activity of the TFs. MYBs regulate a wide variety of biological processes in plants, ranging from their roles in controlling plant development through cell proliferation to their critical roles in diverse plant stress responses (Ambawat et al., 2013).

In this study, we present a detailed analysis of the role of MYB74. The *MYB74* gene has been identified as a downstream target of the auxin biosynthesis intermediate IAM. MYB74 clusters together with MYB41, MYB49, and MYB102 into subgroup 11 of Arabidopsis R2R3-MYB proteins (Kranz et al., 1998). While MYB41 has been identified as a negative regulator of transcriptional responses to osmotic stress (Lippold et al., 2009), MYB102 has been associated with osmotic stress responses and wound signaling pathways (Denekamp and Smeekens, 2003; De Vos et al., 2006). MYB49 was recently found to be involved in the modulation of salt tolerance, cuticle formation, and antioxidant defense (Zhang et al., 2020). As with most of the other members of subgroup 11, MYB74 has so far not been studied comprehensively. A previous study reports on the broad but weak expression of *MYB74* in Arabidopsis. Moreover, the work highlights the transcriptional activation of *MYB74* under salt stress and demonstrates a negative correlation of *MYB74* promoter DNA methylation with its induction under these conditions (Xu et al., 2015). However, the molecular processes downstream of MYB74 are largely unknown. Here, we provide evidence that elevated expression of *MYB74* results in substantial growth retardation, an effect that has also been observed for 35S-MYB41 mutants (Lippold et al., 2009). Furthermore, the conditional overexpression of *MYB74* affects the expression of a considerable number of abiotic stress-related genes and contributes to the modulation of the response to osmotic stress. The results presented here unveil a hitherto unknown molecular link between auxin biosynthesis and the induction of abiotic stress pathways in Arabidopsis. Moreover, our results consolidate the role of IAM as an important small signaling molecule that contributes to the coordination of the trade-off between growth and tolerance to osmotic stress, in part through the transcriptional control of *MYB74*.

MATERIALS AND METHODS

Plant Material and Growth Conditions

Along with the reference genotype *A. thaliana* Col-0 (stock N1092), the following Arabidopsis mutant lines for *MYB74* (At4g05100) and *AMI1* (At1g08980) were used in this study: the *myb74* (SALK_073544C) T-DNA insertion line, the conditional overexpression lines MYB74oe-1 (TPT_4.05100.1D) and MYB74oe-2 (TPT_4.05100.1H) from the TRANSPLANTA collection (Coego et al., 2014), *ami1-2* and AMI1ind-2

(Pérez-Alonso et al., 2021a). Moreover, we used the abscisic acid (ABA) biosynthesis and signaling mutants *aba3-1* (Léon-Kloosterziel et al., 1996) and *abi5-7* (Nambara et al., 2002), respectively. The T-DNA insertion mutant for *MYB74* from the SALK collection was genotyped as described elsewhere (Alonso et al., 2003). The primers used for genotyping are given in **Supplementary Table S1**. After stratification (2 days, 4°C), plants were either grown sterilely on solidified 0.5X MS medium supplemented with 1% (w/v) sucrose (Murashige and Skoog, 1962) or on a mixture of peat and vermiculite (3:1). Plant growth was performed under environmentally controlled short-day conditions (8 h light at 24°C, 16 h darkness at 20°C, 105 µmol photons m^{-2} s^{-1} photosynthetically active radiation). The expression of the transgene in the conditional *MYB74* overexpression mutants MYB74oe-1 and MYB74oe-2, as well as in AMI1ind was induced by adding 10 µM ß-estradiol to the growth medium. In all experiments that employed these lines, corresponding wt control plants were grown on medium supplemented with equal amounts of ß-estradiol. To study osmotic stress responses, the plants were grown on media that were additionally supplemented with 300 µM mannitol. The investigation of heat stress tolerance was performed according to Hsieh et al. (2013). In brief, 24 seeds per genotype were sown on corresponding 0.5X MS media in sealed 90-mm Petri dishes. After the seeds were grown for 6 days under control conditions, they were subjected to a heat-shock treatment (30 min at 42°C). Thereafter, the plants were returned to control conditions and the survival rate was analyzed after 1 week of recuperation.

Plant Hormone Analysis

The contents of ABA, IAA and IAM in 50 and 100 mg of 10 days old sterilely grown Arabidopsis seedlings, respectively, have been analyzed using mass spectrometry. While ABA was assessed by GC–MS/MS analysis according to Pérez-Alonso et al. (2021b), IAA and IAM were quantified by LC–MS/MS as previously described (Pérez-Alonso et al., 2021a). The content of each analyzed metabolite in wild-type Arabidopsis (Col-0) was set to 1. The metabolite contents in the MYB74oe lines were presented in reference to the wild-type values. All mass spectrometric analyses have been conducted in triplicate.

Germination Assay

To analyze the impact of the conditional overexpression on seed germination, 50 seeds of each tested genotype were sown on Protran® nitrocellulose membranes (Whatman) on MS medium supplemented with 10 µM ß-estradiol. The seeds were kept in a growth chamber under previously described standard conditions. The germination process of the different genotypes was periodically monitored under a Leica MZ10F stereomicroscope. To ensure equal conditions, all seeds were harvested at the same time, when the entire siliques had browned. The experiment was carried out in three biological replicates.

Analysis of Stomatal Aperture

Whole leaves from four to 6 weeks-old Arabidopsis plants grown together under control conditions were harvested and the epidermis rapidly peeled. The abaxial epidermis peels were then placed on cover slips. The microscopic observation was done on a Zeiss LSM 880 (Carl Zeiss, Jena; Germany) microscope. The stomatal aperture was analyzed by measuring the quotient of the stomatal width and length using the Fiji image processing software (Schindelin et al., 2012). The experiments were repeated at least three independent times ($n = 25$).

Modeling of the MYB74 and MYB102 Protein Structure

The three-dimensional structures of MYB74 and MYB102 were modeled by using a homology-based approach. The 2.15 Å crystal structure of MYB66 from *A. thaliana* [PDB: 6KKS] (Wang et al., 2020) and the 2.9 Å crystal structure of *Trichomonas vaginalis* MYB3 [PDB: 3ZQC] (Wei et al., 2012) deposited in the Research Collaboratory for Structural Bioinformatics (RCSB) Protein Data Base were used as reference structures. The different structural models were generated by using both the Phyre[2] protein fold recognition server (Kelley et al., 2015) and the I-TASSER protein structure prediction server (Yang et al., 2015). The structural comparison of the obtained models for MYB74 and MYB102 was performed using PyMOL v2.5.0[1] and the InterPro[2] protein classification tool.

RNA Isolation and Gene Expression Analysis by qRT-PCR

For each genotype and condition, 100 mg of plant tissue of seven to 10 days-old sterilely grown seedlings were harvested for total RNA extraction as previously described (Oñate-Sánchez and Vicente-Carbajosa, 2008). First strand synthesis was conducted using M-MLV reverse transcriptase and oligo$(dT)_{15}$ primer, following the instructions of the manufacturer (Promega). Two nanograms of cDNA were used as template in each qRT-PCR. cDNA amplification was performed using the FastStart SYBR Green Master solution (Roche Diagnostics) and a Lightcycler 480 Real-Time PCR system (Roche Diagnostics), according to the supplier's instructions. The relative transcript quantification was calculated employing the comparative $2^{-\Delta\Delta CT}$ method (Livak and Schmittgen, 2001). As reference genes, we used *APT1* (At1g27450) and *GAPC2* (At1g13440; Czechowski et al., 2005; Jost et al., 2007). The quantitative gene expression analysis and metabolite induction studies were carried out as previous described (Pérez-Alonso et al., 2021a), using three biological replicates. In addition, three technical replicates per biological replicate were analyzed. See **Supplementary Table S1** for primer sequences.

RNA-seq Analysis

In this study, we performed two genome-wide expression studies employing mRNA sequencing (mRNA-seq). First, total RNAs from 14 days-old wt, *ami1*, and AMI1ind seedlings treated with methanol (0.5% v/v, mock) or 100 µM indole-3-acetamide (IAM) for 3 h were extracted as described above and quantified

[1]https://pymol.org/
[2]https://www.ebi.ac.uk/interpro/

using a Nanodrop ND-1000® UV/Vis spectrophotometer (ThermoFisher). Overall RNA quality was additionally checked on a Bioanalyzer 2100 (Agilent) by the CNB Genomics Service (Madrid). Library construction and RNA sequencing (50-nt single-end reads) was performed by the Beijing Genomics Institute (BGI, Hong Kong, China) on Illumina HiSeq™ 2000 machines. Basic data analysis, including raw data cleaning, alignment of the clean reads to the Arabidopsis reference genome, and the quantitative analysis of differential gene expression, was performed using the BGI RNA-seq pipeline of standard bioinformatics. Secondly, mRNA from 10 days-old *myb74*, MYB74oe-1, and wild-type seedlings were subjected to mRNA-seq analysis. Library construction and sequencing (150-nt paired-end reads) on Illumina NovaSeq™ 6000 platforms was performed by the Novogene Genomics Service (Cambridge, United Kingdom). The Novogene Genomics Service also provided basic data analysis applying their RNAseq pipeline.

To analyze differentially expressed genes, Vulcano and Venn plots have been generated using the VolcaNoseR[3] and Venn[4] online tools, respectively. For the gene ontology (GO) enrichment analysis we used either the ClueGO application in Cytoscape or the g:Profiler online tool.[5]

Statistical Analysis

The statistical assessment of the data was performed using the JASP v0.16.1 software.[6] Student's *t*-test was employed to compare two means, while two-way analysis of variance (ANOVA), followed by Tukey–Kramer's multiple comparison test, was used for multiple mean comparison. The applied statistical analysis for each experiment is given in the corresponding figure legends. Results were considered significant when the value of $p < 0.05$.

RESULTS

mRNA-Sequencing Reveals a Set of IAM-Responsive Genes in Arabidopsis

IAM is an auxin precursor widely distributed in the plant kingdom (Sugawara et al., 2009; Sánchez-Parra et al., 2014). It is converted into IAA by the virtue of specific IAM hydrolases, including AMIDASE 1 (AMI1; Pollmann et al., 2003), and IAM HYDROLASE 1 (IAMH1) as well as IAM HYDROLASE 2 (IAMH2; Gao et al., 2020) from *A. thaliana*. Previous studies associated the accumulation of IAM with the induction of plant stress responses (Pérez-Alonso et al., 2021a). To gain insight into the biological processes and molecular mechanisms transcriptionally activated by high IAM levels, we profiled the transcriptomes of 14-days old Arabidopsis wild-type, *ami1*, and AMI1ind plants treated with 100 µM IAM for 3 h in comparison to mock-treated wild-type control plants to trigger strong transcriptional responses and provide sufficient substrate for the overexpressed amidase in the AMI1ind plants. As anticipated, given the already reported significant transcriptomic differences between the *AMI1* loss- and gain-of-function lines (Pérez-Alonso et al., 2021a), we identified significant transcriptional responses when the plants were treated with IAM (**Figure 1A**; **Supplementary Table S2**). Interestingly, the responses to IAM were substantially elevated in mutant plants with a manipulated expression of *AMI1* compared to the wild type. This confirms our previous observation that the alteration of *AMI1* expression provokes considerable changes in the transcriptomic profiles of the corresponding plants. As shown in **Figure 1B**, the Venn analysis of differentially expressed genes (DEGs), which was employed to prioritize candidates among the differentially expressed groups in the different genotypes, revealed a small group of 16 DEGs consistently induced under all tested conditions (**Table 1**). The consistent transcriptional activation of these genes under all tested conditions suggested a fast and presumably direct response to IAM. The remaining mRNA-seq data confirmed the notion of an induction of plant stress responses, elicited by the exogenous application of IAM and the genetically manipulated expression of *AMI1* (Moya-Cuevas et al., 2021). A KEGG pathway analysis, using the identified 16 genes as query, provided evidence for the overrepresentation of genes related with the galactose metabolism pathway. Out of the 16 genes the two galactinol synthase genes *GolS2* and *GolS3* belong to this pathway. Interestingly, galactinol synthases seem to be involved in conferring drought tolerance to plants and desiccation tolerance to seeds (Himuro et al., 2014; Lang et al., 2017), which links these genes with the abiotic stress responses triggered by elevated IAM contents. Next, we performed a GO analysis to identify biological processes enriched among the 16 genes. Fourteen of the sixteen genes could be associated to GO terms, and two GO term classifications, response to abiotic stimulus and response to abscisic acid, appeared to be significantly enriched (FDR < 0.05). The groups contained the genes *MYB102*, *GolS2*, *HAI1*, *COR15A* and *MYB74*, *AOC2*, *GolS2*, *GolS3*, *COR15A*, respectively (**Supplementary Table S2**). Our results indicated that a small number of genes that are related with abiotic stress responses show a considerable and relatively quick transcriptional response to IAM, even in conditional *AMI1* over-expressing mutants that convert exogenously applied IAM more rapidly to IAA.

MYB74 and MYB102 Are Structurally Different

Among the identified target genes, the two members of the R2R3-MYB TF family, MYB74 and MYB102, arouse our particular interest. MYB102 has previously been studied in closer detail and has been associated with wounding, osmotic stress responses, and the induction of ethylene biosynthesis (Denekamp and Smeekens, 2003; De Vos et al., 2006; Zhu et al., 2018), while the physiological function of MYB74 remained largely elusive, except its response to salt stress and its putative connection with ABA signaling (Xu et al., 2015; Huang et al., 2018a). Regarding their primary amino acid sequences, the two MYB factors share 65.7% identity. To gain further insight into the

[3]https://huygens.science.uva.nl/VolcaNoseR2/
[4]http://bioinformatics.psb.ugent.be/webtools/Venn/
[5]https://biit.cs.ut.ee/gprofiler/gost
[6]https://jasp-stats.org/

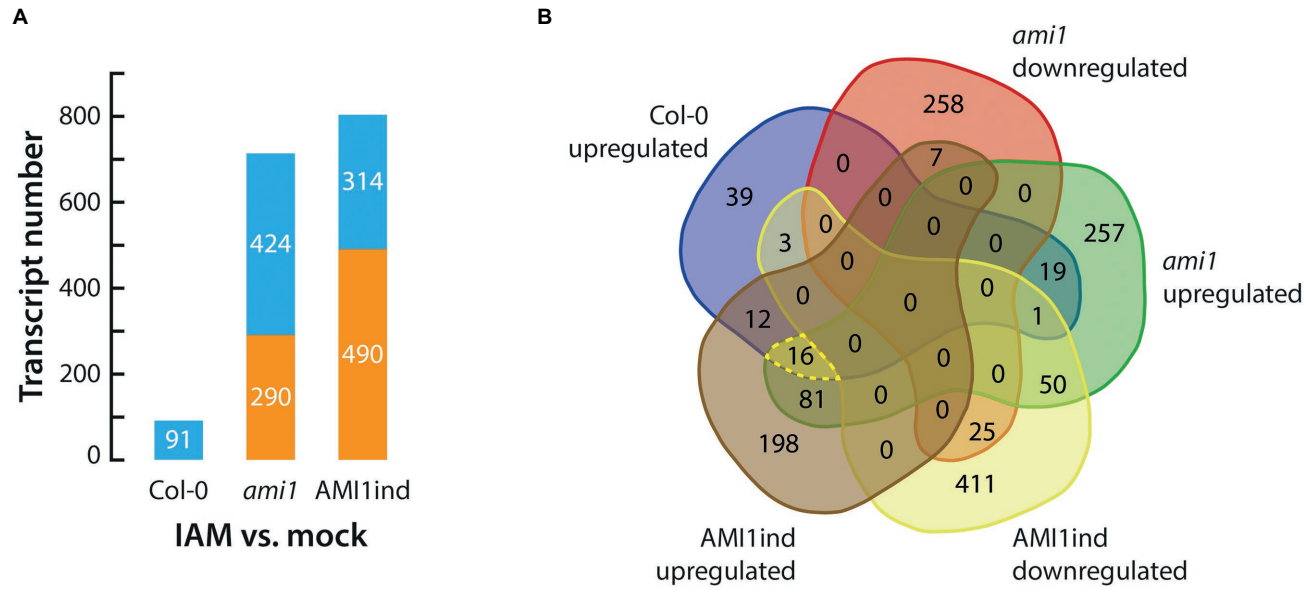

FIGURE 1 | Gene expression analysis of IAM treated plants. **(A)** DEG statistics for 14 days-old Col-0 wild-type and *ami1* as well as AMI1ind mutants treated for 3 h with 100 μM IAM. **(B)** Venn diagram of significantly up and downregulated genes in the investigated genotypes. The group of commonly induced genes among the three genotypes is highlighted by a yellow dashed line.

TABLE 1 | List of genes that were transcriptionally activated (IAM vs. control) by a short-term (3 h) treatment with 100 μM IAM in wild-type (Col-0) plants, the *AMI1* knockout (*ami1*) line, and the conditional AMI1 overexpression mutant (AMI1ind).

Gene ID	Gene name	Differential expression (log_2FC)		
		Col-0	*ami1*	AMI1ind
At1g05100	*MAPKKK18*	1.07	1.63	1.39
At1g09350	*GolS3*	2.03	2.15	2.27
At1g21790		1.01	1.82	1.63
At1g53470	*MSL4*	1.13	1.92	2.02
At1g56600	*GolS2*	1.10	1.60	1.76
At2g36750	*UGT73C1*	1.01	1.68	1.62
At2g39980		1.04	1.24	1.08
At2g42540	*COR15A*	3.18	1.39	2.46
At3g25770	*AOC2*	1.33	1.39	1.03
At3g55500	*EXP16*	1.23	1.33	1.96
At4g05100	*MYB74*	1.44	1.34	1.18
At4g21440	*MYB102*	1.70	3.21	2.23
At4g33930		1.12	1.31	1.27
At5g10410	*PICALM10B*	2.05	1.73	2.02
At5g45950	*GGL28*	1.15	1.82	1.37
At5g59220	*HAI1*	1.35	2.23	2.19

All identified genes showed a significant differential expression (q-value < 0.05).

structural intricacies of the two TFs, we built homology-based protein models using the I-TASSER (Yang et al., 2015) and Phyre² (Kelley et al., 2015) interfaces with the *A. thaliana* MYB66 [6kks] (Wang et al., 2020) and the *Trichomonas vaginalis* MYB3 [3zqc] (Wei et al., 2012) structures as template. The models revealed a substantial structural similarity of the two factors in their conserved N-terminally located DNA binding domains, which are recognizable by the positive surface potential (**Figure 2A**). The DNA binding domain of R2R3-MYB factors is composed of two adjacent imperfect amino acid sequence repeats (R), each consisting of three α-helices (**Figures 2B,D**). The nearly perfect superimposition of the DNA binding (DB) domains (**Figure 2B**) and the largely identical primary amino acid sequence in the N-terminal region (**Figure 2D**) demonstrated the high structural conservation of the two factors in their DB domains. Irrespective from minor displacements, also the anticipated amino acid residues in helix 3 (MYB74: Lys52 and Leu56; MYB102: Lys51 and Leu55) and helix 6 (MYB74: Asn103, Lys106, and Asn107; MYB102: Asn102, Lys105, and Asn106), which are assumed to be responsible for protein-DNA interaction (Wang et al., 2020), appeared structurally conserved. However, as shown in **Figure 2C**, the C-terminal modulator regions, which are responsible for the regulatory properties of the proteins, are clearly divergent. These non-MYB regions contain extensive intrinsically disordered regions (IDRs) that do not fold into stable globular structures, but mediate the interactions with many different signaling molecules and proteins through the formation of a large portfolio of transient structures (Millard et al., 2019). In summary, the *in-silico* structural modeling confirmed shared DNA-binding properties, but do not support the notion of overlapping regulatory functions, because the IDRs of MYB74 and MYB102 are most likely too different to cover similar regulatory purposes.

IAM-Induced *MYB74* Expression Is Independent of ABA

Next, we performed qPCR analysis of *MYB74* and *MYB102* expression in IAM, ABA, IAA, and mock treated wild-type Arabidopsis seedlings. As shown in **Figure 3A**, *MYB74* showed a stronger response to IAM compared to *MYB102*, while the latter responded more strongly to ABA. This finding is consistent

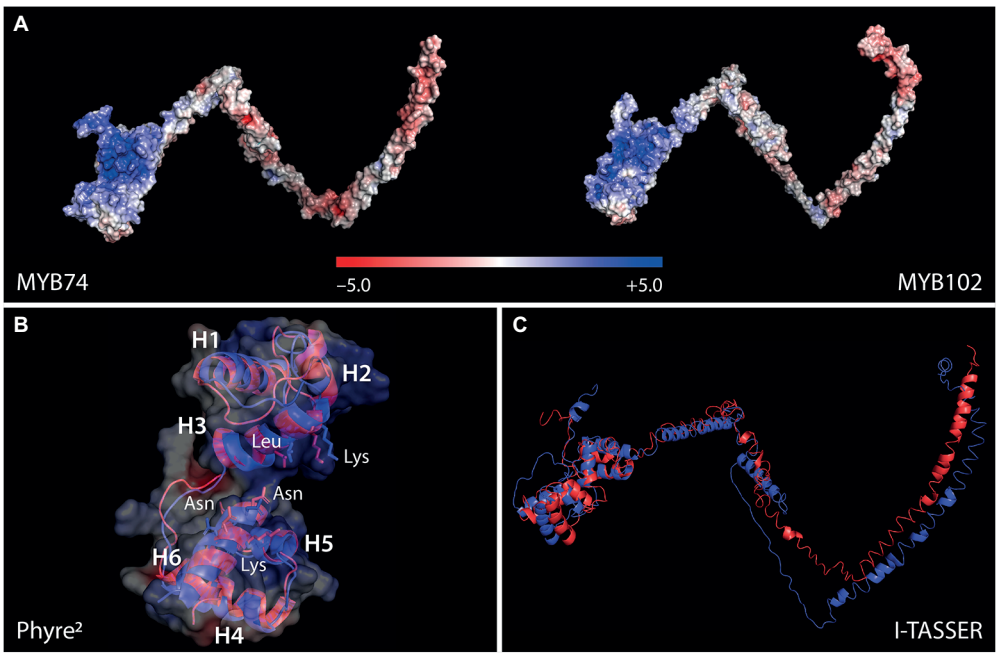

D

```
                                                R2 domain
MYB74   MGRSPCCEKKNGLKKGPWTPEEDQKLIDYINIHGYGNWRTLPKNAGLQRC  50
MYB102  MARSPCCEK-NGLKKGPWTSEEDQKLVDYIQKHGYGNWRTLPKNAGLQRC  49

                                R3 domain
MYB74   GKSCRLRWTNYLRPDIKRGRFSFEEEETIIQLHSIMGNKWSAIAARLPGR 100
MYB102  GKSCRLRWTNYLRPDIKRGRFSFEEEETIIQLHSFLGNKWSAIAARLPGR  99

MYB74   TDNEIKNYWNTHIRKRLLKMGIDPVTHTPRLDLLDISSILSSSIYNSSHH 150
MYB102  TDNEIKNFWNTHIRKKLLRMGIDPVTHSPRLDLLDISSILASSLYNSSSH 149

MYB74   HHHHHQQHMNMSRLMMSDG--NHQ--PLVNPEILKLATSLFS-NQN---- 191
MYB102  H-------MNMSRLMMDTNRRHHQQHPLVNPEILKLATSLFSQNQNQNLV 192

MYB74   --HPNNTHENNTV-NQTEVNQYQTGYNMPGN--EELQSWFPIMD----QF 232
MYB102  VDHDSRTQEKQTVYSQTGVNQYQTNQYFENTITQELQSSMPPFPNEARQF 242

MYB74   TNF---------QDLMPMKTT-VQNSLSYD-DDCSKSNFVLEPYYSD--- 268
MYB102  NNMDHHFNGFGEQNLVSTSTTSVQDCYNPSFNDYSSSNFVLDPSYSDQSF 292

MYB74   -FA-SVLTTPSSSPTPLNSSSSTYINSSTCSTEDEKESYYSDNITNYSF- 315
MYB102  NFANSVLNTPSSSPSPTTLNSS-YINSSSCSTEDEIESYCS-NLMKFDIP 340

MYB74   ---DVNGFLQFQ                                       324
MYB102  DFLDVNGFII--                                       350
```

FIGURE 2 | Structural comparison of Arabidopsis MYB74 and MYB102. **(A)** Electrostatic potential of MYB74 (left) and MYB102 (right). The color code for the estimated electrostatic potential is provided. **(B)** Superimposition of the conserved N-terminally located DNA binding domain. The three helices of the R2 (H1-H3) and the R3 domain (H4-H6) and the amino acids assumed to facilitate the protein-DNA binding are indicated. **(C)** Overlay of the complete three-dimensional structure models for MYB74 (red) and MYB102 (blue). The models have been inferred using the I-TASSER **(A,C)** and Phyre² **(B)** structural prediction server. **(D)** Sequence alignment of MYB74 and MYB102. The R2 and R3 sequence repeats are highlighted in the figure and the three helices of each repeat are indicated by boxes. Domain identification has been carried out using the InterPro classification tool.

with our previous study in which we reported the differential expression of several TFs in the *ami1* mutant, including *MYB74* and *MYB102* (Pérez-Alonso et al., 2021a). Intriguingly, neither *MYB74* nor *MYB102* were transcriptionally activated when

wild-type plants were treated with IAA. For this reason, a partially IAA-dependent regulation through the conversion of IAM to IAA by the IAM hydrolases AMI1, IAMH1, and IAMH2 can likely be ruled out. Given the stronger response of *MYB74* to IAM and its responsiveness to short- and long-term osmotic stress (Watanabe et al., 2018), which further connects the factor with the *ami1* osmotic stress phenotype (Pérez-Alonso et al., 2021a), we focused our attention in the following on MYB74.

While the knockout of *IAMH1* and *IAMH2* has not been reported to translate into altered IAA and IAM levels under control conditions (Gao et al., 2020), the functional impairment of AMI1 in the *ami1* mutant alleles is known to significantly increase both endogenous IAM and ABA contents (Pérez-Alonso et al., 2021a). Therefore, the transcriptional response of *MYB74* could be triggered directly by IAM or proceed *via* the induction of ABA biosynthesis. To further our understanding of the transcriptional regulation of *MYB74*, we quantified the expression of *MYB74* after IAM and mock treatment in wt, *aba3*, and *abi5* seedlings by qPCR. Given that *aba3* is an ABA deficient and *abi5* an ABA insensitive mutant (Léon-Kloosterziel et al., 1996; Finkelstein and Lynch, 2000), we were able to address the question whether the induction of *MYB74* expression is dependent on ABA. As shown in **Figure 3B**, we detected no significant difference in the response of *MYB74* toward the treatment with IAM in the ABA mutants. Notably, the *abi5* mutant showed a slightly lower induction of *MYB74* expression, but the determined difference to the wild-type control was not significant. Together with the missing transcriptional response of MYB74 toward IAA (**Figure 3A**), this result suggested that the response of *MYB74* towards IAM occurs largely uncoupled from the formation of ABA.

MYB74 Negatively Affects Plant Growth

From a previous study (Xu et al., 2015), it is known that *MYB74* is constitutively expressed in the plant in low abundance. The highest levels of expression are detected in leaves and flowers. Furthermore, the authors provided evidence that overexpression of *MYB74* causes salt hypersensitivity during seed germination. To gain more insight into the physiological role of MYB74, we took a reverse genetics approach and performed a more detailed phenotypic analysis of *MYB74* mutants. As with the RNAi lines reported by Xu et al. (2015), the tested *myb74* T-DNA integration line showed only very moderate, if any, differences compared to the wild type, although the *MYB74* expression level in *myb74* was shown to be significantly reduced (**Supplementary Figure S1**). However, the inspection of two conditional *MYB74* overexpression lines, MYB74oe-1 and MYB74oe-2, which are characterized by a

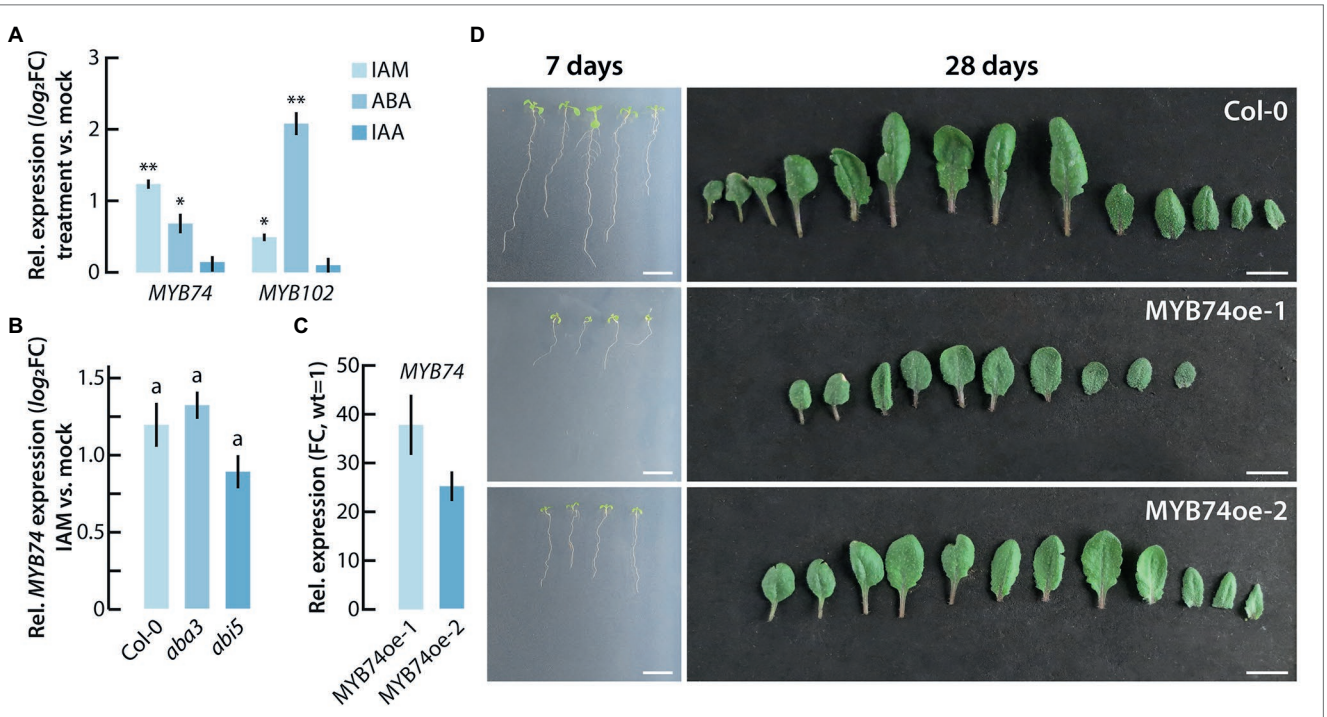

FIGURE 3 | Phenotypic analysis of conditional *MYB74* overexpressor plants. **(A)** Transcriptional activation of *MYB74* and *MYB102* after the short-term treatment of wild-type Arabidopsis seedlings with either 20 µM IAM, IAA, or ABA for 2 h. The data show the means with their corresponding SE ($n = 9$). Student's *t*-test: $^{*}p \leq 0.05$; $^{**}p \leq 0.01$. **(B)** Differential expression of *MYB74* in wild-type seedlings (Col-0), and the ABA mutants *aba3* and *abi5*. The plot depicts the relative *MYB74* expression in IAM versus mock treated seedlings. The bar plots represent means ±SE ($n = 9$). Different letters indicate significant differences between the means of the compared genotypes assessed by ANOVA and a Tukey–Kramer *post hoc* test ($p \leq 0.05$). **(C)** Expression level of *MYB74* in the two conditional MYB74 overexpressor lines, MYB74oe-1 and MYB74oe-2. The expression is shown relative to the gene expression level in wild-type seedlings, which have been set to 1. **(D)** Phenotypic appearance of wild-type (Col-0), MYB74oe-1, and MYB74oe-2 plants grown either for 7 days on sterile 0.5X MS plates (left) or for 28 days on soil (right). Scale bars = 1 cm.

38- and 25-fold overexpression of the transgene (**Figure 3C**), respectively, provided intriguing insight into the function of MYB74 as a negative plant growth regulator. As can be taken from **Figure 3D**, the two independent conditional overexpression lines showed a clear growth reduction when grown under control conditions. Both sterilely grown MYB74oe seedlings and soil grown MYB74oe plants showed considerable growth reductions, which could also be confirmed by the determination of fresh and dry weights of the mutants relative to wild-type plants (**Supplementary Figure S2**).

MYB74 Controls Diverse Abiotic Stress Responses

With the aim to further characterize the physiological function of MYB74, the *myb74* T-DNA insertion line and MYB74oe-1 were subjected to mRNA-seq analysis, comparing their transcriptional profiles to that of Col-0 control plants (**Supplementary Table S3**). Consistent with the phenotypic analysis of the *myb74* mutant, the RNA-seq analysis of the knockout line provided evidence for only a very reduced number of DEGs. Overall, we found five repressed and three induced genes (threshold log_2FC = ±1.25, q-value = 0.05), suggesting that MYB74 plays no critical role under control conditions. On the contrary, as shown in **Figure 4A**, the transcriptional profiling of MYB74oe-1 relative to the wild type disclosed a total of 355 induced and 67 repressed genes (threshold log_2FC = ±1.75, q-value = 0.05). Interestingly, we found *MYB102* to be significantly induced (log_2FC = 2.71) in the conditionally *MYB74* overexpressing line. This is indicative for a secondary transcriptional activation of *MYB102* through the elevated expression of *MYB74* in the transgenic plants.

Taking into consideration that *MYB74* is induced by the abiotic stress-triggered increases in both IAM and ABA levels, it must be concluded that MYB74 is involved in the integration of stress stimuli and the reprograming of the transcriptome to adequately respond to the perceived signals. Functional gene enrichment analyses using the g:Profiler (Raudvere et al., 2019), ClueGO (Bindea et al., 2009), and Metascape (Zhou et al., 2019) tools revealed, among other GO terms and KEGG pathways, the overrepresentation of osmotic stress, water deprivation, desiccation, and seed maturation, development, as well as germination-related gene sets (**Figures 4B,C**; **Supplementary Table S3**). Particularly the abiotic stress-related GO classifications showed a considerable number of shared genes, including *ERF53* (At2g20880), *PXG3* (At2g33380), *COR15A* (At2g42540), *LTP4* (At5g52300), *LTI65* (At5g52300), WSD1 (At5g37300), *GolS2* (At1g56600), *MAPKKK18* (At1g05100), and *RD29A* (At5g52310), some of which (*COR15A*, *GolS2*, and *MAPKKK18*) have already been identified as primary IAM target genes. Notably, *ERF53* was also found to be induced in the *ami1* null mutant (Pérez-Alonso et al., 2021a). With respect to water deprivation response-related genes, we identified *ANAC019* (At1g52890), *ANAC055* (At3g15500), and *ANAC072* (At4g27410) as particularly interesting group members. These plant specific NAC (petunia NAM and *Arabidopsis* ATAF1, ATAF2, and CUC2) TFs have previously been associated with stress responses and the regulation of stomatal aperture (Hickman et al., 2013; Gimenez-Ibanez et al., 2017).

Apart from an involvement in steering flavonoid biosynthesis, MYB74 seems to contribute to the control of the expression of a substantial number of cellulose synthase-like (*CSL*) genes, such as *CSLA1* (At4g16590), *CSLB1* (At2g32610), *CSLB2* (At2g32620), *CSLG1* (At4g24010), *CSLG2* (At4g24000), and *CSLG3* (At4g23990). The expression of genes related with the formation of cellulose and hemicellulose largely determines the biomechanical properties of plant secondary cell walls. Intriguingly, previous studies suggest a role for CSLs in salt tolerance (Zang et al., 2019), root hair morphogenesis (Favery et al., 2001), and organ size determination by altering cell division (Li et al., 2018b). Overall, the significant induction of genes related with osmotic stress protection and damage-repair pathways, including late embryogenesis abundant (*LEA*) and *LEA*-like genes as well as genes coding for proteins with similar characteristics such as the cold-regulated (COR)/responsive to desiccation (RD)/low temperature induced (LTI) proteins, must be highlighted. It remains to be noted that, in comparison with wild-type seedlings, the overexpression of *MYB74* in the MYB74oe lines does not interfere with the endogenous levels of IAA, IAM, and ABA (**Figure 5E**).

MYB74 Overexpressing Plants Show Increased Osmotic Stress Tolerance

Addressing the previously described considerable transcriptional regulation of *MYB74* by abiotic stress cues (Kilian et al., 2007), we confirmed the response of *MYB74* to heat and osmotic stress conditions by qPCR analysis (**Figure 5A**). Taking the previously reported enrichment of abiotic stress- and seed development as well as germination-related genes in the conditional MYB74 overexpression line into account, we further investigated seed germination, and both heat and osmotic stress tolerance of the MYB74oe lines. First, we analyzed the effect of the conditional *MYB74* overexpression on the germination process. As shown in **Figure 5B**, the induction of *MYB74* through the addition of ß-estradiol to the medium clearly interfered with the germination process. The two MYB74oe lines exhibited a significant delay in seed germination, both in terms of seed coat rupture (SCR), defined as the visible vertical opening of the seed coat provoked by the mechanical force exerted by the embryo, and endosperm rupture (ER), defined as the radicle emergence through the seed coat (Iglesias-Fernández et al., 2013). Next, we characterized the primary root growth of MYB74oe lines in comparison to wild-type seedlings under osmotic stress conditions (**Figure 5C**). Apparently, the primary root length of the MYB74oe lines under control conditions was already significantly reduced (**Figure 5C**; **Supplementary Figure S2**). However, when the plants were first germinated on 0.5X MS for 4 days and then transferred to plates containing mannitol, the relative stress response, as defined by the observed primary root elongation, of the MYB74oe lines was clearly less pronounced. While wild-type seedlings showed a reduction of primary root elongation of

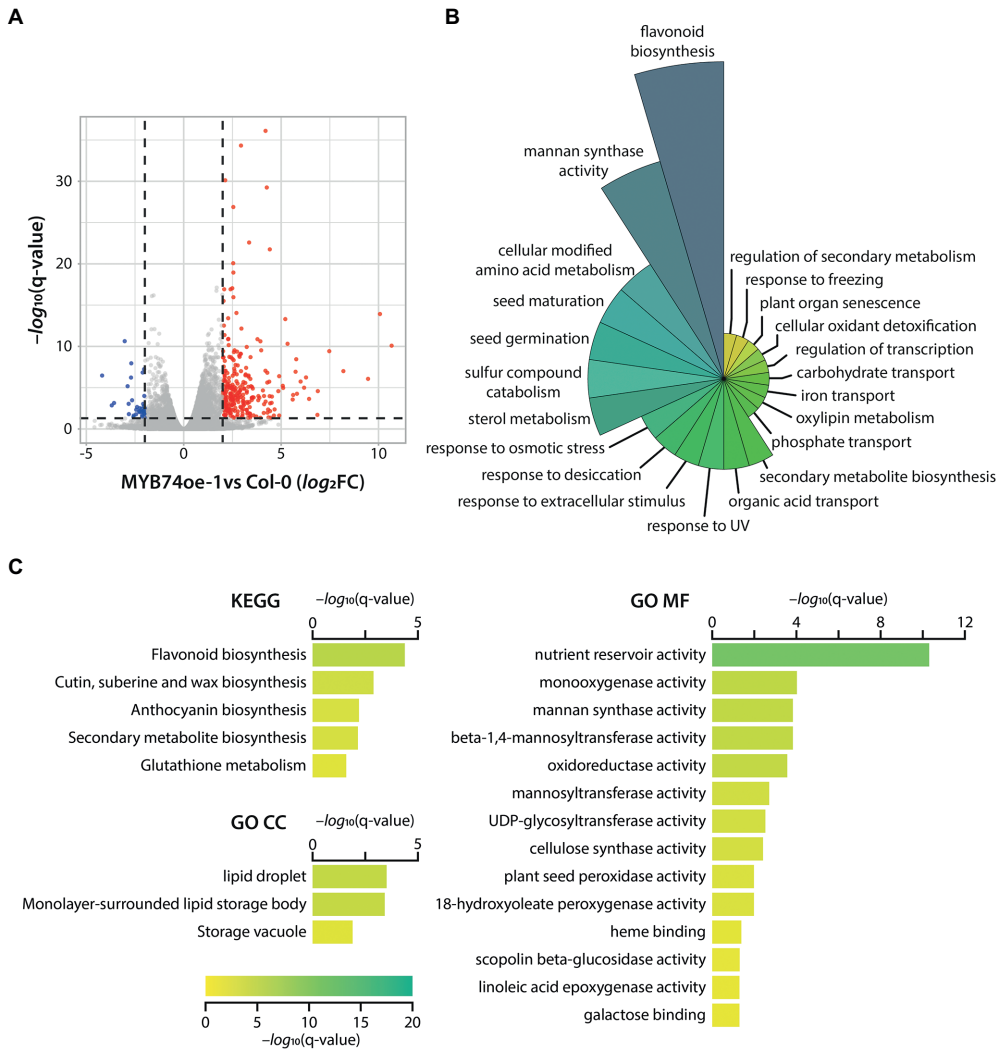

FIGURE 4 | Transcriptomics analysis of differentially expressed genes (DEGs) in the transgenic MYB74oe-1 line. **(A)** Volcano plot of differentially expressed genes in MYB74oe-1 compared to wild-type (Col-0) seedlings. MYB74 acts as a transcriptional activator, as the majority of the DEGs appear to be induced (red dots), while only a small number of genes is repressed (blue dots). Genes with no significant changes (log_2FC = ±1.75, q-value = 0.05) are show in grey. **(B)** Polar plot of biological process-related GO terms enriched in the identified DEGs in MYB74oe-1. **(C)** Bar plots of KEGG pathway (KEGG) and GO cellular compartment (GO CC) as well as molecular function (GO MF) enrichment analysis. The color and length of the bars reflect the significance of the different identified terms, indicated by the legend at the bottom [$-log_{10}$(q-value)]. The graphs only show significantly enriched terms with a q-value <0.05.

52%, the MYB74oe-1 and MYB74oe-2 seedlings displayed a reduction of only 29 and 34%, respectively (**Figure 5D**). Next, we assessed the response of the lines towards a short-term heat treatment. For this, plates with 24 six days-old seedlings were subjected to a heat shock (42°C, 30 min) and the survival rate of the seedlings was monitored after a seven-day long recovery phase. As shown in **Figure 5F**, the survival rate of MYB74oe-1 and MYB74oe-2 seedlings was drastically reduced, which suggested an impairment of the heat shock response (HSR). This promoted us to take a closer look at the expression of HSR-related genes. The mRNA-seq data revealed a significant repression of *HSFA7a* (At3g51910) and the induction of *HSFA6a* (At5g43840). Previous studies have characterized *HSFA6a* as an activator of stress-responsive genes in ABA-dependent signaling pathways and highlighted its involvement in a few other processes, including stomatal movement and water loss (Hwang et al., 2014; Wenjing et al., 2020). Interestingly, *HSFA6a* is not induced by heat, but only by high salt conditions and dehydration (Hwang et al., 2014). HSFA7a, on the contrary, acts in conjunction with HSFA2 in the control of HSR-related genes (Lin et al., 2018). Apart of the differential expression of *HSFA6a* and *HSFA7a*, the mRNA-seq results indicated no differential expression of other HSR-related genes, such as heat shock proteins (*HSPs*), *DREB2A*, or *MBF1c* (Jacob et al., 2017). For this reason, we decided to compare the stomatal aperture of MYB74oe-1 and MYB74oe-2 leaves with that of leaves from wild-type plants. A misregulation of the stomatal aperture could explain

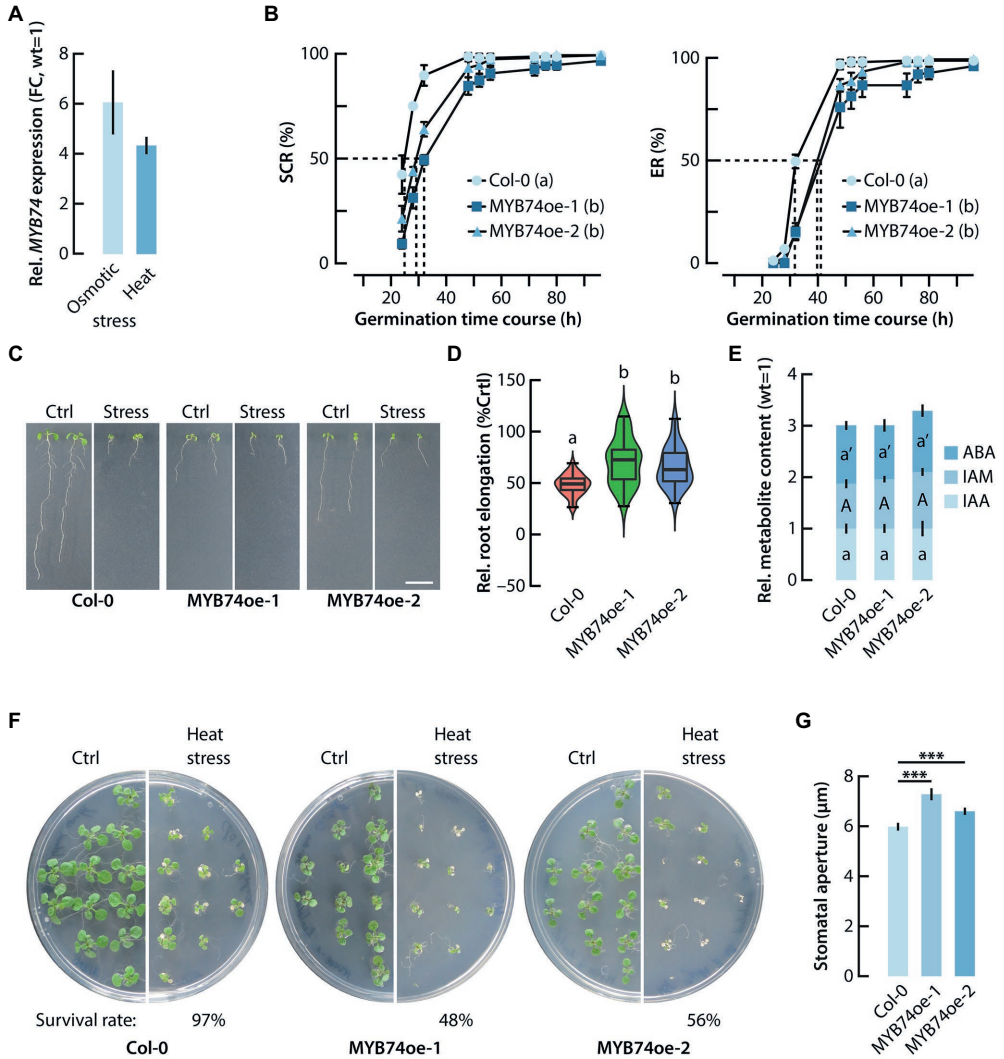

FIGURE 5 | Functional characterization of MYB74oe lines. **(A)** qPCR analysis of the transcriptional activation of *MYB74* by heat and osmotic stress conditions. Gene expression is given relative to the *MYB74* expression in untreated control plants, which has been set to 1. **(B)** Seed germination kinetics in wild-type Arabidopsis (Col-0) and the two conditionally MYB74 overexpressing lines. Seed coat rupture (SCR) and endosperm rupture (ER) time course. Different letters indicate significant differences ($p < 0.05$) in germination of the tested genotypes at t_{50}(h), indicated by the dashed lines. Two-way ANOVA analysis with a subsequent Tukey–Kramer *post hoc* test was employed to statistically assess the data. **(C)** Phenotypic analysis of primary root growth under control (Ctrl) and osmotic stress condition (Stress). To apply osmotic stress, young seedlings were grown on plates containing 300 mM mannitol. Scale bar = 1 cm. **(D)** Violine plot showing the relative primary root elongation response of 4 days-old seedlings that were transferred to plates containing 300 mM mannitol and grown for another 7 days. The primary root elongation of each genotype grown under control conditions was set to 100%. The boxes and whiskers display the median, quartiles, and extremes of the compared datasets ($n = 20$). The colored regions indicate the density distribution of the samples in each genotype and condition. Different letters refer to significant differences between the means of the compared datasets analyzed by ANOVA and a Tukey–Kramer *post hoc* test ($p \leq 0.05$). **(E)** Stacked bar plots representing the relative quantification of endogenous IAA, IAM, and ABA contents in wild-type Arabidopsis and the two MYB74oe lines. The content of each metabolite in wild-type seedlings (Col-0) was set to 1. The metabolite levels in the MYB74oe lines were expressed in reference to the wild-type levels. The stacks show mean values ±SE ($n = 3$). The same letters for each metabolite in the different genotypes refer to a lack of significant differences between the means of the compared datasets analyzed by ANOVA and a Tukey–Kramer *post hoc* test ($p \leq 0.05$). **(F)** Survival rate of Col-0 and MYB74oe seedlings 7 days after a heat shock treatment (42°C, 30 min). The conditional overexpression of *MYB74* reduced the survival rate of the seedlings considerably. **(G)** Comparison of the stomatal aperture of wild-type (Col-0) and MYB74oe lines under control conditions. The overexpression of *MYB74* significantly increases stomatal aperture. Student's *t*-test: $^{***}p \leq 0.001$.

the reduced survival rate of the conditional *MYB74* overexpressor lines through increased water loss. Consistent with the observed reduction of the survival rate of MYB74oe-1 and MYB74oe-2 seedlings after a heat shock, we detected a significant increase of the stomatal aperture of the overexpressor lines (**Figure 5G**). Taken together, our results suggest a role for MYB74 as a negative plant growth regulator. In addition, it must be concluded that MYB74 contributes to the control

of the osmotic stress response in Arabidopsis and interferes with stomatal closure.

DISCUSSION

Transcriptional Insights From the Analysis of IAM Treated Plants

Previous studies unveiled a role for IAM as a putative new signaling molecule in plants, which is further supported by the fact that IAM and IAA regulate largely different subsets of genes, when comparing the transcriptional responses of IAM-treated *ami1* seedlings with those of IAA treated wild-type seedlings (**Supplementary Figure S3**). IAM has been demonstrated to trigger the expression of plant stress response-related genes, induce the formation of ABA, and cause a significant plant growth retardation (Moya-Cuevas et al., 2021; Sánchez-Parra et al., 2021; Pérez-Alonso et al., 2021a). The observed enhanced expression of *NCED3* after IAM application and in IAM accumulating *ami1* mutants indicate that the activation of ABA metabolism is responsible for the deregulation of a considerable number of stress-related genes. In addition, the specific IAM hydrolase *AMI1* from Arabidopsis has been shown to be transcriptionally regulated by several abiotic stress conditions, including drought, osmotic, and temperature stress (Lehmann et al., 2010; Pérez-Alonso et al., 2021a). However, many of the molecular mechanisms downstream of IAM, particularly those related with the observed growth retardation, remained largely undisclosed. Thus, further work was required to shed light on the biological processes activated by the stress-mediated accumulation of IAM in plants.

Transcriptomic analysis of IAM-treated wild-type and *AMI1* mutant plants identified a set of well-known stress-responsive genes (**Figure 1**; **Table 1**), including *MAPKKK18*, *COR15A*, and *HAI1*, which are part of the overall response to drought, cold, and heat stress (Maruyama et al., 2004; Fujita et al., 2009; Li et al., 2017). Furthermore, the experiment revealed the transcriptional activation of two MYB TFs, *MYB74*, and *MYB102*. The two MYB factors belong to the same R2R3-MYB factor subgroup 11 and share considerable primary amino acid sequence similarity (**Supplementary Figure S4**). Notably, neither *MYB74* nor *MYB102* displayed a significant transcriptional response toward IAA, which puts the conversion of IAM into IAA by IAM-specific hydrolases into perspective (**Figure 3A**). Although their N-terminal regions appeared to be highly conserved, the C-terminal IDRs of the two factors, which contain the response regulator domains, showed to be substantially divergent (**Figure 2**).

Overexpression of *MYB74* Has a Detrimental Effect on Plant Growth

In general, MYB factors are expected to be involved in stress responses, but only a modest number has yet been characterized functionally. Interestingly, the four members of R2R3-MYB factor subgroup 11, comprising *MYB41*, *MYB49*, *MYB74*, and *MYB102*, share a common osmotic and salt stress responsiveness (Lippold et al., 2009). Their close phylogenetic relationship (**Supplementary Figure S4**) and their common transcriptional regulation point towards the existence of an intertwined regulatory MYB TF subnetwork that drives transcriptional reprogramming in Arabidopsis to mount appropriate abiotic stress responses.

The four subgroup 11 members are assumed to be transcriptionally controlled by ABA. However, our results point to an additional, ABA independent transcriptional regulation of *MYB74* expression by IAM (**Figures 3A,B**). Most interesting, however, was the observed growth retardation in conditional *MYB74* overexpressing mutants (**Figures 3C,D**, **Figure 5B**). A similar phenotype has been described for constitutively *MYB41* overexpressing transgenic plants (Cominelli et al., 2008; Lippold et al., 2009). MYB41 over-accumulating plants are characterized by increased rates of water loss and by substantially reduced cell sizes, but the underlying molecular mechanisms responsible for the phenotypic alterations remained largely unclear. It remains to be noted that the MYB74oe mutants tested in this study are also prone to increased water loss, as their stomatal aperture was shown to be significantly increased (**Figure 5G**). Such effect is remarkable for a gene that is normally induced in response to heat stress (**Figure 5A**). The transcriptional analysis of MYB74oe-1 compared to wild-type control plants provided no clear evidence for the existence of a molecular mechanism that could explain the pleiotropic growth phenotype of the mutant plants. A closer inspection of the differentially regulated transcription factors, however, revealed the deregulation of two additional MYB factors (**Supplementary Table S3**), *MYB11* and *MYB77*, that most likely contribute to the aberrant growth phenotype of the MYB74 accumulating lines. While the repression of *MYB77* is assumed to negatively affect lateral root formation (Shin et al., 2007), the transcriptional activation of *MYB11* is supposed to interfere with the overall proliferation activity of meristematic cells in Arabidopsis and, thereby, delay plant development (Petroni et al., 2008). However, to confirm and further develop these molecular relationships, much more work is required.

Toward a Role for MYB74 in Orchestrating Plant Stress Responses

The transcriptional profiling data that we obtained for the *MYB74* mutants support our hypothesis that MYB74 has no crucial function under control conditions but is induced when the plants encounter abiotic stress. The considerably higher number of significantly induced genes relative to the number of repressed genes clearly suggests that this MYB TF plays a merely gene activating role (**Figure 4A**), which consequently translates into a negative effect on plant growth. Further enrichment analyses provided evidence for an involvement of MYB74 in the regulation of a broad number of abiotic stress response-related processes (**Figures 4B,C**). As already mentioned, previous studies suggested the induction of the subgroup 11 MYB TFs by heat, osmotic, and salt stress. For this reason, we decided to focus our interest on heat and osmotic stress responses in the characterization of the MYB74oe mutants, because *ami1* null mutants have also been reported to be involved in the osmotic stress response pathway (Pérez-Alonso et al., 2021a) and other abiotic stress responses (Lehmann et al., 2010). The

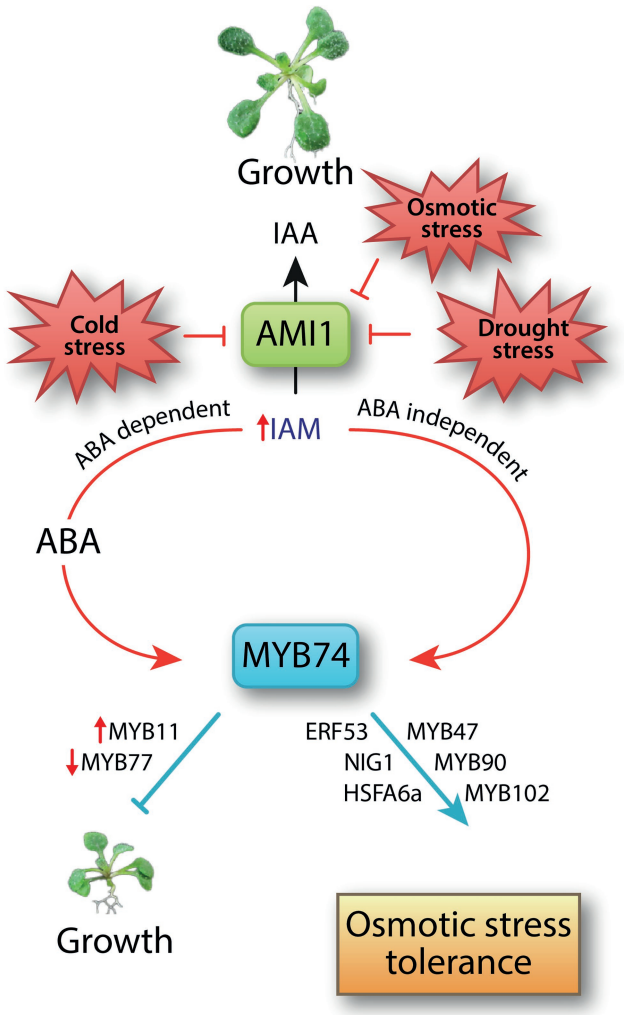

FIGURE 6 | A model summarizing the IAM accumulation-mediated transcriptional activation of *MYB74*. Abiotic stresses, including osmotic stress, suppress the expression of *AMI1* (Perera et al., 2008; Lehmann et al., 2010), which translates into an accumulation of IAM. The auxin precursor IAM triggers ABA biosynthesis (Pérez-Alonso et al., 2021a). Here, we demonstrated an ABA dependent and an ABA independent transcriptional activation of abiotic stress-related TF *MYB74*. IAM directly induces the expression of *MYB74*. The IAM-mediated accumulation of MYB74 results in the transcriptional reprogramming of many osmotic stress-related genes, including further MYB factors, such as the dehydration stress memory gene *MYB47* (Ding et al., 2013) and the abiotic stress-related genes *MYB90* and *MYB102* (Denekamp and Smeekens, 2003; Li et al., 2018a), the ethylene response factor *ERF53* (Hsieh et al., 2013), the basic helix–loop–helix factor *NIG1* (Kim and Kim, 2006), and the ABA-responsive heat shock response factor *HSFA6a* (Hwang et al., 2014). Consequently, MYB74 is assumed to integrate ABA dependent and independent signals and to be involved in plant responses to osmotic stress. At the time, the accumulation of MYB74 suppresses plant growth considerably, possibly through the transcriptional activation of *MYB11*, which is known to be capable of delaying plant development (Petroni et al., 2008), and the repression of *MYB77* expression. MYB77 is involved in the modulation of auxin signal transduction and the control of lateral root formation (Shin et al., 2007).

significantly less pronounced relative primary root elongation inhibition observed in the MYB74oe lines speaks for an enhanced osmotic stress tolerance of the transgenic plants (**Figure 5D**). This notion is further supported by the substantial induction of *LEA*, *LEA-like*, *COR*, *RD*, and *LTI* genes, which are suggested to be involved in conferring an increased stress tolerance to plants through the protection of proteins from inactivation and aggregation and of membranes from disintegration under stress (Nakashima and Yamaguchi-Shinozaki, 2006). Moreover, the transcriptomics data highlighted the transcriptional activation of flavonoid biosynthesis-related genes (**Figure 4B**). Very recently, the accumulation of flavonoids has been shown to alleviate combined heat and salt stress in rice (Jan et al., 2021). Remarkably, the prolonged high-level expression of *MYB74* also linked the TF with processes that are not necessarily interwoven with abiotic stress responses. As an example, we found a series of induced genes that are associated with nutrient deficiency responses in Arabidopsis, including the sulfate-deficiency induced gene *SDI1* (At5g48850) and the response to low sulfur gene *LSU1* (At3g49580), as well as the phosphate deficiency-associated SPX domain genes *SPX1* (At5g20150) and *SPX3* (At2g45130), the *PHO1* sulfate transporter homolog gene *PHO1-H10* (At1g69480), and the phosphate-starvation induced inositol-3-phosphate synthase 2 gene *IPS2* (At2g22240). These data suggest that MYB74 may also be involved in the control of nutrient assimilation. However, to draw further conclusions about the presumably diverse functions of MYB74, additional metabolomics studies will be required.

As summarized in **Figure 6**, we demonstrated the involvement of an ABA dependent and an ABA independent signaling pathway that proceeds directly through the activation by IAM, in the transcriptional regulation of *MYB74*. Our transcriptiomics, physiological, and phenotypic analysis of *MYB74* mutants revealed a contribution of the MYB factor in the control of distinct cellular processes in Arabidopsis, including the positive regulation of osmotic stress tolerance. Moreover, our work uncovered a growth retarding effect through the prolonged overexpression of *MYB74*. Furthermore, it must be remarked that MYB74 seems to also interfere with the regulation of stomatal aperture, rendering the MYB74 over-accumulating substantially more susceptible to heat stress.

DATA AVAILABILITY STATEMENT

The authors acknowledge that the data presented in this study must be deposited and made publicly available in an acceptable repository, prior to publication. Frontiers cannot accept a manuscript that does not adhere to our open data policies.

AUTHOR CONTRIBUTIONS

SP and MW conceptualized the project and were responsible for acquiring the funding. PO-G, M-MP-A, AGO-V, BS-P, JL-M, and SP performed the experiments. PO-G, M-MP-A, AGO-V, BS-P, JL-M, MW, and SP analyzed and interpreted the data. SP wrote the paper with significant input from all other authors. All authors contributed to the article and approved the submitted version.

FUNDING

PO-G is particularly grateful to all members of the Ludwig-Müller lab for their hospitality and to the Universidad Politécnica de Madrid, that financed the short-term stay in the Technische Universität Dresden, Germany, through its "Programa Propio UPM 2021" mobility program. This research was supported by grants BFU2017-82826-R and PID2020-119441RB-100 to SP funded by MCIN/AEI/10.13039/501100011033 and as appropriate, by "ERDF A way of making Europe," by the "European Union" or by the "European Union NextGeneration EU/PRTR."

ACKNOWLEDGMENTS

The *abi5-7* seeds were kindly provided by Jesús Vicente-Carbajosa (CBGP, Madrid, Spain). All other lines were obtained from the Nottingham Arabidopsis Stock Center (NASC).

SUPPLEMENTARY MATERIAL

The Supplementary Material for this article can be found online at: https://www.frontiersin.org/articles/10.3389/fpls.2022.928386/full#supplementary-material

REFERENCES

Alonso, J. M., Stepanova, A. N., Leisse, T. J., Kim, C. J., Chen, H., Shinn, P., et al. (2003). Genome-wide insertional mutagenesis of *Arabidopsis thaliana*. *Science* 301, 653–657. doi: 10.1126/science.1086391

Ambawat, S., Sharma, P., Yadav, N. R., and Yadav, R. C. (2013). MYB transcription factor genes as regulators for plant responses: an overview. *Physiol. Mol. Biol. Plants* 19, 307–321. doi: 10.1007/s12298-013-0179-1

Bindea, G., Mlecnik, B., Hackl, H., Charoentong, P., Tosolini, M., Kirilovsky, A., et al. (2009). ClueGO: a cytoscape plug-in to decipher functionally grouped gene ontology and pathway annotation networks. *Bioinformatics* 25, 1091–1093. doi: 10.1093/bioinformatics/btp101

Coego, A., Brizuela, E., Castillejo, P., Ruíz, S., Koncz, C., del Pozo, J. C., et al. (2014). The TRANSPLANTA collection of Arabidopsis lines: a resource for functional analysis of transcription factors based on their conditional overexpression. *Plant J.* 77, 944–953. doi: 10.1111/tpj.12443

Cominelli, E., Sala, T., Calvi, D., Gusmaroli, G., and Tonelli, C. (2008). Over-expression of the Arabidopsis *AtMYB41* gene alters cell expansion and leaf surface permeability. *Plant J.* 53, 53–64. doi: 10.1111/j.1365-313X.2007.03310.x

Czechowski, T., Stitt, M., Altmann, T., Udvardi, M. K., and Scheible, W. R. (2005). Genome-wide identification and testing of superior reference genes for transcript normalization in Arabidopsis. *Plant Physiol.* 139, 5–17. doi: 10.1104/pp.105.063743

Davies, P.J. (2010). *Plant Hormones. Biosynthesis, Signal Transduction, Action!* Dordrecht, Boston, London: Springer Netherlands.

De Vos, M., Denekamp, M., Dicke, M., Vuylsteke, M., Van Loon, L. C., Smeekens, S. C. M., et al. (2006). The *Arabidopsis thaliana* transcription factor AtMYB102 functions in defense against the insect herbivore *Pieris rapae*. *Plant Signal. Behav.* 1, 305–311. doi: 10.4161/psb.1.6.3512

Denekamp, M., and Smeekens, S. C. (2003). Integration of wounding and osmotic stress signals determines the expression of the *AtMYB102* transcription factor gene. *Plant Physiol.* 132, 1415–1423. doi: 10.1104/pp.102.019273

Ding, Y., Liu, N., Virlouvet, L., Riethoven, J.-J., Fromm, M., and Avramova, Z. (2013). Four distinct types of dehydration stress memory genes in *Arabidopsis thaliana*. *BMC Plant Biol.* 13, 229. doi: 10.1186/1471-2229-13-229

Dubos, C., Stracke, R., Grotewold, E., Weisshaar, B., Martin, C., and Lepiniec, L. (2010). MYB transcription factors in *Arabidopsis*. *Trends Plant Sci.* 15, 573–581. doi: 10.1016/j.tplants.2010.06.005

Emenecker, R. J., and Strader, L. C. (2020). Auxin-abscisic acid interactions in plant growth and development. *Biomol. Ther.* 10:281. doi: 10.3390/biom10020281

Favery, B., Ryan, E., Foreman, J., Linstead, P., Boudonck, K., Steer, M., et al. (2001). KOJAK encodes a cellulose synthase-like protein required for root hair cell morphogenesis in Arabidopsis. *Genes Dev.* 15, 79–89. doi: 10.1101/gad.188801

Finkelstein, R. R., and Lynch, T. J. (2000). The Arabidopsis abscisic acid response gene *ABI5* encodes a basic leucine zipper transcription factor. *Plant Cell* 12, 599–609. doi: 10.1105/tpc.12.4.599

Fujita, Y., Nakashima, K., Yoshida, T., Katagiri, T., Kidokoro, S., Kanamori, N., et al. (2009). Three SnRK2 protein kinases are the main positive regulators of abscisic acid signaling in response to water stress in Arabidopsis. *Plant Cell Physiol.* 50, 2123–2132. doi: 10.1093/pcp/pcp147

Gao, Y., Dai, X., Aoi, Y., Takebayashi, Y., Yang, L., Guo, X., et al. (2020). Two homologous *INDOLE-3-ACETAMIDE (IAM) HYDROLASE* genes are required for the auxin effects of IAM in *Arabidopsis*. *J. Genet. Genom.* 47, 157–165. doi: 10.1016/j.jgg.2020.02.009

Gimenez-Ibanez, S., Boter, M., Ortigosa, A., García-Casado, G., Chini, A., Lewsey, M. G., et al. (2017). JAZ2 controls stomata dynamics during bacterial invasion. *New Phytol.* 213, 1378–1392. doi: 10.1111/nph.14354

Hickman, R., Hill, C., Penfold, C. A., Breeze, E., Bowden, L., Moore, J. D., et al. (2013). A local regulatory network around three NAC transcription factors in stress responses and senescence in Arabidopsis leaves. *Plant J.* 75, 26–39. doi: 10.1111/tpj.12194

Himuro, Y., Ishiyama, K., Mori, F., Gondo, T., Takahashi, F., Shinozaki, K., et al. (2014). Arabidopsis galactinol synthase AtGolS2 improves drought tolerance in the monocot model *Brachypodium distachyon*. *J. Plant Physiol.* 171, 1127–1131. doi: 10.1016/j.jplph.2014.04.007

Hsieh, E. J., Cheng, M. C., and Lin, T. P. (2013). Functional characterization of an abiotic stress-inducible transcription factor AtERF53 in *Arabidopsis thaliana*. *Plant Mol. Biol.* 82, 223–237. doi: 10.1007/s11103-013-0054-z

Huang, Y., Guo, Y., Liu, Y., Zhang, F., Wang, Z., Wang, H., et al. (2018b). 9-*cis*-epoxycarotenoid dioxygenase 3 regulates plant growth and enhances multi-abiotic stress tolerance in Rice. *Front. Plant Sci.* 9:162. doi: 10.3389/fpls.2018.00162

Huang, K. C., Lin, W. C., and Cheng, W. H. (2018a). Salt hypersensitive mutant 9, a nucleolar APUM23 protein, is essential for salt sensitivity in association with the ABA signaling pathway in *Arabidopsis*. *BMC Plant Biol.* 18:40. doi: 10.1186/s12870-018-1255-z

Hwang, S. M., Kim, D. W., Woo, M. S., Jeong, H. S., Son, Y. S., Akhter, S., et al. (2014). Functional characterization of *Arabidopsis HsfA6a* as a heat-shock transcription factor under high salinity and dehydration conditions. *Plant Cell Environ.* 37, 1202–1222. doi: 10.1111/pce.12228

Iglesias-Fernández, R., Barrero-Sicilia, C., Carrillo-Barral, N., Oñate-Sánchez, L., and Carbonero, P. (2013). *Arabidopsis thaliana* bZIP44: a transcription factor affecting seed germination and expression of the mannanase-encoding gene AtMAN7. *Plant J.* 74, 767–780. doi: 10.1111/tpj.12162

Jacob, P., Hirt, H., and Bendahmane, A. (2017). The heat-shock protein/chaperone network and multiple stress resistance. *Plant Biotechnol. J.* 15, 405–414. doi: 10.1111/pbi.12659

Jan, R., Kim, N., Lee, S.-H., Khan, M. A., Asaf, S., Lubna, et al. (2021). Enhanced flavonoid accumulation reduces combined salt and heat stress through regulation of transcriptional and hormonal mechanisms. *Front. Plant Sci.* 12:796956. doi: 10.3389/fpls.2021.796956

Jost, R., Berkowitz, O., and Masle, J. (2007). Magnetic quantitative reverse transcription PCR: a high-throughput method for mRNA extraction and quantitative reverse transcription PCR. *BioTechniques* 43, 206–211. doi: 10.2144/000112534

Kelley, L. A., Mezulis, S., Yates, C. M., Wass, M. N., and Sternberg, M. J. (2015). The Phyre2 web portal for protein modeling, prediction and analysis. *Nat. Protoc.* 10, 845–858. doi: 10.1038/nprot.2015.053

Kilian, J., Whitehead, D., Horak, J., Wanke, D., Weinl, S., Batistic, O., et al. (2007). The AtGenExpress global stress expression data set: protocols, evaluation and model data analysis of UV-B light, drought and cold stress responses. *Plant J.* 50, 347–363. doi: 10.1111/j.1365-313X.2007.03052.x

Kim, J., and Kim, H.-Y. (2006). Functional analysis of a calcium-binding transcription factor involved in plant salt stress signalling. *FEBS Lett.* 580, 5251–5256. doi: 10.1016/j.febslet.2006.08.050

Kranz, H. D., Denekamp, M., Greco, R., Jin, H., Leyva, A., Meissner, R. C., et al. (1998). Towards functional characterisation of the members of the R2R3-MYB gene family from *Arabidopsis thaliana*. *Plant J.* 16, 263–276. doi: 10.1046/j.1365-313x.1998.00278.x

Lang, S., Liu, X., Xue, H., Li, X., and Wang, X. (2017). Functional characterization of BnHSFA4a as a heat shock transcription factor in controlling the re-establishment of desiccation tolerance in seeds. *J. Exp. Bot.* 68, 2361–2375. doi: 10.1093/jxb/erx097

Lehmann, T., Hoffmann, M., Hentrich, M., and Pollmann, S. (2010). Indole-3-acetamide-dependent auxin biosynthesis: a widely distributed way of indole-3-acetic acid production? *Eur. J. Cell Biol.* 89, 895–905. doi: 10.1016/j.ejcb.2010.06.021

Léon-Kloosterziel, K. M., Gil, M. A., Ruijs, G. J., Jacobsen, S. E., Olszewski, N. E., Schwartz, S. H., et al. (1996). Isolation and characterization of abscisic acid-deficient *Arabidopsis* mutants at two new loci. *Plant J.* 10, 655–661. doi: 10.1046/j.1365-313X.1996.10040655.x

Li, Y., Cai, H., Liu, P., Wang, C., Gao, H., Wu, C., et al. (2017). Arabidopsis MAPKKK18 positively regulates drought stress resistance via downstream MAPKK3. *Biochem. Biophys. Res. Commun.* 484, 292–297. doi: 10.1016/j.bbrc.2017.01.104

Li, N., Wu, H., Ding, Q., Li, H., Li, Z., Ding, J., et al. (2018a). The heterologous expression of *Arabidopsis PAP2* induces anthocyanin accumulation and inhibits plant growth in tomato. *Funct. Integr. Genomics* 18, 341–353. doi: 10.1007/s10142-018-0590-3

Li, W., Yang, Z., Yao, J., Li, J., Song, W., and Yang, X. (2018b). *Cellulose synthase-like D1* controls organ size in maize. *BMC Plant Biol.* 18:239. doi: 10.1186/s12870-018-1453-8

Lin, K.-F., Tsai, M.-Y., Lu, C.-A., Wu, S.-J., and Yeh, C.-H. (2018). The roles of *Arabidopsis HSFA2*, *HSFA4a*, and *HSFA7a* in the heat shock response and cytosolic protein response. *Bot. Stud.* 59:15. doi: 10.1186/s40529-018-0231-0

Lippold, F., Sanchez, D. H., Musialak, M., Schlereth, A., Scheible, W.-R., Hincha, D. K., et al. (2009). AtMyb41 regulates transcriptional and metabolic responses to osmotic stress in Arabidopsis. *Plant Physiol.* 149, 1761–1772. doi: 10.1104/pp.108.134874

Livak, K. J., and Schmittgen, T. D. (2001). Analysis of relative gene expression data using real-time quantitative PCR and the $2^{(-\Delta\Delta C(T))}$ method. *Methods* 25, 402–408. doi: 10.1006/meth.2001.1262

Lu, C., Chen, M. X., Liu, R., Zhang, L., Hou, X., Liu, S., et al. (2019). Abscisic acid regulates auxin distribution to mediate maize lateral root development under salt stress. *Front. Plant Sci.* 10:716. doi: 10.3389/fpls.2019.00716

Maruyama, K., Sakuma, Y., Kasuga, M., Ito, Y., Seki, M., Goda, H., et al. (2004). Identification of cold-inducible downstream genes of the *Arabidopsis* DREB1A/CBF3 transcriptional factor using two microarray systems. *Plant J.* 38, 982–993. doi: 10.1111/j.1365-313X.2004.02100.x

Millard, P. S., Kragelund, B. B., and Burow, M. (2019). R2R3 MYB transcription factors – functions outside the DNA-binding domain. *Trends Plant Sci.* 24, 934–946. doi: 10.1016/j.tplants.2019.07.003

Moya-Cuevas, J., Pérez-Alonso, M. M., Ortiz-García, P., and Pollmann, S. (2021). Beyond the usual suspects: physiological roles of the Arabidopsis Amidase Signature (AS) superfamily members in plant growth processes and stress responses. *Biomolecules* 11:1207. doi: 10.3390/biom11081207

Murashige, T., and Skoog, F. (1962). A revised medium for rapid growth and bio assays with tobacco tissue cultures. *Physiol. Plant.* 15, 473–497. doi: 10.1111/j.1399-3054.1962.tb08052.x

Nakashima, K., and Yamaguchi-Shinozaki, K. (2006). Regulons involved in osmotic stress-responsive and cold stress-responsive gene expression in plants. *Physiol. Plant.* 126, 62–71. doi: 10.1111/j.1399-3054.2005.00592.x

Nambara, E., Suzuki, M., Abrams, S., McCarty, D. R., Kamiya, Y., and McCourt, P. (2002). A screen for genes that function in abscisic acid signaling in *Arabidopsis thaliana*. *Genetics* 161, 1247–1255. doi: 10.1093/genetics/161.3.1247

Ogata, K., Kanei-Ishii, C., Sasaki, M., Hatanaka, H., Nagadoi, A., Enari, M., et al. (1996). The cavity in the hydrophobic core of Myb DNA-binding domain is reserved for DNA recognition and trans-activation. *Nat. Struct. Biol.* 3, 178–187. doi: 10.1038/nsb0296-178

Oñate-Sánchez, L., and Vicente-Carbajosa, J. (2008). DNA-free RNA isolation protocols for *Arabidopsis thaliana*, including seeds and siliques. *BMC. Res. Notes* 1:93. doi: 10.1186/1756-0500-1-93

Perera, I. Y., Hung, C. Y., Moore, C. D., Stevenson-Paulik, J., and Boss, W. F. (2008). Transgenic Arabidopsis plants expressing the type 1 inositol 5-phosphatase exhibit increased drought tolerance and altered abscisic acid signaling. *Plant Cell* 20, 2876–2893. doi: 10.1105/tpc.108.061374

Pérez-Alonso, M. M., Ortiz-García, P., Moya-Cuevas, J., Lehmann, T., Sánchez-Parra, B., Björk, R. G., et al. (2021a). Endogenous indole-3-acetamide levels contribute to the crosstalk between auxin and abscisic acid, and trigger plant stress responses in *Arabidopsis thaliana*. *J. Exp. Bot.* 72, 459–475. doi: 10.1093/jxb/eraa485

Pérez-Alonso, M. M., Ortiz-García, P., Moya-Cuevas, J., and Pollmann, S. (2021b). Mass spectrometric monitoring of plant hormone cross talk during biotic stress responses in potato (*Solanum tuberosum* L.). *Methods Mol. Biol.* 2354, 143–154. doi: 10.1007/978-1-0716-1609-3_7

Petroni, K., Falasca, G., Calvenzani, V., Allegra, D., Stolfi, C., Fabrizi, L., et al. (2008). The *AtMYB11* gene from *Arabidopsis* is expressed in meristematic cells and modulates growth *in planta* and organogenesis *in vitro*. *J. Exp. Bot.* 59, 1201–1213. doi: 10.1093/jxb/ern027

Pollmann, S., Neu, D., and Weiler, E. W. (2003). Molecular cloning and characterization of an amidase from *Arabidopsis thaliana* capable of converting indole-3-acetamide into the plant growth hormone, indole-3-acetic acid. *Phytochemistry* 62, 293–300. doi: 10.1016/s0031-9422(02)00563-0

Raudvere, U., Kolberg, L., Kuzmin, I., Arak, T., Adler, P., Peterson, H., et al. (2019). G:profiler: a web server for functional enrichment analysis and conversions of gene lists (2019 update). *Nucleic Acids Res.* 47, W191–W198. doi: 10.1093/nar/gkz369

Sánchez-Parra, B., Frerigmann, H., Pérez-Alonso, M. M., Carrasco-Loba, V., Jost, R., Hentrich, M., et al. (2014). Characterization of four bifunctional plant IAM/PAM-amidohydrolases capable of contributing to auxin biosynthesis. *Plants* 3, 324–347. doi: 10.3390/plants3030324

Sánchez-Parra, B., Pérez-Alonso, M. M., Ortiz-García, P., Moya-Cuevas, J., Hentrich, M., and Pollmann, S. (2021). Accumulation of the auxin precursor indole-3-acetamide curtails growth through the repression of ribosome-biogenesis and development-related transcriptional networks. *Int. J. Mol. Sci.* 22:2040. doi: 10.3390/ijms22042040

Schindelin, J., Arganda-Carreras, I., Frise, E., Kaynig, V., Longair, M., Pietzsch, T., et al. (2012). Fiji: an open-source platform for biological-image analysis. *Nat. Methods* 9, 676–682. doi: 10.1038/nmeth.2019

Shin, R., Burch, A. Y., Huppert, K. A., Tiwari, S. B., Murphy, A. S., Guilfoyle, T. J., et al. (2007). The *Arabidopsis* transcription factor MYB77 modulates auxin signal transduction. *Plant Cell* 19, 2440–2453. doi: 10.1105/tpc.107.050963

Shkolnik-Inbar, D., and Bar-Zvi, D. (2010). ABI4 mediates abscisic acid and cytokinin inhibition of lateral root formation by reducing polar auxin transport in Arabidopsis. *Plant Cell* 22, 3560–3573. doi: 10.1105/tpc.110.074641

Stracke, R., Werber, M., and Weisshaar, B. (2001). The *R2R3-MYB* gene family in *Arabidopsis thaliana*. *Curr. Opin. Plant Biol.* 4, 447–456. doi: 10.1016/S1369-5266(00)00199-0

Sugawara, S., Hishiyama, S., Jikumaru, Y., Hanada, A., Nishimura, T., Koshiba, T., et al. (2009). Biochemical analyses of indole-3-acetaldoxime-dependent auxin biosynthesis in *Arabidopsis*. *Proc. Natl. Acad. Sci. U. S. A.* 106, 5430–5435. doi: 10.1073/pnas.0811226106

Thole, J. M., Beisner, E. R., Liu, J., Venkova, S. V., and Strader, L. C. (2014). Abscisic acid regulates root elongation through the activities of auxin and ethylene in *Arabidopsis thaliana*. *G3* 4, 1259–1274. doi: 10.1534/g3.114.011080

Verma, V., Ravindran, P., and Kumar, P. P. (2016). Plant hormone-mediated regulation of stress responses. *BMC Plant Biol.* 16, 86. doi: 10.1186/s12870-016-0771-y

Wang, B., Luo, Q., Li, Y., Yin, L., Zhou, N., Li, X., et al. (2020). Structural insights into target DNA recognition by R2R3-MYB transcription factors. *Nucleic Acids Res.* 48, 460–471. doi: 10.1093/nar/gkz1081

Watanabe, S., Sato, M., Sawada, Y., Tanaka, M., Matsui, A., Kanno, Y., et al. (2018). Arabidopsis molybdenum cofactor sulfurase ABA3 contributes to anthocyanin accumulation and oxidative stress tolerance in ABA-dependent and independent ways. *Sci. Rep.* 8:16592. doi: 10.1038/s41598-018-34862-1

Wei, S. Y., Lou, Y. C., Tsai, J. Y., Ho, M. R., Chou, C. C., Rajasekaran, M., et al. (2012). Structure of the *Trichomonas vaginalis* Myb3 DNA-binding domain bound to a promoter sequence reveals a unique C-terminal β-hairpin conformation. *Nucleic Acids Res.* 40, 449–460. doi: 10.1093/nar/gkr707

Wenjing, W., Chen, Q., Singh, P. K., Huang, Y., and Pei, D. (2020). CRISPR/Cas9 edited HSFA6a and HSFA6b of *Arabidopsis thaliana* offers ABA and osmotic stress insensitivity by modulation of ROS homeostasis. *Plant Signal. Behav.* 15:1816321. doi: 10.1080/15592324.2020.1816321

Xing, L., Zhao, Y., Gao, J., Xiang, C., and Zhu, J. K. (2016). The ABA receptor PYL9 together with PYL8 plays an important role in regulating lateral root growth. *Sci. Rep.* 6:27177. doi: 10.1038/srep27177

Xu, R., Wang, Y., Zheng, H., Lu, W., Wu, C., Huang, J., et al. (2015). Salt-induced transcription factor MYB74 is regulated by the RNA-directed DNA methylation pathway in Arabidopsis. *J. Exp. Bot.* 66, 5997–6008. doi: 10.1093/jxb/erv312

Yang, J., Yan, R., Roy, A., Xu, D., Poisson, J., and Zhang, Y. (2015). The I-TASSER suite: protein structure and function prediction. *Nat. Methods* 12, 7–8. doi: 10.1038/nmeth.3213

Zang, D., Wang, J., Zhang, X., Liu, Z., and Wang, Y. (2019). Arabidopsis heat shock transcription factor HSFA7b positively mediates salt stress tolerance by binding to an E-box-like motif to regulate gene expression. *J. Exp. Bot.* 70, 5355–5374. doi: 10.1093/jxb/erz261

Zhang, P., Wang, R., Yang, X., Ju, Q., Li, W., Lü, S., et al. (2020). The R2R3-MYB transcription factor AtMYB49 modulates salt tolerance in *Arabidopsis* by modulating the cuticle formation and antioxidant defence. *Plant Cell Environ.* 43, 1925–1943. doi: 10.1111/pce.13784

Zhang, H., Zhu, J., Gong, Z., and Zhu, J.-K. (2022). Abiotic stress responses in plants. *Nat. Rev. Genet.* 23, 104–119. doi: 10.1038/s41576-021-00413-0

Zhou, Y., Zhou, B., Pache, L., Chang, M., Khodabakhshi, A. H., Tanaseichuk, O., et al. (2019). Metascape provides a biologist-oriented resource for the analysis of systems-level datasets. *Nat. Commun.* 10:1523. doi: 10.1038/s41467-019-09234-6

Zhu, L., Guo, J., Ma, Z., Wang, J., and Zhou, C. (2018). *Arabidopsis* transcription factor MYB102 increases plant susceptibility to aphids by substantial activation of ethylene biosynthesis. *Biomolecules* 8:39. doi: 10.3390/biom8020039

Conflict of Interest: The authors declare that the research was conducted in the absence of any commercial or financial relationships that could be construed as a potential conflict of interest.

Publisher's Note: All claims expressed in this article are solely those of the authors and do not necessarily represent those of their affiliated organizations, or those of the publisher, the editors and the reviewers. Any product that may be evaluated in this article, or claim that may be made by its manufacturer, is not guaranteed or endorsed by the publisher.

Advantages of publishing in Frontiers

OPEN ACCESS
Articles are free to read for greatest visibility and readership

FAST PUBLICATION
Around 90 days from submission to decision

HIGH QUALITY PEER-REVIEW
Rigorous, collaborative, and constructive peer-review

TRANSPARENT PEER-REVIEW
Editors and reviewers acknowledged by name on published articles

Frontiers
Avenue du Tribunal-Fédéral 34
1005 Lausanne | Switzerland

Visit us: www.frontiersin.org
Contact us: frontiersin.org/about/contact

REPRODUCIBILITY OF RESEARCH
Support open data and methods to enhance research reproducibility

DIGITAL PUBLISHING
Articles designed for optimal readership across devices

FOLLOW US
@frontiersin

IMPACT METRICS
Advanced article metrics track visibility across digital media

EXTENSIVE PROMOTION
Marketing and promotion of impactful research

LOOP RESEARCH NETWORK
Our network increases your article's readership